AD-767 582

PROCEEDINGS OF THE AFCRL SCIENTIFIC BALLOON SYMPOSIUM (7th), HELD AT PORTSMOUTH, NEW HAMPSHIRE, IN SEPTEMBER 1972

George F. Nolan

Air Force Cambridge Research Laboratories
L. G. Hanscom Field, Massachusetts

3 January 1973

AFCRL-TR-73-0071
3 JANUARY 1973
SPECIAL REPORTS, NO. 152

AIR FORCE CAMBRIDGE RESEARCH LABORATORIES
L. G. HANSCOM FIELD, BEDFORD, MASSACHUSETTS

Proceedings, Seventh AFCRL Scientific Balloon Symposium

GEORGE F. NOLAN, Editor

This research was partially supported by the Air Force In-House Laboratory Independent Research Fund

AIR FORCE SYSTEMS COMMAND
United States Air Force

Unclassified

Security Classification

DOCUMENT CONTROL DATA - R&D

(Security classification of title, body of abstract and indexing annotation must be entered when the overall report is classified)

1. ORIGINATING ACTIVITY (Corporate author) Air Force Cambridge Research Laboratories(LCA) L.G. Hanscom Field Bedford, Massachusetts 01730	2a. REPORT SECURITY CLASSIFICATION Unclassified 2b. GROUP

3. REPORT TITLE

PROCEEDINGS, SEVENTH AFCRL SCIENTIFIC BALLOON SYMPOSIUM

4. DESCRIPTIVE NOTES (Type of report and inclusive dates)

Scientific, Interim.

5. AUTHOR(S) (First name, middle initial, last name)

George F. Nolan, Editor

6. REPORT DATE 3 January 1973	7a. TOTAL NO. OF PAGES ~~488~~ 434	7b. NO. OF REFS 131
8a. CONTRACT OR GRANT NO. N/R b. PROJECT, TASK, WORK UNIT NOS. 66650801 c. DOD ELEMENT 62101F d. DOD SUBELEMENT	9a. ORIGINATOR'S REPORT NUMBER(S) AFCRL-TR-73-0071 9b. OTHER REPORT NO(S) (Any other numbers that may be assigned this report) Special Reports, No. 152	

10. DISTRIBUTION STATEMENT

Approved for public release; distribution unlimited.

Later, this document may be bonded on microfiche.

11. SUPPLEMENTARY NOTES This research was partially supported by the Air Force In-House Laboratory Independent Research Fund.	12. SPONSORING MILITARY ACTIVITY Air Force Cambridge Research Laboratories (LCA) L.G. Hanscom Field Bedford, Massachusetts 01730

13. ABSTRACT

This publication contains the papers presented at the Seventh AFCRL Scientific Balloon Symposium held in September 1972. The papers were presented in three sessions: Tethered and Powered Balloons, Balloon-borne Experiments, and Instrumentation and Balloon Technology.

In the area of tethered balloons, papers were presented on cables, drag and stability characteristics, hull design and analysis, and the results of scientific experiments using tethered balloons as sensor platforms. Papers were presented on a powered spherical balloon and a survey of possible power sources for use by this system.

Presentations during the Balloon-borne Experiments and Instrumentation session included manned balloon flights, precision pointing and control platforms and instrumentation, recovery parachute performance, gondola motion analyses, a balloon radar altimeter, and an overview of French scientific ballooning activities.

During the Balloon Technology session a review was made of the flight results and performance of balloons with volumes in excess of 20 million cubic feet, shape and stress analysis of both nonreinforced and reinforced materials, and fabric tinting to increase solar absorptivity.

DD FORM 1 NOV 68 1473

Unclassified

Security Classification

14. KEY WORDS	LINK A		LINK B		LINK C	
	ROLE	WT	ROLE	WT	ROLE	WT
Balloons Balloon-borne experiments Tethered balloons Balloon materials Balloon design Atmosphere Powered balloons						

Abstract

This publication contains the papers presented at the Seventh AFCRL Scientific Balloon Symposium held at Portsmouth, New Hampshire in September 1972. The papers were presented in three sessions: Tethered and Powered Balloons, Balloon-borne Experiments, and Instrumentation and Balloon Technology.

In the area of tethered balloons, papers were presented on cables, drag and stability characteristics, hull design and analysis and the results of scientific experiments using tethered balloons as sensor platforms. Papers were presented on a powered spherical balloon and a survey of possible power sources for use by this system.

Presentations during the Balloon-borne Experiments and Instrumentation session included manned balloon flights, precision pointing and control platforms and instrumentation, recovery parachute performance, gondola motion analyses, a balloon radar altimeter, and an overview of French scientific ballooning activities.

During the Balloon Technology session a review was made of the flight results and performance of balloons with volumes in excess of 20 million cubic feet, shape and stress analysis of both nonreinforced and reinforced materials, and fabric tinting to increase solar absorptivity.

Acknowledgments

Considerable effort went into the planning, organization, and conduct of this symposium and it is appropriate to thank those who played a large role in its success. The editor is especially grateful to Mrs. Carolyn Meyers for her skillful handling of the mass of correspondence and scheduling activities associated with this undertaking; Miss Joyce Maillett for her long hours of typing; and to Staff Sergeants Gary Johnson and Warren Holzapfel for their outstanding work in operating the visual and sound equipment.

Contents

Tethered and Powered Balloons

Monday, 25 September

Morning: Chairman, James C. Payne
Air Force Cambridge Research Laboratories

Afternoon: Chairman, Thomas J. Dasher
Air Force Cambridge Research Laboratories

Contents

PROCEEDINGS, SEVENTH AFCRL SCIENTIFIC BALLOON SYMPOSIUM

1. A Study of NOLARO Cable for Use With Tethered Balloons

J.S. Ford, Maj, USAF
United States Air Force Academy
Colorado Springs, Colorado

D.E. Jackson, Capt, USAF
AFCRL
Bedford, Massachusetts

1-1. INTRODUCTION

During field operations of a tethered balloon system in May of 1971, failure of the flying line resulted in loss of the balloon. Cable testing after the failure indicated no significant loss of break strength in portions of the cable near the operational failure. Winch testing using a weight and pulley system showed damage to the cable at the same point on the winch as the original failure. It appeared that the failure was due to wearing during balloon operations and not to a weak section of the cable. Laboratory testing was necessary to thoroughly understand all aspects of this failure mode. To accomplish this, AFCRL has undertaken a program with the Engineering Mechanics Department at the Air Force Academy to investigate the incident. This program has the short term goal of isolating and studying the cause of failure and thus taking appropriate steps to prevent future occurrence.

(Received for publication 15 December 1972)

The ultimate goal of the program is to study tether cables, both present designs and promising new ones.

The failure in the field occurred while using a 100,000-ft^2 kite balloon and a 0.52-inch diameter NOLARO cable; NOLARO is an acronym for NO LAY ROPE. It is manufactured by Columbian Rope Company and consists of prestretched polyester yarns contained in an extruded polyurethane jacket.

The 0.52-inch diameter NOLARO cable used in the field operations and this test program has 60 yarns and a nominal jacket thickness of 40 mils. This cable has a rated break strength of 11,500 pounds and weighs 90 pounds per 1000 feet.

The winds at the time of failure were averaging an estimated 40 knots with maximum gusts to 50 knots. These winds were sufficient to cause much sand and dirt to be blown around in the area of the winch. After holding the balloon at 1000 feet above level for 2 hours under these conditions, the cable failed at the first rotating sheave of the winch.

The failure mode seen in the field has been isolated and studied in the laboratory. In studying this failure mode, other modes of wear and damage have also been investigated. This paper describes the tests conducted to date and the results. Also, future plans of the test program are discussed.

1-2. BASIC ASSUMPTION FOR NOLARO TEST PROGRAM

An assumption in the initial test program was that the critical condition for NOLARO is a holding operation with the tether line subjected to cyclic loads superimposed on a basic preload. During a holding condition, which is typical of tethered balloon operations, the material is subjected to traction loads over a short segment of the length for considerable time, whereas the point of application of these loads is continually changing during winching. Cyclic loads, in addition to the basic load due to the balloon, will be present during operation in high wind conditions. These cyclic loads are due to balloon aerodynamics, as well as the dynamic response of the cable.

1-3. PRELIMINARY TENSILE STRENGTH TESTS

The initial steps in the test program were to establish base line data for the static strength of the material and to develop in-house capability to make high-quality eye splices. The material used for the tests was 0.52 inch diameter NOLARO taken from the reel which was in use at the time of the operational failure. Ten 12-foot specimens were tested in tension using a hydraulic Universal Test Machine. The specimens were fabricated with an eye splice at each end and with a thimble

inserted in the eye to protect the fibers. Test values between 9500 and 11,800 pounds were obtained, with the higher values occurring during later tests as splicing techniques were improved. Initial fiber failure occurred in all tests at the beginning of the eye splice, indicating that splicing is a limiting factor in the development of NOLARO breaking strength. These test results are in agreement with those obtained by other researches with like material as described in the reference documents.

1-4. CYCLIC LOAD TEST PROGRAM

After the initial tensile tests were completed, a test program was initiated to investigate the NOLARO/winch interface and the mechanism by which loads were transferred between the two. A test fixture (shown in Figure 1-1) was constructed to simulate a 90° NOLARO/winch interface. The test section consisted of sheave segments of identical geometry and material to that of the Fair Site dual capstan winch. A cross section of a sheave segment is shown in Figure 1-2. The segment is made of aluminum with a molded polyurethane coating. A solid aluminum sheave segment of identical geometry was also manufactured for the test fixture.

The fixture was mounted in an Instron Universal Test Machine as shown in Figures 1-3 and 1-4. To more closely duplicate the boundary conditions existing in actual operations, the primary load cell was extended 4 feet above the normal location on top of the test machine. A clamping fixture was installed on the splices to prevent slip between the polyethylene jacket and the polyester load fibers at those points. A 12,000-pound capacity strain-gauge load cell was mounted on the rear extention arm of the fixture to monitor load behavior in the NOLARO after passing over the 90° sheave section.

During initial testing with this fixture it was observed that the traction available from the 90° sheave segment was not a function of the load but remained at approximately 2000 pounds over a range of primary loads from 3000 to 9000 pounds. Slipping of the NOLARO jacket on the sheave could be observed at the higher loads. Dissection of test specimens which had been loaded to 9000 pounds around the sheave revealed no damage to either the jacket or the fibers. Static tests of specimens which had been tested to 9000 pounds around the sheave resulted in failure loads within the range of previous tensile tests. Specimens loaded to failure around the 90° sheave segment failed at comparable loads, and in the same manner, that is, initial fiber failure occurred at the beginning of the splice. Dissection of these specimens revealed no damage in the sheave area other than the usual hockling of fibers which had failed at the splice.

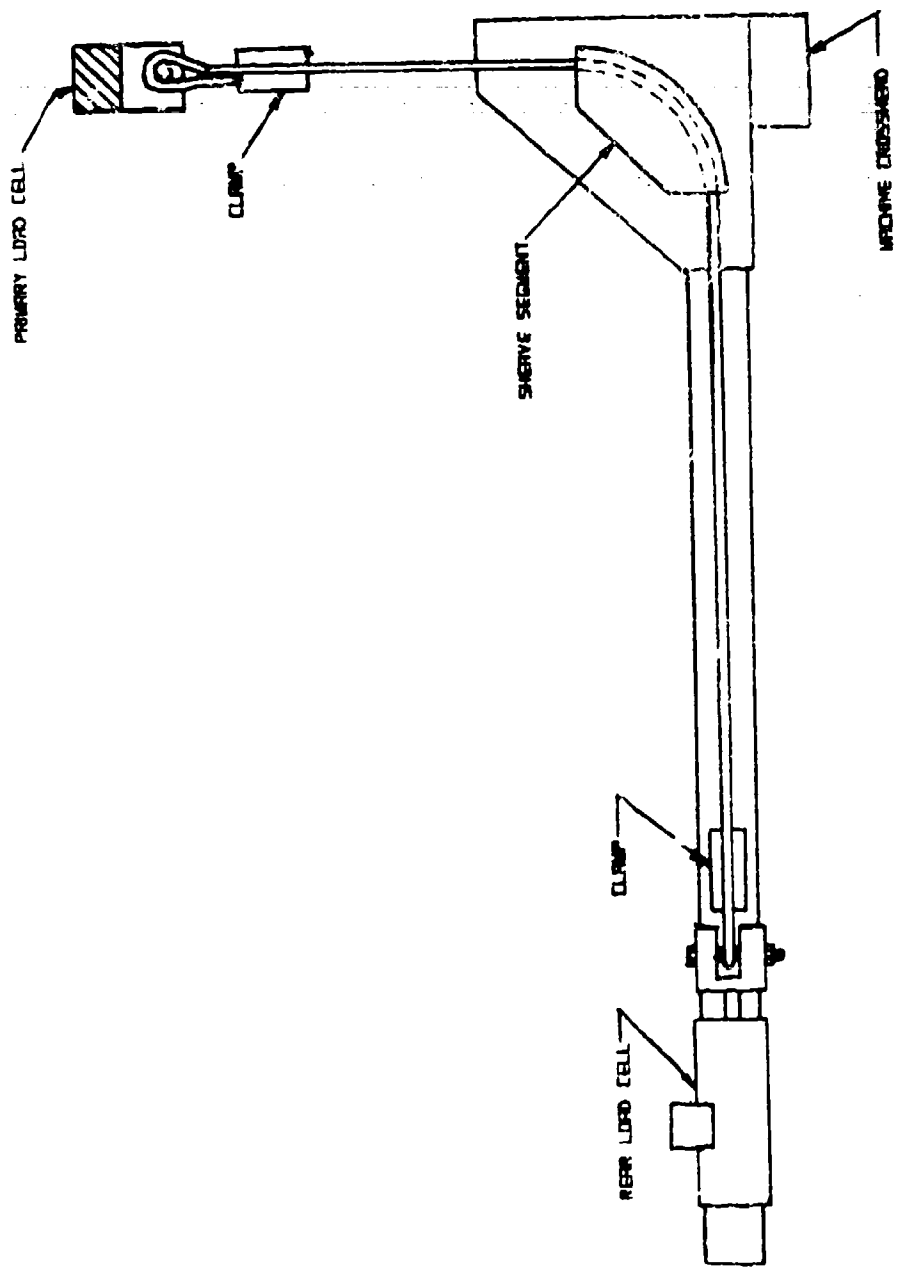

Figure 1-1. Schematic of Test Fixture

Figure 1-2. Cross Section of Test Sheave Segment

A series of cyclic load tests were performed next with a preload of 5000 pounds and a variable load of ±1000 pounds. This loading was considered typical of tether line behavior under moderate to high wind conditions. Duration of the tests varied with the maximum number of cycles attained at this loading condition being 13,500. Rear load cell readings remained almost constant during the cycling tests at a value 2000 pounds less than the upper load limit. No failures of either the NOLARO jacket or the polyester fibers occurred. Fibers were removed from the specimens after tests and compared with untested strands from a similar section of NOLARO under a stereo microscope. Some discoloration and slight abrasion of the fibers which had been in contact with the jacket material was noted; however, tensile tests on these fibers did not indicate that any reduction in strength had occurred.

For the next series of tests, sand with a sieve rating of 15 was introduced into the interface between the NOLARO and the fixed sheave. Since the operational failure had occurred during a s[illegible]dstorm, it was considered highly probable that

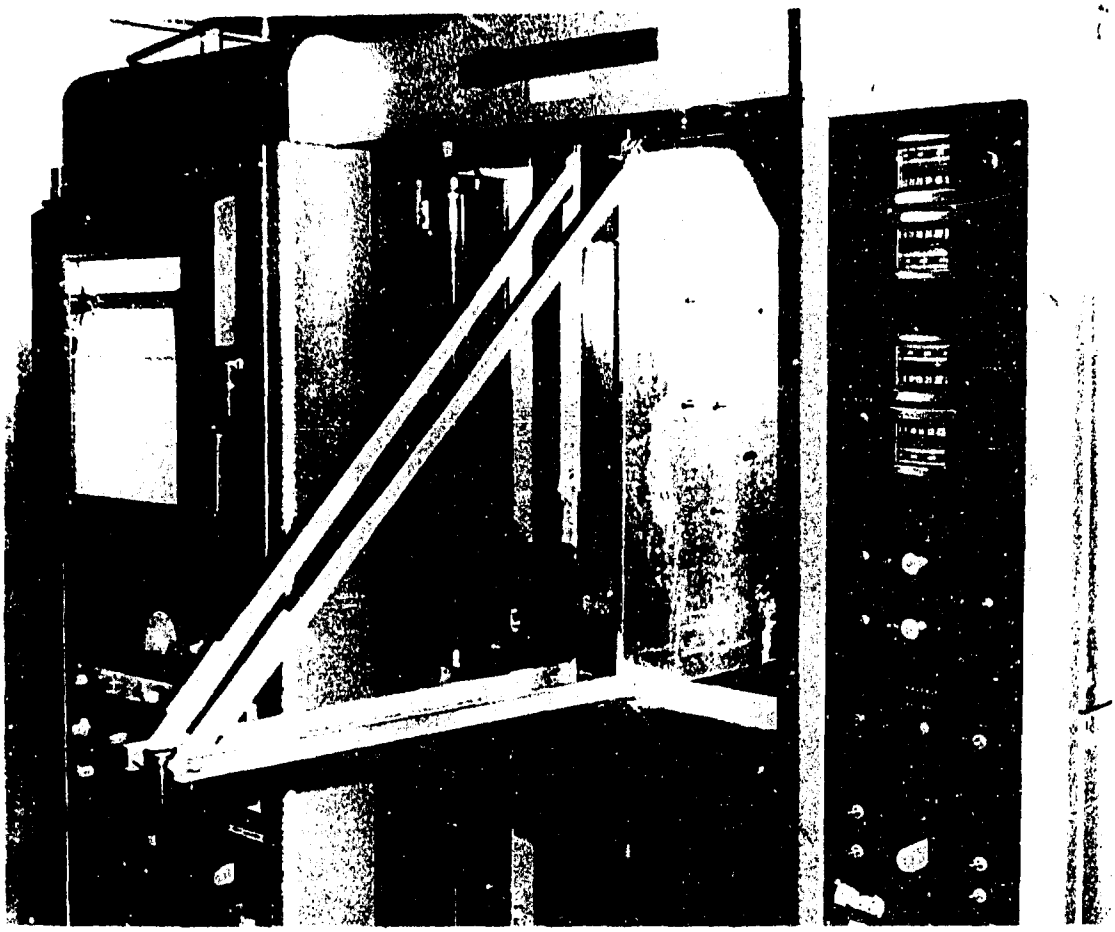

Figure 1-3. Test Fixture in Instron Test Machine (Front)

sand was present in the interface at the time. The introduction of the sand drastically changed the behavior of the NOLARO. Extreme elongations of the jacket material were evident at the point of tangency with the sheave during the initial application of load. Jacket failure occurred at this point after relatively few load cycles. Fiber abrasion and subsequent fiber failure occurred as load cycling continued.

Other friction producing materials, namely commercial belt dressing compound and small spherodized glass beads, were introduced during later tests with similar results. These materials were selected to produce friction without the sharp cutting edges of the sand. Fiber abrasion was less pronounced during tests with these materials; however, the initial jacket failure occurred in the same manner.

The failures observed in the tests with friction materials are considered to be representative of the one experienced in the field; namely, they occurred at the

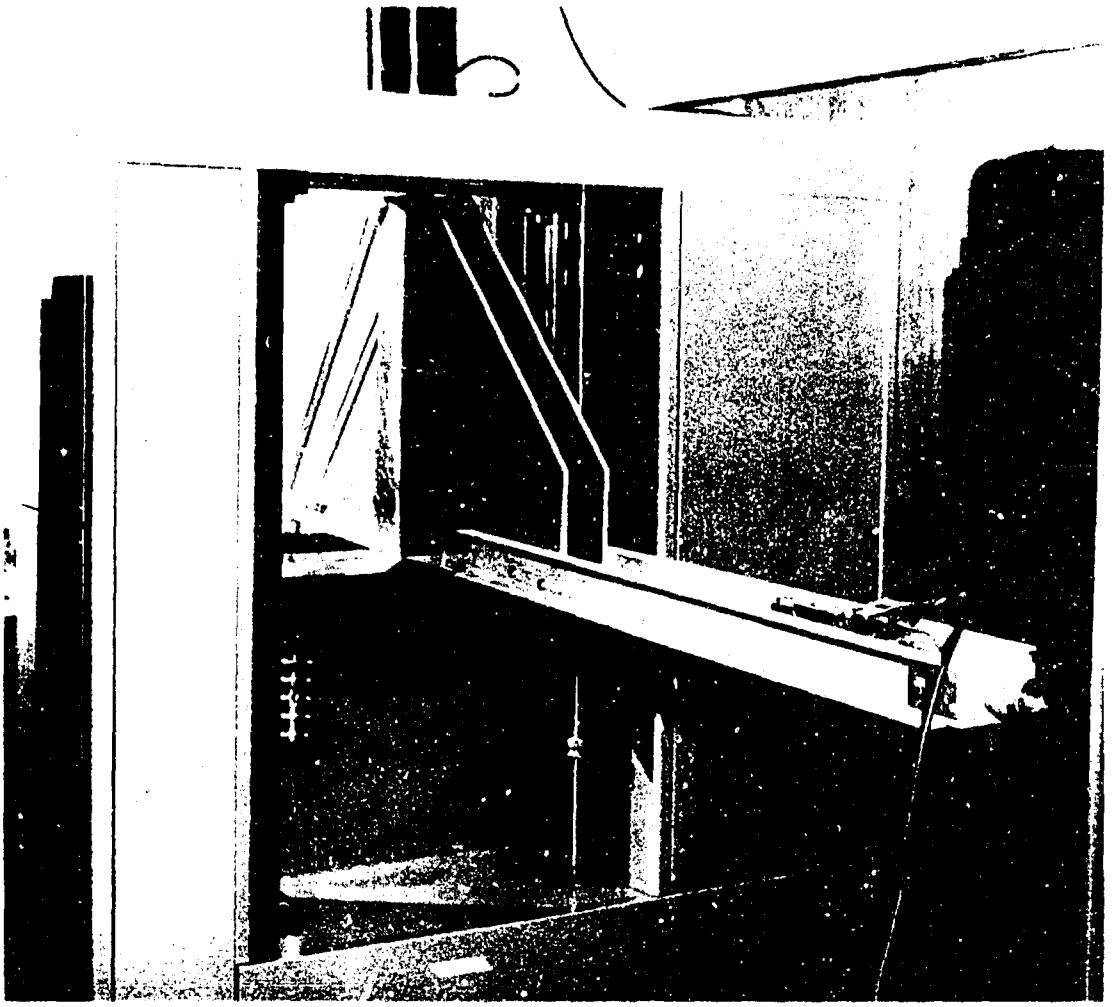

Figure 1-4. Test Fixture in Instron Test Machine (Rear)

initial contact point with the traction drive and were produced by cyclic loads with friction producing material along the interface. A brief explanation of the failure mechanism is presented next. The development of the theoretical model is supplemented with strain data obtained from the NOLAPO jacket during cyclic tests with sand.

1-5. EXPLANATION OF FAILURE MECHANISM

The model used in this discussion is shown in Figure 1-5. It is essentially the same as the test fixture used for the cyclic tests. The coordinate(s) is measured from the loading end of the specimen, and the point of application of the

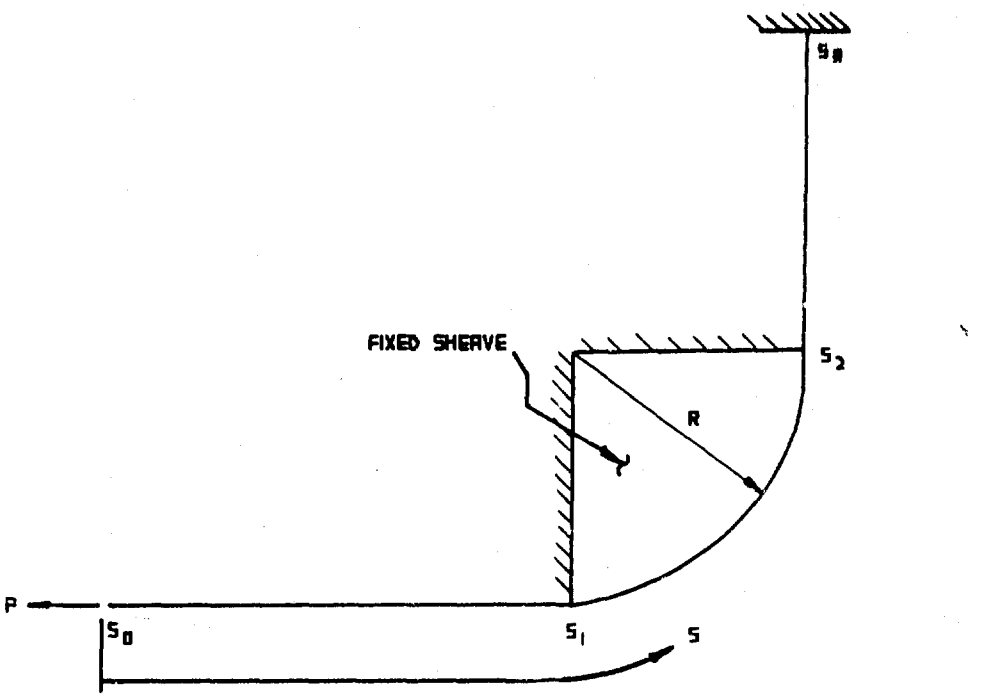

Figure 1-5. Schematic of Test Condition

load (P) is considered to be sufficiently removed from the sheave to represent the boundary conditions of a flying tether line. Friction forces (F) are transmitted to the fibers by means of shear forces in the jacket. The applied load (P) is resisted by these friction forces and by the load at the fixed end of the specimen.

The polyester stress-strain relationship can be considered linear within the range of loading considered; hence, the strain in the polyester bundle as it passes over the 90° sheave section is assumed to vary in proportion to the load in the fibers. Although actual fiber strain measurements were not made, a linear strain distribution along the sheave can be assumed since the fiber/jacket interface through which the friction forces are transmitted is not affected by the surface condition of the sheave. The total elongation of the fibers in the test section can therefore be expressed as the integral of the strains or simply the area under the solid curve in Figure 1-6 which shows assumed fiber strains versus position along the test section.

The jacket strains along the free sections of NOLARO between s_0-s_1 and s_2-s_3 are the same as those of adjacent fibers due to the low modulus of the polyethylene and the molded interface between the two. Friction along the area of contact with the sheave between s_1 and s_2 restrains the motion of jacket and results in a relative slip between the fibers and the polyethylene. The magnitude of this relative motion between the fibers and the jacket is small in the case of a clean sheave.

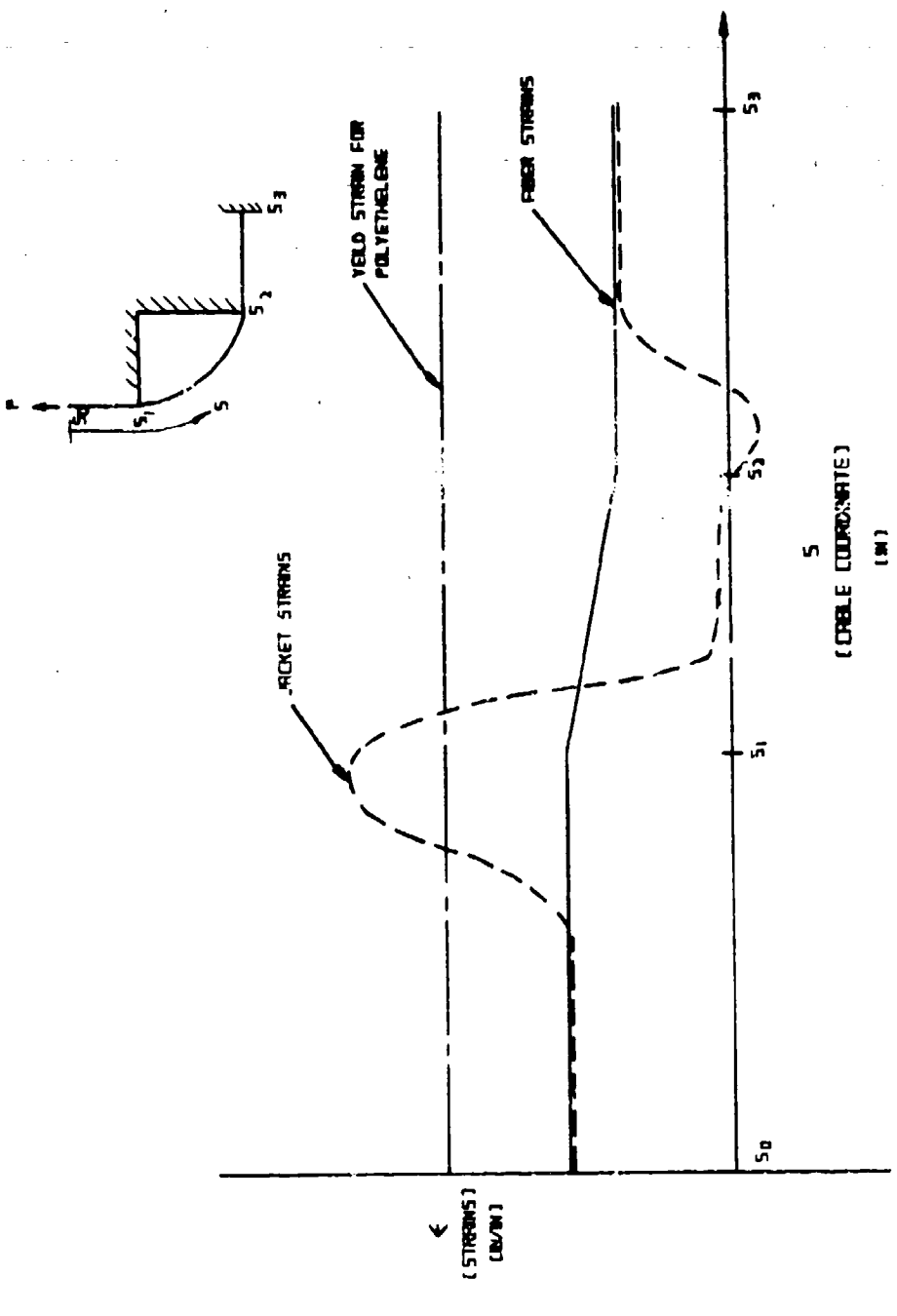

Figure 1-6. Strain in Jacket and Fibers vs Positions

but becomes very large when the jacket is restrained to almost no slip on the sheave by sand or other friction producing materials.

The real significance of the restraint of the polyethylene jacket by high friction on the fixed sheave is seen when the total elongation of the test section is considered. Point s_0 on Figure 1-6 is considered representative of a point on the flying cable sufficiently removed from the sheave. At this point the total elongation of the fibers and the jacket from point s_3, or the fixed end of the NOLARO, must be the same. In other words, the integral of the jacket strains between s_0 and s_3 must equal the integral of the fiber strains over the same length. The dashed line on Figure 1-6 shows measured jacket strains from tests on NOLARO with sand. The curve shows low jacket strains occurring along the contact surface, and more significantly, the very large strains in the jacket which occur as the cable separates from the sheave. These strains, which result from the total displacement condition, considerably exceed the yield condition for the polyethylene. Cyclic loading at this condition produces successive plastic deformation in the jacket at a localized area until rupture occurs.

The jacket failure sequence is clearly shown in Figures 1-7, 1-8, and 1-9. Figure 1-7 shows the specimen in the test fixture after a 2000-pound load was applied. The test marks on the NOLARO were placed at 1/2-inch intervals on the unloaded cable. Figure 1-8 shows the specimen after the application of a 6000-pound load. Over 100 percent elongation in the jacket has occurred locally and jacket failure can be seen on one side of the cable. Figure 1-9 shows the cable after

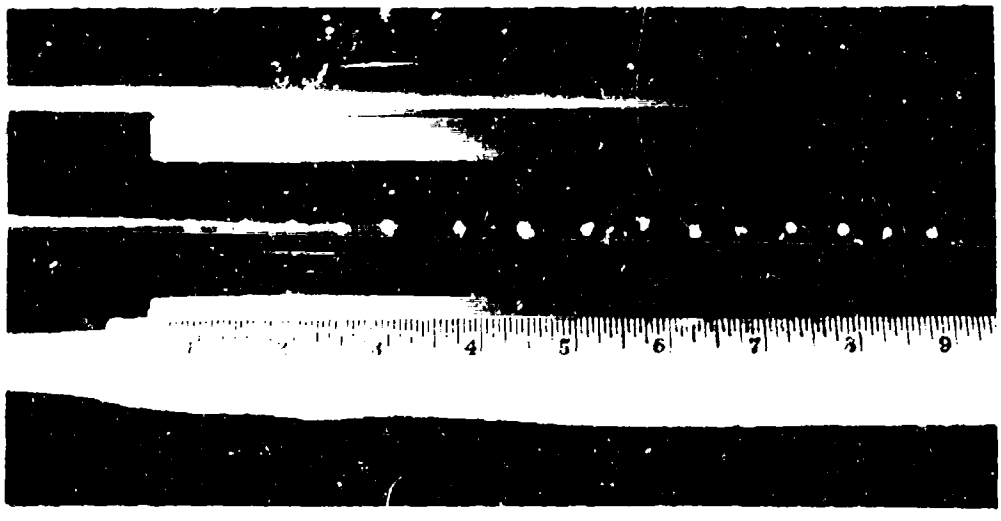

Figure 1-7. Specimen in Test Fixture - 2000-Pound Load Applied

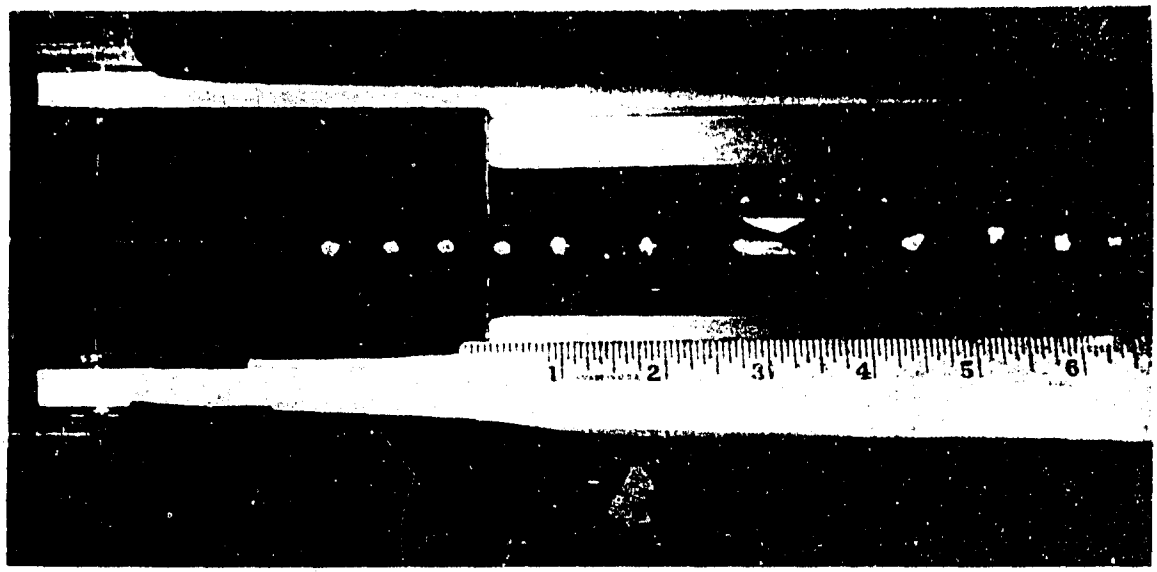

Figure 1-8. Specimen in Test Fixture – 6000-Pound Load (Sand in Interface)

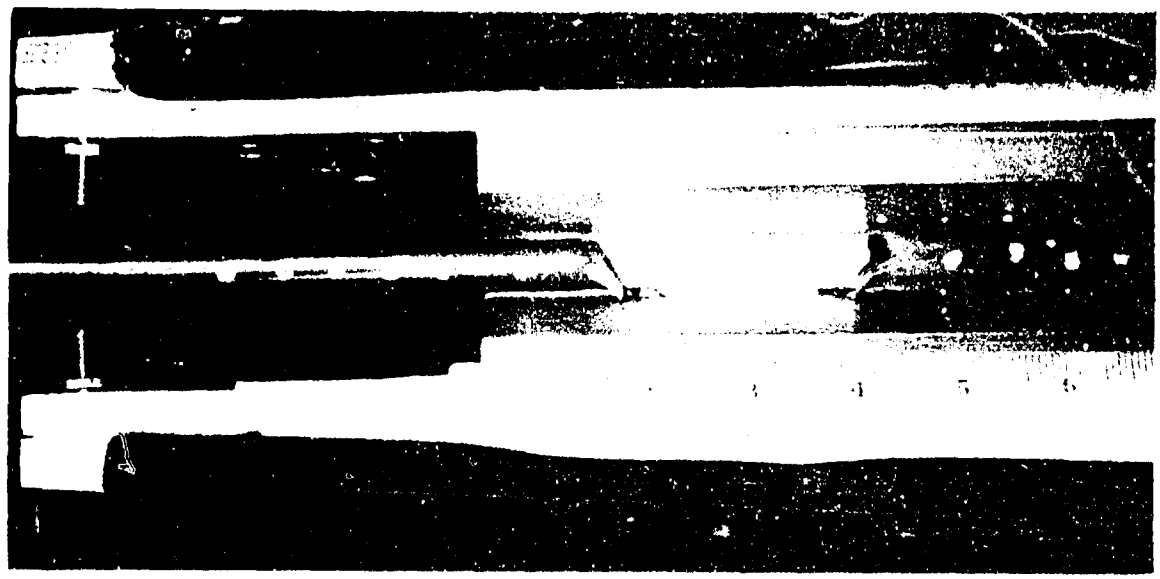

Figure 1-9. Specimen in Test Fixture – After Five Load Cycles 4000 +2000 Pounds (Sand in Interface)

five load cycles of 4000 ±2000 pounds. Considerable separation has occurred at the jacket failure and several fibers have failed due to abrasion. Figure 1-10 shows the failed section of the NOLAR® after removal from the test fixture. Severe damage to the fibers as well as the thinning of the jacket at the failure point is evident in the photograph.

Figure 1-10. Failed Section of NOLARO Removed from Test Machine

The preceding discussion, as well as the measured data and the photographs, applies only to the case of high friction in the area of initial contact with the sheave. As noted before, similar tests under clean conditions did not produce failures of this type. In these tests noticeable slip between the NOLARO jacket and the sheave could be observed, and the large jacket strains at the point of tangency were not present.

1-6. ADDITIONAL TESTING PROGRAMMED

Tests to date have been restricted in the total number of load cycles obtainable due to the relatively low cycling rate of the Instron machine. A new test fixture is currently under construction which will permit the accumulation of a large number of test cycles in a shorter period. This fixture utilizes a 3000-pound force magnetic exciter to provide the cyclic load. Preload of the cable is maintained by hydraulic actuators, and this preload is isolated from the exciter armature by pneumatic springs. A schematic drawing of the design is shown in Figure 1-11. The versatility of the magnetic exciter will provide for a wide range of frequency and load spectrum variations.

The three-wheel tensiometer shown in Figure 1-12 has been developed for use on line during flight operations with NOLARO. This tensiometer has a sensitivity

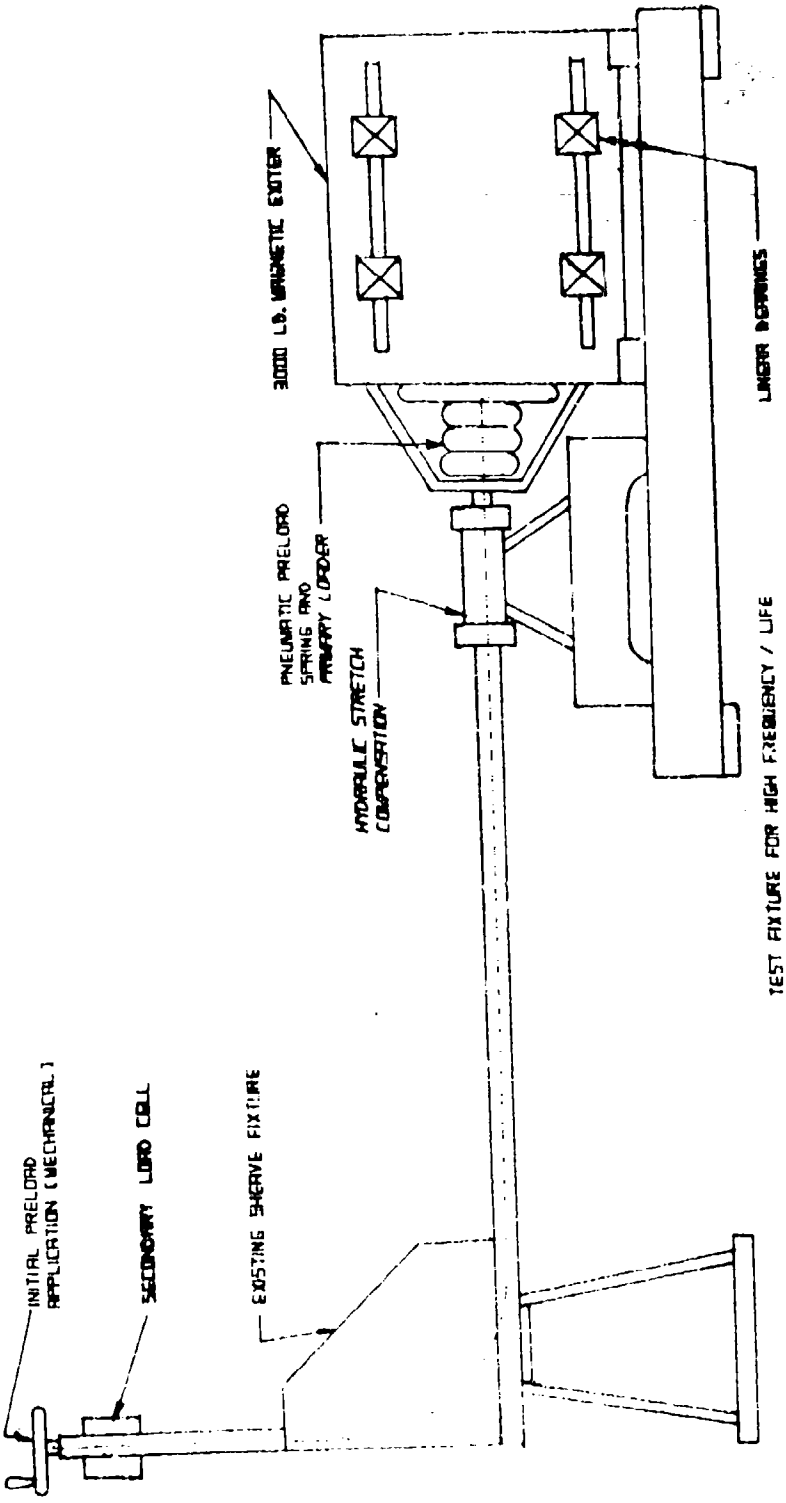

Figure 1-11. Schematic of Proposed High-Frequency Test Fixture

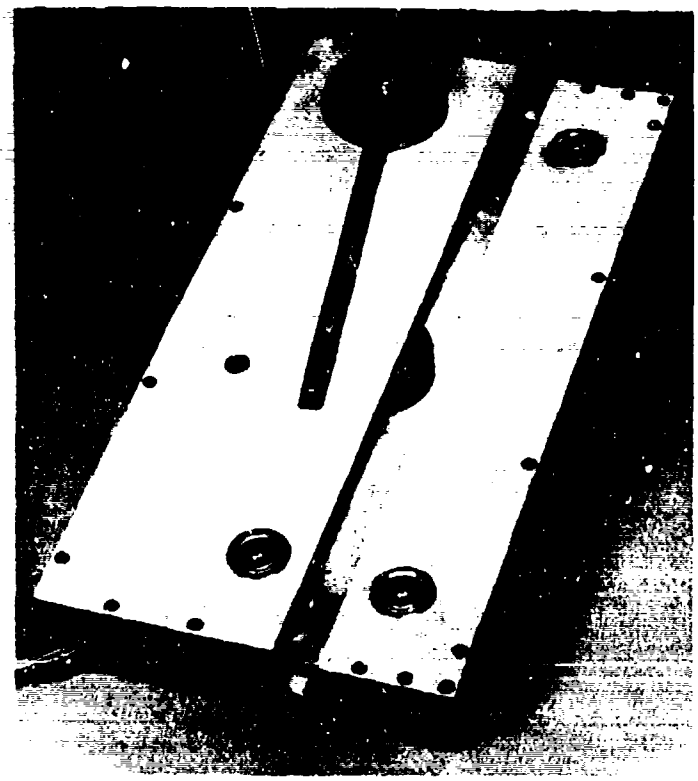

Figure 1-12. Three-Wheel Tensiometer Designed for Measuring NOLARO Loads During Flight Operations

of 1 mV/lb and a frequency response from dc to 1500 Hz. It functions over a range of 500 to 10,000 pounds. Dynamic cable loads during future flights will be measured and recorded on magnetic tape. The data will be analyzed for spectral content as well as used directly as an input to the magnetic exciter.

The tensiometer and test fixture are designed to measure and simulate flight operating conditions as closely as possible, with the primary objective being to determine life expectancy of NOLARO during holding operations. Temperature tests on NOLARO are also planned using an environmental chamber. Tests will be conducted between -60°F and +200°F. The chamber is of sufficient size to permit evaluation of the cable over a partial sheave segment.

1-7. CONCLUSIONS FROM TESTS PERFORMED ON NOLARO TO DATE

1. Limited cyclic loading of NOLARO against a fixed sheave under clean conditions does not appreciably degrade the strength of the cable. Tests have shown this to be true for load conditions of 50 ±20 percent of rated cable strength and up to 15,000 cycles. Test results are identical for both polyurethane and hardened aluminum sheave surfaces.

2. The introduction of foreign matter, in particular sand, into the sheave/cable interface results in a failure of the jacket after relatively few load cycles and subsequent fiber failures due to abrasion of the unprotected polyester.

3. Due to Conclusion 2, field operation with NOLARO should not be conducted under conditions of wind-blown sand unless the winch installation is enclosed. Frequent inspection of the winch surfaces should be made to ensure that a build-up of friction producing foreign matter does not occur. This is particularly important for the first groove on a multiple-groove dual-capstan winch of the type commonly used with NOLARO.

4. Holding operation with NOLARO should be programmed to move the cable frequently by small amounts, thus shifting the critical point along a section of the jacket and preventing accumulative plastic deformation.

5. NOLARO offers a high strength-to-weight ratio necessary for critical applications. The material must be handled with more care than steel cable, but this appears to be a small penalty to pay for the advantages to be gained in increased altitude and payload capability in tethered balloon operations.

6. Further testing of NOLARO is required to determine life expectancy under cyclic loading. Additional testing must be conducted to determine effects of temperature on cable properties.

References

Product Bulletin #R-1a, Columbian Rope Company, Auburn, New York, 1 June 1969.

Tests on NOLARO Tether, Telta Project, Unpublished test data, Patrick AFB, Florida, 20 June 1970.

Contents

2. Aerodynamic Coefficients of Four Balloon Shapes at High Attack Angles

P.A. Peters and H.H. Lysons
Pacific Northwest Forest & Range Experiment Station
Seattle, Washington

S. Shindo
Aeronautical Laboratory, University of Washington
Seattle, Washington

Abstract

This paper presents the results of wind tunnel tests on natural shape, barrage, Class C, and Vee balloons. Lift, drag, and pitching moment of each balloon are presented for an angle-of-attack range from -12° to +102° and a nominal Reynolds Number of 10^6 per foot. The use of each shape as a tethered balloon is discussed. The data will be useful to those responsible for balloon design and performance in logging, or similar large tethered balloon applications.

2-1. INTRODUCTION

Since first introduced in the summer of 1963, tethered balloons have been used to yard logs in the Pacific Northwest as a means of harvesting difficult terrain with little impact on the forest environment from access roads or soil disturbance. In downhill logging, the balloon is typically operated at very high attack

angles. Knowledge of the aerodynamic characteristics of tethered balloons in this operating mode is needed to design the optimum system configuration.

Wind tunnel tests in the United States in the early 1900's were mainly of high fineness ratio bodies with application to airship design (Abbott, 1931). Some testing has been conducted in England on barrage balloons for tethered applications (Simonds, 1963). Recently, extensive pressure and force tests have been conducted in the United States of a natural shape and a kite balloon (Sherburne, 1968; Haak, 1971). However, the above tests have been conducted for a limited range of angle of attack (α), seldom exceeding 20°. A preliminary wind tunnel test of two kite-balloon models in a small subsonic facility provided the first balloon aerodynamic data at $\alpha > 20°$ (Swarthout, 1967). This test indicated the desirability of conducting a more extensive test program in a production facility. This paper presents the results of that subsequent program.

Natural shape, Class C, barrage, and Vee balloon models were tested in an 8- by 12-foot wind tunnel at the University of Washington. Lift, drag, and pitching moment are presented for an angle-of-attack range from -12° to +102°, and a nominal Reynolds Number (R.N.) of 10^6 ft^{-1}. The use of each balloon configuration as a tethered balloon is discussed. The data will be useful for selecting the optimum balloon shape for logging service.

2-2. NOMENCLATURE

α	pitch angle of attack, degrees
α_L	limit angle of attack, degrees
B	buoyant lift, pounds
C_D	drag coefficient, $2D/\rho V^2 \forall^{2/3}$
C_L	lift coefficient, $2L/\rho V^2 \forall^{2/3}$
C_m	pitching moment coefficient, $M/\rho V^2 \forall^{2/3} \ell$
D	drag, pounds
γ	flight path angle, degrees
ℓ	reference length, feet
L	aerodynamic lift, pounds
L/D	aerodynamic lift-to-drag ratio, C_L/D_D
M	aerodynamic pitching moment about center of moments, ft-lb
M_V	pitching moment about tether point due to relative wind, ft-lb

M_y	pitching moment about tether point due to buoyant lift and balloon tare weight, ft-lb
R. N.	Reynolds Number
ρ	density, slugs/ft^3
Σ	sigma, balloon shape parameter
T	tether cable tension, pounds
V	relative wind, fps
$\forall$	balloon volume, ft^3
W	balloon tare weight, pounds
x_T	length from tether point to center of gravity along body centerline, feet
x_B	length from center of buoyancy to center of gravity, feet
y_T	length of perpendicular from tether point to body centerline, feet
sub_e	equilibrium
sub_x	horizontal
sub_z	vertical

2-3. WIND TUNNEL TESTS

2-3.1 Test Procedure

Typical test configurations including model, strut support, and fairing are shown in Figure 2-1. The model has been rolled 90° to use the tunnel yaw axis as the model pitch axis. Pitch angle of attack is obtained by rotating the strut. Forces on the model and strut are transmitted by the strut to a six-component balance system. In the normal configuration (Configuration A), the force transmitted to the balance includes:

1. Weight of the model
2. Desired aerodynamic force on the model
3. Aerodynamic interference effects amongst the model, strut, and fairing
4. Aerodynamic force on the strut.

Forces due to tunnel wall effects were considered negligible. Weight tare corrections were obtained by taking balance readings at all angles of attack with the wind off. Two additional test runs were required at each angle-of-attack setting to correct the data for the effects of items 3 and 4 above. The test configurations and corrections for strut tare are shown in Figure 2-2.

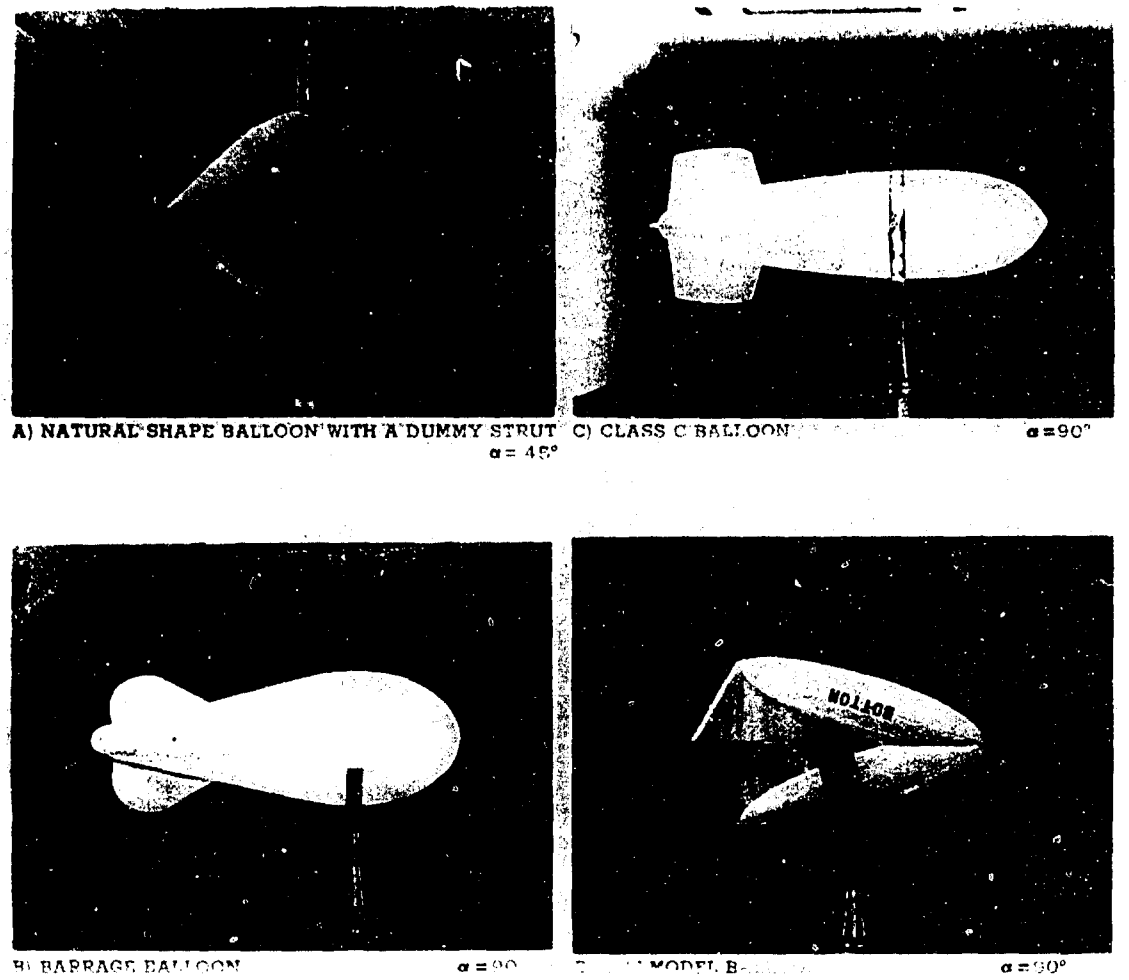

Figure 2-1. Test Configurations in Tunnel

The balance system measures six components of model force: lift, drag, side force, pitching, yawing, and rolling moment. Every model was tested at a zero yaw angle of attack and possessed lateral symmetry. Therefore, side force, yawing moment, and rolling moment should equal zero. The magnitudes of these components corrected for the effects of strut interference were indeed nearly zero (Shindo, 1969 and 1970). Only the components of interest – lift, drag, and pitching moment – are reported here.

A schematic of the wind tunnel facility is shown in Figure 2-3. The tunnel is a subsonic, closed, double-return type. The tunnel tapers down to an 8- by 12-foot cross section at the test section. Top wind speed attainable is 250 mph.

FORCES MEASURED ON SHADED PORTIONS

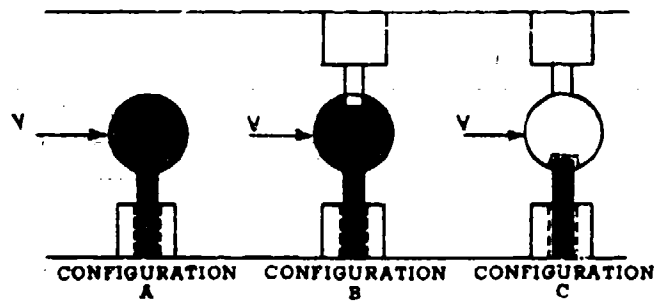

$$\text{Lift} = 2 \times \text{Lift}_A \cdot \text{Lift}_B \cdot \text{Lift}_C$$

$$\text{Drag} = 2 \times \text{Drag}_A \cdot \text{Drag}_B \cdot \text{Drag}_C$$

$$\text{Moment} = 2 \times \text{Moment}_A \cdot \text{Moment}_B \cdot \text{Moment}_C$$

Figure 2-2. Strut Tare Correction Configurations and Equations

The present tests were conducted at constant dynamic pressure of 25.9 lb/ft^2, which corresponds to a wind speed of approximately 100 mph.

2-3.2 Model Descriptions

The balloons in fully inflated condition are represented by rigid models. All models were constructed of white pine and painted white. The hulls were turned on a lathe to insure axial symmetry. Photographs of each model, as they appear in the wind tunnel during the test, are shown in Figure 2-1.

The natural shape is the simplest, possessing axial symmetry and containing no stabilizers. The model is a $\bar{r} = 0$ shape modified at the bottom to represent the natural shape with an attached conical skirt. Generating coordinates for the natural shape model are presented in Table 2-1.

The barrage balloon is a single hull configuration with three aft stabilizers placed 120° apart; it has mirror symmetry with respect to a vertical plane down the centerline. The vertical stabilizer or rudder is directly below the hull. The horizontal stabilizers or fins have the same shape as the rudder but are 80 percent the size. Fin and rudder details are shown in Figure 2-4. Generating coordinates for the barrage balloon hull are presented in Table 2-2.

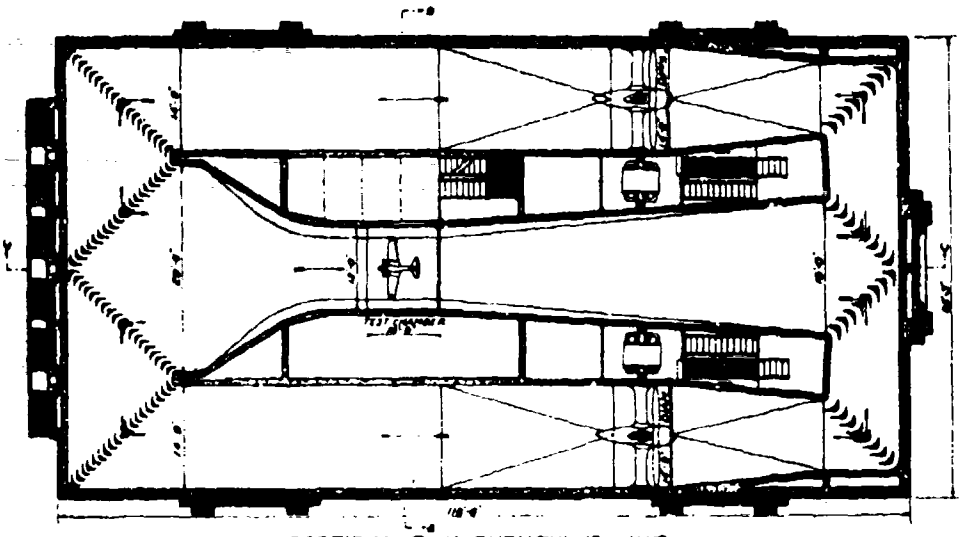

SECTIONAL PLAN THRU TUNNEL AXIS

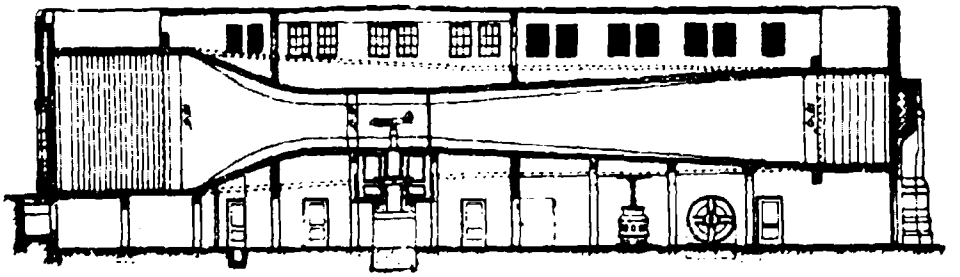

SECTIONAL ELEVATION "C"

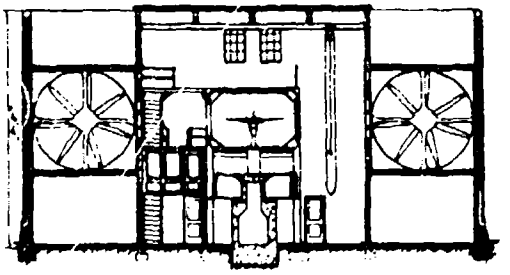

SECTIONAL ELEVATION "B"

Figure 2-3. Wind Tunnel Test Facility

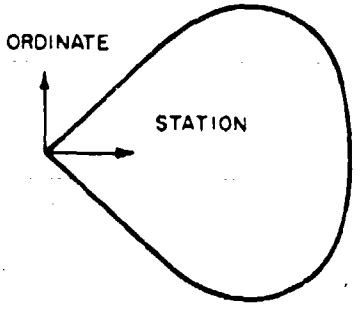

Table 2-1. Ordinates of Natural Shape Balloon

Station (percent length from tether point)	Ordinate (inches)	Station (percent length from tether point)	Ordinate (inches)
0	0	74.8	12.17
14.6	3.42	80.3	11.70
29.2	6.85	85.4	10.95
41.9	9.83	87.7	10.49
46.9	10.70	91.7	9.39
52.0	11.40	94.8	8.12
57.5	11.94	97.1	6.73
63.2	12.27	98.6	5.27
69.0	12.35	99.5	3.78
		100.0 = 25.87"	0

The Class C balloon is a single hull configuration with three aft stabilizers placed 120° apart. The vertical stabilizer is directly below the hull. The geometric details of the stabilizers are shown in Figure 2-5. Generating coordinates for the Class C hull are presented in Table 2-3. By comparison with the barrage balloon, the Class C is more streamlined in both hull and stabilizer design.

The Vee balloon consists of two hulls joined to each other at the forward end and joined to a horizontal stabilizer at the aft end. A single vertical stabilizer is located at the horizontal stabilizer midspan. The geometric details of the stabilizers and their placement are given in Figure 2-6. Generating coordinates of the individual hulls are presented in Table 2-4.

2-3.3 Data Accuracy

Model lift, drag, and pitching moment were measured to a resolution of 0.1 pound, 0.01 pound, and 0.1 in-lb, respectively. The vibration environment was

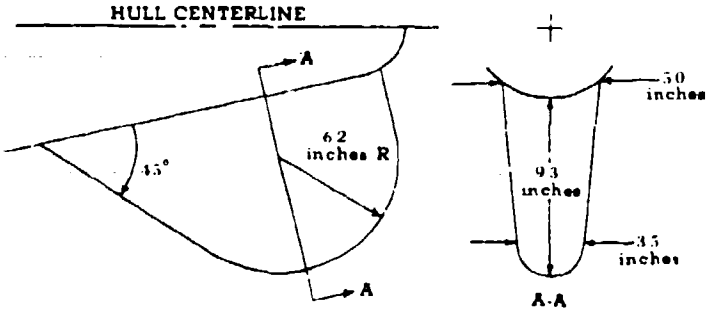

VERTICAL STABILIZER

HORIZONTAL STABILIZERS ARE 80 PERCENT THE ABOVE DIMENSIONS.

TRAILING EDGE OF HORIZONTAL STABILIZERS IN SAME POSITION AS VERTICAL STABILIZER.

Figure 2-4. Barrage Balloon Stabilizers

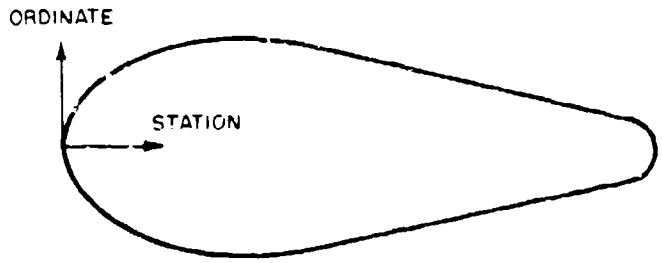

Table 2-2. Ordinates of Barrage Balloon Hull

Station (percent length from nose)	Ordinate (inches)	Station (percent length from nose)	Ordinate (inches)
0	0	23.19	8.88
0.78	1.56	25.68	9.04
2.02	2.94	28.17	9.13
3.27	3.93	30.67	9.17
4.51	4.66	33.16	9.13
5.76	5.23	34.40	9.09
7.00	5.73	35.65	9.04
8.25	6.19	36.89	8.98
9.49	6.57	38.14	8.90
10.74	6.95	39.38	8.83
13.23	7.60	40.63	8.71
15.72	8.06	41.87	8.56
18.21	8.40	95.71	2.60
20.70	8.67	100.00 = 48.98"	0

very low; the amplitude of oscillation was approximately twice the above resolution. This source of error was reduced by averaging.

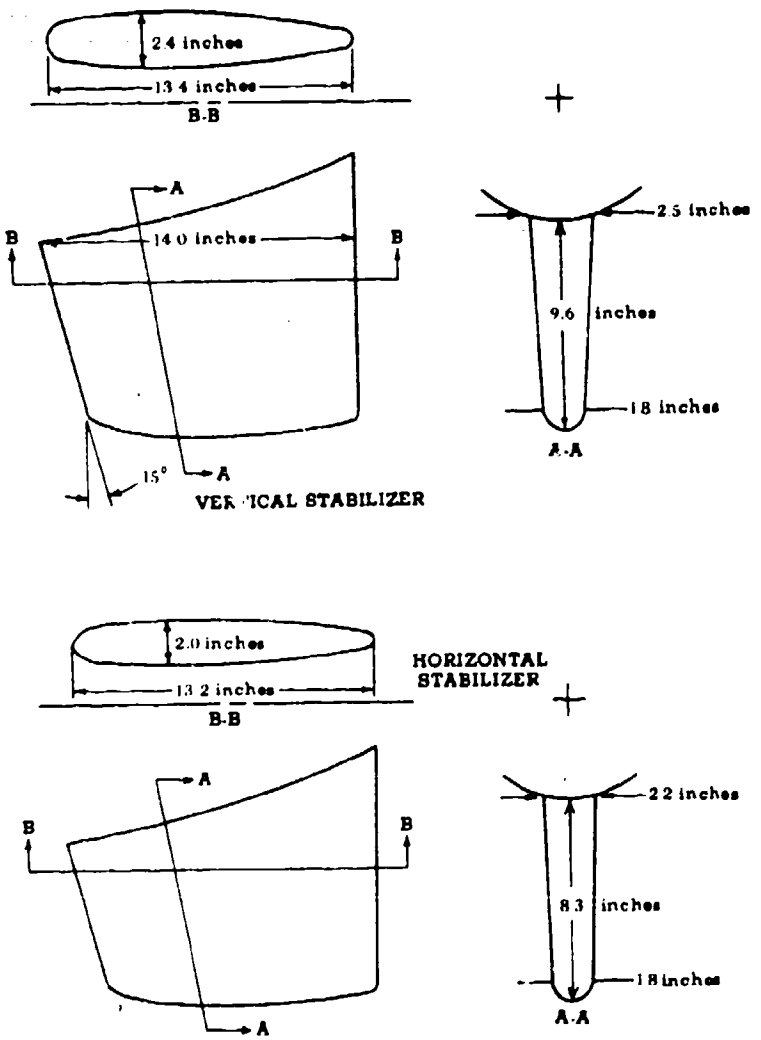

Figure 2-5. Class C Balloon Stabilizers

An additional source of error was introduced in the correction for strut effects. Although the equations for strut correction introduce no error, geometric compromises had to be made in the dummy strut configurations to provide clearance to isolate that part of the configuration for which forces were measured.

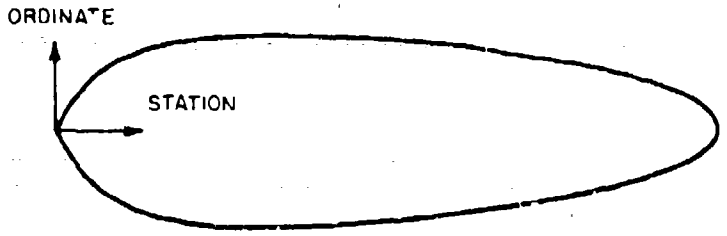

Table 2-3. Ordinates of Class C Balloon

Station (percent length from nose)	Ordinate (inches)	Station (percent length from nose)	Ordinate (inches)
0	0	54.4	7.30
3.2	2.85	57.6	7.20
6.4	4.75	60.8	6.95
9.6	5.85	64.0	6.70
12.8	6.60	67.2	6.45
16.0	7.10	70.4	6.20
19.2	7.40	73.6	5.95
22.4	7.70	76.8	5.60
25.6	7.85	80.0	5.30
28.8	7.90	83.2	4.90
32.0	7.90	86.4	4.50
35.2	7.90	89.6	3.95
38.4	7.85	92.8	3.40
41.6	7.80	96.0	2.65
44.8	7.70	99.2	1.20
48.0	7.60	100.0 = 54.7"	0
51.2	7.45		

An indirect method of assessing this error was to check the data for internal consistency and repeatability. A repeatability check occurred in the angle-of-attack range from 38° to 52°. The support strut for the wind tunnel model has a rotation capability of 65°. To obtain the desired angle-of-attack range of -12° to +102°, the model was mounted in two separate positions on the support strut. An overlap in data was obtained between 38° and 52°. Good agreement in this alpha range is demonstrated in Figures 2-7, 2-8, 2-9, and 2-10.

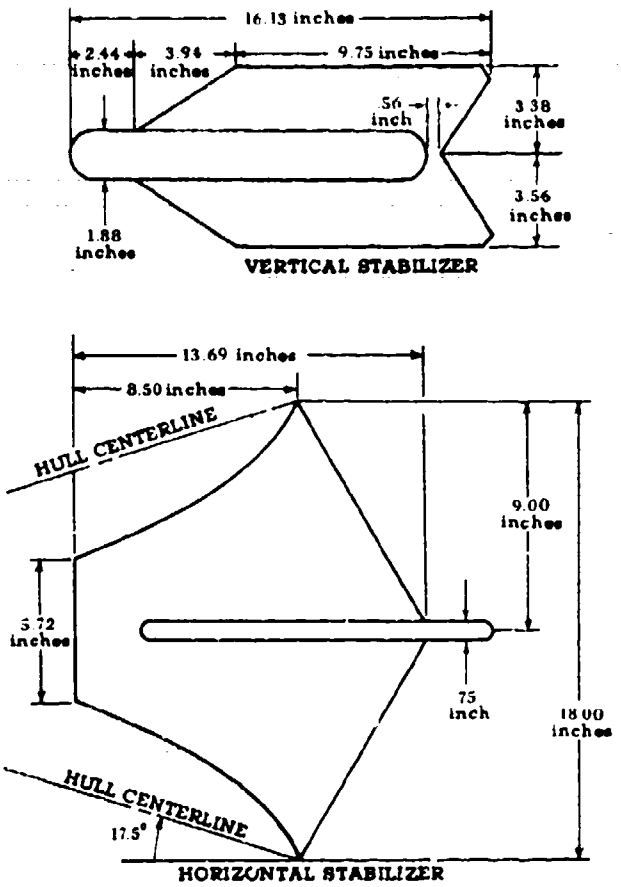

Figure 2-6. Vee Balloon Stabilizers

2-3.4 Data Reduction

Lift and drag were reduced to coefficient form in the standard manner by dividing by the dynamic pressure and reference area. Pitching moment was reduced to coefficient form by dividing by the dynamic pressure, reference area, and reference length.

The reference area selected for each model was the hull volume to the two-thirds power. The hull volume of the natural shape is equivalent to the total volume of the model. For the barrage and Class C shapes, the volume of the fins and vertical stabilizer was excluded. For the Vee balloon, the volume of the vertical stabilizer was excluded.

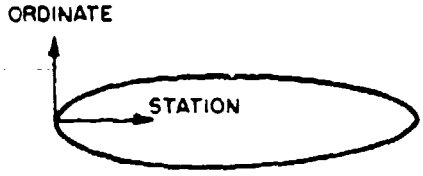

Table 2-4. Ordinates of Each Vee Balloon Hull

Station (percent length from nose)	Ordinate (inches)	Station (percent length from nose)	Ordinate (inches)
0	0	55	3.61
5	1.88	60	3.50
10	2.50	65	3.36
15	2.92	70	3.21
20	3.21	75	3.01
25	3.42	80	2.74
30	3.56	85	2.42
35	3.68	90	2.00
40	3.72	95	1.37
45	3.74	100 = 30.00"	0
50	3.68		

The reference length is the hull length for the Class C and barrage shapes. The reference length for the natural shape is the volume to the one-third power. For the Vee balloon, the reference length is the length of one of the individual hulls.

The center of buoyancy of the kite balloons – barrage, Class C, and Vee – was chosen as the center of moments. The moment center for the natural shape is the load attachment or tether point of the balloon. Some of the pertinent parameters of the configurations tested are shown in Table 2-5. These data are furnished to facilitate comparison with other wind tunnel test results.

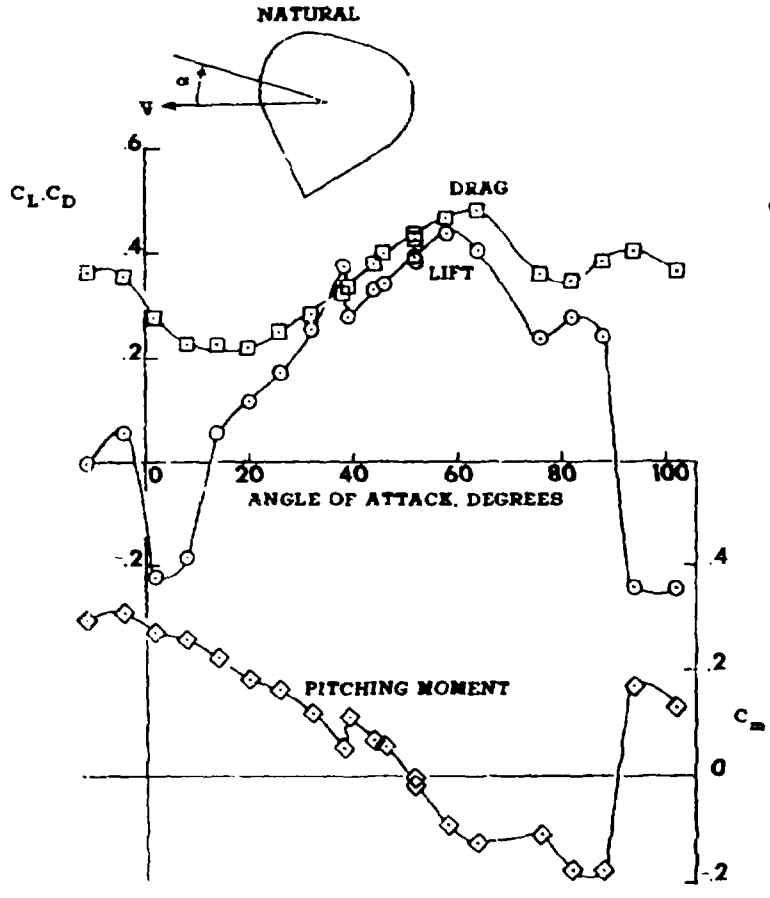

Figure 2-7. Lift, Drag, and Pitching Moment of a Natural Shape Balloon, $\alpha = -12°$ to $+102°$

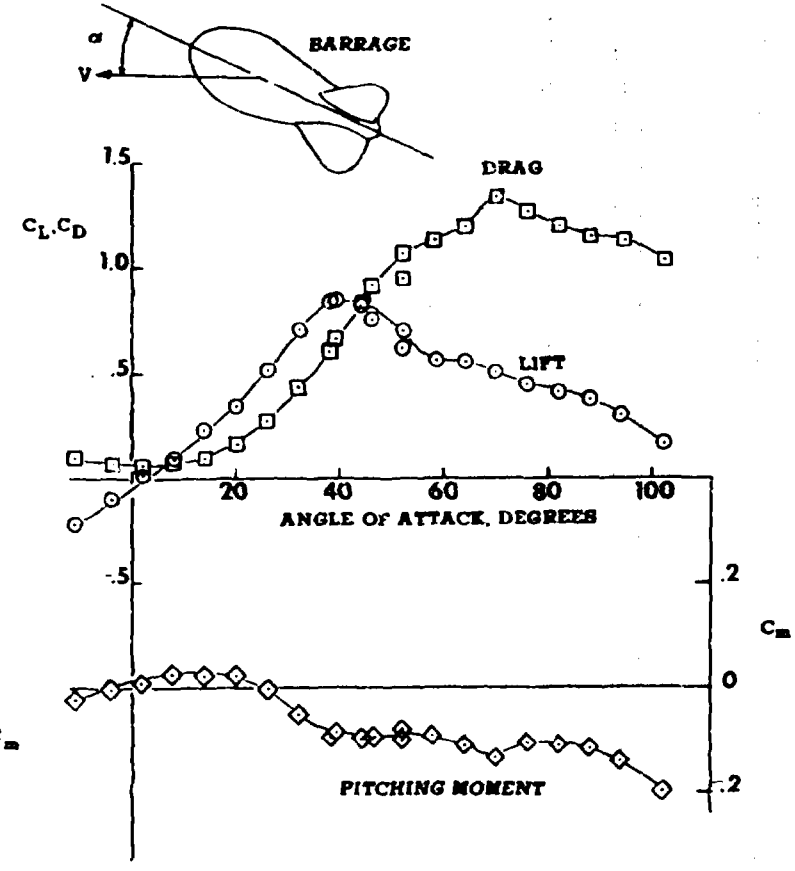

Figure 2-8. Lift, Drag, and Pitching Moment of a Barrage Balloon, $\alpha = -12°$ to $+102°$

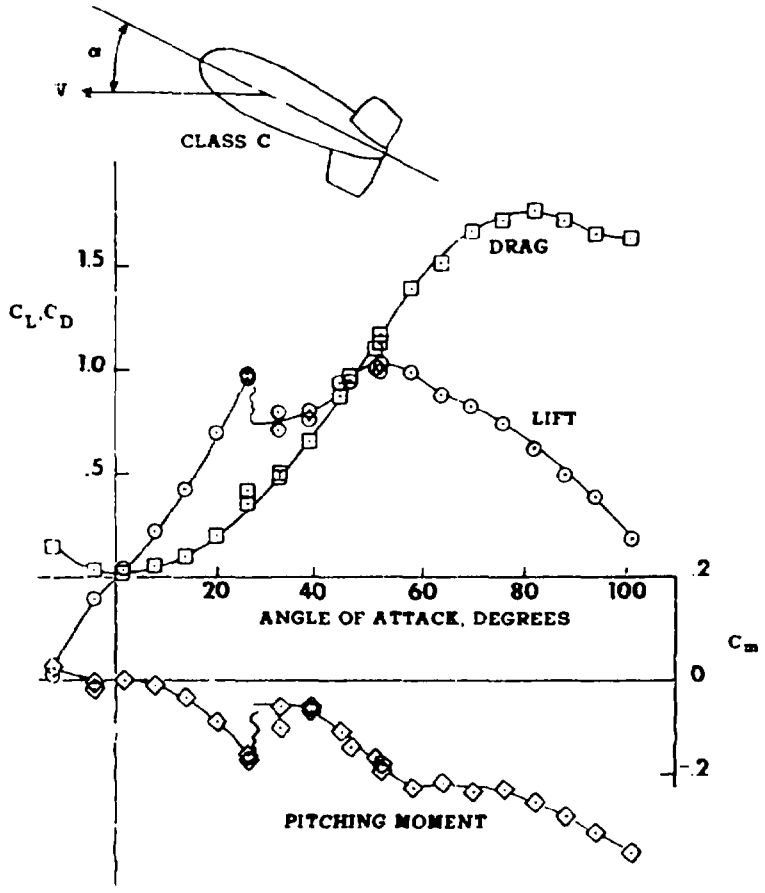

Figure 2-9. Lift, Drag, and Pitching Moment of a Class C Balloon, α = -12° to +102°

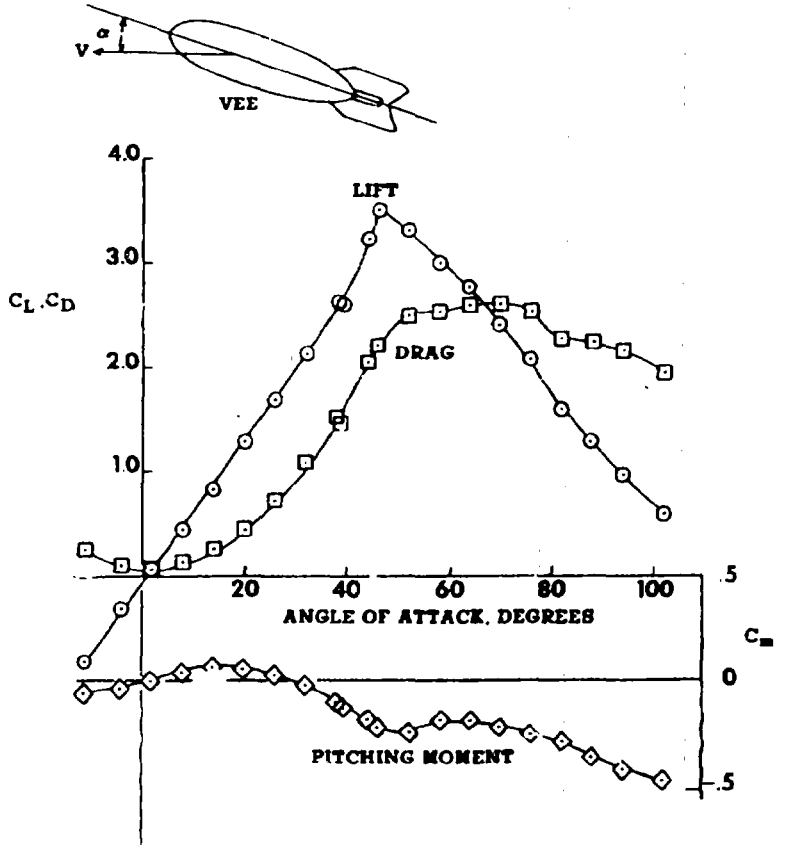

Figure 2-10. Lift, Drag, and Pitching Moment of a Vee Balloon, α = -12° to +102°

Table 2-5. Physical Dimensions of Balloon Models

Balloon	Property					
	Volume (ft^3)	Area $\forall^{2/3}$ (ft^2)	Reference Length (inches)	Center of Moments	Max. Hull Diameter (inches)	Hull Length (inches)
Natural	4.0	2.520	19.0**	Apex	24.7	25.9
Barrage	4.0	2.520	49.0	Body centerline 39% of hull	18.3	49.0
Class C	4.0	2.520	54.7	Body centerline 44% of hull	15.6	54.7
Vee	1.157*	1.102	30.0	Body centerline 14.6" from nose	7.5	30.0

* Includes hulls and horizontal stabilizer

** $\forall^{1/3}$

2-4. SIMULATION AND SCALE EFFECTS

Considerable judgment should be used in the interpretation and use of wind tunnel data on balloons. Two of the principal limitations are the results of:

1. Simulating the balloon by a rigid model
2. Simulating the balloon by a subscale model.

Full scale tests of tethered balloons indicate that flexible body effects may significantly affect the aerodynamic characteristics of balloons. A balloon has a tendency to flatten out on the windward side, which increases the drag force. Drag force estimates from flight data normally indicate higher drag than wind tunnel results (Ferguson, 1965; Menke, 1963).

Aerodynamic similarity is achieved when the Reynolds Number of the wind tunnel model equals the Reynolds Number of the balloon in its reference flight condition. The Reynolds Number (based on $\forall^{1/3}$) for each balloon shape tested is:

R. N. = 1.59×10^6	Natural
R. N. = 1.59×10^6	Barrage
R. N. = 1.59×10^6	Class C
R. N. = 1.05×10^6	Vee

The R. N. of various flight configurations at sea level is shown in Figure 2-11. The R. N.'s of the wind tunnel models are also shown in Figure 2-11 for reference.

The Reynolds Number is a measure of the relative strength of the kinetic and frictional forces in the stream flow. Its principal influence is on the boundary layer and hence affects the friction drag, transition from laminar to turbulent flow, and the location of the separation point. To ensure transition from laminar to turbulent flow, trip strips are sometimes used on wind tunnel models. In the present test, the barrage balloon was tested with and without a trip strip, with no change in measured forces. A 1/8-inch diameter circumferential cord at 10 percent of body length was used as the trip strip.

A classic figure showing the transition region for a sphere is shown in Figure 2-12 (Hoerner, 1951). The natural shape data of this report and that of Sherburne (1966) are also shown in Figure 2-12.

2-5. TEST RESULTS

2-5.1 General

The lift, drag and pitching moment versus angle of attack are presented for each balloon shape. Natural shape, barrage, Class C, and Vee balloon data are presented in Figures 2-7, 2-8, 2-9, and 2-10, respectively.

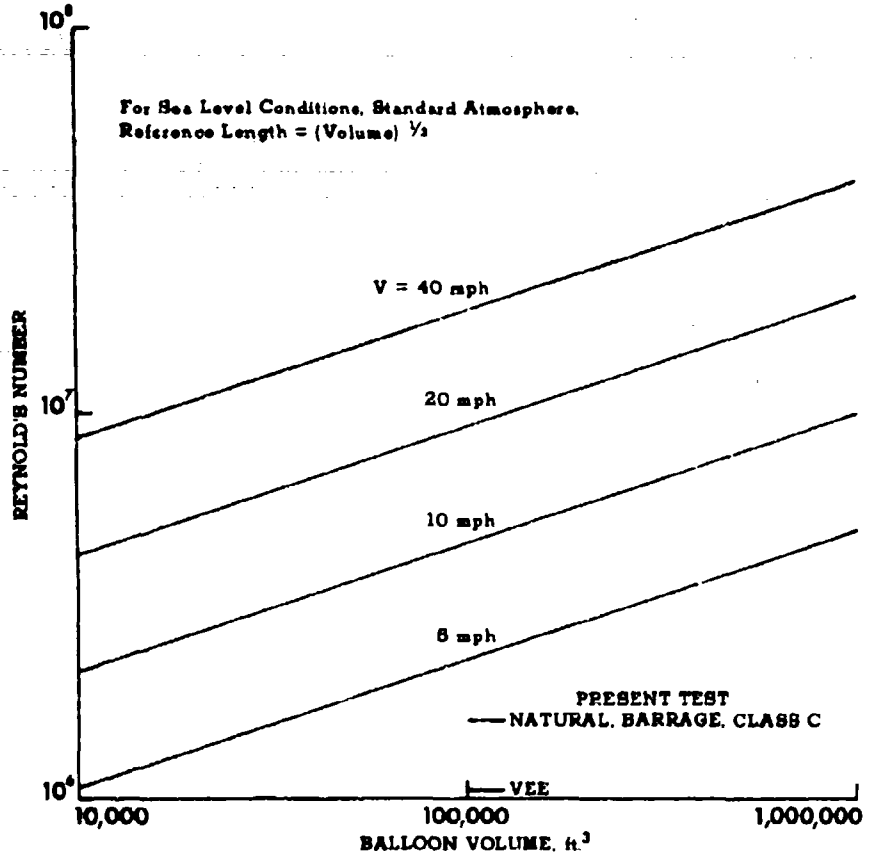

Figure 2-11. Reynolds Number Versus Balloon Volume

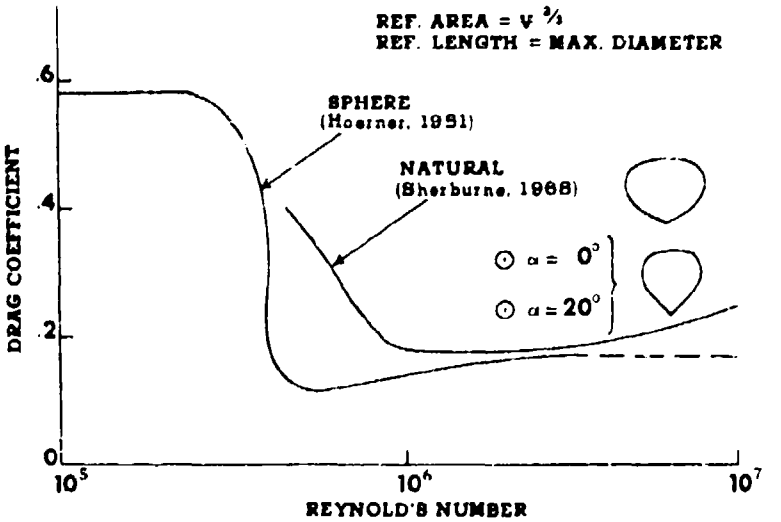

Figure 2-12. Effect of Reynolds Number on Balloon Drag

All data were obtained for a nominal R.N. = 10^6 ft^{-1}. In the following paragraphs, the characteristics of the data for each balloon shape are discussed.

2-5.2 Natural Shape

The lift, drag, and pitching moment of the natural shape are presented in Figure 2-7. An outstanding characteristic of the natural shape is the erratic behavior of the lift curve for small alpha. Lift drops off rapidly at $\alpha = 0°$ and rises just as rapidly at $\alpha = 12°$. A similar behavior was reported by Sherburne (1968). Above $\alpha = 12°$, lift increases until stall occurs at $\alpha = 38°$. Minimum drag occurs at $\alpha = 20°$. The aerodynamic moment about the tether point is predominantly stabilizing. The expected symmetry about $\alpha = 90°$ is demonstrated by the lift, drag, and pitching moment curves.

2-5.3 Kite Balloons

The lift, drag, and pitching moment of the barrage, Class C, and Vee are shown in Figures 2-8, 2-9, and 2-10, respectively. The kite balloons exhibit similar lift, drag, and moment curves. Prominent features are:

1. Linear lift curve up until stall
2. S-shaped drag curve
3. Minimum drag at alpha near zero
4. Moment curve which is predominantly stabilizing.

The Class C balloon lift curve (Figure 2-9) has a double maximum at $\alpha = 26°$ and $\alpha = 51°$. A probable explanation of this result is that the total balloon lift is composed of essentially two parts, that due to the tail surfaces and that due to the body or balloon hull. The lift on the tail surfaces increases until at $\alpha = 26°$ a stall condition occurs on the tail surfaces with a resulting loss in total lift. Above $\alpha = 26°$, body lift continues to increase with alpha until another maximum occurs at $\alpha = 51°$. The center of pressure shifts forward 9 percent of body length between $\alpha = 26°$ and $\alpha = 32°$, supporting the explanation given that lift is reduced at the tail surfaces. This phenomenon is not as pronounced with the barrage balloon because its tail fins are not as aerodynamically effective as those of the Class C balloon.

The coefficient data of the Vee balloon are substantially higher than those of the Class C or barrage balloons. This occurs because the data were normalized by dividing by hull volume to the two-thirds power. If the reference area nad been model surface area of platform area (these may be more meaningful for the Vee balloon), the coefficients would be of comparable magnitude with other configuration data. The lift variation of the Vee balloon is quite unusual, being well approximated by two straight lines.

2-5.4 Lift-to-Drag Ratio

The aerodynamic L/D for the four balloon shapes is presented in Figure 2-13. The barrage, Class C, and Vee balloons show a similar variation of L/D with angle of attack. The L/D is linear with angle of attack at small angles, reaches a maximum at $\alpha \approx 15°$, and steadily decreases with increasing angle of attack.

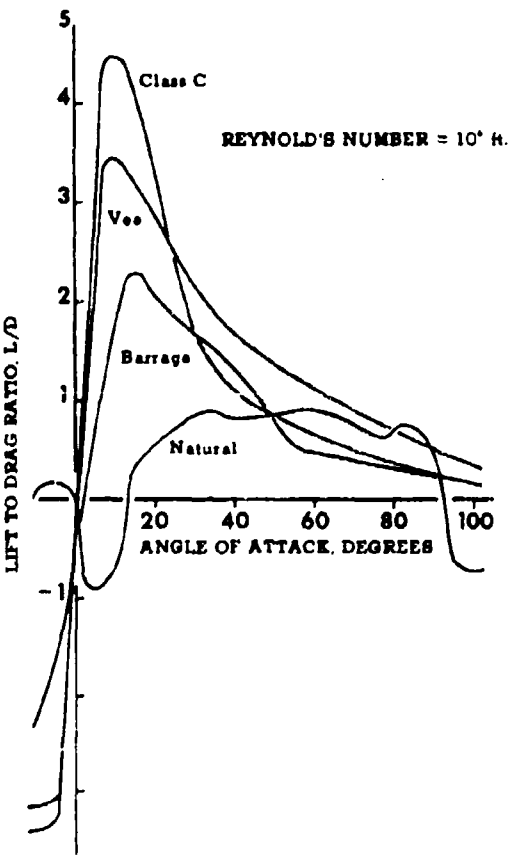

Figure 2-13. Aerodynamic Lift-to-Drag Ratio of Balloons

The natural shape L/D is erratic with small angle of attack. From $\alpha = 30°$ to $\alpha = 90°$, the L/D of the natural shape is essentially independent of angle of attack. In many applications, it is desirable to maximize L/D. The Class C and Vee balloons have advantages over the barrage and natural shape in such applications.

2-6. TETHERED BALLOON APPLICATIONS

In this section, the influence of the longitudinal aerodynamics on the suitability of each balloon as a tethered balloon is discussed.*

2-6.1 Equilibrium Conditions

2-6.1.1 NATURAL SHAPE

A force and moment diagram of the natural shape is given in Figure 2-14.

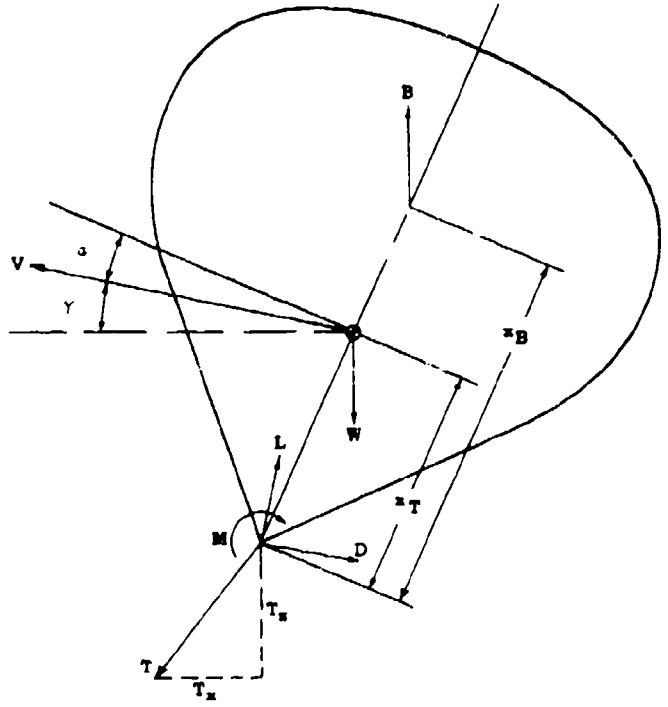

FOR TRANSLATIONAL EQUILIBRIUM:

$$T_x = L \sin\gamma + D \cos\gamma$$
$$T_z = L \cos\gamma - D \sin\gamma + B - W$$

FOR ROTATIONAL EQUILIBRIUM:

$$M + Lx_T \sin\alpha_e - Dx_T \cos\alpha_e + T_x x_T \cos(\alpha_e+\gamma) - T_z x_T \sin(\alpha_e+\gamma) - B(x_B - x_T) \sin(\alpha_e+\gamma) = 0$$

Figure 2-14. Force and Moment Diagram of a Tethered Natural Shape Balloon

*Note that aerodynamic performance is only one of many considerations in the design of a tethered balloon system. Cost, availability, reliability, expected life, tolerance to dynamic loads, and lateral stability are other factors in the selection of a balloon.

The equations for equilibrium in Figure 2-14 can be combined to eliminate cable tension to obtain the following condition for equilibrium:

$$M_V + M_\gamma = 0, \tag{2-1}$$

where

$$M_V = C_m \, 1/2 \rho V_e^2 \forall,$$

$$M_\gamma = Wx_T \sin(\alpha_e + \gamma) - Bx_B \sin(\alpha_e + \gamma).$$

Define the limit angle of attack, α_L, as that for which the aerodynamic pitching moment about the tether point, M_V, equals zero. For the natural shape balloon, $\alpha = \alpha_L$ when $C_m = 0$. From Figure 2-7, $\alpha_L = 51°$ for the natural shape balloon.

Equation (2-1) can be used to obtain the equilibrium angle of attack as a function of velocity and flight path angle. The solution for equilibrium angle of attack is presented in Figures 2-15 and 2-16 for two sizes of natural shape balloon: 250,000 ft^3 and 530,000 ft^3. For example, a level 30-mph wind results in α_e = 11.5° for the 250,000 ft^3 balloon and α_e = 9.5° for the 530,000 ft^3 balloon. Since equilibrium conditions V_e, γ, and α_e are known, cable tensions can be

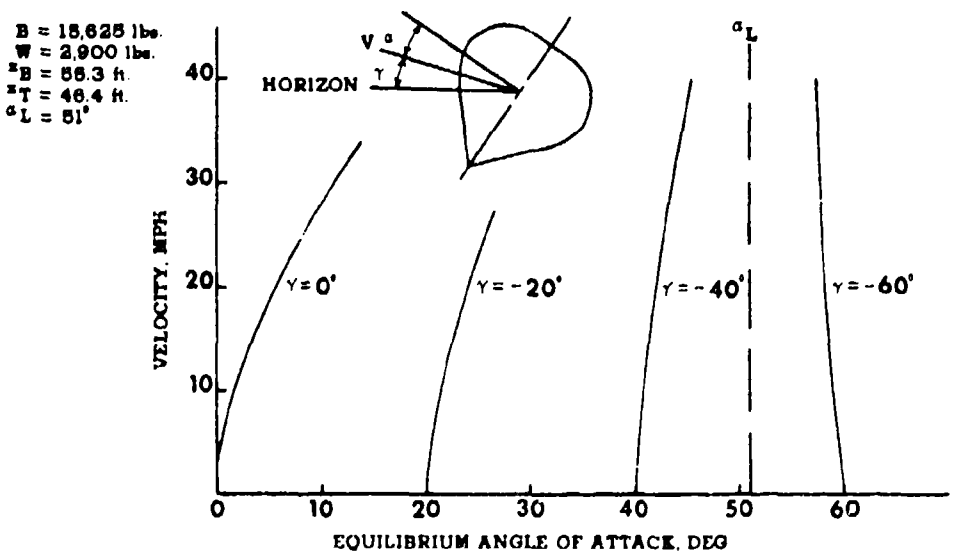

Figure 2-15. Equilibrium Conditions for Tethered Natural Shape, $\forall$ = 250,000 ft^3

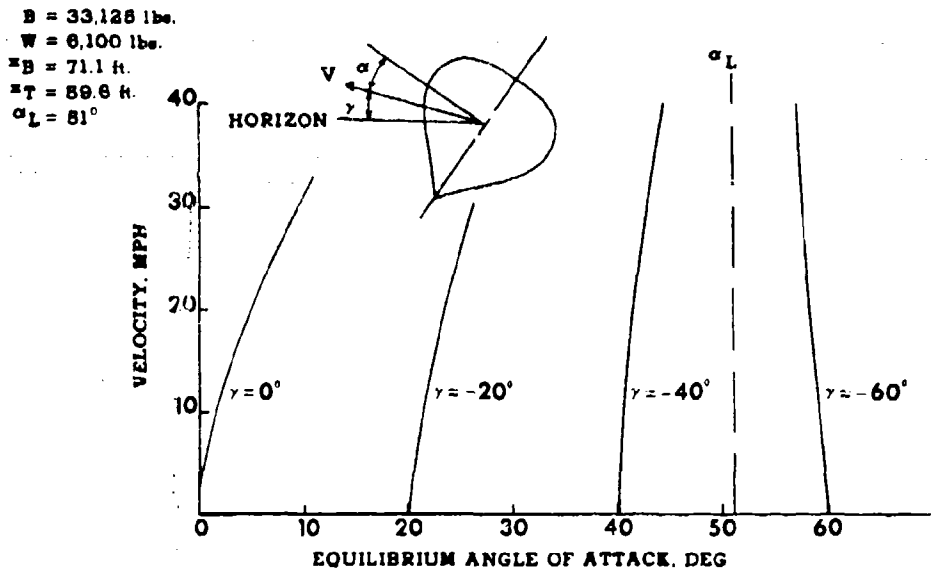

Figure 2-16. Equilibrium Conditions for Tethered Natural Shape, $\Psi = 5{,}000{,}000\ ft^3$

determined using the equations in Figure 2-14. Cable tension for the natural shape tethered balloon in horizontal winds is presented in Figure 2-17.

2-6.1.2 KITE BALLOONS

A force and moment diagram of a kite balloon is given in Figure 2-18. The equations for equilibrium can be combined to eliminate cable tension to obtain the following conditions for equilibrium:

$$M_V + M_\gamma = 0, \tag{2-2}$$

where

$$M_V = C_D \tfrac{1}{2}\rho V_e^2 \Psi^{2/3} [(x_B - x_T)\sin\alpha_e + y_T \cos\alpha_e] + C_m \tfrac{1}{2}\rho V_e^2 \Psi^{2/3},$$

$$+ C_L \tfrac{1}{2}\rho V_e^2 \Psi^{2/3} [(x_B - x_T)\cos\alpha_e - y_T \sin\alpha_e],$$

and

$$M_\gamma = (B - W)[(x_B - x_T)\cos(\alpha_e + \gamma) - y_T \sin(\alpha_e + \gamma)]$$

$$+ W x_B \cos(\alpha_e + \gamma).$$

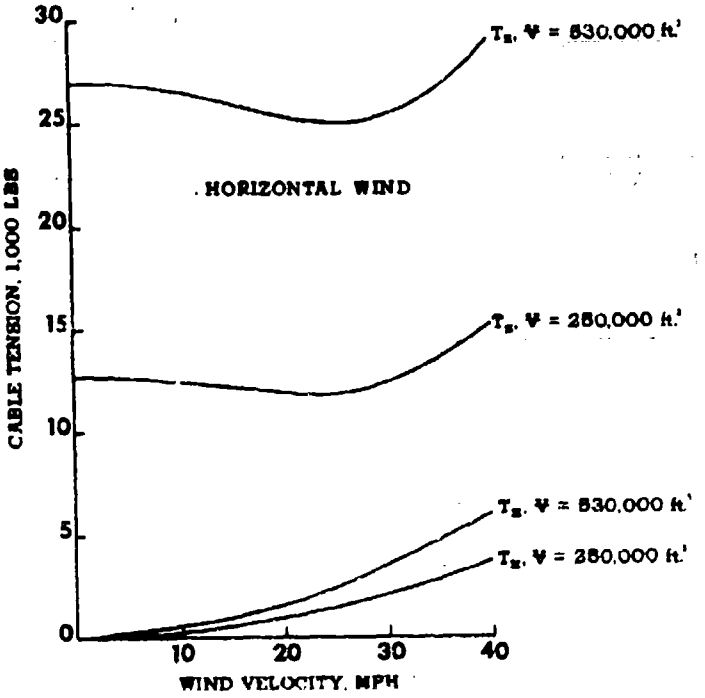

Figure 2-17. Cable Tension in a Tethered Natural Shape Balloon Versus Wind Velocity, $\gamma = 0°$

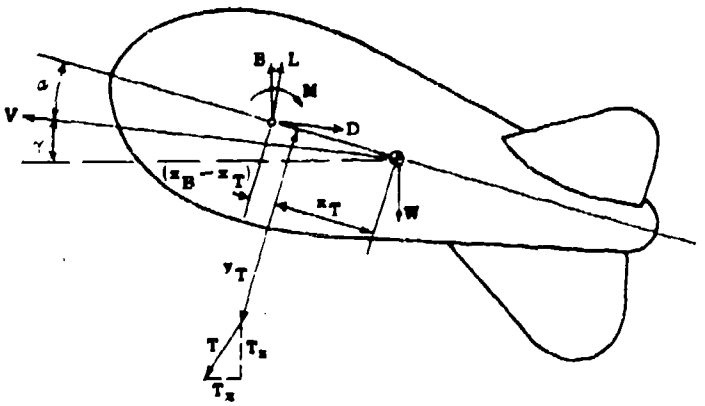

FOR TRANSLATIONAL EQUILIBRIUM:

$$T_x = L \sin\gamma + D \cos\gamma$$

$$T_z = L \cos\gamma - D \sin\gamma + B - W$$

FOR ROTATIONAL EQUILIBRIUM:

$$M + Lx_B \cos\alpha_e + Dx_B \sin\alpha_e + Bx_B \cos(\alpha_e + \gamma) - T_x x_T \cos(\alpha_e + \gamma)$$

$$-T_x y_T \sin(\alpha_e + \gamma) - T_z x_T \sin(\alpha_e + \gamma) + T_z y_T \cos(\alpha_e + \gamma) = 0$$

Figure 2-18. Force and Moment Diagram of a Tethered Kite Balloon

For the natural shape, the apex is the obvious tether point location; for the kite balloon, the tether point location is a design choice.

Select for purposes of discussion a tether point location such that the kite balloon flies level in a calm (Brown and Speed, 1962). The actual tether point location and resultant angle of attack is a design choice influenced by considerations of performance, stability, and survivability in high winds. The effect of tether point location on performance is discussed later in this report; its effect on stability and survivability in high winds is beyond the scope of this report. For level flight in a calm, the tether should be positioned such that:

$$x_T = \frac{B}{(B - W)} x_B. \tag{2-3}$$

Equations (2-2) and (2-3) can be combined to eliminate the longitudinal tether position, x_T, in the mathematical statement of the condition for equilibrium. Therefore,

$$M_V + M_\gamma = 0, \tag{2-4}$$

where

$$M_V = 1/2\, \rho V_e^2 \forall^{2/3} [C_{m_\ell} - \left(\frac{W}{B - W}\right) x_B C_D \sin \alpha_e - \left(\frac{W}{B - W}\right) x_B C_L \cos \alpha_e + y_T C_D \cos \alpha_e - y_T C_L \sin \alpha_e],$$

and

$$M_\gamma = -y_T (B - W) \sin (\alpha_e + \gamma).$$

Equation (2-4) has been used to obtain the equilibrium angle of attack as a function of velocity and flight path angle. The solution for equilibrium angle of attack is presented in Figures 2-19, 2-20, and 2-21 for the barrage, Class C, and Vee balloons, respectively. There are certain general characteristics of these curves:

1. At low velocities, buoyancy effects dominate and $\alpha_e = -\gamma$.
2. At high velocities, aerodynamic effects dominate and $\alpha_e \rightarrow \alpha_{I_\ell}$.
3. More than one equilibrium angle of attack can exist for a given wind speed and flight path (Figure 2-20). The extreme angles of attack correspond to stable equilibriums, and the intermediate angle corresponds to an unstable equilibrium.

4. The importance to the tethered balloon application of the particular value of the limit angle of attack, α_L, is clearly implied.

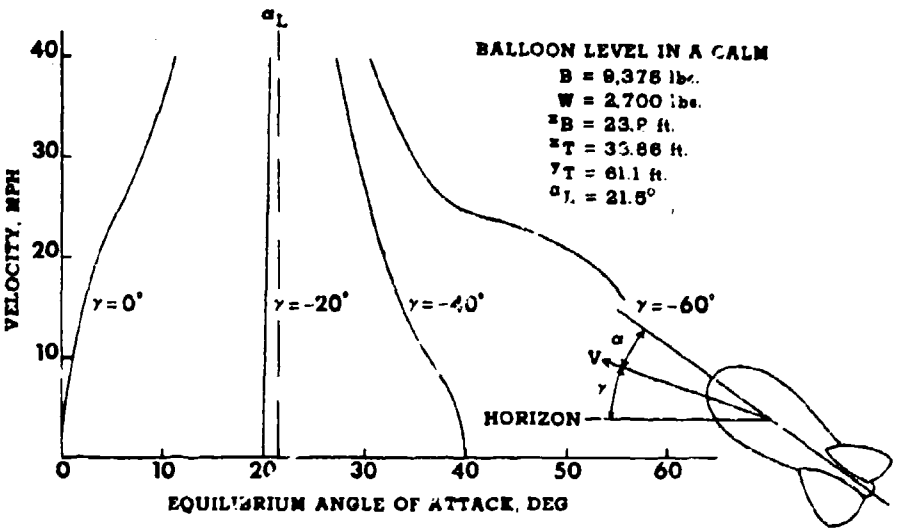

Figure 2-19. Equilibrium Conditions for a Tethered Barrage Balloon $\forall$ = 150,000 ft^3

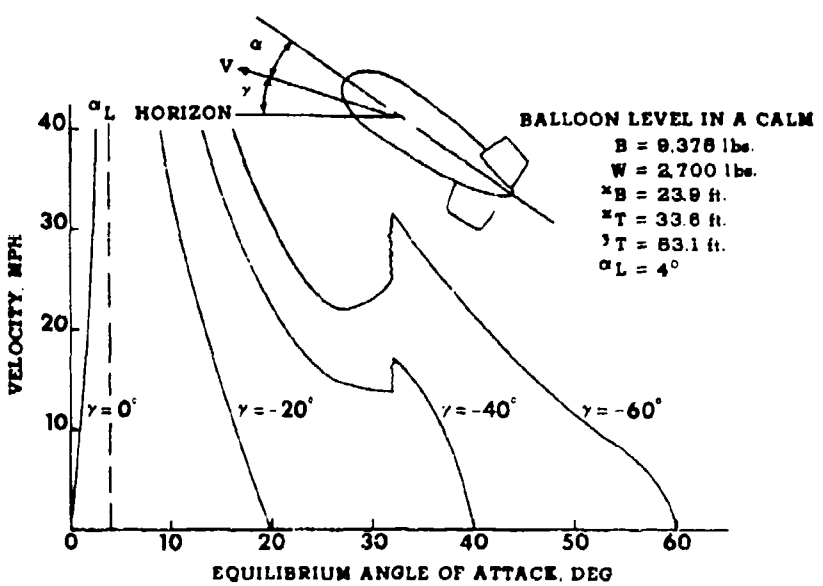

Figure 2-20. Equilibrium Conditions for a Tethered Class C Balloon, $\forall$ = 150,000 ft^3

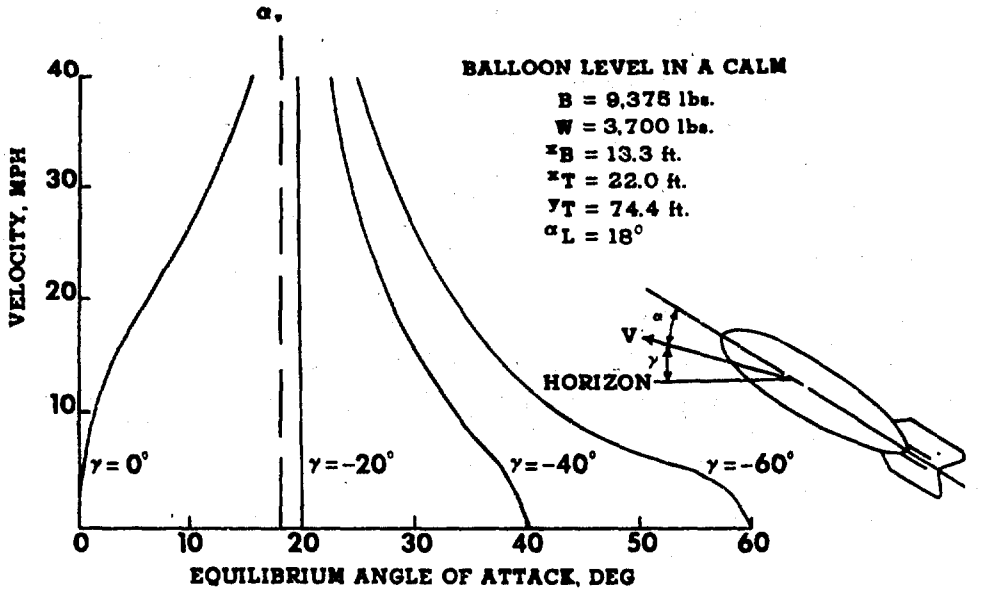

Figure 2-21. Equilibrium Conditions for a Tethered Vee Balloon, $\forall = 150,000\ ft^3$

2-6.2 Effect of Tether Point Location

The designer of the tethered balloon system will want to adjust the parameters at his disposal, normally the location of the tether point, x_T and y_T, to obtain desired performance from the system.

For example: a barrage balloon, $V = 150,000\ ft^3$, is used as a logging balloon for operation at a nominal inhaul speed of 20 mph and a horizontal flight path. How does the lift capability vary with the location of the tether point?

Let T_z be the measure of the lift capability. The plot of T_z versus α for the barrage balloon is shown in Figure 2-22. The angle of attack for maximum lift corresponds to $\alpha = 40°$. At this angle of attack, the horizontal tension is also large and indicates a large power input is required to obtain the maximum lift. By definition, $\alpha = \alpha_{L_o}$ when $M_V = 0$. From Eq. (2-2),

$$C_D [(x_B - x_T) \sin \alpha_L + y_T \cos \alpha_L] + C_m \ell$$

$$+ C_L [(x_B - x_T) \cos \alpha_L - y_T \sin \alpha_L] = 0, \qquad (2\text{-}5)$$

where C_D, C_L, and C_m are all functions of α_L. Since x_T and y_T are both in Eq. (2-5), more than one location of the tether point will satisfy Eq. (2-5). The locus of tether point locations which give a limit angle of attack of 40° is shown in Figure 2-23. The required horizontal position of the tether point is station 47.

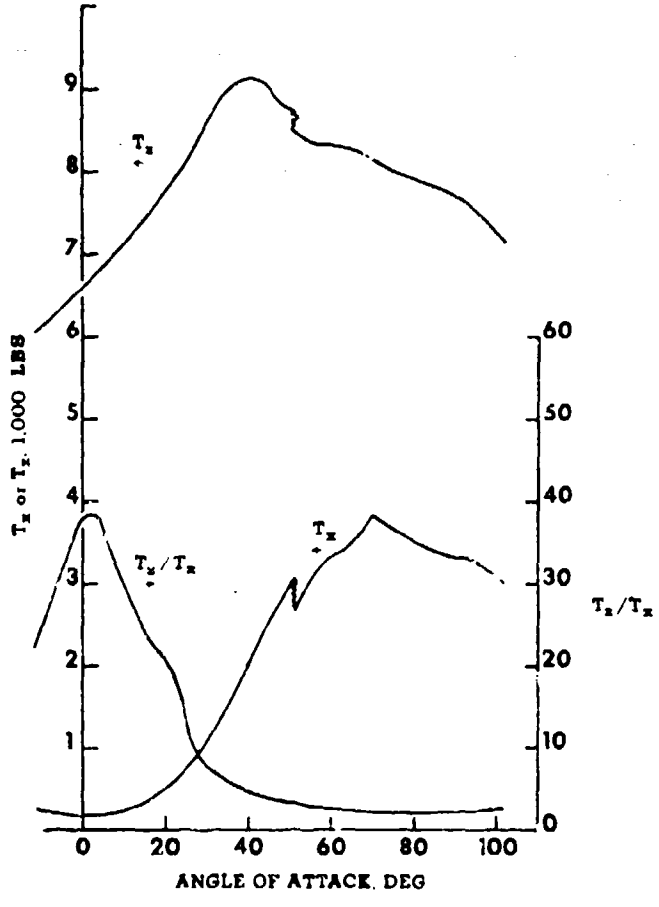

Figure 2-22. Cable Tension of a Tethered Barrage Balloon, $\forall$ = 150,000 ft^3

The vertical location is a matter of convenience. Tether point locations for other limit angles of attack are also shown in Figure 2-23 for α_{l_c} = 10°, 20°, and 30°. In general, as the tether point is located further aft, the limit angle of attack increases.

The balloon attitude in a calm also depends on the tether point location. To fly level with no wind, the tether point must be located at station 32. Forward of station 32, the balloon has a nose down attitude in a calm. Aft of station 32, the balloon has a nose up attitude in a calm.

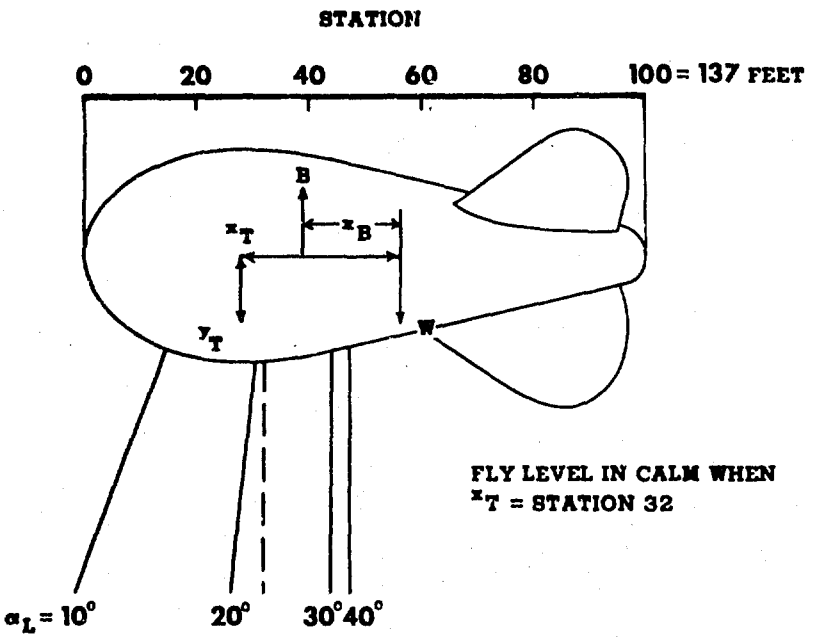

Figure 2-23. Locus of Tether Point Locations to Give a Specified Limit Angle of Attack

2-7. SUMMARY

Wind tunnel tests giving aerodynamic data on three configurations of kite balloons and one design of a natural shape balloon are presented. All four shapes were tested for a wide range of attack angles (-12° to +102°) as typically encountered in balloon logging. These data are needed to design and develop the optimum balloon configuration for use in a balloon logging system.

Principal limitations in the wind tunnel data are the Reynolds Number simulation and representation of a flexible balloon by a rigid model. As a check on the effect of Reynolds Number, a barrage balloon was tested with and without a trip strip, with no change in measured forces. In high winds, deformation of the forward surface of flight test balloons is apparent. Drag force estimates from flight test balloons is apparent. Drag force estimates from flight data normally indicate higher drag than wind tunnel results.

The natural shape exhibits an erratic lift variation with angle of attack. Negative lift occurs between α = -2° to +12°. The kite balloons – barrage, Class C, and Vee – show good qualitative agreement amongst themselves. Each exhibits:

1. A linear lift curve up until stall
2. S-shaped drag curve
3. Minimum drag at alpha near zero
4. A moment curve which is predominantly stabilizing.

Equilibrium conditions of a tethered balloon are presented for each balloon shape. As the relative wind velocity increases, the equilibrium angle of attack approaches the limit angle of attack. The limit angle of attack, by definition, is that for which the aerodynamic pitching moment about the tether point is zero. By developing the relationship between the tether point and the limit angle of attack, it is shown that tethered balloon performance can be substantially controlled by selection of tether point location.

References

Abbott, Ira, H. (1931) Airship Model Tests in the Variable Density Wind Tunnel, NACA Report No. 394.

Brown, I.S.H., and Speed, L.A. (1962) Ballonet Kite Balloons, Design, Construction, and Operation, Royal Aircraft Establishment Report M.E. 24.

Ferguson, W.R. (1965) AFCRL Tethered Balloon Programs, AD 614065, AFCRL Scientific Balloon Workshop Proceedings.

Haak, E.L. (1971) Wind Tunnel Test Results, Family IID Aerodynamically Shaped Balloon, G.T. Schjeldahl Co., Vols. I-V.

Hoerner, Sighard F. (1951) Aerodynamic Drag, published by author.

Menke, James A. (1963) Capabilities of Captive Balloon Systems, AFCRL Scientific Balloon Workshop Proceedings.

Sherburne, Paul A. (1968) Wind Tunnel Tests of Natural Shape Balloon Model, AD 667563, Goodyear Aerospace Corporation.

Snindo, S. (1969) A Wind Tunnel Test of Three Single Hulled Balloons and One Double Hulled Balloon at Extreme Angles of Attack, University of Washington Aeronautical Laboratories Report No. 957-E.

Shindo, S. (1970) Analysis and Discussion of Aerodynamic Characteristics of Balloons Tested in a Wind Tunnel, University of Washington Aeronautical Laboratories Report No. 957-F.

Simonds, M.H. (1963) Low Speed Wind Tunnel Tests on a Kite Balloon Model, Aeronautical Research Council Current Paper No. 643.

Swarthout, Colburn D. (1967) Aerodynamic Forces on Logging Balloons, Master of Science Thesis, University of Washington, Seattle.

Contents

3. Analytical and Experimental Investigation of the Stability of a Balloon Tethered in Wind

L.T. Redd, R.M. Bennett, and S.M. Bland
NASA Langley Research Center
Hampton, Virginia

Abstract

An analytical technique for predicting the stability of a balloon tethered in a steady wind has been developed at Langley Research Center. This technique utilizes computer programs for calculating the stability characteristics of a balloon and for plotting the calculated results. These programs are based on a linearized, stability-derivative type of analysis which includes balloon aerodynamics, buoyancy effects, and static forces resulting from the tether line.

The analytical technique has been applied to a 7.64-meter modified "Class C" shape balloon tethered in steady winds up to 40 m/s. The analytical results obtained compared favorably with experimental data from two tests. This paper briefly describes the analytical technique and presents samples of the analytical and experimental results for the 7.64-meter balloon.

3-1. INTRODUCTION

A tethered balloon is useful for a number of purposes, such as supporting antennas or providing an aerial platform for various measuring instruments. Such operations are often impaired, however, by the occurrence of dynamic instabilities

of the tethered balloon system, especially during strong wind conditions. Although information relating to the stability of towed and tethered bodies, including balloons, has been published (Bairstow et al, 1915 and DeLaurier, 1971; for example), a systematic procedure for the analysis of tethered balloon stability is apparently lacking. In an attempt to fill this need, the Langley Research Center has conducted a general research study aimed at the development of improved techniques for predicting the stability of tethered balloons.

The scope of the above study is indicated by the subjects listed in Figure 3-1. Briefly, this study included the following objectives: (1) derivation of the stability equations for steady wind conditions, (2) adaptation of these equations for use in computer programs to calculate stability characteristics and to plot the result, (3) development of methods for determining derivatives for use in the stability equations (Redd, 1970), and (4) formulation of tow tests to assess the accuracy of the stability analysis. In addition, a trend study was made to determine how the stability boundaries are affected by changes in individual stability parameters.

- STABILITY EQUATIONS
- COMPUTER PROGRAMS
- DERIVATIVES
- TOW TESTS
- TREND STUDIES

Figure 3-1. Important Items in the Langley Tethered Balloon Stability Study

The purpose of this paper is to present highlights of the tethered-balloon stability study conducted at Langley Research Center. A discussion of the assumptions and limitations associated with the stability equations is included, and some typical analytical results are compared with experimental data from the two tests. Samples of the trend studies are also shown.

3-2 SYMBOLS

a	distance along balloon center line from nose to force reference point, meters (see Figure 3-3)
B	buoyancy forces, newtons
C_D	drag coefficient, $\frac{D}{q_\infty S}$
$\mathcal{L}$	balloon geometric center line (see Figures 3-2 and 3-3)
C_L	lift coefficient, $\frac{L}{q_\infty S}$
C_ℓ	rolling-moment coefficient, $\frac{\ell}{q_\infty S\bar{c}}$
C_m	pitching-moment coefficient, $\frac{M}{q_\infty S\bar{c}}$
C_n	yawing-moment coefficient, $\frac{N}{q_\infty S\bar{c}}$

C_Y	side-force coefficient, $\frac{Y}{q_\infty S}$
$\bar{c}$	balloon length, meters
D	aerodynamic drag force, newtons
d_c	tether cable diameter, meters
h_{br}, ℓ_{br}	components of distance from force reference point to center of buoyancy, meters (see Figure 3-3)
h_{cg}, ℓ_{cg}	components of distance from force reference point to center of mass, meters (see Figure 3-3)
h_{k_1}, h_{k_2}	see Eq. (3-A3)
h_{sr}, ℓ_{sr}	components of distance from force reference point to center of gravity of balloon structure, meters (see Figure 3-3)
I_x, I_y, I_z	rolling, pitching, and yawing moments of inertia, respectively, about balloon center of mass, in stability axis system (including aerodynamic apparent inertias), $kg \cdot m^2$
I_{xx}, I_{yy}, I_{zz}	rolling, pitching, and yawing moments of inertia, respectively, about balloon center of mass, in body-reference principal-axis system (including aerodynamic apparent inertia), $kg \cdot m^2$
I_{xz}	product of inertia about balloon center of mass, in stability axis system (including aerodynamic apparent inertia), $kg \cdot m^2$
i	$\sqrt{-1}$
k_{xx}, k_{xz} k_{zx}, k_{zz}	longitudinal tether cable spring constants in earth-fixed axis system, N/m [see Eq. 3-A4) and Neumark (1961)]
k_{yy}	lateral tether cable spring constant in earth-fixed axis system, N/m [see Eq. (3-A4) and Neumark (1961)]
L	aerodynamic lift force, newtons
L, M, N	rolling, pitching, and yawing moments about the x, y, and z axes, respectively, N-m
ℓ	tether cable length, meters
ℓ_{br}	component of distance from force reference point to center of buoyancy
ℓ_{tr}, t_{tr}	components of distance from force reference point to attachment point of tether line, meters (see Figure 3-3)
M_{s_1}, M_{s_2}	see Eq. (3-A3)
m_T	combined mass of balloon structure and inflation gas, kg
m_x, m_y, m_z	masses of balloon in stability axis system (including aerodynamic apparent masses), kg see Eq. (3-A3)

$m_{x,a}$, $m_{y,a}$, $m_{z,a}$	aerodynamic apparent masses associated with balloon accelerations along principal body axes, kg
p, q, r	perturbation rolling, pitching, and yawing rates about x, y, and z axes, respectively, rad/s
q_∞	dynamic pressure of steady wind, $\rho V^2/2$, N/m^2
S	characteristic area of balloon, $V_B^{2/3}$, m^2
T_0, T_1	tension at lower and upper ends of tether cable, newtons (see Figure 3-2)
t	time, seconds
u	perturbation velocity of balloon along x axis, m/s
$\hat{u}$	u/V
V	steady wind velocity, m/s
V_B	volume of balloon gas bag, m^3
W_s	structural weight of balloon (including weight of test instruments and payload attached to balloon), newtons
w_c	tether cable weight per unit length, N/m
X, Y, Z	external forces acting on balloon along x, y, and z axes, respectively, newtons
x, y, z	coordinate distances in stability axis system, meters (see Figure 3-2)
α	perturbation angle of attack of x axis
α_o	balloon angle of attack at trim
β	angle of sideslip
γ_0, γ_1	angles between horizontal and tether cable at lower and upper ends, respectively (see Figure 3-2)
η	real part of characteristic root of stability equations, damping parameter, 1/s
Θ, Φ, Ψ	total Euler angles of pitch, roll, and yaw, respectively (Etkin, 1959)
θ, ϕ, ψ	perturbations of Θ, Φ, and Ψ, respectively
λ	characteristic root of stability equation, $\lambda = \eta + i\omega$, 1/s
ρ	atmospheric density, kg/m^3
ω	imaginary part of characteristic root of stability equations, circular frequency, rad/s

Stability derivatives are indicated by subscript notations:

$$C_{L_\alpha} = \frac{\partial C_L}{\partial \alpha}, \quad C_{\ell_p} = \frac{\partial C_\ell}{\partial \frac{pc}{2V}}, \text{ etc.}$$

Subscripts:

R pertaining to force reference point (see Figure 3-3).

3-3. ANALYTICAL CONSIDERATIONS

3-3.1 General Comments and Assumptions

The stability analysis summarized in this paper is for a balloon tethered in a steady wind as shown in Figure 3-2. The analysis is based on the linearized stability equations such as developed by Etkin (1959) for conventional airplanes;

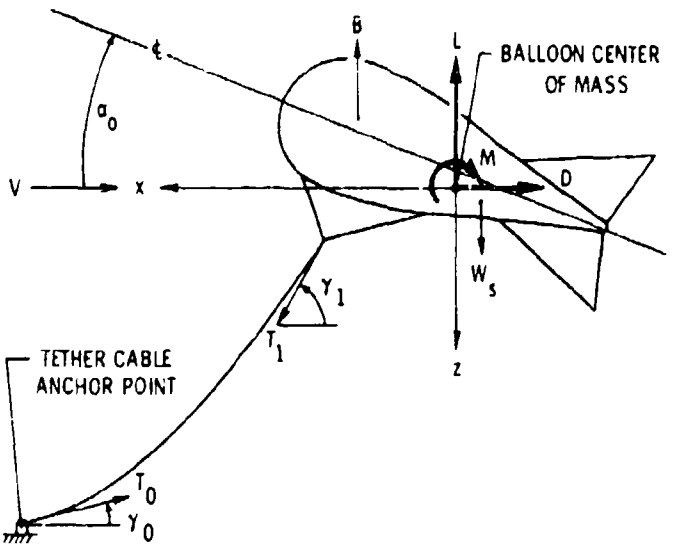

Figure 3-2. Tethered Balloon System in the Steady-Flight Trimmed Condition

however, these equations are modified to include the tether cable forces, buoyancy forces, and the aerodynamic apparent mass. Furthermore, it is assumed that the tether cable anchor point (Figure 3-2) is fixed relative to the earth and that the balloon motion consists of small perturbations about a steady-flight reference condition.

The mathematical model used in the present analysis is also subject to the following additional assumptions:

1. The balloon and bridle form a rigid system whose motions can be completely described with six degrees of freedom.

2. The tether cable is flexible, but inextensible, and has negligible inertia compared to that of the balloon.

3. The cable weight and drag normal to the cable are used in determining the static cable forces and the equilibrium shape of the cable. The cable spring constants (such as k_{xx} and k_{xz}) are determined from the cable shape using the analysis of Neumark (1961).

4. The equations of motion are referenced to the center of mass of the balloon. (The balloon mass includes the mass of the balloon structure, the buoyant gas inside the balloon, and the apparent air mass associated with the balloon accelerations; hence, the balloon mass center is at a different location on the balloon than the structural center of gravity; see Figures 3-2 and 3-3.)

5. There are four kinds of external forces acting on the balloon: namely, aerodynamic forces, tether cable forces, buoyancy forces, and gravity forces (Figure 3-2).

6. The balloon is symmetric laterally and has yaw, roll, and sideslip angles equal to zero when it is in the reference steady-flight trimmed condition.

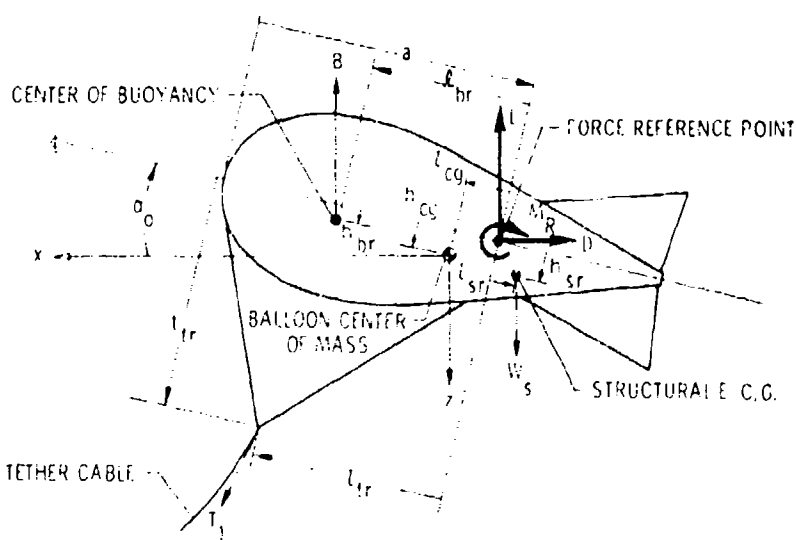

Figure 3-3. Sketch of the Balloon Identifying Pertinent Dimensional Relationships. All arrows are pointing in the positive sense

7. The steady wind velocity (V) is parallel to the horizon; hence, the x-stability axis is also horizontal in the reference trimmed condition [Figure 3-2 and Etkin (1959)].

The preceding assumptions are applicable for most types of tethered balloon systems, especially for those which have relatively light tether cables. These assumptions also lead to the decoupling of the longitudinal and lateral equations of motion.

3-3.2 Stability Analysis

3-3.2.1 STABILITY EQUATIONS

The stability and equilibrium equations used in the tethered balloon analysis are presented in Appendix A for convenience. These equations were derived by applying the assumptions and modifications given in the preceding paragraphs to an analysis similar to that given by Etkin (1959).

The mass and inertia terms in the stability equations include the apparent mass of air associated with the balloon accelerations [see Eq. (3-A3)]. In contrast with conventional airplane analysis, the balloon analysis must include the apparent mass because it accounts for a significant part of the total mass of the balloon system.

The coordinate system and many of the lengths, forces, and moments associated with the stability equations are shown in Figures 3-2 and 3-3. Note in Figure 3-3 that the forces are referenced to an arbitrary fixed point on the balloon center line (that is, force reference point) which is not generally located at the balloon mass center. The reason the forces are treated in this manner is that both the mass of the buoyant gas and the apparent mass are functions of atmospheric density and, hence, the location of the balloon mass center changes with variations in the balloon altitude. The balloon mass center also changes as the payload position and weight are varied. Thus, in solving the stability equations, it is more convenient to use force inputs to the computer programs which are referenced to a fixed point on the balloon rather than to a variable mass center. The computer programs automatically transfer the forces from the reference point to the mass center during the solution of the stability equations.

Although the stability equations shown in Appendix 3-A are derived by assuming that the balloon is tethered in a steady wind to an earth-fixed anchor point, these stability equations are also valid for the balloon towed at a constant velocity over a horizontal surface.

3-3.2.2 STABILITY CHARACTERISTICS

The longitudinal and lateral stability characteristics of the balloon are determined independently from Eqs. (3-A1) and (3-A2) in a manner similar to that used in conventional airplane stability analysis as found in Etkin (1959). Briefly, this method involves the assumption that the stability equations have solutions which are always exponential in form. For example, a typical variable such as θ is of the form $\theta = \bar{\theta} e^{\lambda t}$, where $\bar{\theta}$ is a complex constant. When these assumed solutions are substituted into the longitudinal- and lateral-stability equations and the determinates of the resulting coefficients are set to zero, then solutions for the characteristic root (λ) can be obtained.

Solving Eqs. (3-A1) and (3-A2) in the above manner gives six characteristic roots for both the longitudinal and lateral cases. These roots may appear as complex conjugate pairs (that is, $\lambda = \eta \pm i\omega$) for the oscillatory modes of motion or as pure real numbers (that is, $\lambda = \eta$) for the aperiodic modes. Thus, in each of the longitudinal and lateral cases, it is possible for the balloon to exhibit from three to six modes of motion, depending on whether the roots are complex conjugate pairs or real. Regardless of the number of modes, however, the balloon system is stable when $\eta < 0$ for all modes, neutrally stable when $\eta = 0$ for any mode, and unstable when $\eta > 0$ for any mode.

Computer programs based on Eqs. (3-A1) and (3-A2) were developed for calculating the above stability characteristics and plotting the results. Some typical results from these programs are given in Section 3-5 of this paper.

One principal advantage of the present analysis is that it uses conventional-analytical stability methods to obtain the characteristic roots in terms of the wind velocity. The analyses of DeLaurier (1971, 1972), on the other hand, requires unconventional methods and also a considerable amount of effort to obtain the desired stability roots. These difficulties with the latter analysis result from including the tether cable dynamics in the stability equations. Hence, unless the tether cable dynamics are of appreciable significance, the present stability analysis is the preferable method because of the ease in obtaining solutions to the stability equations.

3-4. TOW TESTS

3-4.1 Objective and Requirements

The primary purpose of the tow tests was to check the validity of the stability analysis by comparing experimentally determined stability boundaries and periods of balloon oscillatory motions with those predicted analytically. To accomplish

this objective, it was necessary to use a long smooth runway in an area where winds were relatively calm. Therefore, the 2-mile skid strip at Patrick Air Force Base, Florida, was used for the tow tests.

3-4.2 Description of the Balloon and Tow-Test Apparatus

The test balloon is shown tethered to the tow truck in Figure 3-4; the balloon's geometric, mass, inertia, and aerodynamic properties are presented in Table 3-1.

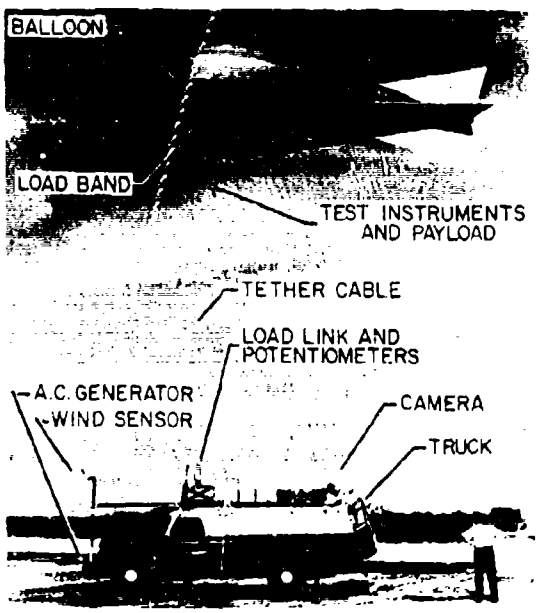

Figure 3-4. Test Balloon and Tow Truck

The basic shape of the balloon is similar to the so-called Class "C" balloon configuration, with the exception that the aft section is conical and the nose is nearly spherical. The essential components of the balloon consist of a helium gas bag constructed of Nylon and Saran, and a "rigid" (that is, not inflated) tail fin assembly constructed of Mylar and balsa. A load band is also attached to the lower portion of the bag which permits variation in the bridle attachment points and, hence, makes it possible to change the balloon trim angle of attack. In a paper, Redd (1970) presents some of the techniques used to determine the aerodynamic relationships listed in Table 3-1, and also gives a more detailed description of the balloon.

Table 3-1. Values of the Stability Parameters for the 7.64-Meter Balloon with Instruments and Payload

Aerostatic Properties:	
Force reference point (Figure 3-3)	
a	4.63 m
Atmospheric density ρ	1.225 kg/m^3
Bridle confluence point (Figure 3-3)	
ℓ_{tr}	3.44 m
ℓ_{tr}	3.82 m
Buoyancy force B	190.4 N
Center of buoyancy	
ℓ_{br}	2.15 m
h_{br}	0. m
Reference area S	7.04 m^2
Reference length $\bar{c}$	7.64 m
Structural center of gravity	
ℓ_{sr}	-0.35 m
h_{sr}	0.38 m
Structural weight W_s	108.1 N
Volume V_B	19.00 m^3
Dynamic Masses and Moments of Inertia:	
Apparent air mass (at $\alpha_o = 0$)	
$m_{x,a}$	5.11 kg
$m_{y,a} = m_{z,a}$	23.93 kg
Center of mass (includes apparent mass)	
ℓ_{cg}	1.10 m
h_{cg}	0.11 m
Mass of balloon structure and inflation gas m_T	14.24 kg
Total moments of inertia (at $\alpha_o = 0$)	
I_{xx}	16.12 kg·m^2
I_{yy}	170.83 kg·m^2
I_{zz}	164.04 kg·m^2

Table 3-1. Values of the Stability Parameters for the 7.84-Meter Balloon with Instruments and Payload (Cont)

Tether Cable Parameters:	
Diameter d_c	0.014 m
Length ℓ	61.0 m
Weight per unit length w_c	0.343 N/m
Normal drag coefficient C_{D_c}	1.17
Aerodynamic Derivatives:	
Derivatives are specified about the force reference point (see Figure 3-3).	
C_L	$0.82(\alpha_o - 0.023) - 5.02(\alpha_o - 0.023)^3 + 111.4(\alpha_o - 0.023)^5$
C_{L_α}	$0.82 - 15.06(\alpha_o - 0.023)^2 + 557.0(\alpha_o - 0.023)^4$
$C_{L_{\dot\alpha}}$	0.089
$C_{L_{q,R}}$	0.685
C_D	$0.0487 + 186.2(\alpha_o - 0.023)^6$
C_{D_α}	$1117.2(\alpha_o - 0.023)^5$
$C_{m,R}$	$-0.0106 + 0.1435\ \alpha_o$
$C_{m_{\alpha,R}}$	0.1435
$C_{m_{\dot\alpha,R}}$	-0.026
$C_{m_{q,R}}$	-0.189
C_{Y_β}	-0.82
$C_{Y_{\dot\beta}}$	-0.089
$C_{Y_{p,R}}$	$0.494 \sin \alpha_o$
$C_{Y_{r,R}}$	0.685
$C_{\ell_{\beta,R}}$	$-0.1435 \sin \alpha_o$
$C_{\ell_{\dot\beta,R}}$	0.
$C_{\ell_{p,R}}$	-0.0237

Table 3-1. Values of the Stability Parameters for the 7.64-Meter Balloon with Instruments and Payload (Cont)

$C_{\ell_{r,R}}$	$-0.178 \sin \alpha_o$
$C_{n_{\beta,R}}$	-0.1435
$C_{n_{\dot{\beta},R}}$	0.026
$C_{n_{p,R}}$	$-0.0641 \sin 2\alpha_o$
$C_{n_{r,R}}$	-0.189

Additional test items shown in Figure 3-4 include a load link used to measure cable tension and potentiometers used for measuring cable inclination angles. The anemometer (wind sensor) shown in the figure was needed to measure the speed and sideslip angle of the tow vehicle relative to the air. Finally, the instruments shown rigidly suspended beneath the balloon were used for measuring pitching and rolling motions of the balloon.

Outputs from the above instruments were recorded on a strip-chart recorder located inside the truck, and the motions of the balloon were recorded by a movie camera mounted on the truck top. Power for the instrumentation, camera, and strip-chart recorder was supplied by an ac generator also shown in the figure.

There were several features of the test equipment and procedures which limited the usefulness of the tow tests. The primary difficulty was that the maximum practical length of tether cable which could be conveniently used was about 61 meters. The reason for this was that the tow cable (consisting of the main tow line, four shielded electrical cables, a small plastic tube, and an extra safety line) would have been too frequently entangled if longer lengths were tried. Also, since some of the primary test data came from the movie film, the maximum length of the tow cable had to be limited to provide good film resolution of the balloon and still allow the use of a wide-angle lens on the movie camera. Additional problems which limited the usefulness of the tests were that the maximum speed of the tow truck was 29 m/s, and the tests were not conducted when surface winds were greater than 2.5 m/s. In spite of these limitations, however, most of the objectives and requirements of the tow tests were achieved.

3-5. RESULTS AND DISCUSSION

3-5.1 Presentation of Results

Typical results of the stability analysis and the tow tests are shown in Figures 3-5 through 3-9. Figure 3-5 shows the variations in the longitudinal-characteristic stability roots (η and ω) with changes in wind velocity; Figures 3-6 and 3-7 illustrate a longitudinal and a lateral mode of motion of the balloon at various velocities; and Figures 3-8 and 3-9 show trend studies which indicate the effects of changes in tether cable length ℓ and directional stability derivative $C_{n\beta, R}$ on the instability velocities.

3-5.2 Modes of Motion

The calculated results shown in Figure 3-5 indicate that the balloon has three oscillatory longitudinal modes of motion at low velocities; however, mode 1 splits into two real nonoscillatory modes ($\omega = 0$) at about 13 m/s. The results also show that the calculated value for mode 2 becomes unstable above about 25 m/s since parameter η becomes positive.

In comparing the calculated results with those measured from the tow tests, it appears from Figure 3-5 that the measured frequencies (ω) and the velocity at

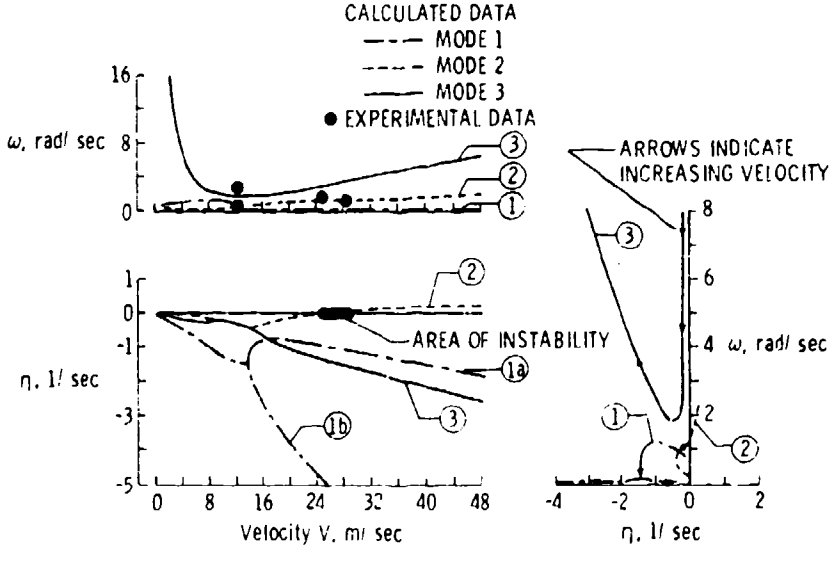

Figure 3-5. Effect of Wind Speed on ω and η for the Longitudinal Case ($\alpha_o = 6°$, $\ell = 51$ m)

the point of instability agree well with those calculated for mode 2. Also, oscillatory balloon motions associated with mode 3 were observed during the tow tests at about 13 m/s.

Note in Figure 3-5 that parameters ω and η are plotted in root locus form, with velocity as the varying parameter. This alternate form for presenting stability data is included for convenience in showing the relationship between ω and η.

Although the results presented in Figure 3-5 are for the balloon configuration for which properties are given in Table 3-1, other balloon configurations were examined in the analysis and tow tests. The results for these configurations are not shown, but were similar to those given in Figure 3-5. The comparison between the measured and calculated points of instability, however, were not quite as good in many cases as that shown in Figure 3-5.

As a means of illustrating typical calculated longitudinal and lateral modes of motion for the balloon, an outline of the tethered balloon and its center of mass are drawn for a sequence of time intervals in Figures 3-6 and 3-7. These plots represent an isolated balloon mode of motion for one cycle of free oscillation at several different velocities. Note that the longitudinal mode of motion shown in Figure 3-6 has characteristic roots η and ω which correspond to those of mode 2 in Figure 3-5.

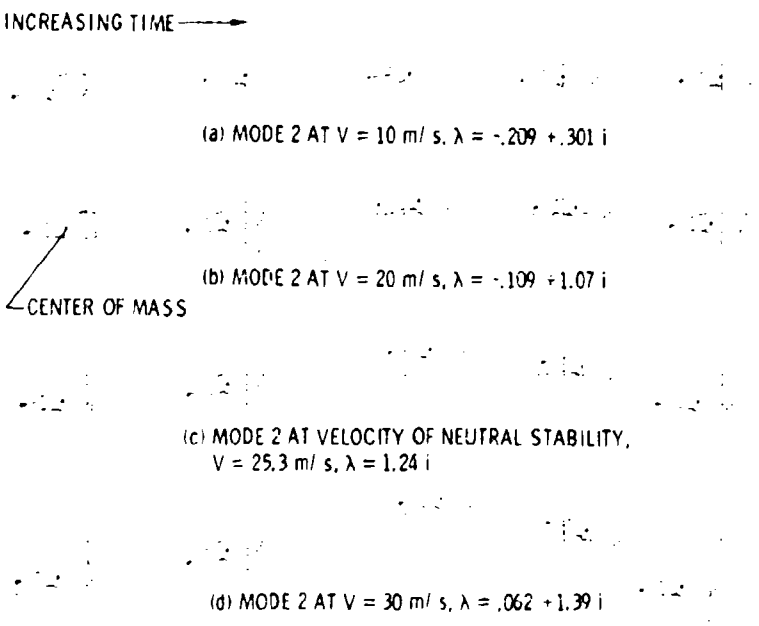

Figure 3-6. Balloon Motion for Longitudinal Mode 2. One cycle of motion is shown for each velocity indicated

For the sake of brevity, however, the lateral characteristic roots of the mode of motion shown in Figure 3-7 are not plotted as a function of velocity in this paper.

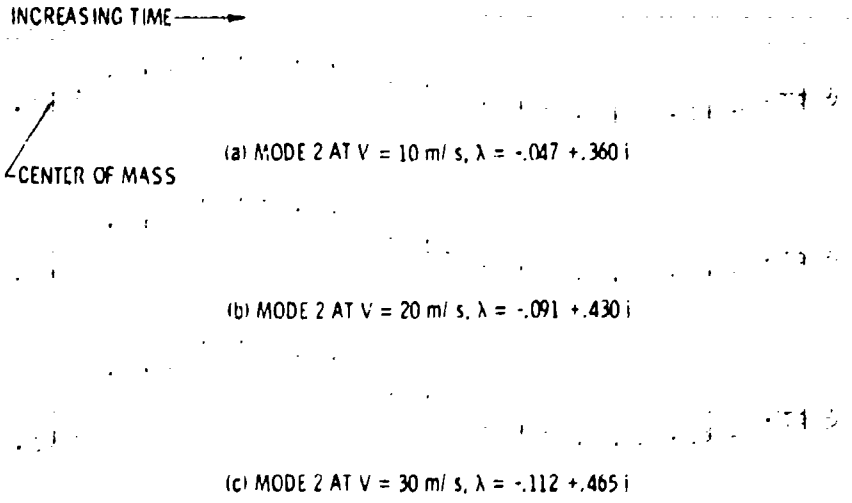

Figure 3-7. Balloon Motion for Lateral Mode 2. One cycle of motion is shown for each velocity indicated

Note that Figures 3-6 and 3-7 do not represent transient response motions in the usual sense which would involve a full description of inputs, initial conditions, and all modes of motion. The purpose of these figures is simply to illustrate the character of a single mode. However, it should be mentioned that the observed behav of the balloon at high tov velocities agrees with the modes of motion illustr Figure 3-6. This result is not surprising since mode 2 is lightly damped or unstable at these velocities and, hence, dominates the motions of the balloon.

(A motion picture showing examples of all the computer-generated modes of motion represented in Figure 3-5, and also the lateral modes of motion, was presented in the oral version of this paper.)

3-5.3 Trend Study

Typical results from the trend study are shown in Figures 3-8 and 3-9. These figures represent only a small portion of the various stability parameters which were considered in the study. Parameters ℓ and $C_{n_{\beta,R}}$ are presented, however, because they have a major effect on the stability boundaries. The data presented in the two figures are for the balloon configuration given in Table 3-1 except for variables ℓ in Figure 3-8 and $C_{n_{\beta,R}}$ in Figure 3-9.

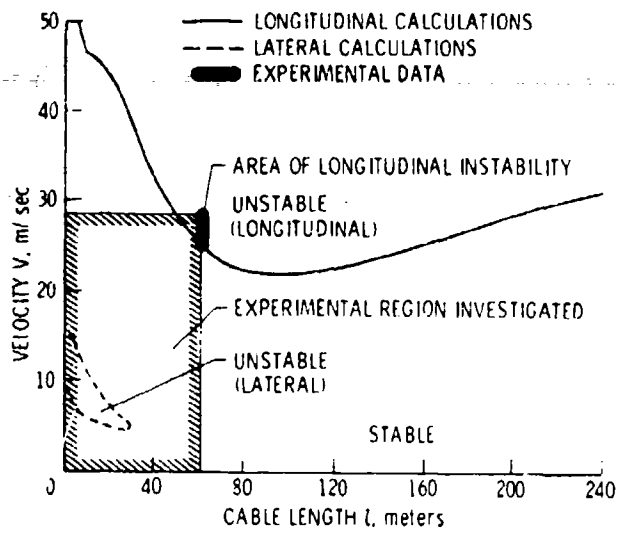

Figure 3-8. Effect of Cable Length on Instability Speed

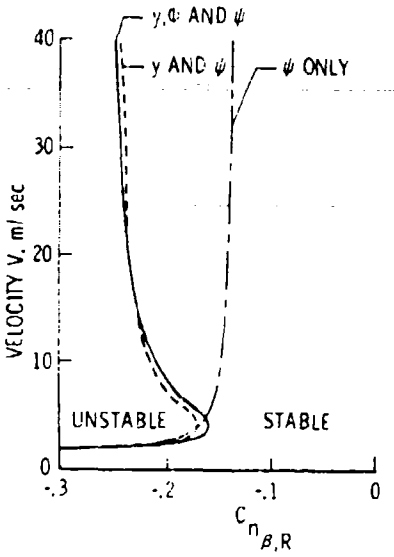

Figure 3-9. Balloon Stability Boundaries for Various Lateral Degrees of Freedom as a Function of Wind Velocity and $C_{n_{\beta,R}}$

The calculated results shown in Figure 3-8 indicate that the balloon has a region of instability for each of the longitudinal and lateral cases. Although no divergent lateral oscillations were measured during the tow tests, large lateral oscillations of limited amplitude were observed when the towing speeds and tether cable lengths were within the range of values for which lateral instability is predicted. Based on this result, it is apparent that the calculated lateral stability data are slightly conservative. Possible reasons for this minor discrepancy between the measured and calculated lateral results are that the dynamics of the tether cable were not included in the analysis, and some of the aerodynamic derivatives used in the analysis may not have been very accurate.

The experimental results shown in Figure 3-8 confirm the calculated longitudinal instability boundary, at least within the region of the tow-test capabilities. Additional experimental data along this boundary could not be obtained because of the limitations of the test equipment. The balloon was towed at velocities ranging from 3 to 29 m/s using tether cable lengths of 5, 33, and 61 meters. No longitudinal or lateral instabilities were found, except as noted.

The significant result shown in Figure 3-9 is that the roll degree of freedom (ϕ) can be eliminated from the stability Eq. (3-A2) without affecting the stability

results appreciably. Also note that the values of C_{n_β} shown in Figure 3-9 are specified about the "force reference point" (see Figure 3-3) instead of the balloon mass center. Thus, C_{n_β} can be negative and the balloon is still stable. When C_{n_β} is transferred to the mass center, it can have slightly negative or destabilizing values and the balloon is still marginally stable. For good lateral stability, however, it would appear that C_{n_β} at the mass center should be positive.

3-6. CONCLUDING REMARKS

A summary of a tethered balloon stability analysis conducted at NASA Langley Research Center has been presented. The analysis was applied to a 7.64-meter balloon tethered in a steady wind and the results were compared with data from tow tests. On the basis of this comparison, it is concluded that the analysis gives good predictions for the frequencies, modes of motion, and instability velocities of a tethered balloon, at least for the configuration and range of parameters studied.

References

Bairstow, L., Relf, E. F., and Jones, R. (1915) The Stability of Kite Balloons: Mathematical Investigation, Advisory Committee for Aeronautics, Reports and Memorandum, No. 208.

DeLaurier, James D. (1971) A First Order Theory for Predicting the Stability of Cable Towed and Tethered Bodies Where the Cable has a General Curvature and Tension Variation, Von Karman Institute Technical Note 68.

DeLaurier, James D. (1972) A Stability Analysis of Cable-Body Systems Totally Immersed in a Fluid Stream, NASA CR-2021.

Etkin, Bernard (1959) Dynamics of Flight, John Wiley and Sons, Inc., New York.

Neumark, S. (1961) Equilibrium Configurations of Flying Cables of Captive Balloons, and Cable Derivatives for Stability Calculations, British A. R. C., R. & M. No. 3333.

Redd, L. Tracy (1970) A Towing Technique for Determining the Aerodynamic Forces on Tethered Balloons, Presented at Sixth AFCRL Scientific Balloon Symposium, Portsmouth, New Hampshire.

Appendix A

Stability Equations

The working form of the stability and trim equations used in the tethered balloon analysis are presented in this appendix.

3-A1. LONGITUDINAL EQUATIONS OF MOTION

X-force:

$$\ddot{x} + \left[\frac{\rho VS}{2m_x}\left(2C_D + C_{D_{\hat{u}}}\right)\right]\dot{x} + \left[\frac{k_{xx}}{m_x}\right]x + \left[\frac{\rho VS}{2m_x}\left(C_{D_\alpha} - C_L\right)\right]\dot{z} + \left[\frac{k_{xz}}{m_x}\right]z + \left[\frac{k_{x\theta}}{m_x} + \frac{\rho V^2 SC_{D_\alpha}}{2m_x}\right]\theta = 0,$$

Z-force:

$$\left[\frac{\rho VS}{2m_z}\left(2C_L + C_{L_{\hat{u}}}\right)\right]\dot{x} + \left[\frac{k_{zx}}{m_z}\right]x + \ddot{z} + \left[\frac{\rho VS}{2m_z}\left(C_{L_\alpha} + C_D\right)\right]\dot{z} + \left[\frac{k_{zz}}{m_z}\right]z + \left[\frac{\rho V\bar{S}\bar{c}}{4m_z}\left(C_{L_{\dot{\alpha}}} + C_{L_q}\right)\right]\dot{\theta} + \left[\frac{k_{z\theta}}{m_z} + \frac{\rho V^2 SC_{L_\alpha}}{2m_z}\right]\theta = 0,$$

Pitching moment:

$$- \left[\frac{\rho V S\bar{c}}{2I_y}\left(2C_m + C_{m_{\hat{u}}}\right)\right] \dot{x} \left[\frac{k_{\theta x}}{I_y}\right] x - \left[\frac{\rho S\bar{c}^2}{4I_y} C_{m_{\dot{\alpha}}}\right] \ddot{z} - \left[\frac{\rho V S\bar{c}}{2I_y} C_{m_\alpha}\right] \dot{z}$$

$$+ \left[\frac{k_{\theta z}}{I_y}\right] z + \ddot{\theta} - \left[\frac{\rho V S\bar{c}^2}{4I_y}\left(C_{m_{\dot{\alpha}}} + C_{m_q}\right)\right] \dot{\theta}$$

$$+ \left[\frac{M_{s_1}}{I_y} - \frac{\rho V^2 S\bar{c}}{2I_y} C_{m_\alpha} + \frac{k_{\theta\theta}}{I_y}\right]\theta = 0. \qquad (3\text{-A1})$$

The dot over the variable indicated d/dt with t in seconds.

3-A2. LATERAL EQUATIONS OF MOTION

Y-force:

$$\ddot{y} - \left[\frac{\rho V S}{2m_y} C_{Y_\beta}\right] \dot{y} + \left[\frac{k_{yy}}{m_y}\right] y - \left[\frac{\rho V S\bar{c}}{4m_y} C_{Y_p}\right] \dot{\phi} + \left[\frac{k_{y\phi} - qSC_L}{m_y}\right]\phi$$

$$+ \left[\frac{\rho V S\bar{c}}{4m_y}\left(C_{Y_{\dot{\beta}}} - C_{Y_r}\right)\right] \dot{\psi} + \left[-\frac{qS\left(C_{Y_\beta} + C_D\right) + k_{y\psi}}{m_y}\right]\psi = 0.$$

Rolling moment:

$$- \left[\frac{\rho S\bar{c}^2}{4I_x} C_{\ell_{\dot{\beta}}}\right] \ddot{y} - \left[\frac{\rho V S\bar{c}}{2I_x} C_{\ell_\beta}\right] \dot{y} + \left[\frac{k_{\phi y}}{I_x}\right] y + \ddot{\phi} - \left[\frac{\rho V S\bar{c}^2}{4I_x} C_{\ell_p}\right] \dot{\phi}$$

$$+ \left[\frac{k_{\phi\phi} \quad h k_2 T_1 \sin\gamma_1 + M_{s_1}}{I_x}\right]\phi - \left[\frac{I_{xz}}{I_x}\right]\ddot{\psi}$$

$$+ \left[\frac{\rho V S\bar{c}^2}{4I_x}\left(C_{\ell_{\dot{\beta}}} - C_{\ell_r}\right)\right] \dot{\psi} + \left[\frac{k_{\phi\psi} + qS\left(\bar{c}C_{\ell_\beta} - h k_2 C_D\right)}{I_x}\right]\psi = 0.$$

Yawing moment:

$$- \left[\frac{\rho S\bar{c}^2}{4I_z} C_{n_{\dot{\beta}}}\right] \ddot{y} - \left[\frac{\rho V S\bar{c}}{2I_z} C_{n_\beta}\right] \dot{y} + \left[\frac{k_{\psi y}}{I_z}\right] y - \left[\frac{I_{xz}}{I_z}\right]\ddot{\phi} - \left[\frac{\rho V S\bar{c}^2}{4I_z} C_{n_p}\right] \dot{\phi}$$

$$+ \left[\frac{k_{\psi\phi} \quad M_{s_2} - h_{k_1} T_1 \sin \gamma_1}{I_z}\right] \phi + \ddot{\psi} + \left[\frac{\rho V S \bar{c}^2}{4 I_z} \left(C_{n_{\dot{\beta}}} - C_{n_r}\right)\right] \dot{\psi}$$

$$+ \left[\frac{k_{\psi\psi} + qS \left(\bar{c} C_{n_\beta} + h_{k_1} C_D\right)}{I_z}\right] \psi = 0. \qquad (3\text{-A2})$$

The mass and inertia properties used in the preceding equations are defined by

$$h_{k_1} = (\ell_{tr} - \ell_{cg}) \cos \alpha_o + (t_{tr} - h_{cg}) \sin \alpha_o,$$

$$h_{k_2} = (t_{tr} - h_{cg}) \cos \alpha_o - (\ell_{tr} - \ell_{cg}) \sin \alpha_o,$$

$$I_x = I_{xx} \cos^2 \alpha_o + I_{zz} \sin^2 \alpha_o,$$

$$I_z = I_{zz} \cos^2 \alpha_o + I_{xx} \sin^2 \alpha_o,$$

$$I_{xz} = -\frac{I_{zz} - I_{xx}}{2} \sin 2\alpha_o,$$

$$= (I_{xx} - I_{zz}) \sin \alpha_o \cos \alpha_o,$$

$$M_{s_2} = \left[(\ell_{br} - \ell_{cg}) B + (\ell_{sr} + \ell_{cg}) W_s\right] \cos \alpha_o - \left[(h_{cg} - h_{br}) B + (h_{sr} - h_{cg}) W_s\right] \sin \alpha_o,$$

$$M_{s_1} = \left[(\ell_{br} - \ell_{cg}) B + (\ell_{sr} + \ell_{cg}) W_s\right] \sin \alpha_o + \left[(h_{cg} - h_{br}) B + (h_{sr} - h_{cg}) W_s\right] \cos \alpha_o,$$

$$m_x = m_T + (m_{x,a} \cos^2 \alpha_o + m_{z,a} \sin^2 \alpha_o),$$

$$m_y = m_T + m_{y,a} - \frac{\rho S \bar{c}}{4} C_{Y_{\dot{\beta}}},$$

$$m_z = m_T + (m_{x,a} \sin^2 \alpha_o + m_{z,a} \cos^2 \alpha_o) + \frac{\rho S \bar{c}}{4} C_{L_{\dot{\alpha}}}. \qquad (3\text{-A3})$$

The tether cable derivatives about the center of mass are

$$k_{\theta x} = h_{k_2} k_{xx} - h_{k_1} k_{zx}; \quad k_{x\theta} = h_{k_2} k_{xx} - h_{k_1} k_{xz},$$

$$k_{\theta z} = h_{k_2} k_{xz} - h_{k_1} k_{zz}; \quad k_{z\theta} = h_{k_2} k_{zx} - h_{k_1} k_{zz},$$

$$k_{\theta\theta} = k_{\theta\theta_D} + k_{\theta\theta_{T_1}},$$

$$k_{\theta\theta_D} = h^2_{k_2} k_{xx} - h_{k_2} h_{k_1} (k_{xz} + k_{zx}) + h^2_{k_1} k_{zz},$$

$$k_{t\theta_{T_1}} = h_{k_2} (T_1 \sin \gamma_1) + h_{k_2} (T_1 \cos \gamma_1),$$

$$k_{y\phi} = - h_{k_2} k_{yy},$$

$$k_{y\psi} = h_{k_1} k_{yy},$$

$$k_{\phi y} = k_{y\phi},$$

$$k_{\phi\phi} = h^2_{k_2} k_{yy},$$

$$k_{\phi\psi} = k_{\psi\phi},$$

$$k_{\psi y} = k_{y\psi},$$

$$k_{\psi\phi} = - h_{k_1} h_{k_2} k_{yy},$$

$$k_{\psi\psi} = h^2_{k_1} k_{yy}. \qquad (3\text{-A4})$$

The expressions for k_{xx}, k_{xz}, k_{zx}, k_{zz}, and k_{yy} are given by Neumark (1961).

3-A3. EQUILIBRIUM TRIM EQUATIONS

The equations describing the equilibrium trim condition of the tethered balloon system are

$$q_\infty S C_D - T_1 \cos \gamma_1 = 0,$$

$$q_\infty S C_L + (B - W_s) - T_1 \sin \gamma_1 = 0,$$

$$q_\infty \, \overline{Sc} C_m + (h_{k_1}) \, T_1 \sin \gamma_1 - (h_{k_2}) \, T_1 \cos \gamma_1 - M_{s_2} = 0. \tag{3-A5}$$

$$\begin{aligned} &\left[(\ell_{tr} - \ell_{cg}) \cos \alpha_o + (t_{tr} - h_{cg}) \sin \alpha_o \right] \left[q_\infty \, S C_L + (B - W_s) \right] \\ &\quad - \left\{ \left[(t_{tr} - h_{cg}) \cos \alpha_o - (\ell_{tr} - \ell_{cg}) \sin \alpha_o \right] C_D + C_m \bar{c} \right\} q_\infty \, S \\ &\quad - \left[(\ell_{br} - \ell_{cg}) \, B + (\ell_{sr} - \ell_{cg}) \, W_s \right] \cos \alpha_o \\ &\quad + \left[(h_{cg} - h_{br}) \, B + (h_{sr} - h_{cg}) \, W_s \right] \sin \alpha_o = 0. \end{aligned} \tag{3-A6}$$

Equation (3-A6) can be solved by Newton iteration to find the equilibrium trim angle α_o for various wind velocities, provided the aerodynamic coefficients C_L, C_D, and C_m are known functions of α_o. Once the trim angle is determined, then Eq. (3-A5) can be solved to find T_1 and γ_1; also, the α-dependent stability coefficients needed for Eqs. (3-A1) and (3-A2) can be calculated.

Contents

4. The HUGO II Tethered Balloon System

E.V. Harrington, Jr., Capt, USAF and
A.S. Carter, Jr.
Aerospace Instrumentation Laboratory
Air Force Cambridge Research Laboratories
C.D. Corbin
G.T. Schjeldahl Company

Abstract

The HUGO II tethered balloon system is described both from a developmental point of view and in terms of its operational capabilities and constraints. Designed to provide continuous information on atmospheric parameters up to 2,000 feet, with the potential of operating up to 4,000 feet, the HUGO II offers a number of engineering innovations in the sensor, TM and data conditioning areas which may have application to other tethered balloon systems. Since the HUGO II will be used in support of the Air Force Weapons Laboratory's TORUS EMP Test System, it will be required to operate at night in FAA-controlled airspace. The approach to the nighttime lighting requirement will be described in detail.

4-1. INTRODUCTION

The Air Force Cambridge Research Laboratories (AFCRL) have entered into a developmental program for the Air Force Weapons Laboratory (AFWL). This program has as its objective to provide an atmospheric data measuring system

to be used in support of the TORUS Electro-Magnetic-Pulse (EMP) Simulator Development Program. The requirements of the system cover a mobile, self-contained tethered balloon system capable of providing temperature, pressure, wind speed and wind direction measurements at selected levels from the ground to an altitude of 2,000 feet above the ground. The system, known as HUGO II, is shown in its flying configuration in Figure 4-1.

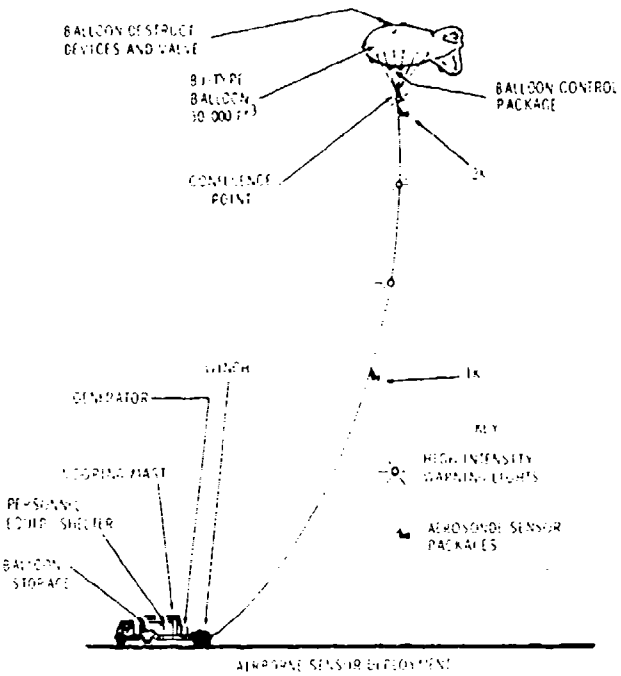

Figure 4-1. Flying Configuration of the HUGO-II Self-Contained Tethered Balloon System

This paper describes each of the major components of the system and their development. The history of the original HUGO I system and some of the limitations inherent in that system are also discussed briefly.

The HUGO II is being developed under contract with the G. T. Schjeldahl Company. Development was started in April 1972. The first flight and test of the system is scheduled for November of this year. The system will be turned over to the AFWL in December 1972.

4-2. HISTORY

The first HUGO system (Figure 4-2) was developed under contract with Vitro Corporation in 1966. That system was designed to measure wind speeds (wind direction was not measured) at four discrete levels: 10, 100, 500, and 800 feet.

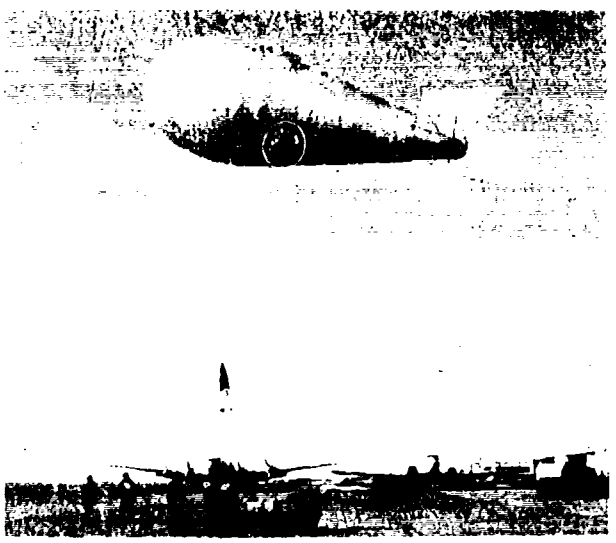

Figure 4-2. HUGO I Developed by Vitro Corporation in 1966

The 10-foot station consisted of an anemometer mounted on a ground anchored mast. The other three stations were deployed at the selected intervals along the tether cable, each consisting of a three-cup anemometer and a mounting bar. Because of the relatively fragile construction of the detachable tail fins on the 3400 ft^3 balloon used on HUGO I, the system was restricted to flight in winds not greater than 15 knots in intensity. (If any one or all of the fins were damaged in flight, the system became unstable.)

All four of the anemometer stations were hard wired to the system trailer. This wiring brought with it a number of disadvantages. One of the biggest problems involved the handling of the signal cable itself, since a wire from a station could easily be broken, and this would not be determined until the system was flying. Also, the system lacked flexibility, since the measuring stations could be attached only at the designated positions and could not be moved to sample at other levels. Another problem involved RF sources which, by inducing spurious signals

in the conductor cable, caused erroneous readings. Located on the trailer was the ground station equipment which provided a meter for viewing the wind speed at each level and a recorder which provided a paper tape record of each level. Because the meters and the recorders could not both be used at the same time, the operator had to choose between a real time viewing of instantaneous wind values and a strip chart recording of smoothed wind data. A further deficiency of the system was that no shelter area for the crew was provided. (This came about because the system could be used only under ideal launch conditions.)

The tether cable was 1/4-inch Dacron braided line. It was normally stored on the drum of a winch located on the system trailer. The winch provided a powered inhaul capability; the lift of the balloon accomplished outhaul. Daytime safety marking was provided by flags attached to the tether cable every 50 feet over the 150-foot point. At nighttime the system was marked by red lights attached to the tether cable every 100 feet. These lights were connected by cabling attached to the tether line to a small power generator on the system trailer.

The HUGO I system has been used on numerous programs and has satisfactorily provided wind profile data to assist in the launching of tandem balloon systems and in dynamic launches involving large cell polyethylene balloons.

Despite its successful use with AFCRL large balloon launching operations, the HUGO I system lacked the flexibility and performance capabilities needed to support the TORUS program. For that reason, a new higher performance system was seen as necessary, and it was agreed that AFCRL would develop such a system for the AFWL.

4-3. BALLOON

The HUGO II system requirements specified that the balloon should be aerodynamically shaped with integral fins, capable of maintaining a maximum altitude of 8,000 feet above mean sea level and 2,000 feet above the ground when lifting all required control instrumentation, sensors, lights, flags and the weight of the tether cable. It had to be operational in winds ranging from 0 to 40 knots and be able to survive in a bedded-down configuration in winds up to 70 knots. The operational life of the balloon would be one year with a storage life of two years.

The balloon (see Figure 4-3) selected for the HUGO II system has a volume of 30,000 cubic feet and is manufactured by Airborne Industries Ltd. of the United Kingdom. It has a 29.5-foot diameter and a 78.4-foot length, weighs 716 pounds, and is constructed of neoprene-impregnated nylon. Its hull is made of two-ply material, while the ballonet and fins are of single-ply construction. In flight, the fins and ballonet are inflated by ram-air scoops with nonreturn sleeves.

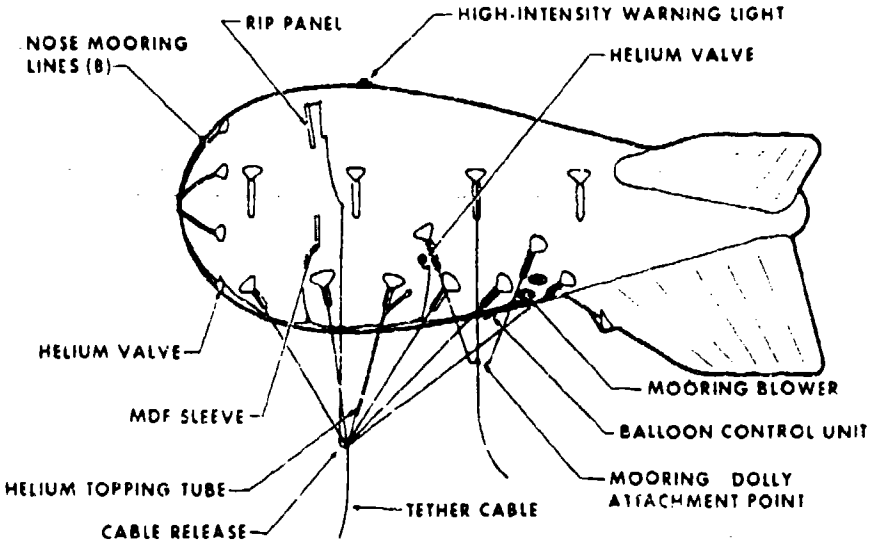

Figure 4-3. 30,000 Cubic-Foot HUGO II Balloon

When the balloon is close to the ground, they are pressured with a 28-volt dc blower installed in a ballonet "deflation sleeve" and connected, via umbilical cable, to ground power. Thus, mooring operations and the moored operating mode are simplified by the streamlined balloon shape.

Figure 4-4 is a functional block diagram of the balloon control subsystem. This subsystem consists of onboard pressure and altitude limit switches and encoded radio command channels which actuate the helium pressure relief valves (one in the nose and one on the port side) and initiate the balloon cut-down actions required by the FAA in the event of cable separation.

When triggered by radio command or by penetration of the 12,000-foot altitude level, the cutdown sequence proceeds as follows:

(1) The tether cable is cut at the confluence point by an explosive cable cutter. As the cable falls away and the balloon rises, a line connected between the cable and balloon rip panel peels the panel off leaving a hole in the balloon helium compartment.

(2) An MDF (mild detonable fuse) circuit is energized. The MDF cuts a slit in the balloon helium compartment.

The port-side helium valve can be opened either by radio command or by automatic activation of the 4-inch H_2O pressure relief switch to provide nondestructive pressure relief. A third radio command function removes power from the command receiver for a predetermined interval, ranging from 0.25 to 5 minutes, to protect the receiver from damage in a severe electromagnetic operational environment.

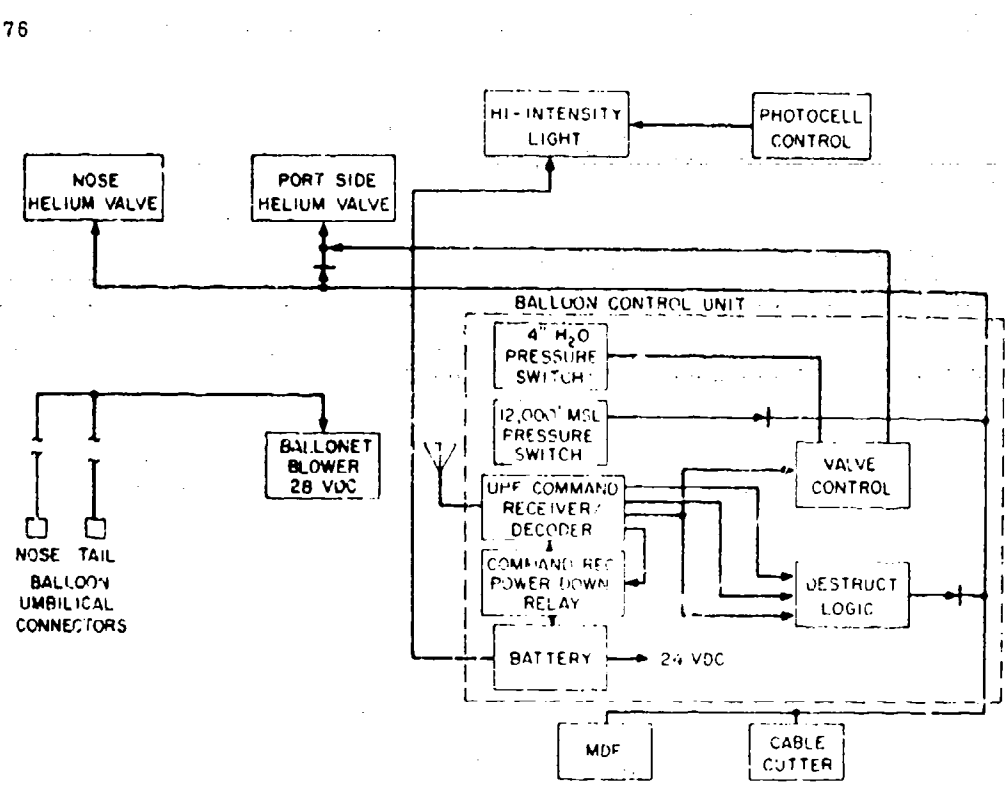

Figure 4-4. HUGO II Balloon Control Subsystem Block Diagram

The high-intensity warning light mounted atop the balloon is powered by batteries in the balloon control unit. It is photocell-controlled and switches on at sunset, off at sunrise.

4-4. BALLOON TETHER CABLE

Preliminary analysis to determine maximum tether cable load considering aerostatic lift, aerodynamic lift, and drag on the balloon in its maximum operational mode (40-knot wind speed) shows that approximately 1,365 pounds are experienced as a worst case. Allowing a safety factor of 2.5, a cable whose minimum break strength is 3,412 pounds was selected.

Four general types of cable were considered for the HUGO II system, of which the first three are dielectric or non-conducting:

(1) Nolaro,

(2) Fiberglass,

(3) Samson braid, and

(4) Steel rope.

All of the above cables satisfy the tether requirements, and each has advantages and disadvantages. Fiberglass cable has the highest strength-to-weight ratio, while steel rope has the highest strength-to-diameter ratio. Nolaro rates last of the four candidates on strength-to-diameter and rates second on strength-to-weight. Fiberglass is unattractive from the handling standpoint, since this construction is quite stiff.

One disadvantage of dielectric cable materials is the insidious degradation of cable strength caused by strand penetration by dirt and other abrasive foreign matter. Although jacketing provides an acceptable solution to this potential problem, it is relatively expensive and bulky. In contrast, steel cable is relatively immune to abrasion. Moreover, it can be wound directly upon the drum without using a traction drive. Use of steel cable is also the least expensive approach, since winches for steel cable are about one-half the price of comparable winches for dielectric cable.

Dielectric cables are generally considered to be less susceptible than steel cables to damage due to lightning and other types of electrostatic discharge, and less likely to carry dangerous electric potentials. (Unfortunately, their use can lull the user into forgetting the danger of conduction by wet and/or dirty dielectric cable surfaces. Conversely, it is easy to remember and respect the electrical conductivity of steel and the need for maintaining good cable grounding and cable avoidance by personnel.) Despite their electrical advantages, dielectric cables were rejected for the HUGO II application because they do not offer the operational reliability, compactness of storage, and easy inspectability of steel cables.

The cable selected is the 3/16-inch diameter Macwhyte 7 × 19 "Hi-Fatigue" aircraft cable. Constructed of 7 strands of 19 wires each, it is extremely flexible, fatigue resistant, and widely used for mooring lines, slings, etc. The construction is 18-8 stainless steel. Wires and strands are pre-formed or shaped to the helical form they assume in the strand and rope, thus reducing friction, kinking, rotation, and fatigue.

4.5 SENSORS

Atmospheric sensors are deployed at three heights in the HUGO II system:

(1) At ground level [actually 25 feet above ground level (AGL)];

(2) At 1,000 feet AGL; and

(3) At 2,000 feet AGL.

These heights are nominal and may be varied as desired. Sensor distributions are as follows:

(1) Pressure altitude (0 to 8,000 feet MSL) (2,000 feet AGL only)

(2) Temperature (-40° to 120°F) (All levels)

(3) Wind speed (0 to 40 knots) (All levels)

(4) Wind direction (0 to 360°) (All levels)

Data from the cable-mounted sensors (1,000-foot and 2,000-foot levels) are transmitted by radio to the ground station. Ground level sensor data are transmitted by electrical cable. All sensor data are displayed on meters and recorded on strip chart recorders simultaneously.

4-5.1 Wind Speed and Direction Sensors

The HUGO II specifications require the wind speed sensors to have a range from 0 to 40 knots with an accuracy of 2 percent or 0.40 mph, whichever is greater, and with theshold readings of 0.6 mph or less. Wind direction must be indicated from 0 to 360 degrees with an accuracy of ± 5 degrees.

A Climatronics Wind Mark III system has been selected for ground wind sensing. Mounted on a 25-foot tower, the Wind Mark III was modified to obtain improved threshold speed, speed measurement accuracy, and directional accuracy to meet the HUGO system requirements. The tower is of truss construction incorporating a hinged base plate for deployment ease and three guy wires and anchors for support against wind loads.

The wind direction and velocity (WINDAV) sensors, developed at the University of Wisconsin for NOAA will be used to sense wind speed and direction at the airborne locations, 1,000 and 2,000 feet AGL. The WINDAV is basically a three-cup anenometer with the unique capability of measuring both wind speed and wind direction as a function of cup rotation. Wind speed is measured by a simple tachometer circuit whose output is a voltage proportional to pulse frequency and, thus, wind speed.

The more difficult wind direction measurement is achieved by utilizing the earth's magnetic field in the vicinity of the instrument. To do this, the WINDAV relies on: (1) a pair of SONY magnetodiodes, which exhibit relatively large changes in resistance with changes in the ambient magnetic field, and (2) a flux concentrator mounted on one of the rotating arms of the anemometer. As the arm cuts the lines of flux of the earth's magnetic field, the magnetodiodes sense the varying local field of the flux concentrator. An ac signal is generated whose positive and negative peaks indicate alignment of the arm with magnetic North and South, respectively. Positive zero crossing indicates West.

The ac signal is not sufficient in itself to determine wind direction. Also necessary is the relationship (in degrees) between the magnetic reference point just established and the azimuthal alignment of the wind vane (aerosonde) on which the rotating sensor is mounted. To ascertain that relationship requires the generation of three more electrical signals.

The first signal is a positive zero crossing pulse designating the point at which the rotating reference arm crosses West. That pulse opens the "gate" of an edge detector pulse counter whose output provides the desired relationship between reference (West) and the aerosonde alignment.

The second signal, the once-around pulse, closes the counter "gate." As the name indicates, it represents one complete revolution of the anemometer shaft. This pulse is developed by a saturating amplifier circuit, which utilizes the output of an electro-mechanical rotational motion transducer consisting of: (1) a light chopper mounted on the rotating shaft and (2) a light-emitting diode (LED) and photocell combination. The point at which that pulse is generated during a rotation is a function of the azimuth position of the vane.

The third signal is the pulse train that is "gated" into the edge detector pulse counter mentioned above. It, too, is generated by the action of the light chopper on the rotating shaft as it cuts the beam of the LED. The latter device, in conjunction with the edge detector counter, produces 360 pulses per revolution. The pulses are operated on in the logic circuit to determine wind direction. They also provide the frequency information for the wind speed measuring circuit. (Recent circuit improvements have rendered the above description somewhat inaccurate. The basic principle is unchanged, however.)

A functional block diagram is shown in Figure 4-5. Note that the base of the WINDAV, along with the LED and photocells, is firmly fixed to and reflects the azimuthal position of the wind-oriented aerosonde. Figure 4-6 shows the

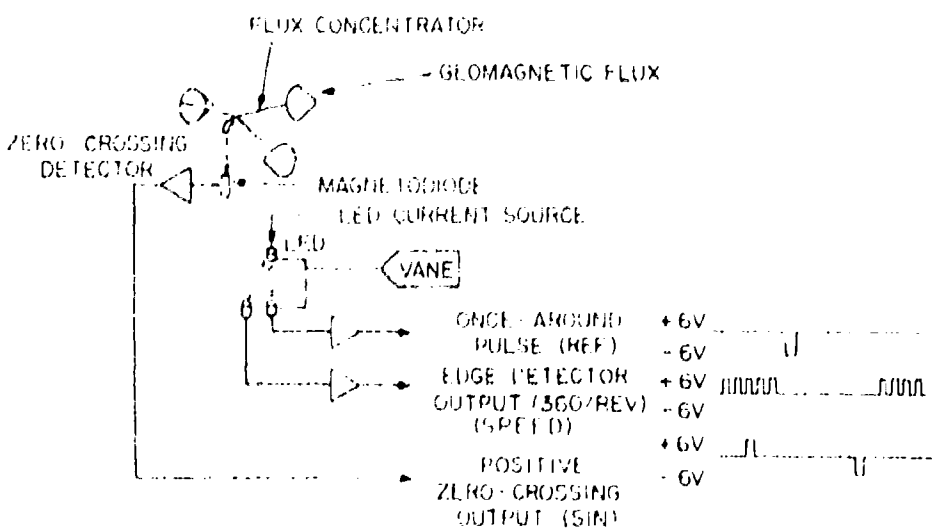

Figure 4-5. WINDAV Functional Diagram

relationship of the pulse train outputs for various wind directions. Referring to that figure, wind direction is determined as follows:

(1) Open the "gate" to the edge detector (ED) pulse counter at the time of a positive zero-crossing. (Reference anemometer arm points West.)

(2) Accumulate pulses in the counter until a once-around pulse occurs to close the "gate."

(3) Add the counts to 270 degrees to arrive at the wind direction. (If total is greater than 360 degrees, subtract 360 degrees.)

Case 1: Once-around pulse closes the gate after one (1) ED pulse. Add this pulse count to 270. Wind direction = 270 + 1 = 271°.

Case 2: Once-around pulse closes the gate after accumulation of 135 ED pulses. Add this pulse count to 270 degrees and subtract 360 degrees, since the total is greater than 360 degrees. Wind direction = 270° + 135 - 360 = 45°.

Case 3: Once-around pulse closes the "gate" after accumulation of 240 ED pulses. Wind direction = 270 + 240 - 360 = 510 - 360 = 150°.

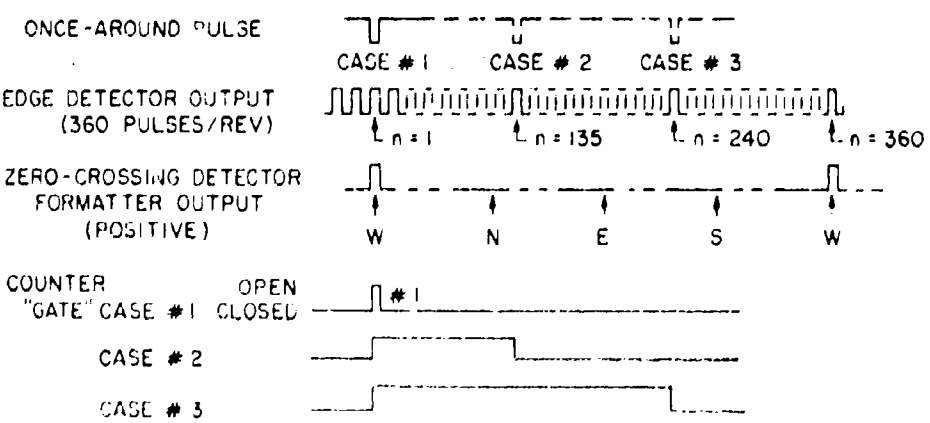

Figure 4-6. WINDAV Pulse Waveforms

4-5.2 Pressure and Temperature Sensors

The aneroid pressure sensor at the 2,000-foot station is primarily for balloon altitude determination. Its measurement accuracy is ± 2mb.

The free air temperature sensors located at each measuring height rely on a vented and shielded thermistor (YECO 43A29). Temperature accuracy is ± 0.5°F with a measuring range of -40 to 120°F.

4-6. TELEMETRY AND COMMAND SUBSYSTEMS

Figure 4-7 is an overall block diagram of the airborne telemetry and command functions. (See Figure 4-4 for more detail on the balloon control and command circuits.)

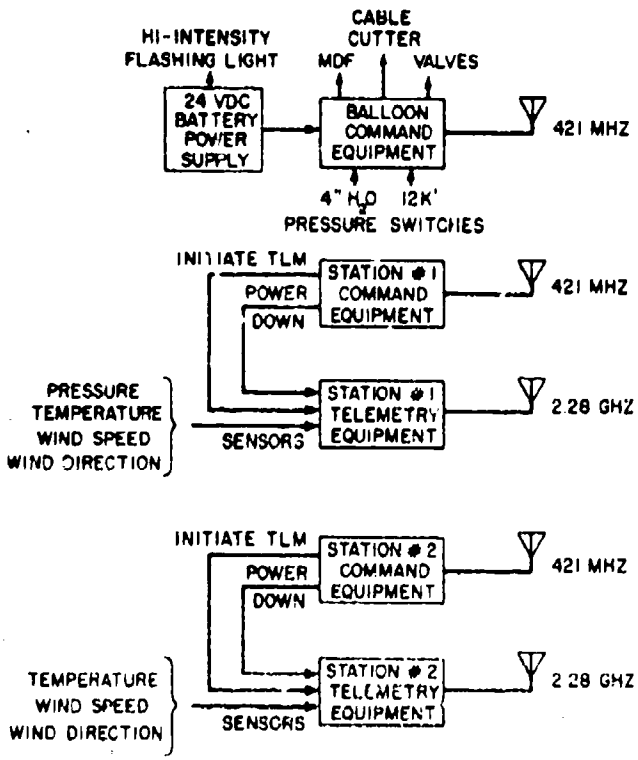

Figure 4-7. Airborne Equipment Block Diagram

The down-link telemetry subsystem employs an S-band carrier frequency of 2.2805 GHz with frequency modulation of the carrier to transmit data from the two cable-mounted sensor stations. These stations are automatically interrogated from the ground in sequential order, and their signals are frequency-multiplexed using subcarrier oscillators (SCOs) operating on four different IRIG channels. (See Figure 4-7.) Each telemetry transmitter has a power output of 100 mW with a crystal controlled frequency stability of 0.003 percent.

The up-link radio command subsystem operates on a UHF carrier frequency of 421 MHz. Tones on five different IRIG channels are used in that subsystem to accomplish the various required functions: initiate telemetry transmission; power-down command receivers; open pressure relief valves; initiate balloon destruct action. Dual command tones are employed for all functions except command destruct, which requires three tones sequentially applied with time-duration coding.

Figure 4-8 is a block diagram of the aerosonde (aerodynamically-shaped sonde). The two aerosondes contain sensors and telemetry signal conditioning and transmission equipment as well as command receivers and decoding circuits. They are battery-powered and capable of continuous normal operation (1/3 duty cycle) for a period of twenty-four hours.

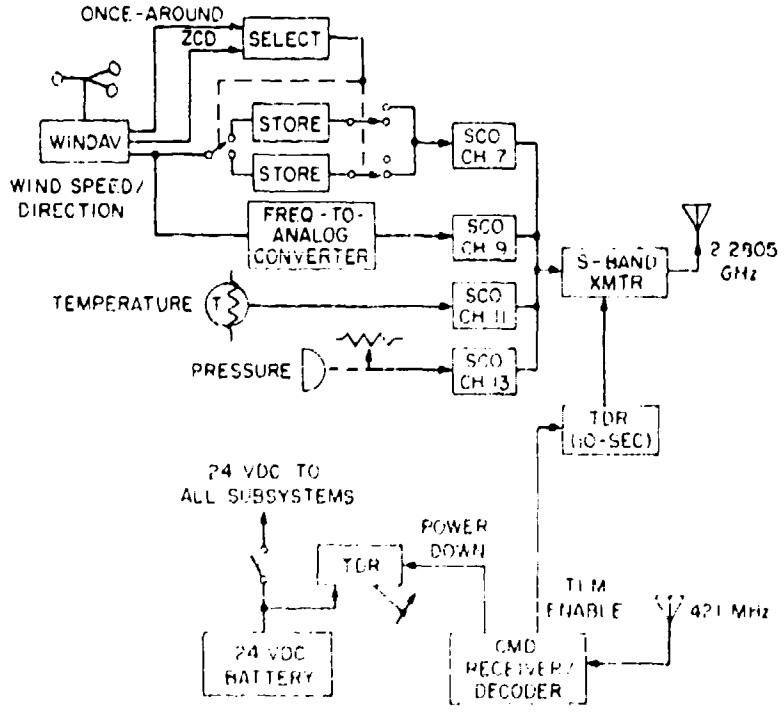

Figure 4-8. Aerosonde Block Diagram

Figure 4-8 also shows the two very important time-delay relays (TDRs) in the command subsystem. When the power-down function is initiated, one TDR is actuated and removes power from all functions, except the TDR itself, for a delay selected before flight (3 seconds to 5 minutes). The other TDR is used to turn on

the telemetry transmitter for a predetermined period (nominally 10 seconds, maximum 30 seconds) when commanded from the ground station.

Figure 4-9 is a block diagram of the functions associated with the ground station equipment mounted in the shelter on the launch vehicle. The key components are the command transmitter and the telemetry receiver. Four subcarrier discriminators are used with the receiver; their output provides the signals for sample-and-hold amplifiers which drive meters and a strip chart recorder. When an aerosonde turns off its telemetry transmission, the most recent signal levels (before turnoff) are maintained by the sample-and-hold circuits and are displayed on the meters and recorder. If the meters are reading in real time, adjacent panel lights glow to indicate that the readings are live.

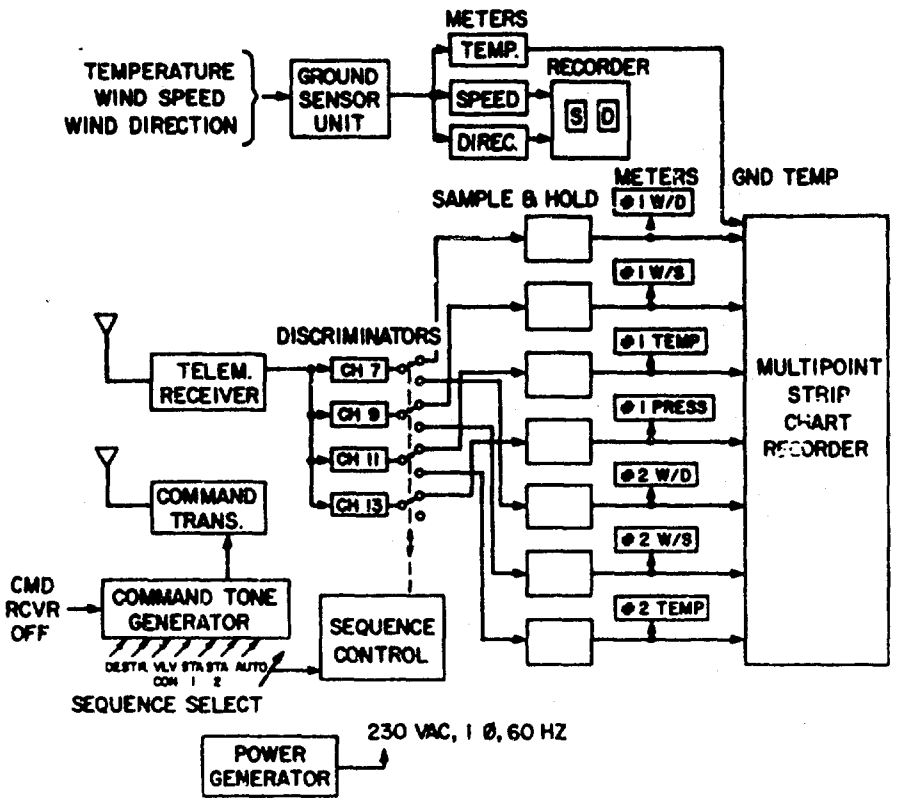

Figure 4-9. HUGO II Ground Station Equipment Block Diagram

The chart recorder gives a record of the pressure (where appropriate), temperature, wind speed and direction at each station. It has a single pen, but up to eight input signals may be time-multiplexed into the recorder. Print rates as high

as 16 samples per second may be selected. Thus, essentially continuous traces are possible with the chart speeds used for aerosonde monitoring.

The two aerosonde stations are interrogated automatically by command sequencer when the "start" switch is depressed. This turns on the command transmitter and keys in the appropriate interrogation command tones (for example, 1 and 5) for the first station. After a 0.5-second delay, the Station 1 sample-hold relays are energized and real time data are recorded for nine seconds. Then the sample-hold relays are released, and the signals are on "hold." Next, assuming a 1-2-1-2 or 1-2-0-1-2-0 sequence had been selected, the second station is commanded on automatically, its data read out for nine seconds, and so on.

An interrogation duty cycle selector switch allows the operator to elect a 0.5 or 0.3 (actually 1/3) station duty cycle. Selecting the 1-2 sequence, with a duty cycle switch setting of 0.5, provides an actual sequence of 1-2-1-2-1-2 and so on. The same sequence selection, with duty cycle switch setting of 0.3, gives an actual sequence of 1-2-0-1-2-0-1-2-0, where -0- is a quiet period during which no telemetry transmissions are made and meter/recorder readouts for both stations are sample/hold outputs. (The quiet period also allows insertion of the transmission from a recently authorized 3rd cable-mounted station when it becomes available.)

Individual momentary switches initiate "command receiver off" and "helium valve open" commands. Each of these switch closures employs two command tones. "Destruct," or balloon cutdown, is initiated by a key switch followed by two additional sequential switch closures, where the operator must manually depress switches for a predetermined length of time.

The aerosonde layout is depicted in Figure 4-10. Basic construction of the shell is G-500 Nopcofoam Corp. rigid urethane foam. A density of 4 pounds per cubic foot was selected for high strength and low weight. The total foam volume is approximately one cubic foot which gives a total shell weight of approximately 4 pounds. The shell will be formed in an enclosed plastic mold, in half sections, with component mounting areas and clearance holes for fasterers and so forth blocked out. Molded surfaces are relatively hard and tough, typically providing a surface strength of approximately 60 pounds per square inch.

4-7. WARNING LIGHTS AND PENNANTS

High-intensity warning lights approved by FAA are used for nighttime operations. Cable mounted at 333 feet, 666 feet and 1,000 feet above the ground (this assumes a nighttime flight altitude of 1,000 feet AGL), they can be seen for distances up to 20 miles in clear weather. An additional light is mounted atop the balloon. (Nighttime operations were limited to 1,000 feet because the additional lights for the 2,000-foot capability exceeded the weight the balloon could handl .)

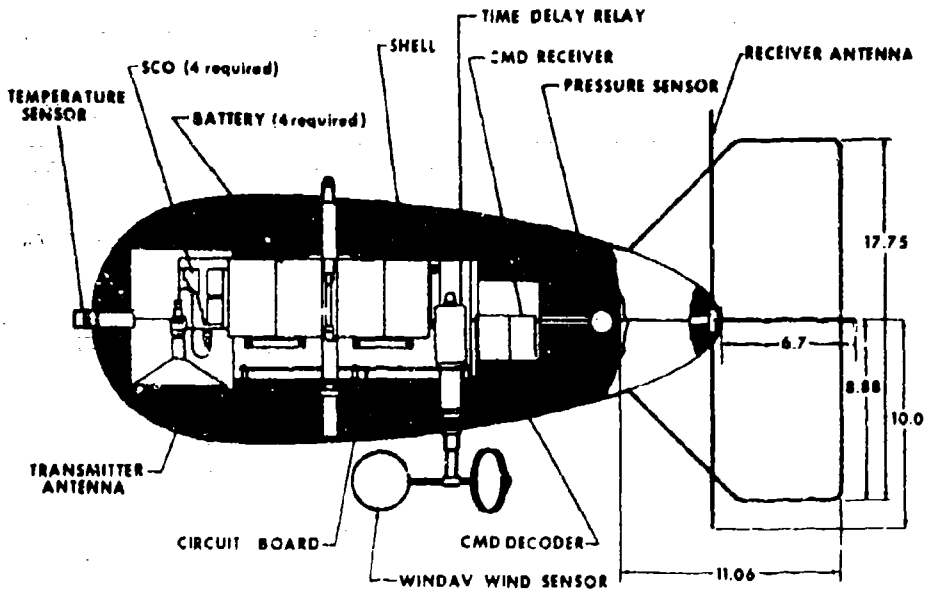

Figure 4-10. General Arrangement of the Aerosonde

Figure 4-11 shows the integrated battery pack/light unit configuration employed for the cable-mounted high-intensity warning lights. The basic light (Symbolic Displays, Inc., Hoskins Division) was adapted from a standard aircraft warning light and has the following characteristics:

Output	1,000 candelas
Flash rate	40 flashes per minute
Weight	1.8 pounds
Control	Photocell (sunrise/sunset-threshold value: 25 footcandles)
Power	1.5 amperes at 12 volts dc.

Two-foot square orange, urethane-coated nylon pennants (also FAA approved and required) are attached by quick-fastening clamps to the cable for daytime operations. They are at 50-foot intervals above 150 feet.

4-8. MAIN WINCH

The HUGO II system employs several small hand winches, described in Section 4-16, and one large powered winch. The latter is referred to as the main winch and is used to deploy and to retrieve the tether cable to which the balloon and sensors are attached. It is capable of pulling in or paying out the the tether cable

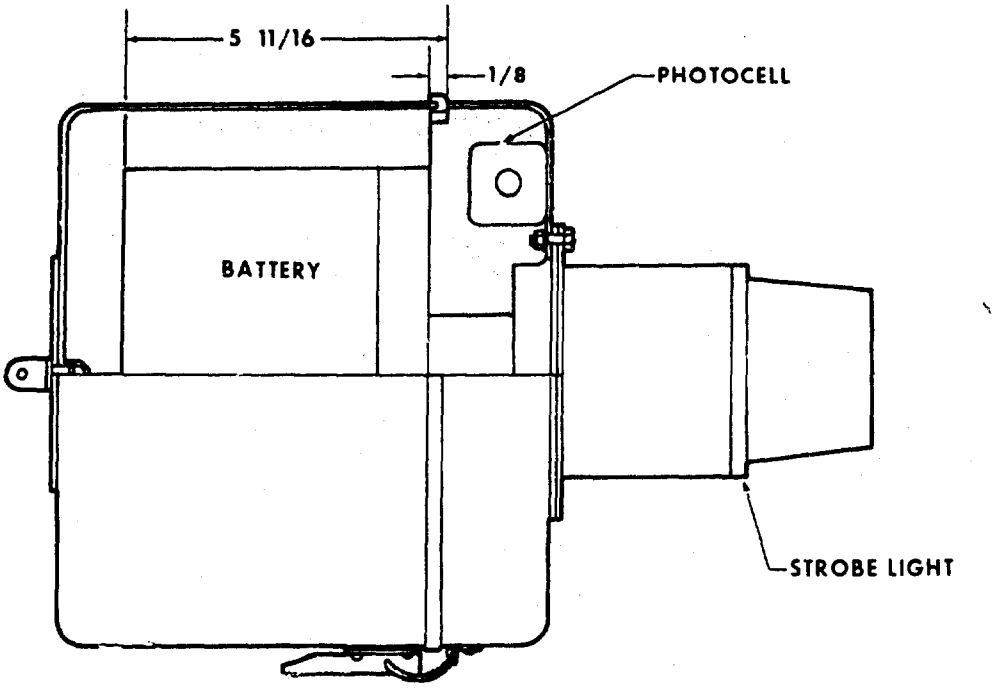

Figure 4-11. Integrated Battery Pack/Light Unit Configuration Used for Cable-Mounted High-Intensity Warning Lights

at a continuously variable rate of 0 - 200 feet per minute and at 1,500 pounds of cable tension. This winch is composed of two units interconnected by hydraulic lines:

(1) Power unit	Engine and hydraulic pump
(2) Drum unit	Drum, level wind, capstan, hydraulic drive.

The main winch has the following features:

Prime mover	Gasoline engine, 21 hp
Drive	Double capstan
Drive coupling	Hydraulic - inhaul and outhaul
Cable feed	Automatic level wind
Storage capacity	6,000 feet 3/16-inch steel cable
Cable monitor	Footage counter
Brake	Funk fail-safe
Drum drive	Chain and sprocket with torque limiter.

4-9. POWER GENERATOR

The power generator selected for the HUGO II system has the following salient characteristics:

Engine	Wisconsin VH4D, 4 cylinder, 4 cycle, air-cooled, 22.5 hp, continuous duty service, 12V battery, starter, 12V generator, quiet muffler, fuel consumption - 2.32 gallons/hour, max.
115V generator	Brushless, 4-pole, 1,800 rpm
Power output	10 kW (12.5 kVA)
Voltage	115/230 V ac, 1 ϕ
Frequency	60 cycles
Voltage regulation	2 percent
Weight	Approx. 900 pounds
Height - 33 1/4 inches	Length - 46 1/4 inches Width - 27 inches

A 55-gallon drum will supply fuel to the engine. A second drum may be located alongside the generator in the event power consumption is large, as when the trailer shelter air-conditioner is used. The generator will have wheels installed to permit easy movement on and off the launch vehicle.

4-10. BALLOON LAUNCH VEHICLE

All components of the HUGO II system have been integrated for transporting in one mobile unit called the balloon launch vehicle. (Figure 4-12 shows the vehicle in transport mode.)

A two-axle, 42-foot long low platform trailer, capable of being pulled by a five-ton cab-over-engine tractor, is employed. Modules for (1) balloon storage, (2) personnel/instrumentation shelter and (3) storage facilities are mounted on the trailer frame. The mooring mast rests on the mast base plate, which is also mounted on the transporter frame. A yoke assembly is provided for cradling the hinged mast in transport mode. The skid-mounted main tether winch is permanently secured to the frame, while the mooring dolly and the dolly-mounted generator are lashed to it during transport.

Two small hand winches are also mounted on the transporter. Four winch locations are shown in the drawing; these are the points where the hand winches will be used depending on the particular phase of the operation: erecting the mast, handling the power generator, hauling the aft confluence to the mooring dolly, or applying tension to the nose confluence line. Obviously, not all of these functions

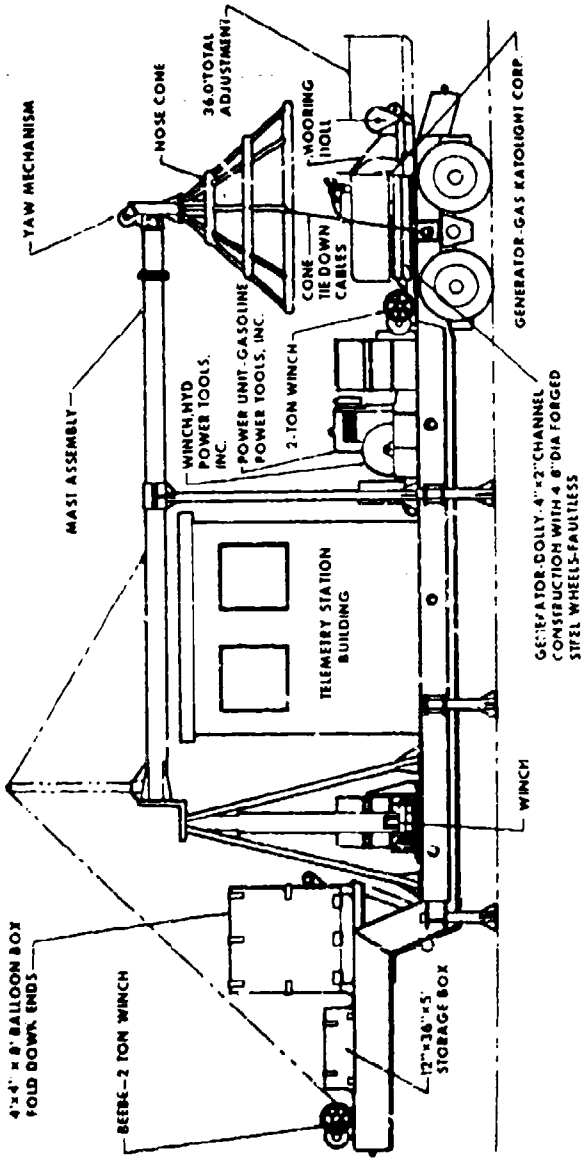

Figure 4-12. Moon Launch Vehicle Housing all HUGO II Components for Ease in Transporting

will occur at the same time. The two hand units provide an effective operational capability for a reasonable cost. They will mount on studs at the points where they are needed. Wood plates with stud clearance holes will be placed over the unoccupied winch locations.

The air-conditioned personnel shelter has working space for two persons, mounting racks for the ground station components, and storage space for the airborne sensor pods. Telemetry receiving/readout and command equipments are arranged in two cabinets. A tabletop near the base of these cabinets provides a convenient writing and working surface. The shelter is heated with a bottled gas heater. Power for lighting and for operation of the ground station electronic equipment is provided by the 10 kW electrical generator. A single cable with a quick-disconnect connector links the two units. Inside the shelter, distribution is initiated at a 100-amp breaker box. A 230-volt breaker handles the air-conditioner load.

Figure 4-13 depicts the moored configuration of the HUGO II system. The 8-inch diameter steel pipe mast satisfies the requirement for mooring the 30,000 ft^3 balloon in winds of 70 knots. Outrigger supports eliminate the need for guy wires. The mooring cone is of tubular aluminum construction and is attached to the yaw assembly at the top of the mast. The yaw assembly is a critical component of the mast, as it permits 360-degree rotation of the mooring cone, plus pitch angle changes of ± 15 degrees.

The mooring dolly, Figure 4-14, is designed for attachment to the aft confluence point of the balloon during mooring in high winds to minimize vertical motion

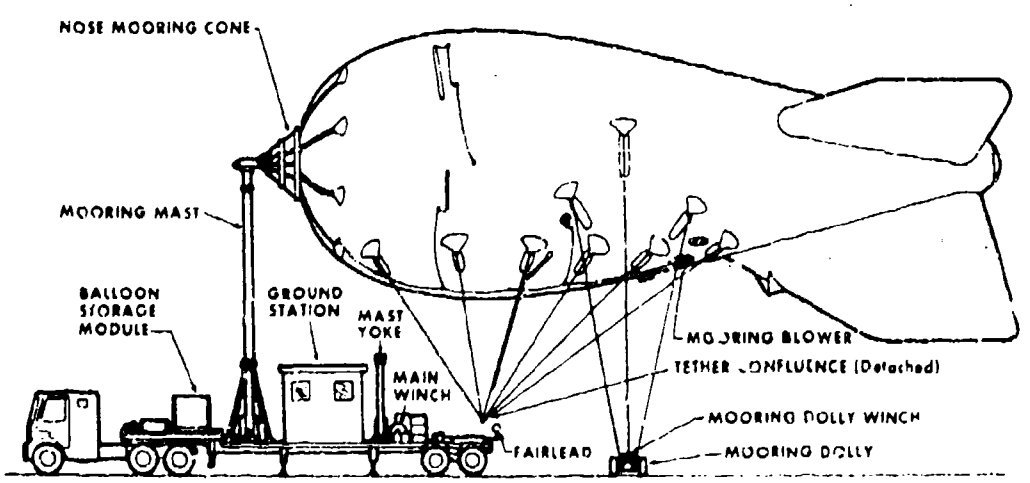

Figure 4-13. HUGO II Moored Configuration

of the balloon. It has two large main wheels (7.50 × 15 tires) and two small (8-in. dia.) auxiliary wheels, parallel to and outboard of the main wheels. In normal operation, only the main wheels touch the ground. Their movement is in the direction of balloon sideways motion or yaw. If the balloon should lay over due to reduced lift, one of the small wheels will also touch the ground. The small wheel's ability to rotate freely should prohibit its digging into the ground, an action which would obviously prevent free sideways motion of the balloon.

Figure 4-14. The Mooring Dolly Attached to Balloon's Aft Confluence Point to Minimize Vertical Motion in High Winds

The unloaded dolly can be moved into position easily by two men. It is then loaded with 100-pound lead weights to a maximum of 1,000 pounds. (Lesser weight may be desirable for light wind conditions to reduce yaw inertia loads.)

The dolly concept depends for its success on the availability of a reasonably smooth surface area. Although it is generally easier and more effective to operate with a track and monorail type of mooring restraint, that concept was rejected for HUGO II because it is not portable.

Figure 4-15 shows the method by which personnel and equipment are protected against electrostatic discharge from the cable as well as lightning strikes on the cable. When the balloon is being raised or lowered the grounding cable clamp is removed from the cable and clipped to the fairlead assembly. In addition, the shelter will be sheathed in a steel mesh bonded to the trailer structure which is, in turn, connected to a ground rod.

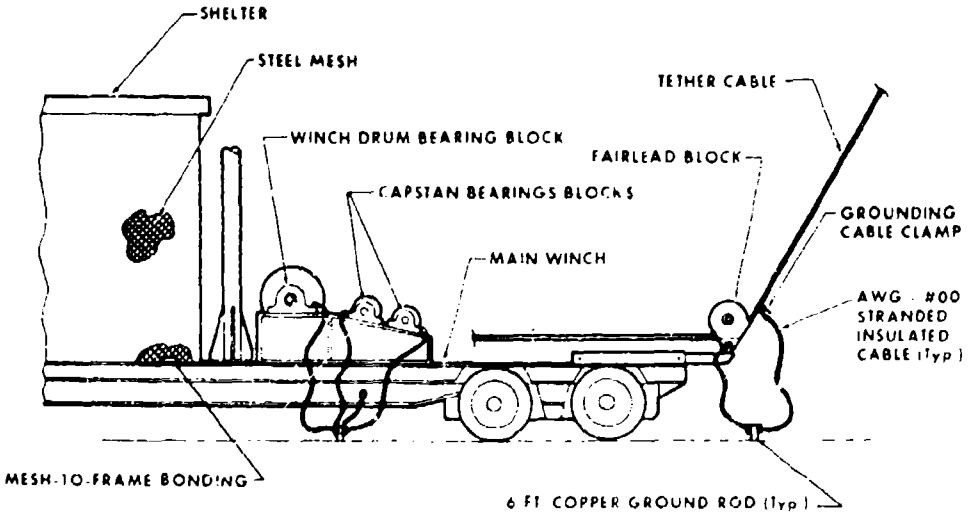

Figure 4-15. HUGO II Electrostatic Protection

Lightning is recognized as a serious hazard to tethered balloon operations. The above provisions will safeguard against static buildup and will provide reasonable emergency protection against lightning, but they are not designed to permit completely hazard-free operation in thunderstorms. The time-tested procedure for avoiding lightning damage is to bring the balloon down to the ground where possible if a lightning threat exists.

Contents

5. Comparison of Balloon-Borne and Tower-Mounted Turbulent Wind and Temperature Sensors

D.A. Haugen and J. Pellegrini, Capt, USAF
Air Force Cambridge Research Laboratories
Bedford, Massachusetts

C.J. Readings and H.E. Butler
Meteorological Research Unit
RAE Cardington
Bedford, England

Abstract

Micrometeorological experiments are conducted to determine the significant properties of turbulent flow in the atmospheric boundary layer. This layer is believed to be roughly 3000 to 5000 feet deep during the day and 1000 to 3000 feet deep during the night. However, the most reliable and complete data available are restricted to depths of only 100 feet and are obtained from sensors mounted on towers. Within the past decade, scientists at the Meteorological Research Unit, RAE Cardington have developed a sensor package for mounting on the tethering cable of a large captive balloon capable of carrying sensors to heights greater than a mile above ground. In September and October 1971, a field program was conducted at Eglin AFB to determine the effects of balloon movement on the cable-mounted sensors. British sensors were mounted at roughly 500 and 1000 feet on the cable of a 15,000-cubic foot barrage balloon and compared with AFCRL sensors mounted at similar heights on the 1200-foot tower at Eglin. Subsequent data analyses have yielded the following results:

a. Balloon movement is primarily horizontal and normal to the prevailing wind direction.

b. Horizontal wind component measurements are, therefore, much more affected by balloon movement than are vertical wind component and temperature measurements.

c. The closer the sensor package is to the balloon, the more marked the effect of balloon movement.

d. At a few hundred feet above ground, nearly all the balloon movement effects occur at scales of motion which are small compared to the physically significant scales that must be studied under turbulent conditions.

5-1. BACKGROUND

Flow within the atmospheric boundary layer is characteristically described as turbulent shear flow. Mean horizontal wind speeds increase with height from zero at the earth's surface to a maximum value somewhere within or near the top of the boundary layer. The surface frictional drag is a basic cause of the vertical shear in the flow. The combination of mean shear and turbulent fluctuations in turn gives rise to a downward turbulent transport of horizontal momentum, a fundamental property of boundary layer flow. Micrometeorologists traditionally obtain quantitative measures of this turbulent transport process by measuring the covariance between horizontal and vertical wind component fluctuations. Knowledge of the behavior of this covariance as a function of height, surface conditions, and thermal stability is a fundamental requirement for understanding the physics of the boundary layer. Similar statements can be made for heat flux to and from the earth's surface, another important property of the boundary layer.

Until recently, however, nearly all micrometeorological experiments have been limited to the so-called surface layer, a layer roughly 50 to 150 feet deep. In part, this has been a desirable limitation for furthering fundamental understanding of boundary layer turbulence, for it is in this layer that the wind shear and temperature gradients are generally the strongest and the momentum flux and heat flux the greatest. The experimental techniques required are easily adapted to instruments mounted on fixed towers and have been pursued by a number of research groups throughout the world during the last several decades. But meteorologists of all disciplines are now well aware that surface layer research has reached a plateau, and widespread motivation exists for extending research studies throughout the planetary boundary layer. Indeed, there are few regions of the atmosphere where less is known about the controlling physical processes than this region between roughly 300 and 5000 feet.

Time scales in this layer vary from a few seconds to several hours, space scales from a few meters to kilometers. Little is known, however, about the variation of turbulent energies as a function of scale size, and experimental meteorologists are currently evaluating a number of techniques for determining this basic property of turbulence. One technique is to carry sensors aloft by using captive balloons, in effect extending sampling heights far beyond those possible with any existing or planned towers. The Meteorological Research Unit, RAE Cardington, in particular, has developed wind and temperature instrumentation packages suitable for mounting on the towing cable of large captive barrage balloons of the type used in England during World War II.

Members of the Meteorology Laboratory, AFCRL, and the Meteorological Research Unit have initiated a joint program to exploit the captive balloon

techniques by using conventional tower-mounted sensors for the surface frictional layer and the British balloon-borne sensors for the bulk of the boundary layer. An elaborate joint program is scheduled for 1973 over a horizontally uniform site in Minnesota. An important aspect of the preparation for these experiments is the obvious need to assess the effect of balloon movement on the response characteristics of the sensors.

The purpose of this paper is to describe a set of experiments conducted at Eglin AFB, Florida in 1971 to obtain comparison data for the two sensing techniques. This was a joint effort with participants from the Meteorology Laboratory, AFCRL, the Aerospace Instrumentation Laboratory, AFCRL, and the Cardington RAF Meteorological Research Unit (MRU).

5-2. EXPERIMENTAL PROCEDURES

The British instrumentation consists of a cup anemometer for measuring total wind speed, a hot wire array to measure the inclination of the wind from the horizontal, and a platinum resistance [illegible] for measuring temperature. (See Figure 5-1.) The sensors are mounted in front of a free-swinging vane which keeps the sensors pointed into the wind. The entire package is clamped to the balloon cable, the significant feature being that the hot wire array is mounted on a damped pendulum which maintains its vertical orientation regardless of tilt in the balloon cable. Data from the three sensors are processed to obtain horizontal and vertical wind component fluctuations and temperature fluctuations.

The AFCRL instrumentation consists of a 3-axis sonic anemometer which provides continuous data on all three wind components and a platinum resistance thermometer for temperature data. These sensors were mounted on 12-foot booms attached to a 1200-foot tower at Eglin AFB at heights of 540 and 1023 feet. (See Figure 5-2.)

The various sensor outputs were transmitted over signal cable to the Meteorology Laboratory's computer-controlled data acquisition system permitting real-time data analysis in the field. Equally important, the data obtained during each experiment were recorded on magnetic tape for subsequent detailed analyses. All the sensors were sampled 20 times per second for each observation period of one hour.

Experimental periods were chosen according to wind direction. Data were obtained only with winds blowing generally from the balloon to the tower. Because of normal safety procedures, experimental flights were made only on days with clear or partially clear skies; no data were obtained during strong convective conditions with rapidly changing up and down drafts. Nighttime experiments were not attempted because of electrical interference from the aircraft warning light system on the tower.

Figure 5-1. MRU Instrumentation. Wind inclination angle sensor is on probe extending to front of instrument, wind speed sensor on right, temperature sensor on left. Signal shaping circuitry is housed in vane, batteries in box hanging on bar

The balloon was launched from a winch truck which was moved as close to the tower as safety permitted. Early in the experimental period, the truck was located 1200 feet north of the tower. As some experience with the operation was gained, however, the truck moved progressively closer. Most of the data were obtained with the truck about 350 feet north of the tower.

Experiments were scheduled for four different balloon altitudes: 1200, 2000, 3000, and 4000 feet. This was done so that subsequent analyses would permit determination of balloon cable movement effects as a function of distance between the sensors and the balloon height. Fifty experiments were conducted during the overall experimental period.

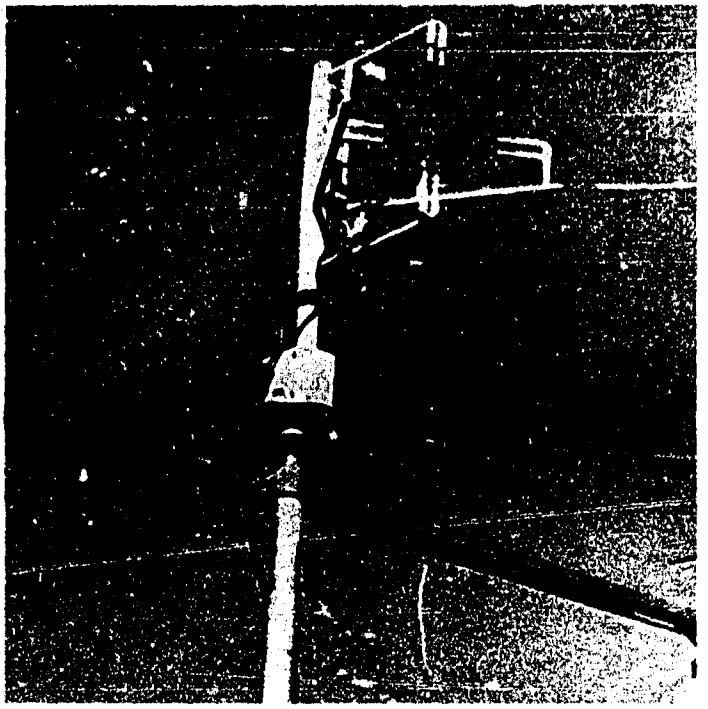

Figure 5-2. AFCRL Instrumentation. Three-axis sonic is oriented into the wind to obtain wind component data. Temperature sensor is mounted on rear post of sonic anemometer

5-3. ANALYSIS PROCEDURES

Each data set was processed to obtain one-hour averages of various statistical quantities chosen for their meteorological significance as well as for their value in evaluating the relative performance of the two experimental techniques. As discussed earlier, we are particularly interested in the vertical flux of momentum and heat. Accordingly, these quantities were the first set of comparison statistics studied. Scatter diagrams for these flux comparisons are given in Figures 5-3 and 5-4. Agreement within ± 20 percent was achieved, a result comparable to similar data sets obtained with like instruments mounted side by side on a tower. There was, however, a systematic divergence in the heat flux comparisons at high values of heat flux. This is most likely due to enhanced vertical motions of the balloon during unstable conditions.

No other obvious balloon movement effect has been found in these data; that is, the average values of the vertical fluxes do not appear to be at all affected by balloon movement or even by distance between the balloon and the sensors on the cable. In part, we feel this result must be a natural outcome, since no data were

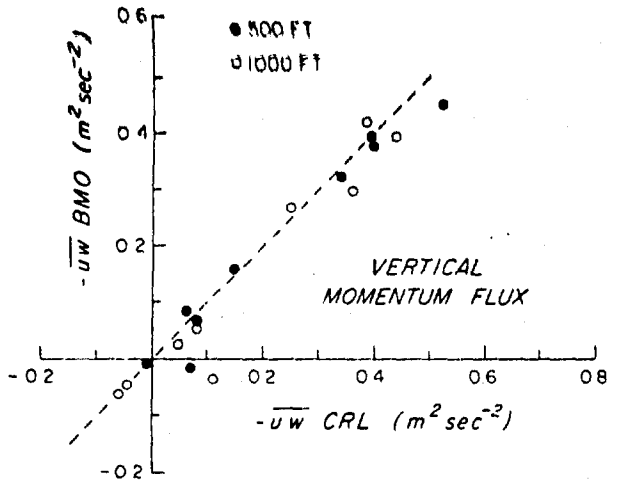

Figure 5-3. Comparison of MRU and AFCRL Measurements of Vertical Momentum Flux

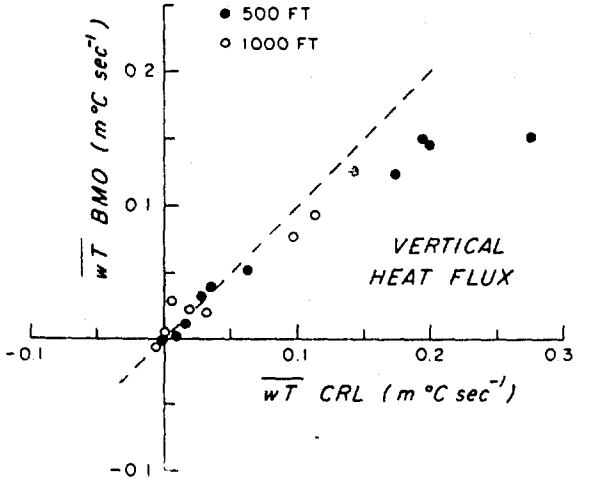

Figure 5-4. Comparison of MRU and AFCRL Measurements of Vertical Heat Flux

obtained during meteorological conditions with strong and abruptly changing vertical motions. As a result, the balloon movement, which certainly does take place, was nearly horizontal. This does have measurable effect on the total speed sensor, of course, but no significant effect on the covariance between horizontal and vertical wind fluctuations (momentum flux) or between vertical wind and temperature fluctuations (heat flux).

Another reason balloon movement effects appear to be negligibly small for these quantities is that the time and space scales of the turbulent eddies contributing

to the vertical fluxes are large compared to scales typical of balloon movement. In fact, the entire data set clearly showed that the turbulent scales are large and elongated markedly along the mean wind, so that we could not obtain suitably stable statistics for comparisons unless the wind was blowing directly from the balloon to the tower. The data shown in Figures 5-3 and 5-4 include only cases where the mean wind direction was within ± 15 degrees of the balloon-tower lines. For wind directions deviating more than 15 degrees from this line, comparisons between the two sets of fluxes showed much more scatter overall with differences of about ± 40 percent or more. The increased scatter can easily be shown to be caused by insufficient sampling of the large eddies and not by differences in experimental techniques. Hence, only data for runs satisfying the ± 15 degree wind direction criterion were accepted as being suitable for comparison analysis purposes. This eliminated all runs with balloon altitudes of 4000 feet, which was unfortunate since these runs should have displayed the least amount of balloon-movement effect.

Another statistic commonly obtained in turbulence research is the variance spectrum. This is simply a breakdown of the variance of any time series which displays the relative contribution to the total variance per unit frequency interval as a function of frequency. Spectrum analyses were made for the vertical wind component, w, the horizontal wind component, u, and the temperature, T, for those runs with good wind directions. The spectral bandwidth obtained ranges from 1 cycle per hour up to 10 cycles per second. We then computed the difference in spectral estimates, normalizing with the spectral estimate obtained on the tower, in an attempt to find balloon movement effects on the individual fluctuating quantities.

The most significant balloon movement effect is found on the horizontal speed data. Since the wind inclination angle seldom exceeds ± 20 degrees, the horizontal wind component, equal to the total speed times the cosine of the inclination angle, is quite similar in behavior to that of the total speed sensor. Lateral movement of the balloon cable, in either a horizontal or vertical plane, must therefore impart relative motion to this component, always in a positive, overspeeding sense. This is shown in Figure 5-5, a plot of normalized difference spectra for the horizontal wind component sorted by balloon height. A general overspeeding effect exists over all frequencies, a tailing off of turbulent energy in the sensor at high frequencies due to frequency-of-response limitations of the cup relative to the sonic anemometer, and an unmistakable balloon movement effect exists over a spectral region centered on a frequency of about 0.3 cycles per second. This latter effect is smaller the greater the distance between the balloon and the sensor, the implication being that about 2000 feet separation between the balloon and sensor is required to suppress adequately the effects of balloon movement.

Three-tenths Hz is the natural frequency of the vane, suggesting that the cable movement is indirectly causing a vane oscillation.

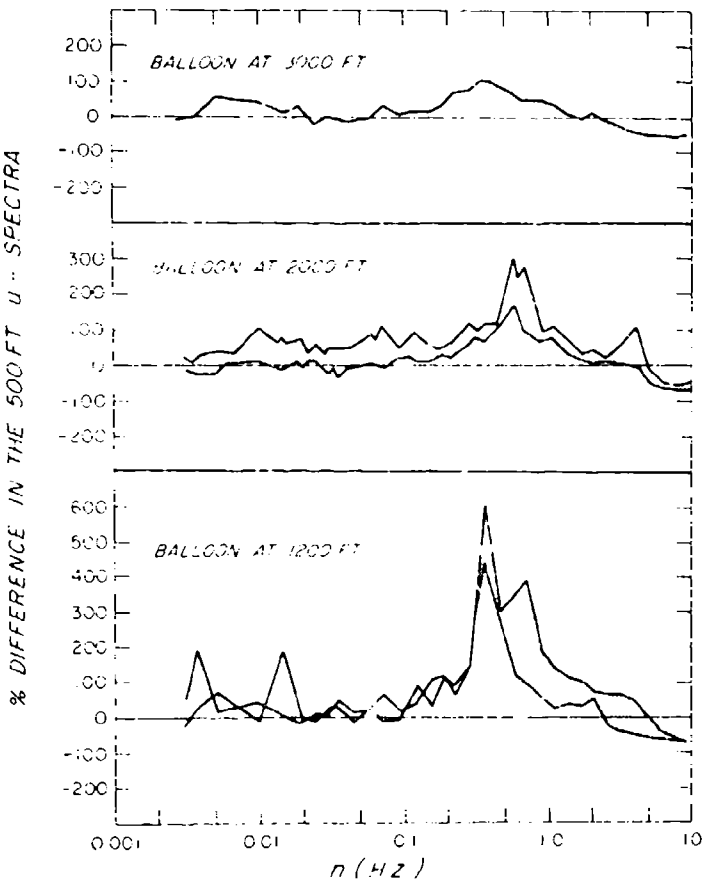

Figure 5-5. MRU-AFCRL Variance Spectrum Differences for Horizontal Wind Component as a Function of Balloon Altitude

Similar plots were prepared for the vertical wind component and temperature fluctuations. However, since the balloon movement was primarily horizontal, no significant balloon movement effect is apparent for these parameters.

A more detailed discussion of these experiments is currently being prepared and will be submitted to the Journal of Applied Meteorology for publication in 1973.

5-4. CONCLUSIONS

In summary, so long as the balloon movement is primarily horizontal in nature, balloon movement effects are essentially restricted to the wind speed sensor alone. Even these can be practically eliminated by maintaining about 2000 or more feet separation between the balloon and the sensor. Most important, the turbulent fluxes of momentum and heat take place at scales of motion quite large compared to the balloon movement scales, and one therefore can sensibly plan boundary layer flux measurements based on the MRU captive balloon techniques. In the field program scheduled for 1973, five British instruments will be flown simultaneously at heights between 200 and 4000 feet, while three AFCRL instruments will be mounted on a 100-foot tower to carefully document the surface layer.

Acknowledgments

We would like to express our appreciation particularly to the balloon flight crew, Aerospace Instrumentation Laboratory, AFCRL, without whose expert participation this program would not have been possible. In addition, many of our colleagues at AFCRL and Meteorological Research Unit, RAF Cardington have participated in this program, and we are pleased to acknowledge the overall team effort which has characterized the experiments.

Contents

6. Balloonborne Aerosol Particle Concentration and Size Distribution Measurements

R. Fenn
Air Force Cambridge Research Laboratories
Bedford, Massachusetts

J. Duichinos and H. Miranda
GCA Corporation
Bedford, Massachusetts

Abstract

An instrument was developed to measure the concentration and size distribution of particulates in the atmosphere.

Since the concentration of natural aerosols in the free atmosphere above the surface layer is less than 1 particle per cm^3, extreme precautions have to be taken to avoid contamination from the instrumentation package, including the balloon itself.

A free balloon flight with this instrument was conducted in October 1970 at White Sands Missile Range, New Mexico. Several interesting aspects became apparent from this flight which are related to the dynamics of the balloon flight itself.

In order to study these phenomena in more detail and to find some possible means for their compensation, a series of flights on a tethered balloon were conducted in the White Sands area in March 1972. With this tethered balloon platform it was possible to fly a variety of ascent and descent profiles with the instrument. Supplementing the tethered balloon flights on a few occasions were airborne measurements of aerosol distributions from a C-130 aircraft.

Various aspects of balloonborne aerosol measurements are being discussed in their relationship to the balloon as the vehicle and measurement platform.

6-1. INTRODUCTION

Advancement in such diversified scientific disciplines as air pollution research, cloud physics, and atmospheric optics depends very much on the capability to measure the distribution and composition of small haze particles (aerosols) in the atmosphere. The number density and the particle size distribution are the two most important parameters in these applications. Because of the extremely low concentration of natural aerosol particles under clear atmospheric conditions and especially at higher altitudes, special care has to be taken that the sampling process and the instrumentation platform do not change or contaminate the natural aerosol sample. Some of the problems encountered in atmospheric aerosol measurements using free and tethered balloons are discussed here.

The aerosol concentration and size distribution are of particular significance for the light scattering properties of the atmosphere. On the other hand, the light scattering properties of the atmosphere have been widely utilized to obtain information on the distribution of aerosols in the atmosphere. The principal advantage of light scattering measurements over direct sampling methods is that no mechanical contact with the particle is required, greatly reducing the danger of changing the aerosol sample in the measuring process. A second important factor in favor of optical measurements is that optical signals can easily be converted into electrical signals which greatly simplifies the problem of data handling; in the case of mechanical particle sampling devices such as impactors or centrifuges, data processing can be a major problem.

Theoretical considerations and experimental results (Kerker, 1967; Shifrin and Perelman, 1967) show that only under very special conditions light scattering measurements on a particle cloud allow one to derive the accurate particle size distribution, concentration and other properties. Much of the uncertainties and ambiguity inherent in particle-cloud measurements can be avoided if the light intensity scattered from single particles is measured. Such optical particle-counting instruments are based on the principle that the particle cloud is sampled through a very narrow light beam. Each time a particle moves through the light beam, a pulse of scattered light can be detected. The intensity of the light pulse is related to the particle size.

Several instruments of this type have been constructed and are commercially available (Air Sampling Instruments, 1966). However, few attempts (Rosen, 1964 and 1968; Junge et al, 1961) have been made to design aerosol counters for high altitude balloon measurements. Particularly during the last few years, the increased interest in stratospheric pollution has created a demand not only for accurate measurements but also for knowledge of the altitude dependence of particle concentration and size.

6-2. AEROSOL COUNTER PRINCIPLE AND DESCRIPTION

From theory (Van DeHulst, 1957) follows that the intensity of light scattered by an aerosol particle into a given direction ϕ is a function of the ratio of particle size to wavelength, r/λ, and of the refractive index of the particle m. This dependence on m can be a source of considerable error in size distribution measurements. The absolute intensity of scattered energy is affected by the particle's refractive index, whereas the angular variation of scattering intensity is much less affected. This leads one to the suggestion to observe the ratio of two different forward scattered intensities as a function of size parameter in order to reduce the disturbing effect of the different refractive indices of various particles.

Penn (1964) shows that over the size parameter range $0.5 < \left(\alpha = \frac{2\pi r}{\lambda}\right) < 5$ (corresponding to a particle diameter range $0.1\,\mu m < d < 1\,\mu m$ with $\lambda \simeq 0.6328\,\mu m$ or approx. $0.63\,\mu m$) it is theoretically possible to measure the particle size by light scattering techniques with an accuracy of 15 percent or better.

The simultaneous measurement at two forward scattering angles also offers the considerable advantage of eliminating errors due to fluctuations of intensity of the illuminating source or due to inhomogeneities of illumination in the scattering volume.

These were the considerations on which the design of a balloonborne aerosol counter was based. (See Figure 6-1.)

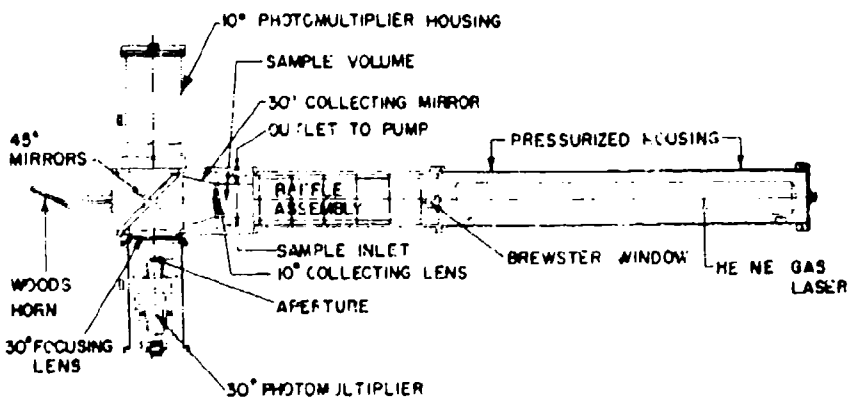

Figure 6-1. Aerosol Counter Optical System

A helium neon gas laser beam of 15 mW power at .6328 μm illuminates the 1 mm^3 scattering volume. The light scattered by aerosol particles entering the

sampling volume is collimated by two annular systems: (1) a lens for the 10-degree light and (2) an off-axis paraboloid of revolution mirror for the 30-degree light. The two beams are directed to each of two photomultiplier detectors. The unscattered direct light is absorbed by a Woodshorn. A carbon-vane oilless pump samples the outside air through the counter. The flow rate is monitored by measuring the pressure drop along a section of the flow channel. The flow rate is in the order of 3 to 5 cm^3/s. The average flow velocity at the sensing volume is 3 to 5 m/s. The minimum transit time of the particles through the sampling volume is approximately 100 to 250 μs. The electronic system processes the information contained in both scattering channels. The data are digitized and recorded on an onboard nine-channel tape recorder for later computer processing on the ground. The circuitry accommodates a dynamic range of four orders of magnitude. In addition to the optical data, several housekeeping functions such as altitude, temperature, and laser output are being sampled.

The aerosol counter can be calibrated with various monodisperse test particles of known size, shape, and refractive index. Excellent particles for this purpose are polystyrene latex spheres suspended in water. These particles are available in several sizes from Dow Chemical. Figure 6-2 shows an example of the response of the aerosol counter to such latex particles of 0.5 μ diameter size. The calibration indicates that the counter accuracy is around ± 10 percent. The actual particle size is derived eventually by using either the absolute intensity of the scattered pulse or the ratio of the two angular signals.

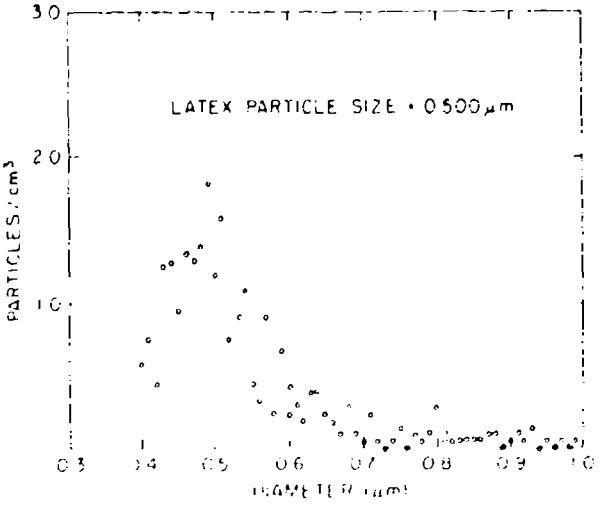

Figure 6-2. Latex Particle Calibration of Aerosol Counter

6-3. BALLOON FLIGHT RESULT

The first balloon flight of the aerosol counter was conducted on 28 October 1970 from the White Sands Missile Range in New Mexico. The pressurized optical housing with electronic chassis and power supply were mounted in an aluminum frame gondola whose sides were covered by reflective aluminum panels for temperature control of the instrument (Figure 6-3). The total payload of the gondola package was approximately 500 pounds. The payload was flown on a two million cubic foot balloon. It was connected to the balloon by a 500-foot letdown reel

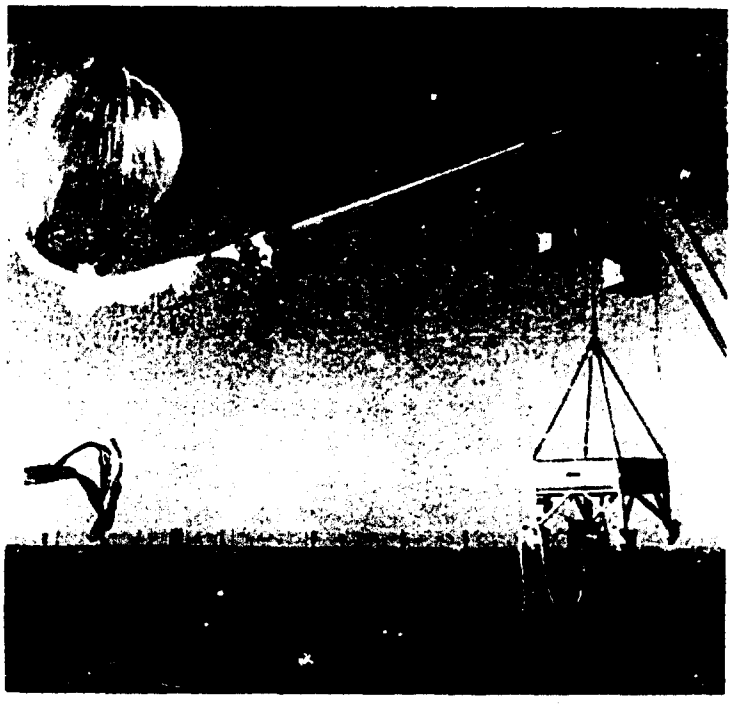

Figure 6-3. Aerosol Counter Gondola During Launch Phase

which was released after launch. The ballast for balloon flight control consisted of 0.4 to 0.6 mm diameter glass beads which were released downward from the instrument gondola through a 10-foot long flexible hose. Since the fall velocity of spheres of this size is >10 m/s, the possibility of entrainment of ballast material into the aerosol counter was negligible in ascent and even during descent. The balloon used for this flight was free of the conventional starch dust (used by manufacturers to avoid sticking of the balloon in packing). Special care was taken

during balloon layout and inflation to avoid dust contamination. The launch occurred at 1402:30 UT (0702:30 MST) from Stallion, White Sands Missile Range (coordinates 33°49'N, 106°40'W). (See Figure 6-3.) The balloon reached a peak altitude of 23.8 km (78K feet), following an east-southeasterly trajectory, and landed at 2100 UT (1400 MST) between Roswell and Artesia, New Mexico (Figure 6-4).

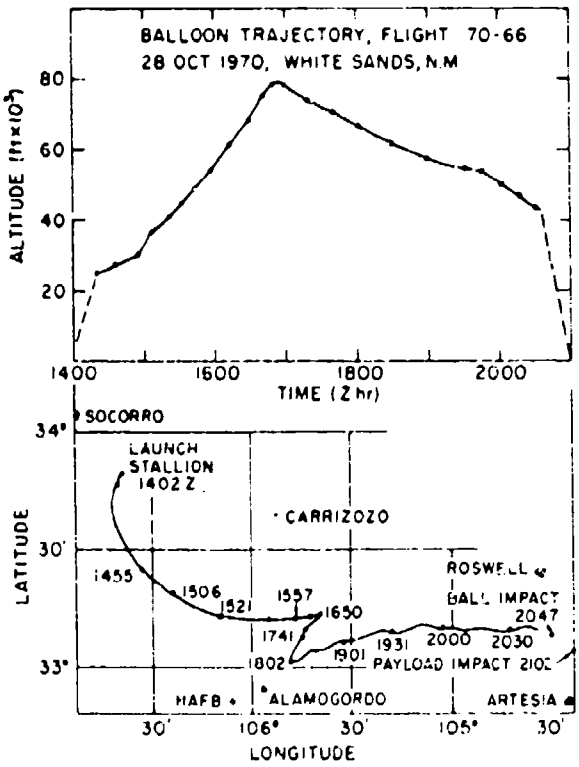

Figure 6-4. Balloon Trajectory Flight H70-66, 28 October 70, White Sands Missile Range, New Mexico

Figure 6-5 shows the vertical distribution of the total number of aerosol particles between 0.2 and 1 μm diameter, as measured in this balloon flight. The aerosol counter was remotely started at 2 km altitude above ground level in order to avoid dust contamination during the launch process. The lack of ascent data between 2 and 8 km and above 15.5 km was due to extremely small or negative flow rates. This condition is caused by the expansion of air in the sample chamber during ascent as the instrument moves to regions of decreasingly lower ambient

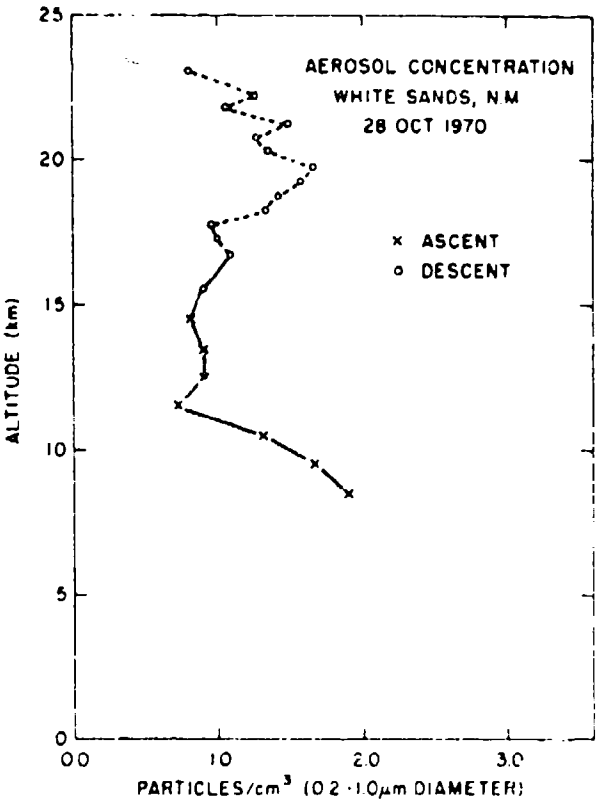

Figure 6-5. Total Aerosol Concentration

pressure. The errors in particle number determination due to this effect become particularly large when sudden changes in the rate of ascent (or descent) occur. These changes are associated with dropping ballast in the control of the balloon flight trajectory. This "exhaling" and "inhaling" effect of the sample volume and resulting errors have been mentioned also by Rosen (1967).

The vertical aerosol profile obtained in this flight does show the characteristic features of the 20-km aerosol layer found originally by Junge et al (1961) and since confirmed by many other experiments. The total particle concentrations measured also agree with data obtained earlier by other experimenters.

For each of the data points indicated in Figure 6-5 the particle size distribution was obtained. An example is shown in Figure 6-6, which gives the size distribution of particles over the size range from 0.2 to 1 μm diameter for the altitude interval from 10 to 12 km during ascent. The distribution follows very nearly an inverse power law with exponent 2.7, in agreement with results obtained by other investigators. A composite of the smoothed size distributions for all

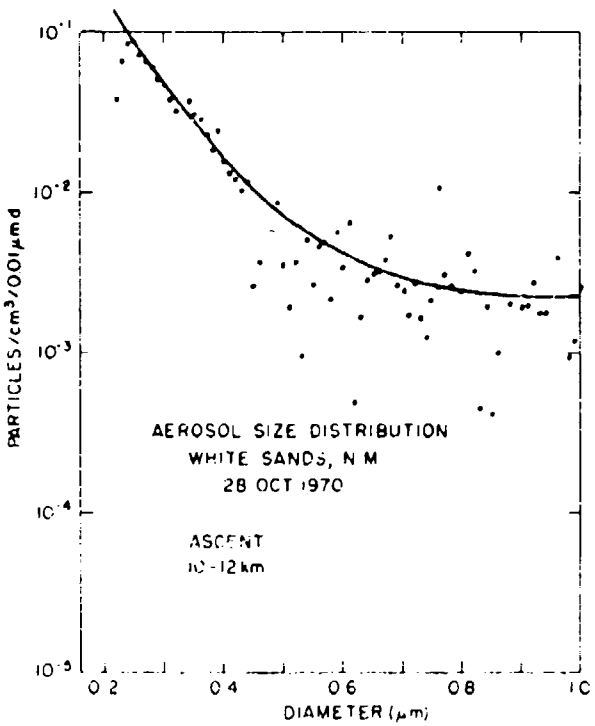

Figure 6-6. Aerosol Size Distribution

altitude intervals is shown in Figure 6-7. The results show a consistent difference in the distribution function between ascent and descent data. The distributions obtained during descent show a deviation from an inverse power law, with a deficiency of small and large particles compared with those from ascent. In general, the distributions fall within inverse power law distributions with exponents 2, 5 and 3. No explanation could be found yet for the differences between ascent and descent data. However, small differences between ascent and descent data were encountered also in earlier investigations by Rosen (1954, 1957, and 1958) and Junge et al (1961).

The discrepancies are much more pronounced in the size distribution measurements than in the total particle concentrations. A number of possible reasons exist for these discrepancies. The particle counts may be accurate, but the ambient aerosol is disturbed by the balloon environment; or the particle counts are incorrect because of the effect of variable flow rate and other factors on the sampling and counting system.

A series of tethered balloon flights were planned in the hope that repeated controlled ascents and descents could provide some indication of the effect of the balloon or of the flight profile on the aerosol counter.

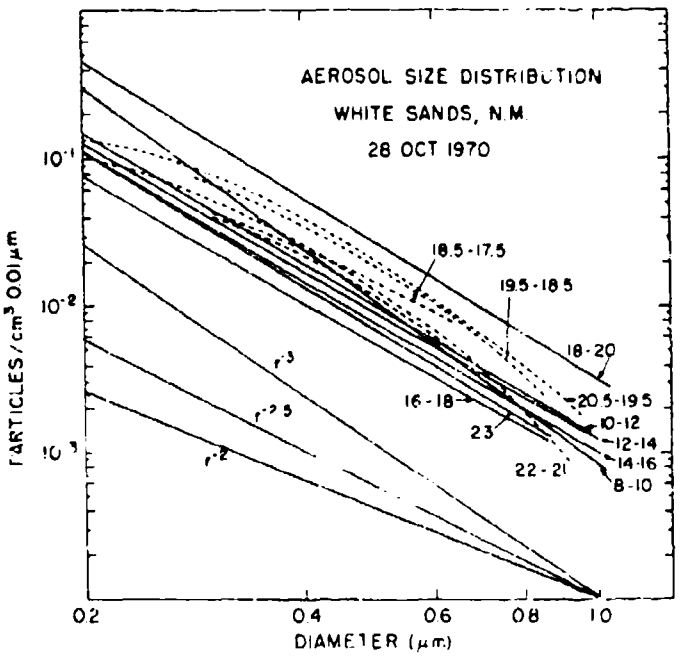

Figure 6-7. Composite of Aerosol Size Distributions for Various Altitude Intervals. Solid lines are ascent, dashed lines are descent data. Altitudes are in km. The three curves at the bottom are theoretical inverse power log size distributions

These tethered balloon flights were conducted during the last week of March and first week of April 1972 at the AFCRL tether balloon site (Fair Site) in the White Sands area, New Mexico. Figure 6-8 shows the balloon gondola arrangement. During the preflight days and the checkout period the instrumentation package was subjected to severe sand and dust contamination.

During the balloon flight period we also had available aircraft measurements of aerosol particles collected by a Royco counter on an AF C-130 aircraft. The Royco counter is a commercially available photoelectric aerosol particle counter which measures particles in the size range from about four-tenths to several microns. This aircraft flew level paths downwind from the balloon at various altitudes to obtain measurements coinciding with the balloon measurements.

Because of limited funding, only a few of the balloon data have been reduced completely at this time. Figure 6-9 shows the balloon flight profile for the flight of 30 March 1972 with the corresponding C-130 aircraft samples. The rate of ascent and descent between the level portions was between 250 and 300 feet per minute. Unfortunately during this flight, as well as during all other flights of the test series, the horizontal wind velocity was always greater than the vertical

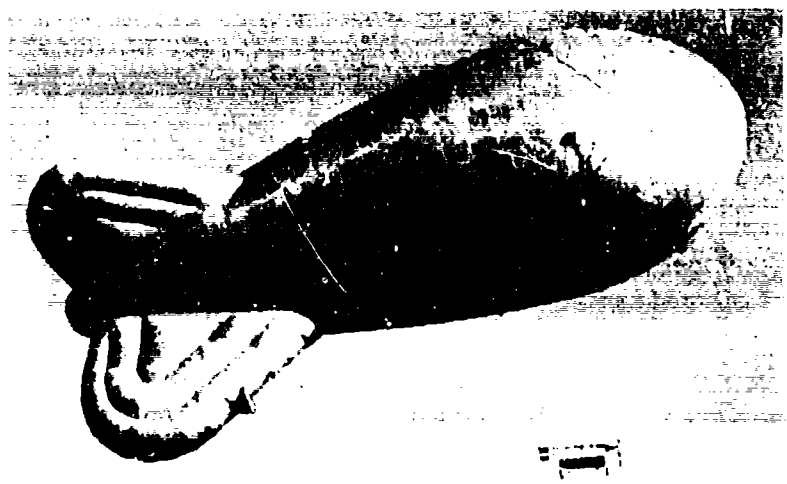

Figure 6-8. Tethered Balloon Flight

balloon velocities, so that no clear answer as to the possible balloon effect on the measurements can be expected. Nevertheless, a number of interesting results were obtained.

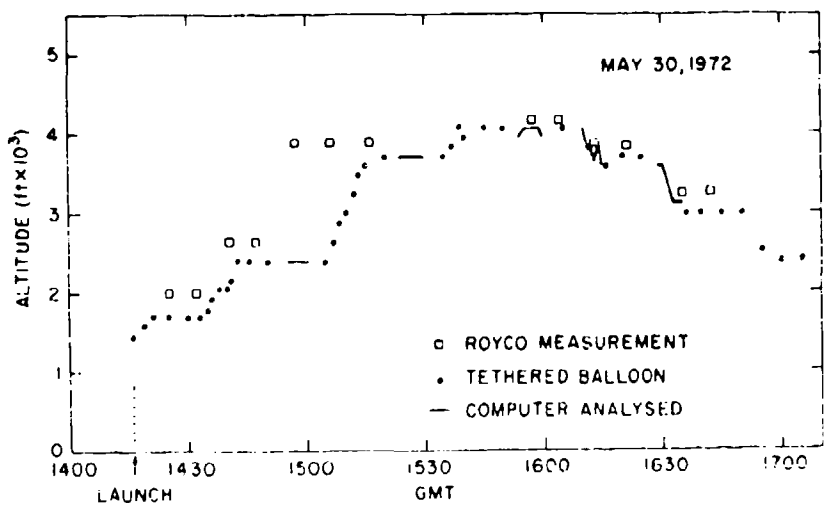

Figure 6-9. Flight Profile of Tethered Flight on 30 May 1972 at White Sands. Squares are C-130 aircraft Royco counter measurements

Figure 6-10 gives results for the flight of 30 March 1972. It shows the total concentration of particles as a function of altitude. The crosses are C-130 aircraft measurements; the dots and bars indicate corresponding balloon measurements; the arrows indicate ascent or descent.

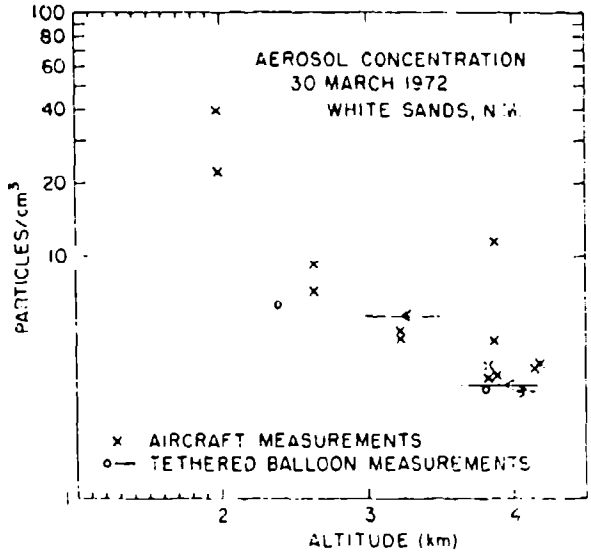

Figure 6-10. Total Aerosol Concentration Profile

The aircraft samples taken at the same altitude vary considerably, even within relatively short time intervals. For instance the measurements at about 2-km altitude are only about 7 minutes apart with sampling times of 2.8 minutes each. During this time interval the aircraft travels a distance of 8 to 9 miles. The samples, therefore, represent a spatial and temporal average. On the other hand, the balloon measurements represent time samples of approximately 5 minutes each with horizontal wind velocities of about 10 miles per hour, thus sampling from a streamline approximately 1/4 mile long. These differences reveal our lack of knowledge about the fine structure of the atmosphere and illustrate the difficulties involved in retrieval of aerosol variations within the range of these variations which can be well within a factor of 2 or 3 or even much higher as observed in some cases.

Figure 6-11 shows the particle size distributions measured at the 3.6 to 4-km altitude level in descent. The balloonborne measurements show a distribution function quite different from the free balloon flight data. This distribution

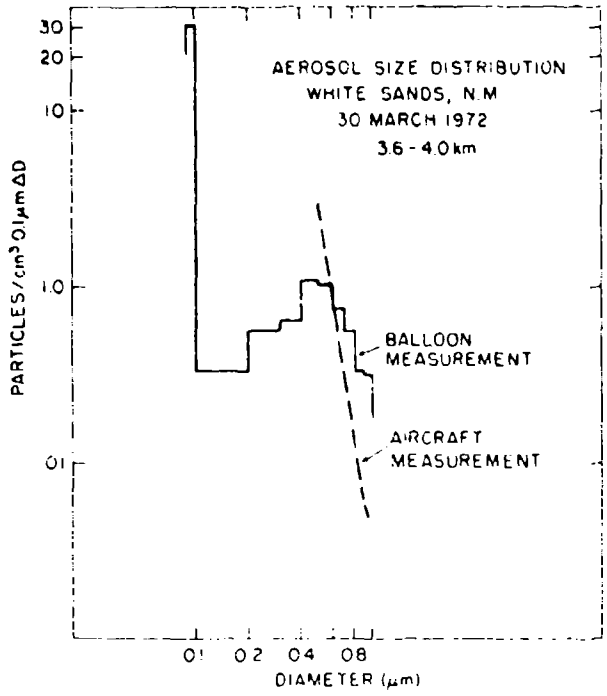

Figure 6-11. Aerosol Size Distribution

with a pronounced peak was found in all samples for the 30 March flight and also in the samples of the 31 March flight. Since the aircraft-based Royco counter only responds to particles $> 0.4\ \mu m$, a comparison of the size distributions is only possible for particles above this size. In general, the aircraft measurements show a size distribution somewhat steeper than the balloon data over this size range. We can give no explanation at the present time for the bimodel size distributions derived from the balloon measurements.

6-4. CONCLUSIONS

The internal consistency within the data derived from the balloon-borne aerosol counters, in free balloon flight ascent and descent as well as in tethered flights, and by comparison with simultaneous aircraft measurements is within a factor of about 2 or 3. Variations of this level, however, are also within the range of normal temporal and spatial fluctuations of aerosol distributions in the atmosphere.

The limited data which have been evaluated indicate the difficulties one encounters if one attempts to correlate aerosol measurements conducted on a scale

equal to or smaller than that for the natural aerosol inhomogeneities in the atmosphere. One might choose a statistical method by averaging over a large number of individual measurements to eliminate natural variations in the aerosol.

Any attempt to resolve variations in atmospheric aerosol distributions which lie within the natural fluctuations from a few individual measurements requires considerable effort, taking into account not only the instrument performance itself, but also its relationship to the test platform.

We are, therefore, considering that in future flights we conduct some measurements of the vertical and horizontal wind components in the gondola environment. It also would be important to measure the electrostatic charge on the balloon to study the possible effect of particle collection. As the demands for predicting the effects of various pollutants on the environment and on our performance within the environment increase, the need for careful aerosol measurement programs and for well-defined research experiment platforms such as balloons or aircraft will be stressed more and more.

Acknowledgments

The experiments described would not have been possible without the enthusiastic and competent support from the AFCRL balloon R&D Test Branch at Holloman AFB. In particular, we appreciate the direction of Maj J. Koehly in the free balloon flight and Capt D. Jackson in the tethered balloon flights.

We also wish to acknowledge the contribution of J. Essex and W. Andon who collected the C-130 aerosol data.

References

Fenn, R. (1964) Aerosol Verteilungen und Atmosphärisches Streulicht, Beitr. Phys. d. Atm. Bd. 37 (Heft 2):69-104.

Junge, C., Chagnon, C., and Manson, J. (1961) Stratospheric Aerosols, J. Met. 18:81-108.

Kerker, M. (1967) Light scattering from colloidal spheres and cylinders, in Electromagnetic Scattering, R.L. Rowell and R.S. Stein, Eds., Gordon and Breach Sc. Publ.

Rosen, J.M. (1964) The vertical distribution of dust to 30 km, J. Geophys. Res. 69:4673-4676.

Rosen, J.M. (1967) Simultaneous Dust and Ozone Soundings Over North and Central America, Report AP 25, School of Physics and Astronomy, Univ. of Minnesota.

Rosen, J.M. (1968) Simultaneous dust and ozone soundings over North and Central America, J. Geophys. Res. 73:479-486.

Shifrin, K.S., and Perelman, A.T. (1967) Inversion of light scattering data for the determination of spherical particle spectrum, in Electromagnetic Scattering, R.L. Rowell and R.S. Stein, Eds., Gordon and Breach Sch. Publ.

Van DeHulst, H.C. (1957) Light Scattering by Small Particles, Wiley, New York.

(1966) Air Sampling Instruments, American Conference of Governmental Industrial Hygienists, Cincinnati, Ohio.

Contents

7. The Powered Balloon System

R. Leclaire, 2/Lt, USAF and A. Korn
Air Force Cambridge Research Laboratories
Bedford, Massachusetts

7-1. INTRODUCTION

A number of organizations within the Air Force and agencies outside the Air Force such as NASA, the Department of Interior and the Department of Agriculture have expressed an interest in having the capability to suspend a payload over selected points on the ground for long periods of time. A. O. Korn of Air Force Cambridge Research Laboratories (AFCRL) developed the concept of a powered balloon to fulfill this requirement. AFCRL has studied (both in-house and contractually) the feasibility of providing a propulsive force on an unmanned, free balloon to accomplish a high-altitude hovering or loitering mission. These studies show that such a system is feasible at altitudes near 60,000 feet over a number of areas at selected times of the year.

The entire concept of powering a free balloon is dependent upon what we call the "minimum wind field." A number of investigations in recent years have been devoted to the phenomena of maximum winds in the atmosphere, especially those related to jetstream activity. Minimum and zero wind fields have received less attention, apparently because they are of little operational importance in the performance of most aerospace vehicles. Minimum wind fields are, however,

extremely pertinent to high-altitude free balloon applications, whenever it is desirable to obtain maximum flight duration with minimum horizontal movement from a fixed geographical location. Figure 7-1 shows a simplified pattern of the winds

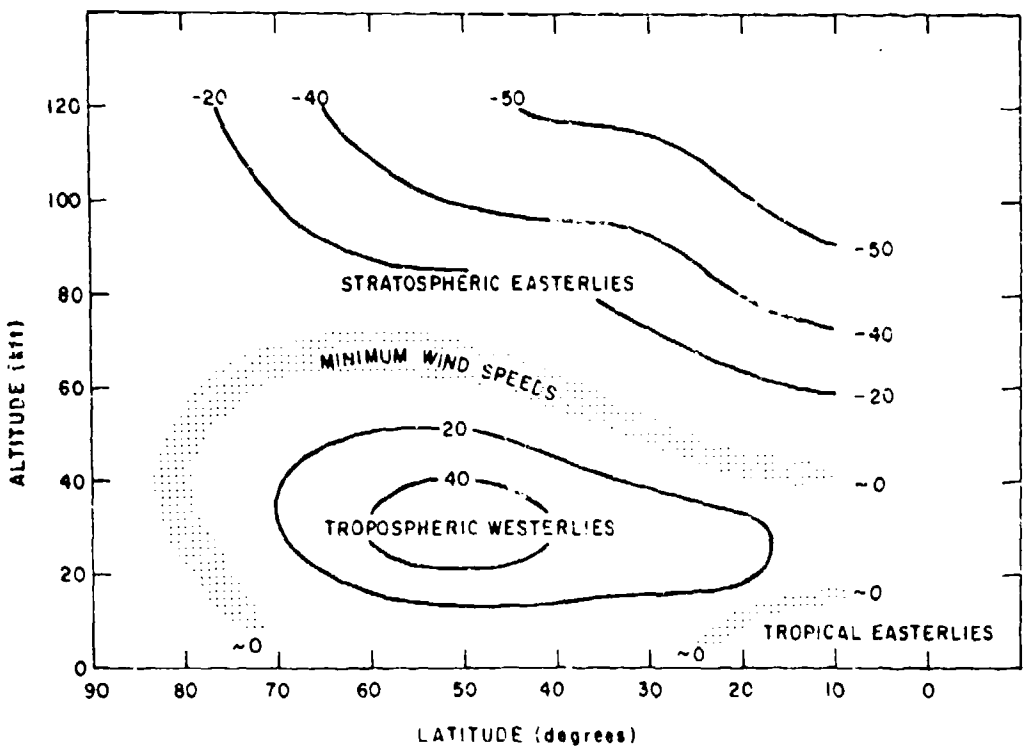

Figure 7-1. Simplified Pattern of the Winds

which cause this phenomenon. Strong westerly winds below strong easterly winds result in a transitional area where the winds are minimum (Figure 7-1). Within this layer there are levels where the winds are essentially zero. Details for the useful application of this phenomenon are explained later.

7-2 HISTORY

For several years the Aerospace Instrumentation Laboratory has been flying unpowered balloons in this minimum wind layer to study the structure of the minimum wind fields and to see if it is possible to keep a flight system over a point on

the ground for extended durations without propulsion. These tests have been encouraging in that we have been able to keep a balloon within a 100-mile radius for up to 100 hours (see Figure 7-2). While the balloon is flying, rawinsonde data are used to find a desired wind region. By ballasting or valving we can use the winds to stationkeep.

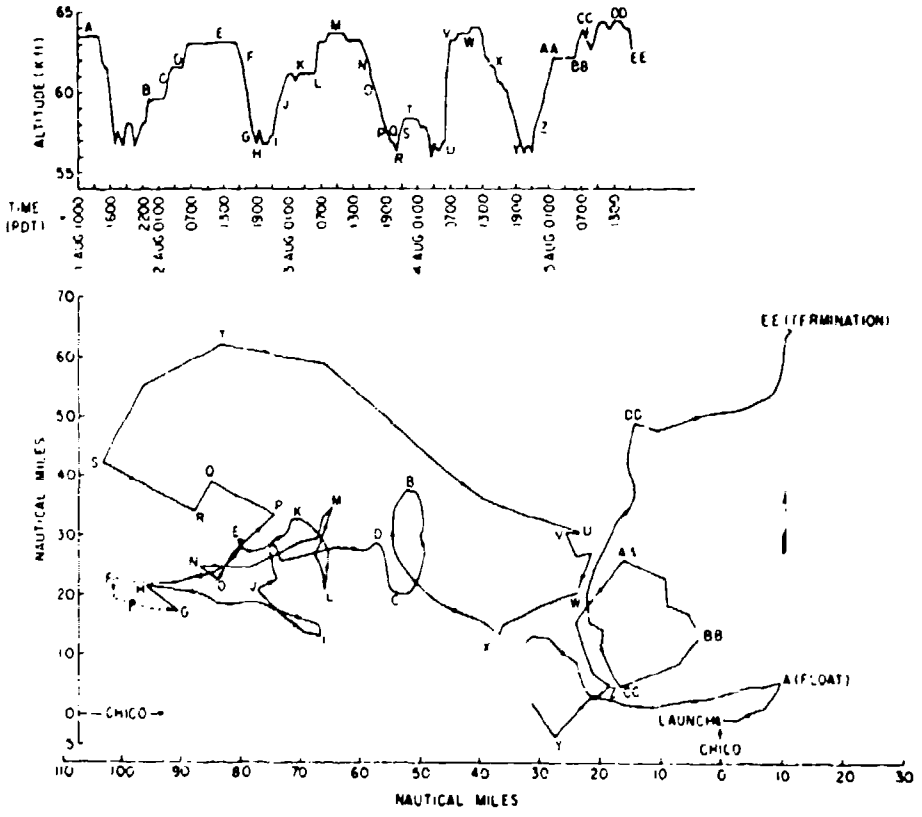

Figure 7-2. Hovering Balloon Flight Track

The concept is shown pictorially in Figure 7-3. The flight system (with its payload attached) is launched in the conventional manner. It ascends to the minimum wind layer unpowered. Upon reaching the min-wind field, the motor is turned

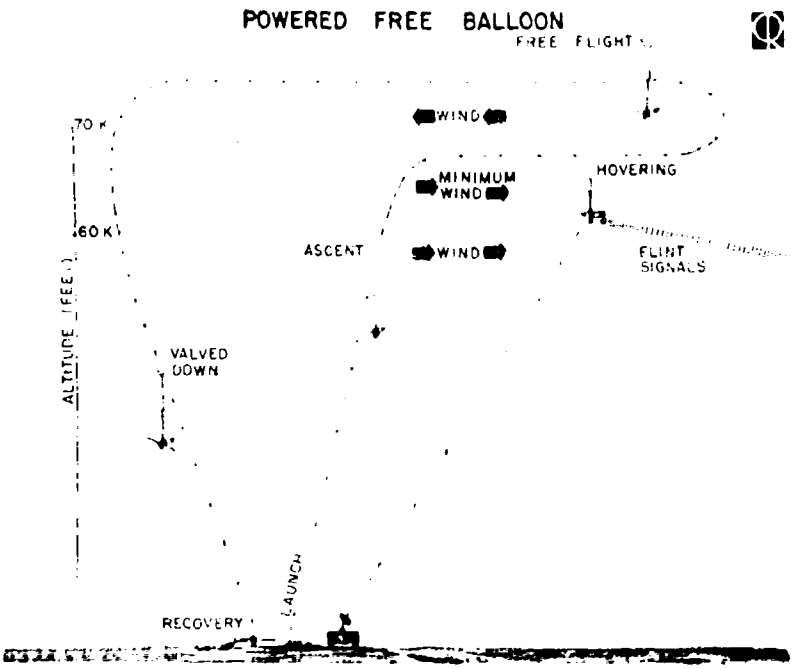

Figure 7-3. Powered Free Balloon Schematic

into the wind by radio control, and stationkeeping is accomplished. After accomplishment of the mission, the payload is recovered.

As a result of this work, a contract was awarded to Goodyear Aerospace Corporation to study the feasibility of supplying just enough thrust to cover all the wind drag on a pressurized balloon and to perform a parametric study to design an economical system for a flight demonstration. A system was designed for demonstration purposes that uses conventional tree balloons and existing hardware and launch equipment. This program was funded by the AFCRL Laboratory Directors' Fund. The demonstration is designed to carry a useful payload of 200 pounds to an altitude of 60,000 feet for 24 hours. It has a powered flight duration of 12 hours (50 percent duty cycle) at a speed of 15 knots and floats without power the rest of the time. Figure 7-4 shows the gondola during testing at Akron. The propeller is 36 feet in diameter, and the gondola weighs 3500 pounds. The rudder is 8 feet 9 inches high and 2 feet 6 inches wide.

The system was flight tested at Holloman AFB, New Mexico on 16 September 1972. After three hours of powered flight, the rudder separated from the payload, and the flight was terminated. In the three hours of powered flight the concept was proven. We were able to move the balloon against the wind. The cause of failure

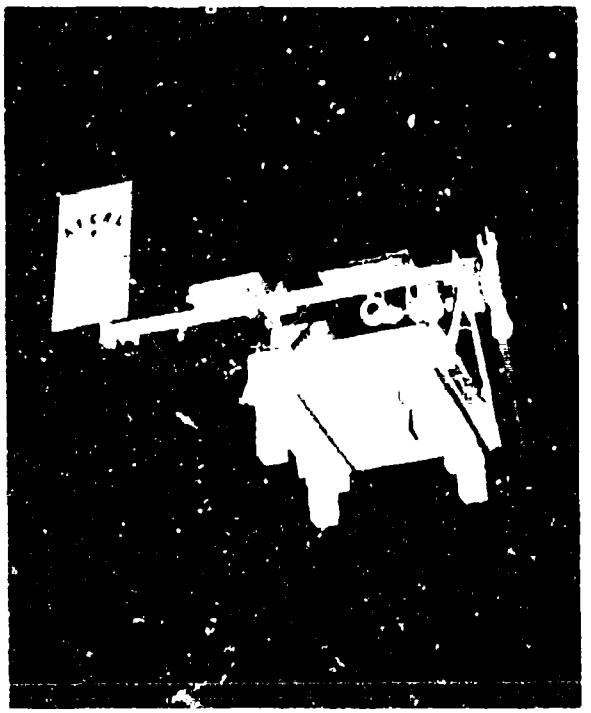

Figure 7-4. Powered Balloon Gondola

is being investigated and believed to be fatigue failure in a 2-inch diameter tube. This is a mechanical problem and not a concept flaw. Current plans call for a re-flight in November of this year.

7-3. COMPARISON WITH DRONES

Because the powered balloon, hereafter known as POBAL, is, after all, an unmanned remotely controlled atmospheric vehicle, its performance must inevitably be compared with the capabilities of drone aircraft. Even a generalized comparison, however, is complicated by the need to place the latest experimental drones – which have remarkably improved endurance and altitude – in a category apart from the other fixed-wing unmanned aircraft.

In altitude, for example, most drones are limited to ceilings well below 60,000 feet; but the newest drones fly above 50,000 feet in the same atmospheric regions as POBAL.

Payloads in the range of 200 pounds are typical of both POBAL and drones. There is at least one drone aircraft that can carry 700-pound payloads, however.

It is in POBAL's unique combination of mission duration, range, and speed that its characteristics differ most radically from any drone. Although immediate goals for current drone development are increased endurance, high altitude capability, and slow speed, the fixed-wing drone aircraft is basically a high speed, long range, short duration vehicle compared to POBAL. The phenomenal 36-hour endurance recently reported for an advanced experimental drone is twice the endurance of its nearest competitor; conventional drones typically have durations of a few minutes. In contrast, the POBAL mission endurance is one week or more with fuel cell power and twenty days to several months with solar cells.

Range, for most drones, is measured in hundreds of miles, whereas POBAL is specifically designed to remain within a very few mile radius of a designated location, while it floats above 60,000 feet throughout its prolonged mission. A drone helicopter obviously would have a similar hovering capability, but its ceiling altitude would be very low, and its duration presumably would be limited by a much greater power requirement than POBAL.

There are at least two other practical considerations. Unlike drones, POBAL is limited to operation during the season of minimum high-altitude winds. It has the great advantage, on the other hand, that balloon payloads can be configured in almost any shape and volume and need not conform to the stringent design specifications required for integration with a drone aircraft.

7-4. REQUIRED DEVELOPMENT

There are several areas requiring major developmental work in order to achieve an operational POBAL system. These are as follows:

(a) Development of a light-weight power supply system
(b) Development of a shaped superpressure balloon
(c) Meteorological studies
(d) Development of altitude-changing capability
(e) Development of navigational equipment.

The two areas requiring the most immediate effort are the development of a suitable power supply and the design of the balloon.

7-4.1 Power Systems

To date, the primary emphasis has been on power requirements. Several studies have been made which indicate that the most likely candidate power sources

for a high altitude, long duration, free powered balloon are an H_2O_2 fuel cell, a solar cell-secondary battery combination, or possibly a turbine engine modified to work at altitude with the proper amount of thrust.

A computer program was written to determine the feasibility and system requirements for a spherical, superpressure balloon powered by solar cells and AgZn secondary batteries. This program considers power requirements, battery capabilities, solar cell capabilities, lift, system weight capabilities, and propeller characteristics and then designs the smallest balloon system consistent with these inputs. Initially, the cadmium sulfide cell seemed a likely candidate due to its very light weight and low cost per cell, and the first program was run using a CdS array. Subsequently, we realized that silicon cells must also be investigated and the program was modified and run for silicon cells. For both cell types we assumed the output to be a cosine function of the angle of incidence.

Figure 7-5 shows a generalized flow diagram of the spherical balloon-solar cell program. With elimination of the daylight loop, it is the flow diagram for an aerodynamically shaped balloon-fuel cell program which was also developed. These programs, consistent with the state of the art, considered the use of solar cells, batteries, and fuel cells which have already been developed. Availability is not assured, however, for the CdS cells. At present they are not in production in the United States, and very limited work is being done in Europe. The existing CdS cells have degradation problems, low efficiency (about 2 to 4 percent), and very expensive interconnectors. These characteristics negate many advantages of CdS cells over silicon.

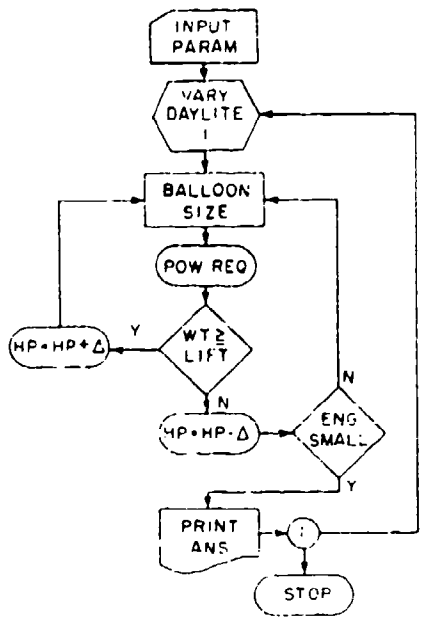

Figure 7-5. Computer Program Flow Diagram

The computer programs indicated that a useful power system will require an output in the range of 3 to 5 kW, or 2 to 10 shaft hp. If solar cells are used, it will probably be necessary to use silicon cells due to availability. They are more efficient than CdS cells, but they are very expensive and somewhat heavier for the same power output ($700,000/kW). The most advanced silicon solar array to date is the flexible, rolled-up solar array (FRUSA), developed by the USAF Aero-Propulsion Laboratory, Wright-Patterson AFB, Ohio. This is a directional array

with a power output of 1.5 kW. It weighs 70 pounds. The weight of the solar cells alone is only 22 pounds and is comparable to the weight of CdS.

We would like to use an undirected array. The balloon surface would be the supporting structure. A directed array would be difficult to launch and control, and its greater complexity increases the probability of malfunction. However, the undirected array presents formidable structural problems and higher cost due to the considerably larger number of cells needed for the array.

7-4.2 Shaped Balloon

Let us now consider the choice of aerodynamically shaped or spherical balloon. The shaped balloon has an attractive coefficient of drag (assumed C_D = 0.07), but the large, lightweight one we require would be difficult to build and launch. The spherical balloon is relatively easy to fabricate and launch, but its C_D is high in comparison (C_D = 0.19); a large power source would be necessary to provide stationkeeping capability.

A comparison of several systems with 15-knot and 20-knot true air speed capability for seven days is shown in Figures 7-6 and 7-7. A spherical balloon is feasible at 15-knot capability, and when meteorological constraints allow its use, this type of balloon should be used. Preliminary studies indicate, however, that far more often a capability of 20 knots will be required, and then one must go to an aerodynamically shaped balloon system.

VELOCITY - 15 KNOTS

DURATION - 7 DAYS

SYSTEM	SHP	POWER WT	TOTAL WT
Round; AgZn+CdS S.C.	5.2	2,930	3,650
Shaped; AgZn+CdS S.C.	1.2	1,010	1,574
Shaped; H_2-O_2 F.C.	.8	375	960

S.C. - Solar Cell

F.C. - Fueld Cell

Figure 7-6. System Parameters: 15-Knot, 7-Day

Duration is another criterion that can change the system design. For very long durations (30 days and up), the only feasible power source is solar cells. For durations up to about 20 days, a fuel cell system is better due to its lighter weight. (See Figures 7-8 and 7-9).

VELOCITY - 20 KNOTS

DURATION - 7 DAYS

System	SPF	Power Wt	Total Wt
Round: Ag/Zn CdS S.C.	18.8	9,413	10,600
Shaped: Ag/Zn-CdS S.C.	2.6	1,590	2,360
Shaped: Ag/Zn-Si S.C.	2.6	1,530	2,240
Shaped: H_2-O_2 F.C.	1.6	495	1,100

S.C. - Solar Cell

F.C. - Fuel Cell

Figure 7-7. System Parameters: 20-Knot, 7-Day

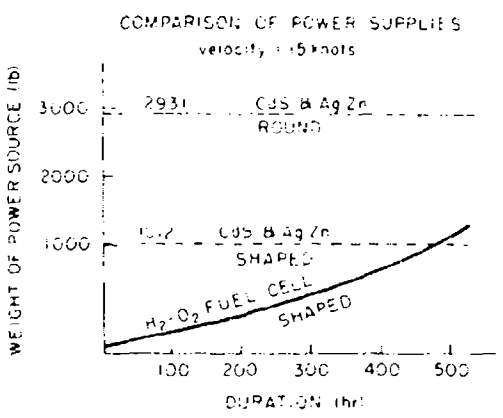

Figure 7-8. Comparison of Power Supplies: V = 15 Knots

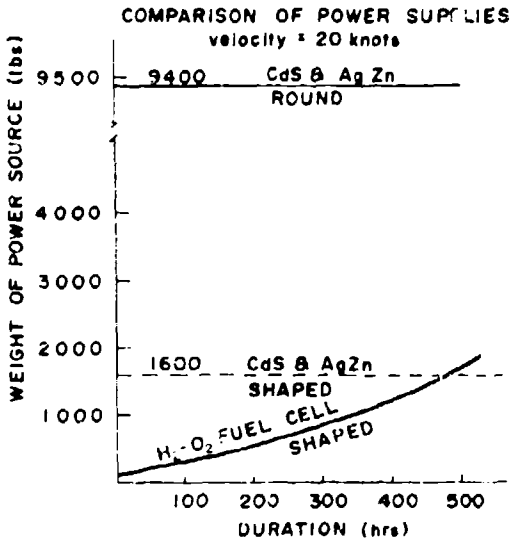

Figure 7-9. Comparison of Power Supplies: V = 20 Knots

The breakeven point is defined by the specific fuel consumption (SFC) and tank weight of the fuel cell system.

Some rules of thumb to use with primary H_2O_2 fuel cells are:

Weight of Reactants	.8 lb/kW-hr
Cryogenic Tankage	1/2 Weight of Reactants
Cell Hardware	30 lb/kW

There are several other types of power supply systems which we are investigating for possible use in this system. These include turbojet and shaft, nuclear power, laser beamed power and the Stirling (closed cycle) engine.

7-4.3 Meteorological

The eventual POBAL system will be limited in its applications because it depends upon the winds for its capabilities. Obviously, if wind speeds are stronger than the velocity capabilities of the system, it will not be able to stationkeep. In order to determine if a powered balloon is feasible for a particular operation, one must know the location, altitude, tolerances for both, duration required, and the time of year. From this information one would derive a climatology for the area. G. Nolan of AFCRL has done a great deal of work in this area. At present Mr. Nolan feels the most helpful charts for POBAL would be similar to the one shown for Las Vegas, Nevada in Figure 7-10. This chart shows the frequency of

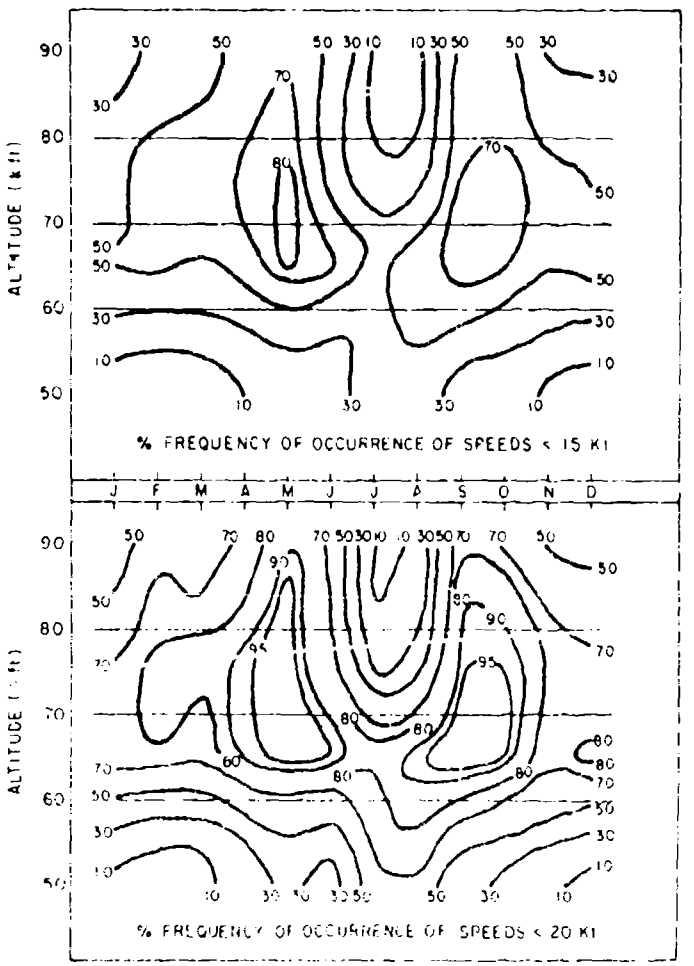

Figure 7-10. Wind Frequency, Las Vegas, Nevada

winds below a velocity of 15 and 20 knots for different altitudes at different times of the year. With this knowledge one could confidently fly a system with a 20-knot capability at 70,000 feet in the spring and fall. This confidence would be enhanced if the system had an altitude control capability of ± 5000 feet. One could seek the most favorable winds to keep on station. Just as important as this information is the knowledge that a system at 85,000 feet in December and January would have little chance of success. In order to properly use the powered balloon concept, a climatology chart must be prepared for the specified area.

7-4.4 Altitude Changing

At present the two most promising methods for changing altitude are air ballast and propulsion-system pitch control. An air ballast system designed by Rand Corporation under USAF contract might be used. It is essentially a balloon within a balloon. This concept will be investigated further. The motor pitch control effect is limited by the thrust available and would allow only small changes in altitude (approximately 2000 feet).

7-4.5 Navigation Equipment

Finally, a navigation system is required. For the test flight, the radar at White Sands Missile Range will be used for tracking, but since radar will not always be available, an on-board tracking capability such as Omega will be required. An autopilot will also be designed for the system.

Since the early 1950's, the primary method for tracking free balloons has been the use of high frequency beacon triangulation utilizing radio bearings taken on signals transmitted from the balloonborne payload. In the mid 60's the need for better positioning was apparent, and work began on several devices for alternate methods of balloon navigation and tracking. In 1966 a miniaturized version of a balloonborne omnirange locating system was proven operational and demonstrated accuracy consistently better than five miles on several balloon flights from Chico, California and Wallops Island, Virginia. These flights proved a theory that only six preselected omnirange frequencies need be employed to provide adequate position coverage across the entire,continential United States at altitudes above 60,000 feet.

The need still prevailed for accurate tracking over remote sparsely settled areas and wide ocean areas. A survey was conducted of other available radio navigation aids as possible candidates for use with balloon systems. Omega emerged as the candidate to meet all objectives. Unfortunately, Omega was a long way from being an operational system.

The Omega system is configured to provide all weather day-night capability. Although it is a hyperbolic system as is Loran, all of the transmitting stations are time synchronized so that it is not necessary to use a given pair of stations as with Loran. The signals are not only time synchronized, but are also phase locked to a common time standard. Omega suits the requirements for a dependable long-range navigation system better than any other system in operation. It has been in limited operational status since the spring of 1966, and four stations are currently on the air, although not transmitting full power. The eventual complete network of eight stations will provide full global coverage with a choice of stations for all areas. Completion is scheduled for 1975.

To utilize the Omega system with CRL balloons, we are developing under contract a balloonborne Omega signal processor with the objectives shown in Figure 7-11. Figure 7-12 illustrates pictorially our use of Omega with a scientific balloon package including a signal processor, which is receiving Omega transmissions from North Dakota, Trinidad, and Hawaii. The retransmission of position information to a remote ground station and a mobile station is depicted by the high frequency telemetry link.

This is probably the navigation system which will be used for POBAL as well as for other AFCRL packages.

7-5. CONCLUSION

Figure 7-13 is an artist's concept of one possible ultimate system. For propulsion it uses a stern mounted propeller and motor, powered by a solar cell array and batteries in this case. Possibly it will instead use a fuel cell for power. It is aerodynamically shaped to reduce the coefficient of drag to an acceptable figure. It will have a 20- to 25-knot capability at 60,000 feet to 70,000 feet, a useful payload of 200 pounds, and a duration of several weeks. It can be used for such varied missions as an intelligence platform; a communications, command and control relay; a sensor technology test platform; pollution control; crop resources and earth resources surveys.

OMEGA SYSTEM

Area Coverage	Global
Time Coverage	Continuous
Frequency	10.2, 13.6, 11.33 KHz
No. of Stations	8
Radiated Power	10 to 25 Kilowatts
Fix Accuracy	1 NM Day 2 NM Nite
Signal Format	Time Sequenced CW
Geometry	Hyperbolic or Circular
Measurement Technique	Phase Difference

Figure 7-11. Omega Systems

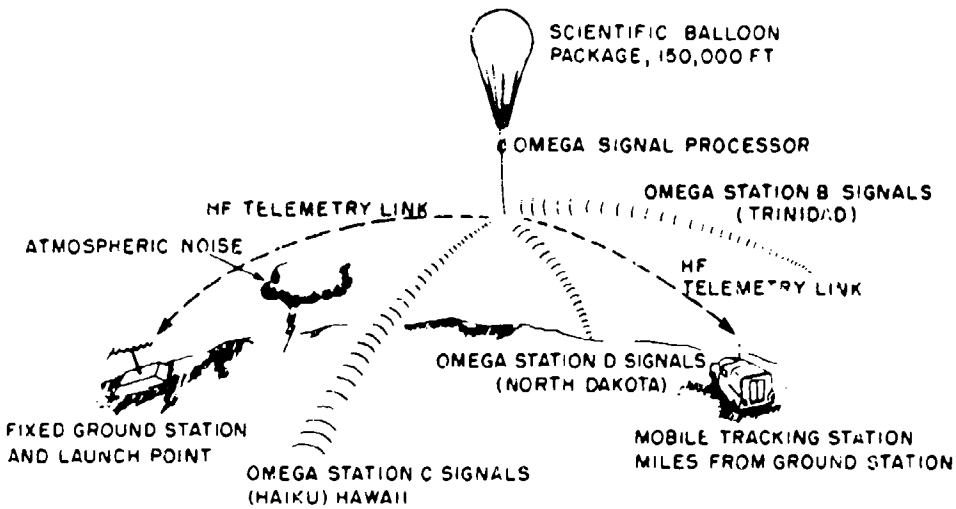

Figure 7-12. Balloon Positioning System

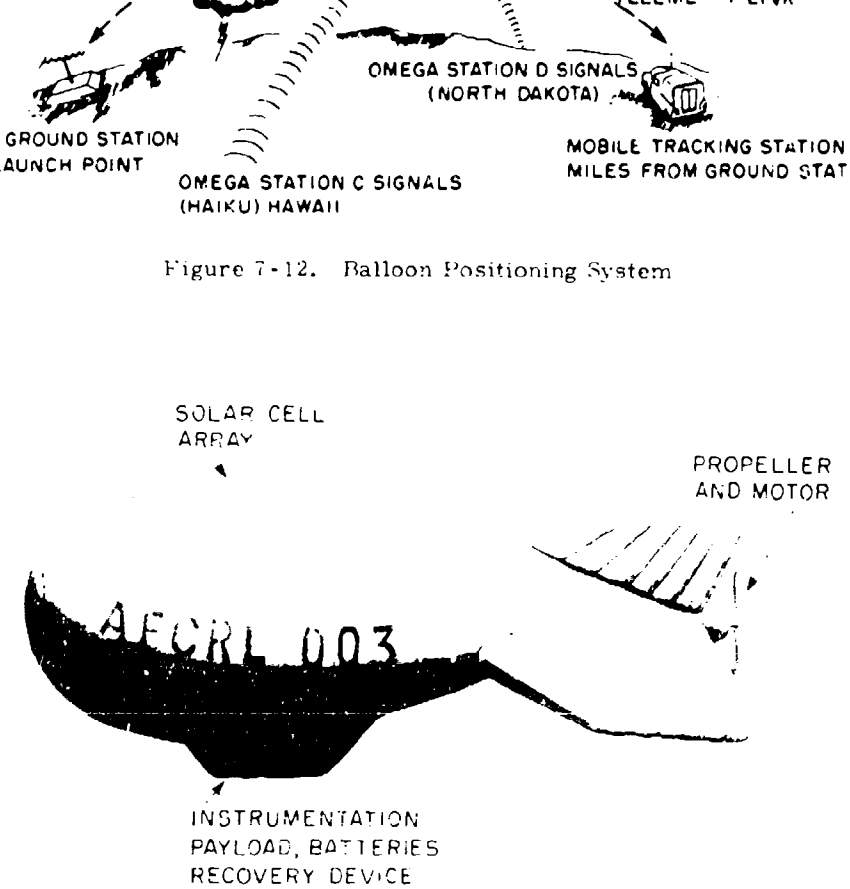

Figure 7-13. Sketch of Ultimate System

This work is several years from completion and operational status. The completed test in September of this year is only the first step. Next the system herein described will be built, based upon detailed study of the design requirements. The flight will determine which areas require additional work. A new system will be built and flown as the last step prior to operational status, if no major problems remain.

Acknowledgments

The authors are grateful to George F. Nolan, Catherine B. Rice and Ralph J. Cowie for technical assistance in preparing this paper.

References

Hamilton, R.C. (1968) Performance analysis and selection of balloon electrical power systems, Proceedings, Fifth AFCRL Scientific Ballooning Symposium (No. 28):297-354.

Massie, L.D. (1971) Flexible rolled-up solar array. Paper presented at Sixth AFOSR Symposium on Advanced Propulsion Concepts, Buffalo, N.Y.

Nolan, G. (1964) High-Altitude Minimum-Wind Fields and Balloon Applications, AFCRL 64-843.

Nolan, G. (1967) A Study of Mesoscale Features of Summertime Minimum Wind Fields in the Lower Stratosphere, AFCRL 67-0601.

Vorachek, J.J. (1968) Investigation of Powered Lighter-Than-Air Vehicles, AFCRL 68-0626.

Vorachek, J.J. (1970) A comparison of several very high altitude station keeping balloon concepts, Proceedings, sixth AFCRL Scientific Balloon Symposium, AFCRL 70-0543 (No. 30):355-382.

Contents

8. Power Sources for a Powered Balloon

C.B. Rice
Emmanuel College
Physics Research Dept.
Lexington, Massachusetts

8-1. INTRODUCTION

When I began to search for power sources suitable for the powered balloon POBAL, the guidelines were fairly well established. It had been determined that, unusual as a propeller would seem at 30,000 feet, with the slow forward speeds and low thrust level required for POBAL, a propeller driven system would work. Of course, the propeller would have to be very large. Inquiries to USAF propulsion specialists and industrial sources to find alternatives had been largely negative, and it was reasonably certain that, at least for the immediate future, POBAL would be propeller driven from an electric motor.

In the previous paper, Lt Leclaire has described his analysis of the energy-to-weight and cost merits of the available fuel cell batteries and solar cell arrays to drive either an electric motor or possibly some other type of converter to keep POBAL on station for several days. He concluded that for periods of more than one day to twenty days, POBAL should be powered by fuel cells, while for longer periods a silicon solar cell array is the most practicable system currently available.

At that point in the planning, in view of the high cost and various complications involved in using fuel cells or solar cells, we wanted to know how far short of

desired performance and cost the other available power sources might be. We also hoped that there might be somewhere another less expensive type of long-duration power device suitable for POBAL.

I was searching for a very lightweight power source or, preferably, a complete system to operate at altitudes above 60,000 feet at speeds under 15 knots, one to deliver approximately 3.5 kilowatts to an electric motor, or 2 to 20 shaft horsepower to a propeller, or 50 to 100 pounds of thrust. The overall weight, including the fuel supply for six days at 50 percent duty cycle, was restricted to 1000 pounds. The device must have throttle control and be capable of many start-stop cycles at altitude.

I sought new developments in high-energy, lightweight batteries, for example, and tried to track down the rumors of breakthroughs in solar cell technology that would appreciably reduce their cost.

8-2. SHAFT ENGINES

Gas turbines have very attractive weight characteristics. Figure 8-1 shows the allowable range for specific fuel consumption versus dry weight for engines delivering 10 and 20 horsepower. These curves presuppose that an engine that meets these fuel and weight limitations produces just 10 or 20 horsepower.

There are some turboshaft engines with dry weight and specific fuel consumption in the desired range. Nominal ratings are misleading, however, because nominal specific fuel consumption is measured under full power output, and nominal power output refers to static operation at sea level. Obviously, at very high altitudes the power output of an airbreathing engine will be considerably reduced – if the engine does not blow out from lack of oxygen to maintain combustion. The maximum altitude for marginal operation and the actual power output at that height are a function of the individual design. Those turbine engines with high compression ratios are most likely to function at high ceiling altitudes, but unfortunately high compression ordinarily is obtained by using multistage compressors which increase the overall weight.

Typical of the smallest turboshaft engines are the AiResearch unit (171 pounds, 403 shaft horsepower) and the Allison (only 139 pounds, 317 shaft horsepower) indicated in Figure 8-1, but neither one operates at sufficiently high altitude for POBAL.

The turboshaft with lowest fuel consumption rate listed in Jane's All the World's Aircraft (1971-1972) or any other source available to us is the Pratt & Whitney ST-9. This advanced, small, high compression ratio engine was built as a single demonstration unit in competition with the General Electric GE-12.

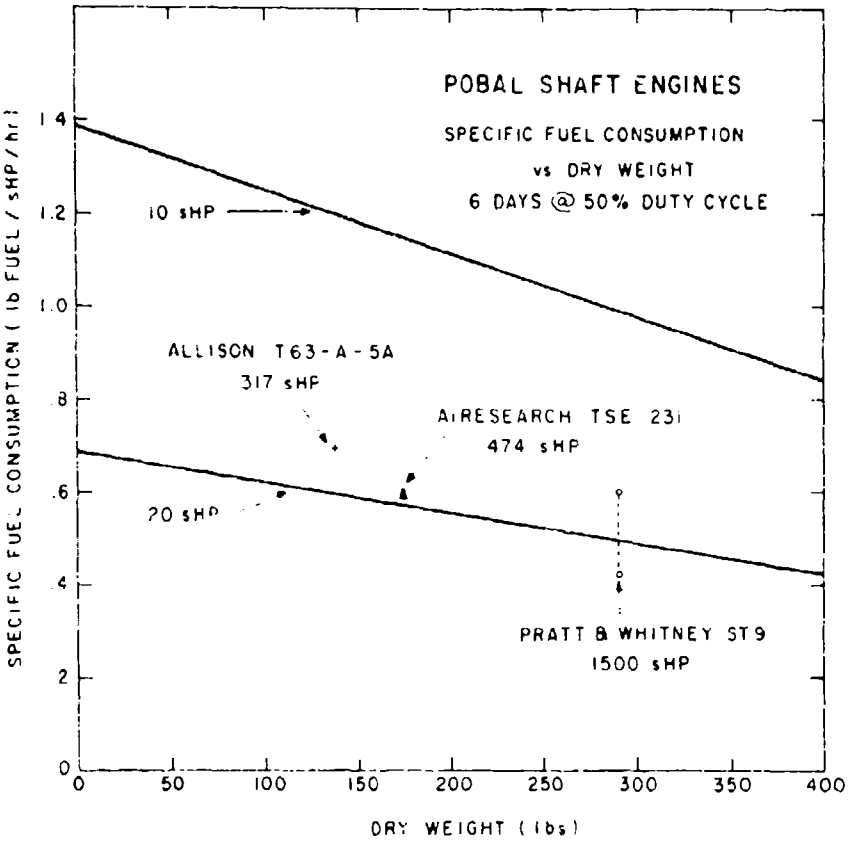

Figure 8-1. POBAL Shaft Engines

Both are rated at 1500 shaft horsepower, so even at their ceiling altitude the output is not likely to be in the 10 shaft horsepower range. Neither engine is available, so the question whether they can be operated above 60,000 feet is academic. After this study was made, the USAF Aero Propulsion Laboratory (E.C. Simpson, letter communication) confirmed our conclusion that turboshaft engines cannot meet the POBAL requirements.

8-3. THRUSTERS

8-3.1 Turbojet Engines

The national inventory of turbojets presents a different situation. There is no difficulty in finding turbine jet engines that function well above 60,000 feet. Some of them propel unmanned aircraft (Miller, 1970; Multiple Roles . . . , 1972). They are not

designed for multistart-stop operation at high altitude, however, and would require an auxiliary starter for POBAL. They weigh upward from a few hundred pounds and produce 1000 pounds or more thrust at sea level.

Figure 8-2 shows allowable weight versus specific fuel consumption for a POBAL device producing thrust. With no allowance at all for dry weight the maximum possible fuel consumption rate per pound of thrust to deliver 50 pounds of thrust to POBAL for 72 hours (50 percent of 6 days) is only 0.28 pounds of fuel per hour per pound. Unfortunately, the very best rate for one of the lightweight turbojets is greater than 1 lb/hr/lb. Even if we could find a turbojet with an auxiliary starter that weighed, for instance, only 100 pounds, and its thrust scaled to altitude was about 50 pounds, it could run for only 18 hours to provide a duration for POBAL of about one and a half days. The USAF Aero Propulsion Laboratory at Wright-Patterson Air Force Base studied this problem also and has assured the Air Force Cambridge Research Laboratories that there is no turbojet engine that meets the POBAL requirements.

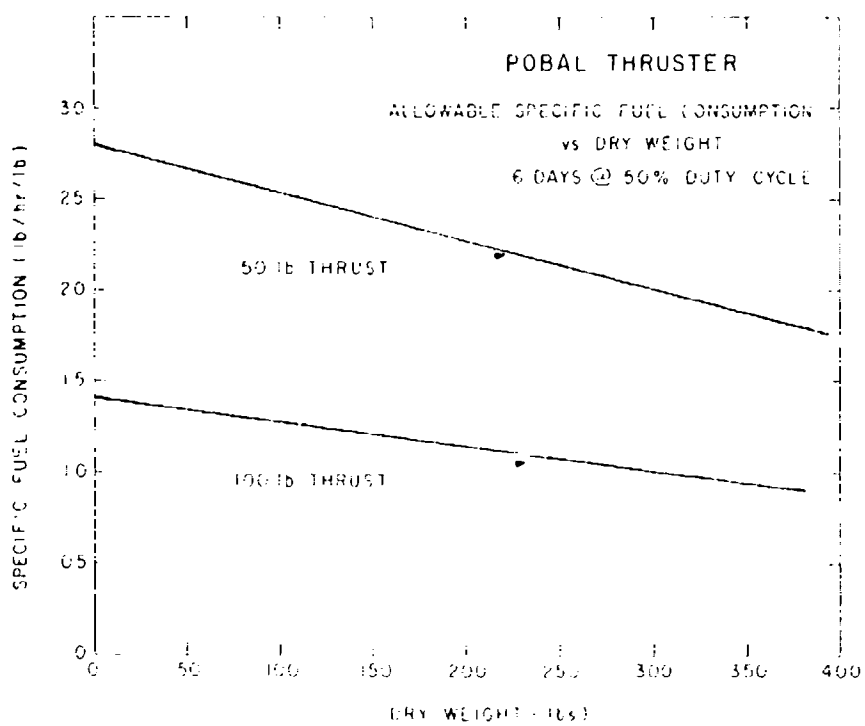

Figure 8-2. POBAL Thruster

8-3.2 Electric Thrusters

Many small thrusters have been developed for special purposes in space flight. "Electric" thrusters in various ways produce a stream of charged particles which is accelerated in an electrostatic or an electromagnetic field. The devices that are now operational develop thrust in micro- or at most millipounds, and their cost is measured in 10^5 dollars (Holcomb, 1972)!

In the same low thrust, high cost category there are the resistojets (Page, 1970) which develop heat by passing current through a solid and thereby heat a stream of gas for propulsion.

8-3.3 Chemical Thrusters

Some simple, chemically-fueled thrusters – small rockets – do produce thrust in the POBAL range. Dry weight is only 10 to 20 pounds, but they burn fuel at 4 to 5 pounds per hour per pound of thrust. Their durations are only a matter of seconds and, in general, they are not throttle-controlled. (The Boeing Lunar Rover Vehicle, the LRV, was powered by supplying each of its four wheels with an electric motor driven by 36-volt silver-zinc batteries. Planned duration was 54 hours.)

8-4. SOLAR HEAT ENERGY

In the early 1960's there was a great deal of solid developmental effort toward systems for converting solar heat radiation into electrical or mechanical energy both for terrestrial uses and for space programs (Menetrey, 1963). Expensive large arrays of solar voltaic cells would be replaced by one or more parabolic mirrors or Frenel reflectors. The solar heat concentrated at the focal point of the mirror would vaporize a liquid to drive a turbogenerator, or maintain the high temperature junction of a thermopile, or heat the cathode of a thermionic generator. One system produced mechanical energy from a closed cycle, Stirling heat engine (Trayser and Libling, 1967).

8-4.1 The Sunflower Power System

Textbooks published as late as 1970 imply that some of these devices for space use are operational. Sunflower (TRW Systems, Inc., 1962) for example, was a 3-kilowatt space power system which weighed only about 700 pounds, just what was needed for POBAL. Although flying a collapsible mirror on a balloon would present somewhat the same complications as a deployable solar cell array, presumably the reflector would be sturdier and much cheaper to build. The Sunflower concept

gained a substantial weight advantage over solar cell systems by storing heat energy as latent heat of fusion in lithium hydride, rather than using rechargeable storage batteries for nighttime operation. The Sunflower reflector was aluminum, 32 feet in diameter, constructed in petal shape so that it could be folded into the nose of a launch vehicle. Liquid mercury in a boiler located at the focal point of the mirror was vaporized by the concentrated heat and drove a 30-pound turbo-generator to produce electrical power.

I traced Sunflower through a progression of contractor reports right up through field tests; then the Sunflower suddenly withered and died. As it can happen in the best-managed R and D efforts, when the complete system was finally assembled, one vital component gave unexpected trouble. In this case it was the sun tracker, which, I understand, was not responsive enough to keep the lens directly pointed at the sun. Without perfect focussing, the device could not produce the maximum concentration of heat energy upon which the design was based. About the same time the SNAP nuclear generators (Systems for Nuclear Auxiliary Power) were thriving, and proposals for multi-kilowatt systems were being implemented. It may be that a few kilowatts of power from a complicated superstructure, however light in weight it might be, were no longer so desirable. At any rate, the additional funds needed to complete Sunflower and several other projects involving solar heat conversion in the 3 to 30-kilowatt range were not forthcoming.

8-4.2 Stirling Engine

Every discussion of small efficient engines mentions the Stirling design. This is a regenerative heat engine which has been studied extensively (Walker, 1971) and is still considered an excellent field for doctoral dissertations. Like all heat engines, its efficiency depends upon attaining a very high temperature differential during the working cycle, and this is still very difficult to achieve in practice. One of the schemes for utilizing focussed solar heat involved a Stirling engine. Some are being manufactured for use in coolant devices, and it has been considered for use with a radioisotope heat source, but I have been unable to find any working unit that might be appropriate for POBAL.

8-5 NUCLEAR POWER

A nuclear device would restrict the usefulness of POBAL by imposing stringent range-safety regulations and limiting the choice of launch sites and trajectories. Several nuclear power plants are now operational for space applications, and others are in various stages of development (U.S. AEC, 1972). Their proponents claim that they are designed and tested to such high standards that they are very safe.

Therefore, range restrictions may eventually be eased. At any rate, SNAP devices are appearing in quite a wide range of power outputs, and in the future one might be used for special-purpose POBAL flights.

Nuclear space power plants are of two types, radioisotope-fueled thermoelectric generators (RTG's) and reactors. The RTG generates heat energy from the spontaneous decay of unstable nuclei and utilizes the heat to maintain the high temperature junction of a thermopile which produces electrical energy. Some of the reactors use heat from nuclear fission in the same way; others heat the cathode of a thermionic generator or vaporize a fluid to operate a turbogenerator. Some of the more recent designs are "particle separators" which separate the oppositely charged products of fission to create a useful electromotive force.

Table 8-1 shows weight and power output of some of the nuclear powered sources developed in the SNAP program for space applications (Kettani, 1970).

Table 8-1. Typical Nuclear-Powered Devices for Space

Radioisotope Thermoelectric Generators	Weight (lbs)	Power (watts)
Snap 3	4	2.5
Snap 9A	32	25
Snap 19	30	25
Snap 27	65	65
Nuclear Reactors (Fission)		
Snap 2 (Particle Collector)		3×10^3
Snap 10A (Thermoelectric)	960	500
Snap 8 (Turbogenerator)	10,000 (est.)	35×10^3

Categorically, we can eliminate the reactors for POBAL, because they are just too heavy. The critical mass of fuel necessary to produce a chain reaction requires a minimum amount of shielding that cannot be further reduced. The 960-pound weight for SNAP 10-A to produce 500 watts would probably not be much less than to furnish only a few watts. At outputs above 35 kilowatts, reactors become very efficient on a power-to-weight basis, but they would be much too heavy for POBAL.

Depending upon the half-life of the radioactive fuel supply, the RTG's, like solar cells, offer very long durations without any weight penalty. The RTG's are considered roughly competitive with conventional solar cell arrays (but probably not with the newest, lightweight, flexible arrays) in power-to-weight characteristics.

The Navy has used RTG's, 2 to 25 watts, on some of the Transit Navigational satellites. SNAP 19's were carried on NIMBUS-B, which failed to orbit. For POBAL use, an RTG should be more rugged than a solar array, and directional problems and nighttime storage provisions would be eliminated, but at the 3 to 5-kilowatt level they would require a large surface area to dissipate the waste heat, and thus would not have any great advantage in compactness to facilitate launch operations. In addition, RTG's are more expensive than solar cell arrays. Radioisotope fuels and thermoelectric materials are very costly. Radioisotopes are also in very limited supply. Thus, the RTG's generally are being used only when solar cells do not work well – on missions within the Van Allen belt or in deep space, for example (Corliss, 1969).

8-6. SUMMARY

Where then do we stand? POBAL altitudes are too high for turboshaft engines. Turbojets are altitude-qualified, but none have low enough thrust, and if they had, their fuel consumption would be at least five times too high! Electric thrusters fall short of the POBAL requirement by a factor of 10^{-4}. Much higher power outputs are in the offing, but they will be reactor-powered and much too heavy for POBAL. The chemically fuelled thrusters consume fuel at 50 times too high a rate, and they are not throttle controlled.

Several systems for converting solar heat had excellent weight and power output for POBAL, but after they were well along in development they met unexpected problems and were abandoned.

The radioisotope thermoelectric generators are a strong possibility for the future, but they involve operational restrictions and are considerably more expensive than solar cells and fuel cells.

8-7. CONCLUSION

I had hoped to find a piece of hardware – an engine, new batteries, a power converter, one already proven – which we could use or adapt for POBAL. What I did find in most instances was a wealth of basic technical information: Congressional hearings and world-wide conferences, surveys and studies, bar graphs comparing energy densities and cost estimates per kilowatt for the various classes of energy conversion devices – and an enormous gap between feasibility and fulfillment! Three programs are indeed spanning the gap in specific categories of energy conversion: the United States Government-sponsored SNAP programs for nuclear devices and the ATEGG program to build components for advanced small turbines

(none small enough for POBAL); and the TARGET (Team to Advance Research for Gas Energy Conversion, Inc.) program sponsored by the natural gas industry.

My point is, however, that if your need for an unusual energy-conversion system exists right now, you should be aware that it is a surprisingly long way in time and especially in money from the reported performance of a promising cell or demonstration unit on a researcher's bench to a battery or power system that will work dependably for you and is available for purchase. In most instances, industry is either unable or unwilling to gamble with the large investment it takes to produce the end product.

It is important to read between the lines of the literature, not because it is in any way falsified, but because it deals almost entirely with theory or, at most, working models operating under laboratory controls.

The literature on fuel cells, for example, describes indirect and direct processes, cells operating on hydrogen, on carbon monoxide, hydrazine, even on bacteria. But when one goes shopping for a fuel cell battery, there is one burning natural gas now operating a model home in Connecticut, and the hydrogen-oxygen units that have been used on space missions. The 2-kilowatt hydrogen-oxygen fuel batteries are feasible for POBAL.

Sir William Grove built the first fuel cell in 1839, but it took a coalition of 33 utility companies in an unprecedented cooperative effort (the TARGET program) to finance the operational natural gas fuel cell unit. And it took the money allocated for the Gemini and Apollo programs to fabricate working hydrogen-oxygen batteries and to provide the operational experience needed to advance the art. And now, if we achieve a powered balloon with twenty-day capability, in all probability it will be powered by a more efficient, lightweight hydrogen-oxygen fuel cell generator that is now being designed for the space shuttle.

References

Corliss, W. (1969) Spacecraft Power, N71-10585, NASA, Washington, D.C.

Holcomb, B. (1972) Survey of satellite auxiliary electric propulsion systems, J. of Spacecraft 9(3):133-146.

Jane's All the World's Aircraft (1971-1972) Paulton House, London, England.

Kettani, M. (1970) Direct Energy Conversion, Addison-Wesley Publ. Co., Reading, Mass.

Menetry, W. (1963) Space applications of solar energy, Introduction to the Utilization of Solar Energy, Zarem and Erway, Eds., McGraw-Hill, New York.

Miller, B. (1970) USAF widens unmanned aircraft effort, Aviation Week and Space Technology:93:19, 46-52.

Page, R. (1970) Advanced resistojet propulsion and control systems for spacecraft, 70-AV/SPT-10. Paper presented at Space Systems and Thermal Technology for the 70's, American Society of Mechanical Engineers, New York.

Simpson, E.C. (1972) Letter communication to Aerospace Instrumentation Laboratory, Air Force Cambridge Research Laboratories.

Trayser, D. and Eibling, J. (1967) A 50 watt portable generator employing a solar powered stirling engine, Solar Energy 11(3,4):153-159.

TRW Systems, Inc. (1962) Solar Rankine System Performance and Status Summary, N65-20791, TRW Systems, Inc., Cleveland, Ohio.

U.S. Atomic Energy Commission (1972) Major Activities in the Atomic Energy Programs Jan-Dec 1971, U.S. GPO 0-484-501.

Walker, G. (1971) Stirling Cycle Machines, University of Bath, Bath, England.

Yaffe, M. (1970) Turbine program sparks new technology, Aviation Week and Space Technology:93:22, 53-57.

(1972) Multiple roles likely for drone aircraft, Aviation Week and Space Technology:96:8, 92-100.

Contents

9. Advanced Airship Concept for Antenna Platform

N.J. Mayer
National Aeronautics and Space Administration
Washington, D.C.

9-1. INTRODUCTION

A study was undertaken by the author for the Naval Research Laboratory during 1970-71 to determine the feasibility of carrying a large phased-array antenna on board a lighter-than-air vehicle. The antenna was cylindrical in form, 800 feet in diameter, 60 feet high along its axial direction, and resembled a circular fence when installed at a normal ground site. The requirement was to transport the antenna to various locations around the world and to operate it from the transport vehicle; hence the lighter-than-air vehicle had to be an airship rather than a balloon.

9-2. CONFIGURATION

A number of possibilities existed in choosing an overall configuration for the airship. Many discussions were held with the mission office regarding variations which might be made in the antenna itself to accommodate the difficult matching of aerodynamic parameters with RF performance requirements. It was clear from the outset that compromises with the overall size would only degrade the RF

characteristics. A further constraint existed in the antenna height. Ground installations contain the natural features of a ground plane which are further augmented by a metal mesh extending outward around the antenna perimeter. Without this ground effect, it was necessary to double the antenna element height to 120 feet to obtain the same RF performance.

The aerodynamic penalties produced by an antenna array external to the airship hull would have raised the drag to intolerable levels. In addition, the weight of an external system and its supporting structure, coupled with the environmental problems, precluded further serious consideration of this approach.

Fully enclosing the antenna appeared more feasible. From a pure radome approach, such enclosure would resemble a torus, with the antenna elements forming diameters for the toroidal ring. The aerodynamics and statics combined indicated that the inner portion of the ring be faired and used as part of the airship hull. These conditions led to consideration of an ellipse of revolution or oblate spheroid as a natural and calculable shape for the vehicle. On this basis, a series of oblate spheroids was generated to solve for two cases:

(1) 120-foot high antenna elements with no ground plane;

(2) 60-foot high element with artificial ground planes of various sizes.

Figure 9-1 is a plot showing elliptical dimensions or the semi-major axis lengths corresponding to various major/minor axis ratios for the two cases.

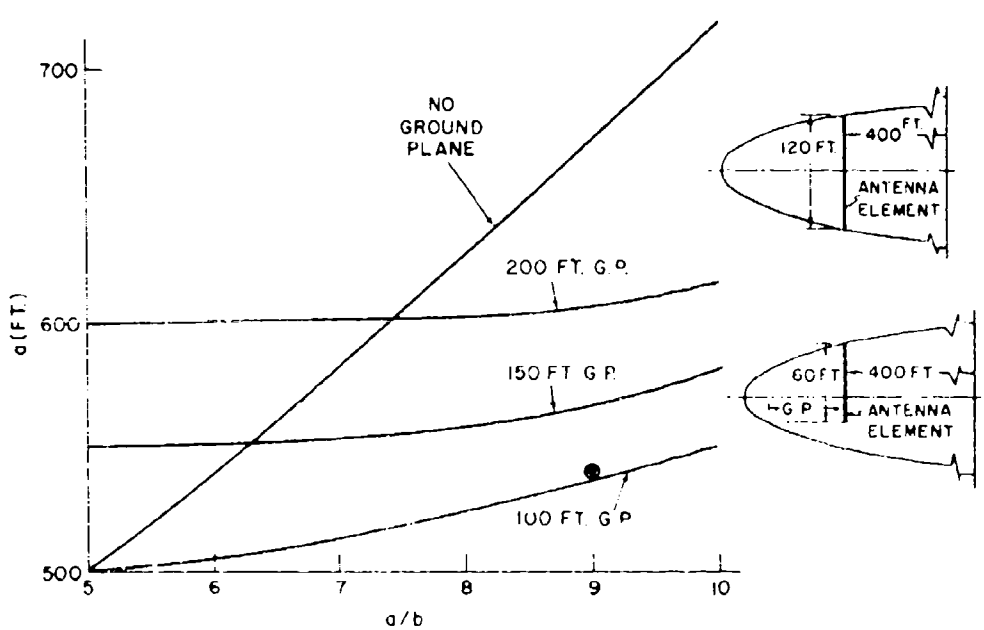

Figure 9-1. Elliptical Dimensions

Aerodynamic efficiency generally favors a/b ratios between 4 and 7 for lowest values of drag of ellipsoidal shapes. It was assumed that the same rules applied to oblate spheroids as well. However, the large overall dimensions of this airship forced consideration of higher a/b ratios in order to keep the maximum height (minor axis dimension) within reason. A study of Figure 9-1 shows that any ellipse located along the "no ground plane" curve will satisfy the function of enclosing the antenna. Similarly, an ellipse located on the various curves (or in between) for ground planes of various lengths will satisfy the enclosure of the shorter antenna elements. As an example, it was evident that for a ground plane of 100 feet, any ellipse with a/b ratios above 5.5 will be of smaller dimensions than one for the case of no ground plane.

The case chosen for detailed study is marked in the figure and was approximately a 9:1 ratio ellipse. This yielded the following dimensions:

Semi-major axis (a) = 538 ft
Semi-minor axis (b) = 60 ft
Ground plane = 113 ft

Oblate spheroid shapes are not inherently stable aerodynamically. To achieve stability, the aft portion of the spheroid was extended an additional 130 feet and tapered to a point. This provided an asymmetrical area aft of the maximum diameter of 168,500 square feet.

Wind tunnel test data (Ware, 1960) for lenticular shapes of lower fineness (a/b) ratios indicated that horizontal fin area of approximately 28 percent of the total planform disc area would provide positive stability for all angles of attack. Higher fineness ratios are stabler. It was assumed that a portion of the aft surface would be used for control, and therefore the additional faired after body seemed adequate for required stability.

From this same source, a vertical fin area of 8 percent of the planform area was indicated for lateral stability. With movable control surfaces, half this amount was assumed to be adequate, which gave a total area of 36,273 square feet.

9-3. VOLUME AND GROSS LIFT

The volume was calculated for the primary lenticular shape, not including the extended aft portion. This gave a total air volume of 72,710,000 cubic feet. Assuming 90 percent of the space usable for lifting gas, a gross lift of 4,054,000 pounds was available.

9-4. SPEED AND POWER

A maximum speed of 80 knots was assumed adequate for the mission. Calculations based on normal propulsive efficiencies gave a total horsepower requirement of 21,800. A 50-knot cruise speed also was assumed.

9-5. STRENGTH AND WEIGHT

9-5.1 Hull

Previous practice for preliminary lighter-than-air design has treated airship hull strength as being determined primarily from the bending moment produced by a high velocity vertical gust at maximum forward speed as a first approximation. Although the equation used normally is applied to ellipsoidal shapes, the calculation was modified to account for the different aerodynamic characteristics of the hull. From this calculation a maximum aerodynamic bending moment of 227,500,000 foot pounds was determined. (See Appendix.)

The detailed determination of weight for the hull assumed conventional rigid airship (Zeppelin) design. Although it was recognized that a final design could be a different type or a combination of several approaches, such as stressed skin, non-rigid, and rigid types, time did not permit investigation of these possibilities. It was assumed that if other than rigid airship design were chosen, the choice would be based upon improved efficiency. Therefore, the approach chosen only erred toward conservativeness which was desirable.

The hull planform was divided into a matrix of cells, each of which measured approximately 100 feet square. Cell and frame weights for the aft extended portion were also included giving a total of 102 cells, as shown in Figure 9-2.

This geometry and subdivision produced a transverse structure consisting of 11 main frames. It was assumed that the transverse bending moment would be 1/3 of the longitudinal moment.

The total weight calculation was based on average cell section weights. For convenience, two average cell sizes were used by dividing the hull into inner (to the antenna location) and outer (to the perimeter) portions. The longitudinal and transverse moments were used to determine member sizes and unit weights. Added to these were weights for wire shear bracing, outer cover, cell netting, valves, and miscellaneous. The total basic hull weight was 1,482,392 pounds.

9-5.2 Empennage Weight

Part of the horizontal stabilizing surface area was included in the calculation of hull weight. A movable surface with an area of 37,500 square feet was added

to the 36,273 square feet of vertical surface for a total of 73,773 square feet. A unit weight of .75 pounds per square foot was assumed for the structure for a total of 55,400 pounds.

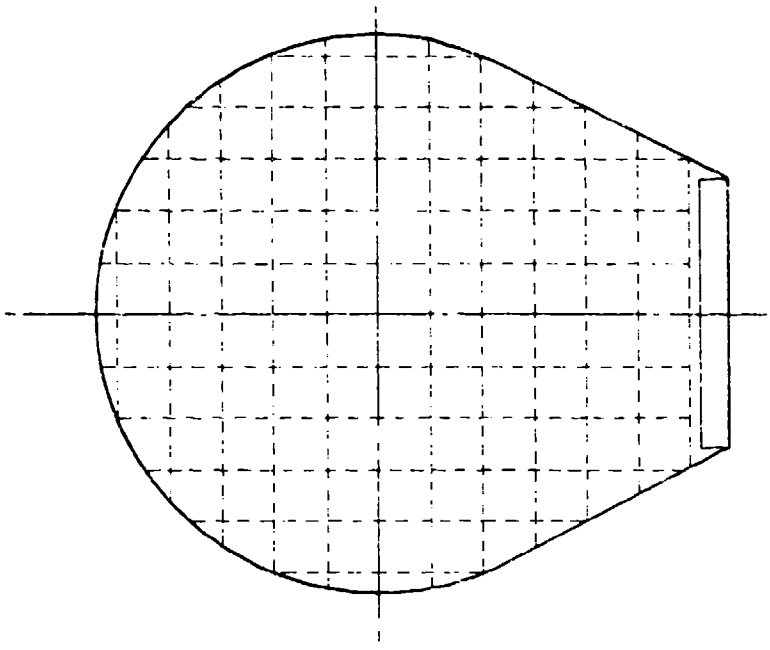

Figure 9-2. Gas Cell Pattern of Hull Planform

9-5.3 Total Structural Weight

The foregoing calculations and estimates were combined with allowances for crew quarters, control car and equipment, and mooring and handling gear to give a total structural weight of 1,600,872 pounds.

9-5.4 Propulsive Weight

The total power requirements can be provided by four turbine engines. As an example, the Rolls Royce Tyne rated at 5,500 shaft horsepower was used with a unit weight of 2,177 pounds. Special gear boxes would be required to reduce shaft speed for very large propellers. An allowance of 1,000 pounds for engine was made. An additional allowance of 1.5 pounds per horsepower was made for a water ballast recovery system. These estimates gave a total of 21,000 pounds.

9-5.5 Military Equipment

The antenna system required 160 coaxial cables weighing 0.2 pounds per foot for a total of 12,800 pounds.

The mission center and electronic equipment was estimated to weigh 150 tons.

The antenna elements and the ground plane would be mounted inside the hull and use structure already estimated for support. The additional weights required for antenna elements and the ground plane were considered negligible in this estimate.

9-5.6 Useful Load

9-5.6.1 CREW

Fifty men were assumed to operate the mission center. An additional 50 men would be required for command, control, navigation, and in-flight engineering. A total weight of 20,000 pounds was allowed for the crew.

9-5.6.2 FUEL AND ENDURANCE

Table 9-1 lists calculated endurance and fuel consumption at various cruising speeds. From these values, 671,000 pounds of fuel are required at 50 knots cruising speed for a total distance of 12,500 miles. At 30 knots, the endurance exceeds 1,000 hours. This speed could be considered a loitering velocity for station keeping. However, the power required is considerably less than the rated horsepower of one engine and would dictate the use of smaller engines to achieve the necessary efficiency.

Table 9-1. Speed, Power and Endurance

v Knots	Hp	Fuel Consumption Lbs/Hr	Endurance Hours
30	1,152	581	> 1,000
50	5,319	2,695	250
60	9,190	4,650	145
70	14,600	7,390	91
80	21,500	11,020	61

9-5.7 Total Mission Weight

The mission weight and the items which add to this weight are listed in Table 9-2. The total of 3,525,672 pounds leaves at least 1,431,000 pounds available for

additional lift, some of which could be utilized for altitude. If all were used for an altitude increase, a ceiling of 12,000 feet could be achieved.

Table 9-2. Total Mission Weight

Weight Empty	
Hull, including empennage	1,600,872
Power plants and ballast recovery system	21,000
Total	1,621,872 lb
Useful Load (including military equipment)	
Mission center	300,000
Antenna cables	12,800
Crew	20,000
Fuel inc. fuel & ballast systems	671,000
Total	1,003,800
Total Mission Weight	2,625,672 lb

9-6. COST

Table 9-3 lists the costs of various airships built or proposed. Several factors affect costs. One is the size of the airship. On the basis of costs per cubic foot, the unit cost will decrease with size. On the basis of numbers of ships built, the costs will decrease (per ship) with an increase in number. Another factor is the comparative dollar value (inflation). All of the figures shown include R&D costs. It is noted that the cost per cubic foot of the ZPG-3W non-rigids is $12.85 per ship including R&D and spare parts, whereas the costs of identical follow-on ships would have dropped to $4.33. Although these latter figures seem high compared to the rest of the data, it should be considered that these were aircraft carrying the most complex electronic systems for search and airborne early warning being flown in the Navy. By comparison, the rigids listed in the table were simple vehicles in this respect. Therefore, the ZPG-3W provided a more comparable baseline for the aircraft under consideration in this study.

A comparison of the data shows a 2 to 1 ratio between small airships and large airships. This decreasing rate appears to reach a constant value above 4 to 6 million cubic feet. If all the foregoing factors are considered, unit cost can be computed as follows:

$$\frac{\text{Cost of ZPG-3W}}{2} = (\text{cost} \times \text{rate of inflation} \times \text{years})$$

$$\frac{\$12.85}{2} + \left(\frac{12.85}{2} \times 0.05 \times 10\right) = \$9.65/\text{ft}^3 \text{ including R\&D costs}$$

$$\frac{\$4.33}{2} + \left(\frac{4.33}{2} \times 0.05 \times 10\right) = \$3.25/\text{ft}^3 \text{ for production aircraft.}$$

Table 9-3. Costs of Various Airships

Airship	Air Volume Size	Year	Cost	$/ft^3
Shenandoah	2,290,000	1923	2,200,000	0.96
Akron-Macon(1)	7,400,000	1931/33	3,979,000	0.54
Hindenburg	7,650,000	1935	2,600,000	0.35
Proposed	1,200,000	1939	1,997,462	1.66
Proposed	3,416,000	1939	2,940,350	0.86
Proposed	10,000,000	1945	7,500,000	0.75
ZPG-3W(2)	1,500,000	1960	19,300,000	12.85
ZPG-3W(3)	1,500,000	1960	6,500,000	4.33

(1) Akron cost was $5,358,000; Macon was $2,600,000.

(2) Based on total cost of $58,000,000 for three airships, spares, all testing and development.

(3) Production follow-on price quote.

As a conservative figure and allowing for the great differences in comparing construction of non-rigids with rigids, a value of $10.00 per cubic foot was suggested. For a prototype vehicle of the airship under consideration, this amounted to $726,000,000.00, including R&D.

9-7. DEVELOPMENT AND CONSTRUCTION

Contracts for the rigid airships Akron and Macon were initiated in October 1926. Actual construction began in November 1929. The Akron was completed and commissioned in October 1931. Comparison of this time with that for other rigid airships shows it to be as good as or better than most. Since in so many cases only single aircraft were developed, or at most two, these figures do not represent production rates. Fabrication periods for follow-on airships can be reduced substantially, as has been demonstrated by both German World War I production and by U.S. production of Navy blimps in World War II. Conservatively, however, schedule estimates ought to be based on time required for initial production of a prototype vehicle. Figure 9-3 shows such a schedule.

Preliminary studies should include a detailed mission analysis to identify other LTA vehicle types and configurations and to confirm the results of preliminary analyses. They should also include a brief but comprehensive wind tunnel project to measure lift, drag, and pitching moment coefficients for some of the body shapes identified. Coupled with this would be a preliminary loads investigation

to establish the magnitude of gust loads, handling loads, and operational loads. An RF study aimed at the general problem of an airoorne system was also suggested. A preliminary structural analysis study should also be included to identify potential problem areas and methods of solution.

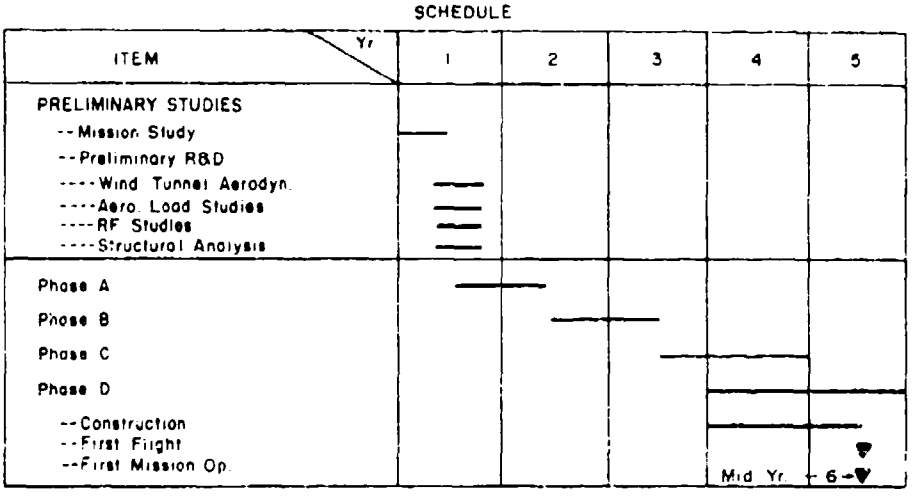

Figure 9-3. Development and Construction Schedule for a Prototype Vehicle

Phase A studies would be limited strictly to a specific lighter-than-air approach. These would explore various relationships between the mission and the aircraft and would establish requirements for the Phase B studies.

Phase B would be a competitive preliminary design study of airship vehicles to perform the mission. It would establish actual size, dimension, and target weights. It would also define the performance expected (range, endurance, speed, RF capability, communication, etc.). It would be coupled with an extensive R&D program in government facilities.

Phase C is the final design phase from which drawings could be released for construction, and, as such, it would only slightly precede Phase D.

Actual construction would occupy approximately 1-1/2 years. First operational use would occur one year later.

This schedule could be compressed somewhat by a combined Phase A and B program (probably non-competitive) and slightly overlapping Phase C with B. This could reduce the schedule by 1-1/2 years.

9-8. OTHER CONSIDERATIONS

This brief study did not allow consideration of many design details which would have to be examined and which would improve the efficiency of the vehicle. For example, the structure forward (or outboard) of the antenna array must be capable of low RF attenuation. Therefore, it would have to be non-metallic and probably a composite material, such as fiberglass-epoxy, or combinations of other advanced composites would be employed. If properly designed, this might be lighter than the aluminum structure assumed in preliminary weight estimates.

This aircraft seems ideally suited to a nuclear propulsion system. If this avenue were used, a number of other propulsive system changes could accompany it, such as electrically powered propeliers. The conventional power plants assumed in the study are not very well suited to the mission, since they do not offer the economy needed for long endurance. The size of the airship suggests that it could easily be capable of non-stop flight around the earth (sub-space orbit) with resupply of consumables by airplane.

The biggest factor in terms of uniqueness is that of the overall size of the aircraft. The study model is almost twice the length, ten times the width, and ten times the volume of the largest rigid airship constructed. If an antenna configuration could be devised with smaller overall dimensions, the size of the vehicle and hence its relationship to an extrapolation of the state of the art would be reduced. For this reason, a concurrent RF research program has been suggested.

The shape of the vehicle even in smaller sizes will produce certain aerodynamic and flight characteristics not previously found in airships. The extreme width of the hull will cause the airship to be responsive to local gust effects; more rolling action could ensue than is found in ellipsoidal forms. It may be necessary to incorporate some means of aerodynamic roll control in addition to the normal static righting moments.

Figure 9-4 compares the study vehicle with the Hindenburg. A profile and more detailed view of the mission airship is shown in Figure 9-5. This view is intended to show typical features rather than exact details. A summary of characteristics of the airship determined in the analysis is listed in Table 9-4.

A smaller antenna system and a smaller vehicle were also studied briefly to serve as a possible feasibility demonstration or experimental model prior to a larger scale version. The dimensions and a comparison with a Hindenburg-size ship are shown in Figure 9-6.

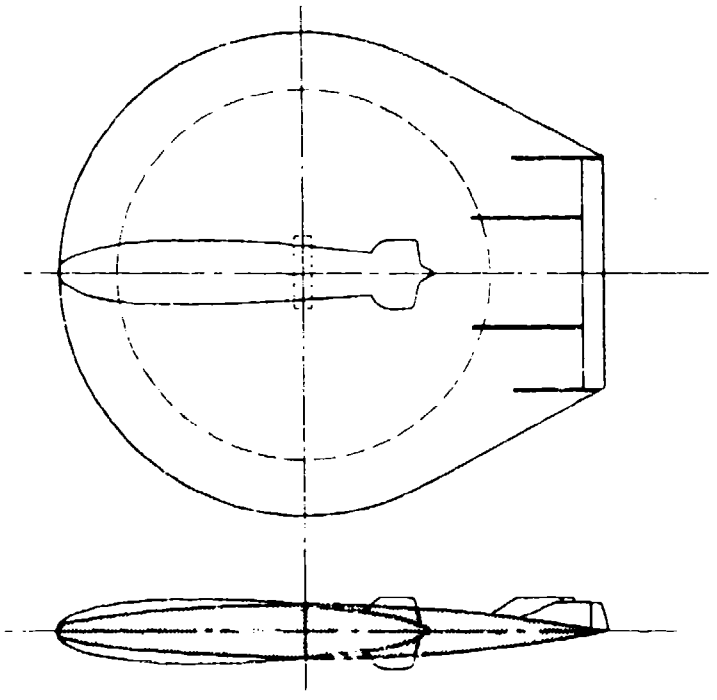

Figure 9-4 Size Comparison of Study Vehicle with the Hindenburg

Table 9-4. Principal Characteristics of Study Airship

Volume (nominal)	65,390,000 ft^3
(max)	72,710,000 ft^3
Length	1,206 ft
Height (hull)	120 ft
Height (above ground)	165 ft
Gross Lift	4,054,000 lb
Weight Empty	1,621,872 lb
Useful Load	1,003,800 lb
Useful Load (max)	2,432,128 lb
Maximum Speed	80 kn
Normal Cruise Speed	50 kn
Range (at 50 kn)	12,500 Nmi
Endurance (at 50 kn)	250 hr

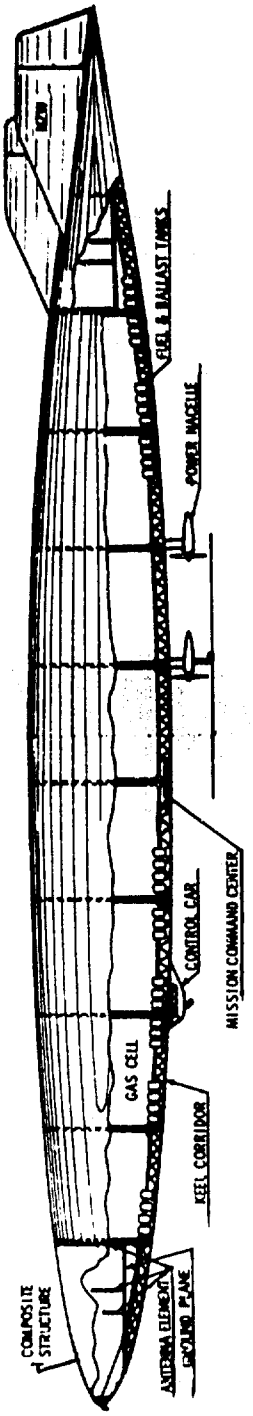

Figure 9-5. Profile View of Study Airship

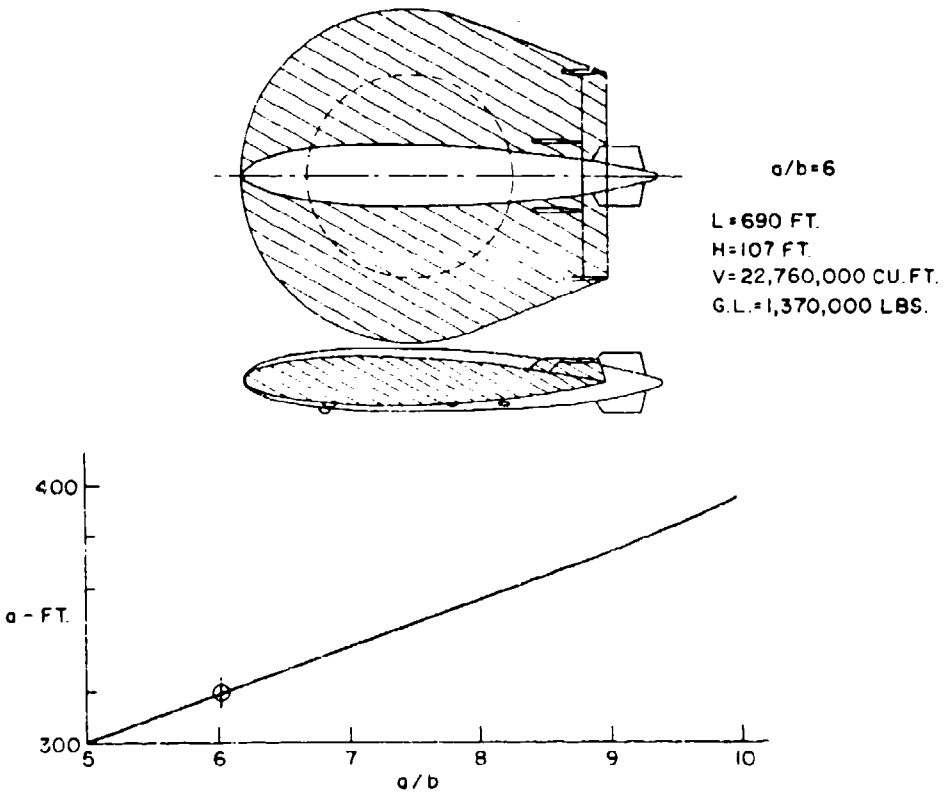

Figure 9-6. Configuration with 400-Foot Diameter Antenna

9-9. TECHNOLOGY BASE

Lighter-than-air is the oldest class of aircraft in the field of aeronautical interest. Even though it started as a discovery by non-scientific people, it soon attracted scientific minds who early applied the principles of Archimedes and the laws of Charles and Boyle. Most of the principles and forms of free ballooning were well developed by the middle of the 19th century.

By the turn of the century, large powered airships or dirigibles seriously began to occupy the enthusiasm and interest of many people as a possible means of public transportation. The initiation of the Zeppelin form of dirigible (rigid airship) and its rapid development during World War I attracted many of the best scientific and engineering minds in the aeronautical field. As the development of this type moved to the U.S., the challenge of this large aircraft and its promise both as a military vehicle and as a commercial aircraft produced many aerodynamic and structural studies and research programs. Great names in both

disciplines, such as Von Karman, Munk, Southwell, and Donnell, produced much of the sound theory and analyses used in the development of U.S. airships. Parallel with this development were advances in materials developments, meteorology, and fabrication techniques. Many of the techniques and technology developed for rigid airships during the late 1920's and early 1930's provided the basis for metal airplane design which followed later.

Most of the serious effort on rigid airships ended in the U.S. with the loss of the ZRS-5 (U.S.S. Macon) and in Germany with the beginning of World War II. During World War II, however, the non-rigid dirigible (blimp) was employed extensively by the U.S. Navy as an ASW and patrol aircraft, providing an impetus to its improvement. During the 1950's, large non-rigid airships were developed as AEW craft and were able to carry electronic equipment that could not be accommodated on heavier-than-aircraft. This development and use of the non-rigid craft by the Navy ended in 1962 and has not been reactivated. Table 9-5 summarizes characteristics of the outstanding airships in each class.

While it can be appreciated that modern design techniques applied to airplanes can also be applied to airships, especially computerized analysis, little on the "art" of airship technology has been documented nor are the experienced personnel available in sufficient numbers to fashion the vehicle. An example of this is found in the development of modern rockets. Even though all the principles were well known to us and to the Russians, both countries were forced to employ the German V-2 designers and personnel to provide the art so necessary to produce workable rockets in large sizes.

Table 9-5. Comparison of Certain Airships and Their Characteristics

Designation	Name	Country	Gas Volume	Length-Ft	Max. Dia. Ft	Hp Total	Max. Speed (Knots)	Yrs Built	Type
ZRS-5 (1)	Macon	U.S.	6,500,000	785	132	4,480	79	1933	Rigid
LZ-130 (2)	Graf Zeppelin II	Germany	6,210,000	804	135	4,500	78	1938	Rigid
ZPG-2 (3)	--	U.S.	1,500,000	403	85	2,550	75	1958	Non-rigid
S-10-A (3)	America	U.S.	202,700	192	46	420	65	1961	Non-rigid

(1) U.S. Navy Fleet Airship
(2) German Consortium (3) = Goodyear Aerospace Corp. Owned and Operated
(3) U.S. Consortium (3) = Goodyear Aerospace Corp. Owned and Operated

9-10. CONCLUSIONS AND RECOMMENDATIONS

This simplified and preliminary study showed that an airship large enough to meet the requirements of the mission represented an order of magnitude increase in volume over the largest ships previously built and flown. Because of its size, shape, and configuration, extrapolations of existing technology would not be sufficient to guarantee success. An early research program would be required to establish design constants for drag, dynamic lift, moments, etc. A generalized structural analysis would be required even for preliminary studies to identify problem areas and possible solutions.

One conclusion should not be disregarded. The mission did not violate any of the aircraft performance requirements for which a lighter-than-air vehicle is suited. In fact, the airship appeared to be the only aeronautical vehicle which could perform the mission. If the vehicle could exhibit satisfactory flight characteristics, it would offer a number of interesting possibilities in terms of a continuously flying aircraft.

In view of the foregoing, it was recommended that a preliminary, but more detailed study be initiated for a lighter-than-air vehicle to accomplish the required mission coupled with a mission analysis to pinpoint range, endurance, and antenna performance requirements.

References

Ware, G. M. (1960) Static Stability and Control Characteristics at Low Subsonic Speeds of a Lenticular Reentry Configuration. NASA TM X-431.

Appendix

Aerodynamic Bending Moment Calculation

$$M = C_M \, q \, V^{2/3} \, L$$

where: C_M = Bending moment coefficient

q = Dynamic pressure

V = Air volume

L = Overall length.

For ellipsoidal shapes Cm = .02

For oblate spheroids, higher values of C_L can be generated for a given angle of attack (α). These would increase the bending moments in proportion.

$$\alpha = \text{Tan}^{-1} \frac{u}{v}$$ where u = gust velocity

v = forward speed

A graduated value of u is assumed with a maximum velocity of 50 fps or an average of 30. Therefore

$$\alpha = \text{Tan}^{-1} \frac{30}{135} = 12.5°.$$

From airfoil data for large aspect ratios $C_L = 1.0$. Correcting for low aspect ratio, $C_L = 0.5$. Therefore,

$$C_M = .02 \left(\frac{.5}{.2}\right) = .05$$

and

$$M = .05 \times 21.6 \times 174{,}000 \times 1206 = 227{,}500{,}000 \text{ ft-lbs}$$

Contents

10. Structural Design Features of a 250,000 Ft^3 Thethered Aerostat

R.G. Witherow
G.T. Schjeldahl Company
Northfield, Minnesota

Abstract

The requirement for an extremely stable, high performance, all-weather tethered aerostat necessitated structural design features unique from previous aerostat designs. The design, fabric selection, and internal pressurization requirements were based quite heavily on the results of a finite element computer analysis. This paper summarizes the structural analysis of the primary aerostat substructures. Both moored and aloft environments are considered.

The initial step in verifying the basic structural design was to test a model of the critical aft hull/empennage region. The results of these tests are also presented.

10-1. INTRODUCTION

The Advanced Programs Division of the G. T. Schjeldahl Company is very optimistic about the future of tethered aerostats, and as such has expended considerable effort in the past three years to achieve a system that performs reliably even when exposed to environmental severities.

Performance can be discussed in terms of operations, aerostatics, aerodynamics and structures. This article deals with the problems encountered by the structural design engineers, how the problems were approached, and further, what has been or is being done to verify that the solutions found are indeed viable.

The intent of the structural design approach was to draw heavily from the technology areas of sister aircraft and aerospace fields where possible and to extend these basic technologies to encompass tethered aerostat design. This technology, coupled with Schjeldahl's years of inflatable fabrication and materials experience, provided a starting point from which to embark toward achievement of an operationally reliable, all-weather aerostat.

The aerostat discussed in this article is 250,000 cubic feet in size – one of three being developed for a commercial application. However, much of the basic technology was developed under a previous program monitored by the Air Force in which three 200,000 cubic foot balloons of different materials were delivered and flight tested.

The most significant lesson learned about structural performance as a result of the 200,000 cubic foot balloon program is simply this: the reliability of an inflatable structure is directly traceable to both design complexity and method of fabrication.

Whereas a portion of the 200,000 cubic foot aerostats were hand sealed, all seams and joints of the 250,000 cubic foot aerostat will be sealed using fully qualified machine methods. Only then can we impose the necessary controls to assure structurally reliable joints.

In terms of design complexity, suffice it to say that constructing an ultimately curved structure from flat patterns can generate significant stress concentrations if the structure is very complex. These concentrations are usually of unpredictable magnitude, since they depend largely on the accumulation of fabrication tolerances.

Lastly, before we get into the specifics of this article, it is good to remind outselves as inflatable structure designers and engineers (since we have a tendency to forget from time to time) that helium and air are necessary structural components – if it leaks, there is no structure; hence, we must concern ourselves with things like permeation and sealing.

10-2. DESCRIPTION OF AEROSTAT STRUCTURE

10-2.1 General Arrangement

The general arrangement of the major components of the 250,000 cubic foot aerostat is depicted in Figure 10-1. Some important general structural features are worthy of note:

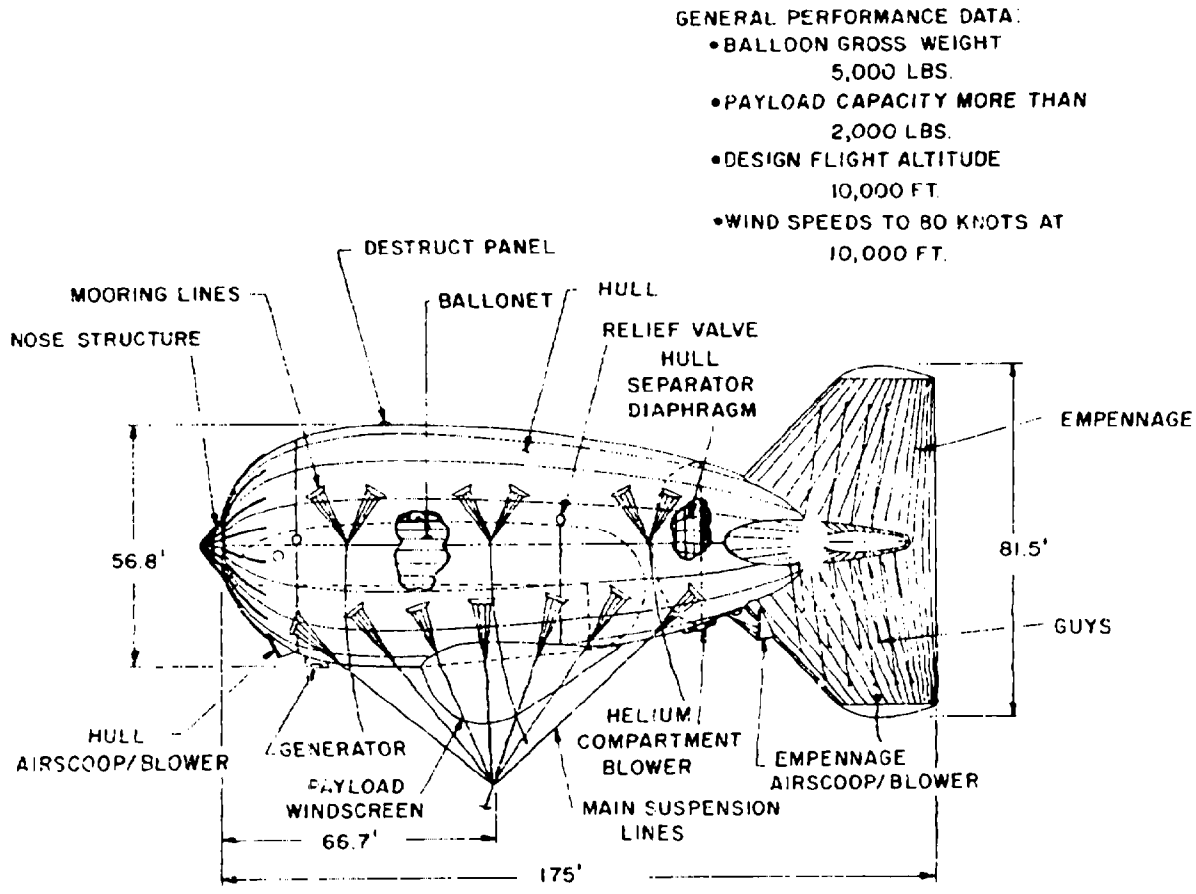

Figure 10-1. Major Components of the 250,000 Cubic Foot Aerostat

(1) The empennage is permanently attached to the hull with T-tapes bonded to the hull interior. All structural T-tapes are bonded to the interior and then internally reinforced and sealed.

(2) The fins are guyed one to another to prevent the possibility of large, rigid body-type rotations (large fin deflection and probable buckling).

(3) The fabrics of construction were discretely chosen based on the end use requirements. These will be discussed in more detail later.

(4) Since the large empennage is well aft on the hull, the pressure requirements for structural rigidity of the aft hull differ from those of the forward hull. To accommodate these different pressure levels, an ellipsoidal diaphragm is inserted in the helium compartment with interconnecting blowers and valves.

(5) Fin ribs run spanwise for maximum flexual stiffness. The ribs are quite unique – borrowing from the concept of a uniform load distributing parabolic shape and are laced rather than a continuous cloth panel.

(6) The main load-carrying suspension patches and the mooring line patches also use the parabolic scallop design approach.

(7) The main suspension lines are sized based not only on strength, but also on relative stiffness to distribute the main tether load into the hull as uniformly as possible.

(8) The nose structure is optimized on a strength-to-weight basis to sustain severe mooring loads and efficiently transfer these loads into the hull fabric without fabric overstress.

10-2.2 Structural Design Criteria

The aerostat is designed to operate in winds to 70 knots MSL and at a constant q of 3.2 in. H_2O aloft. At 70 knots, there is a minimum factor of safety of two on the fabric stresses (both direct and shear) and on hull or fin buckling. Based on aerostatic performance predictions the angle of attack, α, at q = 3.2 inches H_2O will be 6 degrees. These same requirements are imposed under 90-knot MSL winds (q = 5.4 inches H_2O), except that no safety factor is required at this q level.

A separate dynamic mooring loads analysis was undertaken to establish nose structure loads criteria. These results will be defined shortly. A minimum factor of safety of +1.5 to ultimate is used for all metallic members.

To account for the possibility of large vertical gust loads aloft, a gust factor of 4 is used to establish empennage pressures and to size fin guy lines and patches.

10-2.3 Material Designations

The fabrics of construction are pictorially described in Figure 10-2. Most of the materials are laminate constructions composed of Dacron cloth, Mylar, and

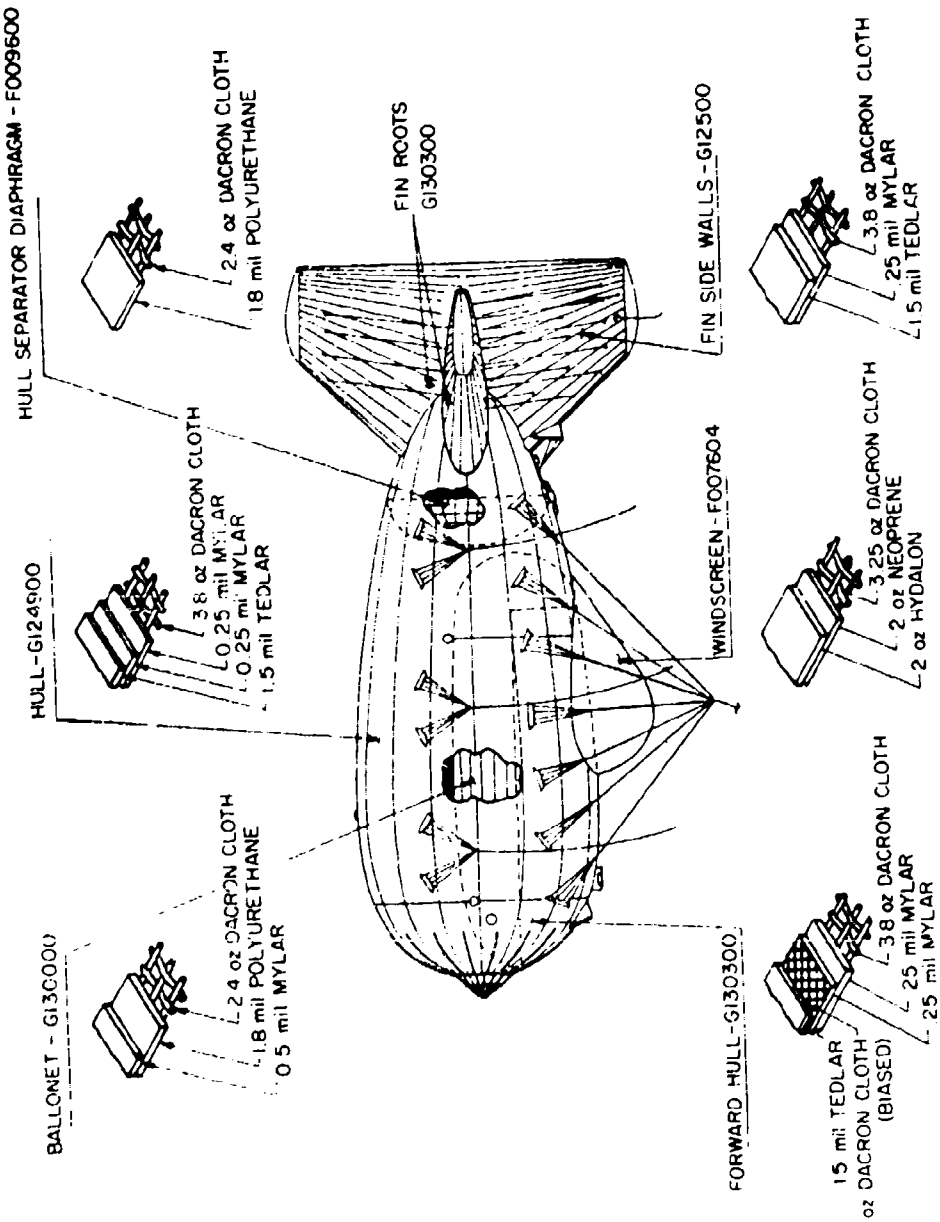

Figure 10-2. Fabrics Used in Construction of Aerostat

Tedlar. The Dacron is the main strength member used to carry direct (hoop and meridional) stresses, whereas the Mylar serves the dual function of providing high shear strength and stiffness and serving as the impermeable membrane. The Mylar provides the same structural function as the biased cloth in conventional coated fabrics. The Tedlar is not a structural membrane; it is the weathering protection for the Mylar and Dacron cloth.

Specific areas of the aerostat do require a higher shear strength material – notably the nose of the hull, which must sustain the high shear loads along the nose beams, and the root areas of the fins, where reverse shear cycling occurs quite frequently. In both these regions, the basic laminate is augmented with a biased Dacron cloth.

10-2.4 Operating Pressures

All of the compartments of the aerostat are pressurized by electrically operated blowers and are maintained at specific levels relative to the freestream q through the use of pressure sensors and valves. The compartment pressure levels are identified in Figure 10-3. In the event of complete power loss (there is a redundant power source), airscoops are provided to maintain some level of pressurization during retrieval.

As previously mentioned, there is a ΔP across the hull separator diaphragm to accommodate the higher pressures in the aft portion of the hull. The higher aft hull pressure is required to prevent the aft hull from buckling when the large lift loads are transferred from empennage to hull at extreme q's. Also, the pressure in the aft hull is maintained at 1 inch H_2O above the empennage pressure to prevent the hull from going flat in the hull/empennage interface region; this could cause severe wrinkling and the resulting stress concentrations.

Fin pressure requirements are based on buckling/collapse load criteria.

10-2.5 Loads Summary

The following loads were used for the structural analysis of the major substructures:

(1) Hull

(a) Pressurization – forward hull = 1.5 + .8q inch H_2O = 4.1 inches = 0.14 psi; aft hull = 4.0 + .8q inch H_2O = 6.6 inches = 0.238 psi.

(b) Buoyant lift – net of 6800 pounds, applied uniformly as a negative gravity loading (0.00213 psi).

(c) Payload – weight 2000 pounds, applied along attachment frame.

(d) Aerodynamic pressure – wind tunnel pressure distribution data at 8 degree angle of attack, q = 0.115 psi (70 knots MSL). (See Figure 10-4.)

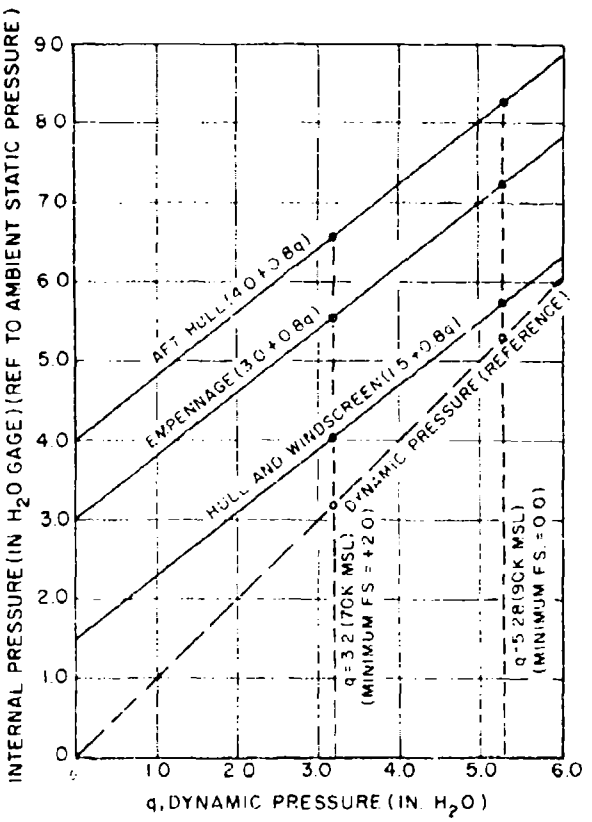

Figure 10-3. Pressure Levels of Aerostat Compartments

(e) Empennage loads – magnitude defined by wind tunnel force data; net lift, drag, and equivalent moment applied to hull around circumference at specific body station.

(f) Skin friction drag – uniform axial type gravity load applied (0.0028 psi) to balance external moments.

(2) Empennage

(a) Pressurization – 3.0 + .8q inches H_2O = 5.6 inches = 0.2 psi.

(b) Aerodynamic pressure – wind tunnel pressure distribution data at 6-degree angle of attack. (See Figure 10-5.)

(c) Skin friction drag – uniform axial type gravity load applied to match wind tunnel drag force data.

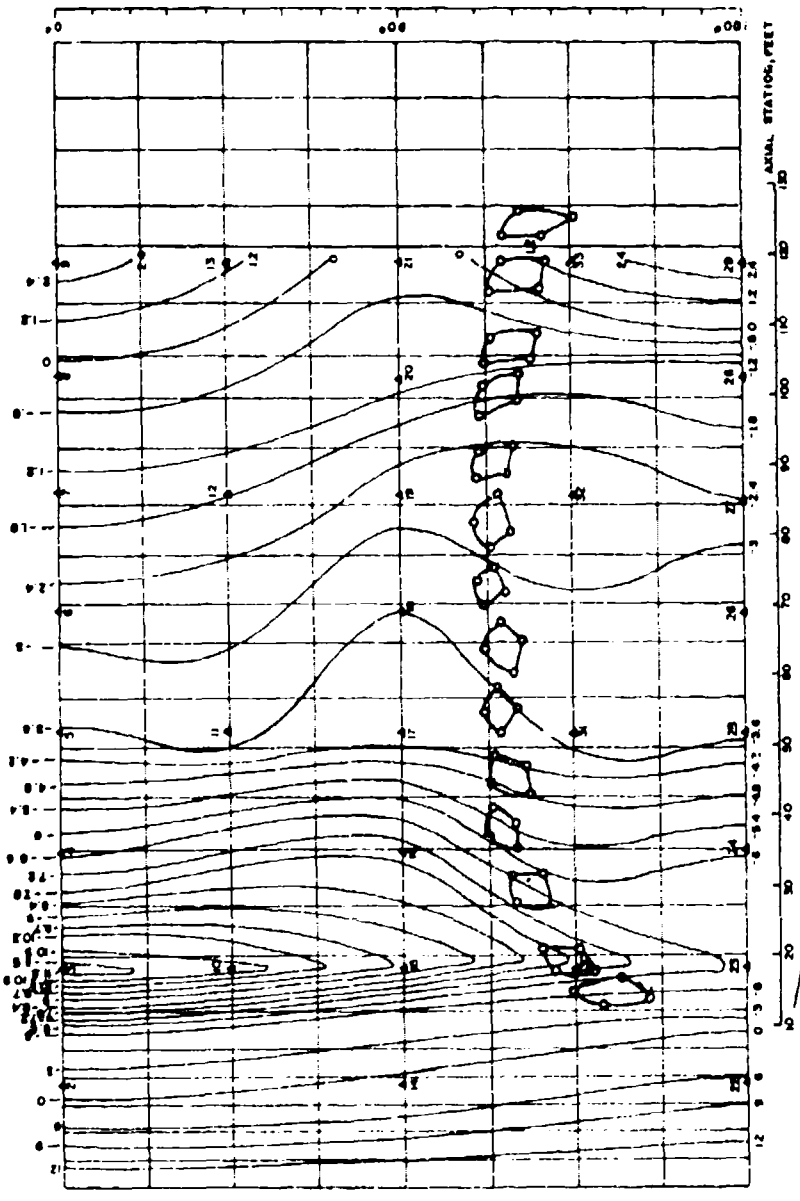

Figure 10-4. Pressure Distribution Map of Hull Superimposed on LD3DX Mesh (180° development of the 250K hull)

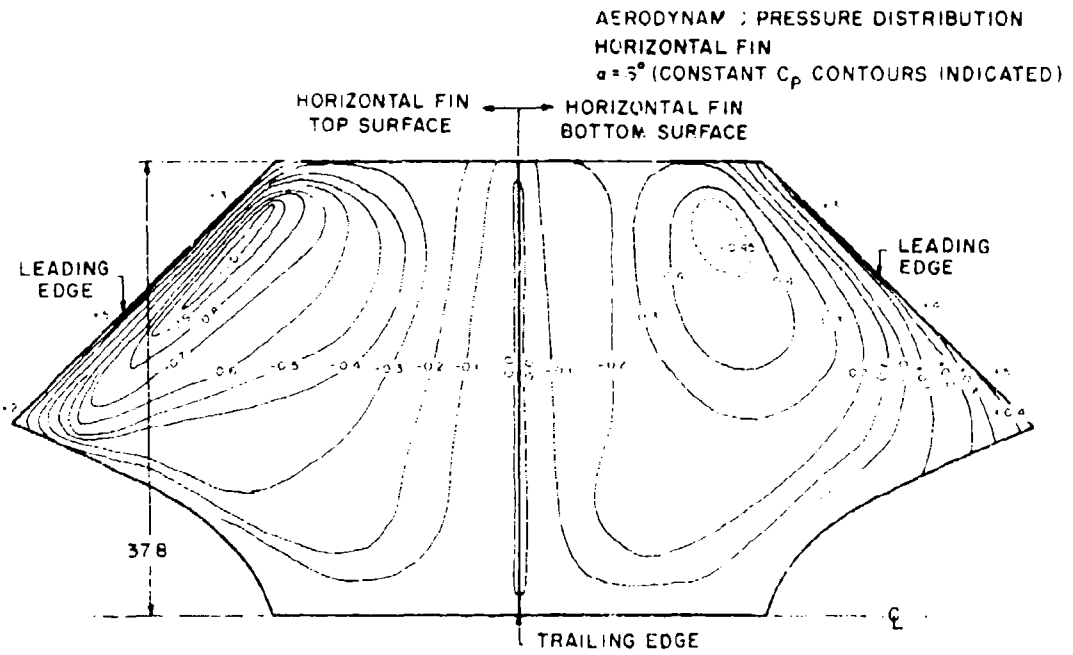

Figure 10-5. Aerodynamic Pressure Distribution of Horizontal Fin

(3) Nose Structure

(a) 25,000 pounds axial and 13,000 pounds side load acting simultaneously as predicted by dynamic analysis. (See Figure 10-6 for rms force versus wind speed predictions.)

10-3. STRUCTURAL ANALYSIS

10-3.1 Method of Analysis

The principal analytical tool used in the stress and deformation analysis of the fabric portions of the aerostat was the large-scale finite element computer program designated LD3DX, Large Deformation Analysis of Three-Dimensional Structures Extended, (Lagerquist, 1972). The computer program is based essentially on the same techniques used by large scale linear structural programs (such as EASE, available through Control Data Corporation), with the necessary extensions to accommodate nonlinear geometry behavior (large deformations) and anisotropic material behavior. Additionally, the program is designed such that external loads may be applied either simultaneously or in sequence as they occur in service.

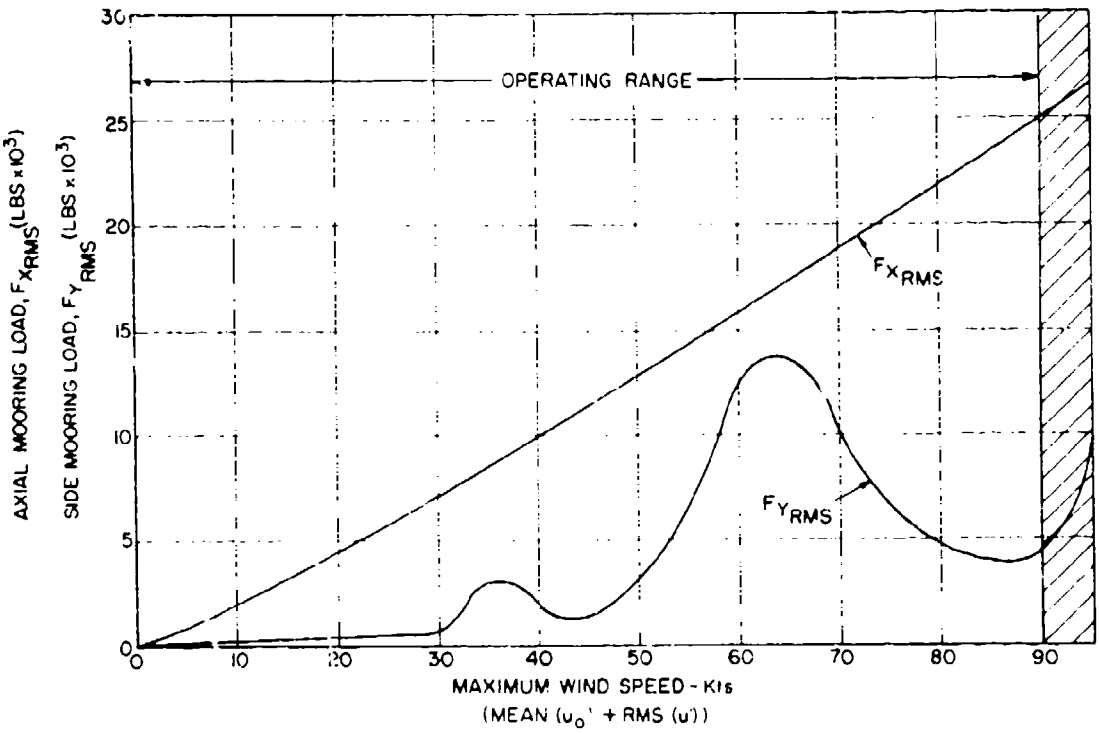

Figure 10-3. Nose Structure Load (RMS force vs wind speed predictions)

LD3DX is also suitable for modeling load lines such as the main suspension lines, fin guys, and fin rib lacing.

Because of the costs associated with a very large element capacity program, LD3DX uses only the core storage allotment of the CDC 6600 computer, so that problem size limitations are more severe than the normal large scale structural computer program. Because of this fact, the aerostat cannot be modeled in its entirety; rather, the hull and empennage substructures are analyzed separately, and then the interface is analyzed in detail. To obtain localized stress patterns and concentrations (as around a suspension patch) a fine gridwork of elements is used in a separate model.

The nose structure was analyzed by combining the capabilities of both LD3DX and EASE.

The elastic constants which describe the behavior of the structural fabric under biaxial load are obtained through the use of a specially designed cylinder test machine.

A separate test fixture is used to burst sample cylinders to obtain fabric and seam allowable biaxial stress levels.

10-3.2 Nose Structure

The nose structure consists of 5-foot deep, 16-foot diameter tubular nose cone and 16 nose beams which are laced directly to the hull fabric. The primary reason for the large number of beams is to reduce the unit shear stress in the hull fabric adjacent to the beams. Additionally, the fabric in this region is reinforced in the shear direction. The large cone diameter/depth ratio minimizes the reaction moment to side loads and, hence, minimizes the bending moment in the tubular nose beams.

The load carrying capability of the nose structure is about six times that of the original nose structure used on the 200,000 cubic foot aerostat, at a weight penalty of less than two to one (approximately 550 pounds for present structure).

The stresses and beam reactions are summarized in Figure 10-7.

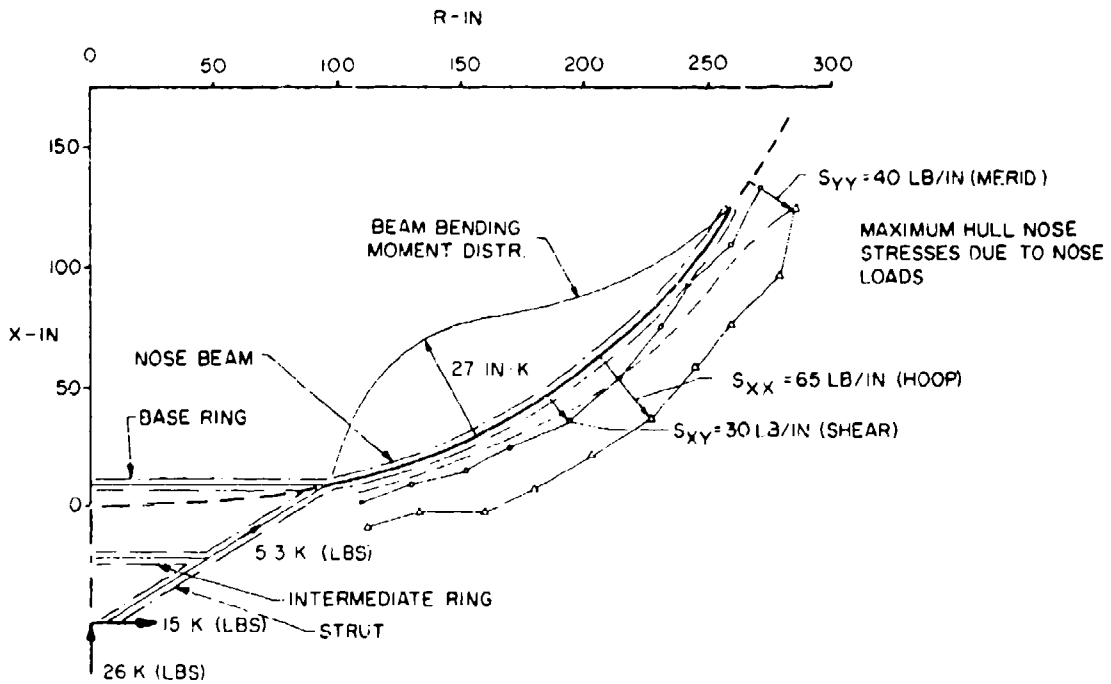

Figure 10-7. Stresses and Beam Reactions of Nose Structure

10-3.3 Hull

Hull stress and deformation magnitudes are illustrated in Figures 10-8 and 10-9, respectively. The deformation is relative to a fixed confluence point.

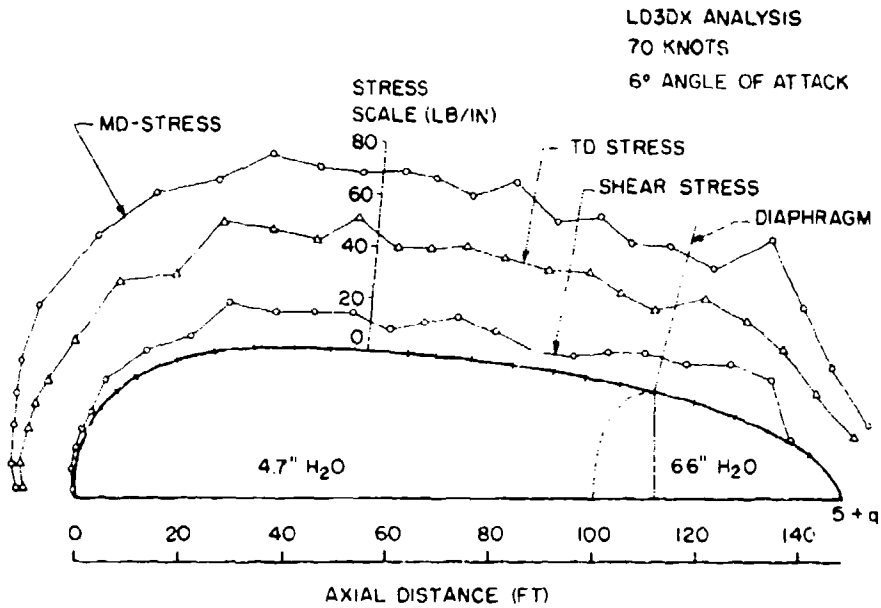

Figure 10-8. Prediction of Maximum Hull Material Stresses

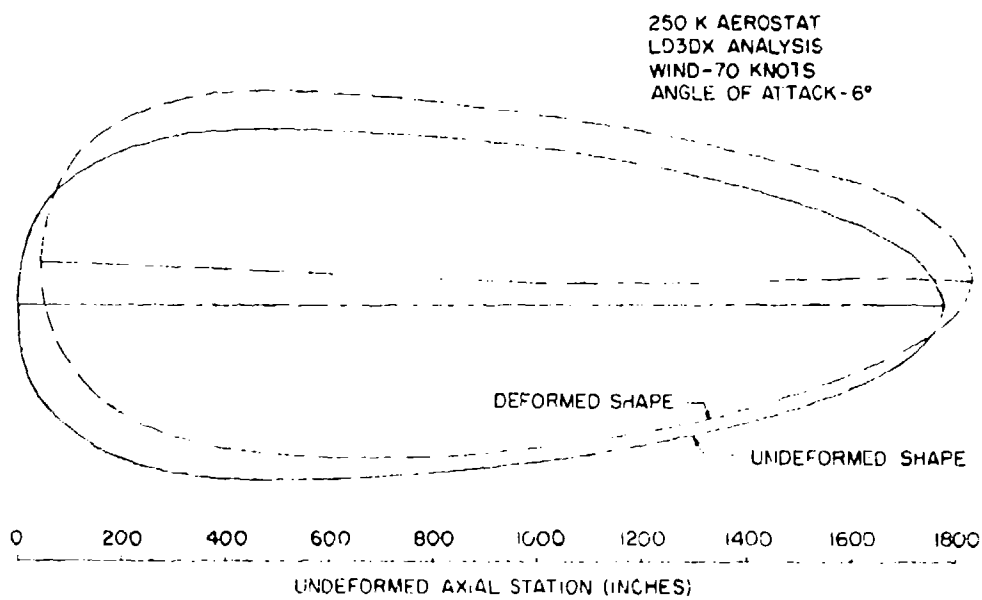

Figure 10-9. Prediction of Hull Deformation Magnitudes

Note that the hull tends to take a "banana" shape and that there is considerable suspension line stretch (that is, confluence point translation) at these extreme loads. Such translations must be minimized, since both angle of attack and stability are functions of confluence point location.

All structural tapes are thread laid for maximum strength and load transfer.

In general, the span between two or more layers of fabric is 12 inches minimum to avoid stress concentrations.

10-3.4 Hull Separator Diaphragm

The diaphragm is ellipsoidal in shape so that it does not interfere with the ballonet. To accommodate hull growth at the diaphragm attachment point, the first 15 inches of cloth is oriented on a bias, and the thread laid tape with its low transverse stiffness is used for bonding the diaphragm to the hull.

The inflated shape of this critical structural section is illustrated in Figure 10-10.

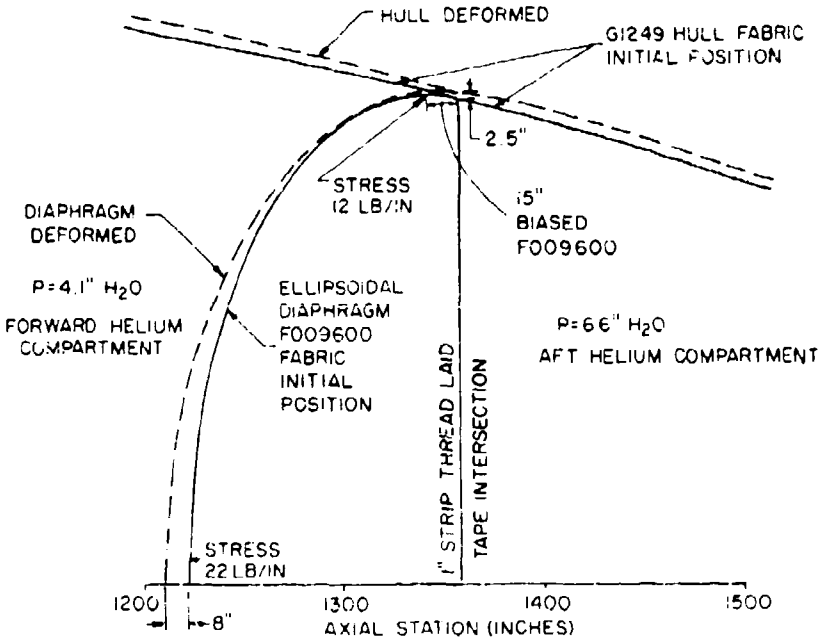

Figure 10-10. Aft Hull Diaphragm Shape Under Q = 3.2 In. H_2O (Knot Slip) Loading

10-3.5 Hull/Empennage Interface

This region is the most critical from a structural point of view, since large stress concentrations can result even though low stresses are predicted, due primarily to the complexity and fabrication difficulties of the attachment. Positive pressure is always maintained across the hull interface to prevent severe wrinkling under extreme loads. Despite this, wrinkling does occur well aft on the hull, but is not expected to affect the hull's load carrying ability. Figure 10-11 illustrates the deformed shape of this region.

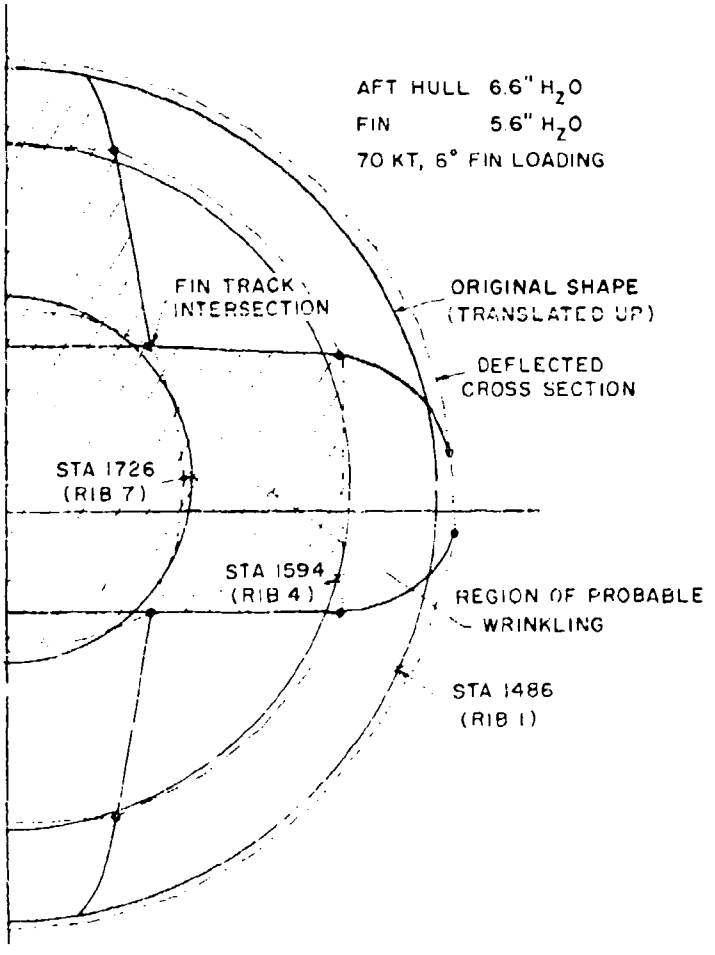

Figure 10-11. Deformation at Hull/Empennage Interface

10-3.6 Empennage

Normally, stresses are quite low in the empennage fabrics except that stress cycling is much more severe. Figure 10-12 depicts the predicted stresses at extreme loads. Failure at extreme loads will probably be due to fin collapse (buckling) rather than fabric failure.

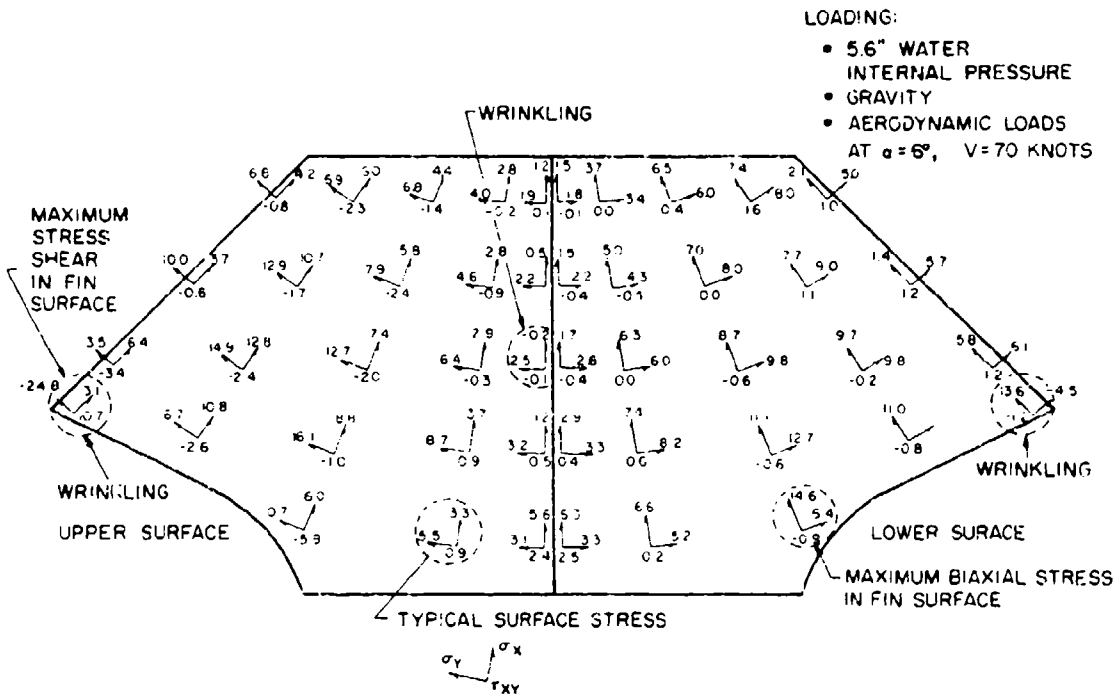

Figure 10-12. Prediction of Maximum Empennage Stresses

10-4. MODEL INFLATION TESTS

An engineering model was constructed to evaluate the critical diaphragm/hull and empennage/hull interfaces. The hull was truncated several feet ahead of the diaphragm attachment point and closed off with a pressurized hemisphere. Only one vertical fin was built to allow us to test the model in a local facility. Figure 10-13 is a photograph of this model at nominal operating pressures. Figure 10-14 is an interesting series of photos taken inside the fin showing the parabolic scallop ribs and lacing.

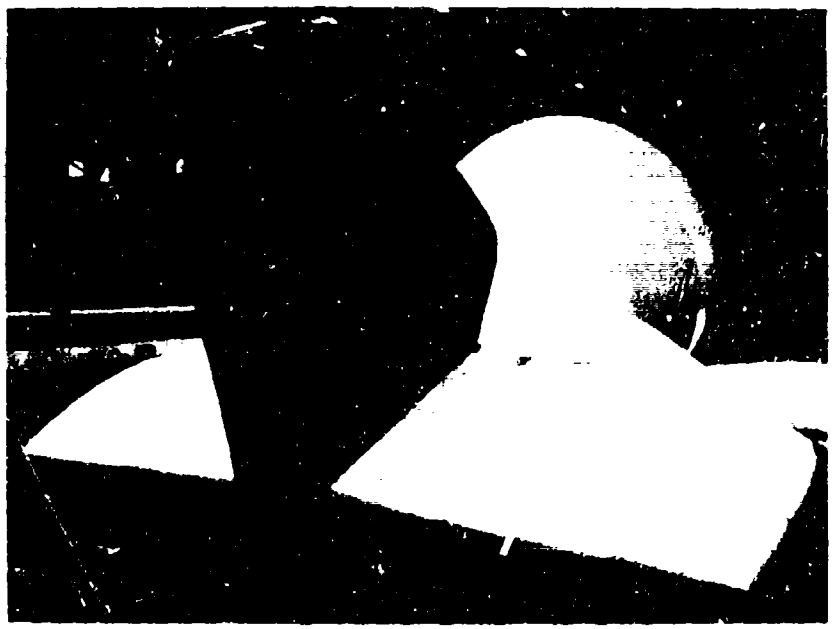

Figure 10-13. Test Model at Nominal Operating Pressures

The tests were quite successful in that the internal pressures expected at a q of 3.2 inches H_2O were achieved without any indication of structural damage. The hull restriction at the diaphragm was almost unnoticeable with test data comparing very well with analytical predictions. The diaphragm took its shape well.

The model proved to be quite valuable, as several minor design and fabrication changes became evident, and we can proceed with the actual aerostat fabrication knowing that we have a superior design.

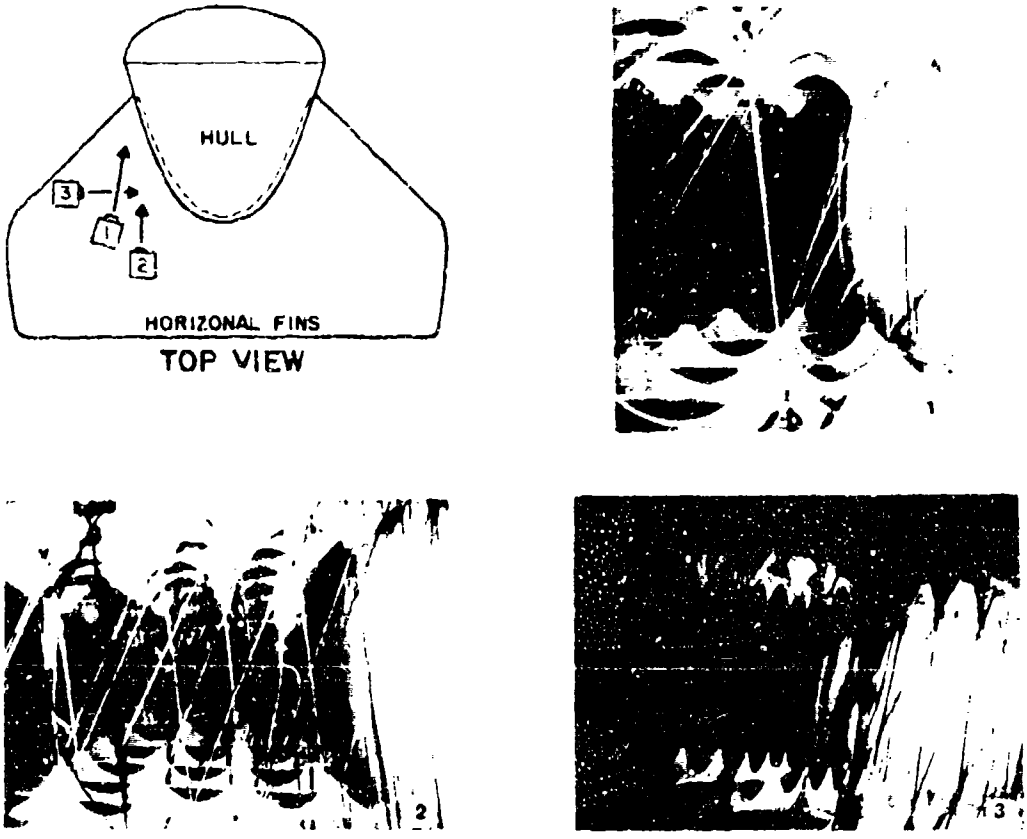

Figure 10-14. Views of Aerostat Fin Showing Parabolic Scallop Ribs and Lacing

References

Lagerquist, D. R. (1972) A computer program to predict stresses and deformations of inflatable structures. Paper presented at this symposium.

Contents

11. A Dynamic Analysis of a Moored Aerodynamically Shaped Balloon Subjected to Atmospheric Turbulence

J.D. DeLaurier
G.T. Schjeldahl Company
Northfield, Minnesota

Abstract

In order to predict the mooring loads on an aerodynamically shaped balloon, a dynamic analysis was performed, where the system's physical model accounted for elasticity of the mooring tower and elasticity and structural damping of the balloon's extreme forebody (including nose structure). Further, the aerodynamic loads due to atmospheric turbulence were calculated from measured meteorological data. The transfer functions, root mean square displacements, and root mean square mooring loads were then obtained for a particular case, with the interesting result that the longitudinal load monotonically increased with increasing mean wind speed, whereas the lateral load experienced peak values at intermediate wind speeds.

List of Symbols

Λ = Balloon elastic forebody length (see Figure 11-2).

A_1-A_8 = Coefficients defined by Eq. (11-14).

B_1-B_8 = Coefficients defined by Eq. (11-15).

List of Symbols

b	=	Characteristic length.
$\bar{b}$	=	Effective aerodynamic length defined in Appendix 11-A.
C_1-C_5	=	Coefficients defined by Eq. (11-7).
$\hat{C}_2$, $\hat{C}_3$	=	Damping coefficients (see Figure 11-2).
C_D	=	Balloon drag coefficient.
$C_{Y\beta}$	=	Balloon sideslip stability derivative.
D_1-D_9	=	Coefficients shown in Eq. (11-16).
E_1-E_4	=	Coefficients shown in Eq. (11-17).
F_x	=	Longitudinal load at the mooring point.
F_y	=	Lateral load at the mooring point.
I_{cm}	=	Moment of inertia of balloon plus enclosed air and gas about its mass center.
i	=	$(-1)^{1/2}$
K_2, K_3, K_4, K_5	=	Spring constants (see Figure 11-2).
m	=	Total mass of balloon plus enclosed air and gas.
m_{ax}	=	Longitudinal apparent mass.
m_{ay}	=	Effective lateral apparent mass defined in Appendix 11-A.
n	=	Integer.
N	=	Maximum value of n.
$P_x(\omega)$	=	Longitudinal turbulence power spectrum.
$P_y(\omega)$	=	Lateral turbulence power spectrum.
$Q_1(i\omega)$, $Q_2(i\omega)$, $Q_3(i\omega)$	=	Displacement transfer functions defined by Eqs. (11-16), (11-17), and (11-9), respectively.
q	=	Dynamic pressure, $\rho U_o^2/2$.
q_1-q_5	=	Coordinates defined in Figure 11-2.
s	=	Laplace transformed independent variable.
S	=	Characteristic area.
U_o	=	Mean wind speed.

$\overline{U}_o$ = Mean wind speed at $\overline{z}$.

u' = Longitudinal gust speed.

v' = Lateral gust speed.

v_o = Maximum amplitude of a v' turbulence component.

x = Balloon axial coordinate (see Figure 11-2).

x_a = Balloon axial coordinate to lateral apparent mass center (see Figure 11-2)

x_{cm} = Balloon axial coordinate to mass center (see Figure 11-2).

x_{cp} = Balloon axial coordinate to lateral center of pressure (see Figure 11-2).

Y_c = Lateral aerodynamic term, $C_{Y\beta}qS$.

$\bar{Y}_c$ = Effective lateral aerodynamic term defined in Appendix 11-A.

z = Height from ground level.

$\overline{z}$ = Reference height from ground level.

z_o = Surface roughness length (Alexander et al, 1971).

α_1-α_6 = Dimensionless turbulence power spectrum curve fitting constants (different for longitudinal and lateral cases).

γ = Lateral gust angle (see Figure 11-2).

ρ = Atmospheric density.

$\Psi(\omega)$ = Turbulence power spectrum as given by NASA (see Appendix 11-C).

Ω = Turbulence frequency (H_z).

ω = Turbulence frequency (rad/s).

ω_o = Incremental value of ω as defined in Appendix 11-B.

Subscripts

$(\ )_{avg}$ = Average value.

$(\ )_{max}$ = Maximum value.

$(\ )_{rms}$ = Root mean square value.

$(\ )_{root}$ = Characteristic root.

Superscripts

$(\dot{\ }), (\ddot{\ })$ = Time derivatives.

$(\bar{\ })$ = Laplace transformed terms.

11-1. INTRODUCTION

This paper deals with the prediction of nose loads on a moored aerodynamically shaped balloon (Figure 11-1). At the beginning of this investigation, static and quasi-static physical models were studied (Kesti, 1971), where it was hoped that by specifying some manner of axial or side gust to a balloon in a quiescent state, design loads could be obtained in the same fashion as for aircraft flying into a step or ramp updraft (Bruhn, 1958). However, it soon became apparent that this approach was inadequate and open to too many arbitrary definitions for the gust's structure and the balloon's response. Therefore, to obtain a realistic idea of the mooring loads, an analysis was performed on a dynamic physical model subjected to continuous atmospheric turbulence.

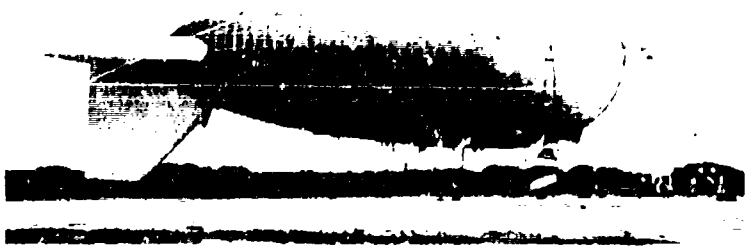

Figure 11-1. Example of Moored Aerodynamically Shaped Balloon

11-2. EQUATIONS OF MOTION

A drawing of the physical model is shown in Figure 11-2, which shows the mooring tower to be modeled by massless springs and the balloon's extreme forebody and nose structure to be modeled by massless springs and dashpots. The rest of the balloon's body is assumed to be perfectly rigid, and further assumptions on the physical model are:

(1) The magnitude of the body's perturbed rotations is small.

(2) The magnitude of the body's angular velocities is small compared with the ratio of the freestream velocity divided by the body's characteristic length.

(3) The aerodynamic forces on the balloon may be accounted for by the concepts of stability derivatives and apparent mass.

(4) The spring constants, K_4 and K_5, are an order of magnitude greater than the damping constants, $\hat{C}_3$ and $\hat{C}_2$, times the highest natural frequency of the system.

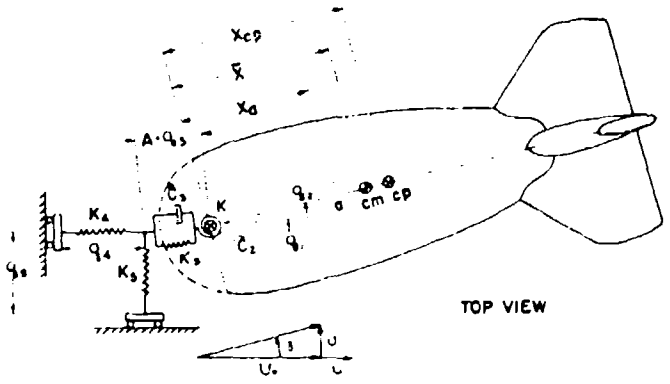

Figure 11-2. The Coordinates of the Physical Model

With assumptions 1, 2 and 4, the resulting equations of motion linearize and uncouple into a longitudinal problem (involving u', q_3, and q_4) and a lateral problem (involving γ, q_1, q_2, q_5), where the longitudinal equations are

$$C_D q S + m_{ax}\dot{u}' + C_D \rho S U_o u' = \left(m + m_{ax}\right)\left(\ddot{q}_3 + \ddot{q}_4\right) + C_D \rho S U_o \left(\dot{q}_3 + \dot{q}_4\right) + K_3 q_3 + \hat{C}_3 q_3 , \tag{11-1}$$

$$q_3 \equiv \left(q_3\right)_o + q_3', \text{ where } C_D q S = K_3\left(q_3\right)_o , \tag{11-2}$$

and

$$q_4 = \left(K_3/K_4\right) q_3 ; \tag{11-3}$$

and the lateral equations are

$$\tilde{m}_{ay} U_o \dot{\gamma} - \tilde{Y}_c \gamma = \left(m + m_{ay}\right)\ddot{q}_5 + \left[m\left(\Lambda + x_{cm}\right) + m_{ay}\left(\Lambda + x_a\right)\right]\ddot{q}_1 + \left(m x_{cm} + m_{ay} x_a\right)\ddot{q}_2 - \left[\left(\Lambda + x_{cp}\right) Y_c / U_o\right] q_1 - \left(x_{cp} Y_c / U_o + \hat{C}_2/\Lambda\right)\dot{q}_2 - \left(Y_c / U_o\right)\dot{q}_5 - Y_c q_1 - \left(Y_c + K_2/\Lambda\right) q_2 , \tag{11-4}$$

$$\tilde{m}_{ay} U_o \left(x_a - x_{cm}\right)\dot{\gamma} - \tilde{Y}_c \left(x_{cp} - x_{cm}\right)\gamma =$$

$$\left[I_{cm} + m_{ay}\left(x_a - x_{cm}\right)\left(A + x_a\right)\right]\ddot{q}_1 +$$

$$\left[I_{cm} + m_{ay} x_a \left(x_a - x_{cm}\right)\right]\ddot{q}_2 + m_{ay}\left(x_a - x_{cm}\right)\ddot{q}_5 -$$

$$\left(Y_c/U_o\right)\left(x_{cp} - x_{cm}\right)\left(A + x_{cp}\right)\dot{q}_1 - \left[x_{cp}\left(x_{cp} - x_{cm}\right)Y_c/U_o -\right.$$

$$\left. C_2\left(x_{cm} + A\right)/A\right]\dot{q}_2 - \left[\left(x_{cp} - x_{cm}\right)Y_c/U_o\right]\dot{q}_5 - Y_c\left(x_{cp} - x_{cm}\right)q_1 -$$

$$\left[Y_c\left(x_{cp} - x_{cm}\right) - K_2\left(x_{cm} + A\right)/A\right]q_2 \ , \qquad (11\text{-}5)$$

and

$$q_5 = -\left(K_2/K_5 A\right) q_2 \ . \qquad (11\text{-}6)$$

Further, $\tilde{m}_{ay}$ and $\tilde{Y}_c$ are functions of the frequency of a given component of the atmospheric turbulence spectrum and are derived in Appendix 11-A.

11-3. SOLUTION FOR THE EQUATIONS OF MOTION

When Eqs. (11-1), (11-2) and (11-3) are combined and the Laplace transformation is made, one obtains the following transformed longitudinal equation of motion:

$$\left(C_1 s + C_2\right)\bar{u} = \left(C_4 s^2 + C_5 s + C_6\right)\bar{q}_3 \ , \qquad (11\text{-}7)$$

where C_1-C_6 are combinations of the coefficients in Eqs. (11-1), (11-2) and (11-3). Further, one may assume that the system has first order dynamic stability, so that from Etkin (1966),

$$s = i\omega \ . \qquad (11\text{-}8)$$

Thus, Eqs. (11-7) and (11-8) combine to give the longitudinal transfer function,

$$Q_3(i\omega) = \frac{C_2 + i\omega C_1}{\left(C_6 - \omega^2 C_4\right) + i\omega C_5} \ . \qquad (11\text{-}9)$$

Now, the atmospheric turbulence is represented by longitudinal and lateral power density spectrums, $P_x(\omega)$ and $P_y(\omega)$, respectively, such that

$$u'_{rms} = \left[2\int_o^\infty P_x(\omega)d\omega\right]^{1/2} \tag{11-10}$$

and

$$\gamma_{rms} = \left[2\int_o^\infty P_y(\omega)d\omega\right]^{1/2} . \tag{11-11}$$

Therefore, one may directly obtain the root mean square value of q'_3 from Eqs. (11-9) and (11-10):

$$\left(q'_3\right)_{rms} = \left[2\int_o^\infty |Q_3(i\omega)|^2 P_x(\omega)d\omega\right]^{1/2} . \tag{11-12}$$

The root mean square value of the axial load at the nose is then given by

$$\left(F_x\right)_{rms} = C_D qS + K_3\left(q'_3\right)_{rms} . \tag{11-13}$$

Similarly for the lateral case, Eqs. (11-4), (11-5) and (11-6) are combined and transformed to give

$$\left(A_1 s + A_2\right)\bar{\gamma} = \left(A_3 s^2 + A_5 s + A_7\right)\bar{q}_1 + \left(A_4 s^2 + A_6 s + A_8\right)\bar{q}_2 \tag{11-14}$$

and

$$\left(B_1 s + B_2\right)\bar{\gamma} = \left(B_3 s^2 + B_5 s + B_7\right)\bar{q}_1 + \left(B_4 s^2 + B_6 s + B_8\right)\bar{q}_2 , \tag{11-15}$$

where A_1-A_6 are combinations of the coefficients in Eqs. (11-4) and (11-6), and B_1-B_6 are combinations of the coefficients in Eqs. (11-5) and (11-6).

Further, Eqs. (11-14) and (11-15) may be combined and rearranged to give, by using Eq. (11-8), the following lateral transfer functions for q_1 and q_2, respectively:

$$Q_1(i\omega) = \frac{\left(D_4 - \omega^2 D_2\right) + i\omega\left(D_3 - \omega^2 D_1\right)}{\left(D_9 - \omega^2 D_7 + \omega^4 D_5\right) + i\omega\left(D_8 - \omega^2 D_6\right)} \tag{11-16}$$

and

$$Q_2(i\omega) = \frac{\left(E_4 - \omega^2 E_2\right) + i\omega\left(E_3 - \omega^2 E_1\right)}{\left(D_9 - \omega^2 D_7 + \omega^4 D_5\right) + i\omega\left(D_8 - \omega^2 D_6\right)} , \tag{11-17}$$

where D_1-D_9 and E_1-E_4 are combinations of A_1-A_6 and B_1-B_6. Therefore, Eqs. (11-11), (11-16) and (11-17) give the root mean square values for q_1 and q_2:

$$\left(q_1\right)_{rms} = \left[2\int_o^\infty |Q_1(i\omega)|^2 P_y(\omega)d\omega\right]^{1/2} \tag{11-18}$$

and

$$\left(q_2\right)_{rms} = \left[2\int_o^\infty |Q_2(i\omega)|^2 P_y(\omega)d\omega\right]^{1/2} , \tag{11-19}$$

and the root mean square of the lateral nose load is given by Eqs. (11-19) and (11-6),

$$\left(F_y\right)_{rms} = K_5\left(q_5\right)_{rms} = \left(K_2/A\right)\left(q_2\right)_{rms} . \tag{11-20}$$

The integration of Eqs. (11-10), (11-11), (11-12), (11-18) and (11-19) were done by a finite element scheme which is explained in Appendix 11-B.

11-4. NUMERICAL EXAMPLE

The moored CBV 250 balloon (see Figure 11-3) was chosen as a numerical example. Its geometric, physical and aerodynamic properties are

$$\begin{aligned}
D &= 148.7 \text{ ft},\ z = 60 \text{ ft},\ x_{cp} = 87.0 \text{ ft},\ x_a = 59.0 \text{ ft},\ x_{cm} = 77.0 \text{ ft};\\
A &= 4.0 \text{ ft},\ \bar{b} = 175.0 \text{ ft},\ S = 3970.0 \text{ ft}^2,\ K_2 = 83300.0 \text{ ft-lb/rad};\\
K_3 &= 12000.0 \text{ lb/ft},\ K_4 = K_5 = 36000.0 \text{ lb/ft},\ \hat{C}_2 = 83.3 \text{ ft-lb-s};\\
\hat{C}_3 &= 36.0 \text{ lb-s/ft},\ m = 565.0 \text{ slugs},\ I_{cm} = 10.98 \times 10^5 \text{ slug-ft}^2;\\
m_{ax} &= 96.0 \text{ slugs},\ m_{ay} = 458.0 \text{ slugs},\ C_{Y\beta} = -2.10 \text{ and } C_D = .06 .
\end{aligned} \tag{11-21}$$

Also, the balloon was assumed to be moored at sea level, with standard atmospheric conditions and a turbulence power spectrum corresponding to strong wind "palmetto" surroundings, as given by Alexander et al (1971). Referring to Appendix 11-C, the longitudinal power spectrum coefficients are

$$\alpha_1 = 6.198,\ \alpha_2 = .845,\ \alpha_3 = .03,\ \alpha_4 = 1.0,\ \alpha_5 = -.63,$$
$$\text{and } \alpha_6 = .076, \tag{11-22}$$

and the lateral power spectrum coefficients are

$$\alpha_1 = 3.954,\ \alpha_2 = .781,\ \alpha_3 = .10,\ \alpha_4 = .58,\ \alpha_5 = -.35,$$

$$\text{and } \alpha_6 = .076 . \tag{11-23}$$

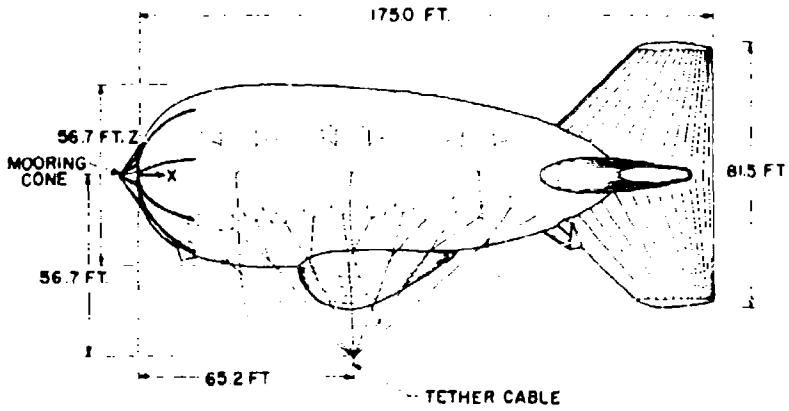

Figure 11-3. The CBV 250 Tethered Aerodynamically Shaped Balloon

Finally, these values were used in the integration scheme discussed in Appendix 11-B, where

$$\omega_o = .005 \text{ rad/s and } \omega_{max} = 10.0 \text{ rad/s}, \tag{11-24}$$

and the results are shown in Figures 11-4, 11-5 and 11-6.

Considering first the rms longitudinal displacement, $(q_3)_{rms}$ (Figure 11-4), one sees that this varies nearly linearly with U_o. This behavior is due largely to the fact that this mode is well damped by C_{ij}, as shown, for example, by the characteristic roots when $U_o = 100$ fps:

$$\omega_{root} = -.063 \pm 13.692. \tag{11-25}$$

Therefore, the resonance spike in the transfer function, (9), was low and well rounded, which contributed to the smoothness of $(q_3)_{rms}$ versus U_o. A further factor was that the aerodynamic terms, C_{ij} and m_{ax}, were assumed to be constant and independent of ω, which also contributed to the smoothness of the longitudinal transfer function.

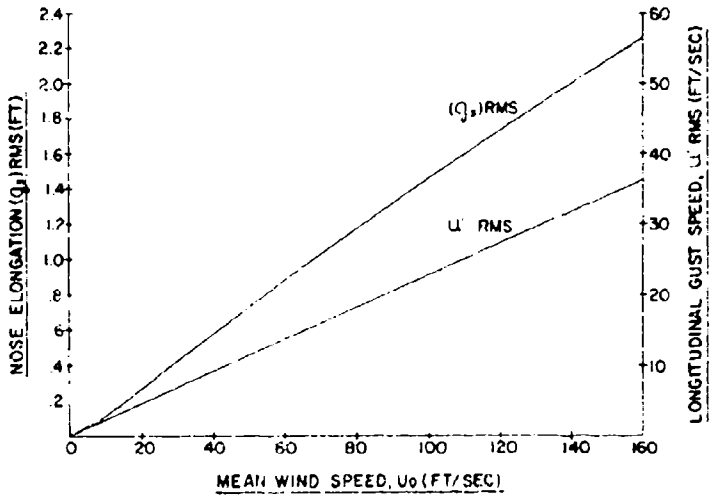

Figure 11-4. The RMS Values of the Longitudinal Gust Speed and Nose Elongation

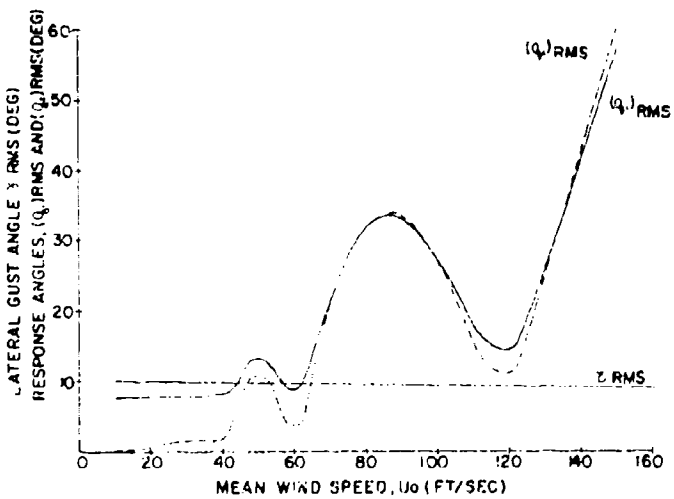

Figure 11-5. The RMS Values of the Lateral Gust Angle and Response Angles

This was not the case for the lateral transfer functions, Eqs. (11-16) and (11-17), where $\bar{Y}_v$ and $in_{\dot{\beta}V}$ vary periodically with ω (see Appendix 11-A), and the lateral aerodynamic coefficient, $C_{Y,\beta}$, contributes only light damping for the combination "bending and swinging" mode. The characteristic root for this mode

when U_o = 100 fps is

$$\omega_{root} = -.018 \pm i5.011 \qquad (11\text{-}26)$$

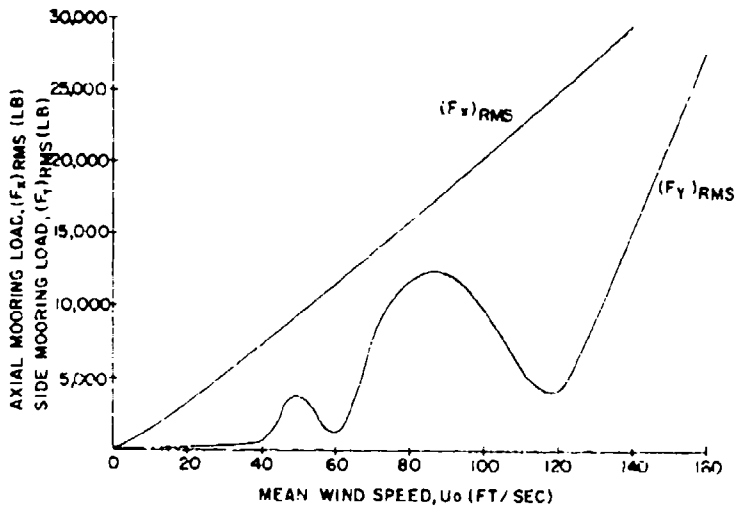

Figure 11-6. The RMS Values of the Mooring Loads

Therefore, the resonance spikes in Eqs. (11-16) and (11-17) were high and sharp, which contributed to the interesting variations of $(q_1)_{rms}$ and $(q_2)_{rms}$ with U_o, as shown in Figure 11-5. One first notes that for $0 \leq U_o \leq 40$ fps, $(q_1)_{rms}$ dominates over $(q_2)_{rms}$ and is nearly equal to the gust angle, γ_{rms}. This is the wind regime where the balloon is swinging nearly in phase with the wind, and bending at the nose is minimal. Where 40 fps $\leq U_o \leq 60$ fps, the first displacement peak is encountered, where the bending angle of the nose, $(q_2)_{rms}$, is nearly equal to the swinging angle, $(q_1)_{rms}$. After a brief reduction at U_o = 60 fps, a second displacement peak is encountered, where again the swinging and bending angles are nearly equal, and further, their magnitudes are very high. Finally, after another brief dip at U_o = 120 fps, they continue up off the graph.

In the regions, 80 fps $\leq U_o \leq$ 100 fps and $U_o \geq$ 130 fps, the magnitudes of $(q_1)_{rms}$ and $(q_2)_{rms}$ are high enough to begin violating the small perturbation assumptions of the theory. However, the structural deformation necessary to allow these angles is so large that the structural spring constant, K_2, would be significantly larger (barring buckling) than its given value, thus limiting the deformations to values less than those indicated by the high peak regions of Figure 11-5.

As a further observation, indications are that q_1 and q_2 act nearly 180 degrees out of phase relative to each other. This has not been checked theoretically, but moored balloon observations and the low theoretical damping of the "bending and swinging" mode of Eq. (11-26) along with the fact that $(q_1)_{rms} \approx (q_2)_{rms}$ in the peak regions, appear to verify this observation.

Finally, Eqs. (11-13) and (11-20) give the mooring loads shown in Figure 11-6. As to be expected from the forms of Eqs. (11-13) and (11-20), these force curves exhibit the same type of behavior relative to U_o as the displacement curves in Figures 11-4 and 11-5, and the preceding discussion about these also applies to Figure 11-6. One important point, though, is that when one is designing to a maximum wind speed, this should be $U_o + u'$. If, for instance, the example system is to be designed to 70 knots (118 fps) maximum wind speed capability, it must be able to withstand any forces encountered within $0 \leq U_o \leq 95$ fps. In other words, the design wind speed, U_o, is always less than the specified maximum wind speed, which is $U_o + u'$.

11-5. CONCLUSIONS

Within the limits of the assumptions on the physical model, this theory provides a design tool for predicting a moored streamlined balloon's rms displacements and loads. The key assumptions are those of small displacements and velocities about the equilibrium position and those of "effective Y_c and m_{ay}", $\tilde{Y}_c$ and $\tilde{m}_{ay}$, for the lateral turbulence inputs. The first step toward improving the theory would be to refine the latter assumptions by considering the phase of the turbulence component as well as its magnitude and wavelength (as discussed in Appendix 11-A). A next step would be to consider large displacement nonlinear motions, although this would then require representative examples of time-dependent turbulence data and would involve a considerable increase in mathematical complexity over the present linear rms analysis.

However, pending comparisons with experimental data, it is felt that this physical model has retained the essential features of a moored balloon system, and that the trends and orders of magnitude of the results for the example are believable. This analysis is a considerable refinement over static and quasi-static physical models, thus warranting its application as a design tool, pending subsequent refinements to the theory.

References

Alexander, M. B., Brown, S. C., Camp, D. W., Daniels, G. E., Fichtl, G. H., Hill, K., Kaufman, J., Smith, O. E., and Vaughan, W. W. (1971) Wind, Terrestrial Environment (Climatic) Criteria Guidelines for Use in Space Vehicle Development, G. E. Daniels, Ed., TMX-64589, NASA: 5.35-5.41.

Bruhn, E. F. (1958) General Loads on Aircraft, Analysis and Design of Aircraft Structures, Tri-State Offset Co., Cincinnati, Ohio: A4.1-A4.14.

Etkin, B. (1966) Transition Between the Time and Frequency Domains, Dynamics of Flight (No. 5), Wiley, New York: 268-270.

Kesti, N. E. (1971) Dynamic Analysis of ARPA Balloon While in Moored Position, SER 0127, G. T. Schjeldahl Co., Northfield, Minnesota.

Appendix A

When one considers the aerodynamic forces on the balloon due to a given component of the atmospheric turbulence, it becomes apparent that these are functions of the component's magnitude, wavelength, and phase. However, the derivation of these functions is involved (one must consider modified crossflow theory for the body and "effective camber" theory for the fin), and the mathematical form of the results is not readily applicable to the transfer function solutions given in the text of this paper. Therefore, a simplified form of these functions was obtained by assuming the turbulence component's phase to be such that the component's maximum amplitude, v_o, always occurs at x_{cp} (see Figure 11-A1). Further, the balloon's effective aerodynamic length, $\bar{b}$, is centered at x_{cp}, so that the average of v' over $\bar{b}$ is given by

$$v_{avg} = \frac{v_o}{\bar{b}} \int_{-\bar{b}/2}^{\bar{b}/2} \cos\left(\frac{\omega x}{U_o}\right) dx \,. \tag{11-A1}$$

So, one may define an "effective Y_c", $\bar{Y}_c$, by

$$\bar{Y}_c = \frac{v_{avg}}{v_o} Y_c \,, \tag{11-A2}$$

which with Eq. (11-A1) gives

$$\bar{Y}_c = Y_c \left| \frac{2U_o}{\bar{b}\omega} \sin\left(\frac{\omega \bar{b}}{2U_o}\right) \right| \,. \tag{11-A3}$$

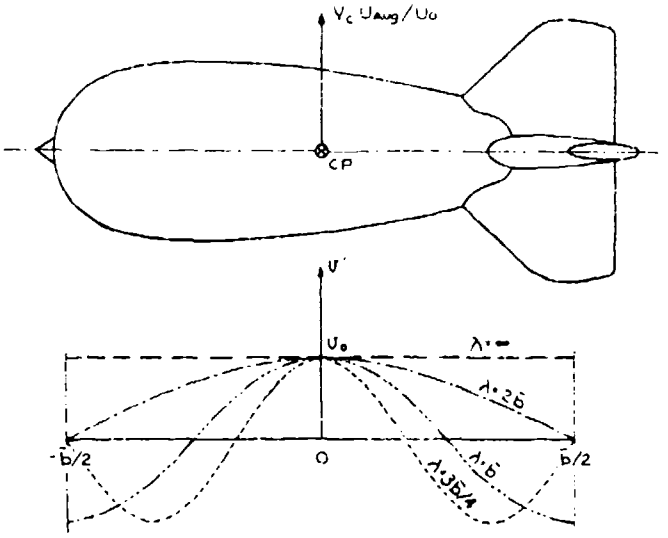

Figure 11-A1. The Assumed Distribution of a Lateral Gust Component

The wave shape for the time derivative of v', $\dot{v}$, is also sinusoidal, so an "effective m_{ay}", $\tilde{m}_{ay}$, may be constructed in the same fashion as $\tilde{Y}_c$:

$$\tilde{m}_{ay} = m_{ay} \left| \frac{2U_o}{\bar{b}\omega} \sin\left(\frac{\omega\bar{b}}{2U_o}\right) \right| . \qquad (11\text{-}A4)$$

Appendix B

Evaluation of the Integrals

The numerical technique for evaluating the integrals, Eqs. (11-10), (11-11), (11-12), (11-18) and (11-19), was to approximate the areas under the function curves by centered rectangles, as illustrated in Figure 11-B1. Thus, the numerical form of Eqs. (11-10), (11-11), (11-18), and (11-19) is

$$u'_{rms} = \left[2\omega_o \sum_{n=1}^{N} P_x(n\omega_o - \omega_o/2) \right]^{1/2} , \qquad (11\text{-}B1)$$

$$\gamma_{rms} = \left[2\omega_o \sum_{n=1}^{N} P_y(n\omega_o - \omega_o/2) \right]^{1/2} , \qquad (11\text{-}B2)$$

$$(q_3')_{rms} = \left[2\omega_o \sum_{n=1}^{N} | Q_3 |(i(n\omega_o - \omega_o/2)|| ^2 P_x(n\omega_o - \omega_o/2) \right]^{1/2} , \qquad (11\text{-}B3)$$

$$(q_1')_{rms} = \left[2\omega_o \sum_{n=1}^{N} | Q_3 |(i(n\omega_o - \omega_o/2)|| ^2 P_y(n\omega_o - \omega_o/2) \right]^{1/2} , \qquad (11\text{-}B4)$$

$$(q_2')_{rms} = \left[2\omega_o \sum_{n=1}^{N} | Q_2 |i(n\omega_o - \omega_o/2)|| ^2 P_y(n\omega_o - \omega_o/2) \right]^{1/2} , \qquad (11\text{-}B5)$$

where ω_o is the ω increment (as seen in Figure 11-B1), and $N = \omega_{max}/\omega_o$.

The integrals rapidly converge when ω_{max} is greater than the largest natural frequency of the system, so it was sufficiently accurate to choose

$$\omega_{max} = 2 \times (\text{largest natural frequency}).$$

For the numerical example, the largest natural frequency was approximately 5.0 rad/s, hence the selection of $\omega_{max} = 10.0$ rad/s.

Further, since the transfer functions of a lightly damped system are usually "spikey," care must be taken to choose an ω_o small enough to evaluate adequately the "spikes" in the curve. For the numerical example, ω_o less than .005 gave negligible differences in the results.

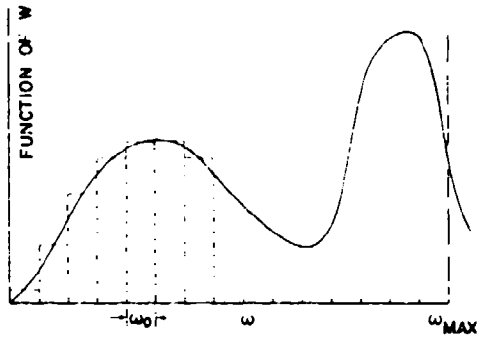

Figure 11-B1. The Centered Rectangle Numerical Integration Scheme

Appendix C

Power Spectrum Functions for the Atmospheric Turbulence

From Alexander et al (1971), exhaustive atmospheric turbulence measurements at Cape Kennedy, Florida have resulted in curve-fitted functions for the longitudinal and lateral turbulence power spectrums:

$$\Phi(\Omega) = \frac{\beta u^{*2}}{\Omega} \frac{\alpha_1 f/fm}{\left[1 + 1.5(f/fm)^{\alpha_2}\right]^{5/(3\alpha_3)}}, \tag{11-C1}$$

where

$$f = \frac{\Omega Z}{U_o}, \quad fm = \alpha_3(Z/\bar{Z})^{\alpha_4}, \quad \beta = (Z/\bar{Z})^{\alpha_5}, \quad u^* = \alpha_6 \bar{U}_o.$$

and

$$\alpha_6 = \frac{.4}{\ln(\bar{Z}/Z_o)}.$$

Further, since

$$\omega = 2\pi\Omega \text{ (rad/s)}, \tag{11-C2}$$

$$u'_{rms} = \left[2\int_o^\infty \Phi(\Omega)d\Omega\right]^{1/2}, \tag{11-C3}$$

and

$$\gamma_{rms} = \left[2\int_o^\infty \frac{\Phi(\Omega)d\Omega}{U_o^2}\right]^{1/2}. \tag{11-C4}$$

Eq. (11-C2) into Eqs. (11-C3) and (11-C4) gives

$$P_x(\omega) = \frac{\Phi(\omega/2\pi)}{2\pi}, \tag{11-C5}$$

and

$$P_y(\omega) = \frac{\Phi(\omega/2\pi)}{2\pi U_o^2}. \tag{11-C6}$$

Contents

12. Tethered and Cable Powered Heavy Lift Balloon Systems Design, Operations, and Applications

R.A. Pohl and K.D. Odney
Raven Industries, Inc.
Sioux Falls, South Dakota

Abstract

Balloon systems are usually categorized by flight profiles which are free flight, tethered, or powered. These flight profiles involve three basic balloon shapes—natural, aerodynamic (streamlined), and spherical superpressure. This paper covers the use of natural shaped balloons in the tethered flight mode, having payload capacities in the range of 10 to 20 tons.

Two applications of this type of system are presented: (1) cable powered, short haul, heavy load transport and (2) low-altitude tethered platforms. These applications involve the use of a natural shape balloon design utilizing heavy coated fabrics which permit long term, continuous operations with heavy payloads. One such system completed some 22,000 hours of operation last year.

A review of existing cable powered, short haul, heavy lift balloon systems used by the timber industry is presented. The three logging systems currently being operated utilize Model 530K balloons (530,000 cubic feet). These systems are capable of transporting payloads of 10 tons at speeds of up to 2,000 feet per minute. Also discussed are the future applications of the short haul transport systems, including ship-to-shore off loading of cargo and construction.

This paper also reviews an existing tethered platform application, a system being developed as part of the TORUS program conducted for the U.S. Air Force.[1] The TORUS balloon support system consists of a Model 815K (815,000 cubic feet) heavy lift balloon, a dielectric quad-tether system, and winching equipment. The Model 815K provides up to 20 tons of payload capacity and is utilized to support an electromagnetic pulse (EMP) simulator. The paper includes a review of balloon system design parameters peculiar to the TORUS application

[1]The work is being conducted under Contract No. A-8075 from EG&G, Inc., Albuquerque, New Mexico, R.L. DesJardin, Program Manager; under Air Force Contract No. F29601-71-C-0109, U.S. Air Force Weapons Laboratory, Kirtland Air Force Base, New Mexico, A.B. Griffin, Program Manager; and sponsored by Space and Missiles Systems Organization (SAMSO).

12-1. INTRODUCTION

Heavy lift balloon systems have been developed for short haul transport and low altitude platform applications. The transport configuration is designed for short haul of high tonnage payloads over difficult or rough terrain and water. Primary applications include mountainous and swamp logging, mining, dam construction, ship-to-shore unloading, moving oil field equipment, and tower erection.

This balloon transport technique has the obvious advantage of moving heavy loads through the air without regard to surface obstacles. While the balloon provides the lift, a simple cable system powered by a double drum winch provides the lateral movement drive. Years of full scale operations in a wide range of weather conditions have proven this method of short haul transport to be reliable and economical.

In another application, heavy lift balloons are used to provide a high-payload capacity, stationary platform at a low altitude. Single or multiple tethers enable the positioning accuracy to be varied. While the equipment is used at fixed sites, it can be relocated to distant sites relatively easily.

A natural shaped balloon was selected for both the transport and platform applications, since it has a high static lift efficiency and good performance characteristics over a wide range of conditions. Since the natural shape is a symmetrical body of revolution which does not produce significant aerodynamic lift, full lift capacity must be provided statically and is, therefore, always available.

Balloon design, materials, manufacturing techniques, ground support equipment, and operational techniques have been developed specifically for the transport and platform applications with the net result being an integrated system for a wide range of applications.

12-2. BACKGROUND

Balloons are usually thought of as being able to carry relatively light payloads to high altitudes. Such systems reflect various degrees of sophistication, including thin film balloons with volumes in the millions of cubic feet, long-duration superpressure designs, and high-altitude, station keeping systems. This paper discusses the other extreme, which is the heavy lift balloon, used at very low altitudes. These systems derive from the high altitude systems for which the basic technology of ballooning was developed.

Low altitude, heavy lift balloons are characterized by payloads of many tons, altitudes usually below 1000 feet, and nearly continuous operation. Such characteristics are the result of the need to provide economic utilization of the system in

commercial applications. This need for a high payload capacity for long durations has led to the development of a class of natural shaped, heavy load balloons which have nearly an all-weather capability. Along with the basic balloon envelope, ground support equipment and operating techniques have been developed for this class of balloons.

The two types of flight regimes in the systems described are (1) heavy loads at low altitudes with lateral movement and (2) heavy loads at low altitudes at fixed points. Both require an extreme duty balloon capable of being maintained in an inflated state for long periods of time (from months to years).

Upon detailed analysis of transport and platform objectives, the natural shaped balloon design was selected. This shape was chosen, since it has a high static lift efficiency, is not dependent upon aerodynamic lift, and can be fabricated with heavy coated fabrics which yield long life cycles. Other parameters, such as the ability to withstand high shock loads, entered into the balloon shape selection. Based on some 50,000 hours of operation, the design selection has proven to be correct.

12-3. BALLOON DESIGN

The highest static life efficiency of any balloon shape is a sphere, and the natural shaped balloon approximates that shape (Figure 12-1). The natural shape does not have any region of excess envelope material or extreme stress concentration. The payload force is transmitted primarily into the balloon meridionally, and the circumferential stress is practically zero.

12-3.1 Shape

A "natural shape" is variable within bounds. A complex shape factor, called Σ, basically describes the relationship between the inflated height and diameter. The Σ value normally varies from 0 to 0.4, where at $\Sigma = 0$ the balloon weight is small compared to the gross lift and at $\Sigma = 0.4$ the payload is light compared to the balloon weight. A high Σ value represents a fatter shape (that is, diameter-to-height ratio is larger). Heavy lift balloons are designed at low Σ values, since the balloon weight is relatively much smaller than the gross lift.

An important feature of a natural shaped balloon is the ability of the design to carry heavy loads with relatively uniform load distribution into the envelope. The uniform distribution also enables this design to take shock loads with minimal stress concentrations and bending moments, as is typical in aerodynamic shape balloons. This basic characteristic of balloon design is of paramount importance to transport operations. A natural shaped balloon is also conducive to the addition of meridional direction load carrying members to the gores to permit heavy payload designs.

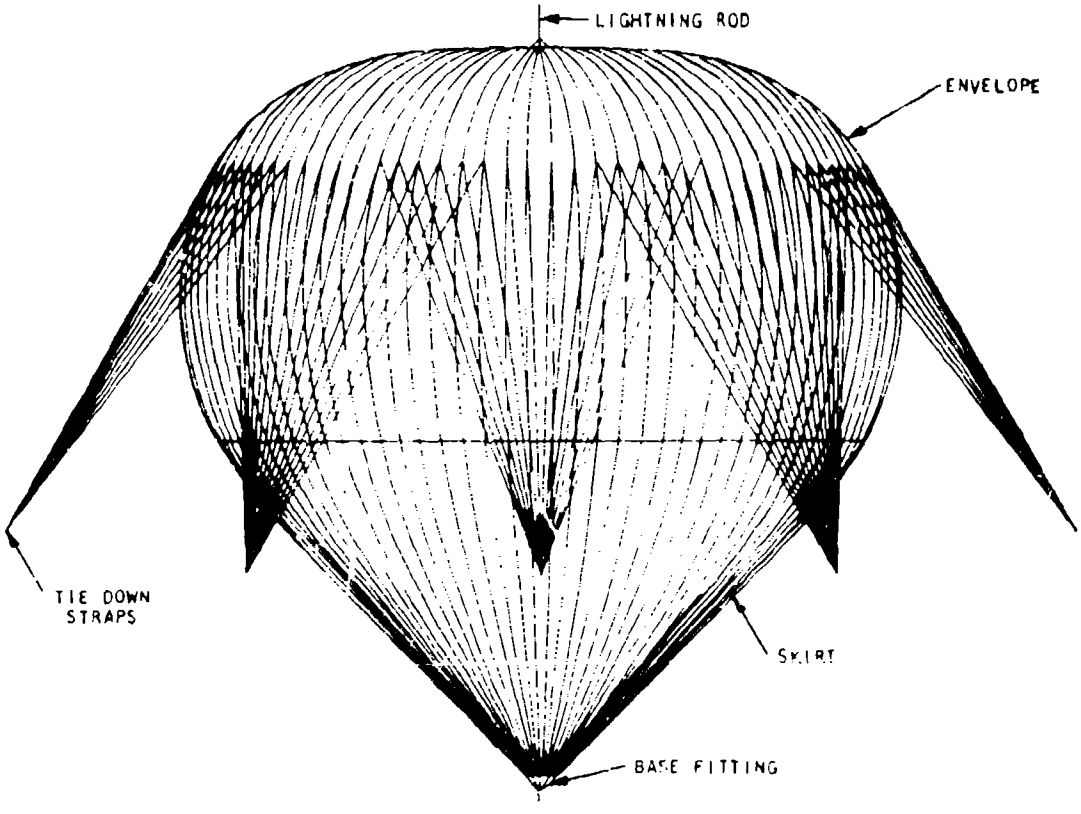

Figure 12-1. Natural Shaped Balloon Configuration

12-3.2 Aerodynamic Considerations

The aerodynamic force coefficient properties of natural shapes are shown in Figure 12-2. Since a natural shaped balloon is a symmetrical body of revolution about the vertical axis, the force coefficients are independent of wind direction. This property is of prime importance in transport functions, because the balloon must operate at or near full lift capacity regardless of wind direction. As shown in Figure 12-2, aerodynamic lift cannot be relied upon under normal wind conditions. In fact, the system will normally operate in the negative aerodynamic lift region. Since system design is predicated on static lift only, this coefficient is not considered in determining maximum usable lift. However, in designing a system for a specific payload, allowance is made in the form of excess static lift for predicted negative aerodynamic lift. This added lift is relatively small, since the negative lift coefficient is encountered only at lower wind speeds.

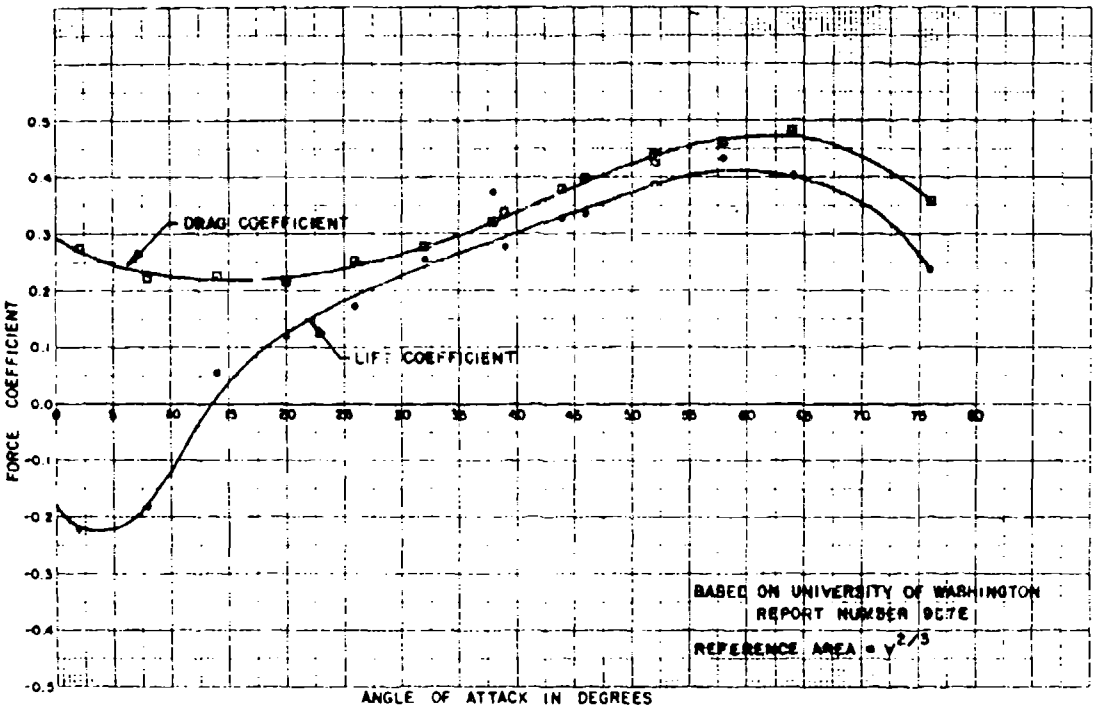

Figure 12-2. Natural Shaped Balloon, $\Sigma = 0.0$, Force Coefficient Variation With Angle of Attack

The drag coefficient for natural shapes generally falls between 0.2 and 0.3 for the Reynold's number range considered applicable in both transport and platform systems. While the drag coefficient range is considerably higher than that of the aerodynamic shaped balloon, for the applications described herein, this disadvantage is greatly outweighed by the advantages of the natural shape, namely, volumetric efficiency, independence of aerodynamic force generation (that is, ability to operate at full lift capacity regardless of wind direction), high mass moment of inertia, gust stability, and uniform envelope loading.

The natural shaped hull is very stable at low altitude operations because of its uniform cross section and the static lift. Gusty wind condition effects on an inverted teardrop shape are small in comparison with an aerodynamic shape, and oscillations typically are slow and quite limited in normal operating configurations.

Envelope stresses in a natural shape are due to the envelope internal pressure generated by the dynamic pressure and the distribution of the payload forces into the envelope. In a 530,000 cubic-foot balloon, the envelope stress induced by a

60 knot wind is 32.1 lb/in (includes an overpressurization factor). The maximum load input to a natural shape is at the skirt/balloon interface. Under a 60-knot flight condition, the load input at this interface is approximately 46,350 pounds. Assuming uniform loading, the skin stress is then 43.1 lb/in, and the gross load input in a 60 knot wind is 75.2 lb/in. The basic fabric strength is approximately 220 psi, thus the safety factor in the "material only" case is approximately 3. In the actual design, the applied loads are carried by the load webbings located on the balloon gores and by the envelope material. A 530,000 cubic-foot balloon has 78 load webbings rated at 2,500 pounds tensile. Considering the load input to the envelope, the safety factor relative to these applied loads will be in excess of 10.

12-3.3 Materials

The envelope material utilized in this class and shape of balloon is a coated dacron fabric weighing 10.75 ozs/yd^2. This material has a tensile strength of approximately 220 lb/in, is ultraviolet resistant, and has a low permeability in the range of 0.3 ls/m^2/24 hrs. The elastomeric coatings are also highly resistant to abrasion and wear.

A continuous loop of steel cable is used as the top end fitting. Load webs attach to this loop. Steel cables connect the load webbings to the bottom end fitting. Lightning protection is provided by a top mounted tower and multiple braided cables extending down the load webbings to the bottom end fitting. This fitting incorporates a multiple swivel and is coupled to double tether lines.

These balloons are normally inflated to 90 percent of their full volume to allow for temperature and pressure altitude changes. At this inflation level, the lower portion of the balloon is slack. A skirt protects the slack portion of the balloon and also serves as a load transfer coupling between the balloon and the bottom end fitting.

12-3.4 Typical Balloon Sizes

Heavy-lift balloon sizes that have been or are currently in operation have volumes of approximately 250,000 530,000 and 815,000 cubic feet. In volumetric comparison to high altitude balloons, these sizes are small. However, since these units are essentially fully inflated at very low altitudes, the payload capacities are large when compared to other types of balloons. The payload range for the above mentioned systems is 11,000 to 40,000 pounds. Balloons with payloads in the 100,000-pound class appear feasible and probably within the state of the art.

The specifications for the three balloon sizes that have been used operationally are shown below:

SPECIFICATIONS

Models	250K	530K	815K
Volume (ft^3, max)	250,000	530,000	815,000
Diameter (ft)	81	105	123
Height (ft)	97	113	121
Approximate Balloon Weight (lbs)	3,000	6,200	8,000
Net Usable Lift (lbs)			
Sea Level	11,000	25,000	40,500
5,000 ft	9,500	20,700	33,790
Approximate Wind Drag @ 25 mph, S.L	2,400	4,100	5,600
Lift-to-Drag Ratio	4.6	6.1	7.0
Lean-over Angle @ 25 mph	12°	9°	8°
Estimated Lift Loss (lb/day)	25	40	50

A 530,000 cubic-foot balloon, as shown in Figure 12-3, is normally flown in winds up to 40 mph. This 105-foot diameter balloon is shown in bedded down condition in Figure 12-4.

In this somewhat sheltered condition, winds of approximately 100 mph have not had any detrimental effect on the balloon.

12-4. CABLE POWERED, SHORT HAUL TRANSPORT

Natural shaped, heavy lift balloons were developed primarily for the logging industry. Large volumes of timber located in mountainous terrain cannot be harvested using ground skidding or cable systems due to their physical limitations, extensive road construction, and deleterious impact on the terrain. Other timber located in rough mountainous terrain is expensive to harvest with conventional equipment and in many cases cannot be transported from the cutting site to a road landing for hauling by truck to processing mills. Mountain road construction costs range from $20,000 to $75,000 per mile, and their usage is being restricted because of the damage to forest regions.

During the mid 1960's Raven Industries, Inc. and Bohemia Lumber Company initiated the development of an airborne log transport system using a natural shaped balloon. The balloon design was selected upon thorough analysis of the operating

Figure 12-3. Model 530K Heavy Lift Balloon

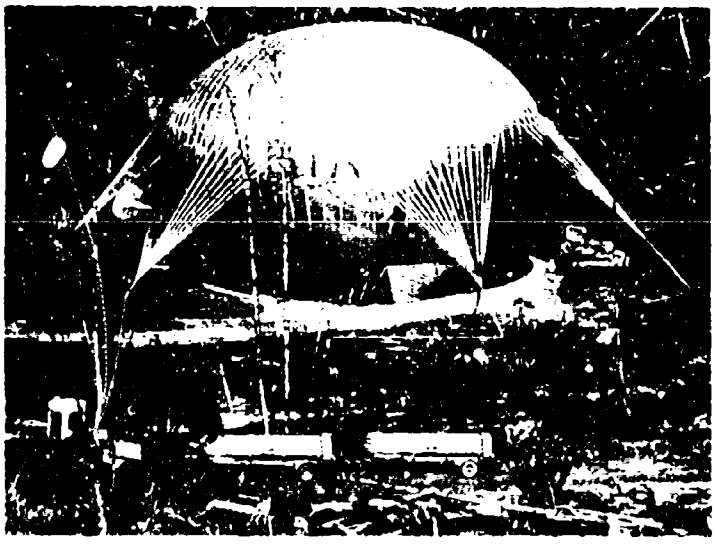

Figure 12-4. Rigged Model 530K Heavy Lift Balloon

requirements and flight regime involved in carrying a payload of logs from the cutting site to the landing site. (This phase of moving logs from the forest to a road site is called yarding.)

Yarding logs with a balloon involves the use of a balloon to supply the lift and a winch-powered cable arrangement for lateral movement. A typical layout is shown in Figure 12-5. The technique can be used practically anywhere a line can be strung—across steep slopes, valleys, swamps, high timber, rivers, and other obstructions. The winch, or yarder (Figure 12-6) as it is commonly called, has two power-driven drums that can be driven through a hydraulic "interlock" or differential. One drum contains the main line which extends to the balloon and

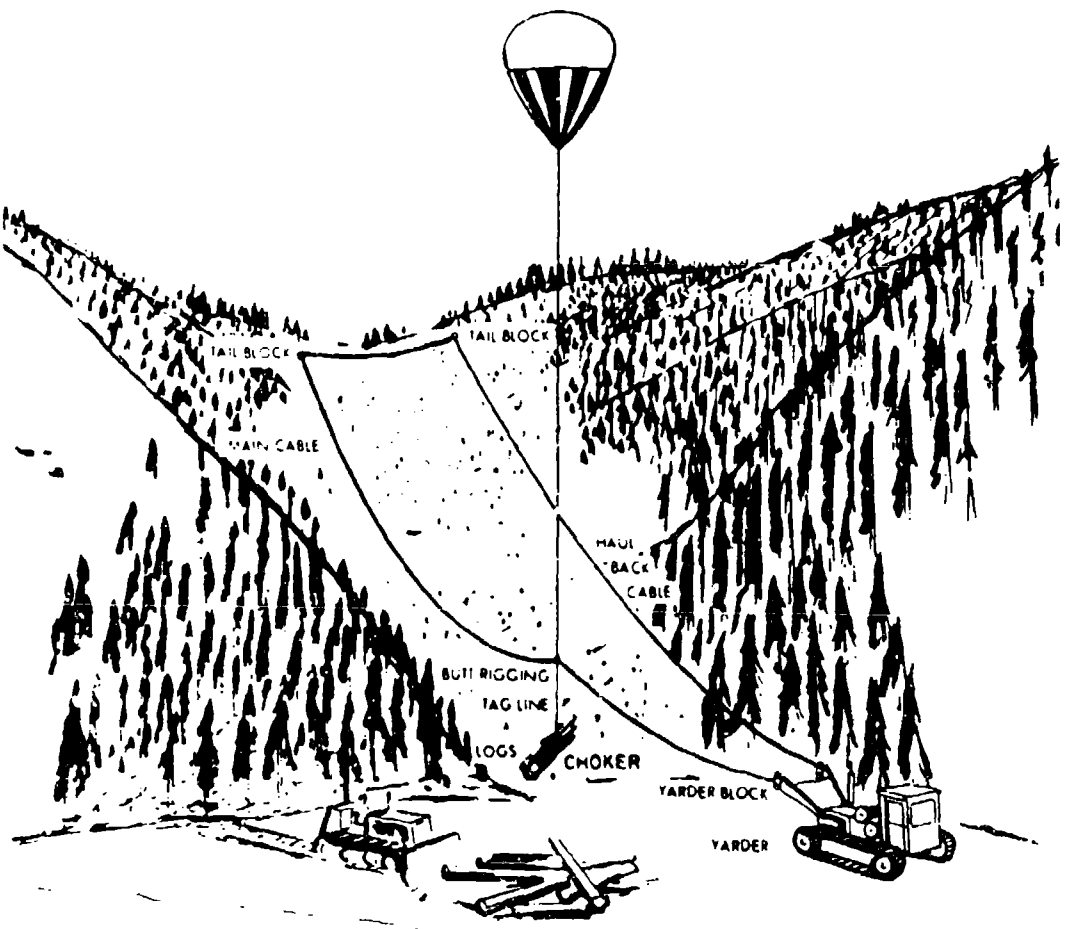

Figure 12-5. Typical Balloon Logging Layout

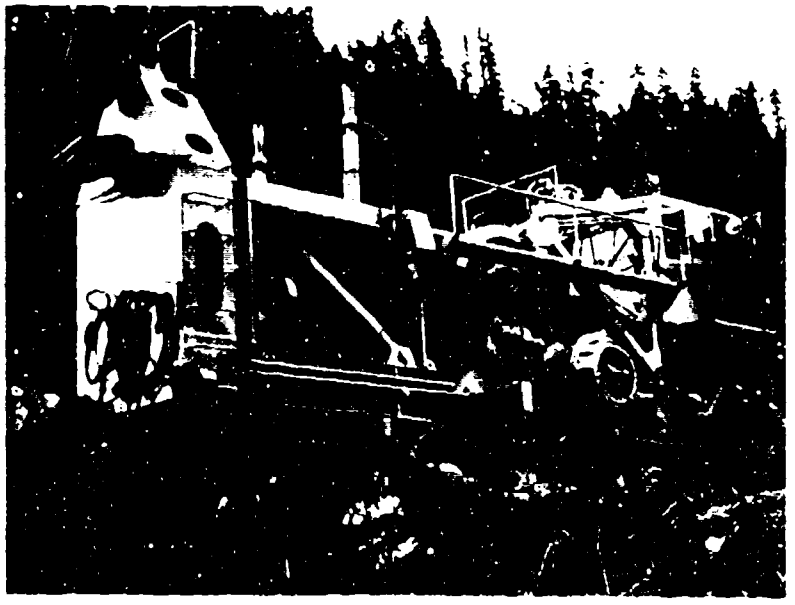

Figure 12-6. Model 530K Yarder

pulls the balloon toward the yarder. The other drum holds and powers the haulback line for the outbound trajectory. With either the mainline and haulback drum locked, the remaining drum feeds line in or out, thus controlling the balloon altitude over a fixed point (the mainline and haulback act as a two-point tether line). The balloon is moved horizontally by letting out on either the haulback or mainline and pulling in the other line. Obviously, these two modes of coupling and uncoupling the haulback and mainline drums in either direction enable the balloon to be flown in a powered trajectory along the cable layout path. Maximum line speed is about 2,000 fpm.

Both lines from the drums go through fairleaders located on a tower on the front of the yarder. The haulback line is passed through a number of stump anchored tailblocks located on the upper end of the timber area being harvested. The free end is attached to the butt rigging, which is the main tether point of the balloon. The mainline extends from the yarder to the butt rigging, forming a closed loop cable system.

The balloon is normally flown 250 to 300 feet above the butt rigging, while the tag line, which extends down from the butt rigging, varies in length up to 500 feet.

Chokers, short cables with quick couplers, are wrapped around the logs connected to the tag line by a ring and toggle connection.

The cable track is initially set up with a light weight "straw line" that enables the one-inch steel cable to be strung through the tailblock layout under power from the yarder. Relocation of the cable layout in a given logging area is done by progressive movement of the tailblocks on the upper end of the area being harvested.

Yarding distances are presently limited to approximately 3500 feet. This distance primarily is determined by the mainline and haulback drum size. Future systems, now in the planning stage, will extend this distance beyond a mile and, possibly, many miles.

A 530,000 cubic foot balloon with a 90 percent inflation level has a net lift of 25,000 pounds at sea level. The nominal log payload range is 20,000 to 22,000 pounds, when allowances are made for the suspended cable and rigging.

The average transported load is lower than this, since the log selection process is done by gross scale estimates rather than a weigh-off, and it is preferable to underestimate weight than to overestimate. One complete cycle will vary from 5 to 8 minutes, depending on the yarding distance, log felling conditions, and timber density. In general, the balloon logging system has a transport rate of 10 to 11 tons over distances up to 3500 feet every 5 to 8 minutes.

Two-shift operations have been utilized, and three shifts are planned in the near future with the use of portable illumination devices. During recent years, some 50,000 hours of full inflation time have been recorded on natural-shaped logging balloons. The only mishaps which occurred during this period were cases in which the balloon was flown in conditions outside the rated flight regime. The three cases were (1) balloon on tether in winds of 100 mph, (2) icing conditions, (3) balloon struck by lightning prior to installation of a lightning protection device.

Relocation of balloon logging equipment is relatively simple. The yarder is track mounted and can be moved short distances under its own power. Larger hauls are made by loading the yarder on a lowboy trailer. The balloon is moved in a tethered state 200 to 300 feet above a transfer vehicle, which is shown in Figure 12-7. Both rubber tired and crawler type transfer vehicles are used. The transfer vehicle is loaded on a lowboy trailer for long moves. The equipment has been moved over distances up to 80 miles in one night.

Other balloon transport applications, either in process or being evaluated, include ship-to-shore unloading and construction operations (a pipeline installation, swamp logging, and mining). A ship-to-shore test project is to be conducted in the very near future on the east coast. A typical ship-to-shore setup is shown in Figure 12-8. Construction project applications will probably be tried soon in a number of different areas.

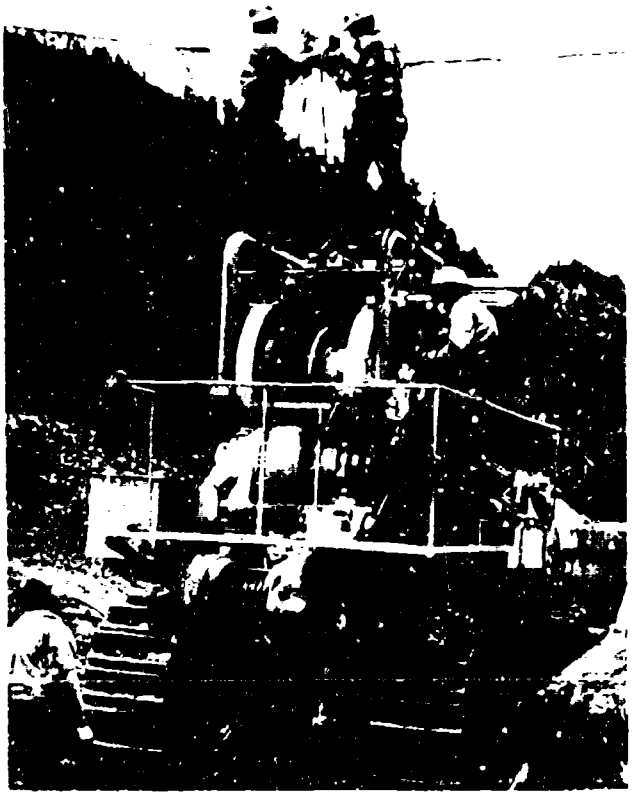

Figure 12-7. Model 530K Transfer Vehicle

12.5. LOW ALTITUDE TETHERED PLATFORMS

The TORUS balloon system is an example of the platform application of heavy lift balloons. TORUS (Transient Omnidirectional Radiating Unobstant and Static) is a portable electromagnetic pulse (EMP) simulator system which uses a Model 815K heavy lift balloon as the support member. The development of this system is being sponsored by the Space and Missiles Systems Organization (SAMSO) and is being monitored by the Air Force Weapons Laboratory at Kirtland Air Force Base, New Mexico. The prime contractor is E G & G, Inc. of Albuquerque, New Mexico.

The TORUS system configuration is shown in Figure 12-9. The major components of this system are the antenna system, the electromagnetic pulse generator (pulser), and the balloon support system. The antenna is a wire cage with a half toroid shape having a major diameter of 100 meters and a minor diameter of

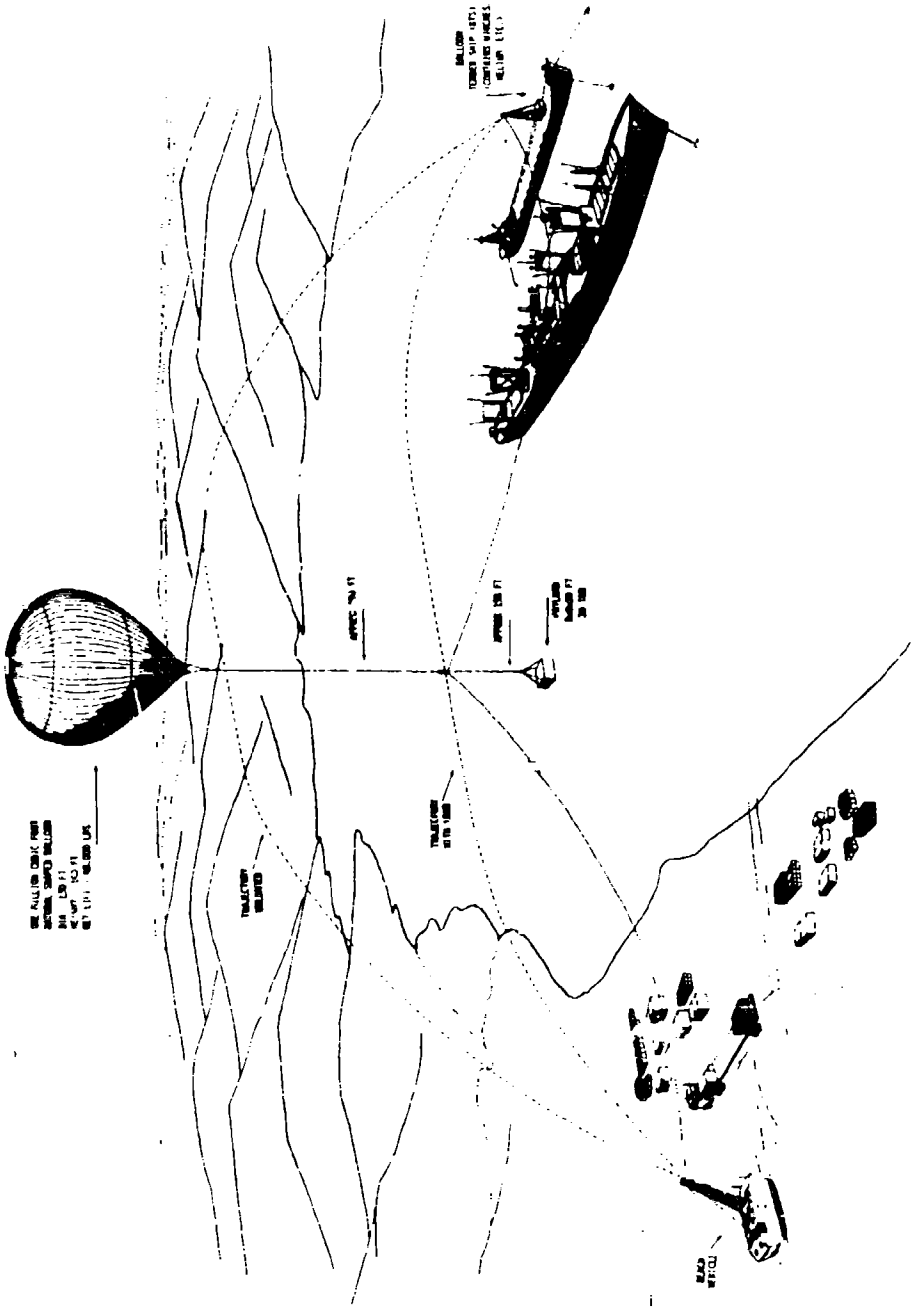

Figure 12-8. Typical Ship-to-Shore Layout

approximately 5 meters. The pulser, provided by Maxwell Laboratories, is mounted within the antenna in any one of seven locations. Support and control of the antenna system and pulser is provided by the balloon support system, which consists of the Model 815K heavy lift balloon, the tether system, and the winching equipment. While these major components of the TORUS System employ largely state-of-the-art techniques, the assemblage of these into the TORUS System has resulted in a uniquely flexible and portable EMP simulator.

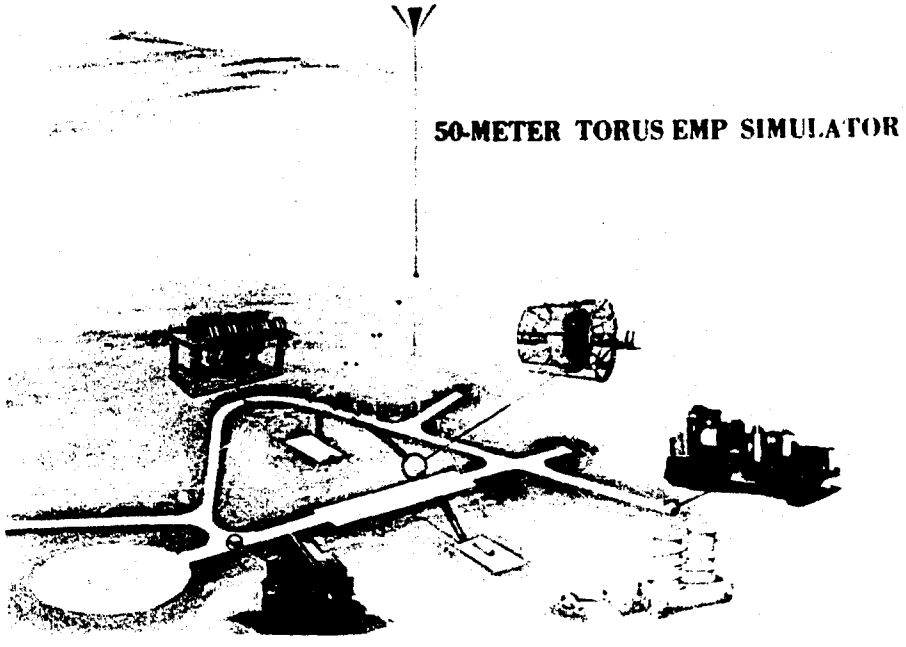

Figure 12-9. TORUS System Configuration

12.5.1 Design Considerations

The TORUS System is designed to operate in the following environmental conditions:

(a) Ground elevation - 0 to 6,000 feet MSL;

(b) Temperature - −20°F to +100°F at ground elevation;

(c) Humidity - 0 to 100 percent (relative);

(d) Wind - 25 knots steady, 40 knots gust.

In addition to these operating requirements, the system is designed to survive the following conditions:

(a) Temperature – -40°F to +120°F at ground elevation;

(b) Winds – up to 70 knots;

(c) Other conditions – The system is designed to withstand combinations of the preceding conditions with rain, snow, hail, lightning, or icing conditions.

The use of the balloon system with a high voltage pulser has resulted in additional specific requirements. Primary among these is a requirement that pertubations of the generated fields be limited as much as possible. Such a requirement imposes restrictions on the proximity of conductors to the antenna while the pulser is being operated. For this reason, the tether lines utilized for TORUS are dielectric.

12-5.2 Balloon Assembly

The Model 815K is shown in Figure 12-10 in the bedding area at the Acceptance Test Site in western South Dakota. In this photograph, the balloon is inflated to approximately 85 percent of its theoretical volume and has a net static lift or approximately 34,000 pounds. Figure 12-11 presents a more detailed description of the balloon assembly, and it can be seen from this figure that the inflation level of 34,000 pounds shown in Figure 12-10 is slightly below that considered to be optimum.

Figure 12-10. Model 815K at TORUS Acceptance Test Site

MODEL 815K

SYSTEM DESCRIPTION

1.	MODEL DESIGNATION	815K
2.	DESIGN TYPE	MODIFIED NATURAL SHAPE ENVELOPE TANGENT HARNESS LOAD SUSPENSION RAM AIR PRESSURIZED SKIRT/BALLONET
3.	FULL VOLUME	816,800 CU. FT.
4.	ENVELOPE DIAMETER	123.25 FT.
5.	HEIGHT (BASE TO CROWN)	121.38 FT.
6.	NUMBER OF TIE DOWNS	9
7.	WEIGHT	8,000 LB.
8.	GROSS LIFT, 90% INFLATION, @ SEA LEVEL	48,500 LB.
9.	DESIGN LIFT AT LOAD FITTING (NET STATIC LIFT), 90% INFLATION, STANDARD CONDITIONS:	
	a. AT DENSITY ALTITUDE OF 0 FT.	40,500 LB.
	b. AT DENSITY ALTITUDE OF 2,000 FT.	37,730 LB.
	c. AT DENSITY ALTITUDE OF 5,000 FT.	33,790 LB.
	d. AT DENSITY ALTITUDE OF 10,000 FT.	27,820 LB.

Figure 12-11. Model 815K System Description

The minimum required inflation level for the TORUS balloon is as follows:

(a) Payload weight including antenna, pulser, and instrumentation - 15,228 pounds;

(b) Tether system - 4,588 pounds;

(c) Stability allowance - 3,700 pounds;

(d) Maximum variation in tether system weight with extremes in antenna tilt angle and pulser location - 500 pounds;

(e) Allowance for moisture pickup in dielectric tether lines and on balloon - 2,000 pounds.

Total fixed weight and allowances equals 26,016 pounds.

In addition to the fixed lift requirement, there is a variable requirement to insure that negative aerodynamic lift is considered. At the TORUS System Acceptance Test Site elevation, this value will not exceed 3300 pounds. Therefore, the total net lift required for operating the system at the Acceptance Test Site is approximately 29,300 pounds. The excess available lift is desirable, since it provides additional stabilization to the system.

12.5.3 Tether System

Both the balloon and the antenna are controlled by the tether system. Two tether line assemblies, each having a length of approximately 340 feet, are attached to the base fitting of the balloon assembly. These tether lines, called the main tether lines, are in turn attached to the tether point fitting. The tether point fitting forms the interface between the main tethers and the anchor tethers, or quad-tether system. These four anchor tethers, each 780 feet long, provide the basic control of the balloon and the antenna through the tether point fitting. Two of the quad-tethers, those on the axis perpendicular to the antenna, are controlled by the winching equipment. The other two anchor tethers, those in the plane of the antenna, are attached to fixed anchors. These two lines are preset to the proper length before lifting the antenna, and all adjustment is made with the lines attached to the winches. The fixed-length anchor tethers also provide the mounting point for the pulleys and lines utilized in shaping the antenna. The relationship of these tether system components can be seen in Figure 12-9.

Since the tether lines must be dielectric, one is limited in the types of lines which may be considered. In the case of the TORUS System, the predicted maximum loads are such that even more stringent limitations are imposed in obtaining a tether line which is both strong enough and flexible enough to permit operation of the system.

The line selected is a double braided synthetic line made by the Sampson Cordage Works under the trade name 2-in-1 Stable Braid. The specifications for this line are shown in Figure 12-12. A description of the assemblies which form the tether system is presented in Figure 12-13.

Both the main tether system, that is, those tether lines between the tether point fitting and the base of the balloon, and the anchor tether lines are of the same material. This is necessary in order that all lines may be winched with the same equipment. The result is that a substantial safety factor is present in all portions of the tether system.

TETHER LINE SPECIFICATIONS

TYPE: SAMSON 2-IN-1 STABLE BRAID

CONSTRUCTION: BRAIDED POLYPROPYLENE CENTER WITH BRAIDED POLYESTER COVER

DIAMETER: 2.25 INCHES

CIRCUMFERENCE: 7 INCHES

BREAKING STRENGTH (AVERAGE): 140,000 LB.

BREAKING STRENGTH (MINIMUM): 123,000 LB.

WEIGHT: 1.40 LB./FT.

Figure 12-12. TORUS Tether Line Specifications

12.5.4 Ground Support Equipment

The ground support equipment consists of two winches, one stationary and one mobile. The two winches are essentially identical, the only difference being the use of an additional hydraulic pump on the mobile winch to drive an auxiliary drum. The stationary and mobile winches are shown in Figures 12-14 and 12-15, respectively.

Designed and manufactured by Otis Engineering Corporation, they are capstan type winches which are diesel powered and hydraulically driven and controlled. The diesel engine drives the hydraulic pumps, the main pump on each winch driving the main hydraulic motor, which in turn drives the capstans through a combination gear and roller chain transmission. The small pumps supply pressure to the hydraulic motors which drive the storage drums through roller chain transmissions. In both winches, the storage drum is connected to a level winding system for cable spooling operations.

The cable enters the winch through a fairlead assembly and passes through a sheave mounted on a hydraulic load cell, providing line tension readout. From this sheave, the cable passes through the capstans, over which the cable is wrapped six

TETHER LINE LENGTHS

	LENGTH	ASSEMBLY* WEIGHT
Main Tethers:		
Assembly No. 1		
Long Length	309 ft.	444 lb.
Short Length	29 ft.	63 lb.
Assembly No. 2		
Segment Length (2 req'd)	169 ft. ea.	259 lb. ea.
Auxiliary Line	48 ft.	89 lb.
Quad Tethers:		
Fixed Lines (2 required)	780 ft. ea.	1,103 lb. ea.
Winch Lines (2 required)	780 ft. ea.	1,103 lb. ea.
Total for System	3,844 ft.	5,526 lb.

* Weight is manufactured assembly weight, including thimbles. Does not represent airborne weight.

Figure 12-13. TORUS Tether Line Assemblies

times. It then passes through the level winding mechanism to the storage drum. Tension is applied to the cable by the capstans, permitting use of a low tension level wind system and storage drum.

A single lever controls speed, direction, and braking of the winch. The brake is a failsafe type and is applied whenever the control lever is in the neutral position, or at any time hydraulic pressure is lost. The system is designed to operate under power in both directions, in-haul and out-haul, from zero to maximum speed, in a continuous, stepless manner. All components of the winch are located on a skid-weldment suitable for anchoring to a permanent site or to a vehicle. General specifications for this Model 40R Winch are shown in Figure 12-16.

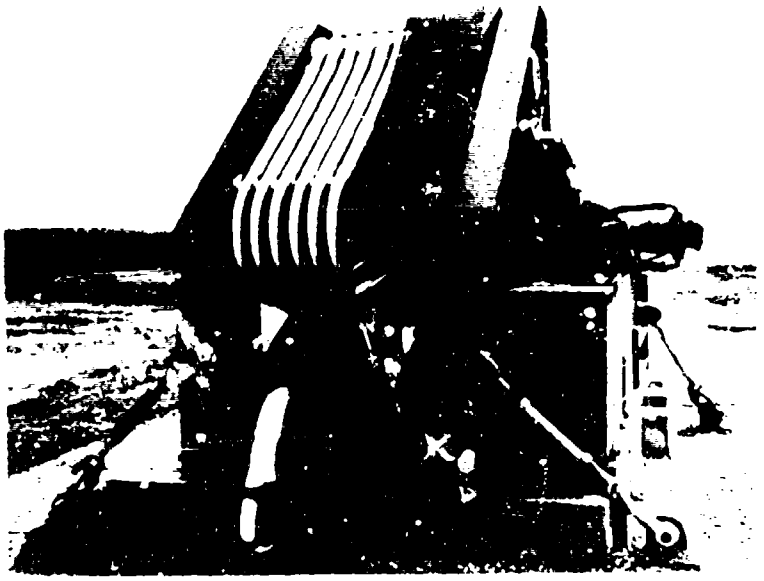

Figure 12-11. [illegible]

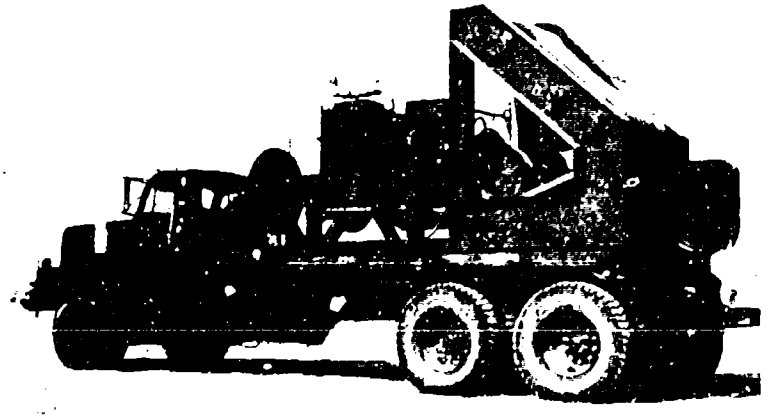

Figure 12-12. [illegible]

MODEL 40R WINCH

GENERAL SPECIFICATIONS

1.	RATED IN-HAUL CAPACITY	40,000 LB.
2.	MAX. IN-HAUL CAPACITY	65,000 LB.
3.	RATED STATIC LOAD CAPACITY	80,000 LB.
4.	CABLE SPEED AT RATED IN-HAUL CAPACITY	25 FPM
5.	DRUM CAPACITY	1200 FT. OF 2¼" DIA. LINE
6.	LENGTH	186 IN.
7.	WIDTH	93 IN.
8.	HEIGHT	103 IN.
9.	WEIGHT	24,000 LB.

Figure 12-16. Model 40R Winch General Specifications

The mobile winch is mounted on an International Harvester M-623 truck. This truck has a normal gross vehicle weight rating of 83,000 pounds. However, a tag axle is added to the truck frame to increase the gross vehicle weight, thus improving stability during balloon transfer operations. The gross vehicle weight of the mobile winch and vehicle is approximately 106,000 pounds, including approximately 52,000 of ballast. Specifications for the vehicle are shown in Figure 12-17.

12-6. CONCLUSIONS

Natural shaped balloons with high payload capacities and long duration flight capabilities have been developed for use as transport vehicles and support platforms. Current commercial operations in the forestry industry have demonstrated that this family of aerostats is both reliable and economical as a primary lift component in an airborne log transport system. Other current and future transport

projects indicate a high degree of versatility for this area of lighter-than-air technology. A tether platform design with a capacity of 40,000 pounds is undergoing initial operation check out and is expected to be a proven system in the near future.

MOBILE WINCH VEHICLE SPECIFICATIONS

1.	TYPE	INTERNATIONAL HARVESTER M-623 TRUCK WITH OTIS ENGINEERING MODEL 40R WINCH
2.	LENGTH	384 IN. (LESS TAG AXLE & BALLAST)
3.	WIDTH	101½ IN.
4.	HEIGHT	164 IN.
5.	WEIGHT:	
	TRUCK AND WINCH	53,860 LB.
	TRUCK-MOUNTED BALLAST (STEEL PLATE)	21,600 LB.
	TAG AXLE AND BALLAST (STEEL PLATE)	30,720 LB.
	TOTAL	106,180 LB.
6.	DRAWBAR PULL (UNCONSOLIDATED SURFACE)	30,000 LB. (LESS TAG AXLE & BALLAST) 40,000 LB. (WITH TAG AXLE & BALLAST)

Figure 12-17. Mobile Winch Vehicle Specifications

Balloon Borne Experiments and Instrumentation

Tuesday, 26 September

Morning: Chairman, Professor Alvin H. Howell
Tufts University

Afternoon: Chairman, Professor David G. Murcray
University of Denver

13. Manned Aerostat Research Flights

K.R. Stehling
National Oceanic and Atmospheric Administration
Rockville, Maryland

Abstract

While most experimenters with aerostat payload requirements these days think in terms of unmanned high altitude systems, a variety of useful, interesting, and practical scientific investigations can be conducted from low altitude (less than 10,000 feet) manned aerostats.

Since 1970, the author, a licensed pilot as well as scientist, has made several flights in the gas aerostat N7749A over the midwestern United States. Flight durations varied from six hours to over 40 hours at altitudes from 3,000 to 10,000 feet. Various Air Force, AFCRL and NASA/University of South Dakota "clinometers" and sky/ground brightness instruments and cameras were carried. Data were collected and are listed on various meteorological and brightness features.

It is shown that such data can be gathered reliably and cheaply and that the aerostat, while old-fashioned (net covered, wicker car, and so forth), performs safely and reliably and permits experiments to be conducted in a steady environment totally free from acoustic, electrical and thermal noise.

Note: Paper not available

Contents

14. Engineering Aspects of a Balloon-Borne Astral Pointing System (BAPS)*

D.L. Guthals
Ball Brothers Research Corporation
Boulder, Colorado

W. C. Gibson
Manned Spacecraft Center
Houston, Texas

14-1. INTRODUCTION

A two-axis stabilized platform was developed to point a scientific package at stellar targets while suspended from a balloon (see Figure 14-1). The requirements imposed by the science were extremely demanding and required considerable use of both an analog and a digital computer to arrive at a satisfactory design.

It was desired to point a telescope with an attached ultraviolet spectrometer at selected stellar targets. The Balloon-Borne UV Stellar Spectrometer (BUSS) has been described elsewhere by Bottema et al (1971) and is further described in a later section of this paper. The telescope optical axis was required to track the target star to within ± 2 arc seconds to attain the desired spectral resolution. Due to physical size and environment dynamics, a multistage pointing concept was used. Detailed servo design information has been described by Gibson et al (1972). The

*This publication results from the work Ball Brothers Research Corporation (BBRC) did for the Planetary and Earth Sciences Division of the Manned Spacecraft Center under Contract NAS 9-13054.

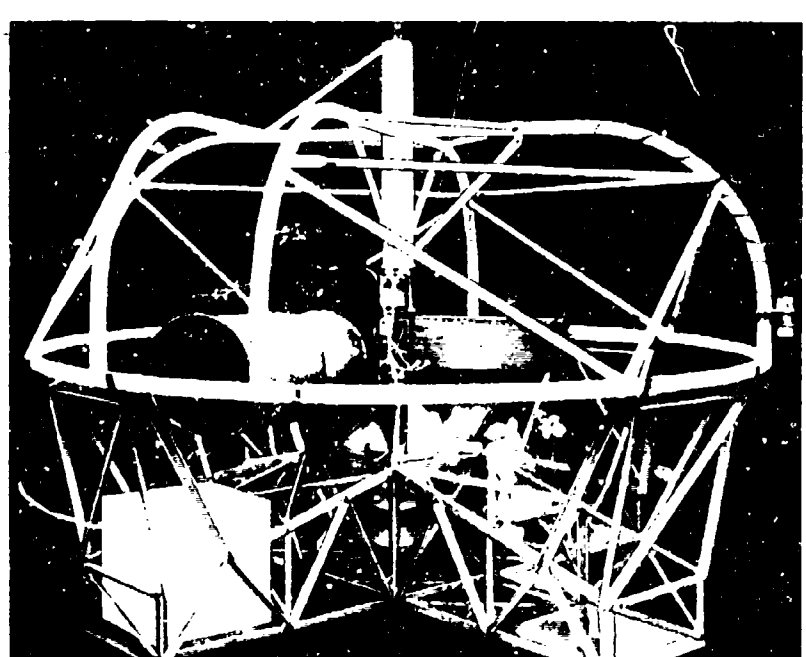

Figure 14-1. Balloon Astral Pointing System

Balloon-Borne Astral Pointing System (BAPS) comprised the first two stages of pointing bringing the telescope axis to within ±1 arc minute of the target star, and a servo-driven secondary mirror was the final pointing stage reducing the error to ±2 arc seconds.

The desired observing program was to be conducted from a balloon floating at no less than 40 kilometers for a period of approximately ten hours. Real time data readout was required to provide for increased flexibility in the observing program. It was also desired to have complete ground based control to allow freedom of target selection at any time during the balloon flight.

The resulting hardware has been flown twice with successful results and, in general, all the design parameters and experiment requirements were met. The scientific results obtained from these flights have been reported by Kondo et al (1972).

14-2. PLATFORM CONFIGURATION

The platform is divided into two basic sections. The upper section is referred to as the pointed section and the lower section as the gondola (see Figure 14-2). The two sections are connected by a semi-rigid support shaft called the azimuth shaft, the upper end of which is connected to the balloon suspension train.

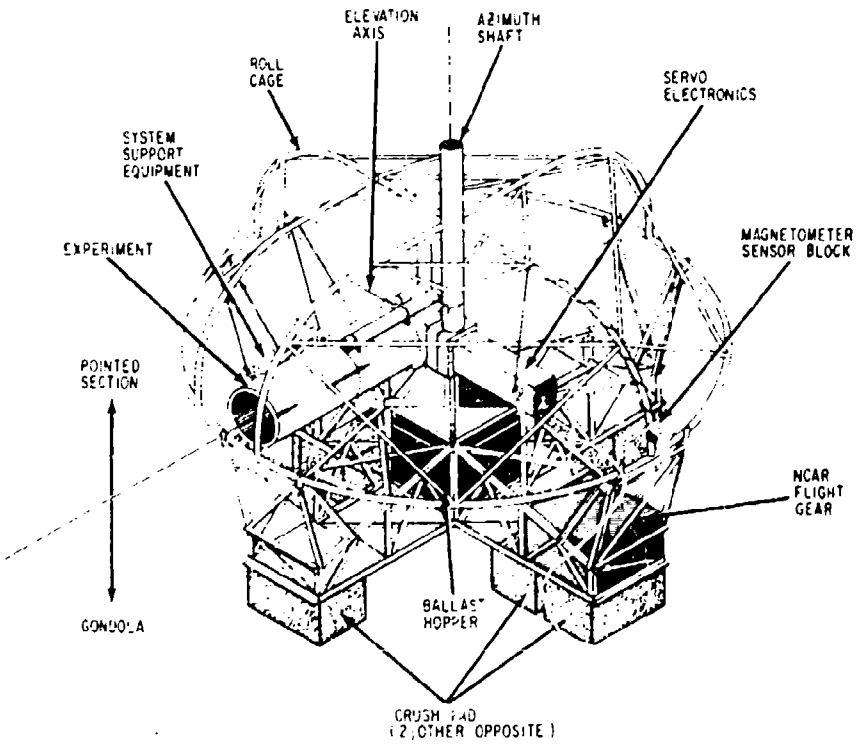

Figure 14-2. BAPS Configuration

Electrical connections made from the gondola section to the pointed section are through a 14-segment brush and slip-ring assembly. The gondola supplies power and pre-decoded command signals through the slip ring assembly, and the pointed section supplies the PCM encoder output through the slip ring assembly to the RF transmitter located in the gondola.

The gondola section serves as a reaction mass for the pointed section as well as the mounting area for the battery supply, command RF receiver and pre-decoder,

RF telemetry transmitter, power control command circuitry, and balloon launch facility flight gear. In addition, a single, centrally located ballast hopper and valve are mounted on the gondola. The ballast hopper is positioned directly in line with a vertical axis through the center of mass of the entire payload. This location reduces to negligible proportions the effect of inuced forcing functions on the servo during ballasting operations required for balloon control.

The gondola is a truss structure fabricated from aluminum angle to reduce the cost of repair and refurbishment. Field damage is easily repairable, since the damaged piece can simply be replaced with another which is cut and formed using common hand tools.

There are apparently as many ways to turn a payload over upon landing as there are people who have flown payloads on balloons. We considered releasing the payload from the parachute upon landing but discounted this approach due primarily to payload safety and payload release system inadequacies. Instead, we assumed that payload turnover would occur, and a protective cage, the roll cage, was devised to protect the experiment and the pointer (see Figure 14-2).

Attached to the bottom of the gondola are crush pads (see Figure 14-3) designed to limit landing loads to less than 15 g (acceleration due to gravity) vertically and 10 g horizontally. The crush pad is a three-tiered device made of laminated aluminum and honeycomb paper panels and blocks of honeycomb cardboard. The tier configuration permits a progressive reduction of velocity in both the horizontal and vertical directions by means of a sequential tearing and shearing action. The paper materials are impregnated with a substance to prevent softening due to water absorption.

The pointed section is mounted to the azimuth shaft by means of low friction load bearings (see Figure 14-2). This section contains all the servo electronics and the PCM encoder and serves as the experiment mount. The experiment is mounted in cantilever fashion to a large flange on the end of a horizontal shaft/yoke fixture referred to as the elevation shaft. There is unlimited rotational freedom around the azimuth axis and 60 degrees rotational freedom around the elevation axis.

Electrical connections made to the experiment are through two large flexible loops of teflon insulated wire. The loops are positioned so as to oppose each other, thereby reducing cable torques around the elevation axis. Mounted to the experiment is the BBRC-built Star Tracker sensor. It is a self-contained unit that is aligned with the telescope. A light shield, which mounts on the telescope baffle, permits operating the star tracker to as close as 30 degrees from the moon.

The pointed section has attached to it a protective structure that prevents damage to it and the experiment in the event that the payload should turn over on landing. This structure also provides a means of mounting the magnetometer sensor

block (see Figure 14-2). The roll cage structure was fabricated from thin walled aluminum tubing and welded together in easily assembled sections. Yoke structures mounted to the gondola transfer inverted loads into the gondola from the roll cage, while at the same time they permit the roll cage to rotate freely with the pointed section.

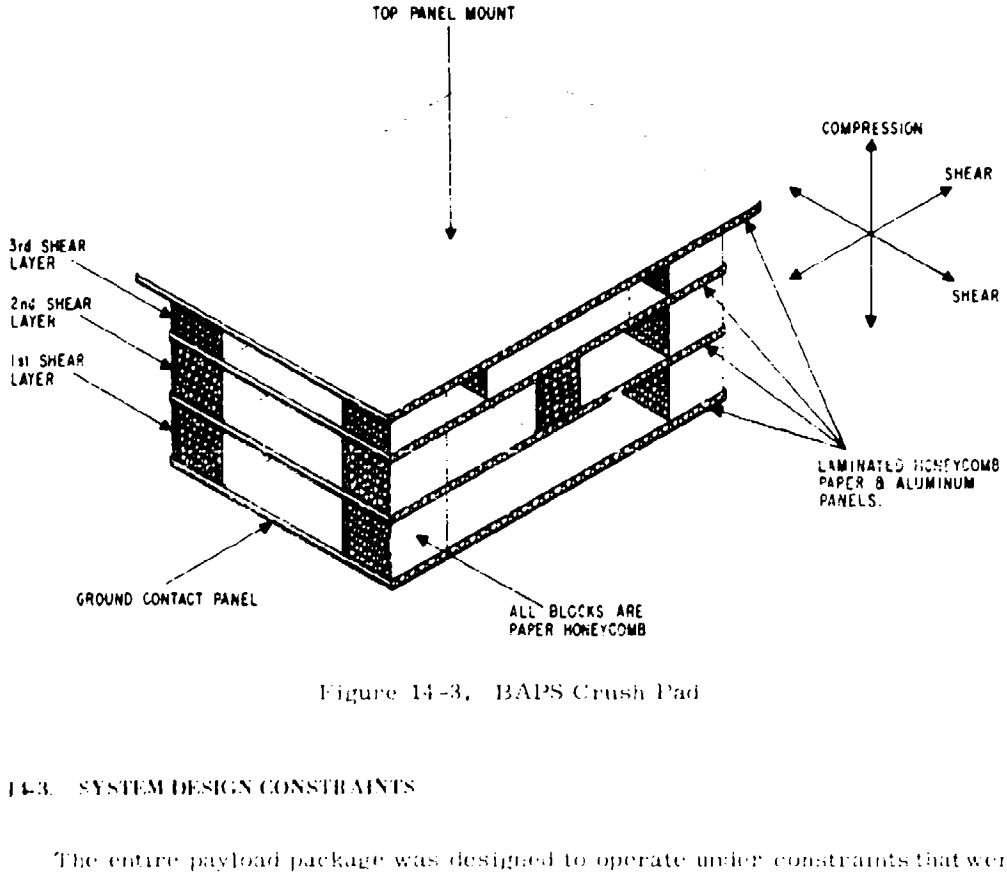

Figure 14-3. BAPS Crush Pad

14-3. SYSTEM DESIGN CONSTRAINTS

The entire payload package was designed to operate under constraints that were either imposed from experience or were assumed. These constraints include balloon-related dynamic forcing functions, parachute opening shock, the probability of payload turnover upon landing, and the maintenance of RF line of sight between the payload and the NCAR launch station.

An attempt was made to model force and function input from the balloon and suspension train to limit the dynamic load constraint. As a result of the computerized model, a special suspension train was designed to decrease the effect of compound pendular motion and dynamic loading.

During the initial design phases, it was difficult to arrive at a specific set of parachute performance characteristics. As a result of conversations with several agencies a design limit opening load of 4 g's was selected.

Since the payload systems required telemetry ground station capability in excess of that available at the launch station, a single ground station was provided by NASA. This implied that the flight would have to take place at or near either of the high altitude, wind turn-around periods.

To meet the scientific objectives, a moderately large telescope and instrumentation system was required which led to a correspondingly large servo and support structure. Since it was desirable to launch using existing NCAR launch equipment and known reliable balloons, the system weight at lift off should have been in the 1500 to 2500-pound range and the 12 to 20-million cubic foot balloon category to attain a float altitude of 40 kilometers. The final design resulted in a lift off weight of approximately 2200 pounds, exclusive of ballast. The balloon used was approximately 15 million cubic feet.

To take advantage of the maximum viewing time during darkness at float, the system was to be launched during evening daylight. This meant that adding insulation to protect against the cold of night would cause system overheating during the light of day. To solve the problem, thermostatically controlled heaters were added to critical areas, and the power capacity was increased.

Due to the critical nature of the optical and servo component alignments, there was concern about the actual launch environment. Data were not available describing the environment presented by the launch vehicle (Tiny Tim). Early in the design stage the vehicle was instrumented and a set of power spectral density curves were derived. These indicated moderate vibration levels with most of the energy contained in the 30 to 50-Hz region. These low levels, it was decided, would have negligible impact on the design.

14-4. SYSTEM CONCEPT

The system concept chosen took advantage, in part, of existing design and used existing MSC telemetry ground equipment to reduce costs and complexity.

The servo system consists of a multiple stage servo using an orthogonal magnetometer pair for the azimuth acquisition sensing element, a potentiometer referenced to local vertical for the elevation sensing element, and a Star Tracker as the final pointing sensing element.

Azimuth acquisition of the target star relies upon knowledge of (a) payload geographical position, (b) target ephemeris data, and (c) the direction of the horizontal component of the earth's magnetic field.

A computer program derived from data supplied by NOAA provided the means for determining the direction of the horizontal component of the earth's magnetic field to less than 0.5 degree. Use of the OMEGA system at the NCAR balloon facility in Palestine, Texas produced geographical coordinates allowing for position determination to less than five miles. However, payload geographical position need only be known to approximately ten miles.

Elevation acquisition of the target relies only upon knowing the geographical position of the payload and target ephemeris data. These data, when referenced to payload local vertical, provide the information needed to program a precision potentiometer in the elevation servo loop.

The acquisition concept required combining these data and issuing a command causing the two-axis servo to point the Star Tracker aligned with the telescope to within a 1 by 3-degree field containing the target star. The expected total azimuth error is ± 1.5 degrees, and the total expected elevation error is ± 0.5 degree.

Real time telemetry data are then used to determine the presence of the desired target to the star tracker. If the data indicate star presence, then a second command is issued which replaces the magnetometer pair sensing element in the azimuth servo loop and the precision potentiometer in the elevation loop with the Star Tracker outputs. The servo then reduces the angular error as seen by the telescope to less than ± 1.0 arc minute in both the elevation and azimuth axes.

The Star Tracker sensor is capable of detecting targets as dim as sixth visual magnitude and can operate over a dynamic intensity range of 100:1. Therefore, with proper aperture sizing, a range of five visual magnitudes is possible. This feature could create a problem in that in a 1 by 3-degree field, it is possible for more than one star of sufficient brightness to exist. To eliminate this problem, the Star Tracker is designed to discriminate with respect to magnitude. The desired target is selected to within 0.3 visual magnitude by ground command.

The elevation and azimuth servos are of the dc coupled analog, null seeking type. Each servo uses a compensation technique that is proportional plus integral in nature.

14.5. TELEMETRY

Since the prime data from the experiment package are digital, and since a high degree of readout accuracy is desired in some of the housekeeping analog data, a PCM telemetry system was selected.

The PCM system is a self-contained package for the encoder and analog-to-digital (A/D) converters and a separate RF transmitter and antenna system.

The PCM format uses a word length of ten bits with a 40 by 50 frame. There are 79 analog channels, four serial digital channels, and 42 discrete bilevel channels per main frame. The system operates at an 8000 bit-per-second rate.

The ground station was provided by MSC, but it was necessary to design and build a prime data converter to permit real time experiment operation.

14-6. COMMAND

That portion of the command system developed under this program was limited to non-RF equipment. All RF equipment was furnished by either MSC or NCAR.

Because of the large number of commands needed to permit acquisition of virtually any target within a hemisphere, a digital type, rather than a discrete function command system, was selected. The servo and instrument functions are both designed for control by the receipt of digital commands.

The command system developed under this program uses a 16-bit digital word (see Figure 14-4). The 16-bit digital word is programmed on the ground to represent the desired function. After transmission and decoding in the payload, the command word is shifted serially into both the experiment and the servo, where it enters a flag bit detector denoting which system, experiment or servo it is intended for. After flag bit detection, the command word is decoded by an address and a function register, and then the command is executed.

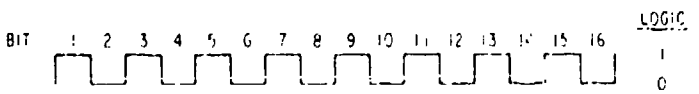

BIT 1 - TAG BIT FOR BAPS OR EXPERIMENT FUNCTION
BIT 2 THRU 4 - BAPS ADDRESS BITS
BIT 5 THRU 16 - BAPS DATA BITS

Figure 14-4. Command Word Format

The command system uses a bi-phase PCM format operating at a 30 bit-per-second rate. A total of 23 bits is sent for each command, with the first seven bits used as a recognization code to enhance system security. In addition to the 16-bit digital command, there are also 32 discrete commands for such functions as power "ON", "OFF", and so forth.

14-7. THERMAL CONTROL

With a few exceptions, all thermal control is passive in nature. The exceptions are the casting housing the lower azimuth bearing and the outer elevation bearing. These are heated using electric heating strips and bi-metal thermostats.

Passive thermal control takes advantage of conserving internally generated heat during servo or other system operation. An extensive thermal analysis was run to determine heat loss from specific hardware areas, and then a thermal insulating scheme was derived for each area. The primary insulating materials used are doubly aluminized mylar and an open cell synthetic foam. The entire pointed section, excluding the roll cage, is appropriately insulated and covered with a layer of lexan to provide both insulation and protection.

The battery, command receiver, telemetry transmitter, command pre-decoder, and power control circuitry that are located in the gondola are housed in a large foam box insulated with doubly aluminized mylar and open cell foam. Also located in the box is a quantity of water. The latent heat of the water is used to effect a thermal inertia for the ten-hour flight period.

14-8. POWER

System power is supplied from a single battery source. Examination of the different battery types currently available quickly led to selecting one of the silver-zinc types. It offered the lowest weight per unit of power. Since the battery had to supply all power for both the experiment and BAPS as well as heater power for both systems, a high-power capacity battery rated at a minimum of 90 ampere hours was selected. Electrolyte outgassing is prevented by individual positive pressure caps on each cell. These operate simply to maintain about four psi by venting from one atmosphere during the ascent.

14-9. SUSPENSION TRAIN MODEL

The suspension train was modeled on an analog computer as both a single cable system and a three-cable system. In the single cable system, it was modeled as a triple pendulum, and in the three-cable system as a double pendulum with no rotation between the cables and the azimuth shaft. The models indicated little difference in frequency of compound pendulation between them; however, there was a sizable difference in amplitude. The single cable showed ± 2 arc minutes, whereas the three-cable would oscillate only a few arc seconds.

The model assumed that the balloon moment of inertia was large enough to be considered rigid. Cable length changes up to 20 feet were predicted to have little effect on the control requirements.

The final suspension train design selected was a compromise between the two approaches (see Figure 14-5). The main train is a 200-foot long single line cable consisting of about 80 feet of parachute and shroud lines and 100 feet of single cable. The remaining distance consists of the azimuth shaft and a 10-foot long section of three parallel cables one foot apart spaced at 120-degree intervals.

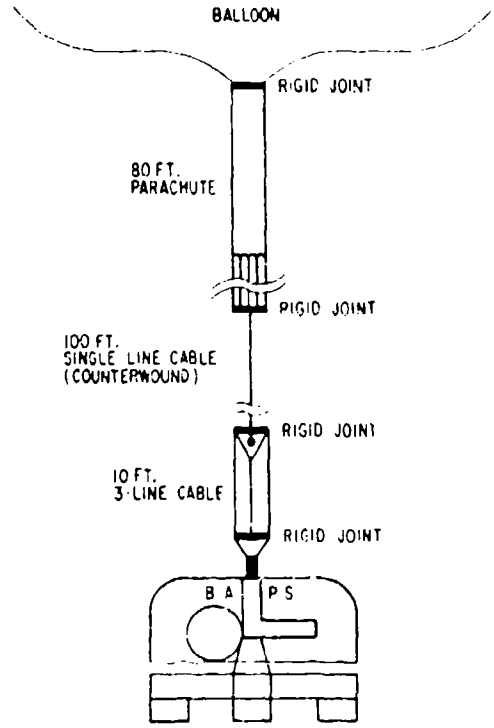

Figure 14-5. BAPS Suspension Train

This combination of single cable and triple cable produced a compound pendulum motion of the azimuth shaft of about 0.5 Hz with an oscillation amplitude of ±1/2 arc minute from local vertical.

14-10. SERVO CONSIDERATIONS

14-10.1 Stow Loop

The azimuth control loop is mechanized to stow the experiment platform to a potentiometer null referenced to the azimuth shaft. The stow drive is rate limited to approximately five to seven degrees per second. A balloon rotation of 1.0 degree per second can be easily handled in stow; however, acquisition time is slightly increased.

The stow mode is used to drive the experiment to the horizontal position over a leg of the gondola, thereby affording further protection upon landing. It can also be used during float to maintain an active system for thermal control purposes while implementing changes to the desired observing program.

14-10.2 Azimuth Loop

A block diagram of the azimuth loop is shown in Figure 14-6. Azimuth acquisition of the three-degree target field is accomplished by commanding the experiment platform relative to the local north-south earth magnetic field line. Two horizontal and orthogonal magnetometers are used to provide azimuth reference from magnetic north. The magnetometer control loop has a bandwidth of about 0.3 cps and points the experiment to a stable null provided by the ground commanded angle and the sensed magnetometer angle. The servo loop is proportional plus "limited" integral; thus, no servo loop pointing error is evident for nominal friction torques of 1.7 lb-in. The integral term is limited to prevent poor performance during acquisition.

A target field 180 degrees away from magnetic north can be acquired in less than 40 seconds. For the 180 degrees acquisition, rates of 20 degrees per second will occur. This high rate is produced because the rate limiting circuit does not prevent rate buildup on the unstable null side during acquisition. For acquisitions of 90 degrees or less, the rate limit is about five to six degrees per second. Acquiring the target star 90 arc minutes away from Star Tracker null takes less than seven seconds.

The azimuth acquisition principle is based on generating the trigonometric identity:

$$\cos \Psi_A \sin \Psi_T - \sin \Psi_A \cos \Psi_T = \sin (\Psi_T - \Psi_A) \qquad (14-1)$$

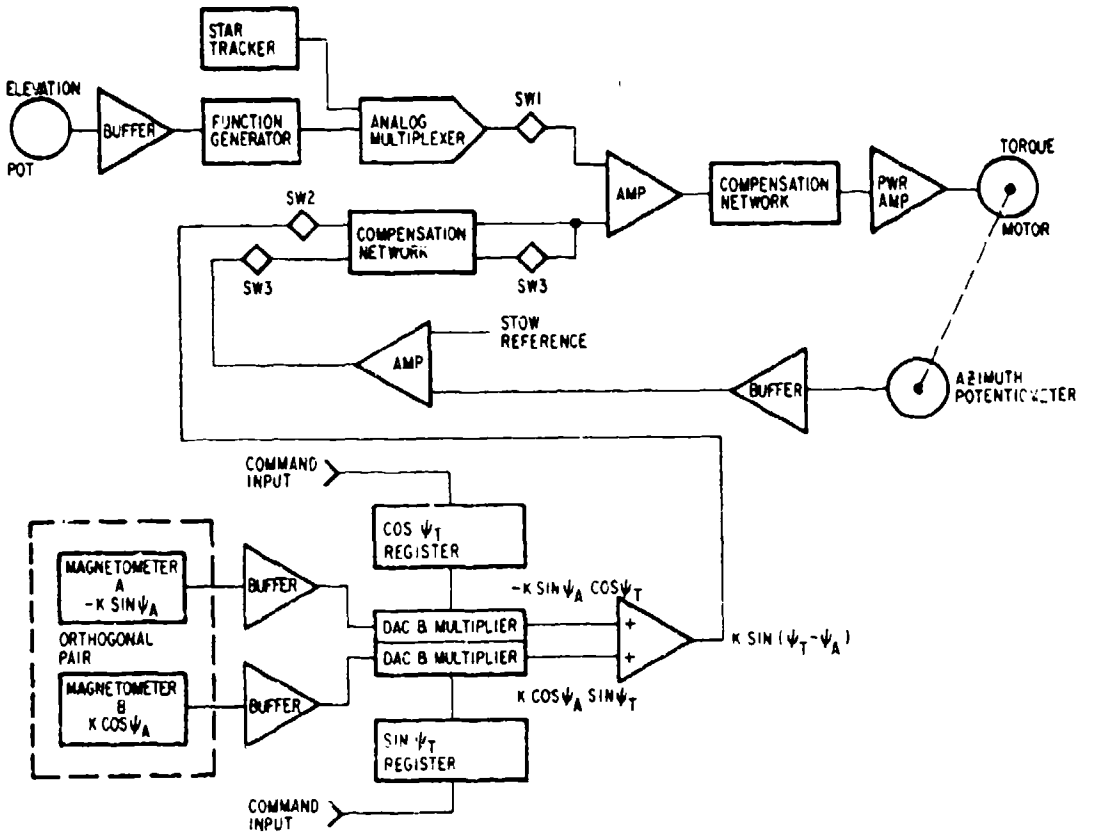

Figure 14-6. BAPS Azimuth Servo Block Diagram

where

Ψ_A = magnetometer angle from magnetic north

Ψ_T = target angle from magnetic north
(Ψ_T is the commanded angle)

The azimuth Star Tracker signal is scaled in an analog multiplier by a scaler that is proportional to the elevation angle of the target. The scaling factor is:

$$S_F = K\text{Sec}\,\theta \qquad (14\text{-}2)$$

where θ = angle above horizontal.

Scaling is necessary to maintain a reasonably constant servo gain; otherwise the effective gain of the azimuth servo will fall off as a function of the cosine of the elevation angle. Scaling of this nature will permit reliable operation up to at least 70-degree elevation angle.

The azimuth Star Tracker control loop also uses a proportional plus limited integral technique. The "steady-state" pointing error is zero considering the friction torque effects and the integrator action. The azimuth Star Tracker loop has a bandwidth of roughly 0.5 cps. Transient effects of direction changes for kinetic friction torque and signal noise from tracking targets of 0 to +5 visual magnitude result in less than 0.4 arc minutes of experiment pointing error. Control bandwidth for this loop which is determined by loop gain and the compensation lead terms must be compromised with torque motor noise output. Battery stored electrical power is consumed proportional to motor noise. The resultant azimuth pointing accuracy is nominally less than 1.0 arc minute.

14-10.3 Elevation Loop

A block diagram of the elevation loop is shown in Figure 14-7. Elevation control was designed to stow the experiment section and point the experiment to a 1.0-degree target field referenced to a potentiometer null. Potentiometer null was set normal to the azimuth shaft. The elevation servo was designed to handle an azimuth shaft oscillation at the simple pendulum frequency with an amplitude of plus-and-minus 1/3 of a degree. As in the azimuth control loops, the elevation control is proportional plus limited integral. The limited integral "washes out" pointing errors in acquisition and track that result from the 1.27 lb-in kinetic friction torque and a maximum 3.0 lb-in torque of mass unbalance around the elevation axis. The elevation acquisition of a target field is rate limited at approximately eight degrees per second; thus, acquisition of a target field 70 degrees from start will require about ten seconds. Acquisition of the target star to within the 1.0-degree field of view will be less than eight seconds. Elevation tracker loop bandwidth is about 1.4 cps. Again, the bandwidth is reduced to decrease torque motor power consumption while tracking the noisy signal from dim targets. Another reason for keeping bandwidth low was to reduce error rate inputs to the experiment section, primary mirror control system. The transient pointing errors in the elevation axis while tracking stars of 0 to +5 visual magnitude are less than 1.0 arc minute.

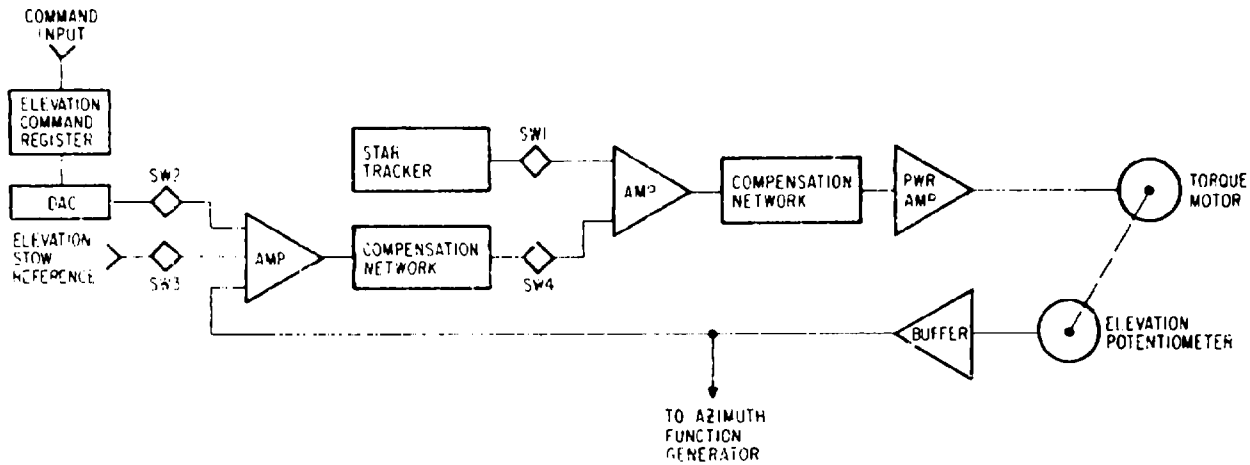

Figure 14-7. BAIS Elevation Servo Block Diagram

14-11. PERFORMANCE

The BAPS has flown three times. On two of the flights, the BAPS was successfully operated with only a few minor problems.

The graphs in Figure 14-8 are plots of Star Tracker pointing error versus time. These data are taken from Flight 2 and are typical of inflight performance. Graphs A and B show initial Star Tracker acquisition in azimuth and elevation, respectively. Note the moderately light damping used to permit sufficient gain while pointing on target.

Graphs C and D are respectively azimuth and elevation Star Tracker pointing error versus time after acquisition stabilization. The predominant error appears at about a 0.8 Hz rate. The forcing function for the error input has as yet not specifically been identified. However, there is evidence to indicate a torsional oscillation of the 10-foot long section of the three-cable suspension train.

Graphs E and F are examples of the worst-case pointing that occurred for relatively short time periods. The predominant motion is in azimuth and is probably a result of torsional suspension line energy coupling into the servo. This is being evaluated and will be corrected.

During the third flight a command system problem developed, and communication with the system was not possible for the entire mission. Prior to the command system becoming inoperative, the BAPS was commanded to point in an easterly direction on the magnetometer loop. It operated in this mode for the remainder of the flight until a thermal problem developed causing overheating and eventual component failure.

The third flight had an unfortunate ending. At release from the balloon, a fitting in the suspension train at the top of the payload separated, permitting the payload to free fall about 130,000 feet to destruction.

The system is being refabricated (with a different fitting) and will be flown again late next year (1973).

14-12. POINTED INSTRUMENT CONFIGURATION AND PERFORMANCE

The scientific instrument, BUSS (Balloon-Borne Ultraviolet Stellar Spectrometer), was mounted to the elevation flange. The BUSS was designed to perform spectrophotometric measurements in the 2770 to 2520 Å spectral interval.

The telescope has a focal length of 300 centimeters and a diameter of 40 centimeters. It consists of an f/3 primary mirror and a secondary mirror with magnification of 2.5. By image motion compensation, an ultimate tracking precision of a few seconds of arc is achieved. The secondary mirror is mounted in

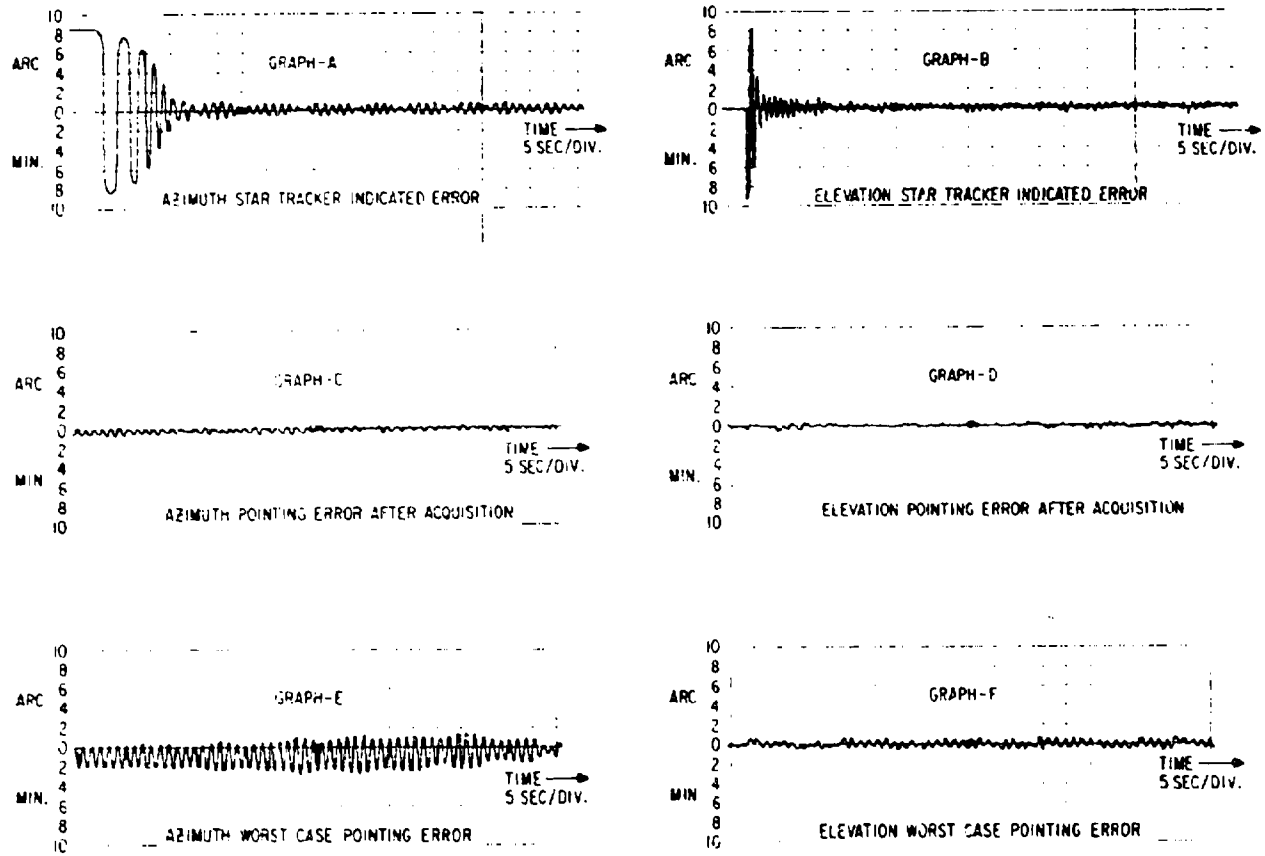

Figure 14-8. Star Tracker Pointing Error Data

a bi-axial flex-pivot gimbal system and can be tilted by means of two small torque motors.

Near the focal plane a dichroic mirror reflects the ultraviolet radiation towards the spectrometer and transmits the visible light towards a star position sensor, which provides the control signals for the torque motors.

In general, tilt of the secondary mirror introduces aberrations in the stabilized image. However, by aspherizing the mirrors to a high degree, the spatial resolution can be made virtually immune to telescope pointing errors of several minutes of arc.

The dispersion of the spectrometer is 3.3 Å/mm, which is obtained by a 2160-groove per millimeter plane grating, used in the second order in an Ebert-Fastie configuration. The grating is fixed, and the spectrum is scanned by means of an image dissecting tube. This technique is uniquely suited for this application, since only a small spectral interval need be covered.

Control circuitry was designed to compensate for slow telescope movements, as well as for jitter. Two parallel networks were incorporated for these tasks. One of these functions as an integrator and provides the motor voltages that are needed to maintain the steady deflections associated with slow variations. The second network serves to compensate jitter. Further details on this are given by Gibson et al (1972).

The position sensor error signals, recorded with stars of visual magnitudes between 4 and 5, correspond to angles of 2.5 arc seconds rms for elevation and 3.0 arc seconds rms for cross elevation. These numbers represent upper limits for the actual motions of the image, since part of the signal fluctuations must be attributed to noise in the sensor.

References

Bottema, M. and Woodruff, R.A. (1971) Third order aberrations in cassegrain-type telescopes and coma correction in servo-stabilized images, Applied Optics 10:(300).

Gibson, W.C., Cuthais, D.L. et al (1972) Pointing and guidance of the BUSS telescope. Paper presented at meeting on Instrumentation in Astronomy, Tuscon, Arizona.

Kondo, Y., Galli, R.T. et al (1972) Observations of the stellar MgII doublet at 2795 Å and 2802 Å. Paper submitted to Astrophysical Journal.

Contents

15. The Opening Performance of 100-Foot and 140-Foot Diameter RSR* Parachutes Near 100,000 Feet with Balloon Borne Payloads

F. Corbalis, Jr., Capt, USAF, A. Giannetti and C. Rice
Air Force Cambridge Research Laboratories
Bedford, Massachusetts

15-1. INTRODUCTION

For many years we have been using modified cargo type parachutes, usually flat circular designs, on balloon systems, and they have worked very well, despite the fact that they are released at much higher altitudes and in a different deployment condition than their designers ever intended. Now that the capabilities of large, plastic balloons have surpassed the load bearing limits for single flat circular canopies of reasonable size, we are using double and triple clusters of 100-foot parachutes to recover the heaviest balloon borne payloads. If we are to penetrate higher ceiling altitudes with heavy loads, however, we must find decelerators with comparable strength and appreciably reduced weight, which will also operate dependably from balloon systems at very high altitudes. There are no adequate criteria for applying scaling procedures to parachute models; consequently, full scale, high altitude parachute testing has become a necessary adjunct to development of advanced balloon systems.

This paper describes two recent balloon flights to test an unusual lightweight, heavy load parachute design above 100,000 feet altitude. In each case, a very large RSR RIBCO canopy was flown in the customary balloon system configuration, unpacked and extended to full unopened length, with the apex attached to the balloon end fitting and the riser extension lines supporting the payload. RIBCO is the manufacturer's acronym for Rapid Inflation Bowline Controlled Opening.

*Recovery Systems Research, Inc.

The RSR RIBCO design offers a substantial weight saving. It also appears particularly suited to a balloon borne application in which the same recovery system must function with either a very heavy or a relatively lightweight payload. (In such experiments, a large portion of the original payload is scheduled for release before the flight is terminated, but for safety's sake the parachute must be capable of recovering the entire initial payload.)

On AFCRL Flight H71-48, the 100-foot RSR parachute carried a 2437-pound load; on AFCRL Flight H72-26, a 140-foot diameter canopy of the same design carried only 611 pounds, close to its minimum load.

The RSR design principle is illustrated in Figure 15-1. The suspension lines around the canopy skirt terminate in several groups, and each group is attached to a point on a control line. The control lines are attached to the payload and to the canopy apex. After the parachute system is cut away from the balloon, the canopy skirt, hanging loose, is free to inflate until the suspension and control lines have extended to their full length. Further spreading is controlled by interaction between the suspension and control lines. In order to fully spread the canopy, sufficient skirt pressure must build up to allow the suspension lines to overcome the tension in the control lines. This bowstring arrangement promotes a smooth opening and tends to minimize the opening and snatch shock forces.

15-2. AFCRL FLIGHT H71-48

On this flight, a 20-foot length of coreless nylon braid was inserted between the riser extension extremities and the tri-plate at the apex of the load bar supporting cables. The 2437-pound payload is shown in Figure 15-2.

After the 5.025-million cubic foot balloon had reached float altitude 101,500-feet above the test range, the parachute system was separated (cut down) from the balloon. Observers using stabilized binoculars followed the flight and descent from a tracking aircraft. The parachute opening and descent were also monitored visually from the ground by theodolite, and the entire flight and descent were tracked by radar. Up-pointing cameras mounted on the load bar photographed the parachute from the time of balloon cutdown until the payload landed.

Snatch and opening shock forces were measured by accelerometers rigidly attached to the center of the crossbar (directly above the center of gravity of the payload) on the payload supporting frame, Figure 15-2. Accelerometer and pressure-altitude data were continuously telemetered from before cutdown time until the system had descended below 15,000 feet. Equilibrium velocities and corresponding drag coefficient values were computed from radar data.

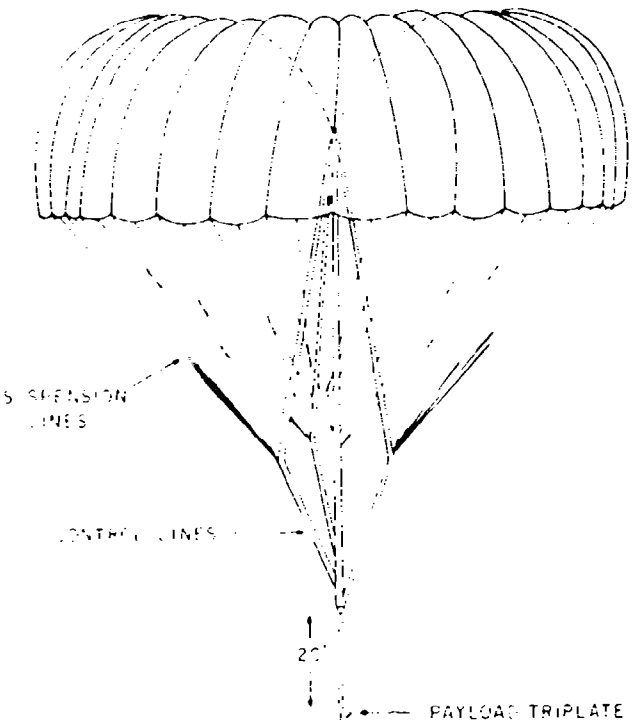

Figure 15-1. RSR RIBCO Parachute

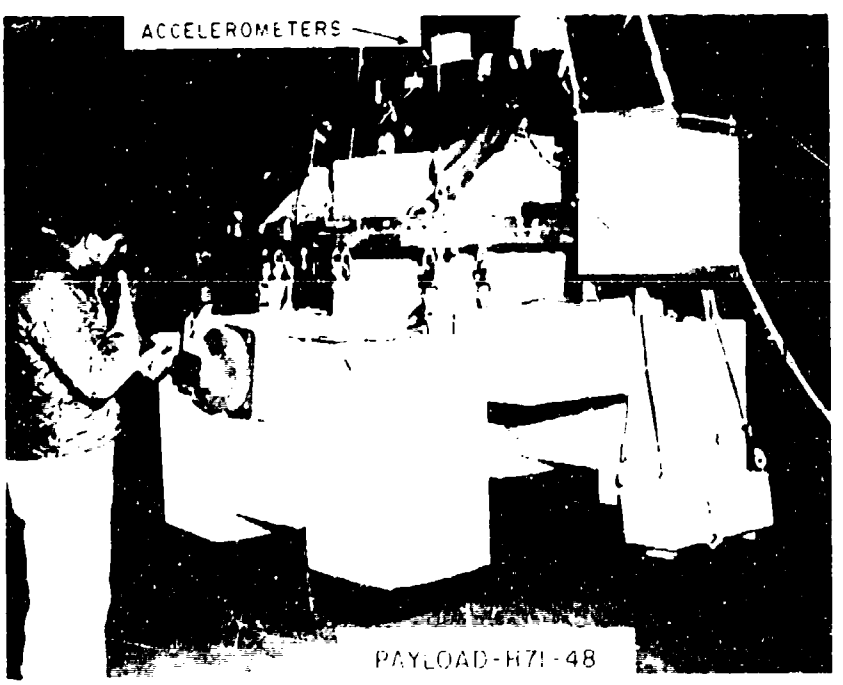

Figure 15-2. ALCRL Flight H71-48 Payload

15-2.1 Accelerometers

The accelerometers were aligned in mutually perpendicular directions local to the crossbar: z, normal to the plane of the bar; x, parallel to the short axis of the bar; and y, along the long dimension of the bar.

Because one of the primary purposes of the experiment was to measure the maximum values of z-directional shock forces, two z-accelerometers were used, one of range 0 to ± 7.5g* and one, 0 to ± 10g. The range of the x and y accelerometers was 0 to ± 2.5g.

15-2.2 Parachute Cutdown and Free Fall

Figure 15-3 is a portion of the telemetered record of the lower range z-direction accelerometer at cutdown. On the far left of the trace where z = 1g, the payload was supported by the floating balloon, and the system was in equilibrium.

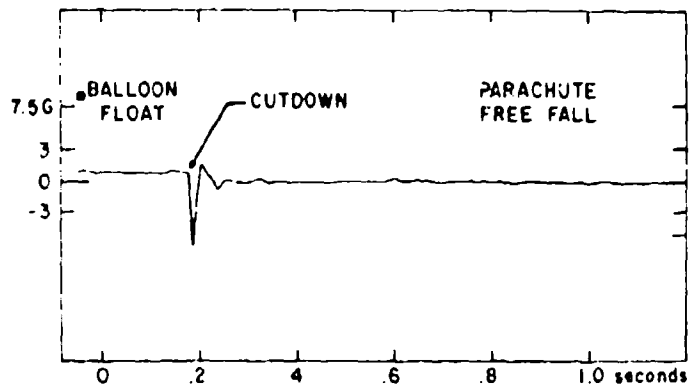

Figure 15-3. Z-Accelerometer Record During Cutdown of 100-Foot RSR Parachute

Then, suddenly, when the parachute was cut away, the release of tension in the supporting cables caused the abrupt reaction, 5.7g downward, at the center of the crossbar where the sensor was located. The direction of this acceleration is consistent with a surface that had been bent in an inverted U-shape while under stress. The photograph, Figure 15-2, confirms this observation. (The cutdown force is not a characteristic of the parachute, of course; rather, it depends upon the stress distribution in the payload structure. It is included here as a matter of interest to experimenters and payload systems designers.) The record shows that for about 3.3 seconds after cutdown the payload was falling freely (z = 0g), and the parachute cable was slack.

*g is acceleration due to gravity.

15-2.3 Parachute Opening Performance Snatch Force

Parachute opening is evident in the z accelerometer data, Figure 15-4. Time is measured in seconds from t = 0 at cutdown. At t = 3.4 seconds, slight tremors about z = 0 indicate that the parachute cables were beginning to tense. At t = 3.66 seconds, a pulse of amplitude 0.95g is the first in a train of oscillations about an average positive value that shows development of some parachute drag force. According to the accepted terminology, this 0.95g force is the parachute snatch force. The oscillation period was about 0.04 seconds.

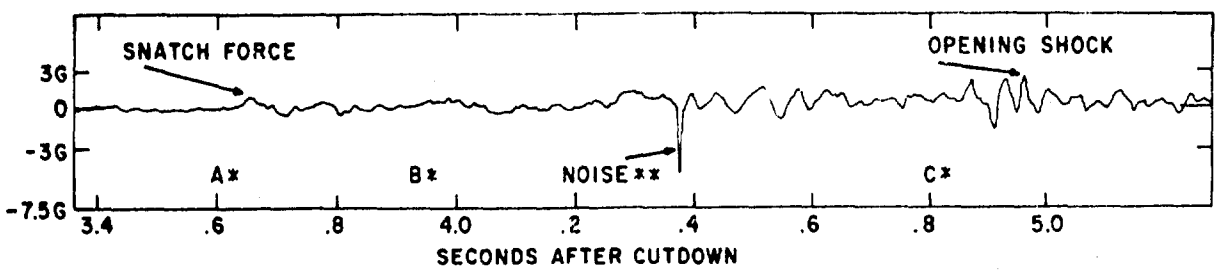

* CORRELATION WITH FILM RECORDS

* OBSERVATIONS FROM FILM RECORD

A. LOAD LINE FIRST BECAME TAUT
B. LOAD LINE REMAINED TAUT THEREAFTER
A. TO B. LINE INTERMITTENTLY SLACK
C. PARACHUTE APPEARED FULLY PRESSURIZED

** THIS RECORD WAS VERIFIED AS NOISE FROM THE TM RECORD. OF SIGNAL STRENGTH.

Figure 15-4. Z-Accelerometer Record During 100-Foot Parachute Opening

15-2.4 Opening Shock

At t = 4.28 seconds, a train of stronger oscillations began. The largest of these pulses, 2.25g at t = 4.96 seconds, is the opening shock force. The average z-direction force was now gradually approaching 1g, and by t = 7.1 seconds the oscillations were completely damped out.

As the system descended between 75,000 and 54,000 feet, z-direction vibrations of much longer period (four seconds) were recorded. Amplitudes were 0.2 to 0.3g about the 1g average. Measurement error was 0.15g.

15-2.5 Film Record

An excerpt from the 128 frame-per-second camera record showed free fall and parachute opening. By counting the number of frames after cutdown, we found

that we could assign approximate times when the various opening stages occurred as observed by the camera. These times correlate suprisingly well with the z-accelerometer records reproduced in Figures 15-3 and 15-4.

For example, on the film by t = 1 second after cutdown, the load line still appeared to be collapsed, but the canopy had already opened. It was not completely pressurized, however. Shortly afterward, it collapsed and reopened. The load line first appeared taut at t = 3.6 seconds. Note on Figure 15-4, point A, that the first appreciable shock force, designated as the snatch force, was recorded close to that time (IRIG). The film shows the load line periodically slackening during the interval between 3.6 and 3.9 seconds. On the corresponding telemetry record the line tension also drops to zero intermittently. After 3.9 seconds, the load line was judged to remain taut, and this is verified by the telemetry record, point B, at four seconds. By 4.8 seconds, the parachute appeared to be fully open. This time according to the telemetry record is at point C, and here the inaccuracy of estimating time by frame counting is evident, because the opening shock actually occurred a little later, at 4.95 seconds IRIG time code.

Figure 15-5 shows several consecutive frames taken at one frame per second by another up-pointing camera in the payload. In frame one, the load line is taut; the floating balloon is supporting the parachute system. In frame two, separation has just occurred. Note in frame three that the canopy had partly opened, although the load line was still slack. In frame four, the load line appears taut; payload snatch evidently had taken place. In frame five the line has partially collapsed, and in frame six the parachute is fully open.

15-2.6 Stability

The relative motion between canopy and load bar appears on the films as strong periodic gyrations that tend to diminish with time. Observers using theodolites reported that while the canopy was developing drag, it was oscillating in an arc of about 100 degrees, but this motion damped out to about 30 degrees. Observers in tracking aircraft noted very little oscillation after the canopy appeared to be fully pressurized.

15-2.7 Transverse Direction Accelerometers

Both accelerometers parallel to the plane of the crossbar recorded very long trains of lightly damped oscillations, which began at the time of parachute snatch and continued throughout the descent.

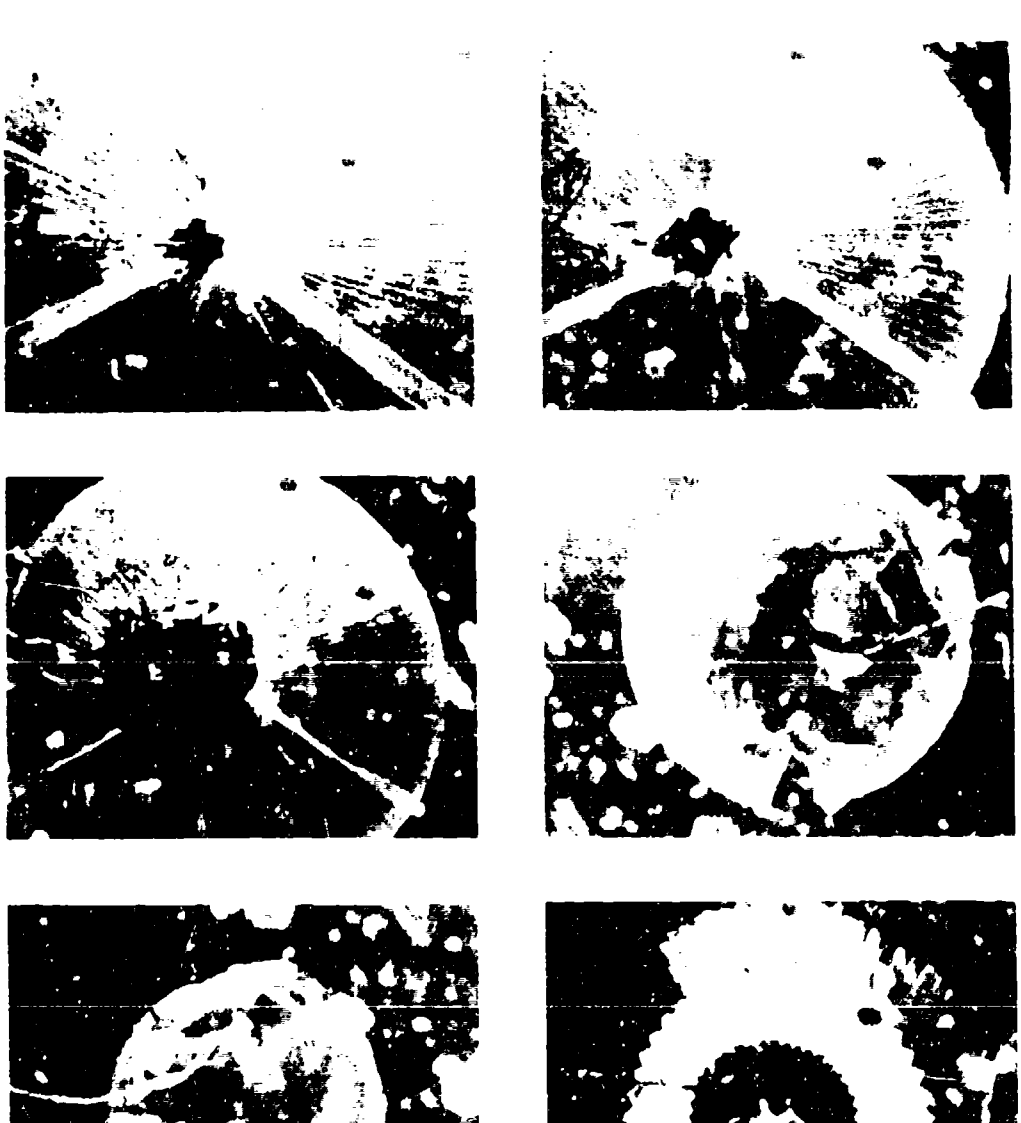

Although the transverse oscillations clearly were initiated by parachute action, their period, 0.6 to 0.8 seconds, is so short that they evidently are internal to the payload loadbar system. The payload consisted of several individual packages hanging from the open square framework, an arrangement which does allow several degrees of freedom for vibrational motions.

15-2.8 Descent Trajectory

Descent time was 31 minutes. The vertical descent trajectory is shown in Figure 15-6. The intervals when acceleration was zero are confirmed by radar velocity data. Between 40,000 and 25,000 feet altitude, the parachute had an equilibrium velocity of 36 feet per second. Finally, as the system descended through the more dense atmosphere below 20,000 feet, it achieved its terminal speed of 23 feet per second.

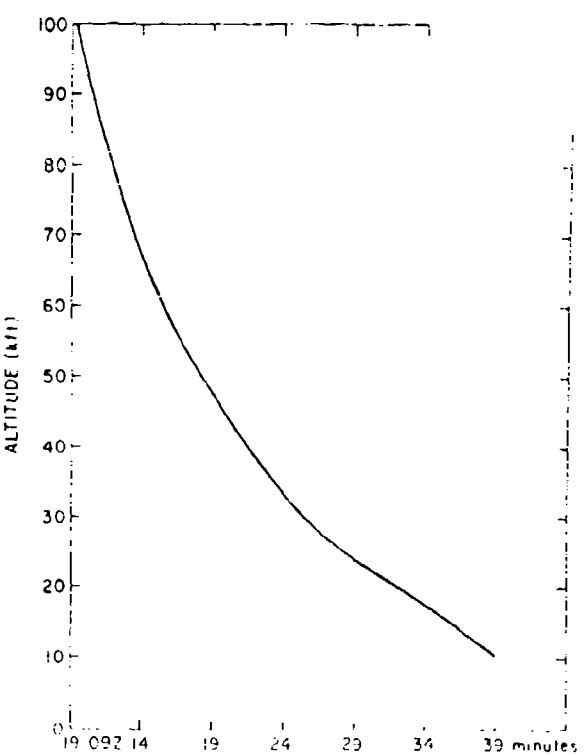

Figure 15-6. 100-Foot ASIR RIBCO Parachute Vertical Descent Trajectory at Air CRU, Eglin AFB, 1971-45

15-2.9 Drag Coefficient

Drag coefficient values were computed at the two equilibrium velocities, using the expression that equates the total descent weight (canopy weight plus payload) to parachute drag force:

$$W = 0.5\rho V^2 AC_D \qquad (15\text{-}1)$$

where C_D is drag coefficient

W = Descent weight
A = Projected area of canopy (mfg. data)
V = Equilibrium velocity
ρ = Air density (mass)

The results are tabulated in Table 15-1.

Table 15-1. Descent Data for 100-Foot Diameter RSR Parachute Test (AFCRL Flight (H71-48)

DESCENT TIME	31 min
TERMINAL VELOCITY	23 fps
DRAG COEFFICIENT	0.95 @ 36 fps (35,000 ft altitude) 1.0 @ 23 fps (15,000 ft altitude)

15-2.10 Balloon vs Aircraft Deployment

The first column in Table 15-2 summarizes the data obtained on this test in which the parachute was released at very high altitude in a unpacked in-line configuration with virtually zero horizontal speed. For comparison, Column 2 shows the El Centro (6511th Test Group (Parachute) El Centro Naval Air Facility, CA) results cited by the manufacturer for a low altitude test in which the parachute was released in the standard packed configuration from an aircraft.

Table 15-2. Comparison of Opening Performance of 100-Foot Diameter RSR Parachute at High and Low Altitudes

RELEASED VEHICLE	BALLOON	AIRCRAFT
Suspended Weight	2437 lbs	2200 lbs
Release Altitude	101.5×10^3 ft	15,840 ft
Snatch Force	0.95g	0.7g
Snatch Time	3.66 s	2.93 s
Maximum Shock Force	2.25g	2.6g
Time of Shock Force	4.96 s	5.33 s
Full-Opening Time	<7.1 s	17.57 s
Terminal Velocity	23 fps	17.7 fps

In view of the differences in manner of deployment and atmospheric density at which these high and low altitude tests were conducted, remarkably consistent results are obtained. The slightly higher snatch force at high altitude may be due to the fact that the canopy had already spready considerably when the control lines first became taut. The much longer filling time at low altitude seems logical when one considers that deployment in the packed configuration from an aircraft is more likely to permit a very gradual blossoming process to take place.

15-2.11 Conclusions

The high altitude performance of the 100 foot RSR Ribco parachute when rigged for balloon use was very satisfactory on this flight test. As predicted by its designers, shock forces were very low and opening time was fast. In the rarified atmosphere near 100,000 feet, it did not exhibit any greater stability than is obtained with conventional canopies similarly loaded. By all other criteria, however, including its appreciably reduced weight, this parachute design appears to offer definite advantages for balloon applications.

15-3. AFCRL FLIGHT H72-26

Two special considerations governed our plan to flight test the 140-foot RSR parachute. We needed to conduct a complete balloon operation to test the reefing arrangement and to discover whatever other special problems might be involved in launching and flying a balloon system with the enormous bulk of material (more than 15,000 square feet) in the canopy. We used a payload of only 611 pounds so

that we could observe the parachute performance under the flight conditions we frequently meet – experiments in which the final descent load is expected to be much less than the required rated strength of the canopy.

15-3.1 Payload

The payload consisted of several instrument packages fastened to a horizontal steel load bar, Figure 15-7. On the advice of the manufacturer, we provided more standoff distance between the canopy skirt and the payload by adding a 10-foot length of coreless nylon braid to each of the two control lines just above the triplate.

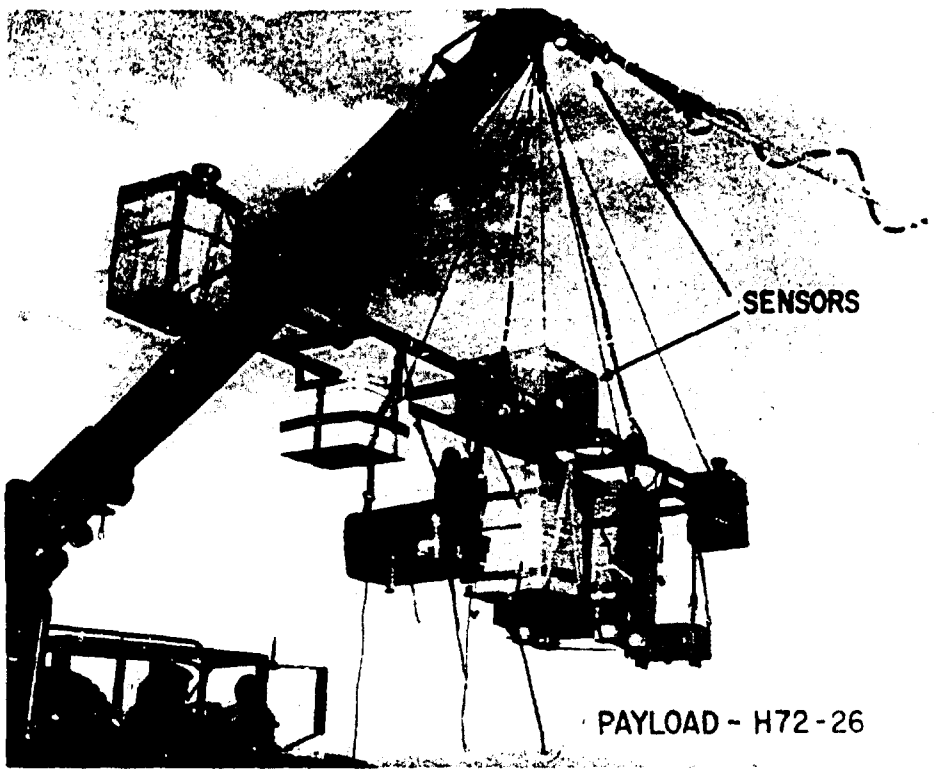

Figure 15-7. AFCRL Flight H72-26 Payload

15-3.2 Sensors

Several additional sensors were carried on this flight. In analyzing the data from earlier parachute tests, we had faced the basic problem of distinguishing between the parachute shock forces we wanted to measure and the particular mechanical

reactions at the location of the sensors due to the distributed stress in the payload structure. For this reason we placed another set of accelerometers above the triplate and measured both payload and load line accelerations. We also placed pitch and roll gyros inside the accelerometer package on the load bar. Films from up-pointing cameras, radar tracking and optical observations from aircraft were also obtained.

15-3.3 Reefing

When the balloon system was assembled for launch, the parachute was reefed at the skirt (Figure 15-8). A reefing ring was sewn approximately 18 inches from the skirt of the canopy. The reefing line was looped under the parachute, and the

Figure 15-8. 140-Foot RSR Parachute With Reefing at the Skirt

two ends were fed through and tied at the reefing ring. Two cannon cutters were employed on either side of the reefing ring to cut the reefing line on command. In order to maintain some tension in the skirt and to prevent the canopy from "snaking" down the risers toward the balloon during inflation, another length of line was tied from the line at the reefing ring to a clevis on one of the risers. Loops of 25-pound test, three-cord cotton were tied at 10-foot intervals along the canopy in order to contain the large amount of material.

15-3.4 Launch and Ascent

All of the 25-pound test cotton ties failed during inflation, and the parachute with the command-controlled reefing tie at the skirt acted like a spinnaker sail during the launch run, (Figure 15-9). This created a dangerous situation and confused the proper release configuration for the balloon and the parachute. When the launch vehicle was positioned properly under the balloon, the parachute was billowing unfavorably to one side or the other, or back over the vehicle. Conversely, when the parachute was properly positioned, the balloon was not. Thus, the vehicle zigzagged down the runway searching for the right conditions until, after travel of about three-quarters of a mile, the payload release was accomplished. Two minutes later, the command for disreef was transmitted, and at the same time the telemetry antenna was dropped. Thereafter, the canopy material was allowed to hang free.

Figure 15-9. 140 Foot Parachute Launch Run, After 25-pound test cotton ties failed, parachute with command-controlled reefing tie at skirt acted like a spinnaker sail.

The film record shows that during the early phase of ascent there were occasions when the canopy partly opened and whipped about, but this is not evident from the accelerometer records. Once the ballon was full, the erratic canopy flagging stopped.

15-3.5 Parachute Opening

The parachute was released from a 2.01×10^6 cubic foot volume balloon at 105×10^6 foot altitude above Holloman AFB, New Mexico.

Figure 15-10 shows consecutive frames from the one frame per second moving picture record of parachute opening. In the first frame, the payload is supported by the floating balloon. The second frame apparently was taken at the moment of cutdown. This parachute had spread considerably while the load line still remained slack, (frame 3). In frame 4, the line had developed some tension and the snatch had taken place. Subsequent frames are typical of the high altitude descent behavior.

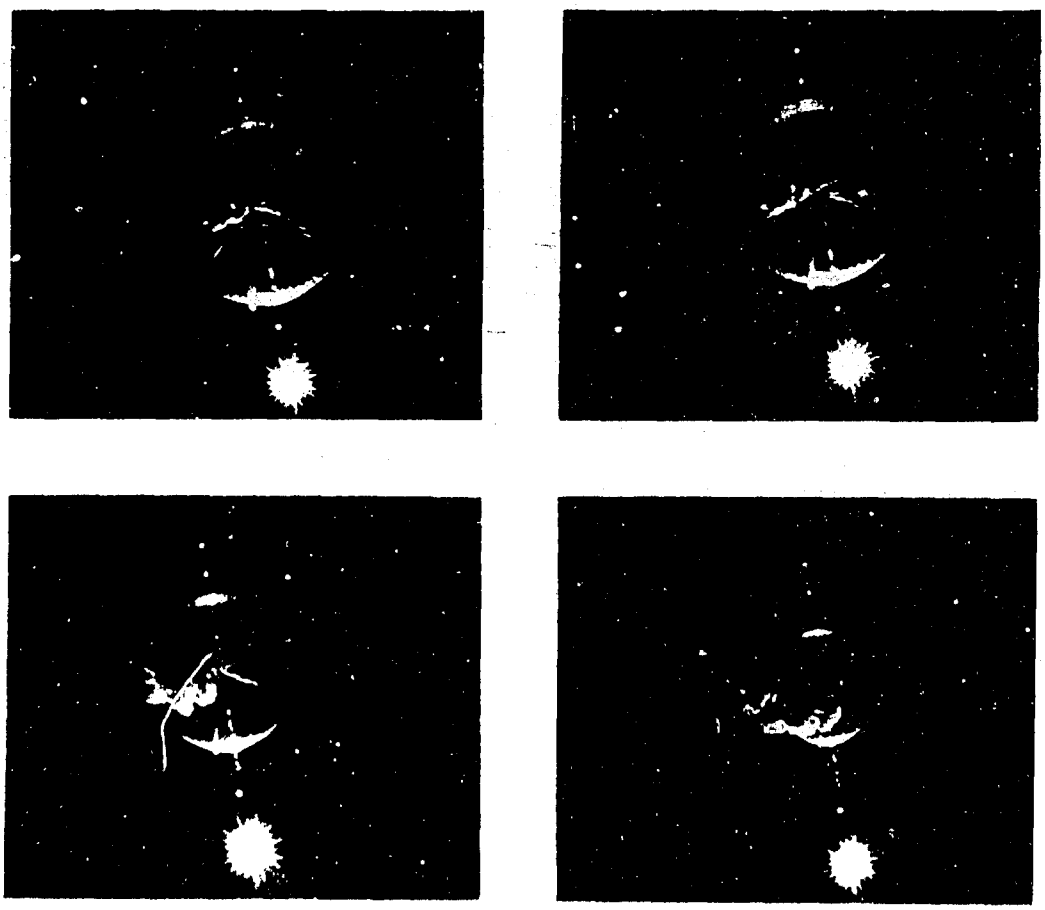

Figure 15-10. One Frame Per Second Camera Record of 140-Foot RSR Parachute Opening (Sheet 1 of 2)

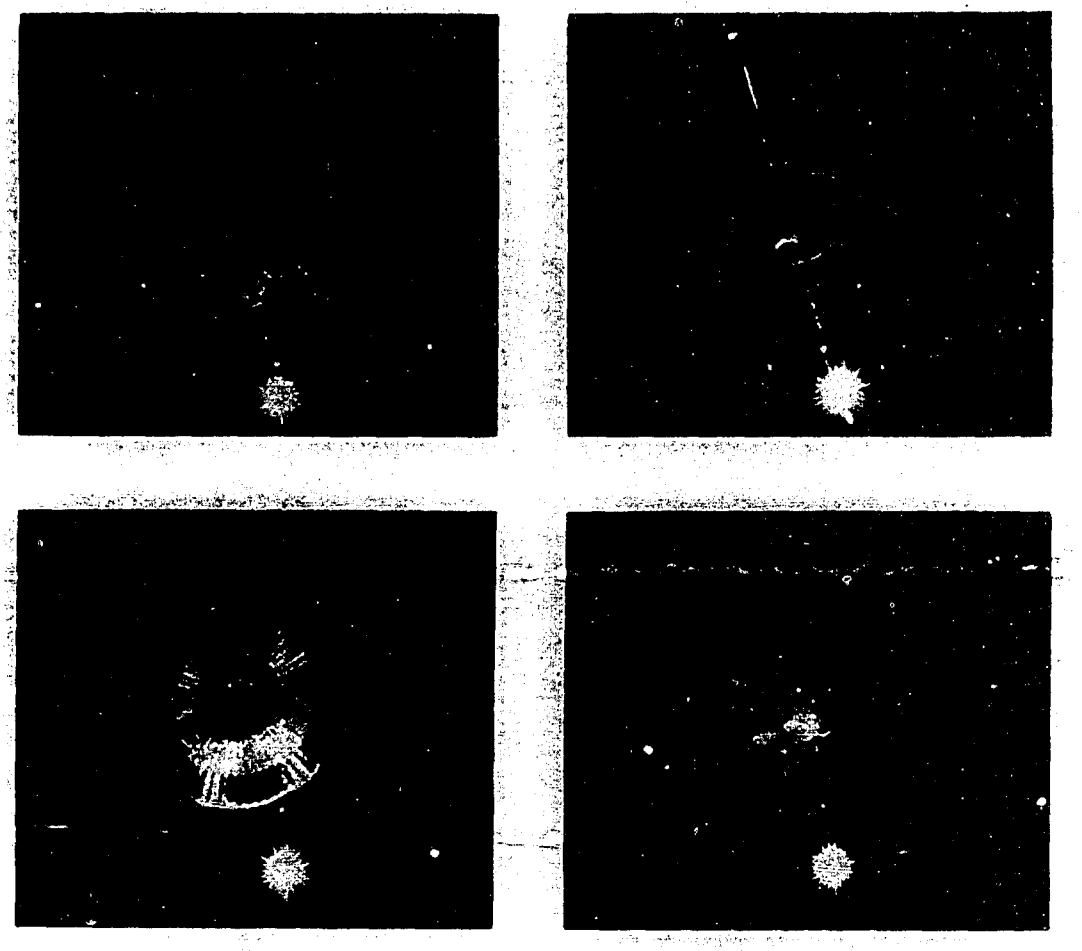

Figure 15-10. One Frame Per Second Camera Record of 140-Foot RSR Parachute Opening (Sheet 2 of 2)

15-3.6 Stability

Observers using stabilized theodolites in the aircraft reported strong gyrations and sporadic motions while the parachute was in the upper atmosphere, but very good stability in the more dense atmosphere.

We can easily reconstruct the parachute opening from the telemetry record. In Figure 15-11 on the far left, both z accelerometers read 1g while the balloon system was floating in equilibrium just prior to cutdown. During the next three seconds the line was slack and the load bar was falling freely (0g). Finally, the parachute lines straightened, and the load line tensed. The snatch force was 2.1g. During the next 1.24 second interval, the line alternately tensed and relaxed, returning to zero tension before beginning to develop a steadily increasing average tension as it vibrated. The maximum force or opening shock was 4.5g. 10.6 seconds after cutdown, the line tension had become essentially steady at 1g ($\pm$ 0.15g).

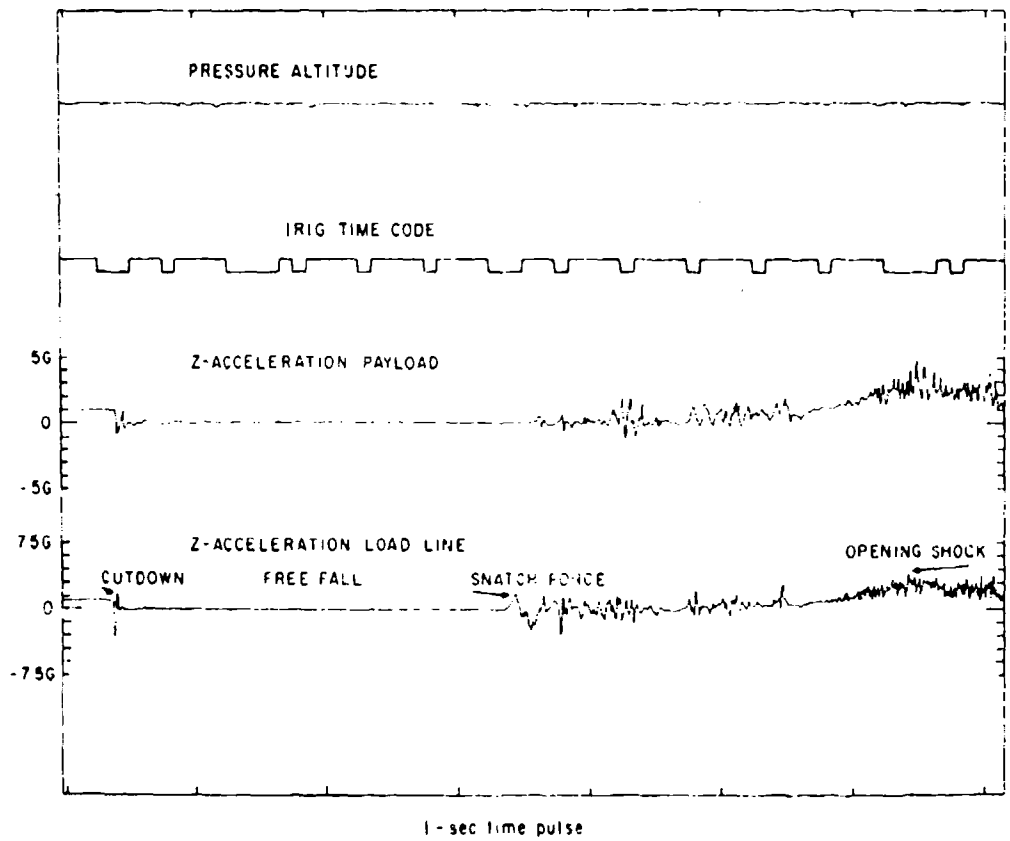

Figure 15-11. Z-Accelerometer Record of 140-Foot Parachute Cutdown and Opening

Table 15-3 summarizes the parachute opening records for both canopies.

Table 15-3. Summary of Results From RSR Parachute Tests

CANOPY	100-ft RSR single canopy	140-ft RSR single canopy
Flight No.	IH71-48	IH72-26
Rigged Weight	128 lbs	221 lbs
Suspended Load	2437 lbs	611 lbs
Release Alt.	101.5 k ft	105 k ft
Snatch Force	0.95 g	2.1 g
Snatch Time	3.66 s	3.05 s

Table 15-3. Summary of Results From RSR Parachute Tests (Cont)

CANOPY	100-ft RSR single canopy	140-ft RSR single canopy
Opening Shock	2.25 g	4.5 g
Time of Opening Shock	4.96 s	6 s
Filling Time	7.1 s	7 s
Terminal Speed	23 fps	20 fps
Descent Time	31 min	93 min

15-3.7 Accelerometer Record

The load line tension record gives a deceptively favorable indication of parachute stability because a steady line tension does not necessarily indicate a descent without gyrations or sporadic motion, particularly when the tension sensor had .15g precision.

During the parachute opening, the transverse forces were greater than 2.5g. About 30 seconds after cutdown there was still some transverse disturbance.

15-3.8 Descent Trajectory

Flight toward the northeast placed the balloon in the vicinity of Clovis, New Mexico. Although impact-disconnect switches operated, the nature of this parachute prevented immediate collapse of the canopy, and the payload was dragged for about one-quarter of a mile. Descent time was 93 minutes.

15-3.9 Equilibrium Velocities

The vertical descent trajectory, Figure 15-12, taken from the barocoder data shows three intervals of constant speed: the first, between about 85,000 feet to 54,000 feet, 27 feet per second; the second, from about 35,000 feet to 20,000 feet, an unusually slow, 10 feet per second, and finally, the terminal velocity from 10,000 feet, about 20 feet per second. These speeds are confirmed by the radar data. The maximum dynamic pressure during opening shock computed from free fall speeds and air density data was 3.5×10^{-2} pounds per square foot.

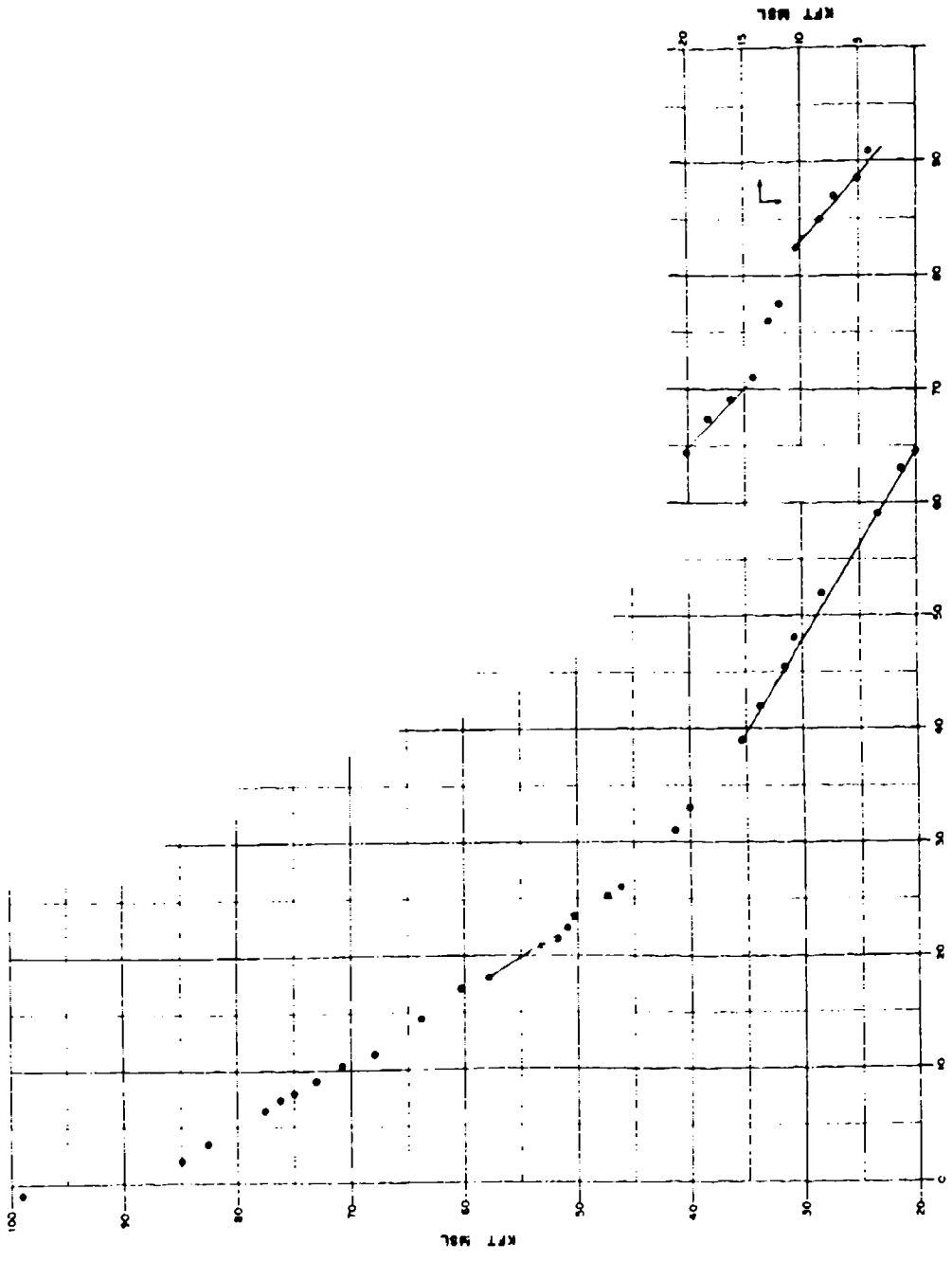

Figure 15-12. 140-Foot RSR Parachute Descent Barocoder Data

15-3.10 Conclusions

(1) The 140-foot RSR parachute under near-minimum load performed safely and had satisfactory opening time and shock force values.

(2) The flight showed the need for an improved reefing arrangement strong enough to contain the canopy during launch and yet sufficiently simple to ensure complete disreef by command operated line cutters. A reefing system we plan to test is shown in Figure 15-13.

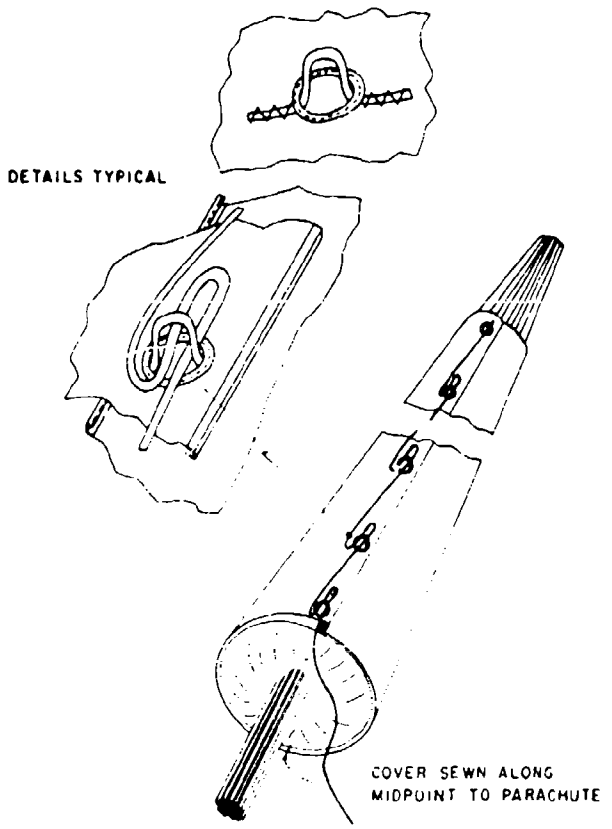

Figure 15-13. Proposed Reefing Method for 140-Foot RSR Parachute

(3) The relative instability of the canopy at very high altitude is entirely reasonable in view of the combination of lightweight payload with large area canopy. The tension in the control lines was actually very small compared to the normal design values. Moreover, turbulent air was detected during the balloon ascent and may still have been present when the parachute was released. If so, this would also contribute to the observed instability.

(4) Evidently the tension in the lines due to the extreme underload condition was not enough to maintain the design shape of the canopy.

(5) The unusually long (93-minute) descent time is also directly attributable to the combination of very large canopy and relatively light load. No practical difficulties arose from this condition.

In summary, the RSR RIBCO parachute shows great promise for heavy load high-altitude applications. Its low weight and simplicity compared to clustered systems makes it very desirable for flights where recovery system must function with either a very heavy or a relatively lightweight payload.

However, further flight tests with this parachute are planned before it will be qualified for routine use in the laboratory.

Contents

16. A Platform and Control System for a Steerable Down-Looking Balloon-Borne Experiment

F.E. Lord
GTE-Sylvania, Inc.
Electronic Systems Group – WD
Mountain View, California

Abstract

A system is described for accurately pointing a laser receiver from high altitudes both by remote control and from an onboard tracker. Provision for control of other functions and real time data readout is included.

The platform is configured uniquely for a down looking experiment by employing a rotating central column upon which the elevation assembly is suspended. Three inverted L-shaped members attached to the column housing contain the heavier equipment, thus creating a momentum sink as well as providing protection around the experiment.

Commands from the ground station are transmitted on a tone modulated FM link and decoded on the platform to control power application, mode selection, axial positioning and experiment operation. The platform azimuth position is referenced to north by means of an ac magnetometer, thus facilitating interception of the upcoming beam. Upon acquisition of the beam, a four-quadrant detector is utilized for automatic tracking during the experiment. The axes employ direct drive torque motors for smoothness of operation and continual achievement of a 0.5 degree pointing accuracy. An FM/FM down link provides for real time data transfer.

The system was employed successfully on a flight from Holloman Air Force Base in October 1970.

16-1. INTRODUCTION

The equipment described in this paper was designed to support a laser propagation experiment that has been described by Woodman et al (1971) in a presentation at another conference. The complete system included both balloon borne and ground based equipment. The balloon borne portion of the equipment received beams of laser energy that were directed at it from the ground, measured various characteristics of interest and transmitted data to the ground where it was displayed and recorded. The field of view of the experiment's sensors was such as to require two axis positioning of the receiving equipment with an accuracy of 0.5 degrees.

Smooth automatic tracking of the beam was required in order that the desired data not be degraded by motion of the optical receiver with respect to the beam. The system was required to gather data at a float altitude of approximately 92,000 feet on an intermittent basis, nominally 20 minutes each hour during an 8 hour flight for a total operating time of 2.7 hours. Consequently, the system had to be arranged in a way that would minimize power consumption between active periods. Since the experiment must look down, there exist the conflicting requirements of providing for unobstructed view and protecting against damage upon landing. In resolving these opposing requirements a unique gondola configuration has been developed and flight proven that is believed to have merit for other down looking applications.

The system block diagram, Figure 16-1, shows both the ground and the balloon borne portions of the system. The laser transmitters are continually directed at the balloon borne equipment by tracking on reflected laser energy. Initially the laser receiver package on the gondola is positioned to intercept the upcoming beam by commands transmitted on the telemetry link. When the upcoming beam is intercepted by the receiving equipment, automatic tracking utilizing error signals developed from the received signal can be initiated. The pertinent data is then transferred to the ground by way of the down telemetry link.

The communication links will be considered briefly, followed by a more detailed examination of the two-axis positioning subsystems and the physical features of the gondola.

16-2. TELEMETRY

Figure 16-2 details the telemetry portion of the system which utilizes the FM-FM technique in both directions. The system is straightforward. The up link employs a 5-tone encoding system to realize 31 distinct commands. On the gondola the received tones are separated by highly selective filters which in turn drive

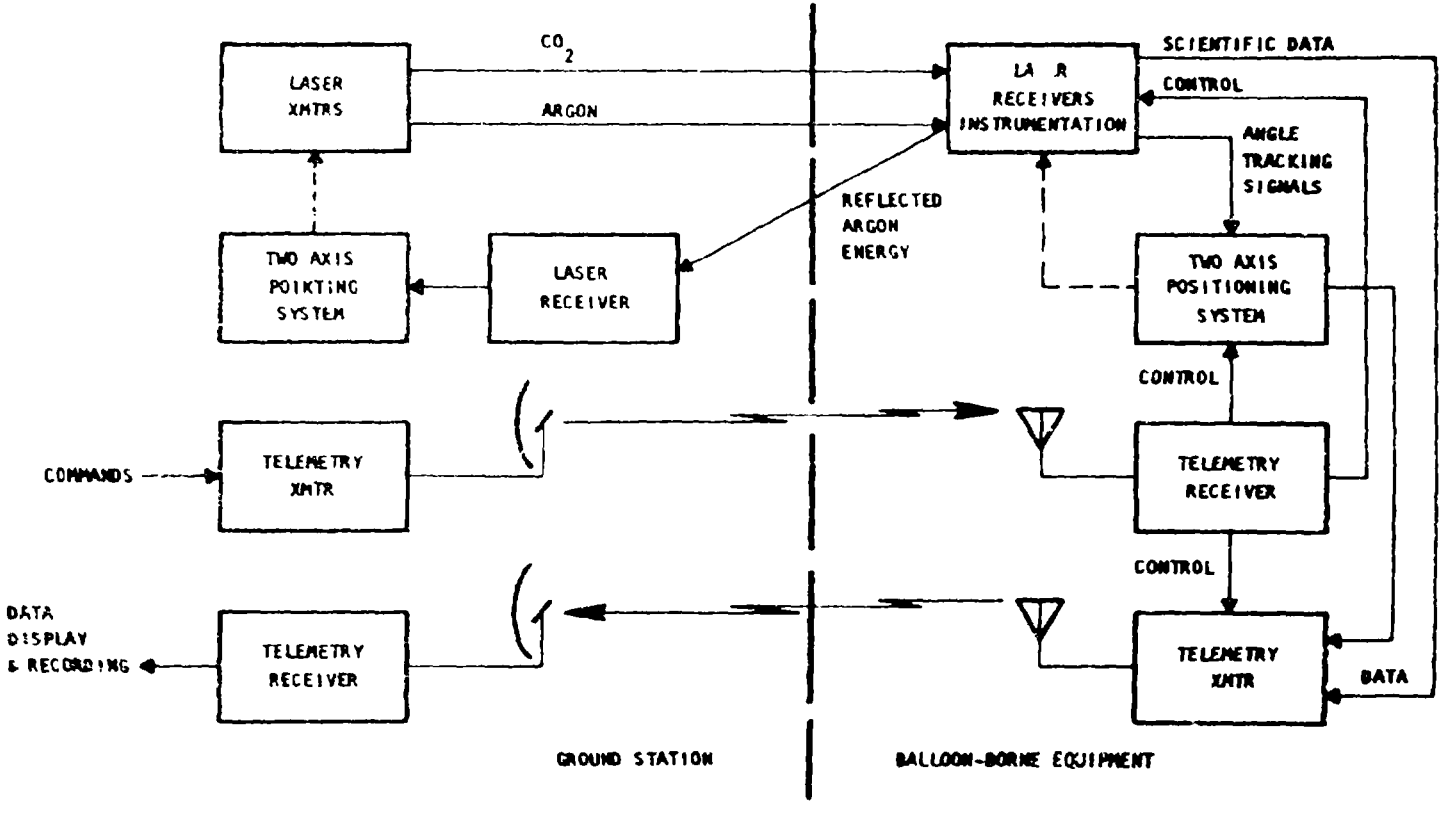

Figure 16-1. Laser Propagation Experiment Block Diagram

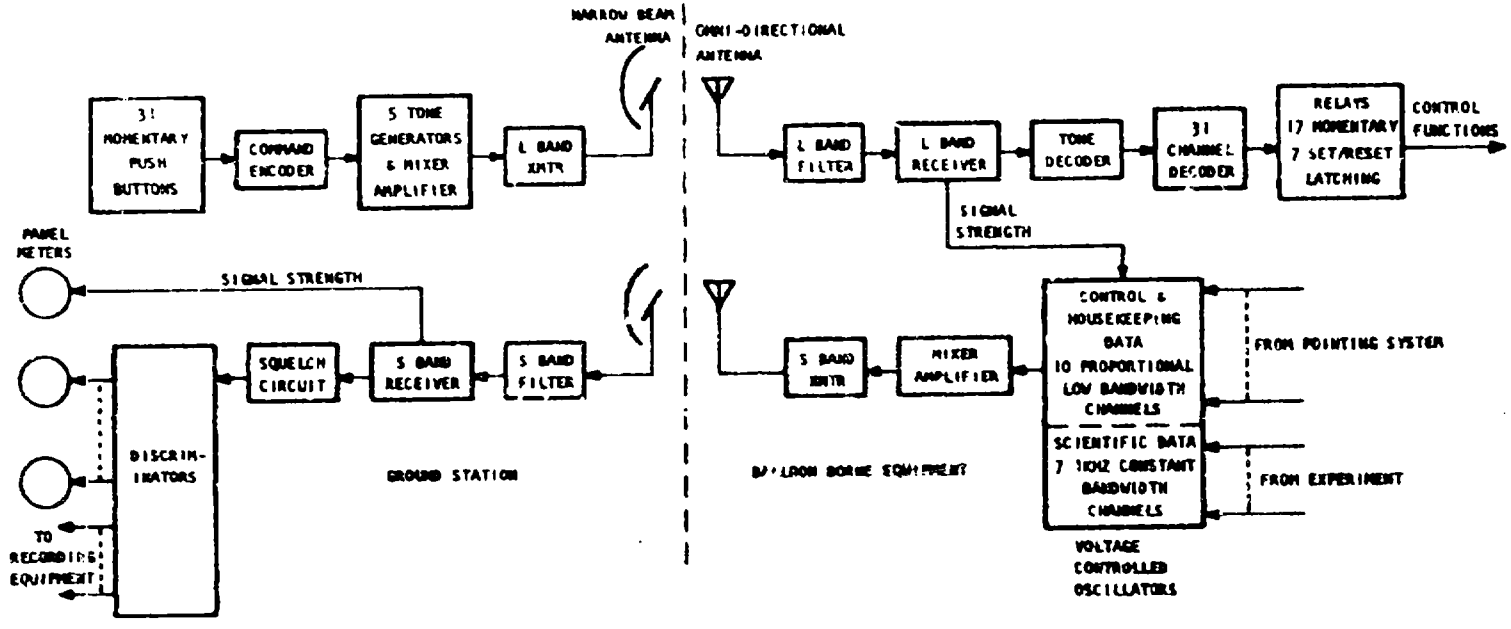

Figure 15-2. Telemetry Subsystem Block Diagram

switching circuitry. The outputs of the switching circuits are decoded to provide for actuation of 17 momentary relays and 7 set/reset latching relays which effect the required control. Positioning, power control, scaling and calibration are accomplished by way of these commands.

The data from the experiment are processed by seven 1-kHz constant bandwidth voltage controlled oscillators (VCO). Ten low bandwidth proportional VCO's handle less critical data from the experiment, control information and housekeeping functions. These latter data include a signal strength indication from the up link receiver which is employed by the operator in manually positioning the up link directional antenna for optimum operation.

At the ground end of the down link, a bank of discriminators detects the data for display on meters and recording. Among the quantities appearing on meters are strength of the down link received signal, which is employed as an aid to telemetry antenna positioning, and pointing data from the experiment in the form of elevation and magnetic true bearing for use in the acquisition procedure. A magnetically actuated flag indicates when the balloon borne equipment is automatically tracking the upcoming beam. The momentary control buttons and indicators that comprise the telemetry operator interface are shown in Figure 16-3. As can be seen on the panel, a considerable number of control functions are concerned with conserving power.

16-3. CONTROL

The control portion of the system is shown in greater detail in Figure 16-4. Inputs are introduced to the control system by way of the command decoder unit of the telemetry system, and information is extracted for down link transmission through the VCO's.

The relatively stationary portion of the gondola contains the heavier items such as batteries, azimuth servo amplifier, and portions of the telemetry equipment. The azimuth drive is a torque motor which along with the slip ring assembly, tachometer and synchro differential comprise the transition between the stationary and trainable portions of the equipment; that is, the stators of these components are part of the stationary structure and the rotors turn with the trainable assembly. It is advantageous for various reasons to carry some of the electronics in the trainable section of the gondola. These items include the elevation servo amplifier, the mode selection circuits, the command decoder and the VCO's and mixer amplifier. The line of sight of the experiment is moved in a vertical plane by the elevation axis which is carried beneath the azimuth axis.

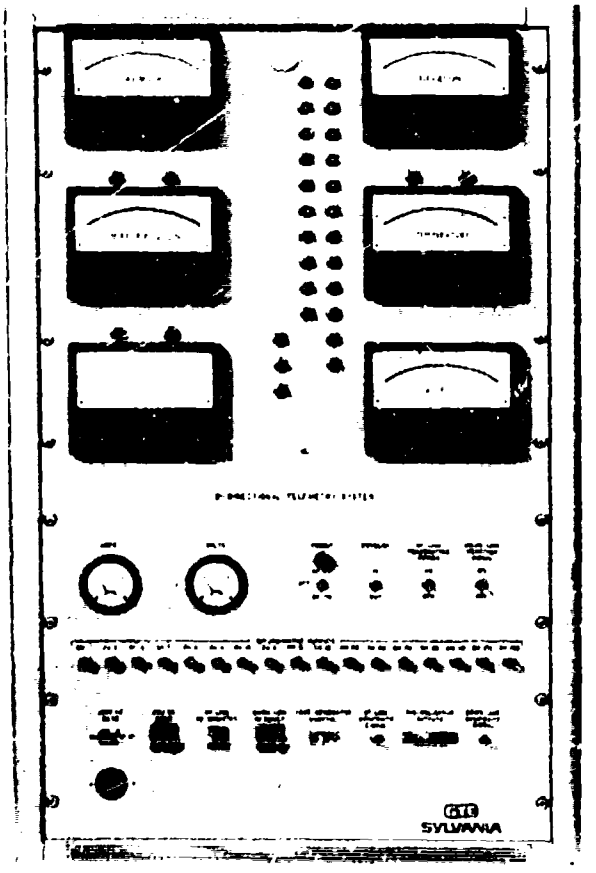

Figure 16-3. Control Panel

The servos which control azimuth and elevation motion are basically the same, except the azimuth torque motor delivers 7 foot pounds of torque compared with 1.2 foot pounds for elevation. Both employ rate feedback stabilization and a standard dc servo amplifier matched to the motor. Potentiometers provide positional data, and brakes hold the axes stationary during nonoperating periods. The principal sources of tracking error include angular drift, oscillatory motion of the balloon-gondola combination, friction of the bearings and slip ring assembly, unbalance on the elevation axis due to loss of liquid nitrogen from a Dewar within the optical experiment, and sensor noise and unbalance. The significant parameters directly influencing servo accuracy are listed in Table 16-1. The servo design contained the total of these errors within the allowable 0.5 degrees. A more sophisticated design could yield higher accuracies, if required.

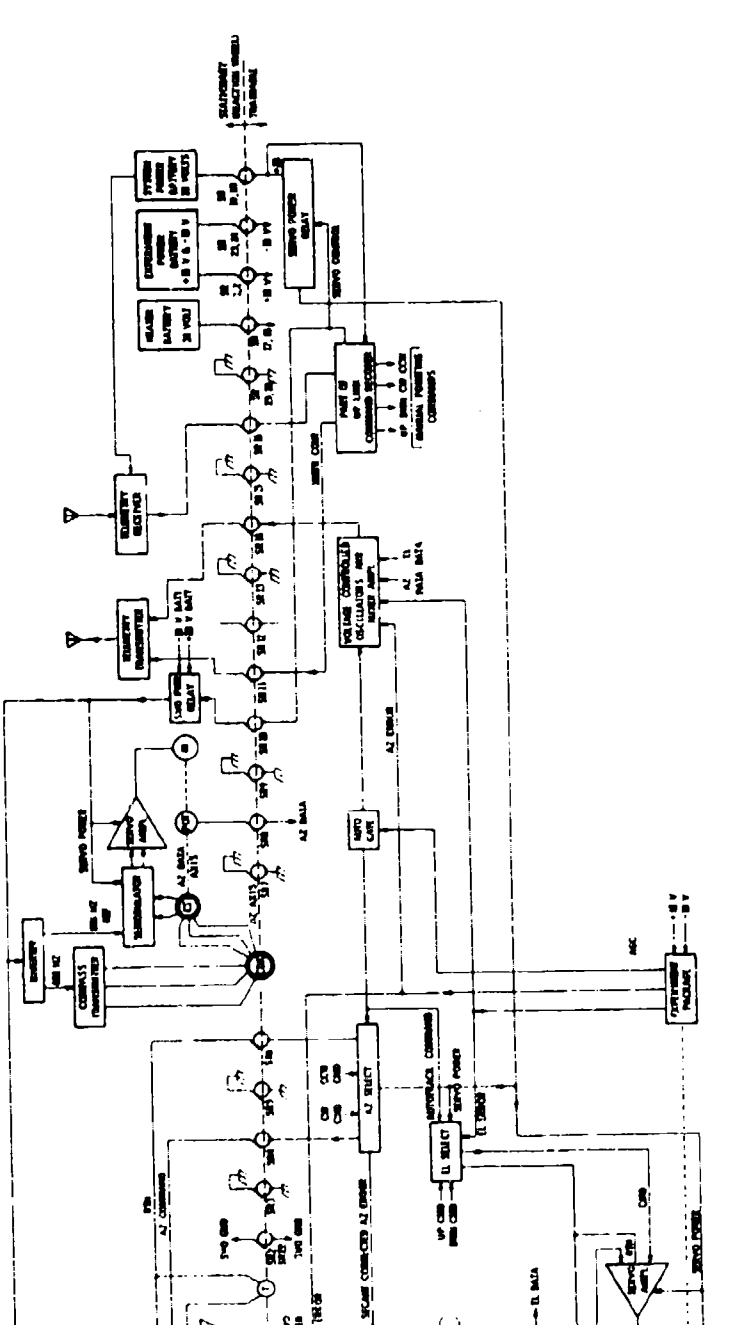

Figure 16-4. Gondola Two Axis Pointing System

Table 16-1. Sources of Tracking Error

	Elevation	Azimuth
Load		
Friction	.25 ft-lb	2.0 ft-lb
Unbalance	.15 ft-lb	--
Motion		
Angular Drift	--	2°/s
Oscillation		
Magnitude	1 degree	1 degree
Period	10 seconds	10 seconds

By combining the magnetic true bearing of the gondola stationary frame with the relative bearing of the experimental equipment with respect to the frame, the magnetic true bearing of the experimental equipment is obtained. A flux gate compass unit similar to one used in military aircraft was employed to measure the position of the gondola frame with respect to north. This choice was favored because this device has a synchro compatible three-wire output and a synchro differential transmitter on the azimuth axis could then serve as the continuous fully rotatable transducer needed at that point. The synchro differential performs an algebraic addition of the bearing quantities to produce the true bearing of the experiment. This three-wire quantity is then converted to potentiometer position by an instrument servomechanism.

The true bearing data from the potentiometer is transmitted to the ground via the telemetry link. The flux gate unit has a nominal accuracy of ± 1 degree which degrades to only ± 1.5 degrees under environmental extremes. This is an accuracy compatible with the 10-degree cone of sensitivity of the tracking sensor. The compass has a pendulous sensing element which allows it to tolerate tilt up to 27 degrees, thus overcoming a possible source of inaccuracy which has been mentioned by Orwig et al (1970) in connection with other positioning systems. Although it was necessary to generate a small amount of 400 and 800-Hz power to excite this device and the demodulator that follows the bearing data synchro chain, this was considered a small price to pay for the advantages obtained.

The elevation data are obtained from a potentiometer coupled directly to the elevation axis. The procedure to acquire the upcoming laser beam is first to depress this axis by the same angle the transmitter on the ground is elevated. Then the experiment is trained to point 180 degrees from the pointing direction of the transmitter mount to arrive at the attitude that looks down along the upcoming beam.

Positioning the experiment is accomplished by way of the CW, CCW, UP and DOWN pushbutton switches at the ground station. As long as one of these pushbuttons is depressed, a relay in the gondola remains closed to apply an appropriate velocity command voltage to the corresponding servo. These switches are effective when the control system is in either the Manual or Automatic mode. However, when upcoming energy is intercepted after the operator has selected the Automatic mode, tracking is started and manual control is lost with no further action on his part through action of the auto gate circuit. This circuit examines the AGC voltage of the sensor amplifier to evaluate the suitability of the received laser signal for tracking. Once started, tracking is broken only if the signal is lost or the operator actuates manual operation. The error signals for automatic tracking are derived from a position sensing photo detector. As the elevation angle becomes large, this sensor's sensitivity to azimuth errors is lowered, prompting the need for the azimuth error signal to be corrected by the secant of the elevation angle. This compensation is obtained by way of a secant function potentiometer on the elevation axis.

16-4. POWER

The power required by the major elements of the balloon borne equipment is presented in Table 16-2. Nickel cadmium cells were chosen for this application

Table 16-2. Gondola Power Requirements

FUNCTION	VOLTAGE	CURRENT (Amperes)	TIME (Hours)	ENERGY (Watt Hours)
TM Receiver	28	.10	8.	22.4
TM Transmitter	28	3.3	2.7	250.0
Control				
Electronics	28	.1	2.7	7.5
	-15	.1	2.7	4.1
Azimuth Servo	28	4.0	2.7	302.0
Elevation Servo	28	1.5	2.7	113.2
Experiment				
Electronics	15	1.1	2.7	44.5
	-15	.60	2.7	24.3
	28	.23	2.7	17.4
Heater	24	4.0	2.7	259.0
Total				1044.4

because of their relatively flat discharge characteristic and tolerance to abuse. If this energy were supplied by a source delivering at the commonly quoted figure of 12 watt hours per pound, a battery weight of 87.0 pounds could be expected. However, the desirability of grouping the batteries by function, allowance for reduced capacity at low temperature, and provision of a margin of reserve resulted in a total battery weight of 175 pounds.

16-5. GONDOLA ASSEMBLY

The balloon borne equipment is pictured in Figure 16-5. This gondola assembly weighs 750 pounds, is 5 feet high and 10 feet across. Its principal features include the central column which rotates in azimuth, the elevation assembly which contains the experimental equipment, and three inverted L structures which house equipment and protect the central zone. Sheet metal members not pictured normally provide a horizontal cover in the upper area of the assembly for the purpose of sun shielding and ballast deflection. The heavier items, including the batteries, located outboard create a sizable momentum sink for the reaction to azimuth motion.

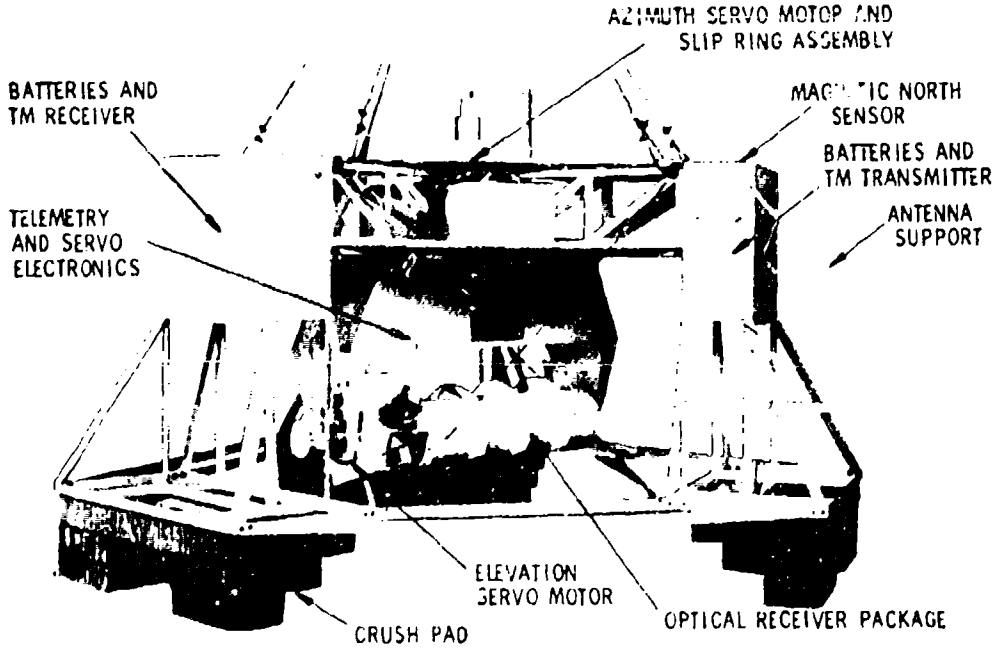

Figure 16-5. Gondola Assembly

The omnidirectional telemetry antennas are mounted on booms which clear the gondola structure by five feet. These turnstile antennas are encased in styrofoam and sealed in a fiberglass shell. The booms are designed to break easily so that the antenna packages will break away and not sustain damage during landing.

Several possibilities were considered for providing extensive coverage of the hemisphere below the gondola while at the same time providing for protection of the experimental equipment upon landing. These included extending and retracting the experiment, extending or pivoting crush pads into place prior to landing and turning a major subassembly of the gondola over after completion of the experiment. Any of these methods would involve mechanisms that would add complexity and cost to the system. The consequences of failure of the device have to be accounted for, and the mechanism itself would be subject to damage upon landing. It must also be considered that any attempt to extend and retract the experiment would most likely reduce the stiffness of the positioning axes and thus compromise their closed loop performance potential. The method employed was simple and reliable, because no moving parts or mechanisms of any kind were involved. The configuration in this case sacrificed visibility in the first 25 degrees below the gondola horizon, a zone that had a low probability of utilization in the mission plan of the experiment. The zone of visibility was made as large as possible by shaping the crush pads to taper toward the experiment, as shown in Figure 16-5, while at the same time maintaining suitable protection in terms of resulting g loads and presence of crushable material for various ways in which the gondola could land. Knowing the energy of the gondola descending at 17 feet per second to be 3360 foot pounds, the ability of various encountered areas of the crush pad to absorb the energy may be examined utilizing the relationship:

$$E = Asd , \qquad (16\text{-}1)$$

where

E = Energy absorbed
A = Area of the crushable material in square inches
s = Strength of the crushable material in pounds per square inch
d = Depth of the material crushed.

In the arrangement shown in Figure 16-6, the first two layers may be regarded as capable of absorbing energy for their entire depth of 1/3 foot, because they are backed by a third crushable layer; that is, the limit on crushable length as compared to original length does not apply layer by layer. The face of the first layer can be regarded as the base of a 1-foot column of material which will crush 75 percent of its length, 3/4 foot. Likewise, the column whose base is the second layer will crush to 75 percent of 2/3 foot, or 1/2 foot.

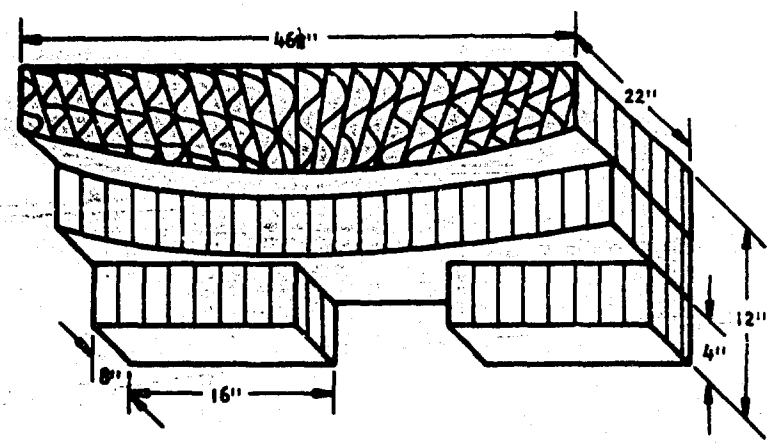

Figure 16-6. Crush Pad Configuration

The resulting g loads are determined from the relationship

$$n = \frac{As}{W}, \qquad (16\text{-}2)$$

where

n = Number of g's
A = Area of crushable material in square inches
s = Strength of the crushable material in pounds per square inch
W = Weight of gondola

The material employed was Vertical Paper Honeycomb Type 1/2" 40-50-0 percent, having a strength of 11 pounds per square inch when employed in 4-inch thickness.

For the pad configuration employed, the g loads and energy absorption characteristics of four different types of impact are shown in Table 16-3. The impacts examined include one in which all the legs encounter the ground simultaneously, a situation where two legs hit at essentially the same time, an instance where one leg hits substantially ahead of the other two, and a case in which one corner, that is, essentially one half of one leg, hits first.

These data show that excessive g loads will result from a perfectly flat landing, although all the energy will be absorbed with only slight crushing of the second layer. Hitting on one corner would crush all the intervening material before the energy was absorbed, resulting in damage to the structure. However, these two cases are ones which are most improbable. A typical landing would most likely involve mainly one leg or at the most the equivalent of two legs. Examination of these two cases shows reasonable g loading increasing in steps as more

Table 16-3. Loading and Energy Absorption for Various Landings

Type of Landing	Crush Pad Performance									
	First Layer			Second Layer			Subtotal Energy Absorb. Cap. Ft-Lb	Third Layer		
	Area In.^{2}	G Load	Energy Absorb. Cap. Ft-Lb	Area In.^{2}	G Load	Energy Absorb. Cap Ft-Lb		Area In.^{2}	G Load	Energy Absorbed
Three Legs	768	11.3	2820	1560	22.8	5712	8532	2580	Not encountered	Not applicable
Two Legs	512	7.6	1880	1040	15.2	3804	5684	1720	Not encountered	Not applicable
One Leg	256	3.8	940	520	7.6	1904	2844	860	12.6	Absorbs remaining energy with 0.65-in. crush
One Half Leg	128	1.9	470	260	3.8	952	1422	430	6.3	Cannot absorb remaining energy without bottoming

material is encountered and all the energy being absorbed before bottoming. Thus, the protection is optimized for the most probable types of landing while at the same time providing protection to a lesser degree for other types.

16-6. PERFORMANCE IN FLIGHT

On October 21, 1970 this equipment was launched from Holloman AFB at 12:15 am. An 8-1/2 hour flight followed, during which the plan of taking data at regular intervals was altered because of some initial difficulties with the laser link. The control system was utilized periodically for the first five hours in unsuccessful attempts to establish tracking by the experiment. This activity consumed approximately 40 minutes of operating time. At 5:37 am laser difficulties were overcome and tracking was established. The balloon borne equipment was operated continuously until 7:59 am for a total of 2 hours and 20 minutes with data being obtained a major portion of the period. Descent and impact at 8:54 am followed. Slight damage of the structure was sustained, but all the equipment remained operable. The year following this successful flight, the sponsoring agency conducted additional experiments, and the vehicle performed successfully on the five flights that were involved.

16-7. CONCLUSION

A relatively simple, reliable concept has been developed into equipment that has been effective in the conduct of down looking experiments. The concept readily can be scaled to other sizes for other types of experimental work.

Acknowledgment

This work was performed for Goddard Space Flight Center, NASA, under Contract NAS5-11679, monitored by Peter O. Minott.

References

Orwig, L. E., Wood, A. P., and Lavoie, P. E. (1970) A payload stabilization and altitude control platform for high altitude balloon experiments, Proc. Sixth AFCRL Scientific Balloon Symposium, AFCRL-70-0543: 49-60.

Woodman, D. P., Minott, P., Boehme, M., Brown, C., Fitzmaurice, M., Kraemer, A., Titterton, P., and Bufton, J. (1971) Balloon atmospheric propagation experiment I (BAPE I). Paper presented at 1971 IEEE/OSA Conference on Laser Engineering and Applications.

Contents

17. Observations of Gondola Motions for High Altitude Flight Systems

R.B. Toolin
Air Force Cambridge Research Laboratories
Bedford, Massachusetts

N.C. Poirier
Northeastern University
Boston, Massachusetts

Abstract

During the past several years a high altitude balloon-borne solar pointer has been used for optical measurements in the atmosphere. The pointer's stabilized line of sight also has provided the opportunity for measurements of gondola motions during ascent and float phases. Results are compared with published studies for very high Reynolds number phenomena. The analysis is qualitative because of the dependence of rotational motions upon minute but nonmeasurable variations in balloon surface contours. The ranges of motions are predictable, but specific values for any particular flight are not.

17.1. INTRODUCTION

It is the purpose of this paper to present some of the measurements and analyses of the dynamical conditions of the balloon borne platforms during high altitude scientific missions. During the past several years our principal concern in

scientific ballooning has been measurements of the attenuation of optical radiation in the earth's atmosphere. A critical element for performance is the basic requirement for a precise and continuous orientation of optical radiometers with respect to the sun. A balloon-borne biaxial sun pointer, developed by the Ball Brothers Research Corporation, is used to attain and to maintain sunlock during the rise and float portions of the flight trajectory. This continuous sunline can be used as the reference for measure of gondola motions.

17-2. MEASUREMENT SYSTEM

Details of the sun pointer and its typical operation have been described earlier (Toolin and Poirier, 1970). However, there are certain broad and also specific features which need emphasis, because they are pertinent to this presentation. Figure 17-1 presents the major features of the pointing control system.

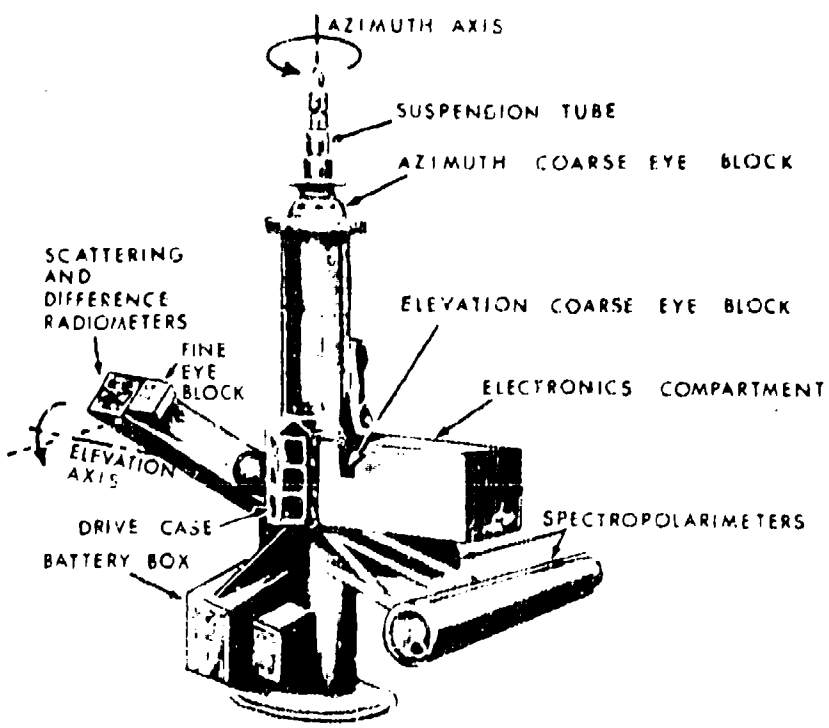

Figure 17-1. Major Features of Balloon-Borne Biaxial Solar Pointer

The pointing control is mounted on the vertical suspension tube which is also the load carrying member joining the balloon to the gondola proper. The horizontal box houses monitor and control electronics and the sensor system which activates pointing in the transverse axis. The section to the opposite side of the suspension tube would be for location of the instrumentation which is to be pointed biaxially with respect to the sun. The fine sensor system, to achieve sunlock within ± 2 minutes of arc, is hard mounted to the instrumentation.

The drive case is the basic structure for the pointed portion of the sun pointer. It is supported on the suspension tube by sets of space hardened ball bearings located at the upper and lower ends of the case. The upward extension of the drive case supports an azimuthally symmetric array of sensors. These generate electrical signals proportional to the angular offset of the sun from azimuthal null and drive the case and all appendages into the sunline. Conversely, once sun lock is achieved, any rotation of the suspension tube due to torquing either from the balloon or from the gondola will generate error signals from the instrument-mounted fine sensors to maintain the sunlock.

A dc torquer motor rated at 1.2 foot pounds is the driver. Its use eliminates the need for gear trains with their attendant backlash and friction problems. An idea of performance can be garnered from a worst case instance we have experienced. A 125-pound instrumentation package with suitable counterweights at the other extreme of the drive case was installed and flown successfully. This weight corresponds to a value 35 percent over design limit. During ground testing the system was mechanically set to a position 180 degrees away from the sun. With application of power, sunlock was attained in less than 25 seconds. The example is extreme. In our complete experience with this system any disruption which produced a displacement exceeding 3 degrees has been negated in less than 3 seconds.

An azimuth position potentiometer is mounted between the pointer structure and the azimuth shaft to provide a 0 to 5-volt signal proportional to the angle between azimuth null (the sunline) and an arbitrary reference on the suspension tube. Its output is a direct measure of the movement of the gondola proper because of the constant stability of the sunline. The few frictional forces in the system are found in the brushing effects in the slip rings and the drag effects in the roller bearings. In any case, the total frictional force of the azimuth system in flight configuration never has exceeded 0.3 pounds.

17-3. ROTATIONAL DATA

For four flights in the program we used the 2.01×10^6 cubic foot polyethylene balloon as the vehicle. The load line length has varied from 60 to 200 feet,

determined by the maximum solar elevation angle for the flight day. For the fifth flight we successfully used the 10.6×10^6 cubic foot polyethylene balloon. In any case, the moment of inertia of the balloon is greater than that of the gondola by a minimum factor of 30 and by a maximum factor of 250.

Figure 17-2 represents the gondola rotational data from one of the four flights. The ordinate is the number of revolutions measured clockwise and counter-clockwise, as a function of time after launch expressed in minutes. Also included

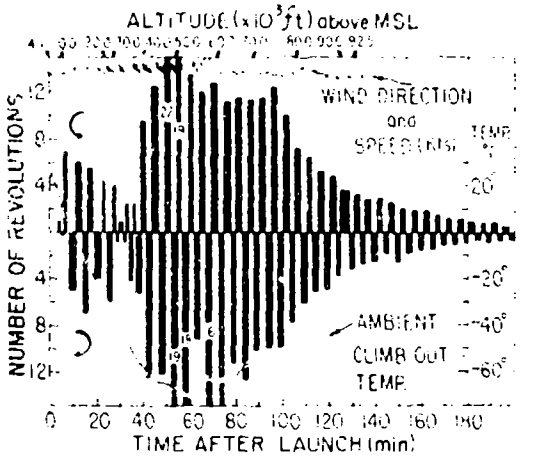

Figure 17-2. Gondola Rotation - First Flight

are the wind velocities expressed in the Beaufort scale and the ambient temperature obtained from a concurrent reading. The motions are markedly symmetrical, at least after the first 50 minutes of flight. Particularly noted is that the motion after float is attained when oscillations decay to immeasurable levels in approximately 60 minutes. This damped oscillation fits well the model presented by Morris and Stefan (1969).

Figure 17-3 tarnishes the orderly image of rotational motion of Figure 17-2. The only common feature is that there are as many rotations in one direction as in the other. There is no similarity in amplitude or time. There is the suggestion of a causal source of rotation due to wind shear in the large amplitude, long duration of rotation at 15,000 feet.

Figure 17-4 illustrates the rotational product of another flight. No data were acquired until the flight system reached an altitude of 35,000 feet because of the pretwilight launch. In this illustration, the Beaufort scale is plotted on the altitude-time line. The magnitudes of rotation compared with the preceding

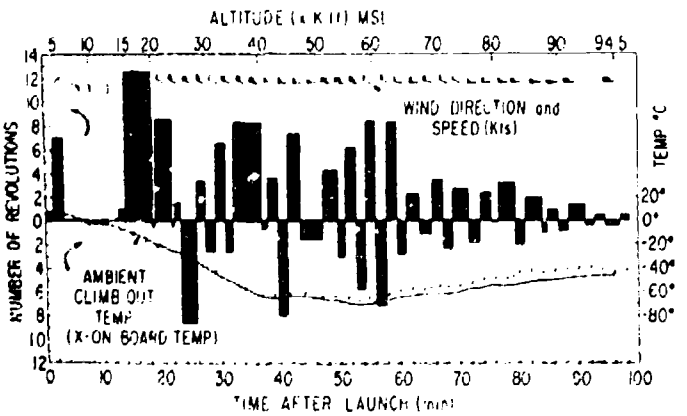

Figure 17-3. Gondola Rotation - Second Flight

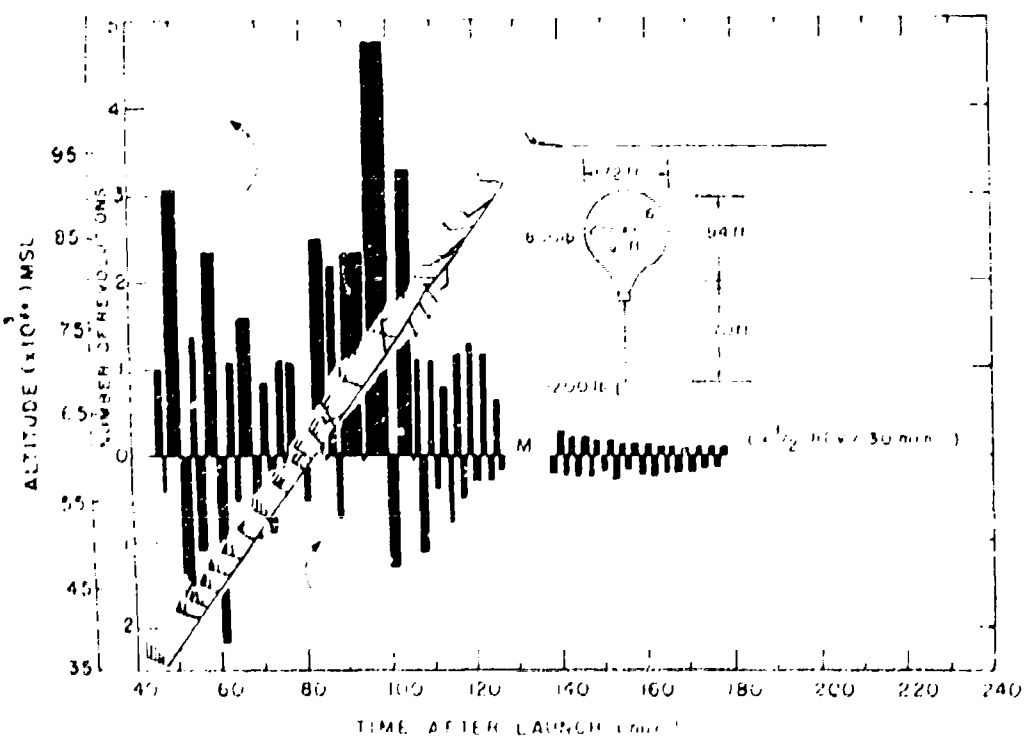

Figure 17-4. Gondola Rotation - Third Flight

experience have decreased, while fine structure has increased, but not proportionately. A possible correlation exists with wind shears - at least for some altitudes,

Figures 17-3 and 17-4 have the common static characteristic that the gross load is substantially greater than for the flight corresponding to Figure 17-2. Indeed, for Figure 17-3 this value is 200 pounds, and for Figure 17-4 it is 400 pounds.

Figure 17-5a is the rotational history for our 10.6×10^6 cubic foot balloon flight. Any correlation with wind shear levels in the atmosphere is not apparent.

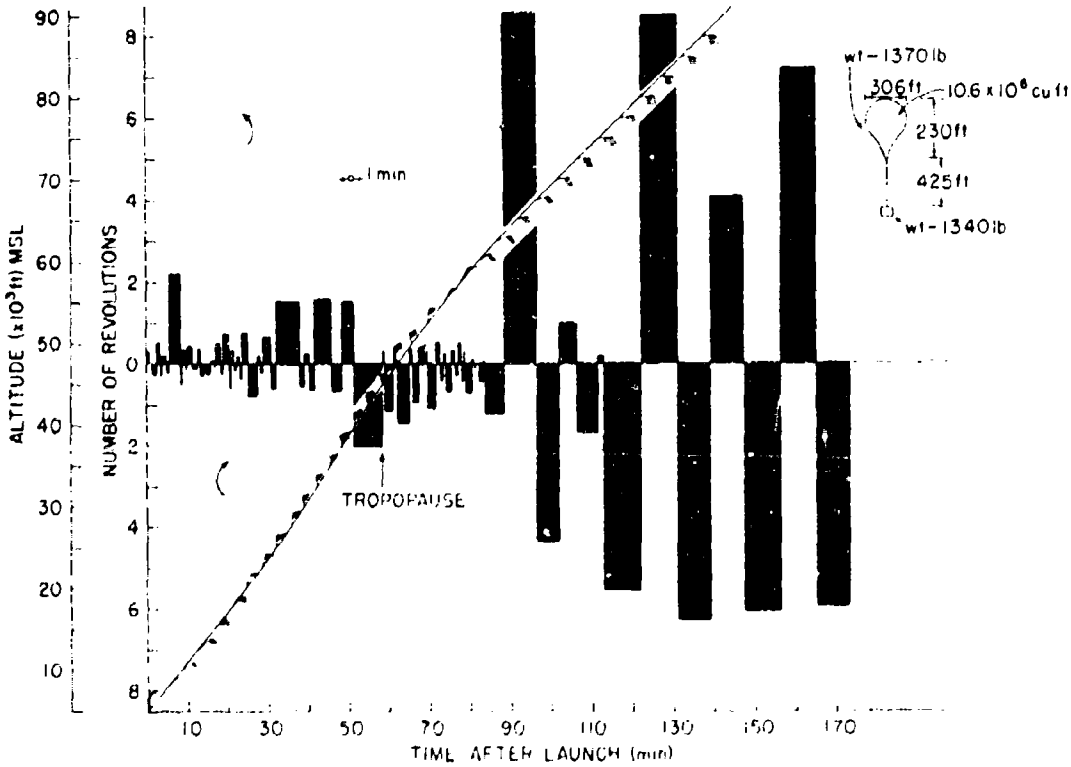

Figure 17-5a. Gondola Rotation During Ascent - Fourth Flight

Indeed, some order seems to appear only above 70,000 feet on its way to 133,000 feet. Figure 17-5b is the continuation of this flight until its termination by cut-down. The potential decay in oscillation is lost because of valving operations. The substantial change in rotation during these periods of low vertical velocities is qualitatively interesting and implies a primary source of rotational motion during float.

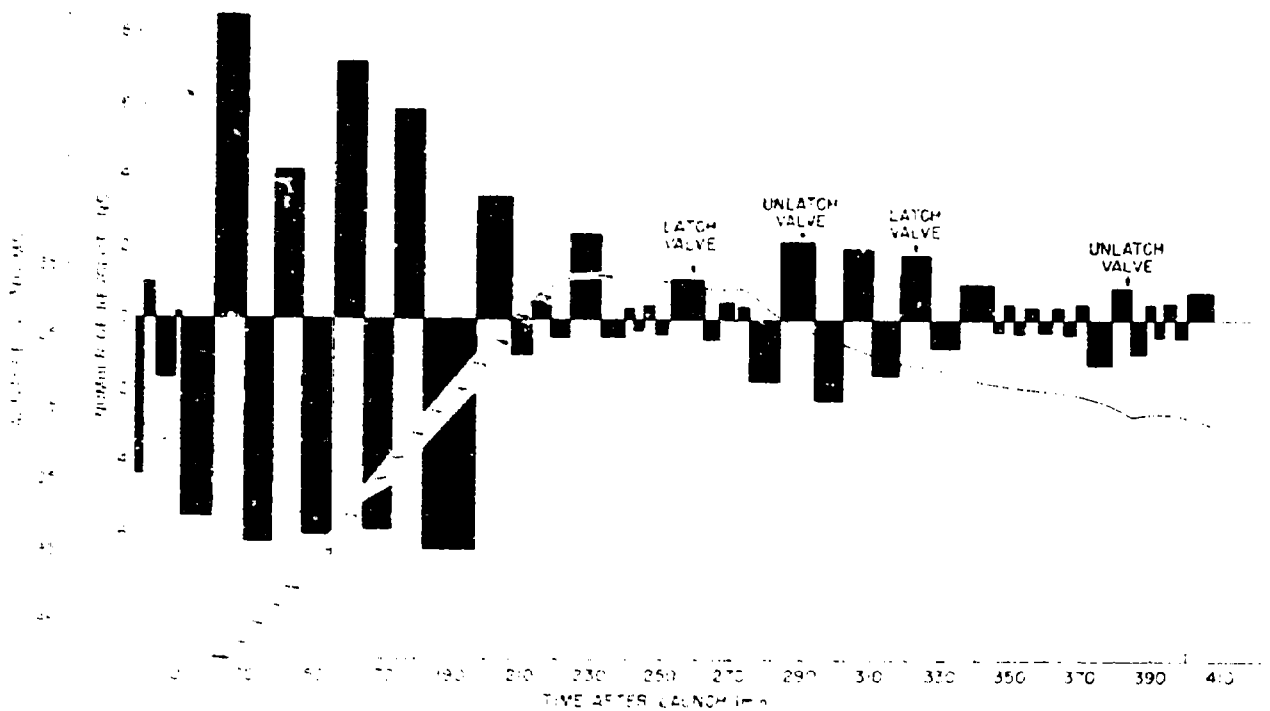

Figure 17-5b. Gondola Motion During Latter Portion of Ascent and Float - Fourth Flight

These preceding data have been collated and arranged in such a manner as to guide those users of the balloon vehicle who also have concern for platform oscillation. The data are presented in terms of a cumulative frequency distribution shown in Figure 17-6. The statistics are based upon the four 2.01×10^6 cubic foot and single 10.6×10^6 cubic foot balloon flights. The graphs show, for example, that the rotation rate of 0.5 rpm or less is realized 50 percent of the time during the rise portion of a flight and that during float the rotation rate never exceeds 0.25 rpm.

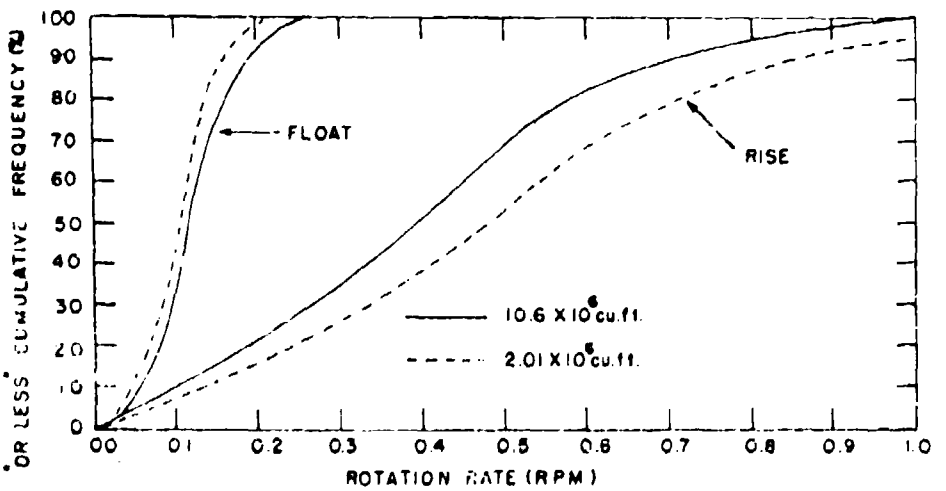

Figure 17-6. Statistical Summary of Gondola Rotation Rates for Loosely Coupled Flight Systems

17-4. INFLUENCE OF THE REYNOLDS NUMBER

The motion of a balloon system through the air is an example of the movement of a sphere through a fluid. Such movements can be described in terms of the Reynolds number and interpreted in terms of the magnitudes of drag and lift forces generated. The flow regime in which the balloon system operates corresponds to the high Reynolds numbers, 10^4 to 10^6. It is recognized as the region where the laminar boundary layer air flow breaks into a turbulent state; the wake is noted by swirls and vortex streets with unsymmetrical pressure variations over the sphere's surface.

Figure 17-7 summarizes the existing knowledge on the behavior of a sphere in a low viscosity medium by demonstrating graphically how the drag coefficient, C_D,

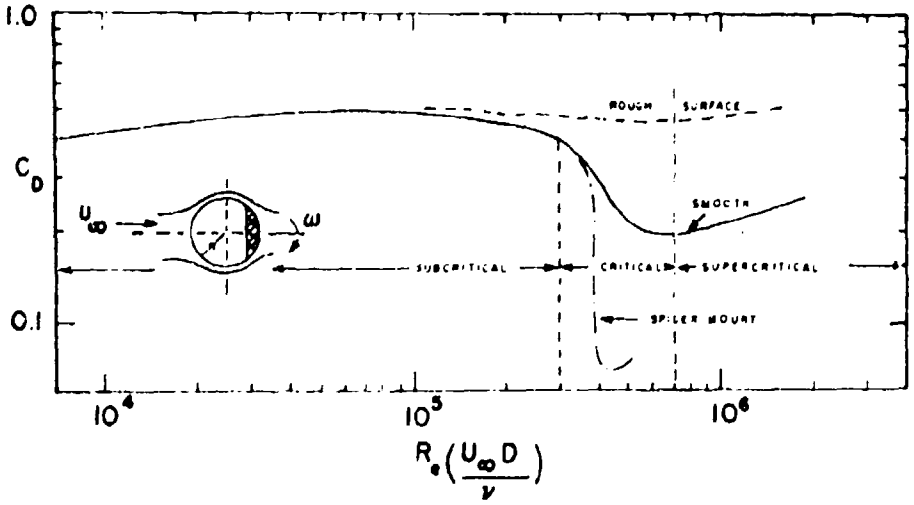

Figure 17-7. Model Curve for Drag Coefficient of a Sphere as Function of High Reynolds Numbers

depends upon the Reynolds number, R_e. The drag coefficient is directly proportional to drag force and inversely related to the square of the free stream velocity and diameter. The Reynolds number is even more simple, since its value depends directly on the free stream velocity and the diameter and, inversely, on the kinematic viscosity. In anticipation, we can realize that for our balloon systems the most important factor is the viscosity, which increases by a factor of 200 over the altitude range, while the diameter increases by a factor of about 6. On this basis, we would look for the super-critical regime to exist in the early portion of a flight, then the critical, and in the later portion of the rise, the sub-critical regime, until the system attains floating altitude when viscous forces attenuate. The illustration and following comments are adapted from a report by MacCready and Jex (1964) and from material by Schlichting (1968). Starting at $R_e = 10^4$, when the laminar boundary layer is commencing to separate, the wake becomes unsteady and leaving in oscillatory fashion. The area of separation on the sphere varies with time and position, indicating fluctuating levels of high and low surface pressures. The wavelength of the wake envelope is much longer than in the high Reynolds number regimes.

In the region between 2×10^5 and 7×10^5 for R_e, we have the critical regime which separates laminar from the super-critical completely turbulent flow. Here the wake is thin, and C_D is on the order of 0.1. But many influences, indeed too many, make this regime ill defined. For example, surface roughness (one percent of the diameter of the sphere) can produce the illustrated curve.

while a spider, or trailing appendage, would exaggerate this regime. Rotation itself strongly influences the extent of this region. When the peripheral speed of the sphere is about three times the free stream velocity, the onset of critical regime occurs at $R_e = 1.5 \times 10^5$. Generally, in our flight systems, the peripheral speed, R_ω, is less than $0.1\ U_\infty$, and the illustrated curves represent this state.

In the supercritical regime, boundary layer separation is turbulent, occurring in the forward section of the spheroid. It detaches quite easily and is readily affected by surface variations.

17-5. DRAG COEFFICIENTS

The arithmetical calculation of drag coefficients is both stimulating and disappointing. Sampling calculations have been made for the flights described by Figures 17-5a and b and Figure 17-4. In the former case, between launch and 30,000 feet, the flight system is operating in the supercritical regime, with Reynolds number of approximately 2×10^6. A $C_D = 0.4$ is appropriate, from inspection of the model curve of Figure 17-7. In the rise portion, between tropospheric penetration and exiting, the value of C_D would be about one-fourth of model value for the supercritical regime of flight. Calculated figures for R_e are of the order of 5×10^5. Above the tropospheric demarcation to float, calculated values of R_e are of the order of 2×10^4, corresponding to the subcritical regime, with an idealized value of 0.4 for C_D.

Drag coefficients can be calculated by the expression relating to a sphere (Schlichting, 1968). The frontal areas of the balloons are determined from the shape curves by Smalley (1960). No consideration is made for relative mass effect or random surface orientation or lack of sphericity. The calculated values follow the model curve almost ideally – except that the absolute values are greater than the model values by a factor of 4!

It would be orderly to correlate the changes in drag coefficient with rotational action of the gondola. However, the very loose coupling between balloon and gondola and the large difference in the moments of inertia of these two bodies negate any such conjecture. The balloon wake effect is a minor energy source when compared with the massive magnitudes of fabric unfolding forces and rudderlike actions.

The distinct variability and longitudinal extent of the wake associated with these large Reynolds numbers do indicate the likelihood of unreal ambient sampling of the atmosphere – unless the sensing system is displaced seven to ten balloon diameters from the vehicle.

17-6. PENDULAR ACTION

Since this paper is intended to summarize the flight performances compiled for this program, a sample pendular measurement presented previously (Toolin and Poirier, 1970) is included. The flight systems have behaved like simple pendula, with amplitudes never exceeding 4 degrees and becoming less than 0.1 degree at float.

Acknowledgments

The authors wish to express their appreciation to the personnel of the Balloon Flight Requirements Analysis, Instrumentation and Test Branches at AFCRL for their continual excellent support and selfless cooperation. Mr. J. Dwyer, AFCRL, has been particularly helpful in the recent phases of this work.

References

MacCready, P., and Jex, H. (1964) Study of Sphere Motion and Balloon Wind Sensors, NASA TM X-53089.

Morris, A., and Stefan, K. (1969) High Altitude Balloons as Scientific Platforms, National Center for Atmospheric Research, Boulder, Colorado.

Schlichting, H. (1968) Boundary Layer Theory, McGraw-Hill, N.Y.

Smalley, J. (1966) Balloon Shapes and Stresses Below the Design Altitude, NCAR-TN-25.

Toolin, R., and Poirier, N. (1970) Sun oriented atmospheric optics measurements using the high altitude balloon, Proc. Sixth AFCRL Scientific Balloon Symposium, AFCRL-70-0543: 75-90.

Contents

18. The French Balloons and Their Application

R. Regipa
Centre National d'Etudes Spatiales (CNES)
Paris, France

18-1. PROGRAMS ACHIEVED

The Centre National d'Etudes Spatiales, since 1972 responsible in France for the development of space techniques for scientific purposes, has directed the work on balloons as complements to probe-rockets and satellites.

This complementarity of balloons is expressed not only in space (where, very schematically, satellites have an influence zone above an altitude of 200 kilometers, balloons below 50 kilometers, and probe-rockets alone are able to cover the intermediate zone), but also in other ways, either as autonomous vehicles for the transport of scientific experiments, or as an integral part of a complex and costly system.

18-1.1 Balloons: Autonomous Vehicles for Transport of Scientific Experiments

The object was to establish a system of exploitation of balloons with the following main characteristics: low cost allowing performance of a large number of tests; facility of putting into use, allowing systematic exploitation in organized centers; and especially, exploitation on demand for scientific campaigns carried out in specific areas and at specific periods of time.

These goals have been achieved with Tetroon stratospheric balloons, a "zero pressure" type, carrying payload weights less than 300 kilograms at altitudes between 30 and 40 kilometers.

18-1.1.1 TETROON BALLOONS

These balloons are in the shape of a tetrahedron at the top of which is attached the payload. They are made from plastic film of constant width which runs from the top along the tetrahedron surface in a spiral form; this hot-air sealing by the covering is continuous and without preliminary cutting. A polyethylene film is used, 25 microns thick and 3.3 meters in standardized width. Very accurate physical, mechanical and geometrical specifications, laboriously established, allow us to obtain constant quality products from our suppliers.

Three manufacturing units have been installed in a plant less than 1000 square meters in surface, two of them for balloon production of volumes greater than 50,000 cubic meters, the other for the production of smaller volume balloons, mainly auxiliary launching balloons.

The tetroon shape allows production at a very good price, but it is not physically adapted to the balloon's realization. Therefore, dimensions are limited to a volume of 85,000 cubic meters and to scientific loads of 200 kilograms. The annual production capacity is 150 balloons of 85,000 cubic meters and several hundred auxiliary balloons.

On request, any volume can be realized from standard polyethylene.

18-1.1.2 LAUNCHING OPERATIONS

The launching method retained uses the "auxiliary balloon". One or several auxiliary balloons of a few hundred cubic meters are filled with hydrogen, tied above the loads to be carried, and tethered to the ground by means of cables with pyrotechnic release. The main balloon is maintained in a launching system with three mobile rods for launching. Weighing is done on a scale supporting the launching system. On either side on the scale we find the inflation bubble and the rest of the main balloon curved on the ground on a protection cover.

After inflation, generally with hydrogen, the balloon is launched; a few seconds later the one or several auxiliary balloons are also launched. These impose ascensional speed to the loads carried, and when all balloons and loads are aligned in the axis of the main balloon, all auxiliaries are released. This launching method was used for several years and was based on a pyrotechnic device commanded by a barometric capsule (working at 1000 meters in altitude). This device caused a few accidents and was recently replaced by an automatic mechanical launching device. Allowing rotation of the experiment in relation to the balloons, it ensures very gentle separations and perfect safety in functioning. Furthermore, it is reusable after each recovery.

This launching method can be used in nonprepared areas without important means on the ground and thus is particularly suitable for scientific campaigns.

Establishing balloon launching stations in France required a thorough study of the problems concerning air traffic safety. These problems motivated the choice of Aire-sur-Adour in the southwest, and in the summer the auxiliary station of Gap in the southeast. All balloons are equipped with active radar response devices and are continuously tracked, not only by CNES, but also by civil and military air traffic navigation departments.

Very precise weather forecasts determine launchings and allow practically 100 percent recovery with the help of aircraft and ground vehicles with homing radio equipment.

Launching stations are equipped with telemetry and remote control equipment and test integration laboratories.

About 150 flights are done each year (see Table 18-1).

18-1.1.3 DEVELOPED EQUIPMENT

These comprise necessary operational equipment for flight realization, scientific equipment for telemetry, remote control and localization, as well as necessary stabilization devices for some experiments. Some scientific equipment follows.

(1) One IRIG standard FM/FM telemetry functions in the VHF range. Remotely controlled is the PCM/PSK type by means of which five functions can be materialized. These two very cheap equipments allow us to carry out low cost flights without recovery, especially outside organized centers.

(2) A more complex telemetry, remote control, and localization integrated system provides either an IRIG standard FM/FM telemetry with a very stable transmitter and very low signal-to-noise ratio, or a very high performance PCM telemetry. Its accuracy is independent from liaison and is increased; the number of emitted parameters can be higher than 100.

Remote control is of the PCM/PSK type with an address system particularly for simultaneous flights allowing the use of the whole instructions capacity. Telemetry transmitter and remote control receiver are linked to a single antenna by means of a duplexer. The addition on the remote control emission on the ground of a localization signal retransmitted by the telemeasurement allows distance localization of the balloon (accuracy of about 3 kilometers).

(3) A stabilized gondola was developed to point a load of about 100 kilos accurately on the sun or on the stars. It works in the following way. The servo control assembly which has the function of orienting the gondola is rigidly linked with the experiment. The gondola which has three degrees of freedom is oriented by means of drive units supplying torques along three axes. The gondola is

Table 18-1. Launching Center Activities

	1967	1968	1969	1970	1971
Flight Number	197	183	146	134	142
Scientific flights	125	141	109	115	120
Technical flights	72	42	37	19	22
Flight Quality					
Operational flights	196	171	142	134	142
Successful	152	148	129	124	124
Balloon failure	31	18	13	10	13
Equipment failure	3	1	1	0	2
Launch fai' re	10	4	0	0	3
Percent Failure	22.5%	13.5%	9.8%	7.5%	12.5%
Performance					
Overall great payload (tons)	12	17	20	20	22,4
Balloon volume ($10^3 \cdot m^3$)	5	6	8,5	8,5	9
Average payload (kg)	60	95	135	152	157
Average volume ($10^3 \cdot m^3$)	25	35	60	63	63
Tracking duration (h)	--	990	830	750	750
Geographic Location of Scientific Flights					
Aire-sur-Adour	102	82	70	71	76
Gap-Tallard	10	19	25	34	17
Campaigns	13	40	14	10	27
Overall number	125	141	109	115	120

suspended from its center of gravity by a table point with three concurring axes. The gondola is uncoupled from the balloon. The drive units are formed by inertia wheels to which desaturating units are added deadheads and vertical axis torque motor.

The detectors are as follows: gyroscope and magnetometer for the acquisition phase; sun or star detector for the pointing phase.

18-1.2 Balloons Associated with a Complex and Costly System

In this case (as in the Eole project, balloons are detectors of physical parameters and are associated with a complex and costly satellite system), balloons become actual mini-satellites, and their reliability must be absolutely ensured.

Production of envelopes (three meters diameter) and gondolas (weight four kilograms, length 10 meters) is extremely elaborate and needs the most modern techniques according to the very strict stresses imposed by the project.

18-1.2.1 ENVELOPE REQUIREMENTS

The thin envelope, light and resistant, must be absolutely leakproof to the particularly fugitive helium gas in very extreme environmental conditions (low temperature at night, solar radiation and ultraviolet rays during the day, and ozone). After a large number of tests on different materials on the ground and in flight, the choice was finally made of a laminated complex film made of two 23-micron polyester films bonded with polyester resin. Each envelope is made of 16 gores joined edge to edge by thermosetting tapes also made with polyester. In order to achieve the results expected, work concentrated essentially on: (1) selection of good quality basic materials by inspection prior to production of the balloons; (2) improvement of existing production techniques to reduce frictions and abrasion of the material; (3) introduction of a systematic inspection procedure during and after manufacturing; (4) conditioning of the envelopes for transport; and (5) launch and prior-to-launch testing.

Finally, at the end of the serial production of 720 envelopes where the cost of inspection plays a big part in the final cost, a sample of 120 balloons was submitted to a complete series of ground tests on mechanical and physical characteristics and then were subjected to flight tests.

These flight tests were performed, as most completion campaigns, from Pretoria (South Africa). This station is equipped with all the necessary test installations for envelope preparation prior to launching and therefore has helped in the setting up of launching procedures for balloons and gondolas in the Eole prototype station in Aire-sur-Adour. Three identical stations have been established in Argentina: Mendoza, Neuquen, and Lago Fagnano.

18-1.2.2 THE EOLE EXPERIMENT

The Eole gondola consists of the following items:

(1) A solar cell generator
(2) A battery and its protection cone
(3) A battery load regulator
(4) A set of pressure, superpressure and temperature sensors
(5) A transponder
(6) An antenna
(7) A ballast bag
(8) A radar reflector.

Five hundred operational gondolas were made. Extremely strict requirements were imposed on the suppliers. Considerations included: (1) Electrical functioning stresses on the stability of different parameters, receiver sensitivity, power supply, reduced consumption; (2) climatic stresses corresponding to storing,

launching and flight; and (3) production stresses imposed by air traffic safety without compromising handling facility, and taking into account mechanical stresses due to flight conditions.

The Eole experiment was at 200 millibars. Collision risks with aircraft had to be evaluated and made known. Even though the collision risk is minimal (probability of 0.0003 per month), important work was carried out to ensure that the collision risk satisfied the safety standards applied to aircraft operations.

Impact tests consisted of throwing gondola parts onto cockpits, jet engine parts and running jet engines, or, inversely, throwing a cockpit or an engine part onto the gondola part to be tested which remained fixed.

Exploitation of these throws allowed us to define production concepts on the density and reliability of the components.

18-1.2.3 EOLE RESULTS

The result of the Eole operation was positive. Scientific data processing necessitated us to obtain daily replies from 250 balloons during a continuous period of 15 days.

The objective was largely achieved. More than 250 balloons in flight during more than 46 days registered more than 250 replies per day during 25 days, and this in spite of a heavy handicap due to the accidental loss of 89 balloons at the very beginning of the sowing.

The technical tracking situation was as follows on the 15th of July 1972:

30 balloons still alive

16 balloons doubtful

433 lost

Among the still operative balloons, the oldest one launched on 29 August 1972 has 321 days of life, and the latest launched on 21 November 1971 has 222 days of life. Mean life duration of operative balloons supplying replies is 255 days. Mean life duration of all balloons is 105 days.

18-1.2.4 FLIGHT TESTS

Preliminary flight tests from Pretoria were carried out with two telemetries of different complexity emitting in the 3-30 MHz range, where the ionospheric reflection allows, by means of multiple reflections, ranges of several thousand kilometers.

The simplest of these equipments is the GHOST telemetry, from an original idea of the American N.C.A.R. A Morse code letter aimed at a given sensor is directly proportional to the frequency of the said sensor. An improved version with four sensors is industrially manufactured, and balloons are tracked by a few very simply equipped reception stations.

A more complex equipment was developed to remedy the faults of the GHOST gondola, including low accuracy of measurements, small number of parameters, no possibility for study of nighttime phenomena. The type of sensor signal being unchanged, the frequency is digitized. A binary word modulates a transmitter in amplitude; 15 parameters are thus emitted. Supply is provided by an Eole battery recharged by a solar generator. Two emitting frequencies are also used; one for day, one for night. The unit with antenna (a 50-meter vertical dipole and an 8-meter horizontal dipole) is quite difficult to launch, but it has allowed us to obtain many conclusive measurements during flights carried out in 1968 and 1969.

Furthermore, note the duration record of 603 days established by a superpressure balloon at 150 millibars equipped with a GHOST gondola.

Discontinuous reception of telemetrics does not allow, except in rare occasions, direct operational use of long flight duration superpressure balloons. Balloons must be integrated in a complex data gathering system, for example, TIROS-N in course of development. On the other hand, these equipments seem sufficient for some technical studies when adjusting the balloons.

18-1.2.5 ALCYON SYSTEM

This system, comprising a zero pressure carrier balloon associated to a superpressure stabilized balloon, was flight tested in March 1970 in Pretoria. The carrier was a tetroon balloon of 10,000 cubic meters, made of 20-micron polyethylene film. The stabilizer was a special balloon 10 meters in diameter, made of laminated polyester (2 × 23 microns).

The stabilization principle was demonstrated, but no operational development of this system was performed due to the complexity and, mainly, the cost necessary to achieve acceptable receipt of scientific data.

18-2 SHORT TERM PROGRAMS

Present budget expectations do not allow us to define important long term programs. But the existing operational, technical, and industrial potentials and credits granted by the French Government nevertheless allow us to ensure continuation of slow but real progress in the use of balloons for scientific programs and mainly for application programs.

Among technically possible realizations, we only retain those that are most economical on a short term basis, unfortunately to the prejudice of prestige realizations.

18-2.1 Free Stratospheric Balloons

The interest in these balloons for scientific experiments leads to pursue and develop their usefulness.

Tetroon balloons will remain at their present development stage with maximum volumes of 85,000 cubic meters for scientific loads less than 200 kilograms.

For the last three years, experimenters have presented more complex experiments of 300 kilograms launched with American "natural shape" balloons of 85,000 and 300,000 cubic meters.

Necessary operational materials already developed and used will be improved, such as launching and weighing systems; unballast caisson, indispensable for flights of 300,000 cubic meter balloons; and different safety and versatility equipments.

The natural increase of requirements following the first successful flights and the cost of American balloons in France, which considerably strained the budget of the Balloons Systems and Projects Department, led to the decision to accelerate the design of our own "natural shape" balloons from 1971. A first flight of a 100,000 cubic meter balloon made of 20-micron polyethylene, reinforced with triplex tapes 20-13-20 and loaded with 400 kilograms, was performed in May 1972.

The industrial development of operational 100,000 and 350,000 cubic meter balloons for 400-kilogram loads is being actively pursued, in spite of difficult safety problems relative to testing above areas with a high population density.

On the other hand, nonsubsidized programs on larger balloons and on stratospheric, superpressure balloons with dissymmetric lobed gores are also being carried out. Furthermore, with cost effectiveness concern, technical and organizational improvements will be brought to all the exploitation phases: preparation, integration and putting into use of experiments and gondolas, flight realization, data reproduction, and so on.

18-2.2 Free Superpressure Balloons

The TIROS-N project brings an important workload to the electronic engineers responsible for the design of balloon gondolas. The performance required from the TIROS-N project mainly test the feasibility of an ultra stable pilot oscillator to ensure accurate localization of the mobile platforms, solely by means of measurements of the Doppler effect in the single sense liaison: platform to satellite. Several test campaigns are projected in Pretoria. Eole-type balloons made of different complex materials will be used with special technological gondolas. Without a long term exploitation program, the industrial production procedure for operational superpressure and free balloons, for long duration flights at altitudes

from 1 to 30 kilometers, with light loads, will be defined to satisfy the large number of proposals for scientific utilizations without delay and at the lowest cost.

This program, very vaguely defined, concerns spherical balloons from 1 to 20 meters in diameter and is part of the general study made on complex materials and on production of low cost leakproof envelopes.

18-2.3 Geostationary Balloons

A large, long term program for the application of geostationary balloons is in the course of study. It leads to very ambitious realizations of power driven platforms, several million cubic meters in volume, stationary and permanent at altitudes above 20 kilometers.

In a first phase, where the essential purpose is to simplify data acquisition during flights of long life free balloons, we start the industrial development of tethered balloons with low operational cost.

Taking into account the strong winds in winter at average latitudes between about 6 to 15 kilometers, maintaining a balloon in this altitude range cannot be considered. On the other hand, balloons situated above 22 kilometers would be of a prohibitive size due to the decrease in density in altitude and to the winds profile. Therefore, two types of balloons can be considered: (1) a tropospheric balloon for 0.2 to 6-kilometer altitudes and (2) a stratospheric balloon for 15 to 22-kilometer altitudes.

18-2.3.1 TROPOSPHERIC TETHERED BALLOONS

Experiments of the National Meteorological Office and the use of such balloons by the Commissariat a l'Energie Atomique (communication presented in 1970 at the preceding AFCRL Scientific Balloon Symposium) show evidence of the feasibility of this vehicle.

Technical developments and present industrialization allow us to intensify their use; they are very light balloons, with low operational cost. A probation model of 65 cubic meters was manufactured and used for the adjustment of a technological gondola allowing mechanical, thermal, and aerodynamic measurements. The Zodiac-Espace Company develops these balloons, and the CNES takes a direct part only in the flight tests.

18-2.3.2 STRATOSPHERIC TETHERED BALLOONS

We cannot possibly imagine a tethered balloon in troposphere, if aerodynamic shapes have not been very carefully studied; this does not apply at high altitude. The natural shape of stratospheric balloons with gores is then imposed because of its excellent aerostatic efficiency. Two experiments made by the National Meteorological Office have shown the feasibility of this system:

(1) In June 1970, a tethered balloon for the first time crossed the zone of jet currents and reached a ceiling of 13,000 meters off Corsica.

(2) In October 1971, a record altitude of 18,000 meters was reached in Guiana.

These vehicles seem well adapted to scientific work, particularly for Meteorology and Aeronomy; therefore, the CNES and the National Meteorological Office have set up a common development program.

Checking of the missions that could use such platforms is being done at present. But, already the first phase of the program is fixed in function of a mission with semi-operational character in the GATE program (GARP Tropical) for the summer of 1974, comprising one main meteorological experiment and auxiliary tests (environment, telecommunications, and so forth).

A technological test of the platform appears also to be necessary in September 1973 at the Guiana Spatial Center.

Appendix A

Technical Development and Industrialization

Besides operational programs, studies on technical development and industrialization were started.

Existing mechanical and electronic industries and the experience of management, organization and technical follow up acquired with probe-rockets and satellites have allowed us to succeed in the realization of gondolas.

On the other hand, the thin plastic film industry, which was very competent in the field of packaging, had to improve, in spite of a lack of industrial and economical motivation, in order to reach a sufficient technical level for the production of balloon envelopes.

First of all, the CNES, inspired by the remarkable American realizations, industrially developed tetroon polyethylene balloons. To succeed it retained for several years all the technical responsibilities and assumed entire financial support of the operation.

However, the Eole project, with a very different budget and real economical and technical motivations raised by its difficulty in realization and its character of a project applicable on a world scale, allowed us to start long term development of balloons.

Finally, the industrial policy of the CNES, which is to let the French and European industry benefit from the results of space research, required us to work in priority with the existing industries, to the prejudice of internal technical developments which very often seem easier and quicker to responsible engineers.

Therefore, the work started on materials and sealing techniques is long and delicate, but the first results show that a specific industrial potential is thus set up and allows us to already foresee future development on a realistic and efficient basis.

18-A1. DEVELOPMENT OF MATERIALS

For each balloon project the materials necessary for the production of the envelope need to be specified.

Criteria for selection: (1) from the project itself (flight level, flight duration, load carried); (2) in function of standards imposed by the use of the balloons (conditioning, launching, ascension, ceiling).

Selection is nevertheless difficult: Properties required are not always expressed in simple and realistic technical terms and are sometimes incompatible; for example, mechanical strength, flexibility and tightness. Products available in industry are ill-adapted and some very interesting materials remain at the research laboratory level because the balloon application does not justify their development. However, from a large number of studies and tests with the help of classical and original means, it was possible to define a first selection of materials for zero and superpressure balloons and also to plan an improvement program.

18-A1.1 Materials for Zero Pressure Balloons

We retained polyethylene (with a low vinyl acetate percentage) among the polyolefin films, mainly for the flexibility quality: 25 microns thick, 3.300 meters wide (folded in 1.650 meters) for tetroon balloons (homogeneous envelope) and 20 microns thick, 1.850 meters and 2.500 meters wide (flat film) for stratospheric balloons with gores (equal stress distribution due to the natural shape). Note the distinction between the gas envelope and the load support with reinforcement tapes.

The main difficulties met in supplying these films are caused not by the widths and thickness required, but by the dispersion of thickness and mainly by the heterogeneity of production within one production run. Consequently, the polyethylene supply is submitted to specifications established from statistical analysis of the physical and mechanical laboratory test results on very large quantities of film.

These specifications have allowed us to succeed in the complete industrialization of tetroon stratospheric balloons (materials and production) without any sensible alteration in the quality of the balloons.

In parallel, the following works were undertaken: (1) Studies in industry for the improvement of the polyethylene extrusion conditions and research of new resins allowing us to obtain films suitable for balloon production; (2) laboratory work, particularly on the visual aspect in polarized light, in order to carry out continuous reception controls and to establish nondestructible methods for the study of physical and mechanical parameters; and (3) systematic control of cold brittleness by two methods: (a) dropping a ball on circular samples and examining the tear; and (b) bursting cylindrical sleeves and recording stresses, pressure and tear.

18-A1.2 Superpressure Balloons

For superpressure balloons (long life duration) no single film could be retained. It was necessary to design multilayer complex materials where each component corresponds to a well defined function. The simplest of these is the laminated 2 × 23-micron polyester, used for the Eole project. The large number of complex possibilities justifies important studies to specify selection criteria and to establish original testing means. Among the means presently used or about to be achieved, we particularly point out the following.

18-A.1.2.1 DETERMINATION OF PERMEABILITY COEFFICIENTS

Transmission of a gas through a polymer is done either by pre-existing pinholes (effusion) or by absorption followed by desorption on the active centers of the material and mainly in the case of complex films by the temporary formation of interstices due to the thermic agitation which stretches the molecular structure.

The permeameter used from a group of exchange cells allows us to test film surfaces between 100 and 1,200 square centimeters. Measurements are made by chromatography and are generally followed by a global leakproof test on spherical balloons of three to four meters in diameter in order to check damages caused by rumpling and abrasion. On this subject, tested balloons are submitted on a vibration bench to very severe reproducible vibration tests.

18-A.1.2.2 AGING TESTS

These allow us to analyze damage of mechanical properties due to the sun ultraviolet rays favored by the presence of ozone in the atmosphere and to evaluate thermo-optic characteristics, in particular, the solar absorption coefficient which acts directly on the thermal equilibrium and pressure of the balloon.

The simulation of environmental parameters with respect to actual flight characteristics required choosing a lamp true to the sun's spectral energetic distribution (xenon lamp), and computing energetic doses received by the balloon

(presence of high pass filters for a specific period of time) as a function of the day time variation of solar ultraviolet lower limit and of solar intensity value and as a function of wavelength with respect to light values, with work in actual time and day/night alternations. Tests also considered temperature conditions and atmosphere composition (pressure ozone ratio).

The simulation is followed by spectroscopic and dynamometric measurements on blank and aged films and is completed by viscometric measurements, allowing us to define the critical wavelength range, the nature of damages, and the effect of different parameters on the damage rates.

These tests are very long to carry out; therefore a new complex system for the whole simulation of balloon meterials representing environmental conditions at all flight levels is just to be achieved. It allows us to simulate in the same time and for a period of several months circular samples of 50-centimeter diameters (1) solar radiation, (2) external environmental atmosphere (pressure, temperature, ozone concentration), (3) internal atmosphere of the balloon (helium pressure), (4) balloon mechanical stresses and their variations over 24 hours.

On the spot measurements are also provided on curvature radius of the sample tested as a function of helium pressure, optic transmission and permeability of the material to helium.

This equipment will be in operation at the beginning of 1973 and will give us an important means for study and selection of balloon materials.

18-A2. DEVELOPMENT OF SEALING TECHNIQUES

Important choice criterion for a material is its capacity for assembling to itself respecting the following specifications: (1) mechanical strength of the seal at least equal to the strength of the base material, (2) slow variation of the elasticity modulus across the sealing to obtain an almost homogeneous envelope, accepting folding, rumpling and energization without a privileged zone of stress concentration, (3) damage of physical properties due to atmospheric factors and aging as low as that of the base film, (4) high continuous sealing speed and constant quality, and (5) if possible, low cost in sealing realization. Numerous sealing methods were studied and used, such as thermal, ultrasonic, hyperfrequencies, and hot and cold welding.

At present, in order to develop industrialization, we retain thermo sealing which corresponds best to the specifications imposed. The hot welding with adhesive, largely used in the Eole project for assembly of laminated polyester films, is retained for specific applications because of its high cost.

Therefore, the sealing function is highly decisive in the definition of new complex materials, and at present it leads us to lay on each side of complex materials a polyethylene or other film with equal properties (in particular, sealing ability, strength, flexibility). This laying is done either by lamination or by extrusion. Furthermore, its presence provides a better aptitude to folding and rumpling in increasing the curvature radius of the folds of the other composing materials which fill the functions of mechanical strength, tightness, non-tearability, and so forth.

One of these complex materials is the Triplex "polyethylene-polyester-polyethylene" 20-12-20 microns thick, which used as a basic complex material, with thoroughly studied properties from well known elements. Other complex materials are now being industrialized with different thicknesses of composing elements; others are reinforced with nets of grids or clothes; for each type of balloon an appropriate complex material can be defined.

With the precaution of selecting the internal elements of the complex materials, such as that their melting temperature be superior to polyethylene, the sealing technique was considerably improved. In fact, these internal elements serve as a melting polyethylene carrier belt, and this unit with constant calorific capacity by length unit can be considered as a heat quantity regulator which allows us to dose the sealing depth.

18-A2.1 Sealing of Complex Materials

Sealing is done in the following ways: (1) heating zones to be sealed at intermediate temperature between the temperature where polyethylene begins to meet (about 130° C) and the melting temperature of the internal elements (about 170° C, for the other polyesters), (2) application under pressure and (3) cooling.

This heating temperature and the thickness of the heated materials determine the heat quantity applied, and define the sealing thickness without risk of damage to the internal elements. Great versatility in the design of sealing equipment and facility in control are thus possible, and this is very interesting for industrialization. Continuous high speed assembly is possible and the speed regularity is not a critical parameter. The necessary heat for adequate warming can be transmitted either by conduction (constant temperature heating roller), by convection (hot air with constant temperature and flow), or by radiation (infrared lamp).

The choice of heat supply and consequently the design of the assembly machine are defined for each seal operation to be carried out.

Example realizations are: overlapped seals, for which it is possible to heat one of the two elements only (for example, a quartz tube placed in one focus of a reflector elliptic cylinder) and edge-to-edge sealing by means of covering tapes,

where the tapes only are heated (generally by contact winding on rollers maintained at constant temperature).

Materials designed in this way are capable of realizing thermo-welding assembiies as in the case of the Eole polyester balloons.

18-A2.2 Correct Positioning

Correct positioning of the elements to be sealed is critical and must be considered in two directions: transversely, to define accuracy of the covering or of the edge-to-edge and in parallel to define the relative balance of lengths.

Transverse positioning is automatically achieved by a system of elastic small rollers slightly tilted and constantly maintaining one edge of the film against a fixed plan, without generating an important effort in the progressing.

Parallel positioning is more difficult to achieve. Without considering, for the moment complicated slave systems, several simple solutions have been designed, with all the more accuracy that the heat lengthening of complex material is very low and that the imposed stresses are reduced. These conditions affect, of course, the design of complex materials machinery.

18-A2.3 Edging

Edging of a thin polyethylene film by a triplex reinforcement tape is possible by applying regulation functions in heat quantity and positioning. An elastic insertion of the film on the tape has to be done, with progressive decreasing of sealing depth from the outside to the inside edge of the tape, which can also keep a very short unsealed portion simply stuck against the film by effect of superficial stresses. For this, it is enough to cool the edge on a specified width after heating the tape at polyethylene melting temperature, before applying to the film. The outside edge maintained very hot allows easy cutting of the polyethylene film on the right of the tape. Thus an edging and cutting system is achieved and by transverse displacement within a program it allows us to define the polyethylene gores cut and edged.

18-A3. INDUSTRIALIZATION

Following an agreement between the Centre National d'Etudes Spatiales and Sodiac, the firm Zodiac-Espace was created in 1970 with the mission to build rapidly a plant specialized in balloon manufacturing, near the Spatial Center of Toulouse where the Balloon Systems and Projects Department is located.

This factory now comprises essentially: (1) a 2200-square meter central building for tetroon and superpressure balloon manufacturing, for materials supplyi and controls service, and for research - prototypes service, (2) a workshop, 10 meters wide and 150 meters long for gores stratospheric balloons manufacturing, and (3) a 1500-square meter building for materials and balloon storage, a workshop for the prototypes adjustment and maintenance of production machines. All these buildings are air conditioned, with dust extraction according to industrial standards, and lighting is particularly well designed.

Three departments were established. The responsible engineers and technical staff were trained at the CNES in the Balloon Systems and Projects Department during the year preceding completion of the building. These are (1) design and prototype service, (2) supplying and material control service, and (3) production service. Constant cooperation was established between the CNES engineers and the Zodiac-Espace executives. It has allowed us to set rapidly into use an important industrial potential for balloon techniques. from now on satisfying numerous practical and theoretical problems.

The technical means available at present are

(1) Testing and material inspection laboratory

(2) Design office

(3) Mechanical workshop

(4) Production units for polyethylene tetroon balloons, consisting of production units for superpressure Eole type balloons, edging machine, mechanical and numerical programmed cutting for production of reinforced polyethylene gores or cutting complex material gores on request, continuous overlapped sealing machine, and fixed and mobile continuous edge-to-edge sealing machines.

Mobile machines can at present operate on a length of 150 meters along a special bench equipped with pneumatic carriers for suspension and presentation of the gores to be sealed.

We also have special machinery adapted to the sealing of auxiliary elements and to the finishing of balloons, and we have different equipment for conditioning and packaging.

These equipments are provided by existing contributions in the CNES and mainly by common CNES-ZODIAC-ESPACE realizations with the help of the local industry trained for several years in these particular techniques. They bring original solutions to the design and realization of electro-mechanical units.

Contents

19. The Flight of ATMOS I: An Extended Test of a Balloon Borne Radar Altimeter at the 100 mb Level

Dr. T.F. Heinsheimer
The Atmospherics Company
Rolling Hills, California

P. Trimm
Trimm Associates

J.P. Pommereau
Service d'Aeronomie, CNRS
Paris, France

Abstract

This report is a short discussion of the prelaunch activities, launch operations and flight performance of the ATMOS-I experiment, flown from Ascension Island on November 5, 1971 by the National Center for Atmospheric Research and the Atmospherics Company.

Carrying an Israeli made radio altimeter (Levanon, 1970) and an NCAR made Digi-Ghost telemetry system (TWERLE Technical Description, 1971), the flight met its objective of demonstrating the validity of the altimeter system in measuring variation of balloon height at the 100-millibar level.

19-1. BACKGROUND

In July 1971, the Service d'Aeronomie, CNRS (Paris, France), and the Atmospherics Company requested the assistance of NCAR in the implementation of

the altimeter portion of the Isentropic balloon (Blamont and Pommereau, 1970) system. NCAR therefore added to its TWERLE-I flight program a test flight, at the altitude range of the subsequent Isentropic test flights, of an altimeter ensemble.

NCAR proposed to use a standard radio altimeter of the type being made in Israel by the Levanon team. The altimeter would be controlled by a Digi-Ghost payload such that it would have sufficient time to make an altitude measurement (approximately 30 seconds) without interference from the Digi-Ghost transmitter (no HF transmission during operation of the altimeter). The altimeter would then pass the data to the Digi-Ghost transmitter, after which it would be telemetered using the Morse code letter forming scheme.

19-2. PRELAUNCH OPERATIONS

The rigging of the system is shown in Figure 19-1 as it appears at altitude. Figure 19-2 shows the packages on the rigging table. In order of its attachment (from the balloon) the equipment was as follows:

(1) a portion of aluminum foil folded into a "bow tie" to serve as a target/reflector for the Ascension FPS-16 tracking radar;

(2) a Ghost package (Litchfield et al, 1967) and a magnetometer cutdown device. The magnetometer assures cutdown if the balloon drifts into the Northern Hemisphere; the Ghost package provides sun angle data (call sign - 82104 QQQ) and provides power for the cutdown device;

(3) the Digi-Ghost and altimeter packages consisting of five structures – the pyramidal solar collector with power supply and transmitter, the Digi-Ghost electronics package, a small box containing a frequency divider and power cutoff circuit, the altimeter package, and the altimeter antenna.

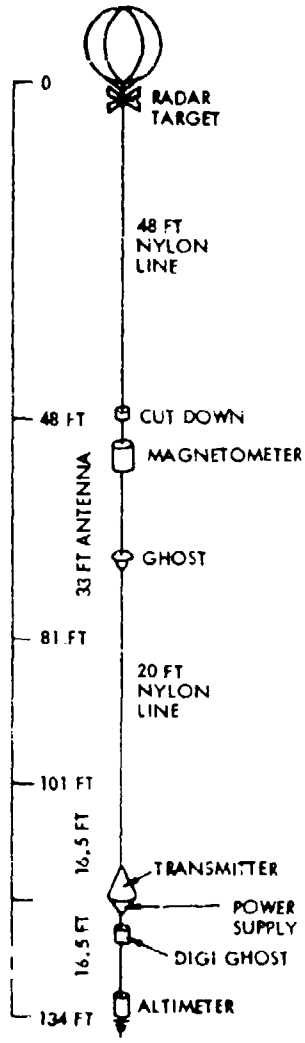

Figure 19-1. Flight Train - ATMOS I

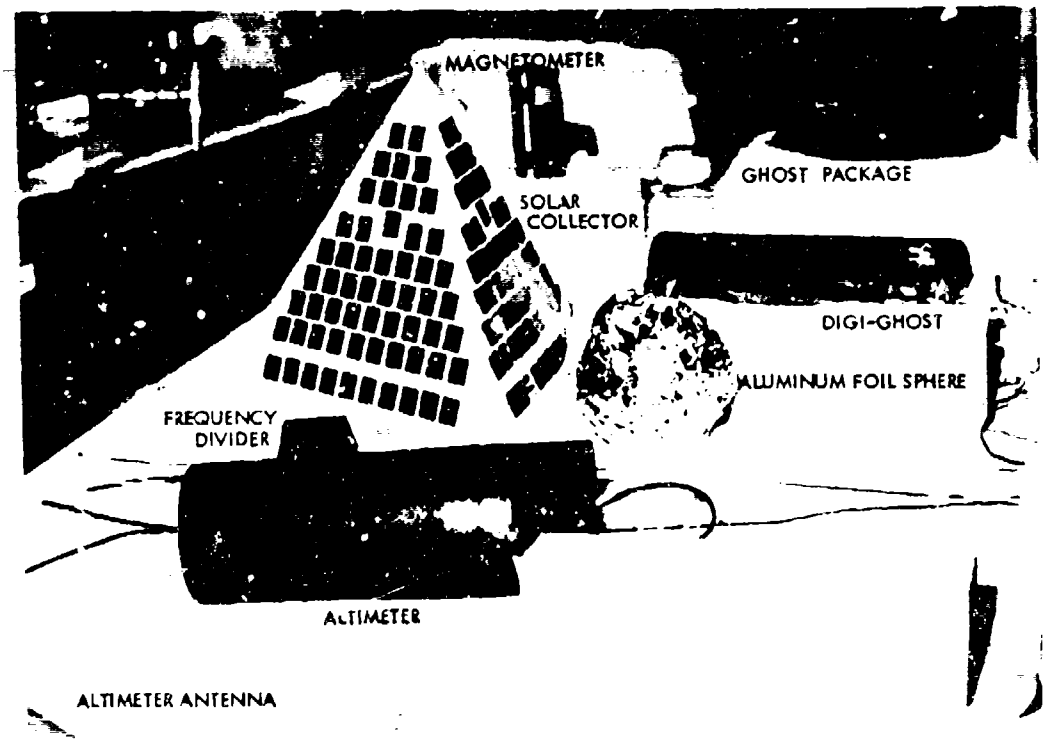

Figure 19-2. ATMOS I on Rigging Table

The ensemble was flown from a Raven 12-foot balloon (Mylar 3/4 × 3/4 mil laminate). The weigh-off sheet is depicted in Figure 19-3. Note that with the total weight of electronics plus rigging of 1079 grams, the planned float altitude was 109 millibars.

19-3. LAUNCH OPERATIONS

The balloon launch was conducted following the standard NCAR dynamic launch technique. The conveyor vehicle carrying the balloon and payload moved along the main runway – with the wind. An extremely smooth liftoff of the balloon and all packages resulted, despite a 20-knot wind and a total flight train length of approximately 150 feet. Liftoff occurred at 0715 GMT, November 5, 1971, through thin low clouds. Figure 19-4 shows the flight train of ATMOS-I just after launch. The code letters for this [illegible] ost flight were "RO"; transmission was at 15.022 MHz.

Balloon Weigh-off 100 ~~200~~ mb flight

Mfr. RAVEN Flight No. 82105 J

NCAR Code No. S/N 140

~~Cap or~~ No Cap

Balloon Mass 2813 Time of Launch 0716

Balloon Volume ~~9.42 m³~~ 25.63 m³ NOV 5 1971

Flight System

Balloon	2813 grams	Weigh-off: D.P. =	16.5 °C
Cut-down	grams	O.P. =	0 mb
Riggi[illegible]	grams	Balloon	2813 grams
2 electronics # = 1079 Rigging		Sleeve	1524 grams
Radar reflector	grams	Fittings (w/o)	300 grams
Ballast	grams	A. TOTAL	4637 grams
TOTAL ~~3282~~ 3010	grams	B. Grosslift	4389 grams
Free lift 12.7% = 497	grams	A - B	248 grams
B. Gross lift = 4389	grams	C.	53 grams
Final readings: left scale - 212		D.	0 grams
right scale - 87		C + D =	53 grams
(final scale readings) TOTAL	299 grams	A - B + C + D =	301 grams

T: 23.2°C
WB: 190
RH: 66%
DP: 16.5°C

FLOAT ALT.: 109 mb.

PAYLOAD: 1079

Figure 19-3. Weigh-Off Sheet – Flight 82105 J

Five measurements were made during the flight:

(1)	sun angle	made by the Ghost payload and used for position determination (Blamont et al, 1970)
(2)	altitude	Digi-Ghost Channel #1
(3)	temperature of the foil sphere (suspended beneath)	Digi-Ghost Channel #2
(4)	reference channel (33K ohm resistor)	Digi-Ghost Channel #3
(5)	internal temperature of Digi-Ghost package	Digi-Ghost Channel #4

For the purposes of this report, reference will be made only to the measurement of altitude and sun angle.

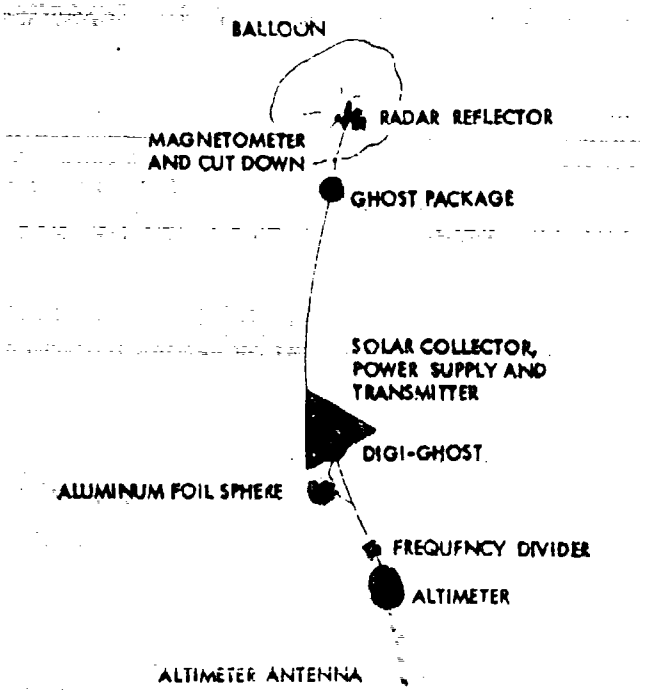

Figure 19-4. ATMOS I at Launch

19-4. FLIGHT TO CEILING ALTITUDE

The launch was tracked by the FPS-16 radar for some 3 hours. Once each second measurements were made of azimuth, elevation and range. A smoothed computed set of data was printed each 10 seconds. The altimeter yielded approximately 30 observations during the 2 hour period of ascent. From these data the flight to altitude is plotted in composite as Figure 19-5. It should be noted that at ceiling the altimeter reads some 40 meters lower than the radar data. This difference corresponds to the distance between the radar target reflector, attached to the load line just beneath the balloon, and to the altimeter antenna, suspended at the bottom end of the load line.

At ceiling, the Digi-Ghost's least significant bit quantization increment of 61.3 Hz limits the altimeter resolution to 22.7 meters of altitude.

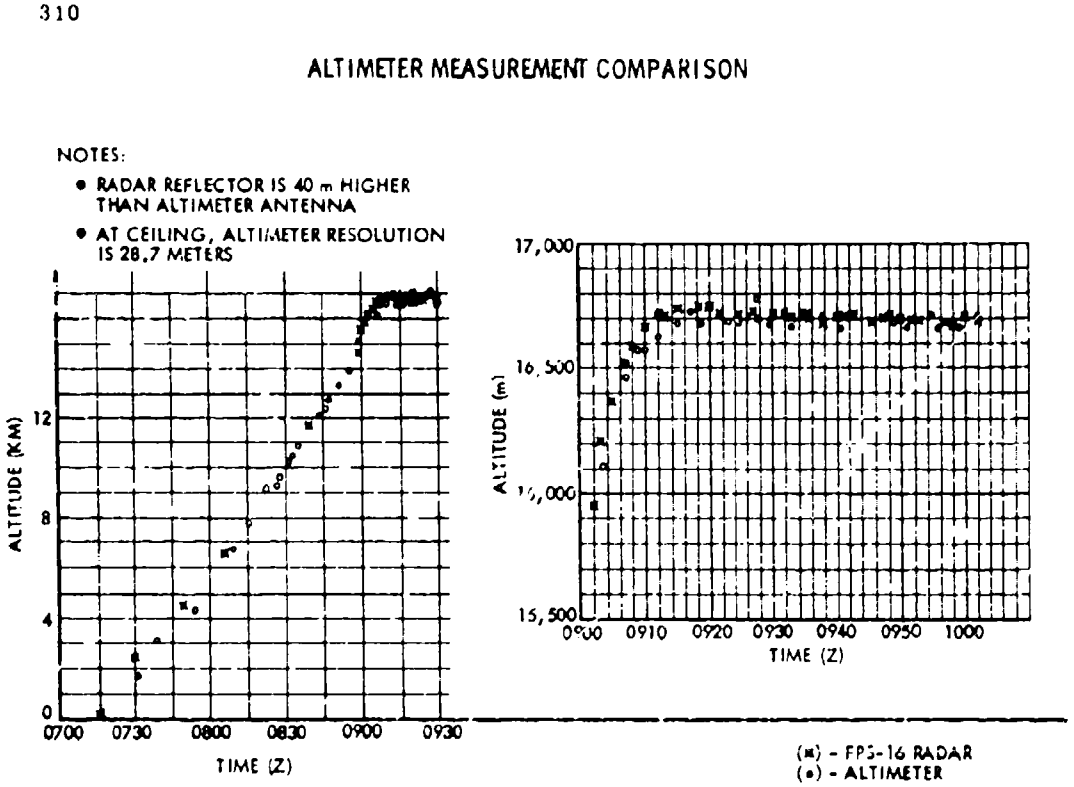

Figure 19-5. Flight to Ceiling Altitude

19-5. ALTITUDE ANALYSIS

The altitude data have been reduced manually using the technique developed by the authors. This technique, as explained in the data logging forms, allows altimeter observations to be rapidly translated into altitude without the use of any computer and with no loss of measurement accuracy or precision. It will allow real time evaluation of system performance in the field, a particularly valuable attribute during the early flights of the Isentropic balloon system when considerable altitude excursions are to be expected.

The daily altimeter data, summarized in Figure 19-6, are found using techniques previously discussed. The forms used to present the detailed daily data have been printed in quantity and are available upon request free of charge to anyone planning to fly a Digi-Ghost altimeter. Figure 19-7 shows a day over land (Africa); Figure 19-8 shows a typical day over water.

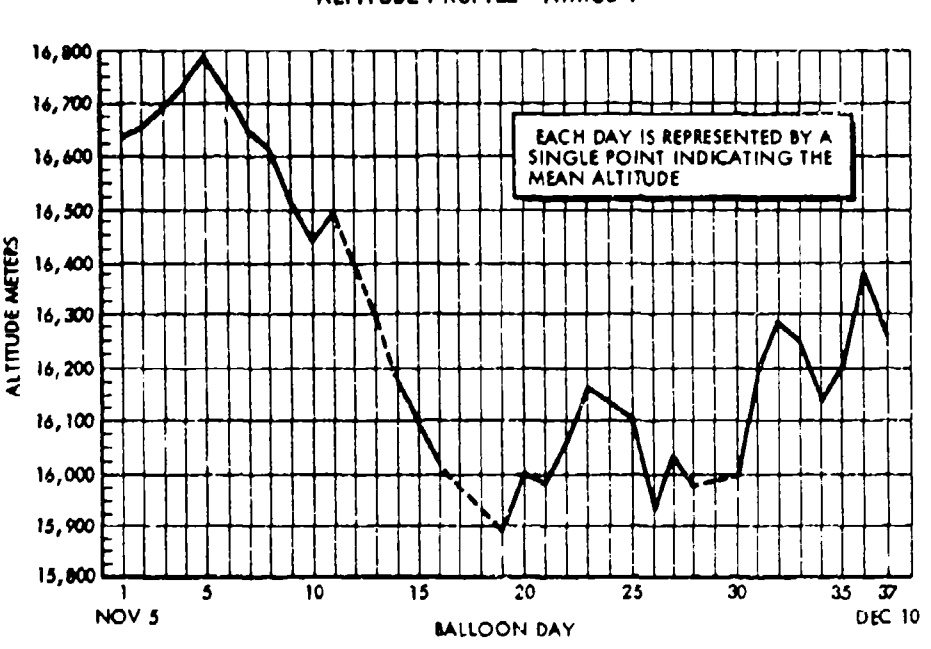

Figure 19-8. Flight Altitude Profile

19-6. TRAJECTORY ANALYSIS

The sun elevation data for the flight was processed in the usual manner, detailed below:

(1) In-flight calibration of sun sensor (see Figure 19-9)

(2) Hand plotting of all data

(3) Longitude by determination of time of local noon.

The altimeter data were also used to establish the trajectory. For each day, the longitude was determined by solar observation, or by estimation if solar data were inadequate or nonexistent. Latitude was then found using the altimeter information, in the following manner. A family of curves was drawn giving the height of the 100-millibar level as a function of the balloon altitude and temperature (assuming the balloon is close to 100 millibars, flying at constant density, and in an isothermal region). These curves have the form shown in Figure 19-10.

For each day, the daily 100-millibar meteorological charts of the Southern Hemisphere are used to provide a plot of the temperature and height of the 100-millibar level along the longitudinal meridian associated with balloon noon. This allows the plotting of curve A.

DATE 16 NOV '71 BALLOON R0 STATIONS P.T. PAGE 1 of 2

atmospherics

MAXIMUM ALTITUDE (METERS)

	N=1	N=2	N=3	N=1	N=2	N=3	N=4	N=1
S				4,521	9,267	14,013	18,759	2,155
D				3,996	8,216	12,436	16,657	2,016
R	18,409			3,577	7,379	11,181	14,982	1,892
G	12,201			3,227	6,691	10,144	13,604	1,781
U	9,209	18,743		2,945	6,116	9,286	12,457	1,683
K	7,340	14,905		2,702	5,639	8,556	11,483	1,589
W	6,090	12,405	18,720	2,497	5,229	7,941	10,663	1,508
O	5,194	10,613	16,032	2,314	4,852	7,390	9,929	1,432
		O_v = ZERO			O_v = 1			O_v = 2

BASE FREQUENCY (Hz)

	N=1,2,3	N=1,2,3,4	N=1
S	200	31,600	63,000
D	4,125	35,525	66,925
R	8,050	39,450	70,850
G	11,975	43,375	74,775
U	15,900	47,300	78,700
K	19,825	51,225	82,625
W	23,750	55,150	86,550
O	27,675	59,075	90,475
	O_v = ZERO	O_v = 1	O_v = 2

INCREMENTS		
MID.		MIN.
0	S	0
490	D	60
980	R	120
1470	G	185
1960	U	245
2450	K	305
2940	W	370
3430	O	430

T (μs)	Corr. (m)
1.2	−180
1.3	−195
1.4	−210
1.5	−225

1. Enter Time and Code Group.
2. Use Max. Altitude Table to find altimeter harmonic (N) & Digital Ghost overflow level (O_v) yielding reasonable altitude.
3. Use Base Frequency Table to find Base Frequency.
4. Use Increment Table to find middle & minor increments.
5. Add Base Frequency to increments for Altimeter Frequency (f).
6. Compute (1 SM f)x 10^8
7. Add "T" correction to give altitude, (h).
8. For balloons at ceiling - do 1-7 only once, then:
   - find resolution element from $\Delta h = c/2\Delta f$ (
   - establish reference Code Group, enter here ____ (Altitude ____)
   - find values of adjacent Code Groups by listing them in order &
   - adding (subtracting) successive resolution elements.

STATION	TIME	CODE	N	O_v	BASE FREQUENCY	INCREMENTS MID	INCREMENTS MIN	ALTIMETER FREQUENCY	ALTITUDE (1 SM f) x 10^8	ALTITUDE T CORR	ALTITUDE (h)
PTA	0730	USR	4	1	39,450	0	430	39,880	15,096	225	14,795
	0753	GUO	3	0	27,675	1960	185	29,820	15,060	225	14,835
	0805	GUO	3	0	27,675	1960	185	29,820	15,060	225	14,835
	0838	QUO	3	0	27,675	1960	60	29,695	15,040	225	14,815
	0902	SUS	3	1	31,600	1960	0	33,560	15,400	225	15,175
	0927	WOO	4	1	35,525	1960	120	39,365	15,260	225	15,035
	0947	R00	(4	R0	Higher Orders		WOO	ΔH = 23 M)			15,139
	1046	500	2	"	"	"	R0	"			15,176
	1105	0WO	1	"	"	"	200	"			15,199
	1126	WWO	1	"	"	"	0WO	"			15,222
	1145	WWO	1	"	"	"	"	"			15,222
	1207	KWO	1	"	"	"	WWO	"			15,246
	1237	R60	3	0	27,675	1470	120	29,265	15,370	225	15,145
	1307	R60	3	0	27,675	1470	120	29,265	15,370	225	15,145
	1329	R60	3	0	27,675	1470	120	29,265	15,370	225	15,145

BALLOON OVER LAND (AFRICA). THE DATA PLOTTED ON PAGE 2 SHOWS LAND CONTOUR ASSUMING BALLOON AT A CONSTANT 16,500 M ALTITUDE.

FIGURE 7A

Figure 19-7a. Daily Altitude Profile – Over Land
(Page 1 of 2 pages)

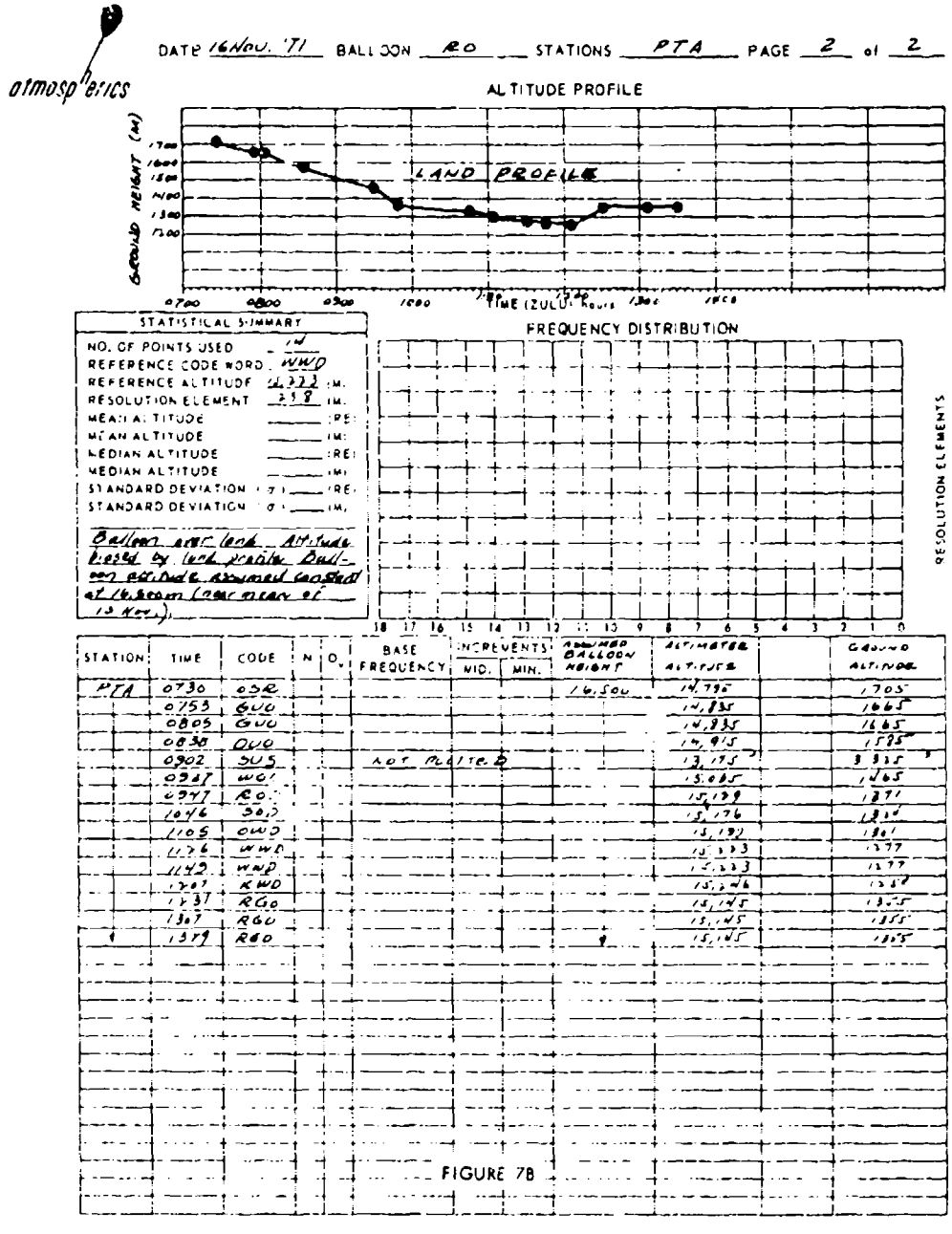

FIGURE 78

Figure 19-7b. Daily Altitude Profile – Over Land
(Page 2 of 2 pages)

atmospherics

DATE DEC 7 '71 BALLOON RO STATIONS BUA, PTA PAGE 1 of 2

ALTITUDE PROFILE

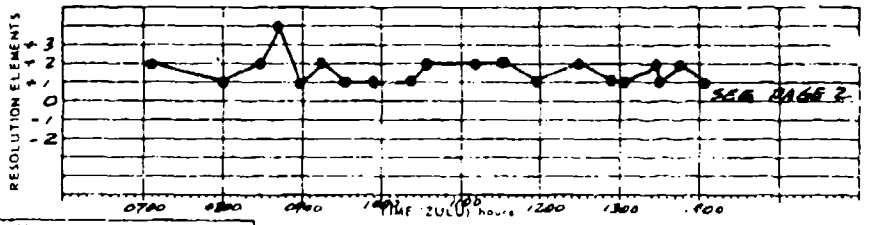

STATISTICAL SUMMARY

NO. OF POINTS USED	38
REFERENCE CODE WORD	URD
REFERENCE ALTITUDE	16,101 (M)
RESOLUTION ELEMENT	26.9 (M)
MEAN ALTITUDE	+.42 (RE)
MEAN ALTITUDE	16,133 (M)
MEDIAN ALTITUDE	+.2 (RE)
MEDIAN ALTITUDE	16,155 (M)
STANDARD DEVIATION	σ .9 (RE)
STANDARD DEVIATION	σ 24 (M)

FREQUENCY DISTRIBUTION

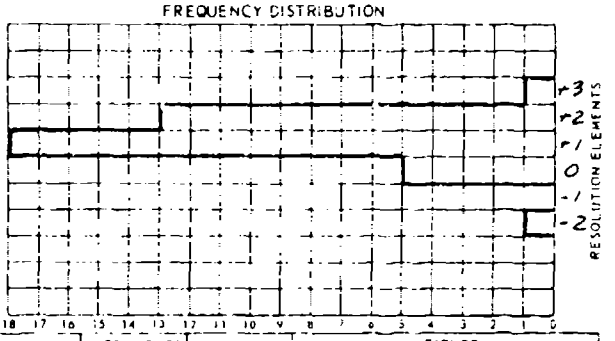

STATION	TIME	CODE	N	O	BASE FREQUENCY	INCREMENTS MID.	INCREMENTS MIN.	ALTIMETER FREQUENCY	ALTITUDE (1,5M ft + ICB)	ALTITUDE T CORR	ALTITUDE (M)
PTA	0707	RRD					+2				
	0759	GRD					+1				
	0825	RRD					+2				
	0841	DRD					+3				
	0857	GRD					+1				
	0918	RRD					+2				
	0932	GRD					+1				
	0953	GRD					+1				
	1020	GRD					+1				
	1037	RRD					+2				
▼	1112	RRD					+2				
BUA	1131	RRD					+2				
PTA	1133	RRD					+2				
	1157	GRD					+1				
▼	1227	RRD					+2				
BUA	1253	GRD					+1				
PTA	1303	GRD					+1				
PTA	1325	RRD					+2				
BUA	1329	GRD					+1				
PTA	1347	RRD					+2				

CONTINUED ON PAGE 2

FIGURE 8A

Figure 19-8a. Daily Altitude Profile – Over Water
(Page 1 of 2 pages)

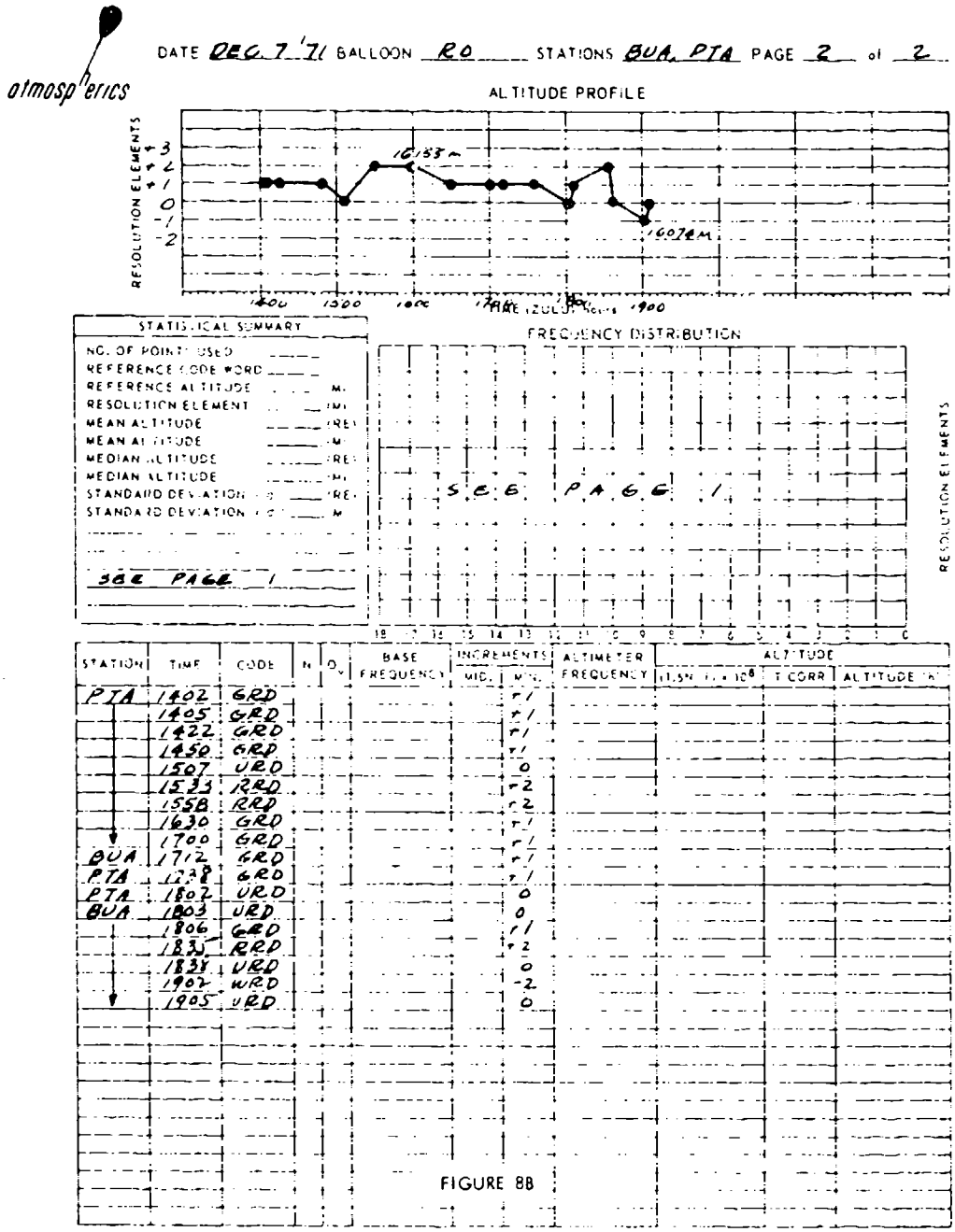

FIGURE 8B

Figure 19-8b. Daily Altitude Profile – Over Water
(Page 2 of 2 pages)

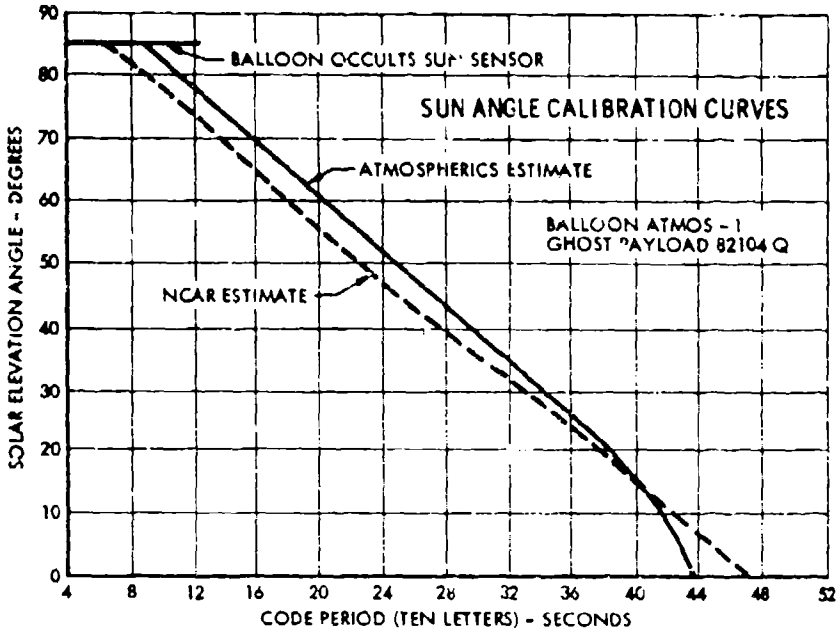

Figure 19-9. Sun Angle Calibration

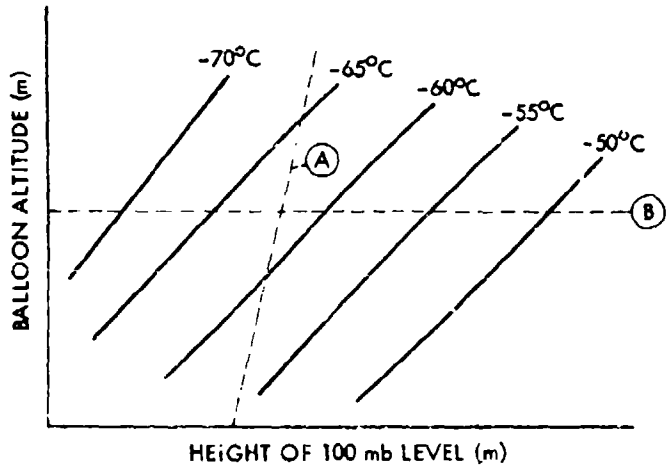

Figure 19-10. Curves Drawn from Altimeter Information

The intersection of curve A with the true altitude of the balloon (mean altimeter value), line B, provides the temperature and height of the 100-millibar level. Consulting the day's 100-millibar meteorological chart yields the latitude required.

As this method is independent of calibration errors of the sun angle sensor, the comparison of latitudes found this way and those found using sun angles alone yields a high confidence trajectory. The resulting trajectory is shown in Figure 19-11.

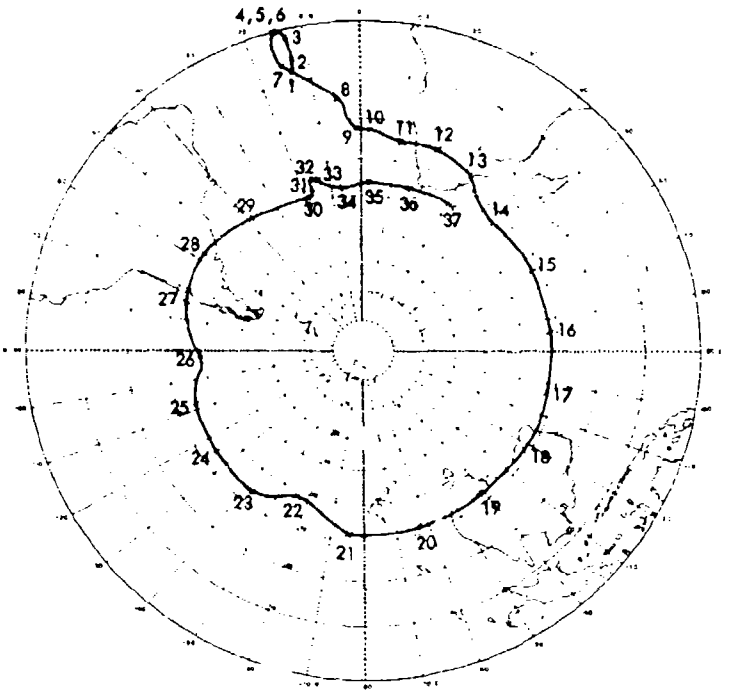

Figure 19-11. Final Trajectory – ATMOS I. Numbers correspond to balloon days from Nov. 5, 1971

19-7. SYNOPSIS OF FLIGHT DATA

Table 19-1 contains a synopsis of the data collected during the flight. The table columns are explained below:

Balloon Day	A count of day/night cycles as seen by the balloon.
Date	The calendar date at Greenwich when the balloon "sees" local noon.
Lat (sun)	The estimated balloon latitude (in degrees) using sun data only (from the QQQ payload).
Lat (alt)	The estimated balloon latitude (in degrees) using altimeter data.

Lat (nominal)	The best estimate of true balloon latitude (in degrees) at local noon using weighted sun and altimeter calculations or extrapolations.
Long	The best estimate of true balloon longitude (in degrees) at local noon using sun calculations or extrapolations.
Balloon Alt	Mean of altimeter readings (in meters) during the day (as shown on the detailed daily data sheets).
100 mb Temp	Best estimate of the temperature at the 100-millibar level at the geographic location of the balloon. This is found by consulting the 100-millibar meteorological charts for the day in question.
100 mb Alt (m)	Same as above, but for altitude.
Δ Alt (m)	Height of balloon (in meters) above (+) or below (-) the 100-millibar surface.
Po (mb)	The estimated pressure at the balloon (to the nearest millibar).

To confirm the analysis (and to identify potential erroneous data points), a temperature versus altitude plot of the points of Table 19-1 was performed. All points fell close to a line of constant density near 176 grams per cubic meter.

The weight of the balloon prior to launch had indicated an expected ceiling at 180 grams per cubic meter. A 2 percent stretching of the balloon volume is entirely reasonable. The balloon was no longer flying stably on balloon days 36 and 37 and was lost on day 38.

19-8. SUMMARY

The flight of ATMOS-1 demonstrated:

(1) The short and long term horizontal motion of a super pressure balloon;

(2) The feasibility of long term, in-flight operation of the Levanon altimeter and the Digi-Ghost combination;

(3) The method of altimeter data reduction and analysis using the indicated forms;

(4) The technique of trajectory analysis using the combination of altimeter, sun angle data, and the daily 100-millibar meteorological charts; and

(5) The direct applicability of this technique to the Isentropic balloon system.

Table 19-1. Summary of ATMOS-1 Flight Data

Balloon Day	Date	Lat (sun)	Lat (alt)	Lat (nominal)	Long	Balloon Alt (m)	100 mb Temp (°C)	100 mb Alt (m)	Δ Alt (m)	Po (mb)
1	Nov 5	(Launch)		8 S	14 W	16,638	-79	16,584†	+ 54	99
2	6	7 S	6 S	6 S	13 W	16,657	-80	16,585†	+129	98
3	7	--	2 S	2 S	13 W	16,692	-80	16,595†	+ 97	98
4	8	4 S	2 N	0	15 W	16,730	-80	16,600†	+130	98
5	9	--	--	--	--	16,793	--	--	--	--
6	10	--	0	0	15 W	16,714	-80	16,600†	+114	98
7	11	6 S	7 S	7 S	15 W	16,648	-79	16,585†	+ 63	99
8	12	--	14 S	14 S	5 W	16,616	-77	16,590	+ 26	100
9	13	25 S	22 S	22 S	1 W	16,511	-74	16,570	- 59	101
10	14	--	23 S	23 S	2 E	16,445	-73	16,550	-105	102
11	15	21 S	24 S	24 S	11 E	16,496	-75	16,550	- 54	101
12	16	21 S	--	24 S	21 E	Overland	-73	16,520	--	--
13	17	24 S	0	27 S	32 E	Overland	-71	16,477	--	--
14	18	26 S	33 S	33 S	46 E	16,180	-69	16,460	-280	105
15	19	--	--	32 S	65 E	16,104	-68	16,435	-331	106
16	20	--	--	32 S	84 E	16,016	-67	16,387	-371	106
17	21	--	--	32 S	103 E	--	-65	16,312	--	--
18	22	--	--	32 S	122 E	--	-58	16,230	--	--
19	23	--	--	32 S	141 E	15,989	-66	16,335	-346	106
20	24	32 S	32 S	32 S	162 E	16,005	-67	16,300	-295	105
21	25	32 S	32 S	32 S	176 W	15,985	-65	16,350	-365	106
22	26	37 S	38 S	38 S	156 W	16,062	-66	16,450	-388	106
23	27	33 S	33 S	33 S	143 W	16,165	-69	16,470	-305	105
24	28	33 S	35 S	34 S	125 W	16,128	-68	16,460	-332	106
25	28	--	36 S	36 S	108 W	16,101	-68	16,390	-289	106
26	29	--	39 S	39 S	91 W	15,938	-65	16,335	-397	108
27	30	--	33 S	33 S	74 W	16,041	-66	16,385	-426	108
28	Dec 1	39 S	33 S	33 S	58 W	15,980	-67	16,320	-340	--
29	2	--	--	36 S	39 W	--	-65	16,290	--	--
30	3	40 S	38 S	38 S	19 W	15,994	-66	16,380	-391	107
31	4	--	37 S	37 S	18 W	16,173	-69	16,435	-262	104
32	5	--	33 S	33 S	17 W	16,284	-71	16,485‡	-201	103
33	6	29 S	34 S	34 S	14 W	16,252	-71	16,470‡	-218	103
34	7	32 S	38 S	38 S	7 W	16,133	-70	16,400‡	-267	104
35	8	34 S	36 S	36 S	3 E	16,202	-70	16,440‡	-238	104
36	9	34 S	--	36 S	17 E	16,370**	--	--	--	--
37	10	34 S	--	36 S	32 E	16,256**	--	--	--	--

* Data estimated or extrapolated
** *Unstable flight*

† Data from meteorological chart of Nov 11
‡ Data from meteorological chart of Dec 5

Acknowledgments

Atmospherics is especially grateful to the following for contributing to the success of the ATMOS-I experiment: Mr. Vincent Lally and the NCAR team, who both supplied the hardware and supported the launch operation; the members of the Ghost network tracking team, particularly Mr. Sanby at Pretoria, South Africa, Mrs. Knight at Christchurch, New Zealand, and the Buenos Aires, Argentina contingent who collectively spent countless hours recording the flight's data; Prof. J. E. Blamont of the Service d'Aeronomie, whose support of the Isentropic research program made this effort possible; and the Royal Air Force, without whose generously offered transportation at least one of the authors would probably still be on Ascension Island.

References

Blamont, J. E., Heinsheimer, T. F., and Pommereau, J. P. (1970) Position determination methods used to track superpressure balloons, Monthly Weather Review 98(No. 10).

Blamont, J. E., and Pommereau, J. P. (1970) Proposition Pour Une Etude Experimentale De La Circulation Stratospherique Par Ballon Isentrope, Service d'Aeronomie, CNRS.

Levanon, N. (1970) Balloon borne radio altimeter, IEEE Transactions on Geo Science Electronics, GE-8(1).

Litchfield, Ernest W., and Frykman, Robert W. (1967) Electronics for around the world Ghost balloon flights, Proceedings of the AFCRL Scientific Balloon Symposium, April 19, 1966, AFCRL 67-0075: 59-67.

TWERLE Technical Description (1971) NCAR, Boulder, Colorado.

Contents

20. High Resolution Solar and Stellar Spectroscopy from Stabilized Balloon Borne Platforms

B. Bates, G.R. Courts, and C.D. McKeith
The Queen's University of Belfast
Belfast, Northern Ireland

20-1. INTRODUCTION

Although a complete study of the emission from the stars across the entire astronomical ultraviolet spectrum (wavelengths 912 to 3000 Å) requires that instruments are contained in sounding rockets or satellites, part of this important spectral region may be observed using balloon borne equipment. Unlike the areas of γ-ray, X-ray and infrared astronomy, in which scientific ballooning has already made an impact, a program of ultraviolet stellar spectroscopy from balloon borne telescopes is yet only in infancy. This is partly due to the severe attenuation by the Earth's atmosphere of incident ultraviolet radiation, since even at the highest balloon float altitudes, observations of stellar spectra remain restricted to parts of the middle ultraviolet (1900 to 3000 Å). In this particular spectral region, attenuation is caused by the overlying atmospheric ozone, and Figure 20-1 shows the expected overhead atmospheric transmission for a float altitude of 40 kilometers.

Because of this wide variation in atmospheric transmission and the uncertainty in applying the necessary corrections, it is unlikely that scientific ballooning can be applied extensively to those stellar observations which require good

photometric accuracy over a wide wavelength range. It is far more appropriate that the balloon program be concentrated on studies of particular spectral lines within the wavelength regions 1900 to 2400 and 2700 to 3000 Å for which the atmospheric transmission is greatest. The latter region is particularly attractive for balloon ultraviolet spectroscopy, since it contains the astrophysically important lines of neutral and singly ionized magnesium [Mg I (2850 Å); Mg II (2795; 2802 Å)]. In addition, sophisticated techniques in high resolution spectroscopy, which have played a significant role in ground based astronomy, are now being developed and applied to this region of the ultraviolet. Such techniques should be well suited to the balloon program.

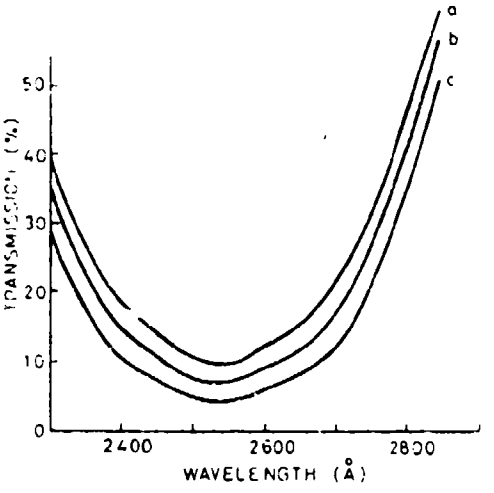

Figure 20-1 Calculated Overhead Atmospheric Transmission for a Float Altitude of 40 Km Based on Published Ozone Concentrations and Absorption Coefficients (McDowell, 1971)

Scientific ballooning offers therefore an excellent opportunity for a program in ultraviolet astronomical spectroscopy (albeit over a limited wavelength range) which will be supplementary to the rocket and satellite program. Our current and future balloon programs are concerned with high resolution observations of the magnesium lines in solar and stellar spectra and in the interstellar medium. These programs are outlined briefly in the following sections.

20-2. HIGH SPECTRAL RESOLUTION STUDIES OF THE SOLAR Mg II LINE PROFILES

The resonance doublet of singly ionized magnesium is formed in the solar chromosphere. Over quiet regions of the solar disk, each line profile has two emission peaks separated by a central absorption core (Figure 20-2). The first high resolution (0.03 Å) rocket spectra showed the detailed structure of these lines but without angular resolution on the disk (Purcell et al, 1963). Subsequently, the aim of the more recent rocket flights (ARU Culham Laboratory/Queen's University; Bates et al, 1971) and balloon flights (Lemaire, 1969) has been to record profiles across the solar disk with both high spatial resolution (several arcsec) and spectral resolution (< 0.04 Å). The Belfast-Culham collaboration has continued with a successful balloon flight (carried out in August 1971 in association with AFCRL) of a Fabry-Perot interferometer spectrograph (resolution 0.016 Å) similar in design to those flown previously in our rocket experiments.

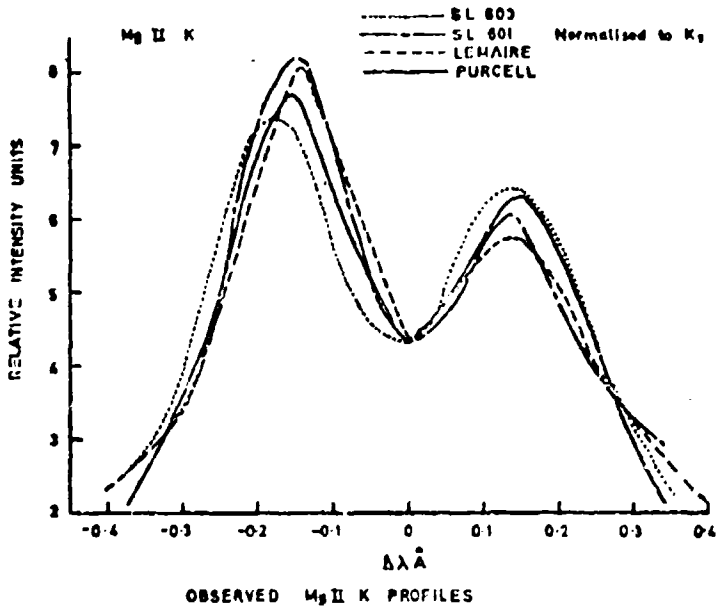

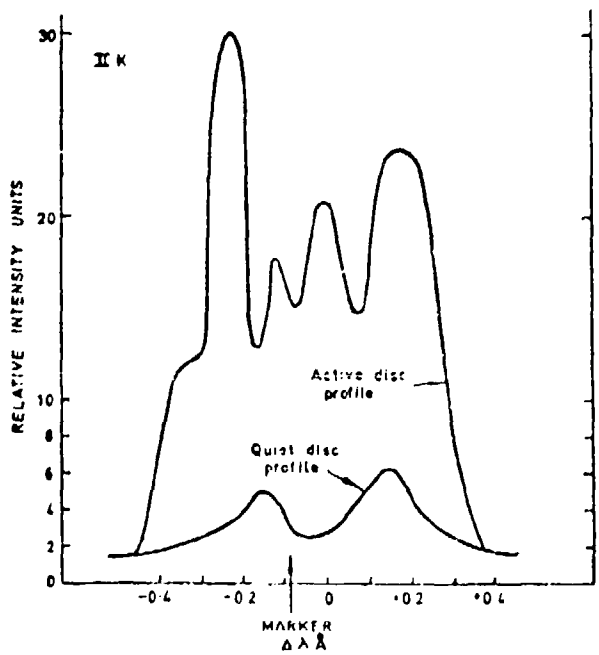

Figure 26-2. Recorded Profiles of the Solar Mg II K Line (2795 Å). Mean profiles for the quiet disk are shown in the upper figure. The lower figure compares profiles for the quiet disk and for an active region. With the method of recording, the wavelength scale corresponds also to a positional change on the solar disk. The peaks in the active disk profile are spatially separated by approximately 30 arcsec (McBride, 1971)

The two main objectives of this flight were (a) to record additional data on the point-to-point variation of the line profiles across the disk, and (b) to compare under the same recording conditions the data from the balloon and rocket flights. This latter information was needed to determine whether our program in high resolution spectroscopy might be seriously influenced by the overlying atmospheric ozone.

The data reduction has yet to be carried out in detail, but it is hoped that the results will be used ultimately for further comparison with synthetic line profiles derived on the basis of existing chromospheric models for the quiet disk and for active regions. The comparison of the rocket and balloon data has shown that the spectra are not influenced by the ozone (at the float altitude of 40 kilometers) other than by the overall attenuation of the incident radiation. The recorded spectra indicate that at this altitude the atmospheric transmission is about 0.4 in general agreement with the data shown in Figure 20-1. The effects of the severe attenuation of the ozone were seen in spectra recorded during the latter stages of the ascent phase, but unfortunately it has not been possible to correlate these completely with altitude, owing to a temporary fault in the operation of the payload at that time.

No undue difficulties were experienced in converting the spectrograph from rocket to balloon flight operation or in making the payload compatible with a Ball Bros. SP-200 biaxial pointer. Careful attention, however, had to be paid to the thermal environment of the instrument and especially to the elimination of thermal gradients in the spectrograph which could lead to a degradation of spectral performance. To this end the spectrograph was contained in a sealed cylindrical envelope in an atmosphere of dry nitrogen at a pressure of 760 Torr. Using appropriate insulation and a suitable choice of surface points, it was calculated that the total energy radiated by the surface would just exceed the total energy absorbed. Fan heaters then supplied the energy balance so that the inside temperature was always under control at the float altitude (McDowell, 1971). At float altitude the desired spectrograph temperature was maintained, but convection losses during ascent were greater than expected, and the instrument fell to a temperature of 8°C. Nonetheless, there was no resultant defect in instrument performance.

Figures 20-3 and 20-4 show views of the instrument and the overall payload assembly.

20-3. STUDIES OF STELLAR AND INTERSTELLAR Mg LINES

In spite of the limited wavelength coverage of the balloon borne instruments, a number of problems in astrophysics can benefit immediately and very readily

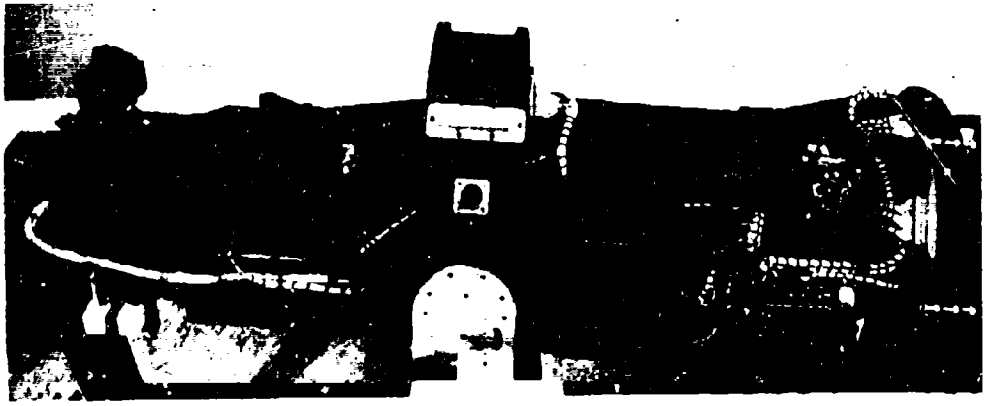

Figure 20-3. High Resolution Interferometer Spectrograph for Studies of the Solar Mg II Resonance Lines

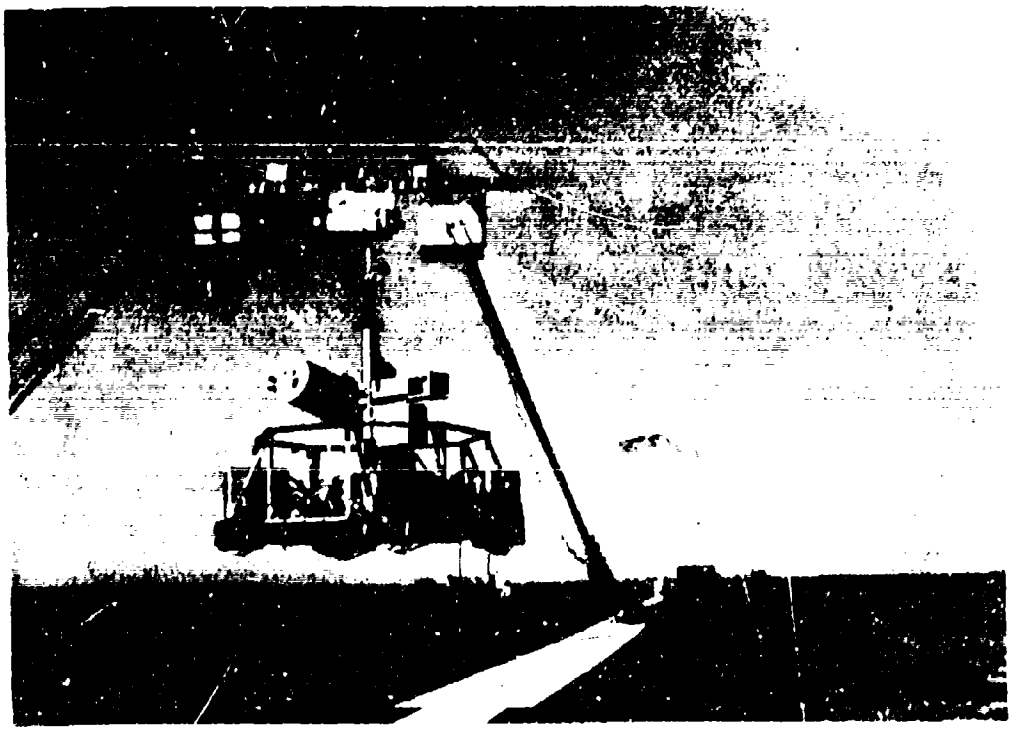

Figure 20-4. Packard-Bell 21" Aperture Coelostat Mounted on a Ball Brothers Solar Tower Telescope, Showing the Spectrograph Unit Mounted on the Optical Table at the Base of the Tower

from a program in scientific ballooning. For certain late-type stars (spectral type GKM) the resonance lines of singly ionized calcium (Ca II, 3934 and 3968 Å) have been observed in emission, and this is believed to indicate chromospheric activity in these stars. The width of the Ca II line has been shown to depend on the absolute visual magnitude (the Wilson-Bappu effect), and the line intensity can be correlated with the age of the star. In the spectrum of the sun it has been very clearly demonstrated that the Mg II lines are much more distinct and prominent than those of Ca II. The theoretical reasons for this are well known and have been outlined (for example, Kondo et al, 1972). The significance is that studies of late-type stars in the Mg II lines should permit an extension of observations over a wider range of spectral type and luminosity than those of Ca II, thus enabling the existing correlations to be extended and interpretations to be examined in greater depth.

Properties of the interstellar gas may be studied through absoption in the resonance lines of interstellar Mg I and II from the continuum of suitable early-type stars used as background sources. Observation of these lines should yield basic information on the interstellar gas "cloud" and "intercloud" regions. It should also be possible to derive reliable estimates of magnesium abundance and from the Mg II/Mg I ionization balance, estimates of electron densities. This latter information in particular is not determined uniquely from ground based studies. Some other considerations of a program in ultraviolet astronomy, including the role of balloons in this program, have been outlined in greater detail (Wilson and Boksenberg, 1969; Bates and McKeith, 1972).

For these problems some compromise has to be made between spectral resolution and observing time. A spectral resolution of < 0.1 Å is really needed for the line profile studies, and because of the low flux levels of the objects under investigation this imposes severe demands on the spectroscopic instruments and the stabilization platforms employed. Further comments on these points are given in Section 20-4.

The first stellar Mg II spectra (resolution ~ 0.25 Å) recorded during balloon flights were obtained in 1971 and have provided some interesting preliminary data on Mg II emission from several stars (Kondo et al, 1972). In Autumn 1972, we plan to fly an instrument with a resolution capability of approximately 0.1 Å for a preliminary survey of interstellar Mg I, II absorption lines. This forms part of a joint series of experiments in collaboration with the Physics Department of University College, London, and the equipment will be flown on a biaxial stellar pointing platform developed and successfully flown by that group.

The payload during assembly is shown in Figure 20-5. The instrument package (comprising an objective grating spectrograph with photographic recording

Figure 20-5. General Payload Configuration of a High Resolution Stellar Spectrograph. (University College, London/Queen's University, Belfast.) The spectrograph is mounted on a stabilized platform developed by the University College Group

and a secondary fine alignment system) is pointed at the chosen object to an accuracy of approximately ±1 arcmin in elevation and azimuth. To realize the required spectral resolution it is necessary that the stellar image be stabilized in the direction of the grating dispersion to about ±5 arcsec. This is accomplished by servo controlling a plane mirror which illuminates the grating and which is operated from a star-position sensor in the fine alignment system. In the direction perpendicular to the dispersion, the image stabilization is determined by the platform pointing accuracy.

20-4. CONSIDERATIONS OF A PROGRAM OF ULTRAVIOLET ASTRONOMY USING BALLOON BORNE TELESCOPES

For our future program and in particular for the studies of the interstellar medium, we would hope to increase the spectral resolution of our instruments to about 0.01 Å. This, together with the need to extend observations to fainter objects, will require an increased collecting area by making use of moderate size telescopes (of the order 0.5 meter diameter).

The telescope and spectroscopic instrumentation will be contained on a stabilized platform capable of arcmin pointing accuracy and a pointing noise value of several arcsec. The Science Research Council has given authorization for a design study to be carried out on stabilized balloon borne platforms which will meet U.K. experimenters' requirements for all aspects of balloon astronomy.

Continuing developments in spectroscopic techniques will also play an important role in the future of ultraviolet spectroscopy from balloon platforms. It is well known that in ground based astronomy interference spectroscopy techniques (especially using the Fabry-Perot interferometer) can outperform diffraction gratings at high spectral resolving powers when used with large telescopes under moderate seeing conditions (Vaughan, 1967). For the balloon program, the use of the interferometer will lead to a considerable relaxation of the pointing accuracy and stabilization requirements for the balloon platform (Bradley, 1968). Although there are a number of practical difficulties associated with extending such techniques into the ultraviolet and applying them to remote operation on a balloon borne platform, considerable gains in luminosity are possible over conventional spectroscopy for high resolution studies over a limited spectral range. Developments in this area in our own laboratory appear very promising for a future balloon program (Bates et al, 1972).

With such improvements in spectroscopic techniques and with the availability of stabilized platforms of arcsec pointing accuracy, then, provided the payload can be maintained at a float altitude well in excess of 40 kilometers for several hours, it seems likely that scientific ballooning can contribute significantly to a program in ultraviolet astronomy during the next few years.

Acknowledgments

This general paper outlines some of our current and future plans in ultraviolet balloon astronomy which are largely being carried out in collaboration with other groups. We wish to thank our collaborators at ARU (Culham), AFCRL and University College, London, and our colleagues at Belfast. The solar program was directed by Dr. R. Wilson (Culham) and Professor D. J. Bradley (Belfast). The overall program is supported by the Science Research Council.

References

Bates, B., Bradley, D.J., McBride, D.A., McKeith, C.D., McKeith, N.E., and Burton, W.M., Paxton, H.J.B., Shenton, D.B., Wilson, R. (1971) Phil. Trans. Roy. Soc. Lond. 270(A):47.

Bates, B., and McKeith, C.D. (1972) Contemp. Phys. 13:225.

Bates, B., Conway, J.K., Courts, G.R., and McKeith, C.D. (1972) Paper to be presented at ICO IX, Santa Monica, October 1972.

Bradley, D.J. (1968) Optica Acta 15:431.

Kondo, Y., Thomas Giuli, R., Modisette, J.L., and Rydgren, A.E. (1972) Paper submitted to Astrophysical Journal.

Lemaire, P. (1969) Astrophys. Lett. 3:43.

McBride, D.A. (1971) Ph.D. Thesis, Queen's University of Belfast.

McDowell, M.W. (1971) Ph.D. Thesis, Queen's University of Belfast.

Purcell, et al (1963)

References

Vaughan, A. H., Jr. (1967) Ann. Rev. Astron. Astrophys. 5:139.
Wilson, R., and Boksenberg, A. (1969) Ann. Rev. Astron. Astrophys. 7:421.

Contents

21. A Control and Instrumentation System with Fine Optical Alignment for a Balloon Borne Ultraviolet Spectrograph

G.W. Ackland and J.G. Firth
Science Research Council
Astrophysics Research Unit
Culham Laboratory
Abingdon, Berkshire, England

21-1. INTRODUCTION

For a number of years there has been active collaboration between the Physics Department of Queen's University College, Belfast and the Science Research Council's Astrophysics Research Unit at Culham, both in the United Kingdom, in the design, construction and commissioning of sounding rocket payloads to study the solar Mg II resonance lines near 2800 Å (Bates et al, 1969; 1971). These payloads have been flown in the attitude controlled heads of British Skylark sounding rockets. These attitude control units point the whole payload at the sun to within a few minutes of arc (Cope, 1964). However, the scientific requirements were such that the sun's image must be positioned at the entrance slit of the spectrograph to within a few seconds of arc. This fine pointing was achieved by using a mechanism developed by the Astrophysics Research Unit (ARU) as part of its own research programme (Black and Shenton, 1965).

A proposal in 1969 to fly a similar experiment suspended from a balloon developed into an international collaborative effort between the United States and the United Kingdom. AFCRL provided, in addition to their own experimental

package, the use of the launch and preparation facilities at Holloman Air Force base, together with all the peripheral requirements for such a flight – telemetry, radio command, batteries, helium and so forth, and in particular the use of the Ball Brothers biaxial solar pointer. Queen's University was to provide the balloon and the ultraviolet spectrometer with its outer housing and mountings, while the ARU was again invited to produce the fine solar pointing system to supplement the 2-arc minute capability of the main solar pointer (Greeb, 1965) together with the associated payload electronics package.

This paper presents some of the requirements and describes some of the facilities for which ARU was responsible.

21-2. OPTICAL ALIGNMENT SYSTEM

The fine pointing mechanism (hereafter called the servo) consists basically of a small imaging mirror mounted on a movable platform directing the sun's image onto a split field error sensor whose outputs, suitably processed and amplified, energize the platform drive motors to maintain the required position. Mounted on the same platform is the main imaging component of the spectrograph which thus maintains the solar image at its correct location on the instrument entrance slit.

Figures 21-1 and 21-2 show the instrument layout as mounted on the Ball Brothers pointer and indicate the locations of the major servo components.

The main imaging element is a concave mirror coated for optimum reflectivity at about 2800 Å and fitted with an aperture or stop disc to reduce the reflected image to the required intensity. The mirror platform is arranged to tilt about two mutually perpendicular axes over angles greater than the specified pointing error of the solar pointer. Ideally, the image error detector should be placed at the instrument entrance slit, but for various reasons, both optical and mechanical, this is not possible, and a compromise solution has been adopted with the unit mounted on a mechanically stiff bracket in the vicinity of the image beam folding mirror.

A target eye is used to activate the servo system only when the relatively coarse pointing of the main solar pointer has brought the payload to within about 1 degree of the sun.

A simplified block diagram of the servo is shown in Figure 21-3 and a mechanical layout drawing in Figure 21-4. Ideally, the two axes about which the mirror platform rotates should pass through the poles of both mirrors to avoid lateral image movement due to relative movement of the poles. This is clearly not possible with both mirrors mounted on a common platform. The pivot points have therefore been arranged to introduce the least error in the axis which moves the solar image across the instrument entrance slit.

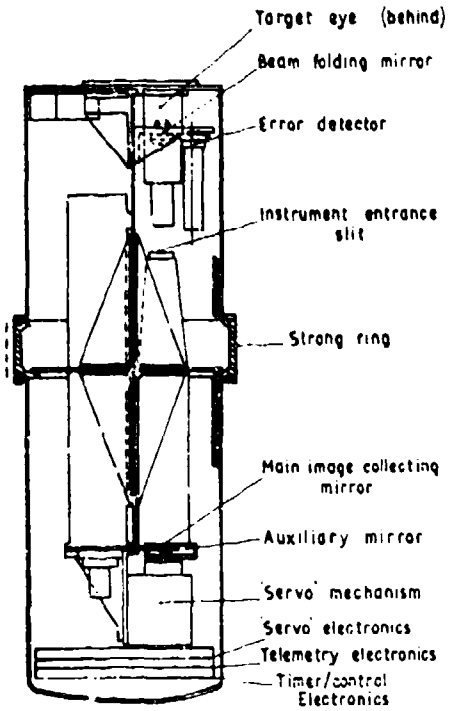

Figure 21-1. Instrument Layout, View 1

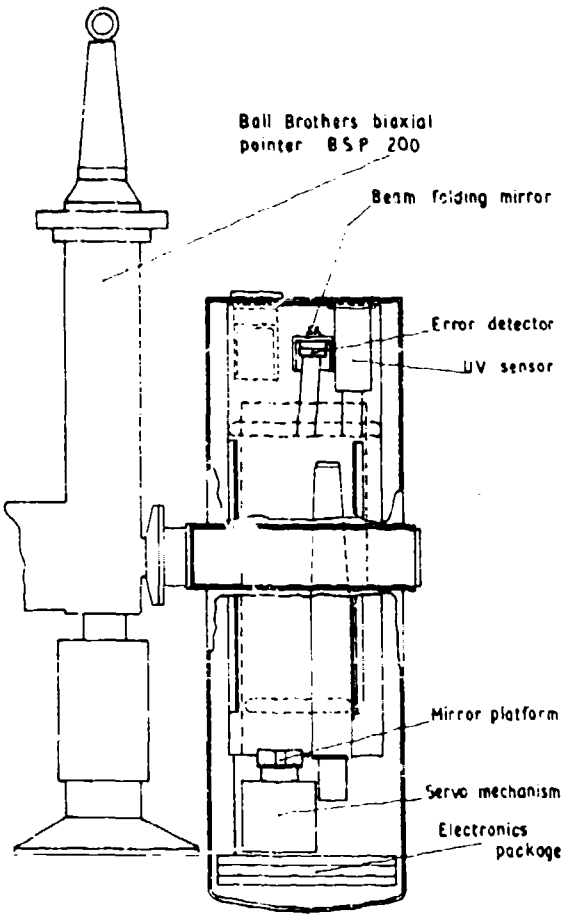

Figure 21-2. Instrument Layout, View 2

An arm or stalk projecting from the rear face of the platform passes through the servo mounting base and is spring loaded against two cylindrical cams whose respective axes are in the same planes as the platform suspension axes. Angular movement of the arm in one axis by rotation of its associated cam causes the arm to slide along the other cam without angular movement in the other axes. The camshafts are driven by two-phase 400-Hz motors through precision gears. Particular attention has been paid to free running and elimination of gear backlash. Preloaded angular contact precision ball bearings are used for the camshaft bearings and for the platform pivots. The overall reduction from the camshaft to the motor is 10,000:1, so that the system inertia is controlled by the friction of the motor and the initial trains of the reduction gear. Angular displacement ac pickoffs are attached to the camshafts to sense the camshaft, and hence the platform, positions. These are so arranged that the null of the pickoffs coincides with the mechanical zero position of the mirror platform.

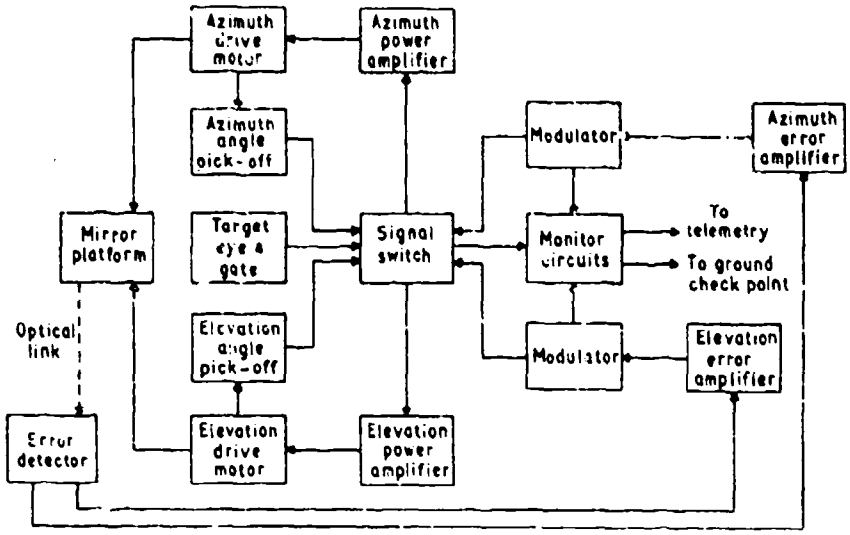

Figure 21-3. Servo Electrical Block Diagram

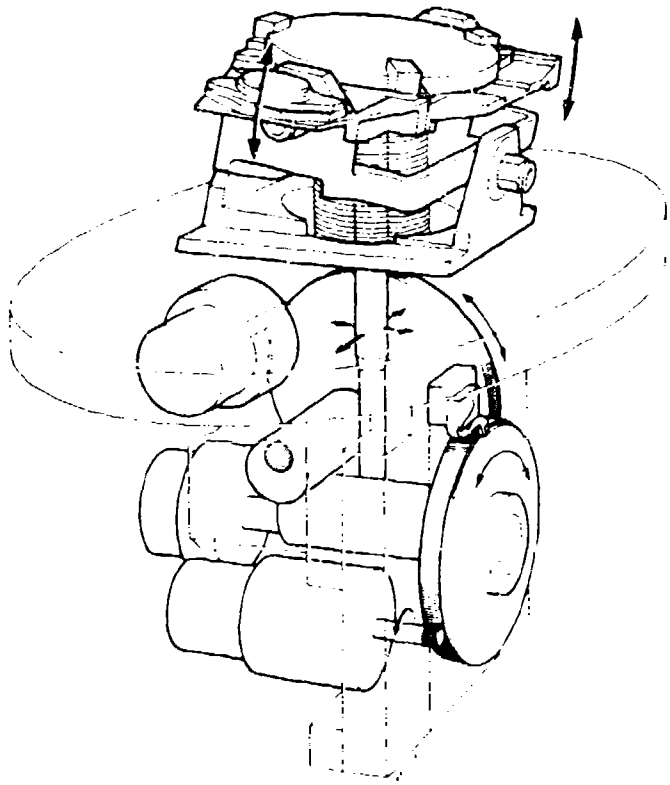

Figure 21-4. Simplified Servo Mechanism

In its quiescent state the mirror platform is held electrically in this position by driving to the zero outputs of the pickoffs. The target eye detects when the payload is aligned with the sun within the working range of the servo system and operates the signal switches, releasing the mirror platform from the control of the cam angle pickoffs and allowing the servo to centre the solar image on the error detector. The signals from the error detector are passed through dc amplifiers, the outputs of which are modulated at 400 Hz, then through the signal switches to the power amplifiers and the two-phase mirror platform motors.

A sectional drawing of the target eye is shown in Figure 21-5. A simple lens produces a solar image at the focal plane where a square aperture is placed. This is sized to produce a field of view of about 2 degrees. A silicon photo voltaic cell fitted with a red glass filter is positioned behind the aperture. The combination of photo cell response (peaking at about 8500 Å) and the red glass pass band (7000 Å to 1000 Å) maintains a more constant solar response from ground level to upper atmosphere and reduces the otherwise significant effects of atmospheric scattering, particularly below 5000 Å.

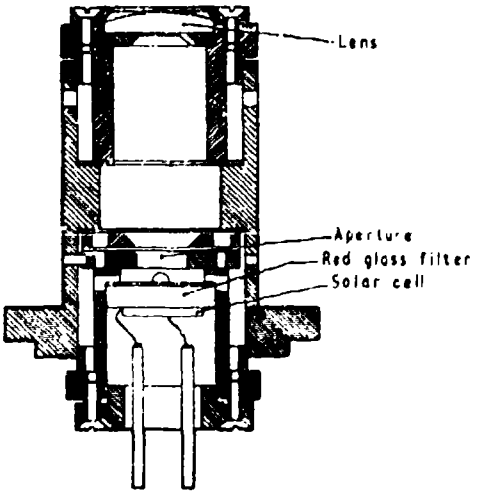

Figure 21-5. Target Eye

The split field error detector consists of four matched triangular silicon photo voltaic cells each covered with a red glass filter (Schott RG9) and placed in a square array giving a field of view of about 4 degrees.

Diagonally opposite pairs of cells are connected in parallel opposition, permitting resolution of errors into two components without the use of auxiliary circuits, but only over the central portion of the field. The outer part of the field is used only during acquisition when simultaneous control in both axes is not required. The error detector and derived signals are shown diagramatically in Figure 21-6. The detector sensitivity is about 20 milliamperes per degree and is adjustable by varying the aperture of the imaging mirror. The complete error detector assembly is held rigidly in a two-axis adjustable mount adjacent to the instrument beam folding mirror.

Five telemetry status output signals are provided. The azimuth and elevation dc error signals are amplified to produce calibrated outputs of 1 volt per 10 arc seconds. The ac pickoff signals indicating mirror platform angular displacement are demodulated and amplified to produce calibrated outputs of 1 volt per 10 arc minutes. Target eye illumination is indicated by a bi-level signal changing from a TTL logical 0 to logical 1.

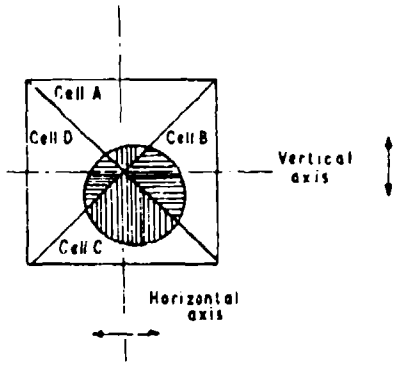

Misalignment	Output
About horizontal axis	B-D
About vertical axis	A-C

Figure 21-6. Error Detector

21-3. TIMING AND CONTROL SYSTEM

The medium used for recording the spectra produced by the spectrograph is 16 millimeter photographic film contained in an electrically driven cassette. The length of time these spectra are allowed to fall on the film emulsion is controlled by the opening and closing of an electrically operated shutter. Another driven mechanism within the instrument is a scanning Fabry Perot Interferometer mount. This rotates in 15 discrete steps each of 16 arc seconds over a total range of only 4 arc minutes. As each spectrum is photographed, another 16 millimeter camera records the actual solar image position relative to a fixed graticule.

A timing and control system is provided to control these four devices over a very wide range of exposure times and in any one of five operational modes. It is designed for operation by three ground initiated signals transmitted over the AFCRL radio command link. The basic operating modes provided are manual control, automatic scanning, and automatic nonscanning (or static). A Ledex sequence switch is used to select the required mode, and this is indexed by an output from the first of the radio commands. The six positions of the switch and the modes selected are shown in Table 21-1.

For each of the six switch positions there are two states controlled by the second and third radio commands respectively. Command number two initiates the "Start" or "On" signal, while command three produces a "Stop" or "Off" signal. Thus, in the Reset mode a "Start/On" signal connects the electrical power supply to the experiment, and a "Stop/Off" command will switch it off (some of the telemetry circuits are connected permanently to enable one of the temperature sensors to be monitored at all times).

Table 21-1. Sequence Switch Positions

Switch Position	Mode Selected
0	Reset
1	Manual
2	Exposure Range 1 FP Scanning
3	Exposure Range 2 FP Scanning
4	Exposure Range 1 FP Static
5	Exposure Range 2 FP Static

The manual mode provides the ground controller with means of opening and closing the instrument shutter as required by means of the two commands. Each time the shutter closes, the instrument and monitor cameras operate and advance the films by one frame each, thus preparing the spectrograph for its next exposure and recording the image position.

In each of the remaining modes, four presettable automatically controlled exposure times are available. In switch positions 2 and 4 the times are as preset (Range 1), while in positions 3 and 5 the Range 1 times are multiplied by a factor chosen between 2 and 10 (Range 2).

In the scanning automatic modes (sequence switch positions 2 or 3) 15 equal exposures are made, one at each step of the Fabry Perot cell. After the 15th exposure a blank frame is inserted on the film, and the system then waits for the next command to be received. If the next command is "Start" a further 15 frames will be made at the next selected exposure time, and so on.

In the static or nonscanning automatic modes (Switch positions 4 or 5) the four selected exposures are made in turn and repeated until either the sequence switch is operated or until a "Stop" command is received.

Whenever a "Stop" command has been received, the exposure then in progress will be completed, the films advanced in both the cameras and the sequence then "held" awaiting the next instruction. If the next command is a "Start" the cycle will recommence from the "hold" position.

As previously mentioned, four different exposure times are available in Range 1, with those values multiplied by a preselected factor of between two and ten in Range 2. A wide range of possible time values has been provided to cater for all foreseeable needs. Each exposure in Range 1 is independently presettable from 0.1 to 9.9 seconds in 0.1-second steps, or from 1.0 to 99 seconds in 1-second steps. Therefore, in Range 2, dependent upon the multiplying factor chosen, exposure times up to 990 seconds are possible.

The actual values, in seconds, chosen for this particular flight were

	Exp 1	Exp 2	Exp 3	Exp 4
Range 1	0.3	1.0	3.0	9.0
Range 2 (Mult. Factor × 3)	0.9	3.0	9.0	27.0

A simplified block diagram of the timing control system is shown in Figure 21-7.

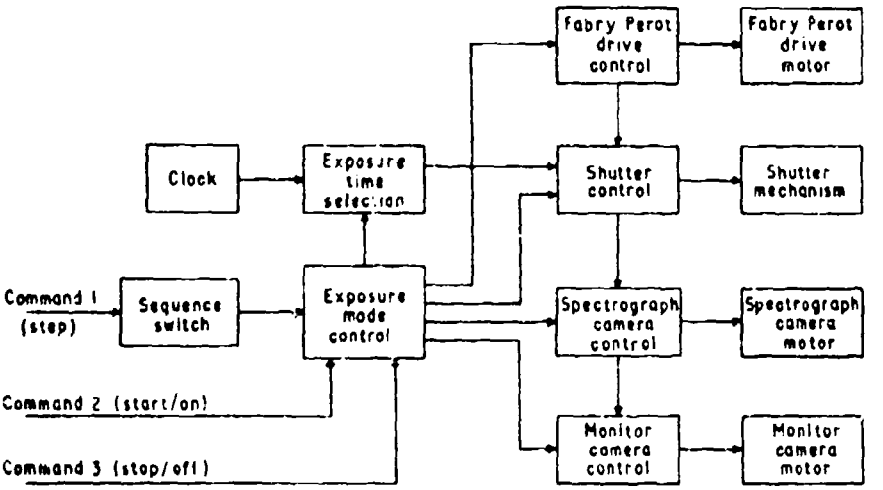

Figure 21-7. Timing and Control System Block Diagram

The timing clock is a silicon-controlled switch relaxation oscillator running at a frequency of 100 Hz. This is divided by 10, and the resultant 10-Hz square wave is used to drive the timing circuits.

The exposure time selector consists of a simple patching system built as an integral part of the timer unit printed circuit board. An impression of the scheme is shown in Figure 21-8. Small screws with crinkle washers under their heads are inserted through holes in the board and make contact with copper strips on the board face and small brass nuts soldered to individual pads at the rear. A similar arrangement is used to select the Range 2 multiplying factor. With screws inserted as illustrated, the chosen exposure values, in seconds, would be

	Exp 1	Exp 2
Range 1	6.4	25
Range 2	25.6	100

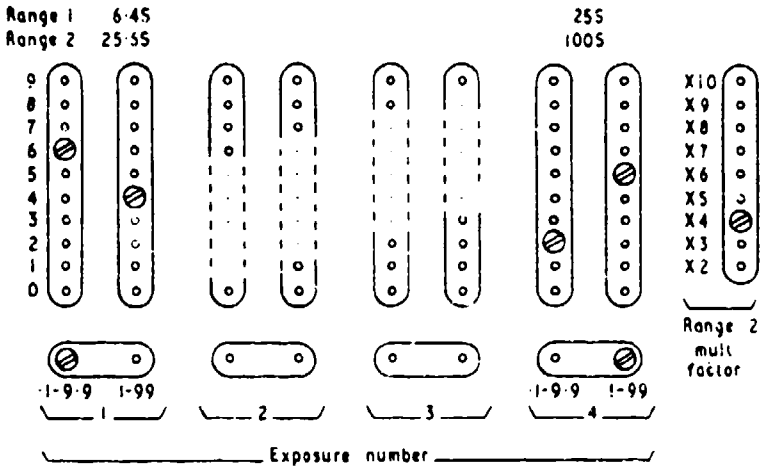

Figure 21-8. Exposure Time Selector

The exposure time selector circuit produces two pulses -- one at the commencement of the exposure period and the other at its end. These pulses pass to the shutter control circuit and open and close the shutter respectively. The shutter itself is operated by a 15-degree bi-directional stepper motor. When the shutter has returned to its closed position, circuits are completed to energize the instrument camera drive motor advancing the film by one frame and to energize the monitor camera recording the image position.

In the automatic scan modes, arrangements are made to advance the instrument films without operating the shutter after the 15th step of the Fabry Perot mechanism, thus inserting a blank frame to assist in subsequent exposure identification.

Control of the various modes of operation is performed by the exposure mode control circuit. Dependent upon the position of the sequence switch and the receipt of start/stop commands, it produces appropriate enable and inhibit signals to control the various instrument functions.

Seven status signals, in binary form, are produced to enable the equipment to be checked before launch and also to monitor its performance during the flight via the telemetry link. They are

(1) Sequence switch position

(2) Sequencer state (This indicates the function actually being performed by the timer. For example, the Ledex switch may have been stepped to its "Reset" position while a long exposure was taking place in the "Automatic Non-scanning Range 2" mode. The status information would therefore be

Sequence Switch Position	"0" indicated
Sequencer State	"5" indicated

At the completion of the exposure the indications would change to "5" and "0" respectively.)

(3) Exposure number (This shows the exposure number of either the exposure taking place or the next exposure.)

(4) Fabry Perot (This indicates from 0-15 in binary form – 4 bits – the cell position.)

(5, 6 and 7). Shutter position, spectrograph camera driving and Fabry Perot driving (These are bilevel signals, and their titles are self explanatory.)

21-4. STATUS INFORMATION

The telemetry system adopted by AFCRL for use on this flight meets IRIG standards as defined in IRIG document 106-60 and its subsequent amendments.

Three subcarrier bands – 13, 15 and 16 – were made available for use by ARU and Queen's University. Time division multiplexing is used on all three bands. Bands 15 and 16 handle analogue information, and the outputs meet IRIG/PAM specifications:

Band 15	10 frames/second	18 samples/frame
Band 16	10 frames/second	30 samples/frame

Both bands are suitable for auto decommutation if the need arises. Band 13 carries digital information and is multiplexed at 10 frames per second with 30 bits of information within each frame. This format is not compatible with standard IRIG decommutating systems but is used in conjunction with the payload checkout unit to display information both during ground checkout and during flight.

The form of the analogue multiplexer outputs is shown in Figure 21-9. Four samples or segments in each frame are taken up by frame sync zero (0V) and full scale (+5.0V) calibrations. Thus 14 segments and 26 segments are available for data on bands 15 and 16, respectively.

The digital multiplexer output waveform has three levels:

$+5.0\,V$ = logical 1
$+2.5\,V$ = logical 0
$<0.4\,V$ = bit sync.

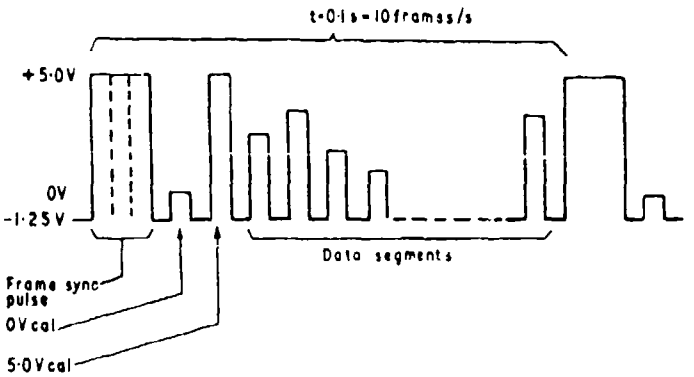

Figure 21-9. Analogue Multiplexer Output Waveform

Part of a typical frame is shown in Figure 21-10. The frame is divided into six 5-bit words, the last bit in each word always being a logical 0. The first

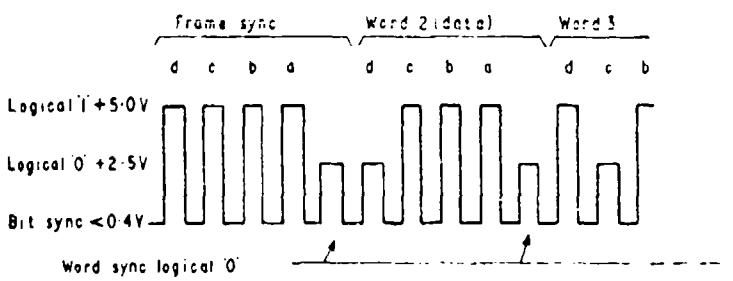

Figure 21-10. Digital Multiplexer Output Waveform

word always contains four logical 1s to form the frame sync signal. In the remaining five data words, four consecutive 1s are forbidden. A bit sync signal (<0.4 V) is inserted after every 1 or 0 level.

A simplified block diagram is shown in Figure 21-11. The master clock runs at 1.8 kHz and is divided by 6 to provide a 300-Hz squarewave to drive the band 13 (digital) and band 16 (analogue) multiplexers. Division by 10 produces 180 Hz to drive the band 15 (analogue) multiplexer.

The 300-Hz signal is counted by the "30 state counter" and provides, at every fifth count, an output to the word sync generator producing a logical 0 at the multiplexer register output for word synchronisation.

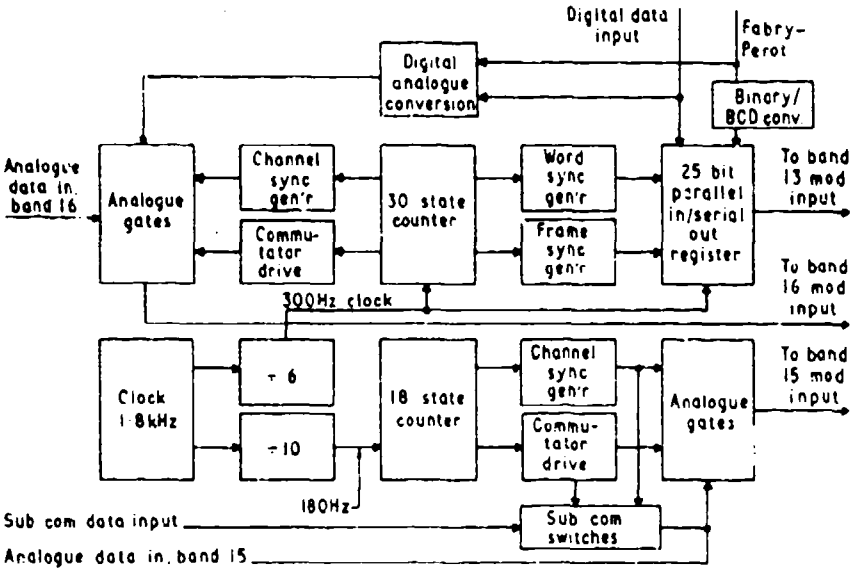

Figure 21-11. Telemetry System Block Diagram

At every 30th count the frame sync generator loads an updated set of data into the 25-bit parallel in/serial out shift register Each word is transmitted most significant digit first with each bit having the significance shown in Table 21-2.

The Fabry Perot position information, in 4-bit binary form, is converted to BCD to be compatible with the multiplexer format and to render further conversion in the ground equipment unnecessary.

The digital information transmitted on band 13 is also transmitted in analogue form on band 15. This enables postflight data reduction to be carried out should it prove necessary. The bilevel signals are compatible with the analogue multiplexer and remain unchanged, but the multibit signals (Fabry Perot position; sequence switch position; sequence state and exposure number) are converted to voltage levels by suitable resistive ladder networks.

Additional outputs from the 30 state counter drive the band 16 channel sync generator and commutator drive circuits. These circuits together with the analogue switches produce a 30-segment frame repeated 10 frames a second. The first five segments are frame sync (2 segments), zero (0V), full scale (5.0 V) calibrations and the ultraviolet sensor EHT monitor. The remaining 25 segments are supercommutated in five groups each of five segments and are used for ultraviolet flux 100 percent full scale, ultraviolet flux 40 percent full scale, temperature sensor number 1 and the servo error detector signals.

Table 21-2. Digital Input Data

Word No.	Bit Ident	Input
2	d	MSB } Sequence Switch Position
	c	
	b	LSB }
	a	Shutter (Bilevel)
3	d	MSB } Sequencer State
	c	
	b	LSB }
	a	Camera Motor (Bilevel)
4	d	MSB } Exposure number
	c	
	b	LSB }
	a	MSB } Fabry Perot position (BCD)
5	d	
	c	
	b	
	a	LSB }
6	d	FP Drive Motor (Bilevel)
	c	Heater
	b	Target Eye
	a	Logical 0

In a similar manner the 1.8-kHz clock output is divided by 10 and fed as a 180-Hz square wave to the 18 state counter, outputs from which drive the band 15 channel sync generator and commutator drive circuits which with the analogue switches produce an 18 segment frame at 10 frames a second. Additional feeds drive the subcommutator switch to subcommutate four housekeeping analogue inputs from the ultraviolet sensor unit to a single segment of the band 15 multiplexer.

The analogue switches consist of FET gates (one for each data channel) with their outputs in parallel. An operational amplifier, connected as a unity gain voltage follower, passes the multiplexed outputs to their respective IRIG modulators. The drive circuits are so arranged that only one switch or gate may be closed at any given time.

An in flight voltage calibration source consisting of an integrated circuit voltage regulator (LM 305) provides a stable, accurate 5.0-volt supply.

The ultraviolet sensor previously mentioned is a calibrated detector mounted behind a transmission filter centred on 2300 Å with a pass band of 80 Å. The sensor provides a measure of the transmission through the atmosphere of the solar

radiation at this wavelength and gives a percentage transmission readout on the real time telemetry display.

Temperature sensors are located at three points within the package. One is near the Fabry Perot unit and is displayable in real time. The others are located one at the front and one at the rear of the package. The outputs are calibrated and adjusted to produce 0 telemetry volts at -40°C and +5.0 telemetry volts at +60°C.

21-5. GROUND EQUIPMENT

The success of this mission depends to a considerable extent on the ability of the ground based observer to control by the use of radio commands the various functions within the experimental package. To enable him to decide on the actions to take he needs to be provided, in real time, with certain data from the instrument. Of particular interest is an indication of the received level of solar radiation as measured by the ultraviolet sensor. This value is the main determinant in deciding, for example, which exposure value should be used and in which mode the instrument should be operated.

A display unit was designed which would accept the demodulated and filtered band 13 and band 16 signals from the telemetry receiving station, decommutate them and present the contained information in an easily assimilated visible form.

During preflight check a 28-volt power source to power the experiment needs to be provided with suitable switching and monitoring arrangements, this in addition to the facility of monitoring the telemetered information. It therefore seemed reasonable to combine all the functions in one package. The resultant test unit is shown in Figure 21-12. (It should be noted that no provision has been made to display the data contained in band 15. This is checked before flight over the telemetry link. The band contains only the digital data in band 13, which is displayed, and such housekeeping information to be of diagnostic interest in the event of a failure.)

The five moving coil panel meters present the following band 16 data:

(1) In flight calibration voltage
(2) Ultraviolet sensor 100 percent full scale
(3) Ultraviolet sensor expanded scale
(4) Fabry Perot temperature
(5) Ultraviolet sensor EHT.

The numerical readout tubes on the right hand side display some of the band 13 digital information:

(1) Fabry Perot position
(2) Exposure number
(3) Sequence switch position
(4) Sequence state.

Below the numerical display five pairs of indicator lamps (one for ON and one for OFF) cater for the remaining band 13 bilevel signals.

(1) Shatter (closed/open)
(2) Camera drive (static/running)
(3) FP drive (static/running)
(4) Target eye (OFF/ON)
(5) Heater (OFF/ON).

Push buttons allow the radio command signals to be simulated during preflight checks without using a radio command channel.

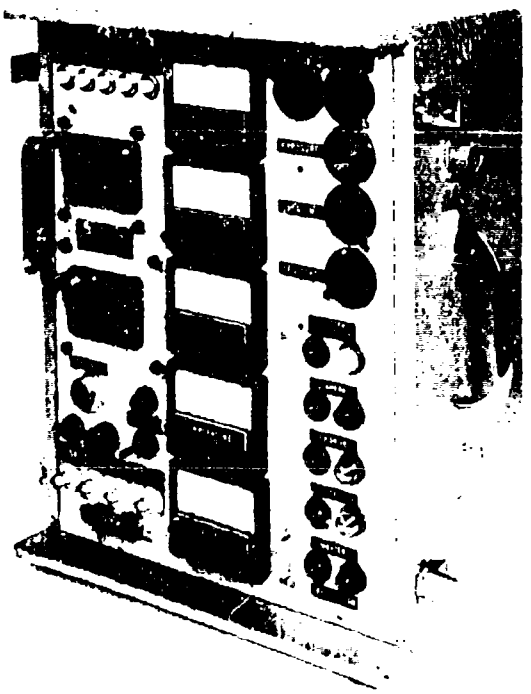

Figure 21-12. Team Test Unit

Test circuits simulating telemetry signals are incorporated in the unit, so that on the operation of the test button a predetermined display can be set up on the various indicators checking the correct operation of the unit. This self check facility is available both preflight and during the balloon flight.

A simplified block diagram of the data display portion of the unit is shown in Figure 21-13. Alternative input jacks are available on each band. The normal data output of the experiment multiplexers is in the range of 0 to +5.0 volts, and the test unit will accept these signals without further processing. However, the outputs available from the telemetry ground station were typically in the range -2.5 volts to +2.5 volts for similar data inputs. A dc level shifting circuit is therefore used during flight to make the incoming telemetry signals compatible with the test unit demultiplexer circuits.

The band 16 signal passes through its input buffer amplifier to the level detector and peak voltage detector. The level detector, set to trigger at -0.8 volts, detects the negative 1.25 volt channel synchronising pulses and locks the 1.2-kHz clock. This in turn drives the channel cycle generator and the sample and hold selector. The channel cycle generator controls the functioning of the peak detector and the sample and hold circuits, while the sample and hold selector determines the order in which the gates are operated. The demultiplexed outputs from band 16, with the exception of the servo error signals, are displayed on the five panel meters. The servo error signals are shifted by 2.5 volts and displayed on an X-Y cathode ray oscilloscope. The ultraviolet sensor 100 percent full scale and expanded scale outputs are also available at the front panel for connection to an external recording device.

The band 13 signal also is buffered and then is applied to the two level detectors. Level detector 2 detects each excursion from 0 to +2.5 volts at the start of each information bit and synchronizes the 300-Hz clock generator. Level detector 1 presets the input stage of the shift register at the end of each logical 1 bit. The information is shifted into the register at the clock frequency. When the frame sync signal (4 logical 1s) appears in the last four stages of the shift register, the frame detector updates the displayed information on the various display devices.

21-6. RESULTS

The experiment was flown on 2 August 1971, launched at 0730 from a runway at Hollonian Air Force Base. The float height of 133,000 feet was reached after 3-1/2 hours and remained at that height for 1 hour when a controlled descent lasting 2 hours to 113,000 feet was initiated. Cutdown then took place, and the gondola landed about 1 hour later at 16,30 hours.

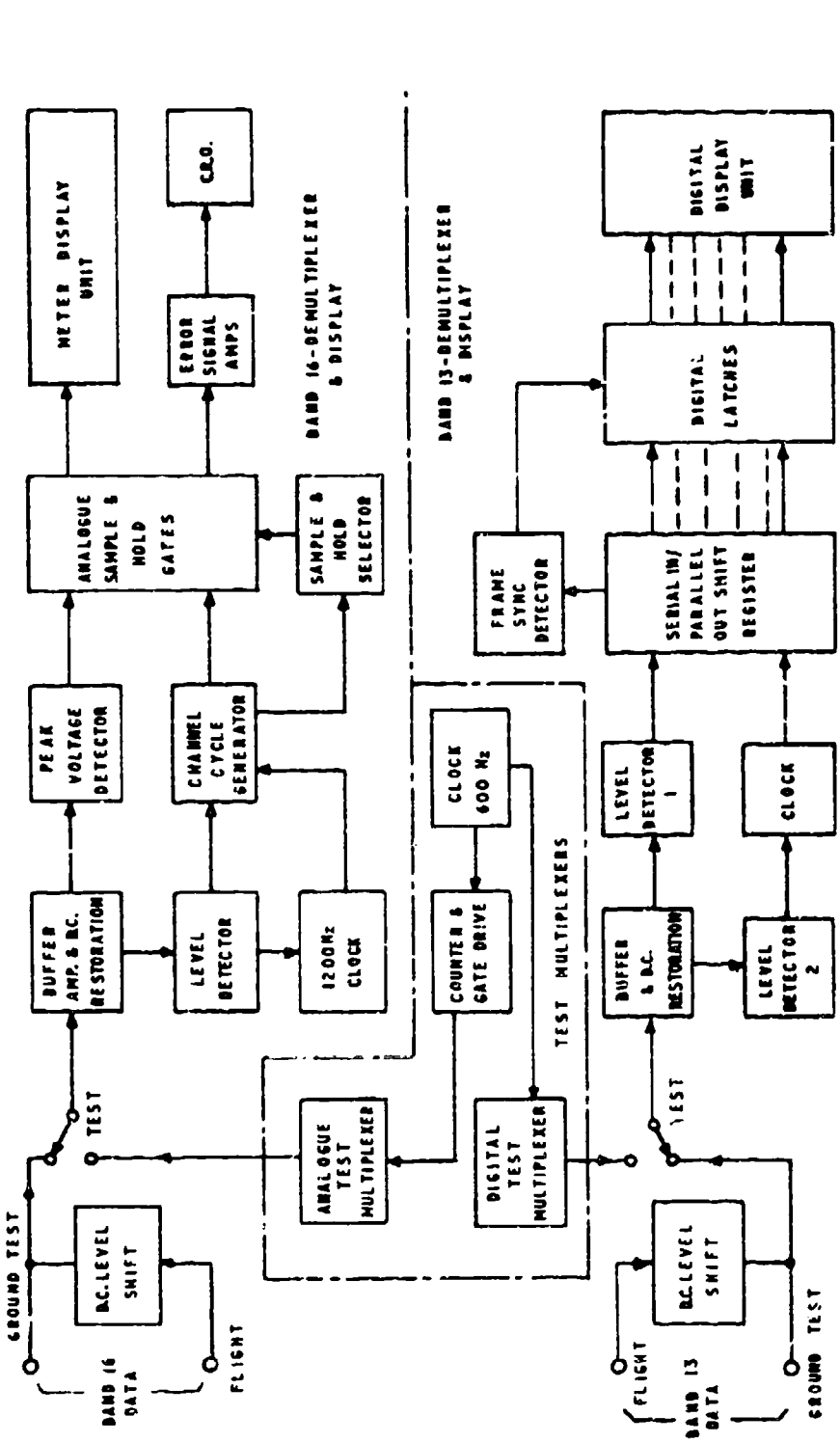

Figure 21-13. Ground Test Unit Data Block Diagram

The camera, film and spectrograph were recovered satisfactorily, moderate damage having been suffered by the outer instrument housing, this resulting from the elevation arm on the biaxial pointer having sheared on impact.

During ascent when the balloon spin rate was high, fictitious start signals caused false exposure sequences. We were unable to investigate the cause after recovery due to the damage to the equipment on landing. We suspect that an intermittent power supply lead may have been the trouble. Prompt action through the radio command system soon returned the system to normal. Apart from this difficulty, all the timing, control and telemetry arrangements worked well, and at no time was difficulty experienced with the radio command system.

The biaxial pointer and our servo had both acquired the sun before release of the balloon, and apart from a few seconds during the launch both systems remained locked on to the sun for the whole flight. Analysis of the image camera film records indicate that at float altitude there was slight drift in both axes over a period of about 2 hours. A mean drift of 4 arc seconds in the horizontal axis and 2 arc seconds in the vertical axis was recorded. The peak-to-peak noise excursions were 12 and 8 arc seconds for the horizontal and vertical axes, respectively. A

A total 240 film exposures were made on the spectrograph recording camera, about 50 of these occurring during the malfunction period.

The spectral data reduction from the flight has yet to be completed, but preliminary studies indicate that the majority of the scientific aims of the experiment were achieved (Bates, McDowell and McKeith, 1971).

Acknowledgments

This paper has outlined some of the equipment designed and built solely for this experiment in a time scale – from commencement to flight readiness – of only 7 months. This would not have been possible without the assistance of our colleagues in the Projects Group at Culham. We should like also to thank our collaborators at Queen's University and at AFCRL. In particular we should like to record our appreciation of the assistance received from Robert B. Toolin and Harry Prevett of AFCRL, Norman C. Poirier of Northeastern University, and especially John Essex, also of AFCRL, for his invaluable help in solving our semantics problems.

References

Bates, B., Bradley, D. J., McBride, D. A., McKeith, C. D., McKeith, N. E., Burton, W. M., Paxton, H. J. B., Shenton, D. B., and Wilson, R. (1971) Trans. Roy. Soc. London A270:47.

Bates, B., Bradley, D. J., McKeith, C. D., McKeith, N. E., Burton, W. M., Paxton, H. J. B., Shenton, D. B., and Wilson, R. (1969) Nature 224:161.

Bates, B., McDowell, M. W., and McKeith, C. D. ( ) Balloon Flight, H71-28, Preliminary Report not yet published.

Black, W. S., and Shenton, D. B. (1965) Peaceful Uses of Automation in Outer Space, Plenum Press, New York.

Cope, P. E. G. (1964) J. British Interplanetary Soc. 19(No. 7):258-291.

Greeb, M. E. (1965) Design and Development of the Balloon Borne Solar Pointer, BBSP 200, Final Report, Ball Brothers Research Corporation.

Contents

22. Operation of a Cryogenically Cooled Infrared Radiometer from a Balloon Platform

E.R. Streed and G.C. Vliet
Lockheed Missiles & Space Company, Inc.
Palo Alto, California

T.P. Condron and J.C. Sullivan
Air Force Cambridge Research Laboratories
Bedford, Massachusetts

22-1. INTRODUCTION

Measurement of the spectral atmospheric emission in the 8- to 13-micrometer wavelength range is of interest to determine the magnitude of the background for stellar observations and to determine the time or spatial variations in gaseous or aerosol compositions. Because of absorption and scattering by lower atmosphere water vapor and carbon dioxide, measurements of the upper atmosphere are severely restricted and limited to special viewing conditions from the ground and from mountain-altitude dry sites.

The use of aircraft, balloons, or rockets can overcome at least 85 percent of the water vapor absorption and reduces the problems associated with condensation on cold optical components. With presently available cooled germanium bolometers (Low, 1961) or doped germanium photoconductive detectors (Caren and Sklensky, 1970), the system performance can be improved significantly by cooling the entire detector field of view (see Figure 22-3). Cryogenically cooled infrared instruments have flown on balloons (Murcray et al, 1969; Jennings and Moorwood, 1971) and rockets (Girard and Lemaitre, 1970; McNutt et al, 1969)

using liquid cryogens, but the system described in this paper is believed to be the first instrument flown which uses a solid cryogen.

The solid cryogen cooled optical system is of unique double focus design to provide a large total field of view (8 degrees) with high out-of-field energy rejection and an optical resolution that approaches the diffraction limit for a 12.7-centimeter aperture. A four-detector Hg:Ge array with eight spectral filters provides spectral coverage from 8 to 13 micrometers.

The purpose of this paper is to describe the instrument, calibration, and performance during three balloon flights. The radiometer was designed and fabricated by the Lockheed Palo Alto Research Laboratory. Calibration was performed at Palo Alto and at the Arnold Engineering Development Center by a team of AFCRL and LMSC personnel.

22-2. RADIOMETER DESIGN

22-2.1 General Description

The electronic, optical, and cooling systems are designed to stand the prelaunch handling of the gondola, remote operation for balloon flights up to 9 hours, and the shock and unattended shutdown on landing. A variation in background emission of about five orders of magnitude is accommodated by a logarithmic amplifier and neutral density filters. Twenty-eight Vdc power is provided by nickel-silver batteries. The system design includes a liquid nitrogen (LN_2) cooled occulting shade located forward of the optical train. The shade and first optical element are covered by a motorized movable cover to protect the optical system from condensation at low altitudes and as a temperature calibration source during flight. The optical train and detectors are conductively and radiatively cooled by solid neon formed in a toroidal tank attached to the aluminum optical barrel. The entire optical assembly and neon tank are enclosed in an LN_2 jacketed double evacuated Dewar.

A frost-free optical system is assured during flight by purging the optical volume with the neon vent gas and mixing the neon gas and warm nitrogen gas at the shade aperture before expulsion to the ambient environment. A separate LN_2 tank, a heat exchanger, and a hot water tank are carried aloft with the balloon to supply the warm nitrogen gas.

The radiometer and Dewar assembly are mounted on a gimbal system operated as part of the gondola equipment to remotely control the viewing angle at 90 degrees (vertical); 45, 30, 15, 10, 5, and 0 degrees (horizontal); or -5 degrees. The main components of the radiometer system are shown in Figure 22-1.

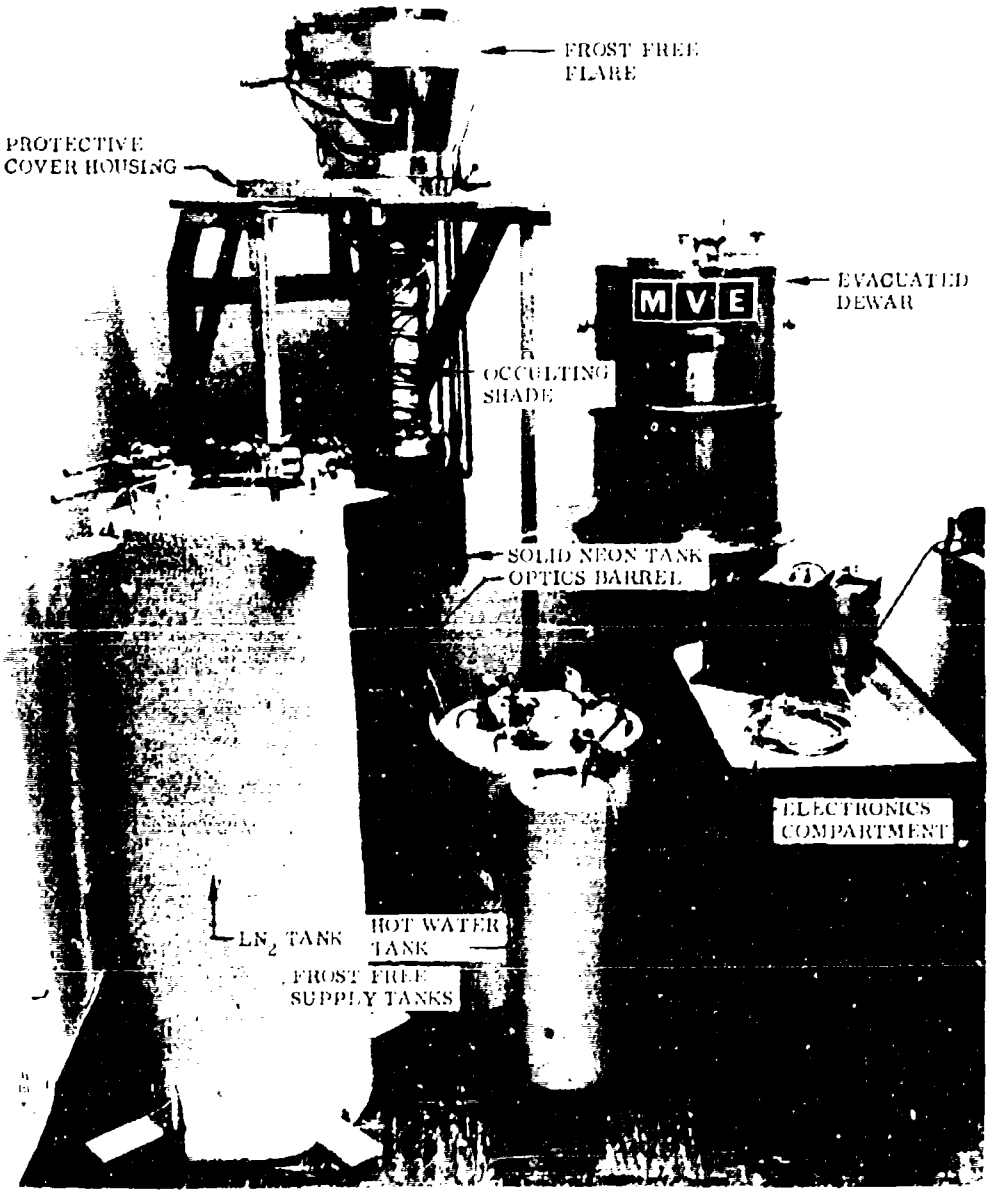
FROST FREE
FLARE
PROTECTIVE
COVER HOUSING
MVE
EVACUATED
DEWAR
OCCULTING
SHADE
SOLID NEON TANK
OPTICS BARREL
ELECTRONICS
COMPARTMENT
LN_2 TANK
HOT WATER
TANK
FROST FREE
SUPPLY TANKS

22-2.2 Optical System

The on-axis double-focusing optical design[4] is conceptually similar to the solar coronagraph but does not use an occulting disk. By using a cooled shade, baffling forward of the optics, and a cooled mask aperture at the first focal plane, the out-of-field energy rejection was measured to reach 10^8 for radiation more than 1/2 degree out of the field-of-view.

The optical system, shown schematically in Figure 22-2, consists of a 12.7-centimeter diameter, 25.4-centimeter focal length germanium collecting lens with one aspheric surface. A three-element array of transfer optics with unit magnification consists of one TI-1173 and two germanium glass lenses. Optical resolution measurements made with the system cold indicated that the optical system is within a factor of two of the diffraction limit at 10 micrometers. All optical elements are antireflection coated to provide maximum transmission in the 8- to 13-micrometer range.

Eight multilayer interference filters deposited on germanium substrates are used to vary the spectral bandpass and bandwidth. The center wavelength, λ_c, and spectral bandpass are listed in Table 22-1. Of the eight neutral density filter positions available, filters with an average transmission of 1.0, 0.2, and 0.02 percent are used. The additional positions are either blanked off or completely open. The filters are positioned with 16 in.-lb starting torque gear-reduced dc motors, a Geneva drive mechanism, and a cam activated microswitch. Each complete turn of the gear head shaft rotates the eight-position mechanism such that the filter rotates 1/8 of a turn. An eight-position switch with resistors is simultaneously rotated 1/8 of a turn to provide a 0- to 5-Vdc monitor voltage. Special bearings lubricated with a graphite-free MoS_2 lubricant, abnormally large bushing clearances, and in-house fabricated $NbSe_3$ motor brushes were used to facilitate operation of the motors at 22°K.

The interior of the aluminum shade is serrated and black anodized to minimize off-axis scattered radiation. The shade is cooled to about 80°K by conducting straps attached to the LN_2 guard Dewar. Thermal isolation from the colder optical system and the warmer Dewar cover is obtained with fiberglass transition adapters.

A conical radiation cone is located in front of the first focal plane and used to support a field stop mask with aperture dimensions of 1.22 millimeters wide by 4.75 millimeters long. Both components are black anodized to reduce scattered radiation reflected back from the chopper.

---

[4] Performed by Optical Instruments Corp., Buena Park, California

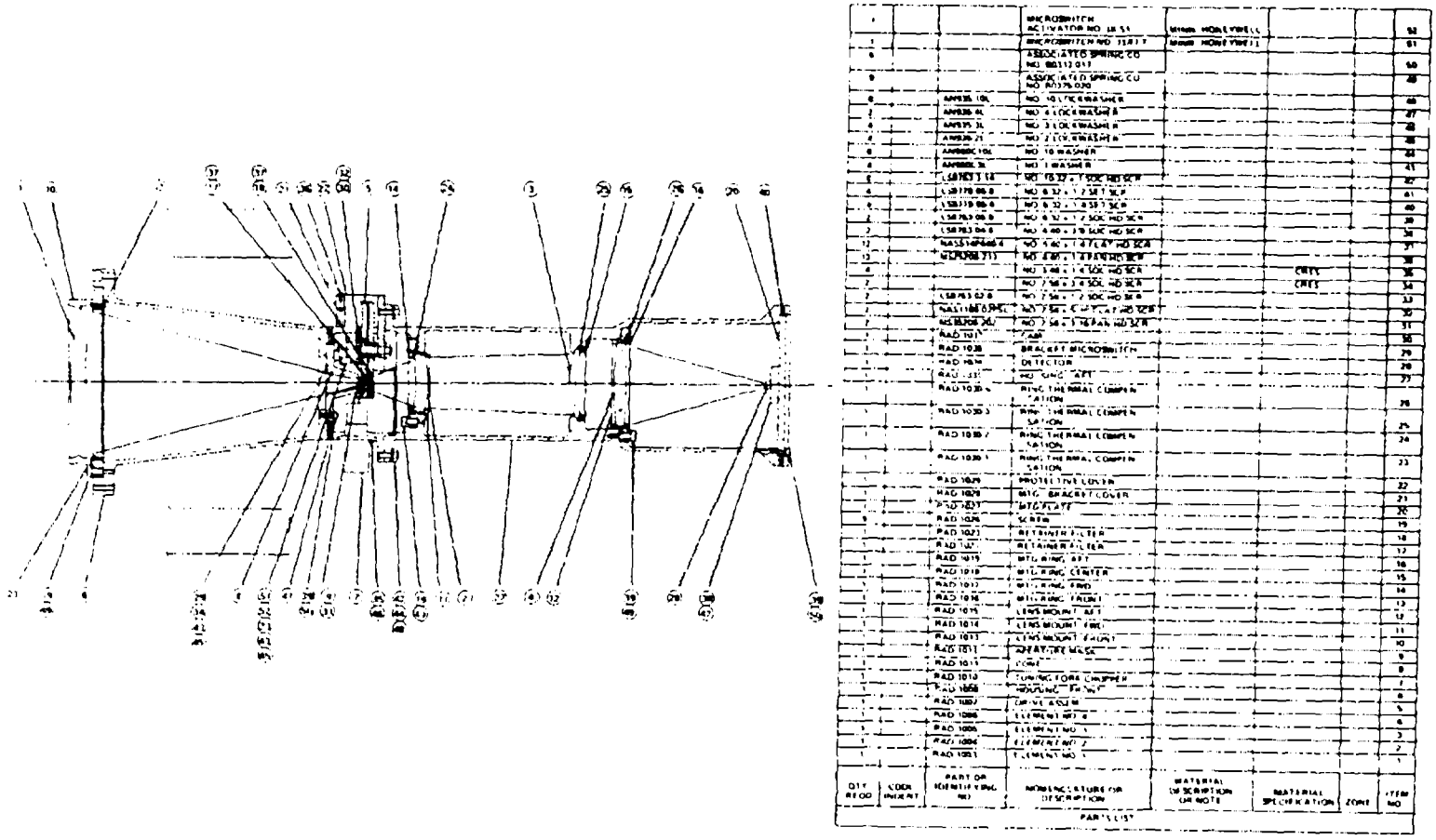

Figure 22-2. Schematic Diagram of Optical, Filter, and Detector Components

Table 22-1. Wavelength and Transmission Characteristics of the Spectral and Neutral Density Filters

Spectral Filters Center Wavelength (μm)	Δλ (μm)
12.03	0.07
10.77	0.10
10.56	0.26
11.99	0.29
11.32	0.74
9.75	1.59
11.62	2.17
10.56	4.75
Neutral Density Filters (Percent Transmission)	
1.0	
0.2	
0.02	
Position for 100% and 0%	

22-2.3 Detection and Electronic System

Optical chopping is accomplished with a vibrating reed chopper located just aft of the field stop. The nominal 200-Hz chopping frequency is controlled by an electronic oscillator located in the electronic chassis. A pickup coil mounted adjacent to the driver coil is used to provide the synchronous signal to the sync generators for each detector amplifier. A 0- to 5-Vdc status voltage is transmitted during flight to monitor the chopper performance.

The four Hg:Ge doped detectors are mounted in a linear array on a copper heat sink attached to an aluminum end plate at the aft end of the optical barrel. Two detectors have an effective solid angle field of view of 1.45×10^{-6} steradians and the other two 4.39×10^{-6} steradians. The spectral response of photoconductive Hg:Ge extends from 2 to 14.2 micrometers with a peak relative response at about 12.5 micrometers. The load resistor and MOSFET source follower are located on the detector mount and cooled to 24°K. The rms noise voltage of a detector unit as a function of background photon flux is shown in Figure 22-3.

The transistorized electronic system, shown schematically in Figure 22-4, consists of the following major elements:

(a) Signal conditioner

(b) Chopper oscillator, synchronous generator

(c) Neutral density and spectral filter drive and monitor electronics

(d) Special power supplies for items a, b, and c

(e) Temperature sensor signal conditioner

(f) Relay and hatch cover drive mechanism

(g) Thermostat and heater for electronic housing temperature control

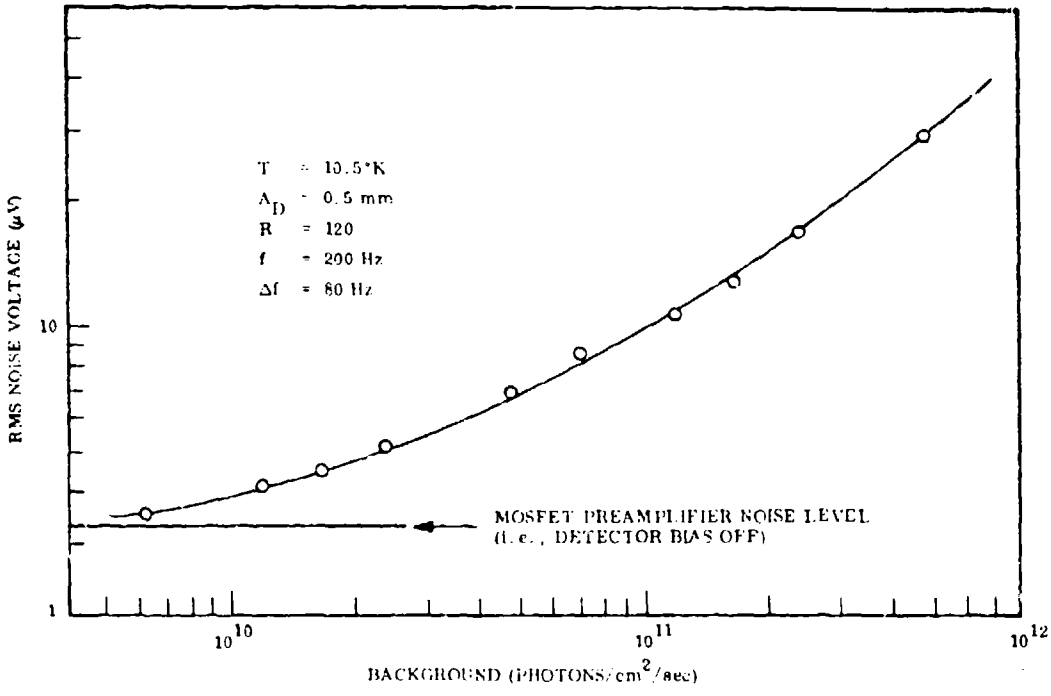

Figure 22-3. RMS Noise Voltage as a Function of Background Photon Flux

The synchronous signal amplifier system employs a preamp, 150- to 250-Hz bandpass amplifier with a gain of three, 200-Hz synchronous demodulator with a 40-Hz output filter, and a 0- to 5-V logarithmic amplifier. An inflight calibration signal is automatically switched to each channel at 0-, 2.5-, and 5.0-V levels when the hatch cover opens or closes.

A 14-channel FM tape recorder is used as the primary onboard recorder with a digital, 4-millivolt resolution recorder used as backup. Frequency modulated telemetry (0 to 5 Vdc) is available using either S-band (2250 MHz) or P-band (240 MHz). Two flux gate magnetometers are installed and calibrated on the gondola to provide azimuth position data during the flight. A central control panel, provided as part of the gondola[1], electrically integrates the radiometer

[1]Designed, built, and checked out by Denver Research Institute.

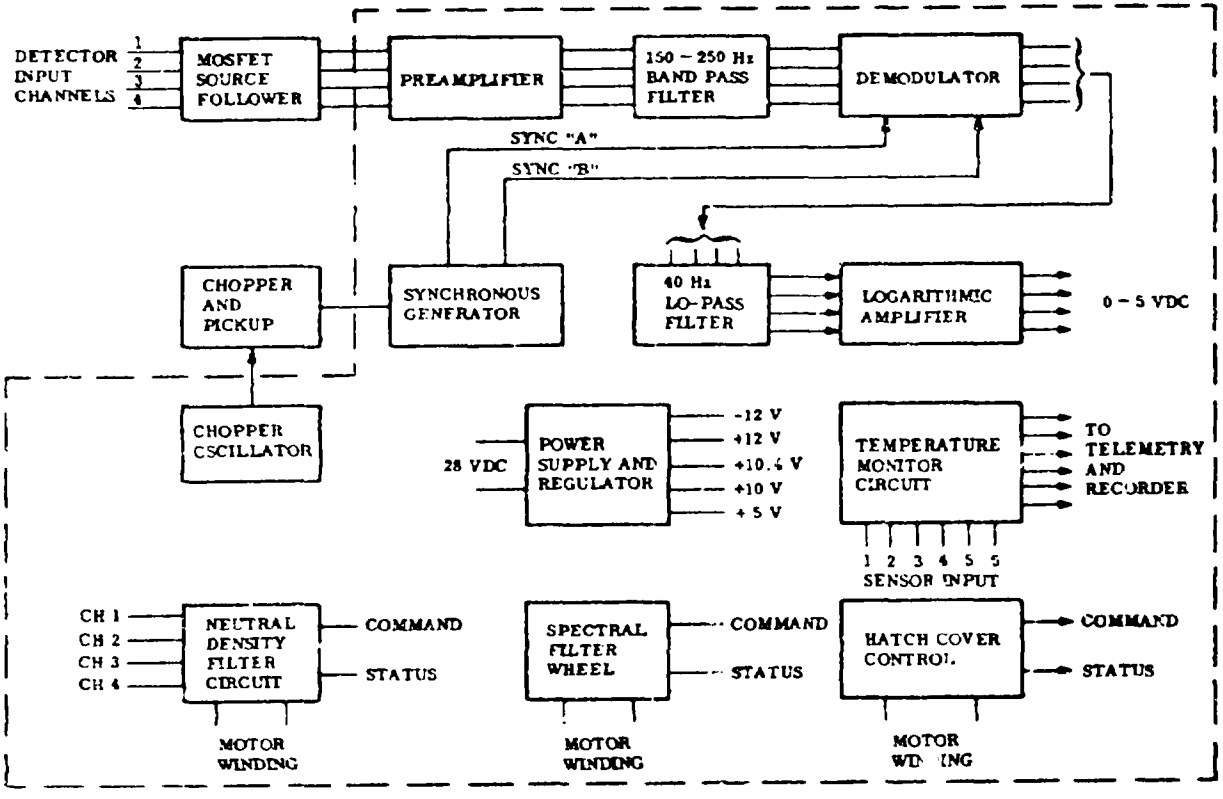

Figure 22-4. Schematic Diagram of Electronic System

with the battery power supply, tape recorders, AFCRL-supplied command package, and the telemetry. The command package is used for preflight calibration of each measurement channel. A breakdown of the electrical power requirements for the major components is listed in Table 22-2.

Table 22-2. Radiometer Experiment Power Requirements

Item	Power (W)	Voltage (V)
Signal Electronics	10	28
Phase Adjust Circuitry	2	
Temperature Sensor Circuitry	6	
Chopper	Negligible	20
Spectral Filter Motor (5% duty cycle)	18* (operating)	12
Neutral Density Filter Motor (5% duty cycle)	18 (operating)	12
Hatch Cover Drive Motor (5 W max.) (intermittent, 20% duty cycle)	18	12
	37	
Electronic Box Heater	56	28
Neon Container Heater	~5	
Total	98	

*Filter and hatch cover motors do not operate simultaneously.

22-2.4 Thermal Control

Temperatures are monitored at six locations to evaluate the system performance prior to and during the flight. These locations include the neon container, shade aft, shade front, hatch cover, flare section, and electronics housing. Platinum resistance thermometers and associated bridge circuits with 0- to 5-Vdc transmitters serve as temperature transducers.

The electronics housing is temperature controlled to 305 degrees ±5°K using two flexible heater blankets, an on-off thermostat, and both flexible and rigid foam insulation. The housing exterior is coated with a white paint for minimum solar absorption. The interior is painted black to increase radiative transfer.

The entire optical, chopping, spectral filtering, and detection system is coupled to the solid neon container. Neon, with a triple point of 24.8°K, was selected because of its relatively high heat of sublimation and safety in handling.

In flight, the neon temperature may get as low as 22°K because of the reduced pressure at operating altitude (~10 mm Hg). The torodial copper neon tank contains copper baffles to keep the gradient between the solid neon and the tank wall to 1°K. Internal coolant lines are provided to permit subcooling and freezing of the neon with liquid helium. The 5.25-liter tank has a hold time of about 10 hours after termination of helium cooling.

22-2.5 Frost Free System

The exposure of cold optical elements to the launch and flight environment can potentially cause condensation problems on the optics or the formation of fog within the field of view. The adopted concept employs a cold neon boil-off gas stream to maintain the front optical window and the shade near the necessary 77°K, and a secondary warm nitrogen gas stream to mix with and warm the cold stream to ambient temperature before it is exposed to the "wet" exterior environment. The cold neon is introduced through peripheral jets immediately forward of the front window, and the warm stream is introduced at the forward end of the shade through jets and a 22.9-centimeter section of porous wall as indicated in Figure 22-5. The outer section of the shade is flared to an angle of 10 degrees, which is beyond direct viewing by the optical system. The warm nitrogen is supplied by an onboard 70-liter tank of LN_2, which is vaporized and heated with hot water.

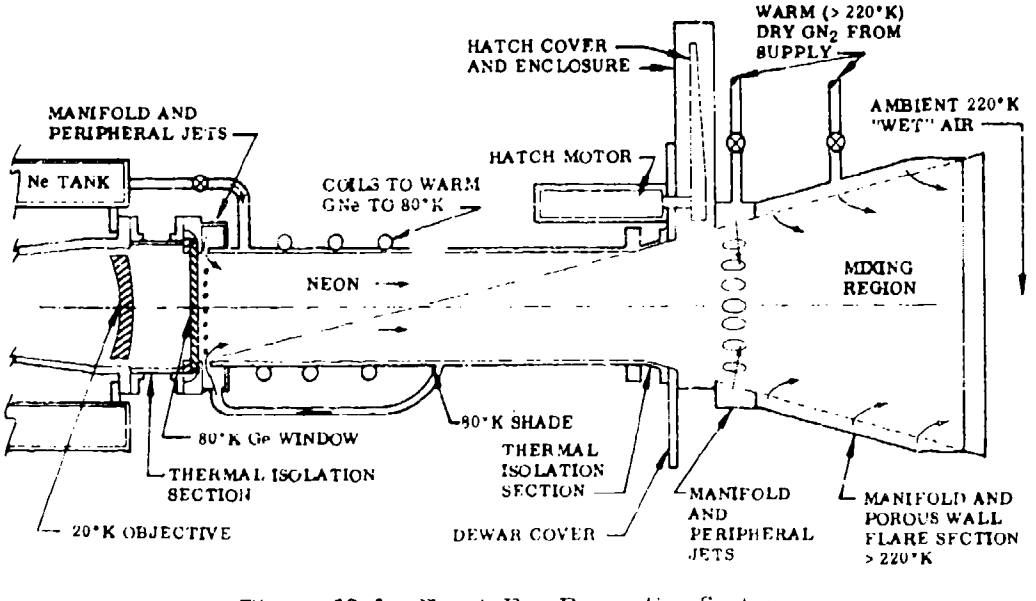

Figure 22-5. Frost-Fog Prevention System

Additional environmental and physical protection for the optical system is provided before launch and during the ascent phase by a movable hatch cover. The 19-centimeter diameter cover is driven by a remotely controlled dc motor with shutoff microswitches at both the open and closed positions. The inside black-coated hatch cover (emittance = 0.92) is temperature monitored to serve as a calibration source when closed.

22-2.6 Radiometer Flight Package

The radiometer assembly, telemetry, tape recorders, storage tanks, batteries, and ballast are mounted on the gondola platform with dimensions of 1.67 meters by 2.36 meters (65 inches by 92 inches). The radiometer Dewar is mounted to the worm gear-driven gimbal system near its center of gravity for ease of rotation and to maintain the gondola in a horizontal position during flight when the radiometer is rotated downward. A list of the major components, cryogens, and gondola typical weights is given in Table 22-3. With the balloon weight of about 700 pounds, the total lifting weight is approximately 2600 pounds.

Table 22-3. Summary of Flight System Weight

Item	Weight (Tare) (lb)	Cryogens (lb)	
Radiometer/Dewar	420		
LHe		14	
LN_2		59	
LN_2 Storage Vessel	128		
LN_2		100	
Water Tank	80		
Water		75	
Electronic Box	40		
Subtotal	674	248	922
Gondola, Battery Recorder, Telemetry Crash Pad			642
Parachute			300
Total			1864*

*For launch on May 16, 1972 (does not include ballast).

22-3. CALIBRATION

Assembly and calibration of the radiometer was conducted in several phases to provide an evaluation and data for the major components as well as the system. The detector array was calibrated with respect to frequency response, responsivity, and noise prior to integration with the optical system. Following installation of the detector array, the absolute responsivity and field of view of each detector were measured using a collimated 873°K blackbody which was apertured down. The apparatus was attached to a rotary table mounted vertically over the radiometer such that controlled movement simulating azimuth and elevation angular rotation with respect to the radiometer optical axis was obtained. The table is remotely controlled to an angular resolution of 3.6 arc seconds in azimuth and 1.0 arc second in elevation. Data points are taken each 0.01 degree until the signal is lost in the noise.

Absolute responsivity measurements were made using a point source and extended source in vacuum. These measurements were later verified with an attachable extended source to permit operation in an air exterior environment. The attachable source, shown in Figure 22-6, is mounted to the top of the LN_2 Dewar flange with a vacuum-tight seal. The blackened copper source surface is machined with 45-degree concentric grooves to provide an emittance of about 0.95

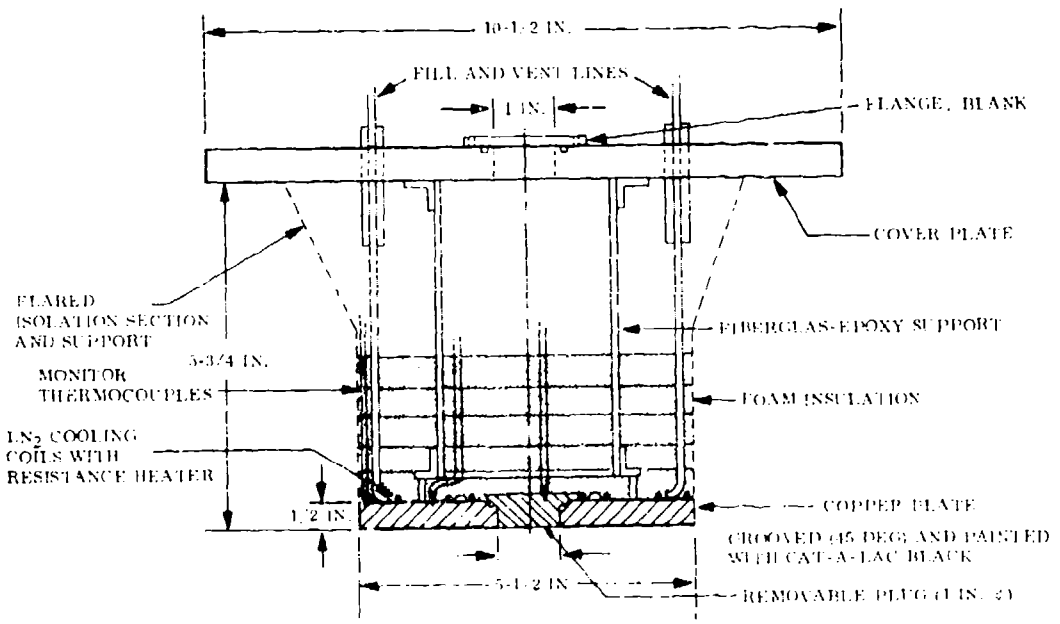

Figure 22-6. Cross Section of Attachable Calibration Source

over the 77 to 300°K temperature range. The temperature is regulated with LN_2 and resistance heating on the backside of the copper plate. Chromel-constantan thermocouples mounted and calibrated in the block serve as temperature transducers. Output voltage for each detector channel is measured for all eight filter positions at sufficient blackbody temperatures to cover the dynamic range. The effective radiance is computed for each source temperature, and plots of output voltage versus the corresponding effective radiance are made for each detector and filter position.

22-4. PREFLIGHT PREPARATION

The low temperature operation of the radiometer requires cooldown operations to commence about 24 hours before the launch. The LN_2 Dewar and the neon tank are filled with LN_2 to provide a thorough soak and elimination of temperature gradients in the optical systems. About 6 hours before launch, the preliminary LHe cooldown is performed in the hangar area for about 2 hours. When the detector temperature reaches 24°K, a checkout of system operation before moving to the launch area is performed. The system is flushed with gaseous helium to ensure no internal pumping of water vapor during transfer to the launch area. With weather permitting, the LHe cooling is resumed to bring the neon tank down to about 35°K. Then the transfer of approximately 11 liters of liquid neon is required to cool the system to 24°K and to fill the neon tank in about 45 minutes. The neon is subcooled for 30 minutes with liquid helium to solidify the neon. Simultaneous vacuum pumping on the LN_2 Dewar is done to freeze part of the liquid and minimize sloshing when the radiometer is rotated. The antifrost LN_2 tank is filled just prior to leaving the hangar area and then topped off just before launch. The water tank is also filled and heated to about 175°F prior to leaving the hangar. The flow of warm GN_2 through the flare section is adjusted for the proper rate after subcooling the neon and blended with the boil-off gas from the neon tank and the LN_2 Dewar just before launch. A view of the radiometer during the LHe subcooling operation on the flight line is shown in Figure 22-7.

22-5. FLIGHT MEASUREMENTS

Three balloon-borne test flights have been conducted with the instrument from Holloman AFB. During the first flight, the FM tape recorder failed and only limited telemetry was obtained, but the cooling system and launch procedures worked satisfactorily.

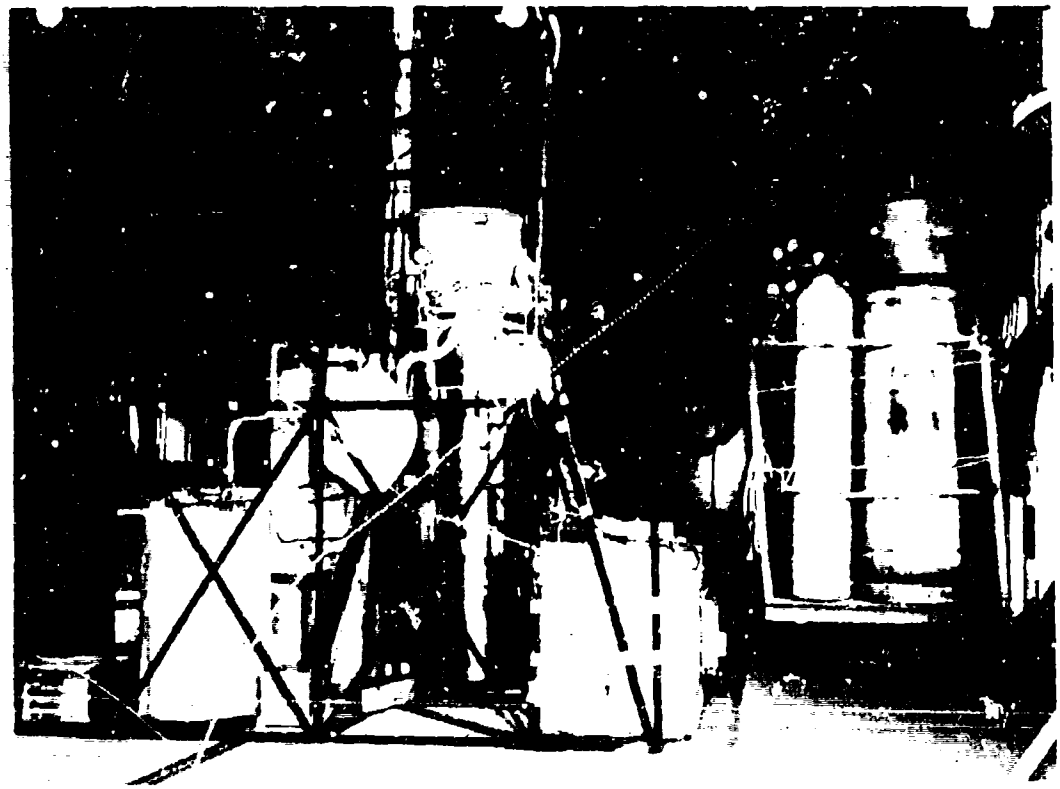

Figure 22-7. Liquid Helium Transfer Operation to Subcool the Neon Just Before Launch

The second flight included a digital tape recorder as backup and utilized [illegible] telemetry. The spectral filter wheel was locked on the 10.5- to 12.75-micrometer filter, and radiance data were obtained from -5 to +15 degrees while at float altitude. A plot of the radiance as a function of elevation angle is shown in Figure 22-8 for two passes.

The third flight occurred on May 23, 1972, and data were obtained with all eight spectral filters for elevation angles from -5 to +30 degrees during a 9 hour flight. Measurements were commenced under dark conditions and proceeded through sunrise, and a complete set of elevation data was obtained during sunlight conditions. Full telemetry and a M tape recording of the data were obtained, but computer reduction had not been performed at the time of preparation of this paper.

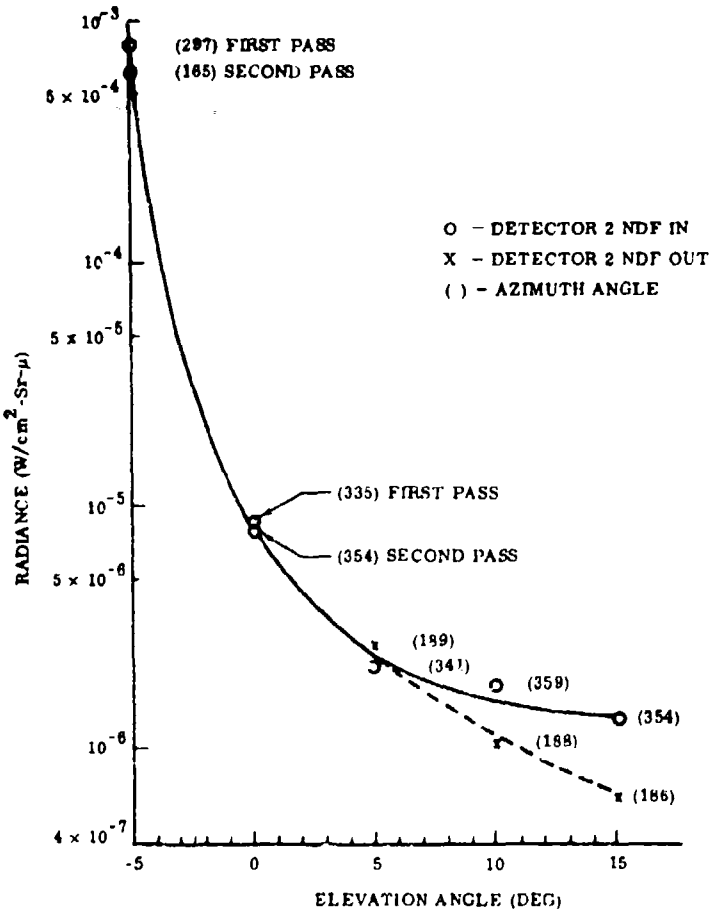

Figure 22-8. Plot of 10.5 to 12.25 μm Atmospheric Radiance as a Function of Elevation Angle

References

Caren, R. P., and Sklensky, A. F. (1970) Cryogenic Requirements of High Performance Infrared Sensors. Paper presented at Space Technology and Heat Transfer Conference, Los Angeles, Ca.

Girand, A., and Lemaitre, M. P. (1970) Profils experimentaux de l'horizon infrarouge de la terre, Appl. Optics 9:903.

Jennings, R. E., and Moorwood, A. F. M. (1971) Atmospheric emission measurements with a balloon-borne Michelson interferometer, Appl. Optics 10:2311.

Low, F. J. (1961) Low-temperature germanium bolometer, JOSA 51:1300.

McNutt, D. P., Shivanandan, K., and Feldman, D. P. (1969) A rocket-borne liquid helium-cooled infrared telescope. I: Dewar and Optics, Appl. Optics 8:2199.

Murcray, D. G., et al (1969) Six-Month Technical Report, Contract F 19628-68-C-0233, ARPA No. 1366.

Contents

23. High Altitude Blast Generation System: Detonable Gas Mixing Experiments

S.F. Fields, Ph.D.
General American Transportation Corporation
Niles, Illinois

Abstract

The overall objective of this program was to investigate experimentally the mixing processes occurring in inflight balloons of the "bar-bell" or ballonet type in which initially separate gases (methane and oxygen) are allowed to mix to form a detonable gas mixture during ascent to cruise or test altitude. This investigation has been carried out by testing appropriately scaled model balloons in the Ballistic Research Laboratories' Blast Sphere Facility.

During two weeks of tests in the blast sphere, a series of gas concentration measurements was made for balloons operating over a range of simulated altitudes from sea level to 50,000 feet. In addition, a series of seven balloon detonations was performed at a simulated altitude of approximately 35,000 feet. The results of these tests confirm the operational feasibility of balloons of the "bar-bell" or ballonet type. In particular, the results establish that balloons of this type quite readily generate gas mixing of the desired efficiency while ascending to test altitude.

23-1. INTRODUCTION

Research previously conducted by the General American Research Division* has demonstrated that explosive sources provided by detonable gas mixtures initially contained in balloons are capable of producing appropriate air blast environments for examining system and component vulnerability. The air blasts produced by gaseous detonations have characteristically smooth shock fronts and are repeatable and analytically predictable. In addition, the buoyancy of certain detonable gas mixtures is ideally suited to high altitude blast simulation applications.

However, before any full scale application of a high altitude blast generation system based on detonable gas mixtures contained in balloons is attempted, certain safety requirements must be met. In particular, safety requirements at the launching site, especially from ships at sea, dictate that balloon configurations be investigated which initially separate the oxygen and fuel gases. By allowing the gases to mix to form a detonable gas mixture only after launch, the risk of accidental detonation at the launching site will be greatly reduced.

The overall objective of this program was to investigate experimentally the mixing processes occurring in inflight balloons of the "bar-bell" or ballonet type in which initially separate gases (methane and oxygen) are allowed to mix to form a detonable gas mixture during ascent to cruise or test altitude.

23-2. THEORY

In principle the "bar-bell" or ballonet balloon (hereafter, ballonet balloon) operates as follows (see Figure 23-1). Initially, the heavier gas (oxygen) is confined to an independent chamber at the bottom of the balloon. This oxygen chamber is fully inflated and therefore taut. The lighter gas (methane) is located in a much larger, partially inflated chamber at the top of the balloon and provides the lift. Gas communication between the oxygen and methane chambers is provided by means of a duct which is closed during launch. During the ascent phase, the duct is opened, and the gases expand in response to ambient pressure reduction. Since the taut oxygen chamber cannot expand, oxygen flows into the top chamber which is free to expand. Oxygen continues to flow until an equilibrium condition exists between the chambers. This equilibrium condition occurs shortly after the upper chamber is fully inflated.

---

*For a summary of previous GARD work in this area, see works by Balcerzak et al, 1966; Balcerzak et al, 1967; Klima et al, 1967a; Klima et al, 1967b; and Lucole and Balcerzak, 1968.

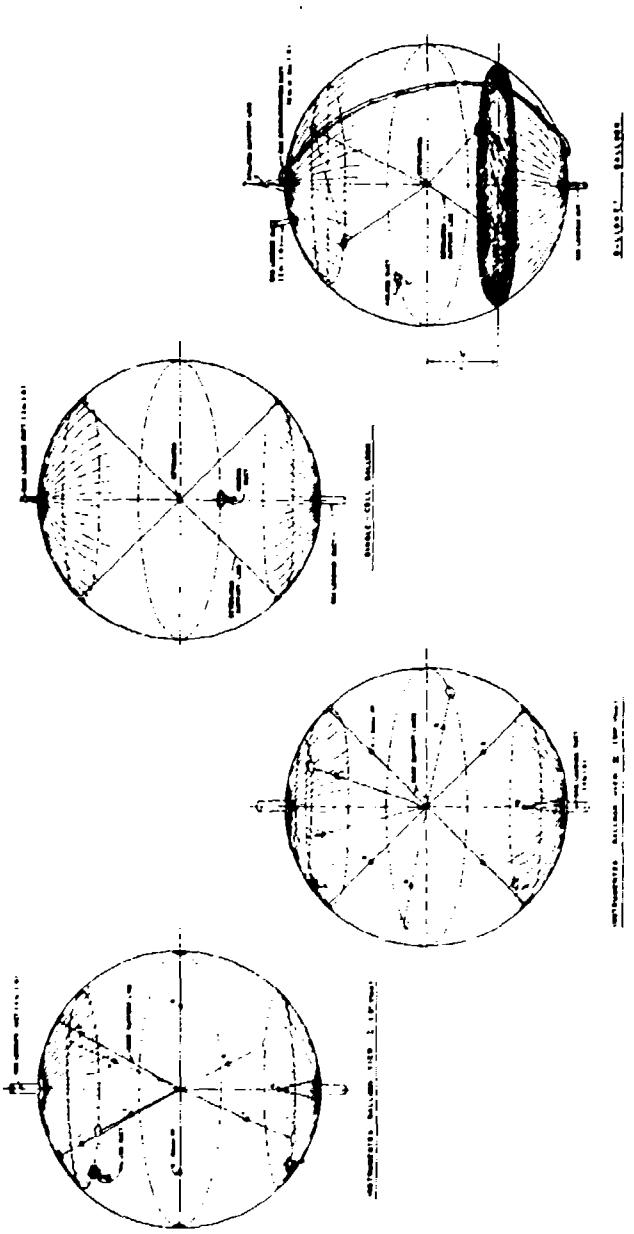

Figure 23-1. Ten-Foot Diameter Model Balloons

In order to simulate the mixing processes that would occur in a full scale ballonet balloon (yield equivalent to 20 tons of TNT at an altitude of 35,000 feet), proper scaling relationships must be determined. It is known that gas mixing will occur primarily due to the action of a turbulent plume formed by introducing heavy gas into the light gas at the top of the balloon (Holmes and Fugelso, 1971). The mixing mechanisms that must be considered to determine appropriate scaling relationships are, therefore, forced convection due to inlet jet momentum, buoyant free convection due to the effect of gravity, turbulent diffusion due to the effect of viscosity, and molecular diffusion.

Theoretical analysis indicates that scaling must be done according to the Froude number, $Fr = U/\sqrt{gD}$, where U is the heavy gas flow velocity into the top of the balloon, D is the balloon diameter, and g is the acceleration due to gravity. In addition to this direct scaling, certain constraints must be satisfied. The Reynolds number, $Re = Ud/\nu$, must be large enough to ensure fully developed turbulent flow. In this expression, d is the inlet duct diameter, and ν is the kinematic viscosity of the heavy gas. At the same time, the pressure head required to drive the flow of heavy gas must be maintained within balloon tolerances. As a result of this, duct sizes are limited as to how small they can be, and the possibility of forced convection is virtually eliminated.

Secondary constraints are imposed by the limited range of ascent rates obtainable in the blast sphere facility (which in turn limits the heavy gas mass flow rates obtainable in a model balloon). Also, since molecular diffusion effects can be shown to be entirely negligible in the full scale case, these effects must be kept as small as possible in any simulation with model balloons.

For a full-scale single-cell balloon, GARD calculations (Calligeros and Hobbs, 1972) indicate that a balloon diameter of 165 feet would be required for a yield equivalent to 20 tons of TNT at 35,000 feet. For scaling purposes, the diameter for a full-scale ballonet balloon with a yield equivalent to 20 tons of TNT at an altitude of 35,000 feet can also be taken as 165 feet. For a typical ascent rate of 1000 feet per minute, the following values of Fr and Re result:

$$Re = 68 \times 10^4 P^*, \quad Fr = .49 . \tag{23-1}$$

The above values of Re and Fr are based on a single duct diameter of 3 feet (approximately equivalent to two 2-foot diameter ducts). For a gas communication duct length of approximately 250 feet, this diameter will produce head losses

---

*Reynolds number computed assuming that the kinematic viscosity of oxygen can be expressed as $\nu = \nu_0/P$, where ν_0 is the sea level value of $\nu(1.5906 \times 10^{-4}$ $ft^2/s)$, and P is the ambient pressure in atmospheres.

of no more than .02 psi. A ballonet should be capable of withstanding a pressure differential of this order.

Similar calculations can be made for a model 10-foot diameter ballonet balloon. For scaling purposes, Froude numbers of about .5 or less are required, as well as a large enough Reynolds number to ensure fully developed turbulent flow. Based on an ascent rate of 3000 feet per minute (this ascent rate is about the highest obtainable with the blast sphere facility and is desirable to minimize molecular diffusion effects), flow calculations result in the following set of values:

$$\underline{d = 2 \text{ in.}}$$
$$Re = 81 \times 10^2 P$$
$$Fr = .43 \qquad (23\text{-}2)$$

$$\underline{d = 3 \text{ in.}}$$
$$Re = 54 \times 10^2 P$$
$$Fr = .19 \qquad (23\text{-}3)$$

Head losses associated with the oxygen flow in the gas communication duct will be negligible in each of these cases.

In order to investigate adequately the performance of the model ballonet balloon over a significant range of Froude numbers, four model ballonet balloons were constructed for the test program, two with a gas communication duct inner diameter of 2 inches and two with a gas communication duct inner diameter of 3 inches.

23-3. PROCEDURE*

Four sets of experiments were conducted during the test series. The first two sets of experiments were performed using carbon dioxide and nitrogen gases and a balloon instrumented (see Figure 23-1) such that the concentration of these gases could be measured versus time at various positions inside the balloon. In this way direct experimental monitoring of various gas mixing processes was possible. Single cell and ballonet balloons (see Figure 23-1) containing oxygen and methane were detonated during the third and fourth sets of experiments. The degree of success in performing these detonations provided further information on the efficiency of the gas mixing processes in question.

*For details concerning gas loading procedures, gas loading systems, balloon systems, and instrumentation systems, the reader is referred to Fields, S. F. (1972).

Teledyne Isotopes of Westwood, New Jersey supplied, installed, and operated the carbon dioxide/nitrogen gas concentration system. This system consisted of nine thermal conductivity cells located inside the instrumented balloon. These cells were referenced to nine other thermal conductivity cells which were left exposed to the blast sphere environment. In this way the effects of temperature and pressure variations on both the primary and reference thermal conductivity cells could be synchronized.

The signal for each primary and reference thermal conductivity cell pair was recorded on a strip chart recorder once every 50 seconds for a period of almost 5 seconds.

For both the single-cell and ballonet balloon detonations, BRL had the responsibility for recording the time of detonation and the time of detonation wave arrival at the surface of the balloon, for making overpressure-time measurements at various positions outside the balloon, and for recording the detonation photographically. Photographic coverage of ballonet balloon deployment during ascent was also obtained.

A schematic of the instrumentation setup for the detonations is shown in Figure 23-2, and a photograph of the blast sphere facility is shown in Figure 23-3.

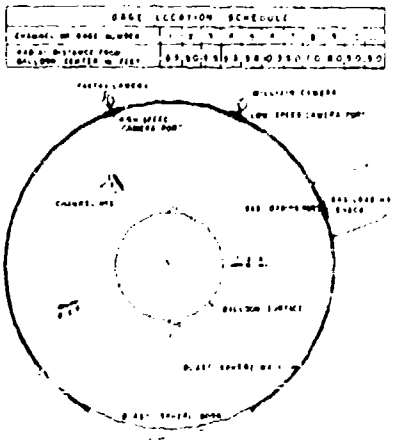

Figure 23-2. Schematic of Layout for Detonation in Blast Sphere, Top View

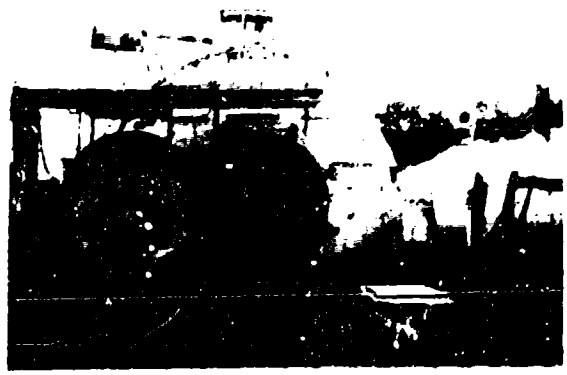

Figure 23-3. Blast Sphere Facility

23-3.1 Molecular Diffusion Measurements

Four molecular diffusion experiments were performed at simulated test altitudes of 20,000 (one experiment), 35,000 (one experiment), and 50,000 feet (two experiments). For each experiment, the instrumented balloon was initially inflated with equal volumes of carbon dioxide and nitrogen gases in a stratified state.

The component gas concentrations were then measured for a period of approximately 20 minutes. To facilitate making accurate gas concentration measurements, full balloon inflation was used to eliminate balloon geometry variations (a balloon superpressure of 1 inch of water was maintained during the course of the measurements).

23-3.2 Plume Measurements

Six plume experiments were conducted ending at simulated altitudes of 20,000, 35,000, and 50,000 feet (two experiments for each altitude). All of the experiments involved heavy gas plumes (carbon dioxide gas loaded into nitrogen gas from the top of the balloon) except for one, which involved a light gas plume (nitrogen gas loaded into carbon dioxide gas from the bottom of the balloon). As for the detonation experiments, the final gas mixture consisted of 60 percent heavy gas and 40 percent light gas by volume.

Plume induced gas mixing was examined by measuring the component gas concentrations versus time at various positions within the balloon during the loading of the second component gas. Full balloon inflation during the loading of the second component gas (performed while descending in the blast sphere) again facilitated making accurate gas concentration measurements by eliminating balloon geometry variations. Descent rates of approximately 100 feet per minute, in combination with the instrumented balloon's 4-inch diameter gas loading ducts, allowed the second component gas to be loaded so that both sufficiently high Reynolds numbers to ensure fully developed turbulent flow and Froude numbers of .5 or less resulted.

23-3.3 Balloon Detonations

For each single-cell balloon detonation (three were performed), the gas loading procedure was to load methane (through the bottom gas loading duct) at sea level. Oxygen was then loaded (through the top gas loading duct) while ascending at a rate of approximately 3000 feet per minute to the test altitude of 35,000 feet. Upon reaching the test altitude and a final gas mixture ratio of $O_2/CH_4 = 1.5$ by volume, the balloon was detonated.

Each experiment was performed using the 3-inch diameter gas loading duct as the top gas loading duct. In conjunction with an ascent rate of 3000 feet per minute, this allowed oxygen gas loading to be performed in a fashion similar to that which was to occur automatically in the model ballonet with the larger gas communication duct during ascent.

For each of the ballonet balloon detonations (four were performed), the gas loading procedure was to load methane into the top chamber and oxygen into the

bottom chamber at sea level. The blast sphere was then evacuated to an altitude of 35,000 feet at a rate equivalent to an ascent rate of approximately 3000 feet per minute. To couteract cooling effects and to obtain a final gas mixture ratio of O_2/CH_4 = 1.5 by volume in the top chamber, the blast sphere was then evacuated to a slightly higher simulated altitude at which full balloon inflation occurred, and the balloon was detonated.

23-4. EXPERIMENTAL RESULTS – GAS CONCENTRATION MEASUREMENTS

Typical gas concentration data for two experiments are shown in Figures 23-4 and 23-5. Figure 23-4 shows portions of the strip chart recording obtained during run number 12, molecular diffusion at a nominal altitude of 20,000 feet. This figure illustrates clearly how slowly gas mixing occurs by molecular diffusion when carbon dioxide and nitrogen are brought into contact in an initially stratified state. The distribution of the two gases inside the balloon at time zero in this figure is due primarily to the gas loading procedure that was used.

Figure 23-5 shows portions of the strip chart recording obtained during run number 6, heavy gas plume ending at a nominal altitude of 35,000 feet. The completeness of plume induced gas mixing throughout the balloon is evident in this figure. As can also be seen, gas mixture gradients decrease with time and are surprisingly small throughout the course of the experiment.

The results of two other gas concentration experiments have been used to generate Figures 23-6 and 23-7. In each of these figures, the percent carbon dioxide volumetric gas concentration is plotted versus vertical height in the balloon for selected times during a particular experiment. In Figure 23-6, zero test time corresponds to the time that loading of the second component gas was completed. Zero test time in Figure 23-7 corresponds to the time at which loading of the second component gas was initiated.

Figure 23-6 again serves to emphasize the relatively ineffective gas mixing caused by molecular diffusion in that the initial stratification of carbon dioxide and nitrogen remains essentially unchanged for the test times considered, except over a small region near the center of the balloon. It should be pointed out, however, that since the diffusion coefficient for a carbon dioxide/nitrogen gas mixture (1.537×10^{-4} ft^2/s for sea level conditions) is smaller than that for an oxygen methane gas mixture (2.222×10^{-4} ft^2/s for sea level conditions), it is to be expected that molecular diffusion will be somewhat more effective for oxygen-methane gas mixtures than for carbon dioxide/nitrogen gas mixtures.

The results shown in Figure 23-7 are typical of those obtained during the plume experiments. They are in excellent agreement with theoretical gas mixture

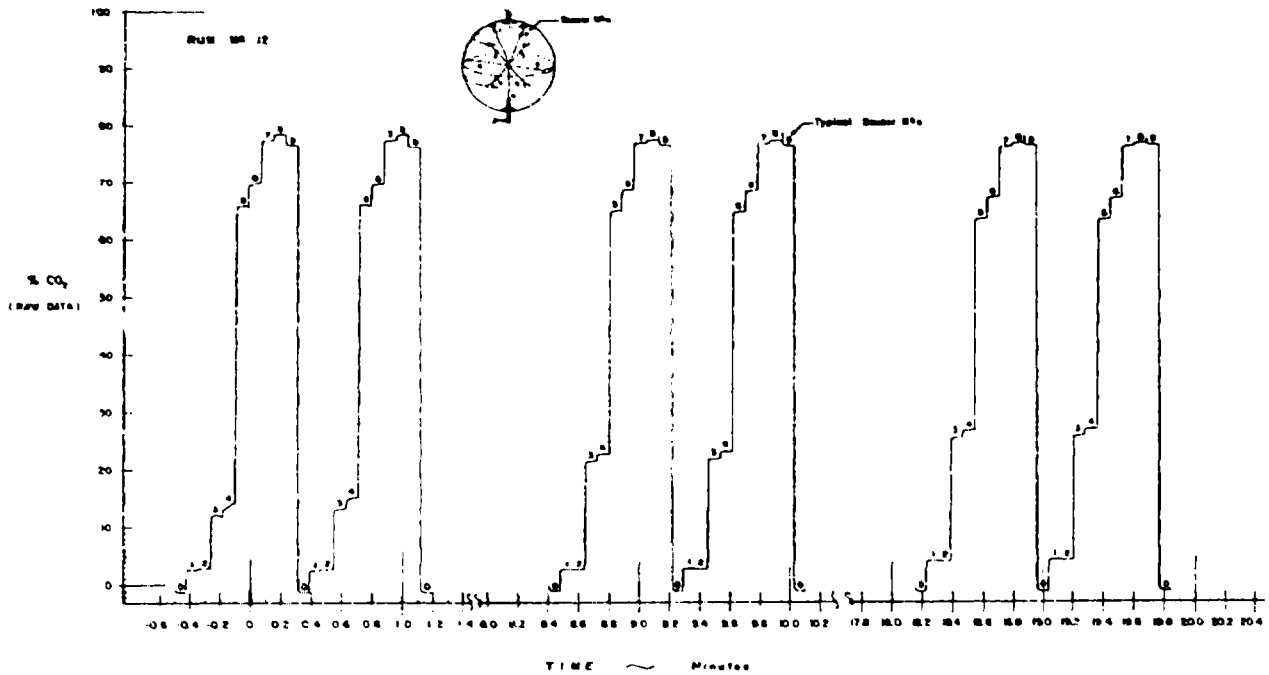

Figure 23-4. Typical Strip Chart Recording for Gas Concentration Measurements: Molecular Diffusion at a Nominal Altitude of 20,000 Feet

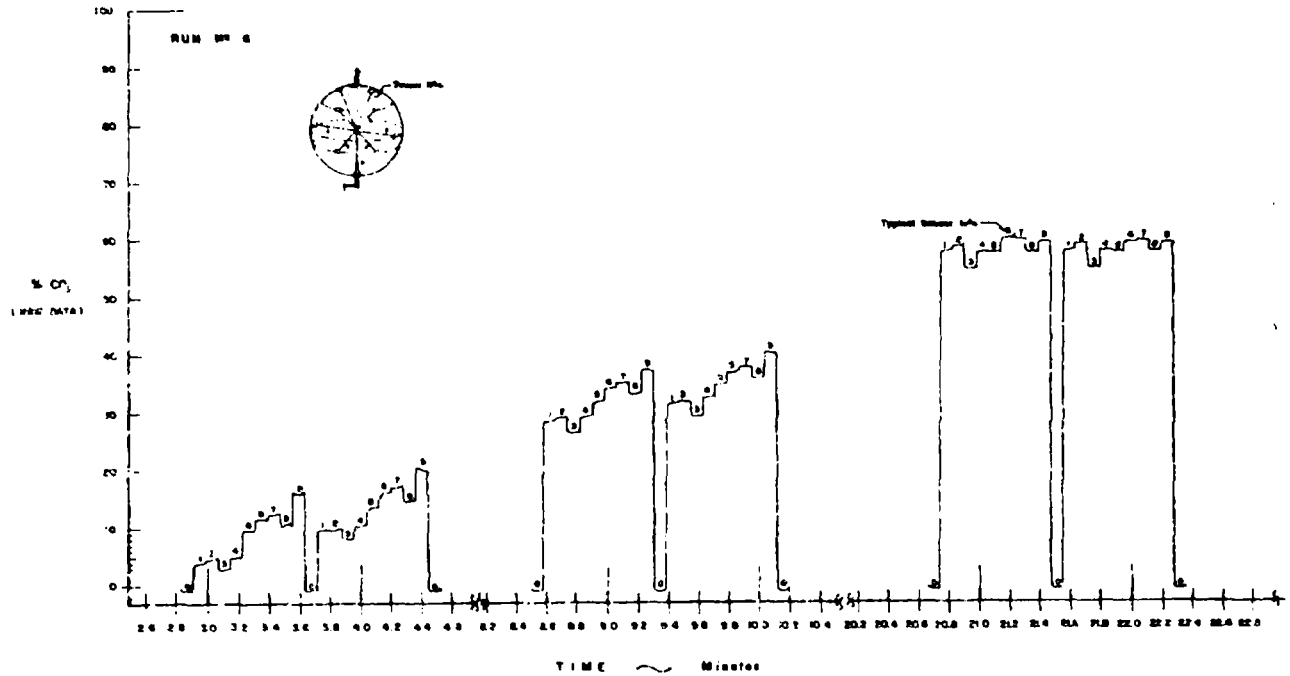

Figure 2-5. Typical Strip Chart Recording for Gas Concentration Measurements: Heavy Gas Plume Ending at a Nominal Altitude of 35,000 Feet

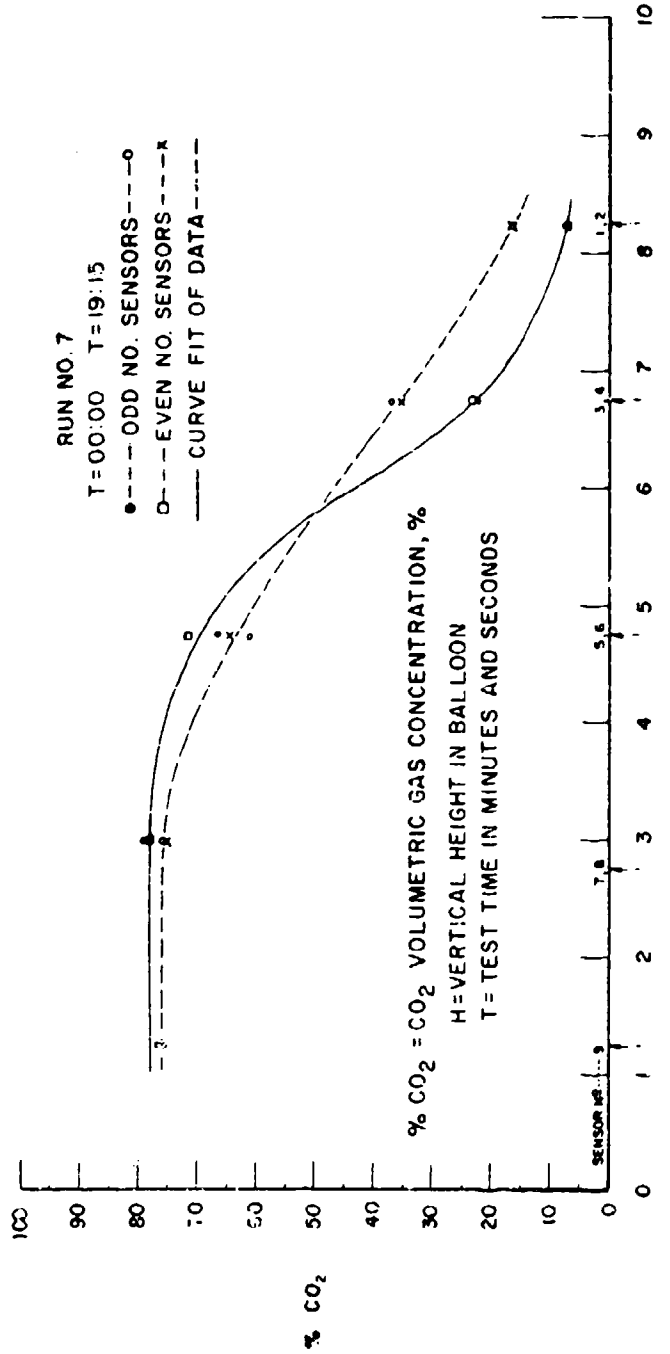

Figure 23-6. Molecular Diffusion at a Nominal Altitude of 35,000 Feet

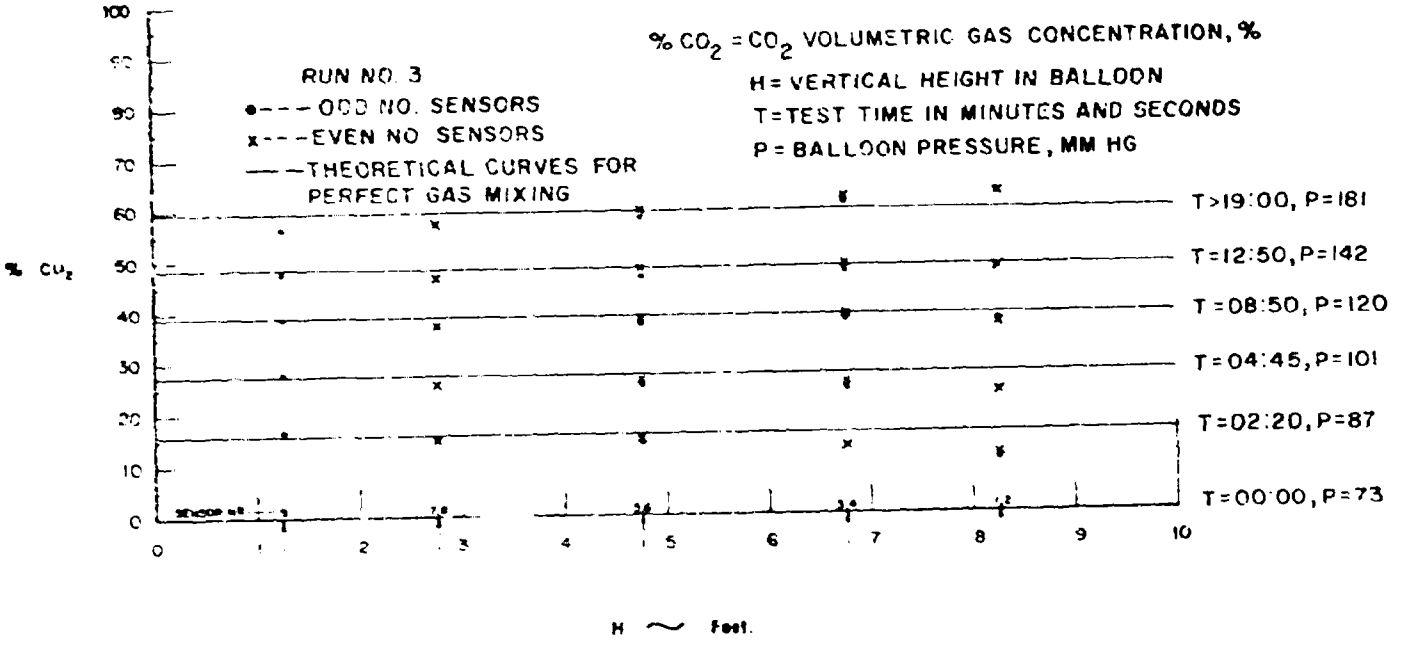

Figure 23-7. Heavy Gas Plume Ending at a Nominal Altitude of 35,000 Feet

values calculated assuming that instantaneous perfect gas mixing occurred during the course of each experiment. Furthermore, the results are expected to underestimate the effectiveness of plume-induced gas mixing for oxygen-methane gas mixtures. Since the ratio of oxygen to methane molecular weight is 1.99 while the ratio of carbon dioxide to nitrogen molecular weight is 1.57, plume buoyancy forces will be greater for the detonable gas case.

23-5. EXPERIMENTAL RESULTS – BALLOON DETONATIONS

A photograph of a fully inflated ballonet balloon is shown in Figure 23-8. Photographs of a fully inflated oxygen chamber (ballonet balloon) and a partially inflated ballonet balloon are shown in Figures 23-9 and 23-10, respectively. The tendency of the fully inflated oxygen chamber to take on a somewhat spherical shape initially is evident in both Figures 23-9 and 23-10.

Kinking of the gas communication duct (ballonet balloon) was encountered on all four of the ballonet balloon detonation experiments and is illustrated in the two photographs of Figure 23-11. This kinking can be attributed to the fact that the ducts were not reinforced and to the fact that they were somewhat longer than they should have been. For all of the ballonet balloon detonation experiments, oxygen flow through the gas communication duct was restricted completely at low altitudes. As a result, the duct did not have to be tied off at sea level to prevent oxygen transfer.

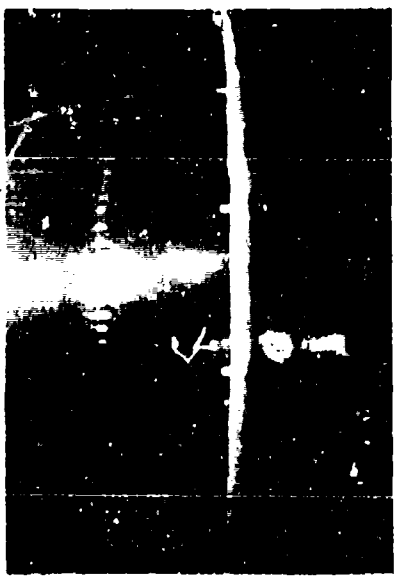

Figure 23-8. Fully Inflated Ballonet Balloon

For one of the ballonet balloon detonation experiments, it appears from the low speed film of deployment that oxygen flow was restricted during ascent to the point that the ballonet burst, allowing oxygen to enter the top chamber from below. According to the data obtained during the molecular diffusion experiments, gas mixing in this case would be very poor. In terms of the high speed camera coverage and the time of arrival and overpressure-time data, a poor gas mixture was indeed obtained during this run. The data indicate that a low order detonation or deflagration occurred.

Figure 23-9. Fully Inflated Oxygen Chamber, Ballonet Balloon

Figure 23-10. Partially Inflated Ballonet Balloon

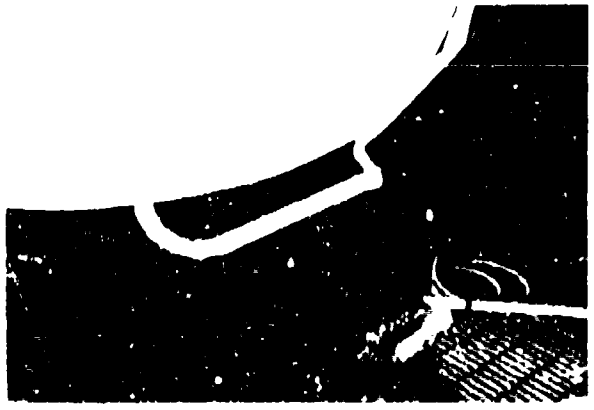

Figure 23-11. Characteristic Pinking of Gas Communication Duct, Ballonet Balloon

Results for the six bonafide balloon detonations, along with curves corresponding to theoretical calculations (Klima et al, 1987a) are shown in Figures 23-12 and 23-13. The figures are for nondimensional peak overpressure and nondimensional shock arrival time versus nondimensional range.

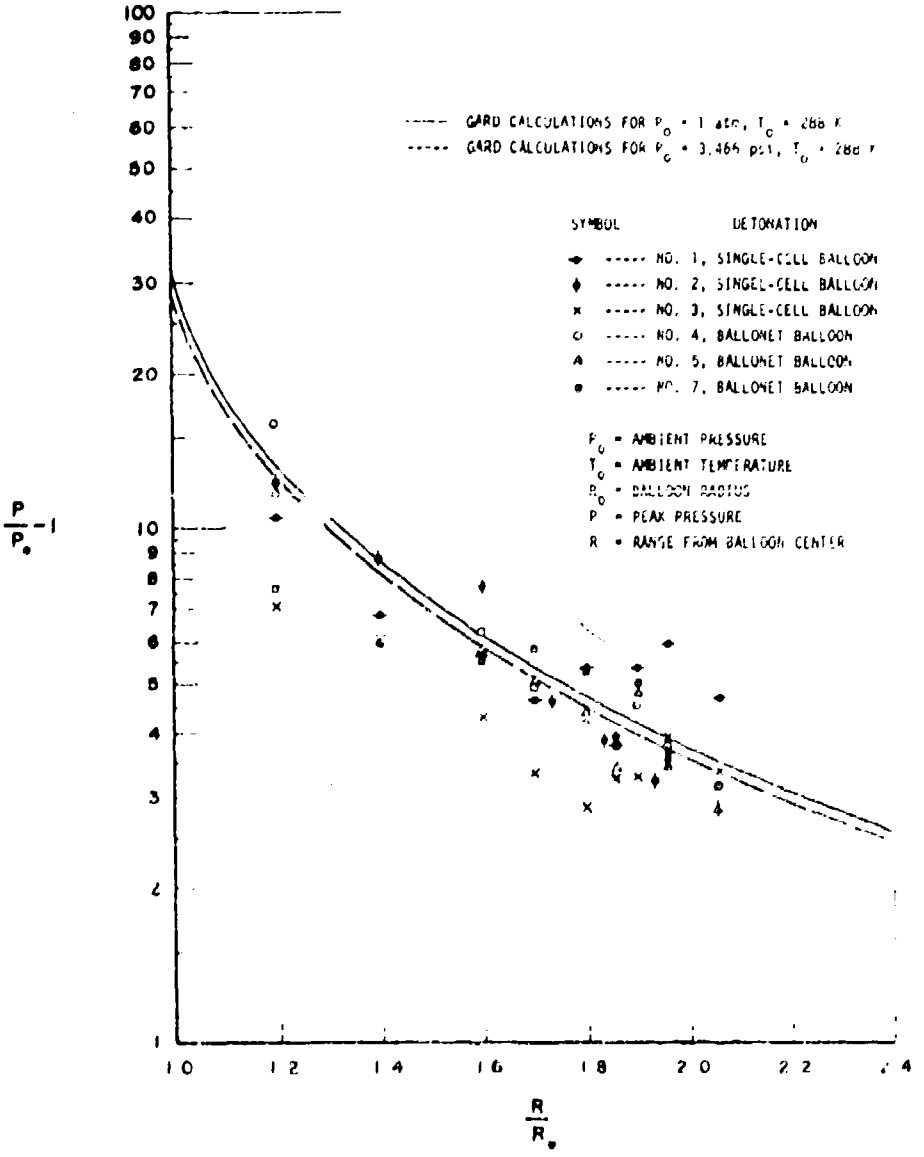

Figure 23-12. Nondimensional Peak Overpressure Versus Nondimensional Range, Composite

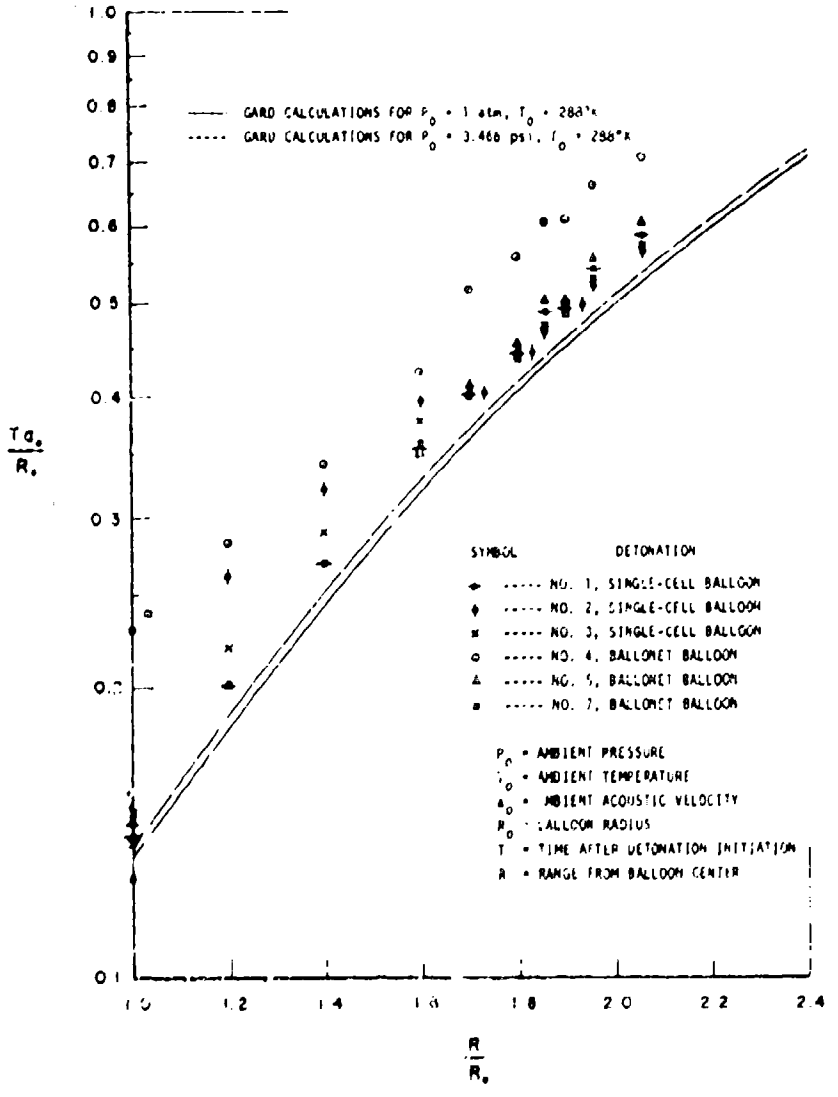

Figure 23-13. Nondimensional Shock Arrival Time Versus Nondimensional Range, Composite

While there is considerable scatter in the data, the nondimensional peak overpressure for these detonations agree reasonably well with the theoretical predictions. In addition, the ballonet and single cell balloon results are quite similar and compare favorably with earlier experimental results presented by Kirrm et al (1967a).

The nondimensional shock arrival times for these detonations are somewhat later than expected according to theoretical predictions, probably because of the finite time required to induce a sustained detonation after detonator firing. Some of this discrepancy may also be due to blast sphere temperatures (and therefore ambient acoustic velocities) having been somewhat lower than those measured (measurements were made only in the vicinity of the blast sphere walls). At any rate, the ballonet and single cell balloon results are once again quite similar and comparable with the earlier experimental results (Klima et al, 1967a).

Finally, one might expect the ballonet balloon results to be somewhat different from the single cell balloon results due to the different effective detonable gas mixture volume (441.8 ft^3 versus 523.6 ft^3) for each type of balloon. However, because of the design of the ballonet balloon and the fact that all the overpressure gages were located close-in in a horizontal plane through the center of the balloon, the effect of the "unused" oxygen chamber volume could not be detected in the ballonet balloon results.

23-6. CONCLUSIONS AND RECOMMENDATIONS

The results of the detonation experiments together with the results of the gas concentration measurements confirm the effectiveness of plume induced gas mixing in balloons of the ballonet type. In terms of gas mixing, the operational feasibility of large scale ballonet balloons has been established. In order to verify operational feasibility completely, it is therefore recommended that a large scale ballonet balloon be tested at altitude. Such a test would also take into account the effects of temperature variation with altitude, which were not simulated during the blast sphere experiments.

The one major problem encountered during the program was the problem of ballonet-balloon gas communication duct kinking. It is recommended that in manufacturing future ballonet balloons, the gas communication duct be suitably reinforced to prevent the possibility of the duct collapsing during ascent.

It is also recommended that an investigation be made into balloon designs which allow the ballonet to collapse to the outer surface of the balloon at test altitude. With such a design the total balloon volume will contain a detonable gas mixture in the final configuration, a larger explosive yield will be realized for the same balloon size, and balloon geometry effects on the detonation and air blast characteristics will be minimized.

Acknowledgments

This work was supported by the Defense Nuclear Agency and administered by the U.S. Army Ballistic Research Laboratories under Contract DAAD05-72-C-0189.

References

Balcerzak, M.J., Johnson, M.R., and Kurz, F.R. (1966) Nuclear Blast Simulation, Part I, Detonable Gas Explosion, DASA 1792-1.

Balcerzak, M.J., Johnson, M.R., and Lucole, S.W. (1967) Nuclear Blast Simulation, Detonable Gas Explosion, Operation DISTANT PLAIN, DASA 1945.

Calligeros, J.M., and Hobbs, N.P. (1972) A Concept Definition Study for Dynamic Testing of Interceptor Missiles to Blast(U), Kaman AviDyne Final Technical Report, Draft (KATR-84), Secret.

Fields, S.F. (1972) High Altitude Blast Generation System: Detonable Gas Mixing Experiments, GARD Final Technical Report, Draft (1550).

Holmes, L.B., and Fugelso, L.E. (1971) The mixing of gases in a spherical cavity, Appendix F in Underground Detonable Gas Explosions, MIRACLE PLAY Test Series, DASA 2676.

Klima, R.J., Balcerzak, M.J., and Johnson, M.R. (1967a) High Altitude Blast Generation System, Part I, Theoretical and Experimental Analysis, DASA 2303-I.

Klima, R.J., and Balcerzak, M.J. (1967b) High Altitude Blast Generation System, Part II, Design and Economic Study, DASA 2303-II.

Lucole, S.W., and Balcerzak, M.J. (1969) High Yield Detonable Gas Explosions, Sledge Technique, DASA 2302.

Balloon Technology

Wednesday, 27 September

Morning: Chairman, John McFall:
National Aeronautics and Space Administration

Contents

24. Review of Recent Performance of Large Balloons and Balloons with Payloads in Excess of 3000 Pounds

J.R. Nelson and P.J. Osborne
Winzen Research Inc.
Minneapolis, Minnesota

24-1. BALLOON DESIGN ACHIEVEMENTS

Since the last review of StratoFilm® polyethylene balloon performance given at the Balloon Symposium in 1970, the frequency of large and heavy load balloon flights has increased significantly. (Table 24-1 summarizes those flights from January 1970 to September 1972.) As a result of the demand for higher altitudes and heavier payloads, there has been an increased emphasis on a continual evaluation of balloon design, materials, fabrication and launching techniques. In particular, this has produced the need for a more intensive investigation into the mechanical properties and performance of very thin films. The development of a high quality sealing machine has resulted in consistent, uniform seals for thin films, including nylon material, with seal test strengths exceeding the specifications. Successful flights of 0.35 mil StratoFilm® balloons have been accomplished, and fabrication of the largest balloon ever, a 48 million cubic foot volume of 0.35 mil material for AFCRL, has just been completed. A nylon film has been extruded which has excellent balloon film properties and has a strength of about four times that of polyethylene for the same weight. It appears that 0.35 mil is the limit for StratoFilm® in regard to the extrusion of a uniform film. However, it is possible to extrude a uniform quality film of nylon material as low as 0.2 mil thickness.

Table 34-1. Heavy Load (>3000 lb) and Larger (>20 MCF) StratoFilm® Balloon Flights From January 1970 to September 1972*

Vol. (MM)	Shell (mil)	Cap (mil)	Dia. (ft.)	Wt. (lb)	Date	Location	P. L. (lb)	Alt. ($\times 10^{-3}$)	Remarks
40.1	.5	.7/.7	500.5	2937	4/4/72	Alice Spgs,	1634	148.0	Success, 26.9 hr SN 1
37.74	.45	.8	489.9	1946	9/17/72	Holloman AFB, N. M.			Success SN 1
36.36	.5	.7/.7	483.2	2830	4/15/72	Alice Spgs, Australia	2118	-	Failure, split at launch, SN 1
36.36	.5	.7/.7	483.2	2802	6/17/72	Palestine, Texas	1525	148.4	Success, 11-1/4 hr SN 3
35.85	.5	.9	481.5	2044	2/3/72	Longreach Australia	11001	-	Ground abort, high winds, SN 1
33.85	.45	.5/.5	452.8	1892	11/7/70	Mildura, Australia	1552	-	Failure at 40 K SN 1
33.85	.45	.5/.5	452.8	1868	10/16/70	Mildura, Australia	1423	145.0	Success, 14.3 hr SN 2
33.85	.45	.5/.5	452.8	1840	7/1/70	Churchill, Manitoba	1568	-	Failure, split at launch, SN 3
33.85	.45	.5/.5	452.8	1878	7/1/70	Churchill, Manitoba	1568	-	Failure, split at launch, SN 4
30.5	.6	.7/.7	434.64	2581	5/19/71	Palestine Texas	34301	-	Failure at 89 K SN 1
30.5	.6	.7/.7	434.64	2597	7/2/71	Palestine Texas	1248	142.0	Success, 5 hr SN 2
30.5	.6	.7/.7	434.64	2318	7/13/71	Palestine Texas	1270	142.0	Success, 4.6 hr SN 3
30.5	.6	.7/.7	434.64	2565	11/2/71	Palestine Texas	1359	-	Failure at 75 K SN 4
30.5	.6	.7/.7	434.64	2521	5/31/72	Palestine Texas	2249	132.5	Success, 6.2 hr SN 5
30.5	.6	.7/.7	434.64	2578	7/7/72	Churchill Manitoba	1563	153.7	Success, 17.3 hr SN 6
30.18	.45	.7	434.36	1335	8/26/71	Palestine Texas	8065	133.0	Success, 5.3 hr SN 6
30.18	.45	.7	434.36	1357	8/18/71	Palestine Texas	.0941	-	Failure at 80 K SN 6
28.8	.7	.7/.7	410.99	2594	10/14/70	Palestine Texas	2270	134.0	Success, 8.3 hr SN 4
28.8	.7	.8/.8	410.99	2716	5/25/71	Palestine, Texas	3940	128.9	Success, 43.9 hr SN 2
20.84	.7	.7/.7	382.5	2319	9/4/70	St. Paul, Minnesota	2994	132.0	Success, 345.0 hr SN 2
20.84	.7	.7/.7	382.5	2330	5/12/71	Sioux Falls, S. Dak.	3232		Success, 40 hr SN 1
20.84	.7	.7/.7	382.5	2319	6/7/71	Sioux Falls, S. Dak.	3008		Success, 20 hr SN 3
20.8	.8	.9/.9	378.1	2907	9/9/72	Palestine Texas	4538	120.5	Success, 11.6 hr SN 12
20.8	.8	.9/.9	378.1	2883	9/20/71	Palestine Texas	2947	127.2	Success, 10.2 hr SN 3
20.8	.8	.9/.9	378.1	2987	5/7/71	Palestine, Texas	4840	116.9	Success, 11.8 hr SN 4
20.8	.8	.9/.9	378.1	2897	9/18/70	Palestine, Texas	4807	119.4	Success, 7.9 hr SN 5
20.8	.8	.9/.9	378.1	3048	9/29/70	Palestine, Texas	5135	117.3	Success, 27.6 SN 6
20.8	.8	.9/.9	378.1	3001	5/25/71	Palestine, Texas	5209	120.5	Success, 7.3 hr SN 8
20.8	.8	.9/.9	378.1	2950	10/6/71	Palestine, Texas	4510	115.8	Success, 10.6 hr SN 9
20.8	.8	.9/.9	378.1	2872	2/18/72	Palestine, Texas	4471	-	Failure at 51.7 K SN 7
20.36	.6	.8/.8	377.37	1937	11/27/70	Parana Argentina	1059	126.9	Success, 4.9 hr SN 2

*Does not include those flights in 1970 reported at Balloon Symposium of Oct. 1970.
†Balloons with payloads in excess of maximum recommended.

Table 24-1. Heavy Load (>3000 lb) and Larger (>20 MCF) StratoFilm® Balloon Flights From January 1970 to September 1972* (Cont)

Vol. (MM)	Shell (mil)	Cape (mil)	Dia. (ft)	Wt. (lb)	Date	Location	P. L. (lb)	Alt. ($\times 10^{-3}$)	Remarks
20.36	.6	.6/.6	377.37	1932	12/1/70	Parana Argentina	1875	124.8	Success, 0.8 hr SN 3
20.36	.6	.6/.6	377.37	1971	5/4/72	Pierre, S. Dak.	2899	121.5	Success, 24.5 hr SN 4
20.36	.6	.6/.6	377.37	1886	11/16/71	Parana Argentina	1770	-	Failure, L.T. pulled out. SN 5
20.36	.6	.6/.6	377.37	1945	11/16/71	Parana Argentina	1770	138.0	Success, 7.4 hr SN 6
20.36	.6	.6/.6	377.37	1951	5/4/72	Palestine Texas	2316	121.3	Success, 23 hr SN 7
20.36	.6	.6/.6	377.37	1840	5/3/72	Pierre S. Dak.	2899	-	Ground abort, high winds, SN 9
20.11	.5	1.0	376.91	1814	5/9/72	Palestine Texas	1175	139.1	Success, 10.6 hr SN 1
20.1	.6	1.0	377.81	1768	6/15/70	Palestine Texas	1343	139.0	Success, 6.6 hr SN 1
15.0	.7	.7/.7	334.85	1829	5/18/70	Palestine Texas	3467	121.8	Success, 13.7 hr SN 5
15.0	.7	.7/.7	334.85	1957	9/28/71	Palestine Texas	3173	-	Failure at 74.8 K SN 20
15.0	.7	.7/.7	334.85	1927	9/28/71	Palestine Texas	3204	118.0	Success, 20.3 hr SN 21
10.6	1.0	1.5	305.86	2115	2/13.71	Palestine Texas	4101	107.0	Success, 6.5 hr SN 330
10.6	1.0	1.5	305.86	2176	7/13/70	Holloman AFB, N.M.	3708	116.0	Success, 3.7 hr SN 346
10.6	1.0	1.5	305.86	2149	9/17/70	Holloman AFB, N.M.	3810	-	Failure at 80 K SN 347
10.6	1.0	1.5	305.86	2117	7/20/70	Holloman AFB, N.M.	3210	112.0	Success, 3.7 hr SN 348
10.6	1.0	1.5	305.86	2177	5/1/71	Palestine Texas	3888	107.5	Success, 7.1 hr SN 393
10.5	1.5	1.5	304.9	2718	1/29/70	Chico AFB California	4246	104.7	Success, 4.3 hr SN 1
10.5	1.5	1.5	304.9	2675	7/10/70	Palestine Texas	4586	104.0	Success, 5.5 hr SN 3
2.9	1.5	-	192.4	990	4/21/71	Palestine Texas	3041†	91.1	Success, 10.5 hr SN 75
2.9	1.5	-	192.4	1010	5/13/71	Palestine Texas	3050†	92.3	Success, 10.9 hr SN 78
2.9	1.5	-	192.4	990	8/1/72	Palestine Texas	3029†	91.0	Success, 8.5 hr SN 86
2.9	1.5	-	192.4	989	8/11/72	Palestine Texas	3002	90.3	Success, 10.1 hr SN 95

Tandem Systems

Vol. (MM)	Shell (mil)	Cape (mil)	Dia. (ft)	Wt. (lb)	Date	Location	P. L. (lb)	Alt. ($\times 10^{-3}$)	Remarks
38.3	1.5	1.5/1.5	465.8	9800	1/6/71	Holloman AFB, N.M.	11214	N/A	Failure at 50.0 K, Main balloon SN 1
38.19	1.5	1.5/1.5	465.87	9800	8/26/72	Holloman AFB, N.M.	13798	N/A	Failure at 48 K, Main balloon SN 2
18.9 .33	1.5 2.0	-	358.7 D 96.94	9308	3/17/72	Palestine Texas	7426	101.7	Main balloon SN 1 Success, 1.9 hr Launch balloon SN 3
6.97	1.5	1.5/1.5	264.93	6393	5/14/71	Palestine Texas	6378	84.2	Main balloon SN 1 Stratoscope Success, 2.5 hr
6.87	1.5	1.5/1.5	264.93	6144	2/10/72	Palestine Texas	6401	83.2	Main balloon SN 2 Stratoscope Success, 1.2 h.

When this capability is added to that of the superior sealing of the film, the construction of large, lightweight balloons which can attain very high altitudes is now realizable. Further investigation of film properties and fabrication of nylon balloons are continuing under the sponsorship of AFCRL and NCAR.

Other design achievements have been the capability of attaching larger ducts to the balloon, the development of the segmented clamp apex fitting and the development of the reefing sleeve. The latter will be covered in section 24-2.

Previously, the largest ducts used were 40 square feet in area, which meant that for some of the larger balloons as many as 12 ducts would be necessary consistent with the ducting requirements. However, due to improvement in fabrication techniques, ducts of 100 square feet area are now being used with a consequent reduction in the number of ducts required.

The segmented clamp fitting which securely holds the balloon film and load tapes at the balloon apex has performed flawlessly in every case, sustaining a load of 25,000 pounds on one flight and 90,000 pounds in a ground pull test. Hence, its continuing use is assured as the demand for heavier payloads increases.

In the category of single cell balloons of capacity larger than 20 million cubic feet there have been 38 flights since 1970, of which 28 have been successful (that is, the balloon reached and maintained float altitude). The two most notable successes were the largest balloon (46 million cubic feet) ever flown, in Australia this year and the 37.7 million cubic foot, 0.45 mil balloon flown at Holloman Air Force Base this month. The 46 million cubic foot balloon carried a payload of 1834 pounds at an altitude of 148,000 feet for more than 26 hours. The 37.7 million cubic foot balloon attained a float altitude in excess of 160,000 feet. Of the eleven unsuccessful flights, two were classified as ground aborts (termination of launch due to excessive gusty winds, mechanical or electronics failure, and so on), and nine were classified as balloon failures (failure of the balloon system itself). In the case of two of the failures the payloads were in excess of the values Winzen Research recommended as maximum for the strength of the film material. One failure was the result of an unfortunate accident when an inflation tube pulled out of the balloon during the inflation procedure. Helpful information was received from the launch crew on how this failure was incurred. As a result, the inflation tube attachment design has been modified. Significantly, most of the failures occurred very soon after launch or at low altitude, which has prompted a closer investigation of possible problems associated with the dynamic launching of large, thin film balloons. These problems are examined in section 24-2.

In the category of balloons carrying payloads in excess of 3090 pounds, which covers a volume range from 2.9 to 30.5 million cubic feet, there have been 25 flights of which 21 were successful. One of the balloons, 30.5 million cubic feet, had a payload 15 percent in excess of the maximum recommended. It managed

to reach a maximum altitude of 86,000 feet before starting to descend due to excessive gas leakage. The other failures were of a 20.8, a 15.0 and a 10.6 million cubic foot balloon.

The demand for heavier payloads has spurred the development of the tandem balloon system. This system was developed primarily to overcome the problems associated with the dynamic launching of large balloons with very heavy payloads. Since 1970, five tandem systems have been launched which have incorporated a StratoFilm® main balloon and in one case a StratoFilm® launch balloon as well. Three of the flights were successful and two were unsuccessful due to main balloon failures. One system carried a payload of 11,200 pounds and failed at 50,000 feet; the other carried a payload of 13,800 pounds and failed at 48,000 feet.

Two successful flights were for the evaluation of the Stratoscope program, and each system had a scrim mylar launch balloon with a 6.9 million cubic foot StratoFilm® main balloon. The first was flown in May 1971 and carried a payload of 8400 pounds at an altitude of 84,000 feet for nearly 3 hours. The second was launched in February 1972 and carried a 9400-pound payload at 83,000 feet for over 1 hour before the flight was terminated. Because of the high cost of mylar in relation to polyethylene, it was decided to evaluate a system which used polyethylene for both balloons. This system, which had a main balloon volume of 19 million cubic feet, was launched in March 1972 and carried a 7400-pound payload at an altitude of 101,700 feet for over 1-1/2 hours. As a consequence of the success of this flight the construction of another Stratoscope system is now underway, using the polyethylene design for both balloons. The main balloon will have the same configuration as that used for the two previous Stratoscope balloons. The launch balloon will be constructed of 2.5 mil StratoFilm® double wall and will have a volume of 465,000 cubic feet. This flight, another in the evaluation of the Stratoscope system, will be launched some time next year.

24-2. INNOVATIONS FOR IMPROVED LAUNCHING TECHNIQUES

Since the Sixth AFCRL Scientific Balloon Symposium float altitudes, payload weights and balloon sizes have continued their upward trend, as indicated in section 24-1. This progress has not been achieved without some trauma, however, since the economics of ballooning require that development costs of balloon progress must be teamed with actual scientific research flights. Analysis of the flight records show that most of the failures of giant balloons were during the launch phase or were flight failures potentially caused by launch damage. The problem presented was whether to make balloon design changes to overcome existing launch technique problems or to develop new launch techniques. We felt that the latter

approach merited a thorough attack, because balloons are going to get much larger than current models.

In the development of the current state of giant balloons, many improvements in design and manufacturing have been made, but relatively few innovations have occurred in launch techniques.

Development in design of large balloons has resulted in more expanded computer programs to provide shapes for multiple caps of different thickness and lengths, for various types of superpressure and subpressure shapes, and for incremental weight distribution data. Hi-slip StratoFilm® reefing sleeves with thin rip panels were designed and have been in use for several years. These sleeves were not optimum, but offered a measure of protection against ground damage, launch sailing and ascent sailing.

Many manufacturing developments were accomplished, such as the first obvious step of lengthening the production plant. Great improvements were made in material handling, such as full gore width winders and dispensers, handling and packaging machinery to prevent any stress on the balloon from manufacture to shipment. Heat sealing equipment was revolutionized to provide micro control of temperature, pressure and speed, with elimination of virtually all manual expertise requirements. This development was essential to provide optimum sealing strength for a wide range of thicknesses, from total layers of under 1 mil to over 20 mil. Development of very thin StratoFilm® also has made such giant balloons feasible.

Considerable effort has been extended in improving launch techniques for very heavy payloads and large balloons by using a tandem balloon system that consists of a strong, smaller launch balloon with a transfer duct into the main balloon. This provides a tight bubble which is relatively unaffected by ground wind and positive slow motion, as well as controlled letup and launch without aerodynamic flailing about. Unfortunately, this type of system bootstraps considerable weight that increases operating costs (helium and handling equipment) as well as initial balloon costs for a given load-altitude mission.

The platform-roller launch technique with mobile launch vehicle has been polished for many years, until a reasonable success ratio of 5000-pound payload launches have been achieved with balloons of up to 20 million cubic foot inflated volume. What is a reasonable success ratio? The latest Winzen Research Flight Report of over 800 flights or attempted flights during the last 3 years indicates a success ratio of 91 percent. If we eliminate experimental film flights, no-test situations, and ground and launch aborts, the success ratio is 97.2 percent. However, of balloons over 20 million cubic feet in size, the overall success ratio falls to 76 percent. As indicated in section 24-1, the major portion of the 24 percent

failures either occurred at launch or were low altitude topouts caused by launch damage. Following is a detailed analysis of some of these flights or launch failures.

Some fine photography in 16 millimeters was done by Raven Industries of two 33.8 MM balloon back-to-back failures at Ft. Churchill, Canada in 1971. The film was loaned to us by the program sponsor, the Office of Naval Research and NASA so that the failures could be analyzed. Both failures occurred under ideal launch conditions with not enough wind to riffle the wind sock. What little wind there was caused a slight side drift as the bubble came up. The data, reported in a failure analysis report to ONR, showed that the large ratio of lift to bubble weight caused a motion toward the launch vehicle of 4 knots. The high lift acceleration caused a very large diameter mushroom cap which, when the sail developed, called for very rapid deployment of the 0.45 mil material from a tight rope to fill out the sail. This started a tear in the lower part of the cap area which split to the apex, and failure resulted. The second failure was almost a duplicate of the first.

This leads to the conclusion that it is desirable to reduce the ratio of lift to launch bubble weight, which in turn reduces the initial acceleration and velocity toward the launch vehicle. This can be accomplished by letting more bubble up through the roller before launch, the extent of which is determined by launch environment, but preferably before a large lift is achieved to prevent abrasion of the balloon or popping holes from entrapped air. Secondly, it is desirable to have a slight wind (4 to 7 knots) from the balloon bubble toward the launch vehicle to reduce the relative wind to near zero, since the bubble ascent causes a velocity toward the launch vehicle of 4 to 5 knots.

These criteria were applied to the launch of a 46 MM cubic foot balloon in Alice Springs, Australia in May of this year. This flight carried Dr. Lewin's X-ray telescope with a liftoff gross inflation of 5490 pounds to 148,000 feet with a flight duration of 26 hours. The following wind of about 7 knots at launch gradually lifted the balloon so that it did not fully clear the ground until about half way to the launch vehicle, and no appreciable sail developed.

A few days later, the same payload after recovery and recalibration was attached to a 36 MM cubic foot balloon. The same criteria were applied again, except that the surface calm seemed deeper up to about 5 knots at about 1000 feet. The balloon failed shortly after release. Most people present felt that the conditions were almost identical to the 46 MM flight, but side pictures showed that the 36 MM balloon was completely off the ground, and most of the balloon was parallel to the ground shortly after release.

Examination of the balloon showed a triangular tear in the middle of a gore with the point toward the top of the balloon. This tear split up to the apex. Examination of the movies and imprint at the start of the tear showed that the apex fitting did not accelerate as rapidly as the bubble film dropping it, relatively speaking, into the bubble. Then, as the bubble picked up the load, the apex was snapped upward, and a nut on the fitting caught and tore a hole. Design protection against this type of failure has been made. This problem might well have been the source of failures where balloons topped out at low altitudes with apparent holes.

In anticipation of dynamic launch technique limitations, a program to develop a new launch technique for giant balloons was sponsored by the Office of Naval Research and NASA in 1971. It has been rather generally acknowledged that the optimum method of launching a balloon is from vertical inflation. Unfortunately, this launch method requires the seldom experienced condition of dead calm to an altitude over a thousand feet.

The main preventative of the optimum vertical inflation launch, wind, moves the uninflated balloon portion over the ground when the bubble is inflating so abrasion protection is required. If there is no restriction on the gas bubble, the undeployed material will inflate like a sail; so the gas bubble must be restrained to a reasonably tight bubble such as that achieved with a launch roller. One who has tried to hold the end of an inflation tube during inflation with the wind in the wrong direction knows that aerodynamic flailing is a problem. Wind effects on the inflation tube must be eliminated.

These problems have been resolved successfully with a 0.25 MM cubic foot balloon. A reefing sleeve has been developed for a series of ground inflations. It consists of a fabric sleeve lined with hi-slip StratoFilm®. The fabric is a portable ground cloth which permits movement over reasonably clean ground or pavement without balloon damage. The reefing sleeve is secured every few feet with a circumferential draw line that can be released by pulling a pin. With these pins tied together the length of the sleeve, they can be pulled sequentially like a zipper as the bubble inflates to a vertical position of the balloon. This maintains a tight bubble with a maximum cone angle of about 50 degrees during the entire inflation. During the test of a simulated 750-foot gore length balloon using an anchor line, it was found that the 18-knot wind force on the pin pulling line and the elongation of this length would release several pins at once. The procedure was therefore changed to use the lanyard release of pins only to unzip most of the sleeve during the erection phase. The bypassed pins were then released by self-contained squib cannon cutters as the bubble grew to full inflation. Other pins were released by baroswitch-controlled cutters as the balloon ascended to maintain control of the undeployed balloon for sailing protection during wind shears.

To prevent flailing of the inflation tube or tubes, they were encased in a fabric sheath and attached to a flange on the reefing sleeve and to a flange on the balloon. This procedure operated in excellent fashion on the last five ground inflation tests in winds between 15 and 18 knots.

The bubble must be prevented from twisting which might choke off the inflation tube, so two handling lines were installed near the bubble equator. The patches for these lines are capable of handling 200 pounds of pull in any direction. To prevent sudden surges of force on the balloon, a length of bungee cord was inserted in a longer loop of line in each handling line. The force to pull this bungee taut was 25 pounds, but the torque required to prevent bubble twisting never reached this extension even under 18 knot wind forces.

The ongoing program with this sleeve development incorporates a flight test of the .25 MM balloon and then ground and flight tests of a 1 MM cubic foot balloon. These tests will be followed by manufacture of a 2 million and a 7 million cubic foot balloon under the ONR-NASA contract. The latter two balloons will be flight tested by NCAR at Palestine, Texas.

Our feeling is that this reefing sleeve design or an improved version of this design will provide a launch procedure that will open the door for super giant balloons and payloads far in excess of those presently considered.

Contents

25. The Effect of Material Deformation on the Shape and Stress State of a High Altitude Balloon

Dr. H. Alexander and P. Agrawal
Stevens Institute of Technology
Hoboken, New Jersey

Abstract

Presently used balloon design procedures do not account for the effect of material deformation on the shape and stress state of a balloon and assume a state of zero circumferential stress. Using an approximate constitutive theory for transversely isotropic (balanced) and anisotropic (unbalanced) films, it is demonstrated that the zero circumferential stress state is impossible, and the shape of a fully inflated balloon can be quite different from the design (undeformed) shape. This shape difference under certain load situations can give rise to quite large stresses that could cause balloon failures.

Modifications to the present balloon procedures that include deformational effects are proposed, as well as methods of analysis to predict the true circumferential loading to be expected in high altitude balloons. The proposed constitutive theories are verified through comparison with experimental data obtained in uniaxial and biaxial stress state experiments performed over a full range of balloon temperatures.

25-1. INTRODUCTION

As a result of the requirements placed on the balloon designer by the user to carry heavier payloads to ever higher altitudes, the demands placed on the balloon structure have increased to the point where the usual assumptions of zero circumferential stress and no material deformation in the design of natural shape balloons

are no longer valid approximations of the actual stress and deformation states. A need exists for a realistic analysis of the stresses actually developed in a balloon. Such an analysis must account for the effect of material deformation and should be an adjunct to any balloon design program. It could be an important aid in modifying balloon design procedures to better utilize material strength and prevent regions of high stress concentration.

This paper describes a simple, conservative analysis that uses relatively little computer time and gives a reasonable approximation of the stress field in a balloon.

25-2. THEORETICAL ANALYSIS

25-2.1 Basic Assumptions

The commonly used natural shape balloon design procedure assumes that the deformed shape is not very different from the design shape (equilibrium can be taken on the undeformed shape) and that the circumferential stresses are everywhere zero. A rotationally symmetric shape is then determined that will be in equilibrium under the applied pressure, balloon weight and payload. This shape is used as a guide in the production of the balloon from a series of gores that are heat sealed together with load tapes at their junctures. It has been noted, however, that upon inflation, a balloon does not remain rotationally symmetric but goes into a regular shape with scalloping of the film between the load tapes (see Figure 25-1).

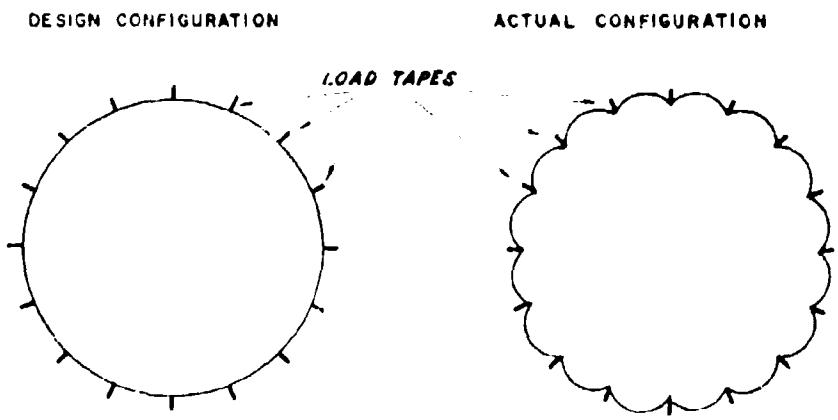

Figure 25-1. Comparison of the Design and Actual Configurations of the Cross Section of a Natural Shape Balloon

Noting this and the fact that the deformations of the balloon film will be small in the temperature range of interest, the analysis of this paper has been performed assuming that the load tapes, which are fairly rigid compared to the film, follow the design shape at ceiling and a computed bubble shape at all other altitudes. The film is then assumed to deform into a circular cross-section shape between adjacent tapes. All excess material at altitudes below ceiling is assumed to go into a sail that sustains no loading. Consequently, all loaded gores are assumed to be similarly loaded (see Figure 25-2).

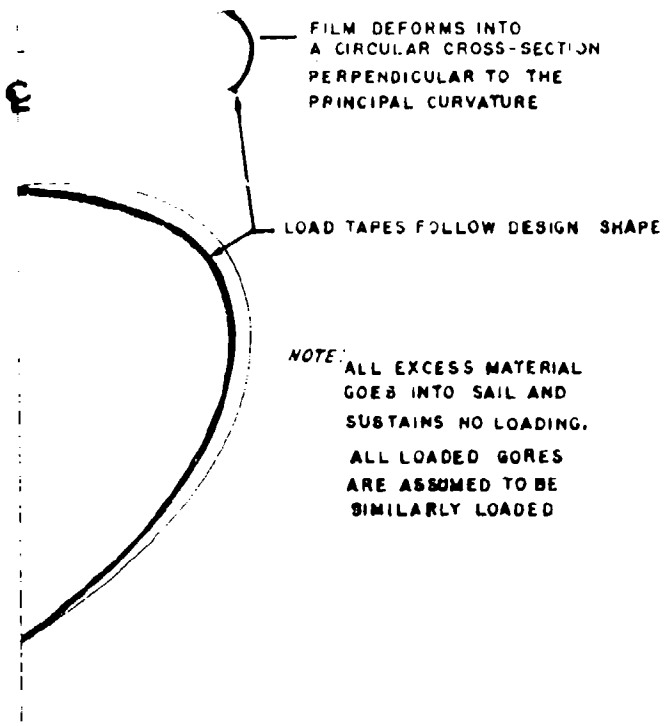

Figure 25-2. Scheme of Analysis for a Taped, Natural Shape Balloon

25-2.2 Film Constitutive Theory

Polyethylene, throughout its entire temperature range in balloon use (see Figure 25-3) is an anisotropic viscoelastic-plastic material. An exact stress-strain-time relationship for such a material is extremely difficult to establish. Upon establishment, it would not be practical for use in balloon design. However, certain simplifying assumptions can be made. If the range of plastic response (beyond the yield stress) is considered as failure, the plastic nature of the material can be

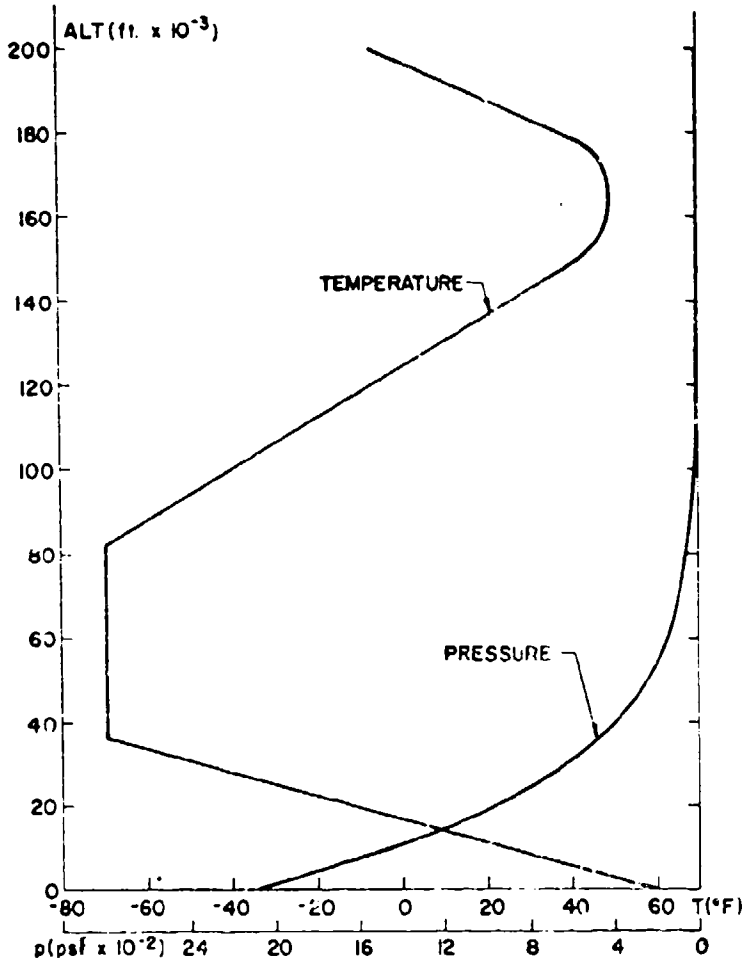

Figure 25-3. Standard Atmosphere

eliminated from the constitutive theory. At flight temperatures, the viscous response is small at operating stress levels and can be neglected. It remains then to establish a constitutive relation of an anisotropic elastic material.

Recognizing the orthotropic nature of blown films and assuming linearity between engineering stress and simple strain (Alexander and Weissmann, 1972), the following two-dimensional constitutive relation is obtained:

$$\epsilon_t = \frac{1}{E_1}\,\sigma_t - \frac{\nu}{E_2}\,\sigma_m \qquad (25\text{-}1)$$

and

$$\epsilon_m = \frac{1}{E_2}\sigma_m - \frac{\nu}{E_2}\sigma_t \qquad (25\text{-}2)$$

where ϵ_t is the transverse strain, ϵ_m is the meridional strain, σ_t is the transverse engineering stress, σ_m is the meridional engineering stress, E_1 is the transverse modulus, E_2 is the meridional modulus, and ν is the meridional to transverse Poisson's ratio. Assuming incompressible behavior under load, the Poisson's ratio, ν, has been found to be approximately .679 for all temperatures for DFD-5500 film. For the purposes of this report that value will be used.

The modulus versus temperature characteristic of various polyethylene balloon films has been determined in the earlier report of Alexander and Weissmann (1972). They are reproduced here in Figures 25-4 and 25-5. In the temperature

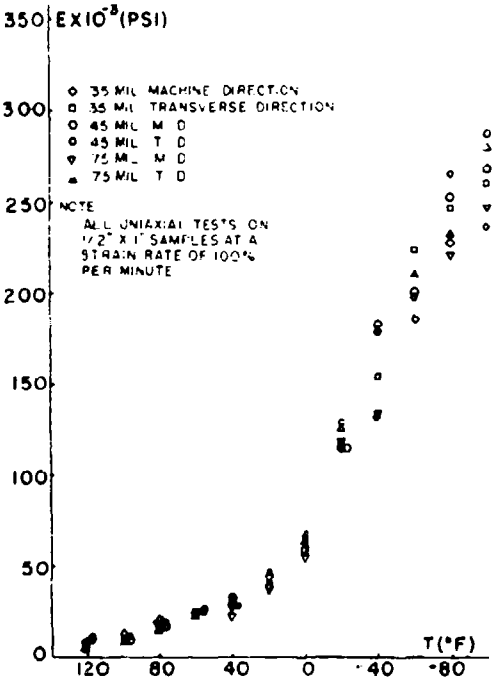

Figure 25-4. Modulus Versus Temperature for Thin StratoFilm

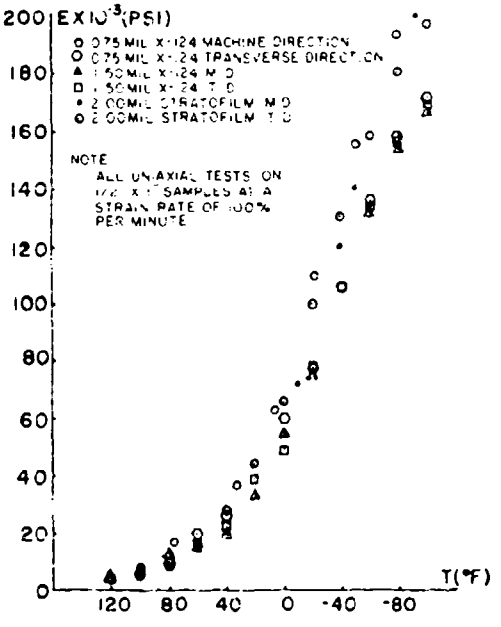

Figure 25-5. Modulus Versus Temperature for Polyethylene Balloon Films

range of interest, the modulus varies from 15,000 to 250,000 psi. The yield stress, which determines the limits of applicability of the analysis, was also found by Alexander and Weissmann (1972). Typical yield stress versus temperature characteristics are shown in Figure 25-6. However, one should not assume that

stress levels below the yield stress are always safe stresses, since it has been shown by Kerr and Alexander (1968) and Alexander and Weissmann (1972) that launch temperature preloading can cause failures at quite low burst stresses at the tropopause.

Analyses of the type presented in this report can never be utilized to their fullest extent until gross lot-to-lot variations in film properties are eliminated. This assurance of consistency and how to obtain it is the subject of other investigations of the authors (Alexander, 1972).

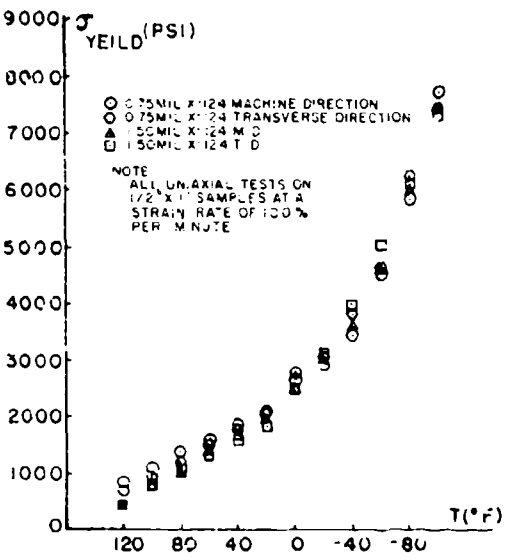

Figure 25-6. Yield Stress Versus Temperature for Polyethylene Balloon Films

25-2.3 Load Tape Constitutive Theory

On the basis of preliminary testing reported by Alexander (1972), an approximate constitutive relation was established for load tapes that assumes linearity between the load tape force, F_{tape}, and the meridional strain, ϵ_m, with the constant of proportionality (a tape "modulus") as K,

$$F_{tape} = K\epsilon_m \tag{25-3}$$

For 500-pound load tapes, the tape "modulus" was found to be approximately represented by the following empirical relationship:

$$K = \frac{5000}{85}\ (110-T)\ \text{lb}, \tag{25-4}$$

where T is temperature (°C).

25-2.4 Analytical Details

Force equilibrium in the meridional direction yields

$$F_{tapes} + F_{film} = 2\pi R_c t_m, \tag{25-5}$$

where F_{tapes} is the total force in the load tapes, F_{film} is the total meridional force in the film, R_c is the circumferential radius computed by the natural shape balloon design program, and t_m is the average meridional force per inch of balloon circumference computed by the balloon design program. Substituting Eq.(25-3) into Eq. (25-5) and noting that

$$F_{film} = \sigma_m 2\pi R_c h \tag{25-6}$$

yields for equilibrium in the meridional direction,

$$nK\epsilon_m + \sigma_m 2\pi R_c h = 2\pi R_c t_m , \tag{25-7}$$

where n is the number of deployed gores.

Assuming that the film deforms into a circular cross section perpendicular to the principal curvature directions, taking force equilibrium perpendicular to the balloon film surface yields

$$\frac{\sigma_m}{R_m(1+\epsilon_t)} + \frac{\sigma_t}{r(1+\epsilon_m)} = \frac{p}{h} + w \sin\theta , \tag{25-8}$$

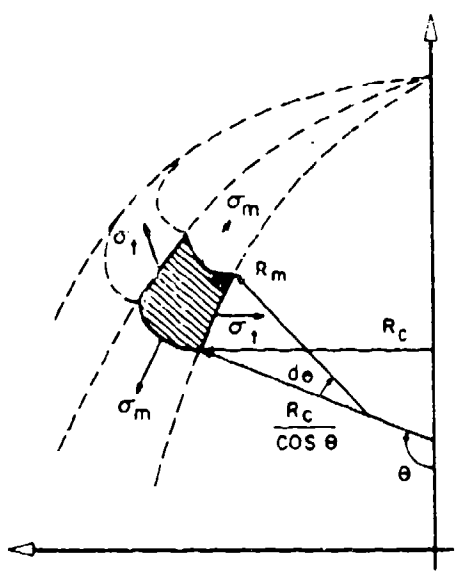

Figure 25-7. Free Body Diagram of an Element of a Balloon Gore

where R_m is the meridional radius of curvature of the design shape, r is the deformed transverse radius of curvature, p is the pressure difference across the balloon skin, h is the undeformed thickness of the balloon film, w is the weight density of polyethylene, and θ is the angle made by the design shape with the vertical axis of the balloon (see Figure 25-7).

Referring to Figure 25-8, it is necessary to establish a relationship between the transverse stretching and the strain, ϵ_t. The opening angle of the undefined shape can be expressed as

$$\alpha = \sin^{-1}\left(\frac{\ell \cos\theta}{2R_c}\right) , \tag{25-9}$$

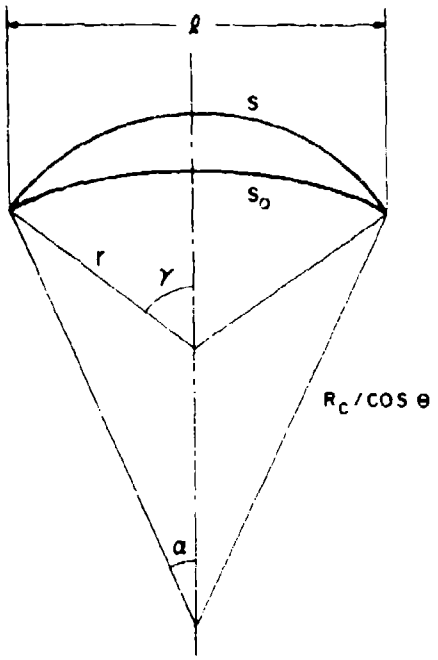

Figure 25-8. Undeformed and Deformed Cross Sections of a Balloon Gore

and the undeformed length is therefore

$$S_o = \frac{R_c}{\cos\theta}\,\alpha\,. \tag{25-10}$$

The deformed length is given by

$$S = r\gamma, \tag{25-11}$$

where

$$\gamma = \sin^{-1}\left(\frac{\ell}{2r}\right). \tag{25-12}$$

Therefore,

$$\epsilon_t = \frac{S}{S_o} - 1 = \frac{r\sin^{-1}\left(\frac{\ell}{2r}\right)\cos\theta}{R_c\,\alpha} - 1\,. \tag{25-13}$$

Equations (25-1), (25-2), (25-7), (25-8), and (25-13) constitute a system of five equations in the five unknowns. σ_t, σ_m, ϵ_m, ϵ_t and r. The quantities R_c, ℓ, θ, p, h and t_m are all obtained from the standard balloon design solution at each level on the balloon. Combining these equations yields the single nonlinear algebraic equation,

$$F(r) = \left[\frac{nk\nu}{ER_mQ} + \frac{1}{r(1+\epsilon_m)}\right] \sigma_t \quad \frac{BE_2}{R_mQ} - \frac{p}{h} - w\sin\theta = 0, \tag{25-14}$$

where

$$E = nK + 2\pi R_c h E_2, \tag{25-15}$$

$$Q = \frac{r\cos\theta \sin^{-1}\left(\frac{\ell}{2r}\right)}{R_c \alpha}, \tag{25-16}$$

$$1+\epsilon_m = \frac{A}{C}(Q-1+B\nu) + B + 1, \tag{25-17}$$

$$A = \frac{\nu}{E_2}\left[\frac{nK}{E} - 1\right], \tag{25-18}$$

$$C = \frac{1}{E_1} - \frac{nK\nu^2}{E_2E}, \tag{25-19}$$

$$B = \frac{2\pi R_c t_m}{E} \tag{25-20}$$

and

$$\sigma_t = \frac{Q - 1 + B\nu}{C}. \tag{25-21}$$

Equation (25-14) is solved for r using the Newton-Rhapson method. It is then possible to evaluate the other four unknowns, σ_m, σ_t, ϵ_m, ϵ_t. However, it should be noted that the ϵ_m computed will be the strain of the tape-film interface and not of the film at the center of the gore. Consequently, a correction is made that accounts for the increased ϵ_m in the gore center due to the increased meridional radius of curvature. It is found from geometric considerations that

$$\delta R_m = r - \frac{R_c}{\cos\theta} + \frac{1}{2}\sqrt{4\left(\frac{R_c}{\cos\theta}\right)^2 - \ell^2} - \frac{1}{2}\sqrt{4r^2 - \ell^2} \tag{25-22}$$

and, therefore, the corrected ϵ_m, $\bar{\epsilon}_m$, is

$$\bar{\epsilon}_m = \epsilon_m + \frac{\delta R_m}{R_m} . \qquad (25\text{-}23)$$

Substituting $\bar{\epsilon}_m$ for ϵ_m in Eqs. (25-1), (25-2), (25-8) and (25-13), these four equations are solved for the four unknowns σ_m, σ_t, ϵ_t and r. Equation (25-7) cannot be satisfied, since it represents meridional force equilibrium at the tape-film juncture. Combining Eqs. (25-1), (25-2), (25-8) and (25-13) yields the single nonlinear algebraic equation,

$$\frac{E_2 \bar{\epsilon}_m}{R_m Q} + \left[\frac{\nu}{R_m Q} + \frac{1}{r(1+\epsilon_m)}\right] \sigma_t - \frac{P}{h} - w \sin\theta = 0 , \qquad (25\text{-}24)$$

where

$$\sigma_t = \frac{\epsilon_t + \nu \bar{\epsilon}_m}{\frac{1}{E_1} - \frac{\nu^2}{E_2}} \qquad (25\text{-}25)$$

and

$$\epsilon_t = Q - 1 . \qquad (25\text{-}26)$$

Equation (25-24) can then be solved for r using the Newton-Rhapson method. Then σ_t, ϵ_t and σ_m are evaluated through the use of the governing equations.

25-3 THE STRESS ANALYSIS OF A SAMPLE BALLOON

To demonstrate a typical balloon stress analysis, a fully tailored, taped 5 million cubic foot balloon was chosen. A complete description of the sample balloon is given in Figure 25-9.

25-3.1 Stress Analysis With the Cap and a 488-Pound Payload

With the balloon in its design configuration with the cap and a 488-pound payload, the design shapes and the load tape configurations were computed at launch and at a number of altitudes up to ceiling. At all altitudes below the ceiling altitudes, the balloon was assumed to have 10 percent free lift. In this first attempt at balloon stress analysis, no superpressure region was allowed at the base of the

balloon. This causes a conservative analysis, an advantage in attempting to validate design work.

DESCRIPTION OF SAMPLE BALLOON

GORE PATTERN: TAPERED TANGENT BASE, FULLY TAILORED APEX.

MAXIMUM VOLUME: 5.025×10^6 CU. FT.

DIAMETER: 238.9 FT.

TAPE TYPE: POLYESTER, 500 LB.

GORE MATERIAL: 1.0 MIL POLYETHYLENE.

GORE LENGTH: 324 FT.

CAP LENGTH: 110 FT.

CAP MATERIAL: 1.0 MIL POLYETHYLENE.

DESIGN MINIMUM PAYLOAD: 468 LBS. FLOATS AT 119,000 FT.

MAXIMUM PAYLOAD: 4500 LBS. FLOATS AT 92,100 FT.

Figure 25-9. Description of the Sample Balloon

Using the design configurations to position the load tapes, the stresses and the strains in the balloon film were computed using the method outlined in section 25-2. Figures 25-10 and 25-11 show the transverse and machine direction stresses as a function of position on the balloon gore from the top end fitting to the maximum diameter. The high stresses near the top are probably due to the flat top result of the design program, a configuration that previously has been shown to violate force equilibrium on a deformed shape (Kerr and Alexander, 1965). Disregarding these high stresses near the top of the balloon, it appears that the highest stresses occur between 20,000 and 40,000 feet altitude, about 12 feet from the top of the balloon. In general, however, the stresses are rather low. This would be expected since the payload is quite low for this balloon.

Inspection of the transverse strain characteristic (Figure 25-12) yields some very interesting results. During the pass through the tropopause, there is a small region of negative transverse strain on each gore between 12 and 24 feet from the top of the balloon. This region would look like a flattening of the balloon in the region. Figure 25-13 shows a "circumferential stress band" reported by Baker (1966). This picture, taken of a 9 million cubic foot balloon at 54,600 feet, shows a flattened region almost exactly as predicted by Figure 25-12. This is an alternate explanation for Baker's "stress band."

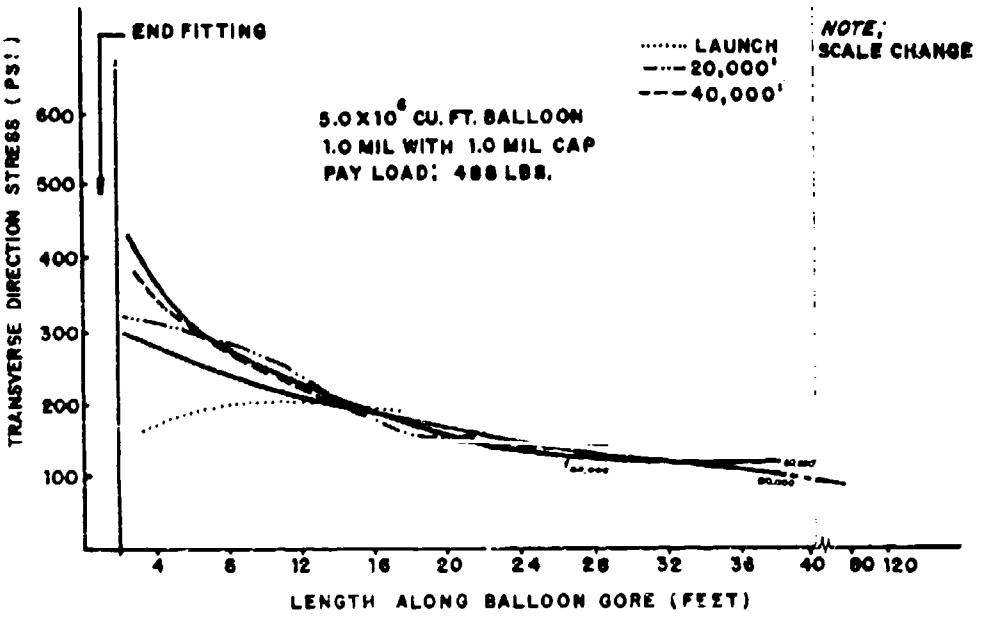

Figure 25-10. Transverse Stress Characteristic with 488-Pound Payload

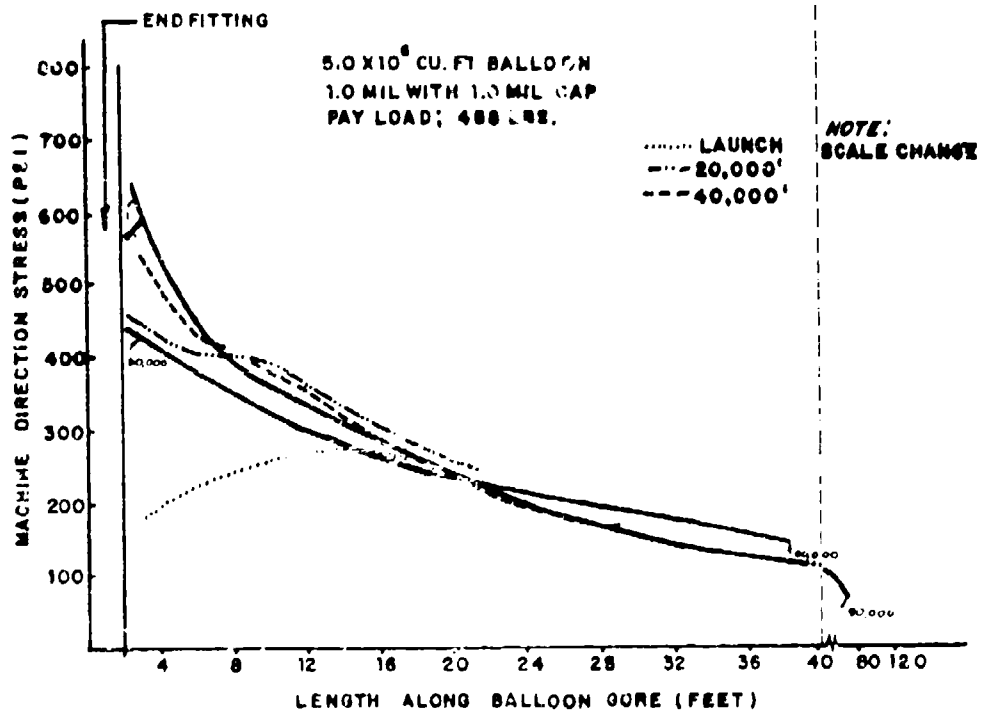

Figure 25-11. Machine Direction Stress Characteristic with 488-Pound Payload

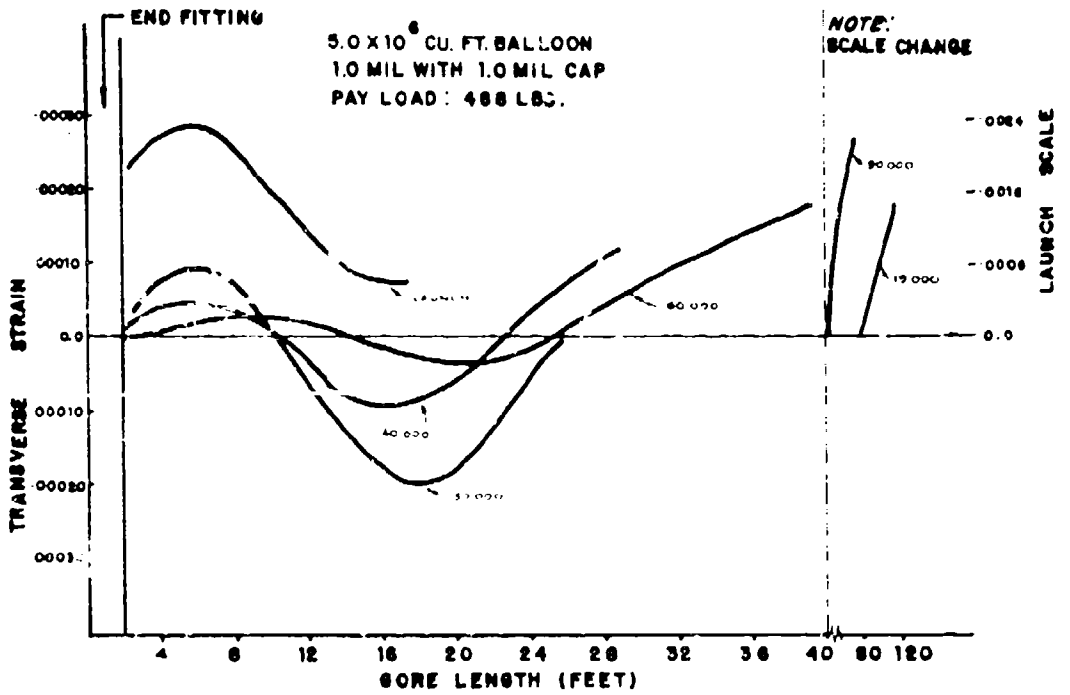

Figure 25-12. Transverse Strain Characteristic with 488-Pound Payload

25-3.2 Stress Analysis Without the Cap and a 488-Pound Payload

The load tape configurations were again computed at launch and at a number of altitudes up to ceiling, and the stresses and strains in the upper region of the balloon were found. Figures 25-14 and 25-15 show the transverse and machine direction stresses for this case. Here again the maximum stresses occur between 20,000 and 40,000 feet altitude approximately 12 feet from the top of the balloon. Most of the tropopause failures of this balloon have occurred in this maximum stress region.

25-3.3 Stress Analysis With the Cap and a 4500-Pound Payload

With this maximum payload, the stresses and strains were computed. The transverse and machine direction stress characteristics are shown in Figures 25-16 and 25-17. Again the maximum stresses occur at the tropopause. However, the stress values are quite large. If the stresses were really this high, the balloon would probably fail. Since balloons of this type have flown with 4500-pound payloads, the sources of error in the analysis were carefully evaluated. Since 500-pound load tapes were not available to the authors at the time of this study,

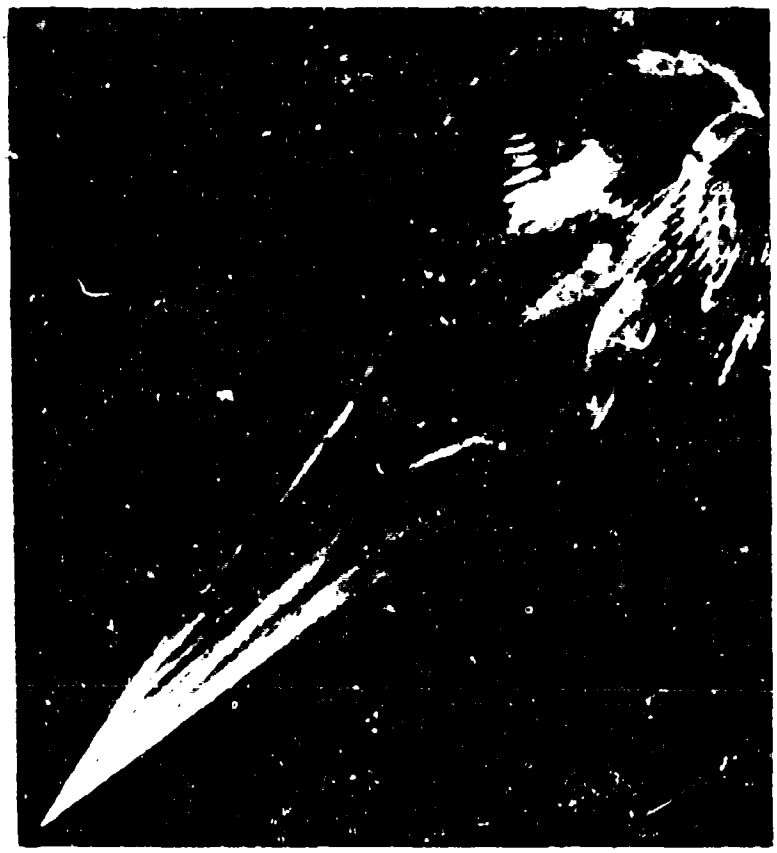

Figure 25-13. Negative Strain Region in a Balloon at the Tropopause (October, 1972)

the modules used was extrapolated from work with lower load tapes. This was considered a major source of error in the analysis. Consequently, the load tape modulus was doubled and the stresses were recomputed. The new results are shown in Figures 25-14 and 25-15. With these "1000-pound" load tapes, the stresses are brought down to reasonable levels. It is interesting to note that at the maximum diameter, the cross-direction stress has been almost unaffected by the load tape change. This seems to reflect that the load tapes carry almost no load at the maximum diameter, a fact that has been observed in ground inflations of balloons (Peters, 1972).

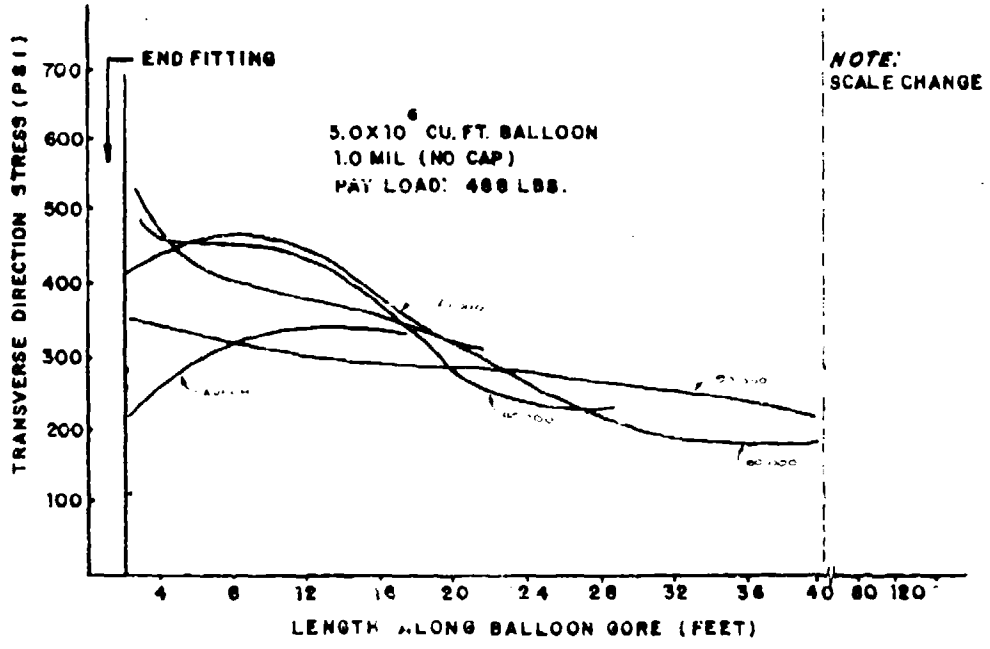

Figure 25-14. Transverse Stress Characteristic for Uncapped Balloon with 488-Pound Payload

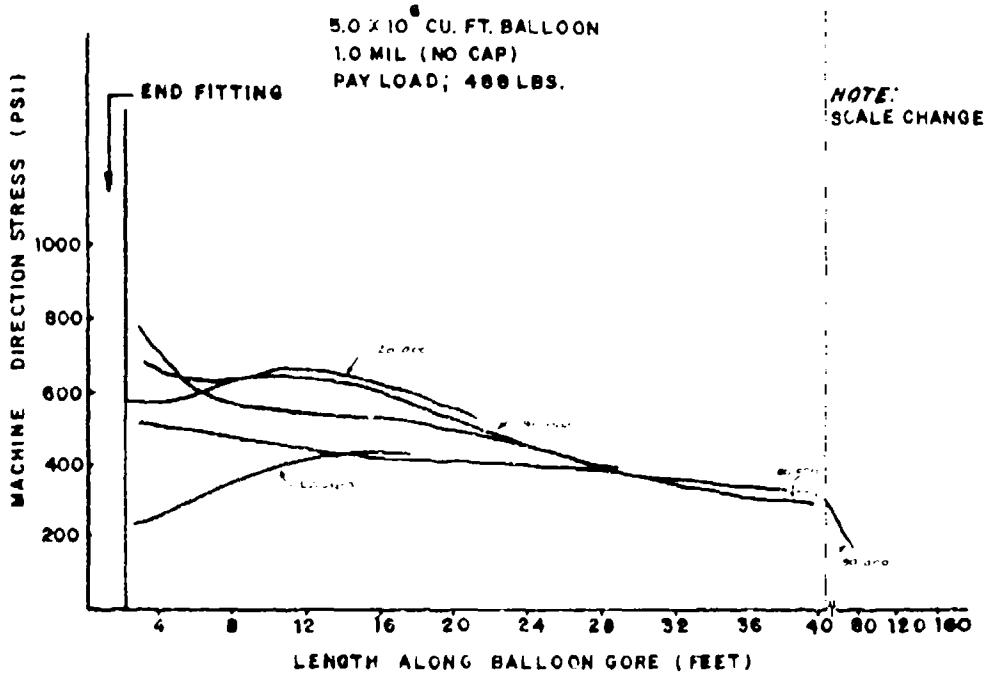

Figure 25-15. Machine Direction Stress Characteristic for Uncapped Balloon with 488-Pound Payload

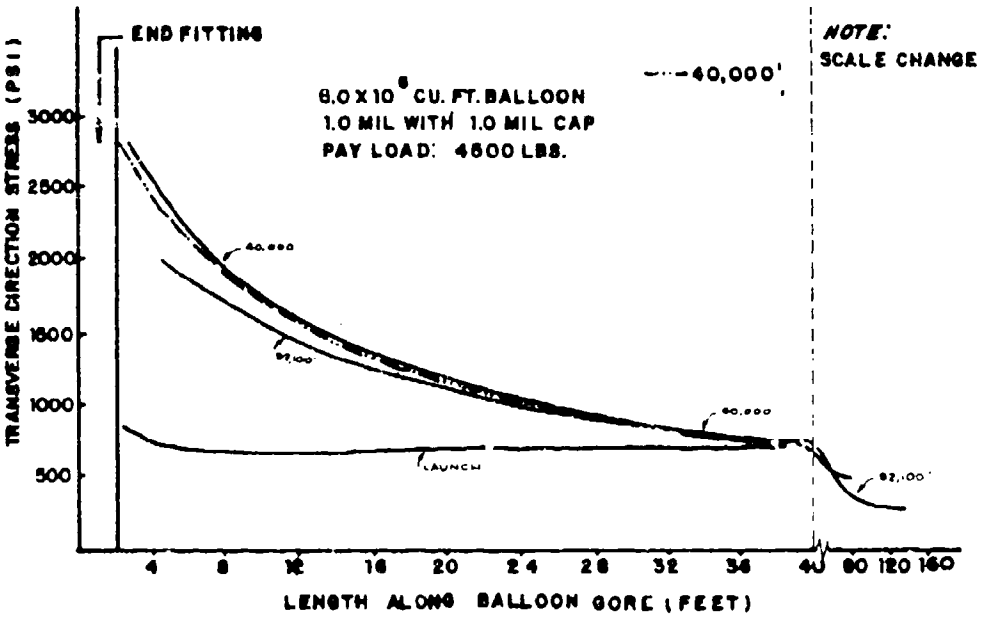

Figure 25-16. Transverse Stress Characteristic with 4500-Pound Payload

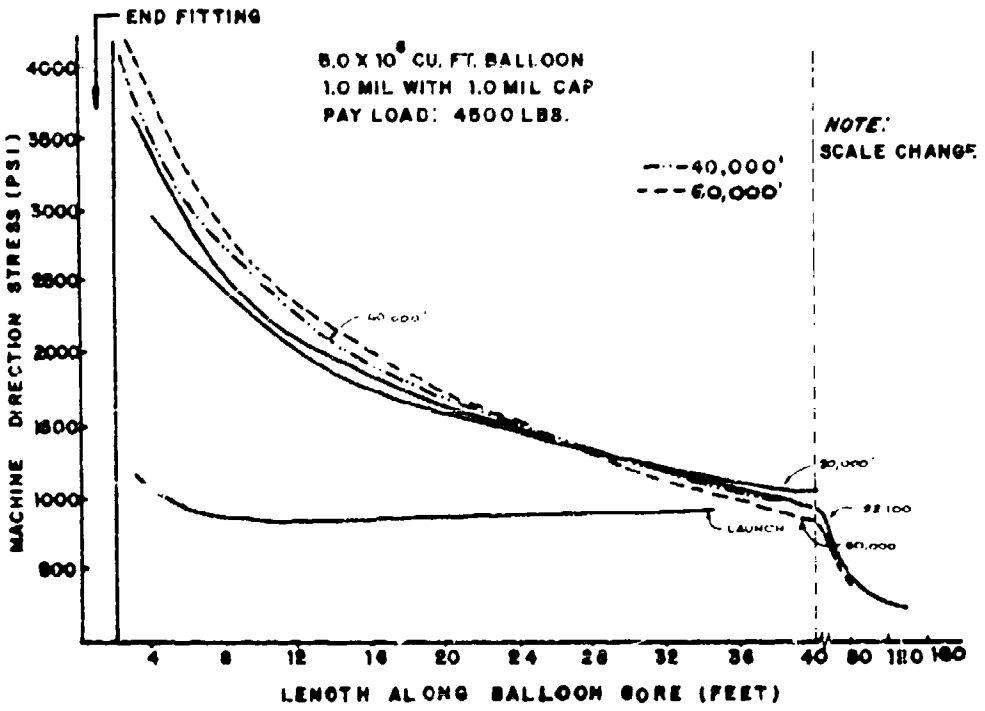

Figure 25-17. Machine Direction Stress Characteristic with 4500-Pound Payload

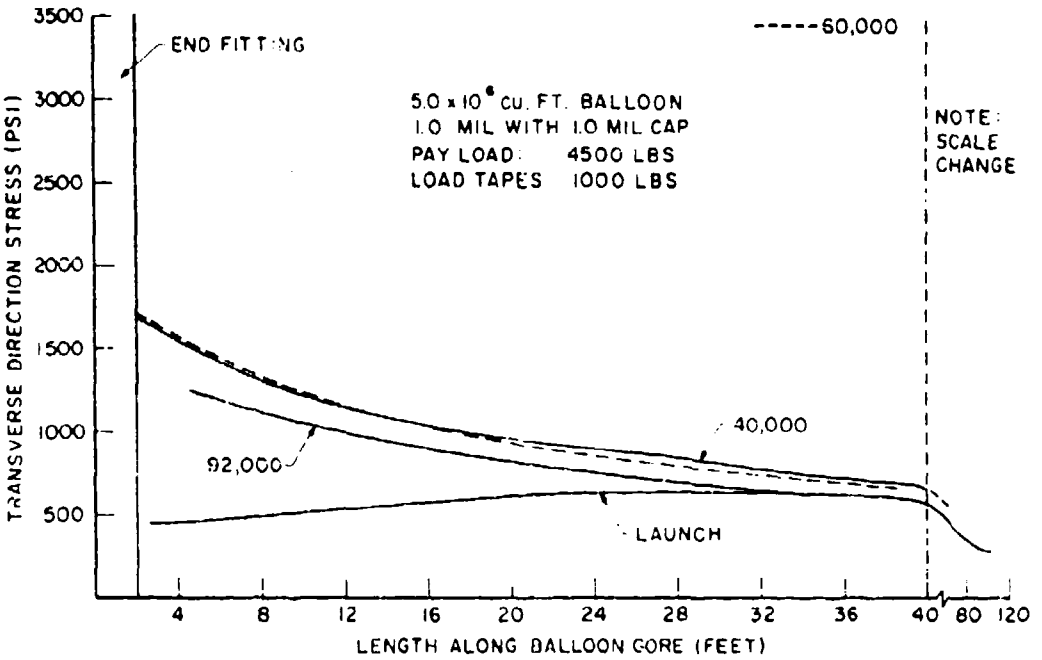

Figure 25-18. Transverse Stress Characteristic with 4500-Pound Payload and "1000-Pound" Load Tapes

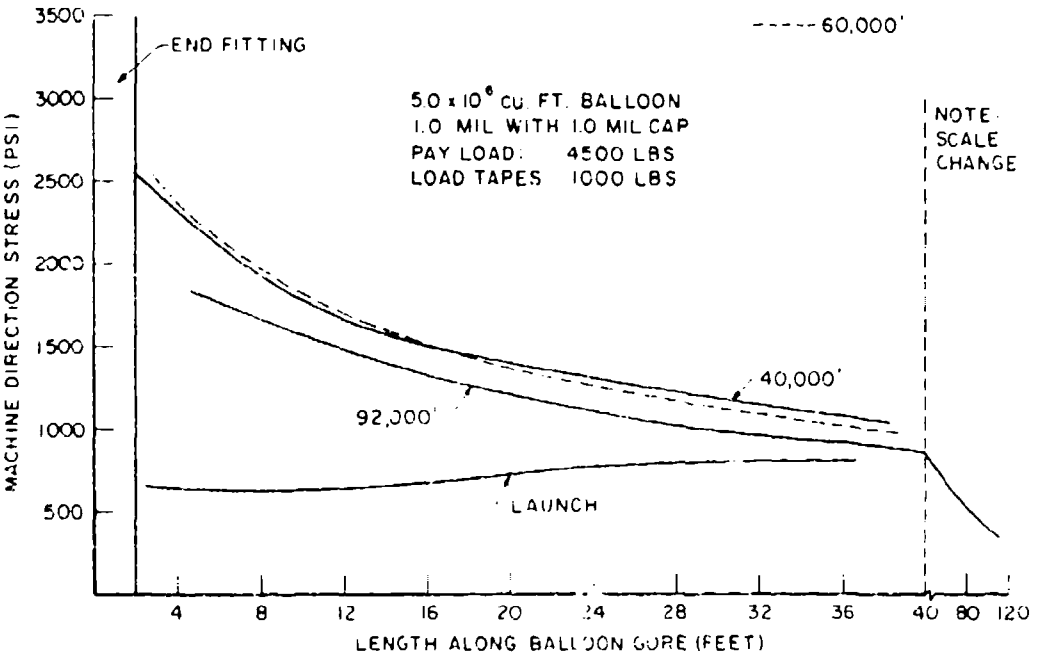

Figure 25-19. Machine Direction Stress Characteristic with 4500-Pound Payload and "1000-Pound" Load Tapes

25-4. CONCLUSIONS AND RECOMMENDATIONS

The analytical procedure presented in this paper provides a simple, conservative calculation of the stress field in a high altitude balloon throughout its entire flight history. It uses little computer time and can easily be incorporated into the balloon design procedure.

Of course, there are improvements that can be made. These are included in the following recommendations for future work:

(1) The subpressure region should be accounted for at all altitudes below ceiling.

(2) A better constitutive relation should be developed for polyethylene film.

(3) A better constitutive relation should be developed for load tapes.

(4) The material constants for the film and the load tapes should be more accurately determined.

(5) The analysis should be improved to account for nonhomogeneity of strain across the gores and to better determine the geometric configuration at the top of the balloon.

At the conclusion of this work it is expected that the analysis will be incorporated into the AFCRL balloon design program and that balloon design procedures will then be modified to better utilize balloon material strength and prevent regions of high stress concentrations.

References

Alexander, H. (1972) The Strength and Deformation Analysis of Flexible Balloons, Stevens Institute Report ME-RT-72004 (AFCRL-72-0236).

Alexander, H., and Weissmann, D. (1972) A Compendium of the Mechanical Properties of Polyethylene Balloon Films, Stevens Institute Report ME-RT-72001 (AFCRL-72-0068).

Baker, H. (1966) Balloon stress band analysis, Proc., Fourth AFCRL Scientific Balloon Symposium, pp. 75-96.

Kerr, A.D., and Alexander, H. (1965) Shape and Stress Analysis of Rotationally Symmetric Balloons, New York University Report NYU-AA-65-11.

Kerr, A.D., and Alexander, H. (1968) On a Cause of Failure of High Altitude Balloons, New York University Report NYU-AA-65-28 (AFCRL-68-0486).

Pavey, M. (1972) Private Communication.

Contents

26. Analysis of a Yarn Reinforced Laminate for Balloons and Other Structural Uses

V.L. Alley, Jr.
NASA Langley Research Center
Hampton, Virginia

Abstract

Equations are developed for analyzing and optimizing diagonally and longitudinally reinforced membranes used as a structural material. The relationships between the geometric and mechanical parameters are studied, and some design criteria are proposed. Buckling criteria are examined in depth, and the selection of parameters to yield maximum stable load ranges is treated. Through the appropriate selection of different materials and the use of the optimization criteria, multifold improvements in performance are predicted without a weight penalty. Test data and theoretical results for the flight-proven Viking Balloon Launch Decelerator Test (BLDT) balloon material are shown to give very good correlation.

26-1. INTRODUCTION

A lightweight high-strength reinforced mylar laminate has been developed in connection with the Balloon Launch Decelerator Test (BLDT) project of the Viking program. The material is for use as the gas bag structure of the main (lower) balloon of the large free-flight, two-stage balloon used to carry aloft the Mars reentry capsule and decelerator system of the Viking payload.

Balloons have many other current and potential uses, and their reliability, load capability, and application could be extended by improvements in the materials, improvements in the fabrication techniques, reduction in cost, and improvements in the balloon material manufacturing techniques. Balloon research has been minimal and has slowed the growth of balloon use for varied applications. Balloon interest is of a national scope and far exceeds the specific involvement in the Viking Project.

For example, balloons are being used for freight hauling, logging, microwave relay stations, television surveillance, radar platforms, a variety of military applications, border monitoring, and night and day surveillance. They are capable of extensive measurements of Earth resources, atmospheric samplings, high-altitude optical and radiation research, pollution detection, and weather watches. They are useful for high altitude drop tests of research payloads of sizable weights, for fish spotting, and for stable platforms for large antennas. Other possible applications are for police surveillance of urban areas using infrared optics, the transportation of prefabricated units (such as houses) by helicopter tows, balloon supported tramways for short haul moving of cargo and or people, and control of lighting in critical areas and over dry forests.

The many applications for balloons are an impetus to improve and advance and optimize the materials that are used for balloon construction. The potential seems to exist to greatly improve current materials to the point that a fourfold increase in the material ultimate capability can be realized within the same weight constraints.

Furthermore, in regard to the material elastic properties, essentially nothing has been done to acquire the material coefficients needed to do structural analyses of the membrane systems. These coefficients are known to be nonlinear functions of the membrane stresses in the material. In order to accomplish sophisticated structural analyses on balloons or inflatable membrane structures, it is essential that a macroscopic approach to the material mechanical behavior be used. In order to achieve this type of analysis, it is desirable to have a full set of the generalized Hookian coefficients for the composite planar laminate. These coefficients are nonlinear and stress dependent and fail to meet the usual reciprocity or symmetric conditions that are found with ordinary structural materials. Consequently, the six coefficients that are a maximum for two-dimensional stress solutions of usual materials need extending to a total of nine independent nonlinear Hookian coefficients for a complete understanding and a full and accurate assessment of the material behavior.

The problems associated with measuring and data processing for acquiring the generalized set of Hookian coefficients for a macroscopic treatment of a filamental material previously have been outlined in detail (Alley and Faison, 1972a and b).

These procedures are equally applicable to the laminates used for balloon construction. Kenner (1972) has investigated examples of the use of the nonlinear Hookian coefficients in large deflection nonlinear membrane analyses by finite-element methods. These references indicate the vast amount of material data necessary for adequately analyzing membrane structures and reveal the great void that exists in such information on fabrics, membranes, and laminates currently in use as structural materials.

The present paper deals primarily with developing and optimizing a balloon material with specific application for the Viking Project. The proposed Viking qualification test balloon is a tandem type having a .5 million cubic foot launch balloon that carries aloft the main balloon having a full inflation capacity of 34,000,000 cubic feet at the float altitude of 120,000 feet. The balloon system is initially charged with 300,000 cubic feet of helium at sea level, and as it ascents and the atmospheric pressure drops, the helium expands and transfers from the launch balloon to the main balloon until it reaches its fully expanded size of approximately 34,000,000 cubic feet. A very critical situation exists in this type of balloon, in that as it passes through the tropopause its materials are subjected to the severe cold quench reaching temperatures around -70° to -90°F. At these temperatures, the usual polymeric membrane material of the balloon reaches a highly glasseous phase where it becomes extremely brittle, and failure is induced by almost any small strain. Unfortunately, during this tropopause phase the balloon has not been fully inflated to the smooth, uniform axisymmetric onion shape and, as a result, the irregular semi-inflated shape is subject to many nonaxisymmetric perturbations which in turn produce shear stresses and local stresses and aggravate the stress condition at the low temperature. In addition, current balloon design technology is almost totally based upon the analysis of the balloons for a completely asymmetric condition. Very little, if any, quantitative information exists as to the significance of asymmetric geometries and how they affect biaxial stresses and the shear stresses that are introduced.

In the early phases of the Viking program, a rectangular yarn-reinforced mylar laminate was proposed that is widely known as leno scrim laminate. The leno scrim laminate has been used extensively in smaller balloon construction in the past. It is comprised of a mylar base membrane that is hot rolled to a Dacron yarn scrim that has a rectangular pattern of usually five threads per inch in the transverse direction and six threads per inch in the longitudinal direction of the fabric. The fundamental principle of the laminated structure of the balloon is that the reinforcing yarn is designed to take the primary loads, whereas the base membrane of mylar is designed to provide a gas barrier only. An inherent violation to this principle exists in the geometric characteristics of the leno laminate by virtue of its inability to resist shear forcing except within the mylar membrane.

The validity of this concern was studied by finite element structural analyses and followed up with experimental tests. These analytical results and experimental tests clearly indicated that there was an adverse degeneration in the structural ability of the leno scrim laminate at tropopause temperatures aggravated by the presence of shear loading. To establish realistic levels of shear for balloons is currently impossible; however, consideration should be given to the real problem that shears do exist in the inflation stages in particular. A materials development program was initiated through the Viking Project to obtain a material with increased structural integrity over that of the leno scrim laminate with the major objective being to carry the biaxial stresses along with the presence of moderate shear stresses.

A related and comprehensive report on some of the experimental results on candidate materials for the Viking application is given by Niccum (1972). Manufacturing problems are discussed, and the technique and facilities for biaxial testing with shear is given attention.

This paper considers the optimization of the reinforcement pattern with respect to the amount and distribution of the yarn relative to the base membrane. The equations for considering these factors are developed in detail, and numerical data are acquired to show the near-optimum geometric and mechanical characteristics to be achieved and incorporated in design and implemented in balloon material production. Also, correlation of theoretical with experimental results is presented.

26-2. SYMBOLS

A_{ij}, A_{im}	Cross-sectional areas of diagonal yarn and longitudinal yarn, respectively, in.^{2} (m^2)
AE_{ij}, AE_{jm}	Project of cross-sectional area and Young's modulus of the ij and jm diagonal yarns, lb (N)
AE_{im}	Product of cross-sectional area and Young's modulus of the im longitudinal yarn, lb (N)
C_{11}, C_{22}, C_{33}, C_{12}, C_{21}	Coefficients of matrix, Eq. (26-15a), unitless
E_y, E_m	Young's modulus of yarn material and membrane material, respectively lb/in.^{2} (N/m^2)
Et	Membrane modulus of elasticity times membrane thickness, lb in. (N/m)
f_{ij}, f_{jm}, f_{im}	Forces in the ij and jm diagonal yarns and in the im longitudinal yarn, respectively, lb (N)
P_x, P_y	Average applied membrane loads per unit length in the x and y directions, respectively, lb/in. (N/m)

p_{xy}	Average applied membrane shear load per unit length, lb/in. (N/m)
$q(\theta, \mu) = \zeta_{1,cr}/\psi$	Characteristic function relating optimum conditions, unitless
r_1, r_2	The larger and smaller root of the membrane stability Eq. (26-23), respectively
t	Thickness of membrane, in. (m)
t_a	Thickness of adhesive coating on membrane, in. (m)
u, v	Displacement in the x and y directions, respectively, in. (m)
$\overline{w}$	Specific weight, weight per unit area of the reinforced membrane, lb/in.^{2} (N/m^2)
x, y	Orthogonal coordinates, longitudinal and transverse directions, respectively, in. (m)
γ_{xy}	Shear deformation, unitless
ϵ_x, ϵ_y	Strain in the x and y directions, respectively, unitless
$\zeta_1 = \frac{EA_{im}}{Etx_j}$	Parameter, unitless
$\zeta_2 = \frac{EA_{ij}}{EA_{im}}$	Parameter, unitless
$\zeta_3 = \frac{\rho_m E_y}{\rho_y E_m}$	Parameter, unitless
θ	Angular orientation of the diagonal yarns with respect to the x axis, degrees or radians
$\lambda = (t + t_a)/t$	Parameter, unitless
μ	Poisson's ratio, unitless
ρ_y, ρ_m	Density of yarn material and membrane material, respectively, lb/in.^{3} (N/m^3)
σ_x, σ_y	Stresses in the x and y directions, respectively, lb/in.^{2} (N/m^2)
$\sigma_{max, min}$	Designates the maximum and minimum principal stresses, lb/in.^{2} (N/m^2)
τ_{xy}	Shear stress, lb/in.^{2} (N/m^2)
Δ_{ij}	Elongation of the ij yarn, in. (m)
ϵ_{im}, ϵ_{ij}	Strain in the im and ij yarns, respectively, unitless

Subscripts:

i, j, m	Designate nodes, or subscripts, unitless
u	Designates "ultimate"

Matrices:

$[\ ]\ \{\ \}\ |\ |$

Denote square, column, diagonal, inverse, and transpose matrices, respectively.

$[\ ]^{-1}\ \cdot\ [\ ]^{T}$

26-3. ANALYSIS

The derivation follows for the equations relating yarn forces, membrane stresses, and related strains to the applied uniaxial loads and applied shear. Also, the conditions necessary for membrane stability are defined.

26-3.1 Assumptions

The derivations are based on small deflection-linear theory and assume isotropic behavior of the membrane. The assumption of elastic behavior is poor for both the membrane and yarn at room temperature and for large strains. However, for tropopause temperatures for which balloon materials are primarily critical, and for which this analysis is directed, the assumptions are reasonably good. In the use of Hooke's law, the coefficients of interactions of the first and second kind are considered zero, and material conservativeness or symmetry is assumed. In addition, it is assumed that compressive forces cannot be sustained in either the yarns or membrane without buckling, and no external tensile and/or shear forces are applied. An exception to the assumption that compressive stresses can be sustained in the yarns membrane is stable.

26-3.2 Repetitive Pattern

The analysis of a uniformly stressed infinite field of fine mesh, reinforced material can be reduced to the analysis of one element of the repeating pattern. For example, the diagonally reinforced material used in the Viking balloons reduces to repeated parallelograms of the sort shaded in Figure 2601(a). With closer inspection and consideration, it is seen that further simplification can be achieved even within the parallelogram, since the left-hand half of the shaded parallelogram is antisymmetric to the right-hand half. Hence, the problem can be reduced to

the analysis of a single triangular element of the material such as indicated in Figure 26-1(b) by the i, j, m element.

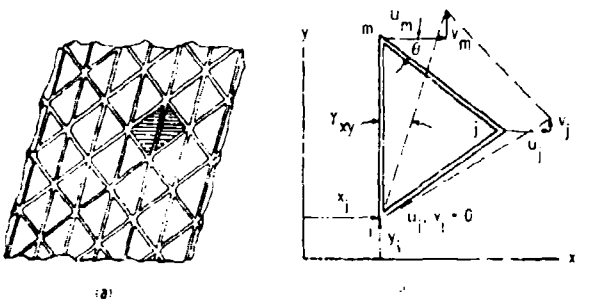

Figure 26-1. Uniformly Stressed and Skewed Reinforced Membrane and Basic Triangular Element

In the following section, the stresses in the membrane and the forces in the yarns will be explicitly derived in terms of the strains.

26-3.3 Membrane Stresses and Yarn Forces

Assume that the total stress field is due to uniform strain in both the y and x directions and shear deformation γ_{xy}, such that any point relative to the x, y coordinate system will experience the displacements.

$$u = \epsilon_x x \quad \gamma_{xy} y \tag{26-1}$$

$$v = \epsilon_y y \tag{26-2}$$

For convenience and simplification, choose the origin of the x, y coordinate system to coincide with the ith node, and set $u_i = v_i = 0$. Substituting the coordinates for the jth and mth nodes will yield the nodal displacements in terms of the uniform field strains and shear deformation; that is,

$$\begin{Bmatrix} u_i \\ v_j \\ u_m \end{Bmatrix} = \begin{bmatrix} x_i & 0 & y_i \\ 0 & y_j & 0 \\ 0 & 0 & 2y_j \end{bmatrix} \begin{Bmatrix} \epsilon_x \\ \epsilon_y \\ \gamma_{xy} \end{Bmatrix} \tag{26-3}$$

since

$$y_m = 2y_j \text{ and } x_m = 0$$

and

$$v_m = 2y_j \epsilon_y = 2v_j . \tag{26-4}$$

For later convenience, Eq. (26-4) is carried separately from the matrix set since it is linearly related to the second row of Eq. (26-3). The membrane forces are assumed linearly related to the strains by the usual stress-strain relationships. If the stresses are multiplied by the membrane thickness, then the membrane forces are obtained and the membrane force-strain relationship result is as follows:

$$\begin{Bmatrix} \sigma_x t \\ \sigma_y t \\ \tau_{xy} t \end{Bmatrix} = \frac{Et}{1 - \mu^2} \begin{bmatrix} 1 & \mu & 0 \\ \mu & 1 & 0 \\ 0 & 0 & \frac{(1-\mu)}{2} \end{bmatrix} \begin{Bmatrix} \epsilon_x \\ \epsilon_y \\ \gamma_{xy} \end{Bmatrix} \tag{26-5}$$

The extensions of the yarns to maintain compatibility with the nodal displacements produce yarn strains and yarn forces. Consider, for example, the yarn running from node i to node j (Figure 26-1b). For small deflections, the elongation of ij is

$$\Delta_{ij} = u_j \cos\theta + v_j \sin\theta_{ij} - u_i \cos\theta_{ij} - v_i \sin\theta_{ij} . \tag{26-6}$$

But it is readily seen that

$$\cos\theta_{ij} = \frac{x_j - x_i}{\sqrt{(x_j - x_i)^2 + (y_j - y_i)^2}} \tag{26-7}$$

and

$$\sin\theta_{ij} = \frac{y_j - y_i}{\sqrt{(x_j - x_i)^2 + (y_j - y_i)^2}} . \tag{26-8}$$

Substituting Eqs. (26-7) and (26-8) in (26-6) and dividing the results by the yarn length will yield the strain in the yarn. In a similar manner and with appropriate interchanges of subscripts, the strains in the other yarns can be expressed. Multiplying the strains by their respective cross-sectional areas and Young's moduli

will give the forces in the three yarns. Recalling that the ith node was chosen as the origin, hence, x_i, y_i, u_i, v_i, and x_m are zero. Also, observing that $v_m = 2v_j$, then the forces in the yarns can be expressed as

$$\begin{Bmatrix} f_{ij} \\ f_{im} \\ f_{jm} \end{Bmatrix} = \frac{y_j AE_{im}}{x_j^2 + y_j^2} \begin{bmatrix} \frac{x_j}{y_j}\frac{AE_{ij}}{AE_{im}} & \frac{AE_{ij}}{AE_{im}} & 0 \\ 0 & \frac{x_j^2 + y_j^2}{y_j^2} & 0 \\ \frac{x_j}{y_j}\frac{AE_{jm}}{AE_{im}} & \frac{AE_{jm}}{AE_{im}} & -\frac{x_j}{y_j}\frac{AE_{jm}}{AE_{im}} \end{bmatrix} \begin{Bmatrix} u_j \\ v_j \\ u_m \end{Bmatrix} \qquad (26\text{-}9)$$

Substituting Eq. (26-3) into Eq. (26-9) will yield the yarn loads in terms of the strains.

$$\begin{Bmatrix} f_{ij} \\ f_{im} \\ f_{jm} \end{Bmatrix} = \frac{y_j^2}{x_j^2 + y_j^2} \begin{bmatrix} AE_{ij} & & \\ & AE_{im} & \\ & & AE_{jm} \end{bmatrix} \begin{bmatrix} \left(\frac{x_j}{y_j}\right)^2 & 1 & \frac{x_j}{y_j} \\ 0 & \frac{x_j^2 + y_j^2}{y_j^2} & 0 \\ \left(\frac{x_j}{y_j}\right)^2 & 1 & -\frac{x_j}{y_j} \end{bmatrix} \begin{Bmatrix} \epsilon_x \\ \epsilon_y \\ \gamma_{xy} \end{Bmatrix} . \qquad (26\text{-}10)$$

26-3.4 Average Applied Loads

Reinforced membranes are generally judged by the force per unit length they can sustain – uniaxially, or for combinations of membrane loads. An inspection of the following diagrams will show that the total laminate forces per unit length can be defined simply by considering the equilibrium (Figure 26-2). Summing the forces in the y direction over the pitch "$2x_j$" gives the average running load in the y direction of

$$p_y = \sigma_y t + \frac{f_{ij}\, y_j}{2x_j\sqrt{x_j^2 + y_j^2}} + \frac{f_{im}}{x_j} + \frac{f_{jm}\, y_j}{2x_j\sqrt{x_j^2 + y_j^2}} . \qquad (26\text{-}11)$$

Similarly, summing forces on Figure 26-2(b) in the x direction over the pitch $2y_j$, gives the average running load in the x direction.

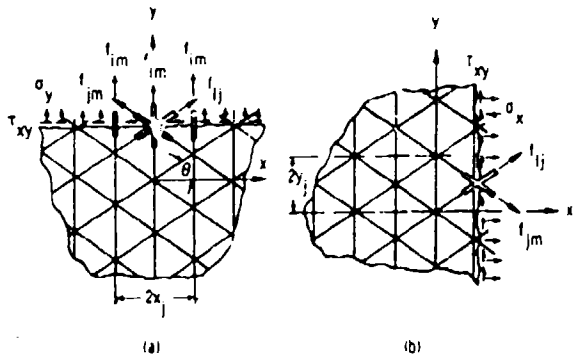

Figure 26-2. Boundary Forces on Edges

$$p_x = \sigma_x t + \frac{x_j f_{ij}}{2y_j \sqrt{x_j^2 + y_j^2}} + \frac{x_j f_{jm}}{2y_j \sqrt{x_j^2 + y_j^2}} \tag{26-12}$$

The average running shear (or shear flow) along the edge can be found from summing, over the pitch length, the boundary forces along the cut edges of either Figure 26-2a or 26-2b; that is,

$$p_{xy} = \tau_{xy} t + \frac{f_{ij}}{2\sqrt{x_j^2 + y_j^2}} - \frac{f_{jm}}{2\sqrt{x_j^2 + y_j^2}} \tag{26-13}$$

Equations (26-11), (26-12), and (26-13) can be succinctly stated in matrix form as

$$\begin{Bmatrix} p_x \\ p_y \\ p_{xy} \end{Bmatrix} = \frac{1}{2\sqrt{x_j^2 + y_j^2}} \begin{bmatrix} x_j & 0 & x_j \\ y_j & & y_j \\ y_j & \dfrac{2\sqrt{x_j^2 + y_j^2}}{x_j} & y_j \\ x_j & & x_j \\ 1 & 0 & -1 \end{bmatrix} \begin{Bmatrix} f_{ij} \\ f_{im} \\ f_{jm} \end{Bmatrix} + \begin{Bmatrix} \sigma_x t \\ \sigma_y y \\ \tau_{xy} t \end{Bmatrix}. \tag{26-14}$$

26-3.5 Explicit Solutions

Equations (26-3), (26-5), and (26-10) express the displacement, membrane stresses, and yarn forces explicitly in terms of strain. It is desired to achieve

expressions for these parameters, along with the strain, in terms of the applied loads given by Eq. (26-14). This is achieved forst by substituting Eqs. (26-5) and (26-10) into Eq. (26-14) and solving the matrix equation for the strains; that is

$$\begin{Bmatrix} \epsilon_x \\ \epsilon_y \\ \gamma_{xy} \end{Bmatrix} = \frac{1}{Et} \left[\frac{\frac{y_j^2}{x_j^2}}{2\left(1+\frac{y_j^2}{x_j^2}\right)^{3/2}} \begin{bmatrix} \frac{x_j}{y_j} & 0 & \frac{x_j}{y_j} \\ \frac{y_j}{x_j} & 1 & \frac{y_j}{x_j} \\ 1 & 0 & -1 \end{bmatrix} \begin{bmatrix} \frac{AE_{ij}}{Etx_j}\frac{x_j}{y_j} & & 0 \\ & \frac{2AE_{im}}{Etx_j}\frac{x_j^2}{x_j^2}\left(1+\frac{y_j^2}{x_j^2}\right)^{3/2} & \\ 0 & & 0 \\ & & \frac{AE_{jm}}{Etx_j}\frac{x_j}{y_j} \end{bmatrix} \right.$$

$$\left. \begin{bmatrix} \frac{x_j}{y_j} & 0 & \frac{x_j}{y_j} \\ \frac{y_j}{x_j} & 1 & \frac{y_j}{x_j} \\ 1 & 0 & -1 \end{bmatrix}^T + \frac{1}{1-\mu^2} \begin{bmatrix} 1 & \mu & 0 \\ \mu & 1 & 0 \\ 0 & 0 & \frac{1-\mu}{2} \end{bmatrix} \right]^{-1} \begin{Bmatrix} p_x \\ p_y \\ p_{xy} \end{Bmatrix}. \qquad (26\text{-}15)$$

For future convenience, Eq. (26-15) may be denoted as

$$\begin{Bmatrix} \epsilon_x \\ \epsilon_y \\ \gamma_{xy} \end{Bmatrix} = \frac{1}{Et} \begin{bmatrix} C_{11} & C_{12} & 0 \\ C_{21} & C_{22} & 0 \\ 0 & 0 & C_{33} \end{bmatrix}^{-1} \begin{Bmatrix} p_x \\ p_y \\ p_{xy} \end{Bmatrix} \qquad (26\text{-}15a)$$

and performing the inverse operations and observing that $C_{21} = C_{12}$, and $EA_{ij} = EA_{jm}$, then

$$\begin{Bmatrix} \epsilon_x \\ \epsilon_y \\ \gamma_{xy} \end{Bmatrix} = \frac{1}{Et(C_{11}C_{22}-C_{12}^2)} \begin{bmatrix} C_{22} & -C_{12} & \\ -C_{12} & C_{11} & \\ & & \frac{C_{11}C_{22}-C_{12}^2}{C_{33}} \end{bmatrix} \begin{Bmatrix} p_x \\ p_y \\ p_{xy} \end{Bmatrix}. \qquad (26\text{-}15b)$$

If

$$\theta = \tan^{-1}\frac{y_j}{x_j}$$

and

$$\zeta_1 = -\frac{EA_{im}}{EA_{ij}}$$

$$\zeta_2 = \frac{EA_{ij}}{EA_{im}}$$

then the coefficients of Eq. (26-5a) or Eq. (26-15b) are as follows:

$$\left.\begin{aligned} C_{11} &= \frac{1}{1-\mu^2} + \zeta_1\,\zeta_2\,\frac{\cos^4\theta}{\sin\theta} \\ C_{12} &= C_{21} = \frac{\mu}{1-\mu^2} + \zeta_1\,\zeta_2\,\sin\theta\,\cos^2\theta \\ C_{22} &= \frac{1}{1-\mu^2} + \zeta_1 + \zeta_1\,\zeta_2\,\sin^3\theta \\ C_{33} &= \frac{}{2(1+\mu)} + \zeta_1\,\zeta_2\,\sin\theta\,\cos^2\theta \end{aligned}\right\}. \qquad (26\text{-}16)$$

Substituting Eq. (26-15b) into Eqs. (26-5) and (26-10) will yield the membrane forces and yarn forces as functions of the applied loads.

$$\begin{Bmatrix} \sigma_x t \\ \sigma_y t \\ \tau_{xy} t \end{Bmatrix} = \frac{1}{(1-\mu^2)(C_{11}C_{22}-C_{12}^2)} \begin{bmatrix} C_{22}-\mu C_{12} & \mu C_{11}-C_{12} & \\ \mu C_{22}-C_{12} & C_{11}-\mu C_{12} & \\ 0 & 0 & \frac{(1-\mu)(C_{11}C_{22}-C_{12}^2)}{2C_{33}} \end{bmatrix} \begin{Bmatrix} p_x \\ p_y \\ p_{xy} \end{Bmatrix}$$

$$\begin{Bmatrix} f_{ij} \\ f_{im} \\ f_{jm} \end{Bmatrix} = \frac{x_j \zeta_1 \zeta_2 \sin^2\theta}{(C_{11}C_{22}-C_{12}^2)} \begin{bmatrix} (C_{22}\cot^2\theta - C_{12})C_{11} - C_{12}\cot^2\theta & \frac{(C_{11}C_{22}-C_{12}^2)}{C_{33}\tan\theta} & \\ -C_{12}\frac{\cos^2\theta}{\zeta_2} & -C_{11}\frac{\cos^2\theta}{\zeta_2} & 0 \\ (C_{22}\cot^2\theta - C_{12})C_{11} - C_{12}\cot^2\theta & \frac{-(C_{11}C_{22}-C_{12}^2)}{C_{33}\tan\theta} & \end{bmatrix} \begin{Bmatrix} p_x \\ p_y \\ p_{xy} \end{Bmatrix}.$$

Equations (26-15b), (26-17), and (26-18) provide all the essential data on the strains, stresses, and yarn forces. However, these equations are valid provided the normal stresses and yarn forces are all positive, with one exception. Compressive (or negative) stresses occur with buckling when the minimum principal stress is equal to or less than zero. Yarn buckling is assumed to occur whenever the membrane buckles. However, it can be shown that compressive yarn forces can exist when the membrane is stable, and this phenomenon can occur for small yarn placement angles, θ, along with low transverse strain.

26-3.6 Buckling Bounds

The maximum and minimum stresses in the membrane are given by

$$\sigma_{max,\,min} = \frac{\sigma_x + \sigma_y}{2} \pm \sqrt{\left(\frac{\sigma_x - \sigma_y}{2}\right)^2 + \tau_{xy}^2} \tag{26-19}$$

Substituting Eq. (26-17) into Eq. (26-19) yields the expression for the principal stresses in terms of the coefficients given by Eq. (26-16).

$$\frac{\sigma t_{max,\,min}}{p_y} = \frac{1}{2(1-\mu)(C_{11}C_{22} - C_{12}^2)} \left\{ C_{11} - C_{12} + (C_{22} - C_{12})\frac{p_x}{p_y} \right.$$

$$\left. \pm \frac{(1-\mu)}{(1+\mu)} \sqrt{\left[(C_{22} + C_{12})\frac{p_x}{p_y} - (C_{11} + C_{12})\right]^2 + \left[\frac{(C_{11}C_{22} - C_{12}^2)}{C_{33}}\frac{p_{xy}}{p_y}\right]^2} \right\} \tag{26-20}$$

The maximum principal stress is obtained by using the plus sign of the radical. The minimum stress is obtained by using the minus sign. For the minimum stress to be equal to or greater than zero, σ_x and σ_y must be equal to or greater than zero; hence, from Eq. (26-19)

$$\frac{\sigma_x + \sigma_y}{2} \geq \sqrt{\left(\frac{\sigma_x - \sigma_y}{2}\right)^2 + \tau_{xy}^2}, \tag{26-21}$$

where the radical on the right-hand side is known to be the maximum shear stress, $\tau_{xy\,max}$.

Squaring both sides of Eq. (26-21) and simplifying yields

$$\sigma_x \sigma_y \geq \tau_{xy}^2 \quad \text{for } \sigma_{min} \geq 0. \tag{26-22}$$

Substituting Eq. (26-17) into Eq. (26-22) and rearranging yields the conditional equation for a stable membrane and for the conditions in which the foregoing equations are valid.

$$(C_{22} - \mu C_{12})(\mu C_{22} - C_{12})\frac{p_x^2}{p_y^2} + \left[(C_{12} - \mu C_{12})(C_{11} - \mu C_{12}) + (\mu C_{11} - C_{12})(\mu C_{22} - C_{12})\right]\frac{p_x}{p_y}$$

$$+ (\mu C_{11} - C_{12})(C_{11} - \mu C_{12}) - \left[\frac{(1-\mu)(C_{11}C_{22} - C_{12}^2)}{2C_{33}} - \frac{(1-\mu)(C_{11}C_{22} - C_{12}^2)}{2C_{33}}\frac{p_{xy}}{p_y}\right]^2 \geq 0. \quad (26\text{-}23)$$

Equation (26-23) is an inequality of quadratic form in p_x/p_y, and when solved for its roots it will relate the parameters defining the bounds and regions of stability. If r_1 and r_2 are the roots of Eq. (26-23) and r_1 is the larger of the two, then buckling in the membrane does not occur if

$$\mu C_{22} - C_{12} \geq 0$$

and

$$(p_x/p_y - r_1)(p_x/p_y - r_2) \geq 0. \quad (26\text{-}24)$$

Thus a stable membrane exists for these conditions if

$$p_x/p_y > r_1$$

or

$$0 < \frac{p_x}{p_y} < r_2 \text{ provided } r_2 \text{ is positive.}$$

However, if

$$\mu C_{22} - C_{12} < 0,$$

then the condition for stability is

$$(p_x/p_y - r_1)(p_x/p_y - r_2) < 0, \quad (26\text{-}25)$$

and a stable membrane occurs only if

$$r_2 < p_x/p_y < r_1$$

and

$$0 < p_x/p_y .$$

The latter equality is always satisfied, since only positive p_x/p_y values are necessary and practical to the real problem.

26-3.7 Weight Constraint

A major objective is to minimize the membrane principal stress, σt_{max}, without a weight penalty. By an uninhibited application of yarn reinforcement, the stress obviously can be reduced, but at the expense of objectionable weight. A constraint relationship can be generated that will permit parameter variations while maintaining a fixed weight of the reinforced membrane.

From Figure 26-1b, it can be seen that the weight of a single triangular element is equal to the sum of the weight of the triangular membrane, one-half the sum of the weights of the two diagonal yarns, one-half the weight of the longitudinal yarn, and the weight of the adhesive coating. The sum of these weights divided by the area of the triangular element is the specific weight $\bar{w}$ of the reinforced membrane; that is,

$$\bar{w} = \rho_m t \left[\left(\frac{A_{im}}{x_j t} + \frac{A_{ij}}{x_j t \sin\theta} \right) \frac{\rho_v}{\rho_m} + \lambda \right] , \tag{26-26}$$

where

$$\lambda = \frac{t + t_a}{t} . \tag{26-27}$$

Utilizing the ζ_1 and ζ_2 parameters and letting

$$\zeta_3 = \frac{\rho_m E_v}{\rho_v E_m} , \tag{26-28}$$

then Eq. (26-27) becomes

$$\bar{w} = \rho_m t \left[\left(1 + \frac{\zeta_2}{\sin\theta} \right) \frac{\zeta_1}{\zeta_3} + \lambda \right] . \tag{26-29}$$

If $\bar{w}$ is constrained to a specified value, then ζ_2 can be expressed as a function of ζ_1 and the other physical properties as

$$\zeta_2 = \left[\left(\frac{\overline{w}}{\rho_m t} - \lambda\right)\frac{\zeta_3}{\zeta_1} - 1\right] \sin\theta . \tag{26-30}$$

Now $\frac{\overline{w}}{\rho_m t} - \lambda$ will always be positive. Also, since only positive material characteristics are meaningful, then

$$\zeta_1 \leq \left(\frac{\overline{w}}{\rho_m t} - \lambda\right) \zeta_3 \tag{26-31}$$

if a constrained specific weight is to be a constraint.

Using the constrained value of ζ_2 given by Eq. (26-30) and the limitation imposed on ζ_1 by Eq. (26-31), then Eq. (26-20) is of primary value for minimizing the membrane stress with respect to the applied loads by varying the many parameters of the laminate.

26-4. DISCUSSION AND RESULTS

In the foregoing section, the expressions for membrane stress, yarn forces, and stability criteria were derived. In this section, practical consideration of these analytical results will be discussed in view of the selection of optimum parameters, and some comparisons with test data will be shown.

26-4.1 Stability of the Membrane

The root systems and stable regions are illustrated in Figure 26-3 to show their importance to the laminate's performance. A generalized "b" form of the quadratic stability equation (Eq. [26-23]) is used in Figure 26-3 to show the effects of signs. This is essentially a graphic display of Descarte's rule of signs for the two forms of the equality. Since a good laminate should be tolerant to a wide range of p_x/p_y values (0 to 1.0, perhaps), it is evident that the conditions of the A and B coefficients leading to (c) and (d) for $\mu C_{22} - C_{12} \geq 0$ and (a) and (b) for $\mu C_{22} - C_{12} < 0$ are pertinent for a wide range of laminate performance.

It can be shown that the factor $\mu C_{22} - C_{12}$, associated with the two different inequalities displayed in Figure 26-3, is identically zero if

$$\zeta_1 = \left(\frac{\overline{w}}{\rho_m t} - \frac{t - t_a}{t}\right)\frac{E_y \rho_m}{E_m \rho_y}\,\frac{\sin^2\theta\,(\cos^2\theta - \mu\sin^2\theta)}{(\mu\sin^2\theta\cos^2\theta - \mu\sin^4\theta)} = \psi q(\theta,\mu). \tag{26-32}$$

This value of ζ_1 is henceforth defined as $\zeta_{1,cr}$ and is an important relationship in light of its influence on root characteristics and also on optimum performance.

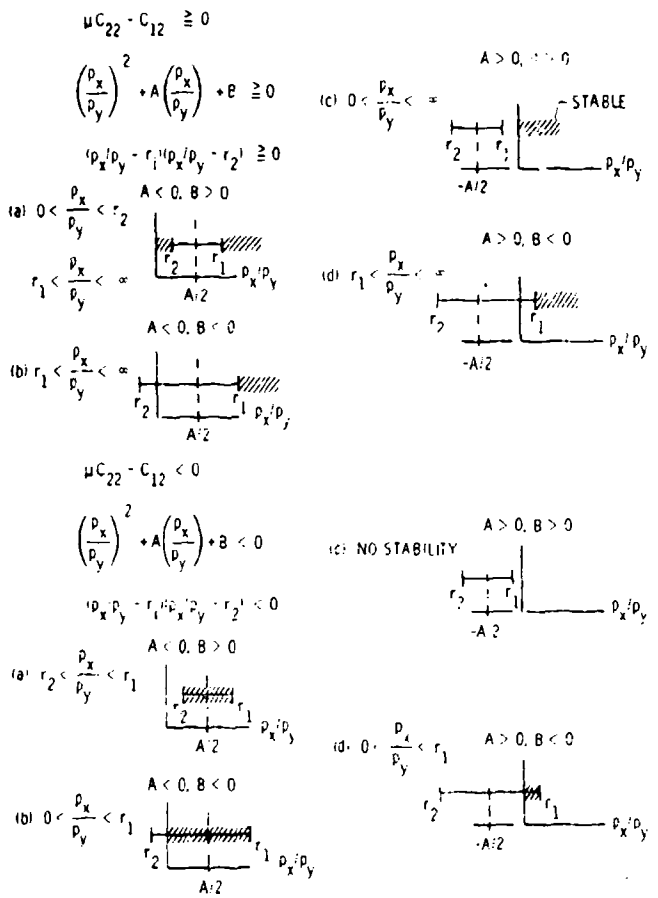

Figure 26-3. Roots and Stable (Shaded) Ranges for Various Conditions of the "b" Form of the Quadratic Stability Equation

The function of the $q(\theta, \mu)$, being independent of all of the laminate characteristics except θ and μ, is tabulated in Table 26-1 for a useful range of thetas.

Figure 26-4 illustrates the dramatic difference in root locus plots for a different relationship of ζ_1 to $\zeta_{1,cr}$. For $\zeta_1/\psi > 0.39$, the typical root system is always continuous with $0 < \theta < 90°$ as shown in Figure 26-4a for $\zeta_1/\psi = 0.60$ (Viking). If $\zeta_1/\psi < 0.39$, there will be a range of θ's in which $\zeta_1 < \zeta_{1,cr}$, and the asymptotic root behavior as illustrated in Figure 26-4b for $\zeta_1/\psi = 0.067$ will occur.

The system of Figure 26-4a offers the most stable situation, although the characteristics of Figure 26-4b are not generally objectionable unless the region between the asymptotes possesses r_1 roots much less than unity and r_2 roots significantly greater than zero.

Table 26-1. $\zeta_{1,cr}/\psi$ Versus θ for $\mu = 0.3$

θ	$q(\theta,\mu) = \frac{\zeta_{1,cr}}{\psi}$	θ	$q(\theta,\mu) = \frac{\zeta_{1,cr}}{\psi}$
0	0	35	0.3856
5	.0244	40	.3893
10	.0981	45	.3684
15	.1693	50	.3169
20	.2485	55	.2222
25	.3137	60	.0588
30	.3600	65	-.2280

$$q(\theta,\mu) = \frac{\sin^2\theta\,(\cos^2\theta - \mu\sin^2\theta)}{(\mu\sin^2\theta\cos^2\theta - \mu\sin^4\theta}$$

$$\psi = \frac{\bar{w}}{\rho_m t} \cdot \frac{t + t_a}{t} \cdot \frac{\rho_m}{\rho_y} \cdot \frac{E_y}{E_m}$$

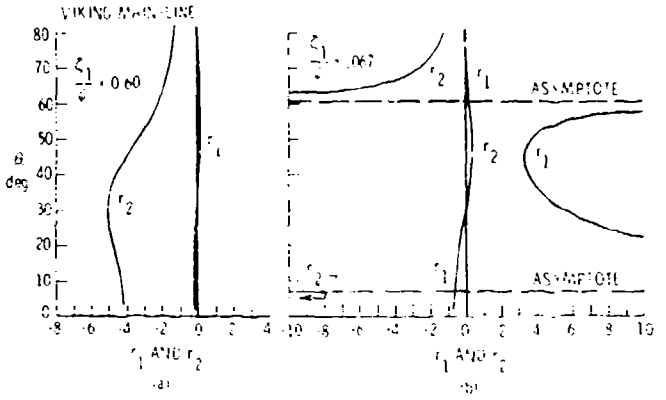

Figure 26-4. Root Locus Plots Versus θ for Values of ζ_1/ψ Greater Than and Less Than 0.39

26-4.2 Viking Load Factors

The Viking BLDT material has a ζ_1 value of 1.66 times the $\zeta_{1,cr}$ value. The diagonals are placed on a 30° angle with intended apices intercepts with longitudinals spaced two per inch. The basic dimensions and characteristics follow on Table 26-2.

Table 26-2. Characteristic Data for the Viking BLDT Balloon Material at -90°F

AE_{ij} (440 denier Dacron yarn)	60.86 lb (270.7 N)
$A\Xi_{im}$ (1300 denier Dacron yarn)	181.2 lb (806.0 N)
t	0.00035 in. (0.889×10^{-5} m)
t_a	0.00015 in. (0.381×10^{-5} m)
ρ_m	0105 lb/in.^{3} (13,575 N/m^3)
ρ_y	0.05 lb/in.^{3} (13,575 N/m^3)
E_m (isotropic mylar)	6.2×10^5 kb/in^2 (4.27×10^9 N/m^2)
E_y	11.28×10^5 lb/in.^{2} (7.78×10^9 N/m^2)
x_j	0.50 in. (0.0127 m)
μ	0.30
$\sigma_{m,u}$ (vendor's data)	18,000 lb/in.^{2} (1.24×10^8 N/m^2)
$\sigma_{y,u}$ (vendor's data)	140,000 lb/in.^{2} (9.65×10^8 N/m^2)
$f_{im,u}$ (1300 denier)	22.39 lb (99.59 N)
$f_{ij,u}$ (440 denier)	7.58 lb (33.72 N)
$\overline{w}$	0.576×10^{-4} lb/in.^{2} (0.397 N/m^2)
ζ_1	1.67 unitless
ζ_2	0.3359 unitless
ζ_3	1.500 unitless
λ	1.4286 unitless
$w/\rho_m t$	3.29 unitless
ψ	2.796 unitless
area/denier (Dacron)	0.123×10^{-6} in.^{2}/den. (0.793×10^{-4} mm^2/den.

26-4.2.1 COMPUTED LOAD FACTORS

The load factors $p_y/\sigma_m t$ for the Viking material have been computed from the inverse of Eq. (26-20) for the applicable coefficients given in Table 26-2, and the results are shown in Figure 26-5. Two cases are presented. Figure 26-5a shows the load factor $p_y/\sigma_m t$ for the mainline Viking BLDT material ($\zeta_1 = 1.67$). Figure 26-5b shows similar data, but for $\zeta_1 = \zeta_{1,cr}$. There is considerable difference in the behavior of the load factor with the transverse load p_x/p_y. For low

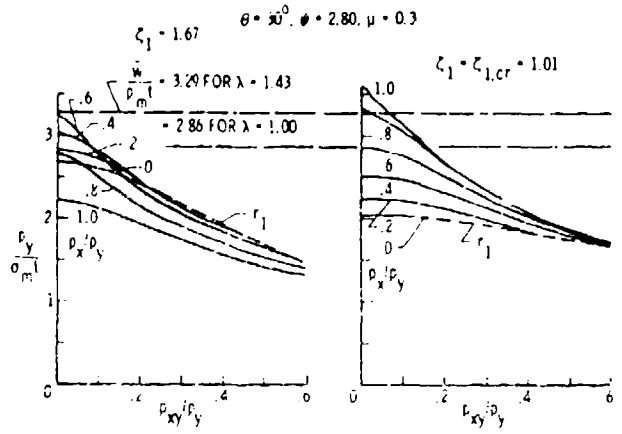

(a) Viking Mainline BLDT Material

(b) Viking Optimum ζ_1 and θ

Figure 26-5. Load Factors for 30° Reinforced Membranes of the Viking Type

values of shear, the mainline material is better than the $\zeta_1 = \zeta_{1,cr}$ material for low values of p_x/p_y. However, as the transverse load is increased, the mainline Viking material hits a maximum and then degrades. The $\zeta_1 = \zeta_{1,cr}$ material continues to improve with increasing p_x/p_y loading. Of most importance is the minimum performance the materials possess under the possible combined loading. For example, if the design requires a material to sustain biaxial loads ranging from $1 \leq p_x/p_y \leq 1.0$ in the presence of shear loads that might range from $0 \leq p_{xy}/p_y \leq 0.6$, then Figure 26-5a shows a minimum $p_y/\sigma_m t$ ratio of 1.32. For $\zeta = \zeta_{1,cr}$ Figure 26-5b shows a minimum $p_y/\sigma_m t$ ratio of 1.67. For Figure 26-5a, the $p_x/p_y = 1.0$ curve is the minimum bound, and for Figure 26-5b, the $p_x/p_y = r_1$ (the largest root of the stability equation) is the minimum bound. A similar stability bound exists in Figure 26-5a, except that it is not the minimum bound of the data for the range of loads.

Also shown in Figure 26-5 are the weight ratios of the complete laminate to the film. If the adhesive is assumed of equal strength and similar elastic behavior to the base membrane, then λ is taken as unity, and the weight ratio is 2.86. If the adhesive is considered nonload carrying and only additive weight, then λ is 10/7 for the Viking material and the weight ratio is 3.29. A good measure of the efficiency of the reinforcement is the comparison between $p_y/\sigma_m t$ and $\overline{w}/\rho_m t$. The weight ratio indicates the extent of weight increase over the base membrane, and the load factor indicates the increase in load/unit length that can be carried by the composite with respect to the load carried by a unit length of the membrane. It is apparent that a weight penalty is suffered in order to provide a material capable of sustaining biaxial loads along with shear. However, for both the optimum ζ_1 and nonoptimum ζ_1 cases, the laminate load factors outperform the weight increases for low values of shear and, if the adhesive is considered, comparable to the base membrane ($\lambda = 1$). A parasitic adhesive is obviously an inefficient feature, and the strength ratio is less than the weight ratio.

26-4.2.2 TEST DATA

Viking material of the type of Figure 26-5a has been tested extensively at the G. T. Schjeldahl Company and at NASA Langley Research Center. Tests were performed with cylinder test specimens (Alley and Faison, 1972a; Niccum, 1972). Both test programs were performed in -90°F temperatures representing the tropopause environment for which the material performance is most critical. The test data have been correlated with the theoretical data, and the results are presented in Figures 26-6a and 26-6b.

In order to make the comparison, it is necessary to assume that only stable membrane data are applicable. Also, the parameters necessary for stability are known only from the analytical data, and the test points are selected by such. In addition, it must be assumed that failure occurred in the test specimen when $\sigma_m t = \sigma_{m,u} t$ (the ultimate membrane force). Hence, for a test point having a known p_y, $\tilde{p}_x/p_y$ and p_{xy}/p_y, if $\sigma_m t = \sigma_{m,u} t$, then since for linear analyses, the stresses are proportional to the forces, it follows that

$$\frac{p_{y,u}}{\sigma_{m,u} t} = \frac{p_y}{\sigma_m t} \quad . \tag{26-33}$$

The right-hand side of Eq. (26-33) is obtained from Eq. (26-20) which is the equally valid ratio for the ultimate conditions equated on the left. Since only vendor values generally are available for the ultimate membrane stress, $\sigma_{m,u}$, a more appropriate value was extracted from the test data by use of a least-square fit. Letting

$p_y/\sigma_{m}t_i$ = ith calculated data

and

$\frac{p_{y,u}}{\sigma_{m,u}t_i}$ = ith test data ,

then the best fit between the calculated and test data for k test points is obtainable, provided

$$\frac{\partial}{\partial\left(\frac{1}{\sigma_{m,u}t}\right)} \sum_{i=1}^{k} \left(\frac{p_{y,u}}{\sigma_{m,u}t_i} - \frac{p_y}{\sigma_m t_i}\right)^2 = 0 . \qquad (26\text{-}34)$$

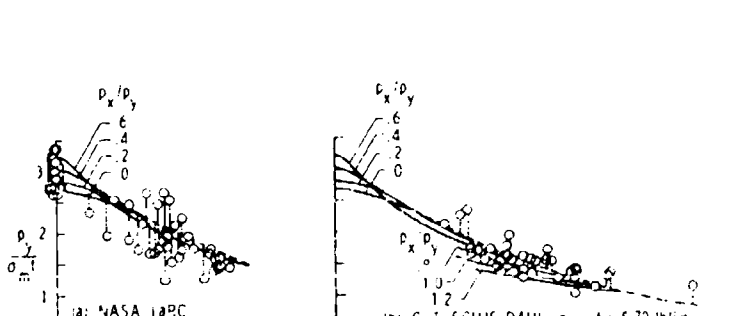

Figure 26-6. Comparison of Theoretical and Experimental Membrane Load Factors $\frac{p_y}{\sigma_m t}$ for Viking Mainline Balloon Material

Equation (26-34) yields the value of $\sigma_{m,u}t$ that provides the best fit; that is

$$\sigma_{m,u}t = \frac{\sum_{i}^{k} p_{y,u_i}^2}{\sum_{i}^{k} \left(\frac{p_y}{\sigma_m t}_i\right) p_{y,u_i}} . \qquad (26\text{-}35)$$

From 47 stable test values acquired at the LRC, the value for $\sigma_{m,u}t$ was determined to be 8.36 lb/in. (1464 N/m). From 40 stable values tested at the

Schjeldhal Company, the value for $\sigma_{m,u}t$ was determined to be 5.70 lb/in. (998 N/m). The comparisons of the test data by the foregoing methods are shown in Figures 26-6a and 26-6b for the LRC tests and for the Schjeldahl tests, respectively.

The vendor data for the membrane ultimate would indicate values around 6.3 lb/in. (1103 N/m). However, it should be understood that the 0.35-mil thick membrane tested had been coated with a polymeric adhesive film giving a total thickness of about 0.5 mil. If the adhesive has comparable elastic and ultimate strain conditions, then it can be expected that the ultimate membrane strength could obtain values as large as 9.0 lb/in. (1576 N/m^2). The analysis permits treating the adhesive contribution in only two ways. It can be assumed that no strength is added by the adhesive and only weight addition results. In such a case,

$$\lambda = \frac{t + t_a}{t}$$

where t_a is the adhesive thickness and t is the bare membrane thickness. However, if, on the other hand, the adhesive is assumed to have physical and mechanical characteristics equal to the base membrane, then λ is taken as unity and t is considered to denote the combined thickness of the membrane and adhesive. In either case, the manipulation is carried out within the definition of the ψ coefficient.

The differences between the Schjeldahl and LRC $\sigma_{m,u}t$ values obtained from least-square considerations could be attributed to the differences in the seam effects, since the test cylinders were of different diameters. It is thought the seams contributed less to strength in the larger test specimens used by the contractor. Also, most of the Schjeldahl test points were for large values of p_{xy}/p_y, where the determination of stable or unstable membrane behavior is highly sensitive and less accurate. The indications are that if membrane buckling occurs, the failure level is considerably lower than the ultimate tensile mode of failure and would lead to a low value of $\sigma_{m,u}t$ if the least-square analysis included data points from the unstable regions.

In Figure 26-6, the test points are defined by circles at their respective p_{xy}/p_y and $p_y/\sigma_m t$ values. Leaders are drawn from each test point to the appropriate ρ_x/p_y value for the test. For an exact agreement, no leader would be required. Considering the large variations experienced in the rupture of reinforced laminates, it is felt that the theoretical and test correlations are very good and clearly substantiate the characteristic behavior of the laminate with the controlling parameters. Perhaps the lower plastic and more elastic characteristics of polymers at the very low temperatures attributed to the generally good analytical predictions of failure by use of the linear theory.

26-4.3 Optimum Parameters

It has been found that for $\zeta_1 = \zeta_{1,cr}$ the minimum load factor, $p_y/\sigma_m t$, encountered is a maximum for all possible combinations of likely loads. This is shown graphically by the data of Figure 26-7 for a yarn placement angle of 30°. These curves represent the minimum envelopes of data, such as those displayed for the load factor $p_y/\sigma_m t$ given on Figures 26-5 and 26-6 for various ranges of p_{xy}/p_y and p_x/p_y. These envelopes, called mini-bounds and shown in Figure 26-7, have been computed for values of ζ_1 from 0.50, 0.75, 1.00, 1.50, and 2.00 times the critical ζ_1 for the 30° reinforcement angle. The envelopes are shown for values ψ 0.75, 1.00, 1.50, and 2.00. For all cases of ψ and particularly for the larger values, the best load factor to accommodate any possible combination of loads from $0 < p_x/p_y < 1.0$ and $0 < p_{xy}/p_y < 0.6$ is obtained for $\zeta_1 = \zeta_{1,cr}$ and for the largest value of ψ.

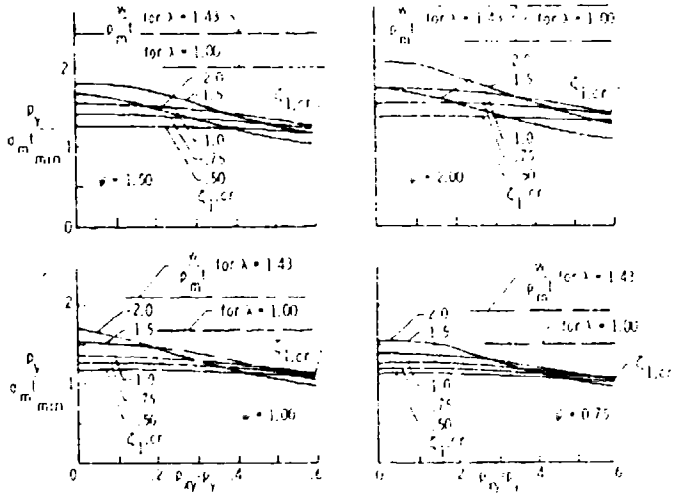

Figure 26-7. Mini-bounds, $0.5 < \zeta_1 < 2.0$, $0.75 < \psi < 2.0$, $\theta = 30°$, $\zeta_3 = 1.5$

Figure 26-8 shows the load factor for only $\zeta_1 = \zeta_{1,cr}$ data and for variations in ψ and θ for the range of p_{xy}/p_y from 0 to 0.6 and for the minimum envelope of p_x/p_y data from 0 to 1.0. It is clearly evident that larger values of ψ are favorable for increasing the load factor, although this increase is generally obtained at the expense of increased weight. Through use of a three-dimensional graph, the data for $p_{xy}/p_y = 0.6$ have been displayed for $\psi = 1.50$ and 2.79 for placement angles of 20, 40, and 50° in addition to the 30° data. These curves

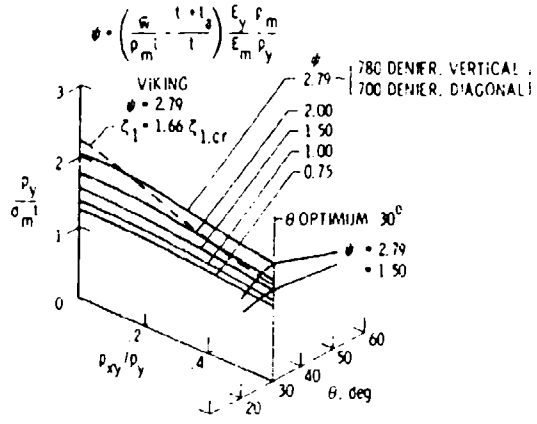

Figure 26-8. Variation of Load Factor With ψ, θ, and $\frac{p_{xy}}{p_y}$ for $\zeta_1 = \zeta_{1,cr}$ and $0 < p_x/p_y < 1.0$

indicate that the mini-bounds are maximum in the proximity of 30° for the ranges of loads and parameters studied.

Shown in Figure 26-8 is the dashed curve of $p_y/\sigma_m t$ for $\psi = 2.79$ and $\zeta_1 = 1.66\ \zeta_{1,cr}$, which are the characteristics for the Viking BLDT material. In this case, ζ_1 was not the optimum $\zeta_{1,cr}$, and the cost of using a ζ_1 of 66 percent larger than optimum is seen by comparing the dashed curve with the optimum case for $\psi = 2.79$ and $\zeta_1 = \zeta_{1,cr}$. For values of p_{xy}/p_y greater than about 0.1, the $\zeta_1 = \zeta_{1,cr}$ curves indicate better performance. The Viking BLDT material has 1300 denier Dacron longitudinals on .5-inch spacing and 440 denier diagonals. If the Viking material were modified for $\zeta_1 = \zeta_{1,cr}$, it would call for 780 denier longitudinal yarns and 600 denier diagonals.

If ζ_1 is constrained to equal $\zeta_{1,cr}$, then ζ_2 defined by Eq. (26-30) is reduced to a function of μ and θ only; that is,

$$\zeta_2 \quad \left(\frac{1}{q(\theta,\mu)} - 1\right)\sin\theta \quad \text{for } \zeta_1 = \zeta_{1,cr}. \tag{26-36}$$

Since the C's of Eq. (26-16) that are pertinent to all solutions are functions of ζ_1, ζ_2, θ and μ, setting $\zeta_1 = \zeta_{1,cr}$ advantageously reduces the solution of the reinforced membrane to the two independent parameters, ψ and θ, along with specified design load ranges and Poisson's ratio.

It should be cautioned that constraining ζ_1 to equal $\zeta_{1,cr}$ has not been adequately investigated for low yarn placement angles and for large yarn placement

angles around $\theta = 60°$. The generalization of declaring $\zeta_1 = \zeta_{1,cr}$ as optimum for all θ's is not intended, and qualifications in regard to such are beyond the scope of this paper.

26-4.4 Yarn Forces

To this point, it has been tacitly assumed that laminate failure initiates in the membrane. This is essentially the conclusive finding of the testing for the Viking material, but is not necessarily true of reinforced membranes conceived for other combinations of parameters. The yarn force equations are furnished as Eq. (26-18). Dividing Eq. (26-18) by x_j and p_y will provide a useful nondimensional form that is defined as the yarn force factor. In Eq. (26-18), if f_{jm} is subtracted from f_{ij}, it is easily proven that for $0 \leq \theta \leq 90°$, and for positive values of p_x/p_y and p_{xy}/p_y that f_{ij} is always larger than f_{jm}. Hence, consideration of the diagonal yarn forces are limited to analysis of f_{ij} only since it has the larger load. However, the diagonal yarn jm is lightly loaded in comparison to ij and needs consideration in regard to yarn buckling.

26-4.4.1 YARN STABILITY

A second and somewhat unique mode of instability is indicated as the existence of yarn compression in yarn jm, while the membrane is stable and in tension. This phenomenon is virtually a result of Poisson's ratio and is aggravated mainly by low placement angles of the diagonal yarn along with low transverse strain.

From Eq. (26-18) it can be seen that for yarn tension to exist in both diagonals

$$\frac{p_x}{p_y} \geq \frac{C_{12} - C_{11} \tan^2\theta + \dfrac{\left(C_{11}C_{22} - C_{12}^2\right)}{C_{33}} \dfrac{p_{xy}}{p_y} \tan\theta}{C_{22} - C_{12} \tan^2\theta}. \qquad (26\text{-}37)$$

The value of θ that will always maintain yarn stability for positive values of p_x/p_y is determined by setting $p_x/p_y = 0$ in Eq. (26-37) and solving for the $\tan\theta$. Observing that the denominator in Eq. (26-30) is always positive at least for $0 < \theta < 60°$, then

$$\tan\theta \geq \left| \frac{C_{11}C_{22} - C_{12}^2}{2C_{11}C_{33}} \frac{p_{xy}}{p_y} \right| + \sqrt{\left(\frac{C_{11}C_{22} - C_{12}^2}{2C_{11}C_{33}} \frac{p_{xy}}{p_y} \right)^2 + \frac{C_{12}}{C_{11}}} \qquad (26\text{-}38)$$

valid $0 < \theta < 60°$.

For $p_{xy}/p_y = 0$, and by recourse to Eq. (26-16), Eq. (26-38) reduces to the simple fact that

$$\theta \geq \arctan \sqrt{\mu} \quad (\text{for } p_{xy}/p_y = 0) \tag{26-39}$$

and for all positive values of p_x/p_y to yield stable yarns.

This result indicates that θ should be considered only for values greater than the angle whose tangent is the square root of Poisson's ratio. Beyond this consideration, buckling of the yarns on an unbuckled membrane is difficult to envision, and it is suspected that the yarns are constrained by the membrane and do take some compression. Hence, to limit the scope of this paper, negative yarn forces for low values of p_x/p_y will be assumed possible if a stable membrane exists.

26-4-4.2 YARN LOAD FACTORS FOR VIKING MATERIAL

The yarn load factors for the longitudinal yarn (m) and the heavily loaded diagonal ij have been computed by use of Eq. (26-18) for the Viking membrane material. These data are displayed in Figure 26-9 for the usual ranges of applied loads.

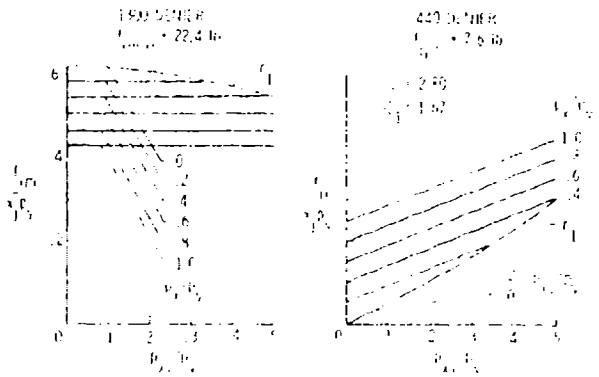

Figure 26-9a. Yarn Force Factors for the Viking Membrane Balloon

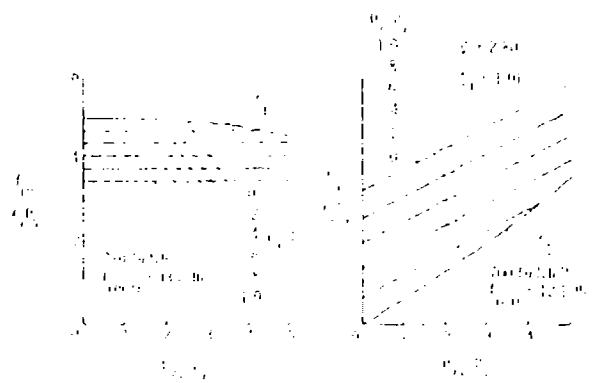

Figure 26-9b. Yarn Force Factors for the Viking Membrane Balloon

In both the mainline and optimum ζ_1 cases of Figures 26-9a and 26-9b, the longitudinal yarn force factors $f_{im}/x_j p_y$ are nearly constant with shear loading. For both cases, the longitudinal yarn loads are reduced by application of the transverse load, p_x/p_y, and the importance of the transverse load in maintaining yarn (and membrane) stability is indicated by the stability bound, r_1. The denier values for the yarns commensurate with the ψ and ζ_1 values are given in the figure. For $\zeta_1 = \zeta_{1,cr}$, the yarn weights are more evenly distributed between the longitudinal and diagonals than in the mainline viking case. The diagonal yarn varies nearly linearly with the shear force p_{xy}/p_y, as well as with the transverse force p_x/p_y. The values of the ultimate forces of the yarns are shown on the figure and are proportional to the denier value.

An illustration of converting from the nondimensional to dimensional form will help in understanding the magnitudes of the results and in showing how to use the generalized data. From Figures 26-5a and 26-5b, the membrane load factors are given for the Viking mainline balloon material and for the Viking optimum $\zeta_1 = \zeta_{1,cr}$ case, respectively. To illustrate, consider an ultimate load condition where $p_x/p_y = 0.6$ and $p_{xy}/p_y = 0.4$, and use the ultimate membrane load $\sigma_{m,u}t = 8.36$ lb/in. (1464 N/m) obtained from the LRC test data.

For the Viking mainline

$$\frac{p_{y,u}}{\sigma_{m,u}t} = 1.83 \text{ , from Figure 26-5a for } p_x/p_y = 0.6 \text{ , } p_{xy}/p_y = 0.4 \text{ .}$$

For the Viking optimum $\zeta_1 = \zeta_{1,cr}$

$$\frac{p_{y,u}}{\sigma_{m,u}t} = 2.05 \text{ from Figure 26-5b.}$$

Then for $\sigma_{m,u}t = 8.36$ lb/in. (1464 N/m) the ultimate longitudinal loads are

$p_{y,u} = 15.30$ lb (68.06 N) Viking main line

$= 17.14$ lb (76.24 N) Viking optimum $\zeta_1 = \zeta_{1,cr}$.

From Figures 26-9a and 26-9b the im and ij force factors for the Viking mainline and optimum $\zeta_1 = \zeta_{1,cr}$ cases are

Mainline	Optimum $\zeta_1 = \zeta_{1,cr}$
$\frac{f_{im}}{x_j p_y} = 0.503$	$\frac{f_{im}}{x_j p_y} = 0.406$

Mainline	Optimum $\zeta_1 = \zeta_{1,cr}$
$\frac{f_{ij}}{x_j p_y} = 0.312$	$\frac{f_{ij}}{x_j p_y} = 0.411$.

Using the above $p_{y,u}$ values and $x_j = 0.50$, the yarn forces can be computed for both the mainline and optimum cases, as

$f_{im} = 3.88$ lb (17.3 N)	$f_{im} = 3.48$ lb (15.5 N)
$f_{ij} = 2.39$ lb (10.6 N)	$f_{ij} = 2.52$ lb (15.7 N)

Comparing these values with the ultimate yarn forces given in Figure 26-9 shows that for the mainline material f_{im} is only 17 percent its ultimate, and f_{ij} is 31 percent its ultimate at the load p_y that would fail the membrane. The unequal distribution and low percent of loading is less than desirable. For the optimum $\zeta_1 = \zeta_{1,cr}$ case, the f_{im} and f_{ij} values at membrane failure are 26 percent and 29 percent, respectively. These yarns are more equally loaded but considerably less than their ultimate values. In Figure 26-10, dimensional values of interest, such as considered above, are shown for optimum $\zeta_1 = \zeta_{1,cr}$ cases for a general range of ψ. These data have been selected for the express design condition of $p_x/p_y = 0.6$, $p_{xy}/p_y = 0.4$, $\lambda = 3/2$, and $\sigma_{m,u}t = 8.36$ lb/in. (1464 N/m). It is readily seen that the weight, $\overline{w}$, mounts steadily with ψ.

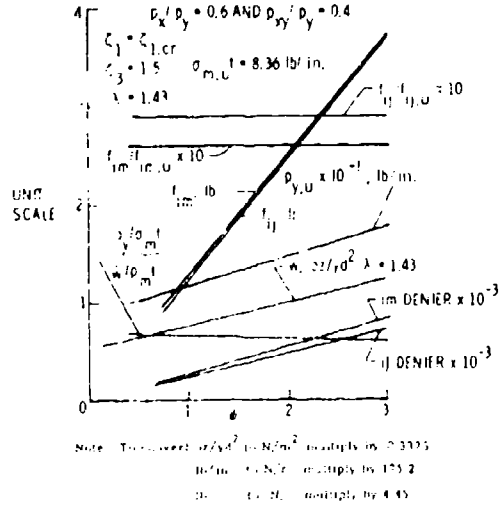

Figure 26-10. Dimensional Results at Membrane Failure for Dacron Reinforced Mylar Film Loaded to $p_x/p_y = 0.6$ and $p_{xy}/p_y = 0.4$

As could be expected, the ultimate longitudinal loads of both the membrane and yarns increase with the weight (and with ψ). The efficiency which is measured by dividing the load factor by the weight ratio

$$\left(\frac{p_y}{\sigma_m t} \Big/ \frac{\overline{w}}{\rho_m t}\right)$$

decays slightly with increasing ψ. It is indicated that maximum efficiency is obtainable with no reinforcement. That is, a homogeneous membrane is capable of using its weight to the best advantage in whatever fashion the load is applied. This is generally true if the reinforcement is of a similar material as the membrane. However, the efficiency ratio can be increased above unity by the appropriate combinations of materials. Nevertheless, even if reinforcement using materials similar to the membrane is done, the methods of this paper are important to minimizing the loss in efficiency from using weight other than homogeneously. In addition, reinforced membranes provide a redundant structural system and add rip-stop control, not features of most homogeneous membranes.

In order to achieve at membrane failure significantly higher ratios of yarn loading to yarn ultimate loads ($f_{im}/f_{im,u}$ and $f_{ij}/f_{ij,u}$), it is found that an order of magnitude change in ψ will be required. The criterion for near simultaneous failure is considered in the following paragraphs.

26-4.4.3 SIMULTANEOUS YARN AND MEMBRANE FAILURE

For a well balanced design, it is desirable that both $\sigma_m t$ and f_{im} (or f_{ij}) reach their ultimate strength values simultaneously with the application of an ultimate load combination. Now, f_{im} from Eq. (26-18) is of the form

$$f_{im} = p_y x_j f_1 (\zeta_1, \zeta_2, \zeta_3, \mu, p_x/p_y, p_{xy}/p_y). \tag{26-40}$$

Also, $\sigma_m t$ from Eq. (26-20) is of the form

$$\sigma_m t = p_y f_2 (\zeta_1, \zeta_2, \zeta_3, \mu, p_x/p_y, p_{xy}/p_y). \tag{26-41}$$

Dividing Eq. (26-40) by Eq. (26-41) yields

$$\frac{f_{im}}{x_j \sigma_m t} = \frac{f_1}{f_2} = \left(\frac{f_{im}}{x_j p_y}\right)\left(\frac{p_y}{\sigma_m t}\right). \tag{26-42}$$

From elementary linear one-dimensional stress-strain relationships

$$f_{im} = \epsilon_{im} AE_{im} \tag{26-43}$$

$$\sigma_m = \epsilon_m E_m \, . \tag{26-44}$$

Substituting Eqs. (26-43) and (26-44) into Eq. (26-42) and recalling the definition of ζ_1 yields

$$\frac{f_{im}}{x_j \sigma_m t} = \frac{\epsilon_{im}}{\epsilon_m} \zeta_1 \, . \tag{26-45}$$

Substituting Eq. (26-45) into Eq. (26-42) results in

$$\frac{\epsilon_{im}}{\epsilon_m} = \frac{1}{\zeta_1} \left(\frac{f_{im}}{x_j p_y}\right)\left(\frac{p_y}{\sigma_m t}\right) \, . \tag{26-46}$$

When the product of the im yarn force factor and the membrane load factor divided by ζ_1 equals the im yarn's ultimate strain divided by the ultimate membrane strain, the desired theoretical simultaneous failure of yarn and membrane is achieved. A similar expression for the diagonal ij can be derived and is similar to Eq. (26-46) with the exchange of the im subscripts with ij and an additional division by ζ_2.

Failure occurs first in the yarn if the following inequality is true:

$$\frac{1}{\zeta_1}\left(\frac{f_{im}}{x_j p_y}\right)\left(\frac{p_y}{\sigma_m t}\right) > \frac{\epsilon_{im,u}}{\epsilon_{m,u}} = \frac{\epsilon_{ij,u}}{\epsilon_{m,u}} < \frac{1}{\zeta_1 \zeta_2}\left(\frac{f_{ij}}{x_j p_y}\right)\left(\frac{p_y}{\sigma_m t}\right) \tag{26-47}$$

If Eq. (26-47) is true, the particular yarn that fails first is the yarn for which the product of the yarn force factor and the membrane load factor is the greatest.

It should be mentioned that the ultimate strain ratios used in Eq. (26-47) are more appropriately the equivalent linear strains to failure and not the plastic ultimate strain ratio. They are best determined by

$$\frac{\epsilon_{im,u}}{\epsilon_{m,u}} = \left(\frac{\sigma_{im,u}}{\sigma_{m,u} t}\right)\left(\frac{E_m t}{E_{im}}\right) = \left(\frac{\sigma_{ij,u}}{\sigma_{m,u} t}\right)\left(\frac{E_m t}{E_{ij}}\right) \, . \tag{26-48}$$

The product factors of Eq. (26-47) for the Viking material are several times smaller than the ultimate strain ratios. This indicates that failure would be consistently experienced in the membrane as was verified by the test program. To achieve simultaneous failure, it appears necessary to use different material combinations. In Figure 26-11, the relationship between the strain ratios ($\epsilon_{im,u}/\epsilon_{m,u}$) and ψ is shown for different combinations of materials and for a laminate weight of about 1 oz/yd^2 (1/3 N/m^2). Polyethylene membranes with Dacron yarns offer insufficient improvement. PRD-49 type III yarn on mylar is to the opposite end of the desired range and yields laminates that would fail consistently in the yarns. The PRD-49 type IV yarn, that has greater strength than the type III and a lower modulus of elasticity, comes close to meeting the desired strain ratio.

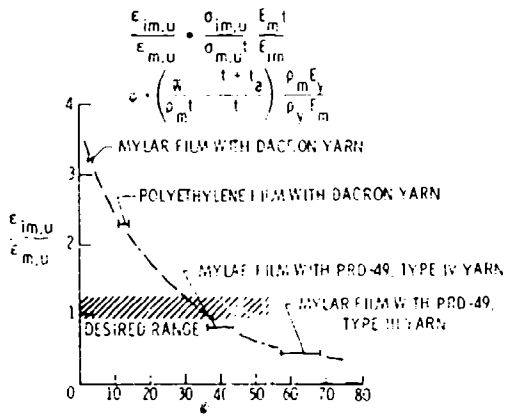

Figure 26-11. Relationship Between Strain Ratios and ψ Ranges for 1 Oz/Sq Yd (1/3 N/m^2) Laminates

In Figure 26-12, the computed strain ratios are shown for a PRD-49 type IV material of identical weight to the Viking mainline material. The ψ parameter is 36 and $\zeta_1 = \zeta_{1,cr}$. The longitudinal yarns are 950 denier, and the diagonals are 850 denier. The film is 0.35 mil mylar. For its laminated weight to film weight ratio of 3.3, it yields a load-to-film strength ratio of 11 to 14 for the range of $0 < p_x/p_y < 1.0$ and $0 < p_{xy}/p_y < 0.6$. The failure initiates in the diagonal yarn which is seen from Figure 26-12b for the p_{xy}/p_y value of 0.4 and $p_x/p_y = 0.6$. The failure would occur when $p_y = p_{y,u} = 98.6$ lb/in. (439 N/m). For this condition, f_{im} is 83 percent its ultimate, and the membrane is 86 percent its ultimate. This contrasts to an ultimate load of 15.3 lb/in. (68.1 N/m) for the same weight Viking mainline material for the same loading combination. These figures suggest

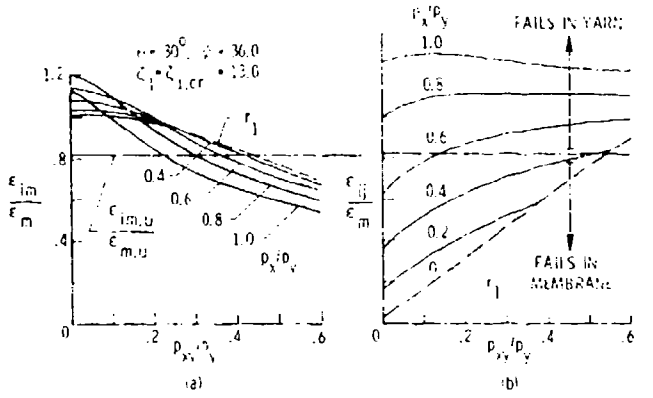

Figure 26-12. Yarn to Membrane Stress Ratios for PRD-49 Type IV Yarn on Mylar

the potential improvement from optimizing the laminate design, in view of minimizing membrane stress for the selected placement angle, and in striving for simultaneous yarn and membrane failure. Other combinations of yarns and membranes that offer even greater improvements are silicon carbide whiskers on mylar and S-glass filaments on polyethylene film.

26-4.5 Some Practical Considerations

To approach the near optimum conditions discussed above, a number of potential obstacles are faced. Present manufacturing fails to achieve the desired apices intercepts assumed for the classical analysis. In addition, uniformity in the membrane is seldom obtainable even with a single element by virtue of adhesive flow, adhesive splatter in the case of yarn coating techniques, and imprints from the lamination rollers. Also, the failure of present adhesive compounds to match the membrane physical characteristics is a departure from the ideal, and the lack of unstrained initial conditions can perturbate the theoretical performance. In addition, plastic instead of elastic behavior will modify the calculated performance. Current developments are active in adhesive syntheses to yield better mechanical characteristics, and efforts are being considered to achieve laminate materials with better apices intercepts. Improved testing facilities are under construction to permit more controlled test conditions and better observation of the modes of failure. Since PRD-49 yarn has become available, plans exist to acquire sample laminates for test qualification of its potential performance.

26-5. CONCLUSIONS

Equations for analyzing the membrane stresses, yarn forces, stability criteria, and some optimum parameter relationships have been derived.

Cold temperature test data for laminate failure under biaxial and shear loads are correlated with the theoretical results and show very good prediction capability.

The optimum stiffness of the longitudinal yarns to membrane stiffness is established. Along with this, the ratio of ultimate strain of the yarn to ultimate strain of membrane is shown to be a controlling parameter in achieving the efficiency of simultaneous yarn and membrane failure. These controlling parameters lead to the conclusion that it is necessary to reinforce with a material of different mechanical characteristics than the membrane to achieve a laminate load-to-membrane strength factor greater than the laminate weight-to-membrane weight penalty.

Investigations indicate that multifold improvement for comparative weight is possible through use of high modulus PRD-49 type IV reinforcement on a mylar membrane. Even more significant improvements are indicated for silicon carbide reinforcement on mylar and S-glass reinforcements on polyethylene film.

The mechanical characteristics for the Viking BLDT balloon material and a partially optimized version are provided in detail. The mechanical performance is investigated for a transverse loading varying from zero to that equal to the longitudinal load along with variations in the shear flow from zero to 0.6 the longitudinal load.

A unique mode of instability is discovered characterized by yarn compression in the presence of a stable tension field membrane. A full treatment of this phenomenon is beyond the scope of this paper, and the problem is generally circumvented if the yarn placement angle is taken larger than the arctan of the square root of Poisson's ratio.

References

Alley, V.L., Jr., and Faison, R.W. (1972a) Experimental investigation of strains in fabric under biaxial and shear forces, J. Aircraft 9(No. 1):55-60.

Alley, V.L., Jr., and Faison, R.W. (1972b) Decelerator fabric constants required by the generalized form of Hooke's law, J. Aircraft 9(No. 3):211-216.

Kenner, P.M. (1972) Structural analysis of a parawing during deployment, J. Aircraft 9(No. 2).

Niccum, R.J. (1972) Comparison of Polyester, Film-Yarn Composite, Balloon Material Subjected to Shear and Biaxial Loading, NASA CR-2047.

Contents

27. Tinting of Balloon Fabrics to Increase Their Solar Absorptivity

D.M. Smith
NASA Langley Research Center
Hampton, Virginia

Abstract

During passage through the cold troposphere, Mylar reinforced laminates experience embrittlement that severely reduces the structural capacity of the materials. Nearly transparent materials currently in use absorb between 6 and 15 percent of the solar energy they encounter. Tinting can increase the absorptivity to approximately 90 percent, if desired. The techniques and problems associated with tinting balloon fabrics to vary their solar absorptivity and surface emittance are discussed.

Experimental data are presented on the radiative characteristics of various degrees and types of tints studied at the Langley Research Center (LRC). Results of trajectory studies for balloons with various ratios of solar absorptivity to surface emittance are presented. The impacts of tinting of various aspects of flight, such as rate of ascent, thermodynamics of the balloon, valving and ballasting, and mission planning, are discussed. This paper represents portions of work from an LRC support task for the Advanced Research Projects Agency.

27-1. INTRODUCTION

During the ascent of high altitude balloons, the thin film of Mylar or polyethylene used to envelope the helium gas experiences progressively lower temperatures that can reach a minimum of -100°F during passage through the troposphere.

This temperature history occurs because of the drop in temperature of the atmospheric air with increasing altitude between ground level and the troposphere and the expanding helium gas inside the balloon. The low temperatures cause the film to become brittle, which in turn increases the risk of structural failure because of the film's reduced strength capacity. One source of energy – the sun – is not being utilized to full advantage to increase the film temperature, since the current clear films have a relatively low solar absorptivity (.06 to .15). This paper presents the results of a study conducted to determine the feasibility of tinting clear films of mylar and polyethylene to increase their solar absorptivity and thus reduce the possibility of structural failure due to film embrittlement. The study was divided into two parts: (a) characterization of thermal radiation properties of tinted films, and (b) evaluation of tinted films in terms of their effect on the ascent trajectory of a balloon. Experimental values of the solar absorptivity, transmissivity, reflectivity, and infrared emissivity of tinted film samples are presented. The results of trajectory studies which investigated the impact of various shades of tinting on the rate of ascent, film temperature, valving and ballasting requirements, and mission planning are also presented.

27-2 METHODS USED TO DETERMINE THE RADIATIVE CHARACTERISTICS OF TINTED FILMS

Tinted films made by two different processes have been investigated. One type of tinted film is obtained by adding various percentages of carbonblack to the adhesive used to bond the film and the reinforcing Dacron filaments together. The adhesive is applied as an even coating to the film, and the Dacron filaments are then placed on top of this coating. This is the normal process for manufacturing the clear balloon films currently being used. The second type of tinted film considered was obtained by applying a dye that completely penetrates the film. This type of film is truly a tinted film in that the tint is in the film rather than being added with the adhesive coating. Details of how the dyes are applied are not precisely known, because the processing companies consider them proprietary. Samples of these tinted films, both the mylar and the polyethylene, were tested for their radiative characteristics. The two instruments used were the Beckman DK-1A spectroreflectometer, which was used to determine the absorptivity, transmissivity, and reflectivity of the samples in the solar spectrum, and the Gier-Dunkle DB-100 infrared reflectometer, which was used to determine the reflectivity, transmissivity and emissivity in the infrared spectrum.

The Beckman DK-1A spectroreflectometer is an instrument used to expose test specimens to radiated energy on a single wavelength. The spectro-reflectometer scans between the wavelengths of 0.25 micron and 2.65 microns at a

prescribed rate, directly measuring the transmissivity or the sum of the transmissivity and reflectivity. Raw data from the instrument are in the form of a curve showing either transmissivity or the transmissivity-reflectivity sum versus wavelength.

Figure 27-1 shows the integrating sphere on the spectroreflectometer and the location of the sample for the transmissivity and the combined transmissivity-reflectivity measurements. For the transmissivity measurement, the sample is

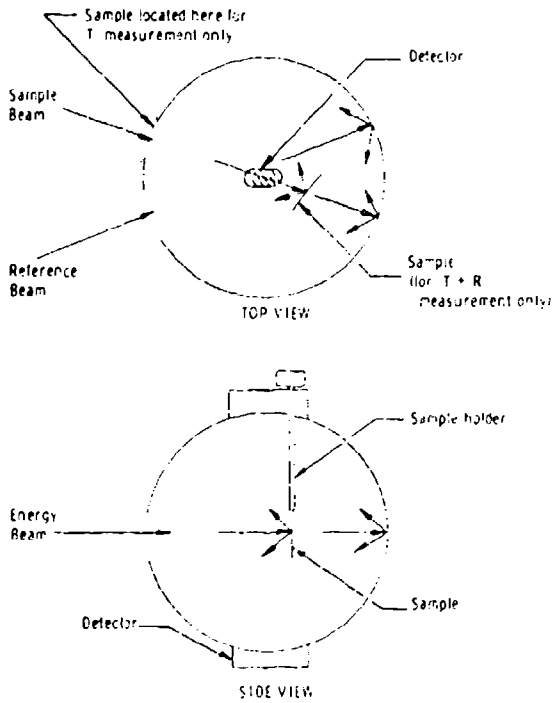

Figure 27-1. Schematic of Integrating Sphere on Beckman DK-1A Spectroreflectometer

placed over the opening that allows a beam from the energy source to enter the sphere. The detector is exposed alternately to a beam that passes through the sample and to a beam that passes unobstructed through the second opening in the sphere. The signals are compared, and the transmissivity is recorded. For the transmissivity-reflectivity sum measurement, the sample is placed inside the sphere and mounted on a frame that allows the energy beam to pass directly through and reflected off the surface of the sample is collected by the sphere.

The detector then measures the sample beam and the reference beam and records the transmissivity-reflectivity measurement

The solar spectrum is considered to be between the wavelengths of 0.17 microns and 4.00 microns. Figure 27-2 shows a curve of emissive power of a blackbody versus the product of wavelength and temperature. The sun can be

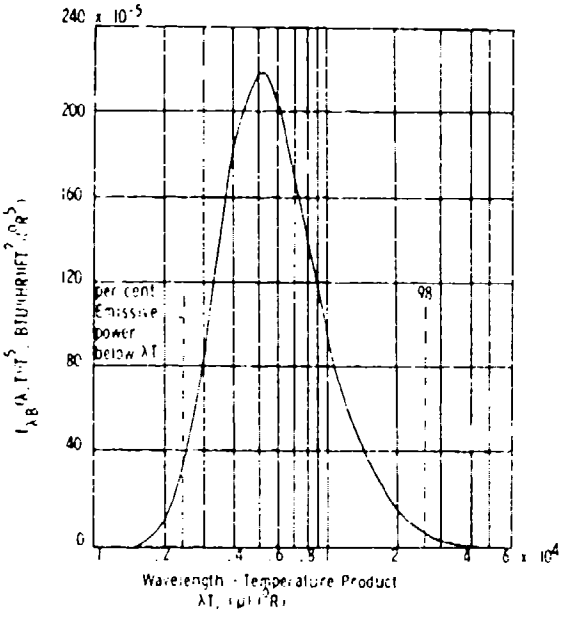

Figure 27-2. Plauck's Spectral Distribution of Blackbody Hemispherical Emissive Power (Edited from Siegal and Howell, 1968)

assumed to emit a blackbody which is at a temperature of 10,000°R. It can be seen from this curve that approximately 97 percent of the emissive power of the sun is between 0.25 micron and 2.65 microns, which are the limits of the Beckman spectroreflectometer. Thus, it is clear that the solar spectrum is adequately scanned in these tests.

The Gier-Dunkle DB-100 reflectometer measures the reflectivity of a test specimen in the infrared region of the spectrum with the specimen at room temperature. The sample is cyclically exposed to two rotating semicylindrical cavities which are at different temperatures. A vacuum thermocouple views the sample and monitors the varying energy that is reflected by the sample from the two cavities. This signal is compared with the signals from high reflectivity and

low reflectivity standards to determine the reflectivity of the sample. Complete details of the working principles of the Gier-Dunkle DB-100 are given by Nelson et al (1966). Since the samples are transparent, a second reading must be taken with the sample backed with a highly reflective surface so that the emissivity and transmissivity may be determined. How these two values are calculated from the two readings will be shown in section 27-3 of this paper.

27-3. DATA REDUCTION

When radiative energy strikes a transparent body, the body will absorb, reflect, and transmit the energy. The absorptivity, reflectivity, and transmissivity define the proportions into which the incoming energy is divided. Their sum must add to 1.

$$A(\lambda) + R(\lambda) + T(\lambda) = 1 . \tag{27-1}$$

Therefore, by measuring $T(\lambda)$ and $T(\lambda) + R(\lambda)$, all three values can be determined as a function of wavelength. This reasoning was applied to the data gathered with the Beckman spectroreflectometer.

The integrated average of each of these three quantities over the solar spectrum is used in radiation heat transfer analysis. The integrated average for absorptivity, for instance, is obtained from the following expression:

$$A = \frac{\int_{\lambda_1}^{\lambda_2} A(\lambda)\, I(\lambda)\, d\lambda}{\int_{\lambda_1}^{\lambda_2} I(\lambda)\, d\lambda} \tag{27-2}$$

where A is the average solar absorptivity and $I(\lambda)$ is the solar emissive power as a function of wavelength. Planck's spectral distribution of emissive power for blackbodies is used for $I(\lambda)$.

$$I(\lambda) = \frac{2\pi C_1}{\lambda^5 \left(e^{C_2/\lambda T} - 1\right)} \tag{27-3}$$

where C_1 and C_2 are constants and T is taken to be 10,000°R as previously noted. The T and R values are determined from expressions similar to Eq. (27-2).

Since a balloon is a transparent enclosure, solar energy transmitted through one surface element on the balloon may strike a second surface element, reflected energy from the second element strikes a third element, and so on. An expression was derived by Germeles (1968) for the effective solar absorptivity of a transparent balloon. This expression is

$$A_{eff} = A\left(1 + \frac{T}{1 - R}\right). \qquad (27\text{-}4)$$

This is the value for solar absorptivity used in the trajectory studies to determine tinted balloon performance and film temperatures. Measurements taken with the Gier-Dunkle reflectometer are used to determine tinted film emissivity. As previously mentioned, two measurements must be taken, since the sample is transparent. The first measurement is made on the sample alone. This reading gives the sample reflectivity. A second measurement is made with the sample backed with a highly reflective surface to determine the emissivity. The reflectometer actually gives a second reflectivity reading which must be used with the first reflectivity reading to calculate the emissivity. The calculation is based on the following reasoning (see Figure 27-3):

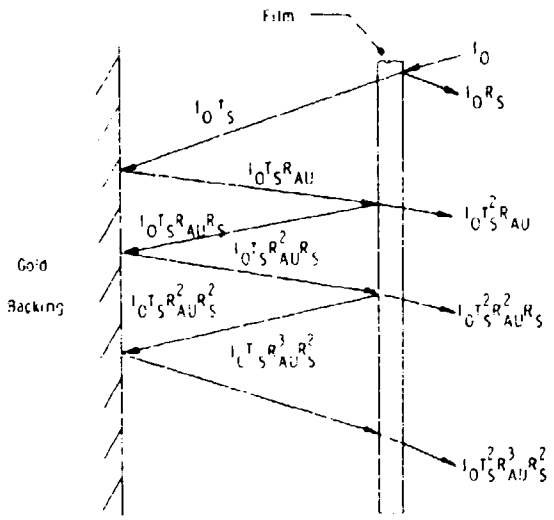

Figure 27-3. Derivation of Equation for Calculating Infrared Transmissivity and Emissivity from Gier-Dunkle DB-100 Reflectometer Measurements

$$I_O(R_S + T_S^2 R_{AU} + T_S^2 R_S + T_S^2 R_{AU}^3 R_S^2 + \text{--}) = \; _O R_M$$

$$R_M = R_S + R_{AU} T_S^2 (1 + R_{AU} R_S + R_{AU}^2 R_S^2 + \text{--})$$

$$R_M = R_S + R_{AU} T_S^2 \frac{1}{1 - R_{AU} RS} .$$

The R_S and R_M are the first and second reflectometer readings, respectively, and R_{AU} is the reflectivity of gold. The sample transmissivity, T_S, may be now calculated:

$$T_S = \left[\frac{(R_M - R_S)\ (1 - R_{AU} R_S)}{R_{AU}}\right]^{1/2} \tag{27-5}$$

Now using the equation

$$A_S + R_S + T_S = 1 \tag{27-6}$$

where A_S is the infrared absorptivity of the sample, and using Kirchoff's Law to assume $E_S = A_S$, where E_S is the sample emissivity, the emissivity is determined from

$$E_S = 1 - R_S - T_S . \tag{27-7}$$

Since the balloon film radiates from both sides, the balloon radiates energy to itself on the interior which must be transmitted through the film. In a derivation similar to that for the effective absorptivity, an expression for the effective emissivity can be found (Germeles, 1966),

$$E_{eff} = E_S (1 + \frac{T_S}{1 - R_S}) \tag{27-8}$$

where T_S and R_S are evaluated in the infrared spectrum.

27-4. THERMAL RADIATION PROPERTIES OF TINTED MYLAR AND POLYETHYLENE FILMS

Table 27-1 lists all the radiation properties for 15 samples with various shades of tinting. These properties were either measured directly or they were calculated using the formulas described previously. Figures 27-4 through 27-7 show the effects of tinting on the transmissivity and transmissivity plus reflectivity curves in the solar spectrum.

Table 27-1. Thermal Radiation Properties for Balloon Films

Material Type	Thickness Mils	Solar Spectrum (.25 - 2.65μ)				Infrared Spectrum				$(A/E)_{eff}$
		T	R	A	A_{eff}	T	R	E	E_{eff}	
Mylar Composite	.33	.82	.14	.04	.078	.537	.12	.343	.552	.142
Orange Mylar (film dyed)	2	.667	.099	.234	.433	.377	.12	.503	.717	.604
Blue Mylar (adhesive dyed)	3 (film) 1.5 (adhesive)	.695	.108	.197	.35	.234	.091	.675	.848	.413
Frosted Mylar (etched)	1	.81	.155	.035	.069	.491	.122	.387	.604	.114
Mylar Composite (india ink spray coat)	.33	.402	.146	.452	.663	.445	.11	.445	.668	.99
Mylar Composite (blue dye spray coat)	.33	.681	.097	.222	.394	.593	.119	.288	.482	.818
Grey Mylar 1% CB (1% carbonblack in adhesive)	.33 (film) .2 (adhesive)	.712	.058	.23	.418	.590	.129	.281	.478	.875
Grey Mylar 3% CB (3% carbonblack in adhesive)	.33 (film) .2 (adhesive)	.575	.053	.372	.597	.588	.129	.283	.474	1.26
Grey Mylar 7% CB (7% carbonblack in adhesive)	.33 (film) .2 (adhesive)	.274	.048	.678	.873	.525	.13	.345	.554	1.58
Grey Mylar 1% CB (1% carbonblack in adhesive)	.5 (film) .2 (adhesive)	.691	.079	.23	.403	.564	.125	.311	.512	.789
Grey Mylar 3% CB (3% carbonblack in adhesive)	.5 (film) .2 (adhesive)	.551	.059	.34	.618	.551	.122	.327	.532	1.16
Grey Mylar 7% CB (7% carbonblack in adhesive)	.5 (film)	.275	.048	.677	.873	.494	.128	.378	.592	1.475
Polyethylene Composite	1	.845	.112	.043	.084	.733	.11	.157	.286	.294
Polyethylene Coated with Adhesive	1	.88	.083	.037	.073	.684	.113	.203	.36	.202
Grey Polyethylene (Grey tint in film)	1	.819	.066	.115	.216	.828	.111	.061	.118	1.83
Polyethylene 1% CB (1% carbonblack in adhesive)	1 (film) .2 (adhesive)	.681	.053	.266	.47	.702	.11	.188	.336	1.40

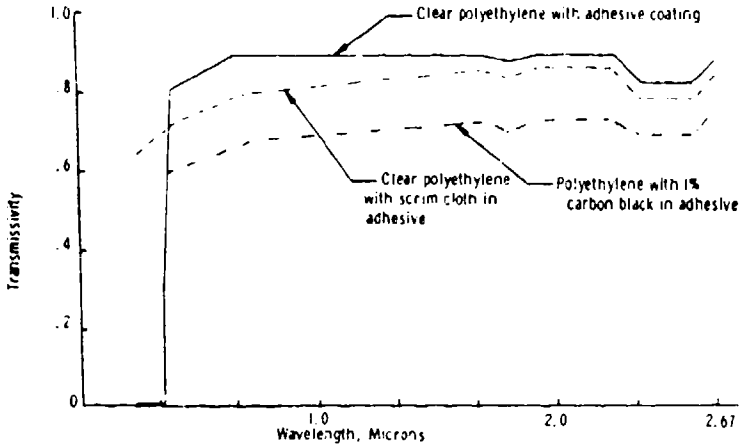

Figure 27-4. Transmissivity Versus Wavelength in Solar Spectrum for Polyethylene

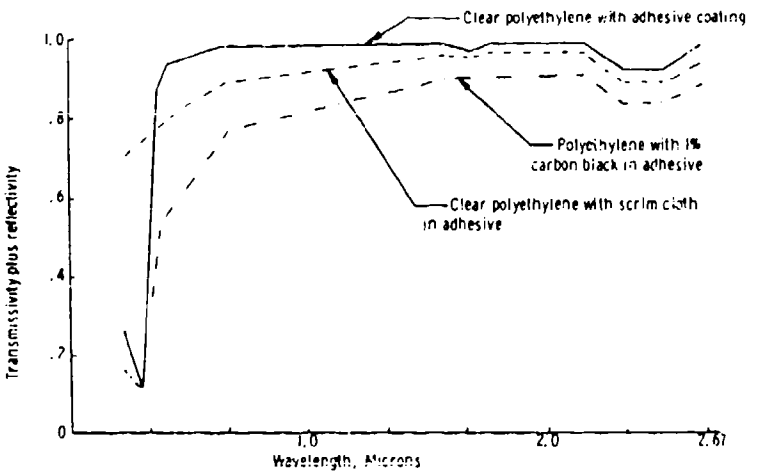

Figure 27-5. Transmissivity Plus Reflectivity Versus Wavelength in the Solar Spectrum for Polyethylene Samples

The carbonblack tinting lowers the curves over the entire spectrum, while the orange and blue dyed Mylar produce increased absorptance in the visible range of the spectrum. It can be seen that a wide range of effective solar absorptivity and effective emissivity can be obtained. A measure of the degree of tinting can be determined by calculating the solar absorptivity to emissivity ratio. A material with an $(A/E)_{eff}$ larger than 1.0 is classified as a solar absorber, while a material with an $(A/E)_{eff}$ less than 1.0 is considered to be a solar reflector.

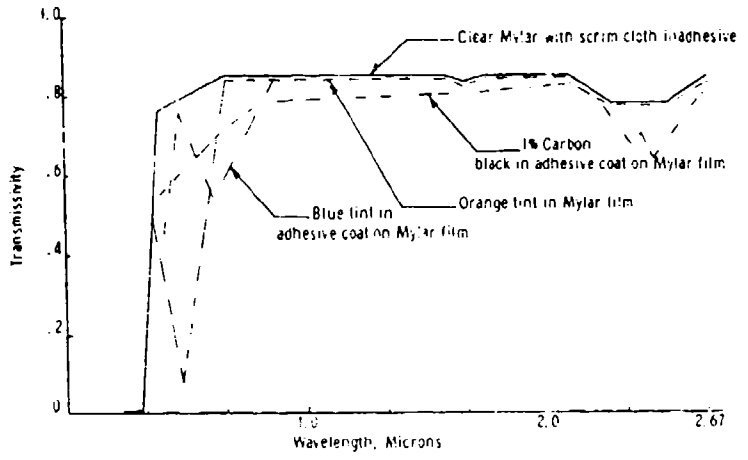

Figure 27-6. Transmissivity Versus Wavelength in the Solar Spectrum for Mylar Samples

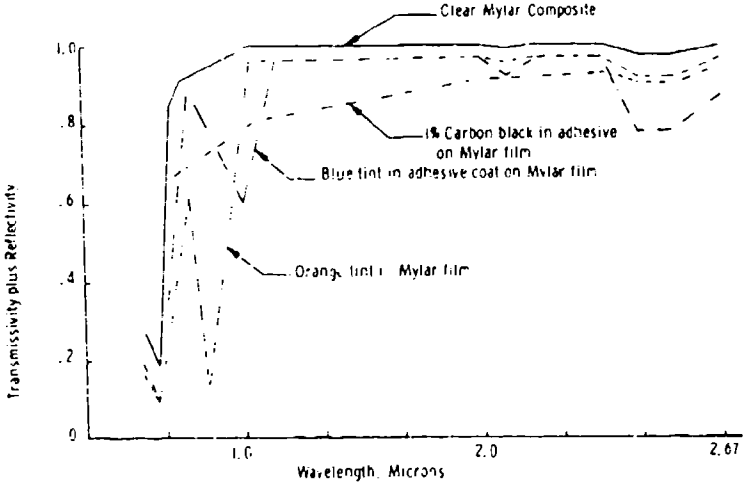

Figure 27-7. Transmissivity Plus Reflectivity Versus Wavelength in the Solar Spectrum for Mylar Samples

Tinting that produces an intermediate $(A/E)_{eff}$, that is, 0.4 to 1.0, is preferable to the tints that produce $(A/E)_{eff}$ ratios greater than 1.0, because balloons made with a material of a higher ratio have a higher equilibrium temperature during the sunlight floating period.

The lowest value of effective absorptivity for the tinted Mylar was 0.35 for the Mylar with blue dye in the adhesive. Very small amounts of carbonblack in the adhesive drastically increased the solar absorptivity. These data indicate only small changes in the effective emissivity when a tint is added to the film.

Therefore, an increase in the solar absorptivity increases the $(A/E)_{eff}$ almost proportionally. The exceptions are the orange and blue tinted Mylar and the Mylar composite that was tinted with an India ink spray coat. The higher values of emissivity for the orange and blue Mylar are related to the larger film thickness, while the increase in emissivity of the spray coated Mylar is due to the India ink.

Data from tests on the polyethylene samples indicate the solar absorptivity is substantially increased for a small amount of tinting. The emissivity values for the polyethylene films are relatively low, and by increasing the solar absorptivity, the $(A/E)_{eff}$ for polyethylene is greater than 1.0 in all cases. While this does not create a problem during balloon ascent, high film temperatures will occur during the floating period. Lower values of $(A/E)_{eff}$ can be obtained by reducing the amount of carbonblack below one percent or by reducing the amount of tinting dye.

27-5. RESULTS OF TRAJECTORY STUDIES

To determine how effective tinting a balloon film can be in terms of increasing the film temperature during ascent, analytical studies of the trajectory of tinted balloons were made. The study involved the use of a computer program originally developed by Germeles (1966) and recently modified by Kreith (1971). The program solves six nonlinear ordinary differential equations which describe the vertical motion of a spherically shaped balloon. These equations describe the forces on the balloon, the rate of volume change of the balloon, the rate of change of temperature of the gas used for buoyancy, and the rate of change of mass of the balloon gas. The dependent variables, which are a function of time, t, are the following:

$Z(t)$	altitude of the balloon
$T_g(t)$	balloon gas temperature
$T_f(t)$	balloon skin fabric temperature
$V_g(t)$	volume of balloon gas
$U(t)$	vertical velocity of balloon
$M_g(t)$	mass of balloon gas

Parameters which must be given by the user are the atmospheric properties, the balloon gas properties, the infrared radiation field, the balloon fabric properties, the payload weight, the valving and ballast schedule, the drag coefficient for the balloon, the launch location and time, and the initial conditions of the six dependent variables. Complete details of the program are given by Kreith (1971).

For comparison purposes, the tinted balloons were exposed to the same environment. Figure 27-8 shows the atmospheric temperature profile versus

altitude that was used in the analyses. The temperature reaches a low of -100°F in the troposphere. This profile is typical of a summer day in White Sands, New Mexico. Sky conditions were assumed to be clear, and launch time was 6:00 a.m.

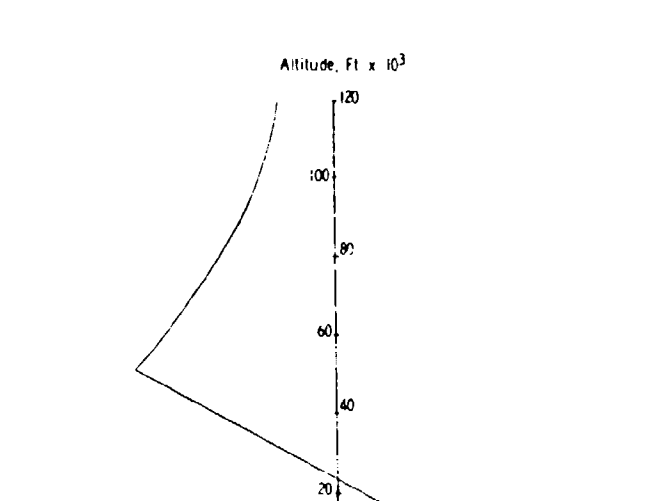

Figure 27-8. Atmospheric Temperature Versus Altitude Profile Used in Trajectory Studies

Payload weight was assumed to be 6000 pounds, and float altitude was assumed to be 120,000 feet. This corresponds to a balloon volume of approximately 35 million cubic feet. The radiative thermal properties for each balloon fabric, the valving schedule, and the initial free lift were the only variables changed during each analysis. The balloon vertical velocity was limited to 2000 feet per minute to prevent increased convective cooling that would reduce the temperature increase gained by tinting the film. The main variables of interest are the film temperature and balloon velocity, along with the valving and ballasting requirements. Figures 27-9 and 27-10 show comparisons of the tinted Mylar and polyethylene film temperature profile versus altitude. Both the clear Mylar and polyethylene films reach a temperature of approximately -100°F during troposphere passage. By increasing the solar absorptivity, the minimum temperature can be raised to -25°F using films with an $(A/E)_{eff}$ greater than 1.0. However, during the floating period at 120,000 feet the film temperature would be 100 - 110°F during the sunlight hours. This temperature is acceptable if the mission is completed during this time.

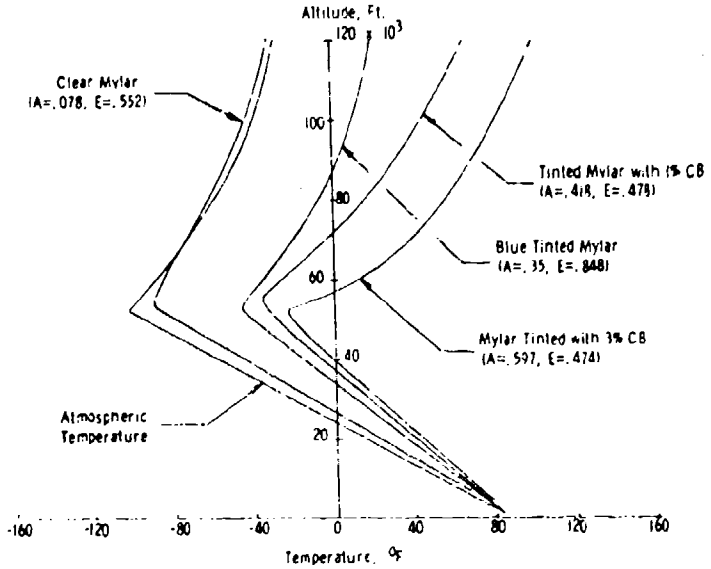

Figure 27-9. Film Temperature Versus Altitude for Tinted Mylar Balloons

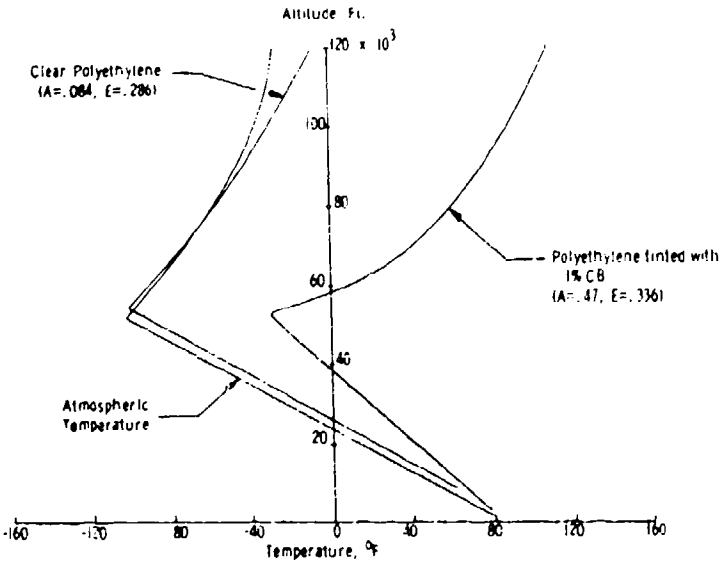

Figure 27-10. Film Temperature Versus Altitude for Tinted Polyethylene Balloons

During the night the main source of heat to the balloon is the infrared radiation from the earth. The helium temperature will approach -70°F, and in order to

maintain the balloon at 120,000 feet, 3000 pounds of ballast have to be released for a blue tinted mylar balloon (A = .35, E = .848). This would limit the mission life to one day-night cycle. A solution to this problem is to tint only the portion of the balloon that is unfurled between ground level and the troposphere. According to the trajectory calculations, the balloon volume at 80,000 feet, where the atmospheric temperature is -60°F, is 5.6 million cubic feet. Basing surface area calculations on a spherically shaped balloon, 29 percent of the fabric of a balloon whose volume is 35 million cubic feet when fully inflated would be directly exposed to the atmosphere. This area could be tinted to an $(A/E)_{eff}$ ratio of 1.0, and the remaining fabric, which would be covered with an insulated sleeve until it is unfurled, would be made with the clear film which has a low solar absorptivity. Analysis of the temperature distribution on a balloon skin made with two materials which have different values of absorptivity and emissivity has not been conducted. Substantially reduced ballast requirements are anticipated.

Venting of the helium gas is required during ascent to maintain the vertical velocity of less than 2000 feet per minute. Venting requirements can be relieved by reducing the initial free lift at ground level. The free lift is defined as the difference between the weight of the air displaced by the balloon and the total weight of the balloon and payload. Usually, the initial free lift is 8 to 10 percent of the total weight. It can be reduced to 2 percent of the total weight when a tinted film with $(A/E)_{eff}$ of 0.8 to 1.0 is used.

Table 27-2 lists the venting schedule versus altitude for tinted balloons. The vertical velocity of a typical balloon versus altitude is shown in Figure 27-11.

Table 27-2. Helium Venting Rate During Ascent for Tinted Balloons (Maximum Vertical Velocity of 2000 Feet Per Minute)

	Altitude, Feet	Pounds of Lift Lost Per Second
Clear Mylar	0 - 120,000	0
Blue Mylar	0 - 13,000	0
	13,400 - 18,500	0.25
	18,500 - 49,000	1.0
	49,000 - 120,000	0
Mylar Tinted with 3% Cb	0 - 15,000	0
	15,000 - 22,000	0.25
	22,000 - 55,000	1.85
	55,000 - 60,000	0
	60,000 - 74,000	2.0
	74,000 - 120,000	0

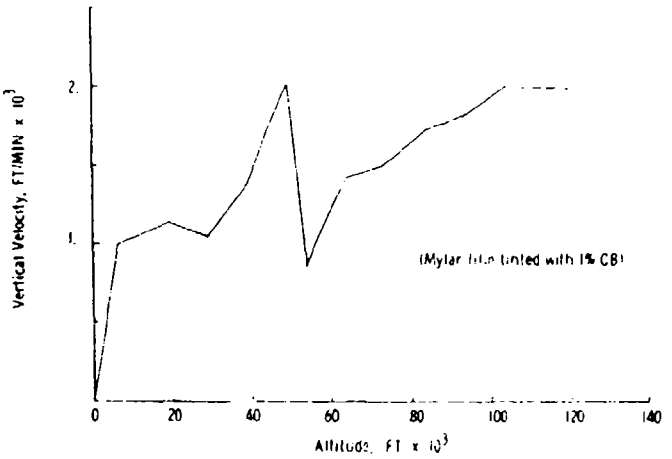

Figure 27-11. Typical Tinted Balloon Vertical Velocity Versus Altitude

The balloon velocity tends to increase as it approaches the troposphere and again as it approaches float altitude. These venting requirements should not present a problem in controlling the balloon's ascent.

27-6. CONCLUSIONS

It has been demonstrated that tinted Mylar film can be manufactured and that by using tinted film as the balloon skin the film minimum temperature can be increased from -100°F to -25°F. Higher film equilibrium temperatures occur at the float altitude, causing increased ballast requirements if the mission life requires a tinted balloon to pass through a day-night cycle. A solution has been proposed that only that portion of the balloon exposed to the atmosphere when the balloon passes through the troposphere be tinted. The tinted polyethylene samples had $(A/E)_{eff}$ ratios greater than 1.0. Balloons made of these materials will have high equilibrium temperatures during the sunlight floating period. The $(A/E)_{eff}$ can be reduced by decreasing the amount of carbonblack in the adhesive or tinting dye. Tinting only a portion of a polyethylene balloon would also be beneficial.

References

Germeles (1966) Vertical Motion of High Altitude Balloons, Technical Report IV, Arthur D. Little, Inc., for the Office of Naval Research.

Kreith, F. (1971) Performance of High Altitude Balloons, NCAR-TN/STR-65.

Nelson, K. E., Luedke, E. E., and Bevans, J. T. (1966) A device for the rapid measurement of total emittance, J. Spacecraft 3(5):758-760.

Siegal, R., and Howell, J. R. (1968) Thermal Radiation Heat Transfer, Vol. 1, NASA SP-164.

Contents

28. A Computer Program to Predict Stresses and Deformations of Inflatable Structures

D.R. Lagerquist
G.T. Schjeldahl Company
Northfield, Minnesota

28-1. INTRODUCTION

An important part of the evaluation of designs for inflatable structures such as balloons is the prediction of stresses and deformations experienced by the structure during its service lift. Classic small deflection linear theory analysis techniques are not applicable to most inflatable structure problems, since the deformations due to loading are large, and changes in geometry must be accounted for in the analysis. Simplified approximate methods of analysis are often sufficient for structures of simple geometric shape subject to certain loading conditions. However, more general complex problems require more sophisticated analytical techniques.

In order to have the capability of solving a broad class of inflatable structure problems, G.T. Schjeldahl Company engineers have coordinated the adaptation of a large-scale computer program especially for analyzing this type of structure. This program, designed LD3DX (Large Deformation Analysis of Three-Dimensional Structures, Extended), uses the finite element matrix method of analysis (Przemieniecki, 1968) which has become so important in computerized structural analysis and design techniques over the past decade. The geometrically nonlinear

equilibrium solution is obtained by a form of the Newton-Raphson iteration technique, combined with an incremental loading procedure.

Input to the program are the initial geometry of the structure modeled with truss (rod) and/or membrane shell elements, material properties, and loading conditions. The program computes displacements and stresses for the entire strucrure.

LD3DX was adapted from a program developed for a shell structure design technique at the University of California in Berkeley (Smith and Wilson, 1971). The program was modified by Engineering Analysis Corporation, Redondo Beach, California under the direction of Robert G. Witherow of the G. T. Schjeldahl Company. Further modifications were incorporated by Schjeldahl engineers. The program was written in Fortran IV language for the Control Data Corporation 6600 computer. A special version of the program was adapted for smaller analysis problems using a remote terminal time sharing system on a CDC 6400 computer.

28-2. METHOD OF ANALYSIS

In the finite element method of structural analysis, the actual structure is idealized by a discrete set of structural elements connected at node points. Inflatable structures generally exhibit membrane-type behavior and may involve cable suspension systems. Therefore, available elements in the LD3DX program are triangular or quadrilateral membrane elements and rod elements. The structure can have arbitrary geometry, material properties, and boundary conditions. Figure 28-1 shows an example of a model for an inflatable structure with internal lacing. These plots were produced by the computer program and can be used to check the original geometry input to the program. It is also possible to produce plots of the final deformed geometry.

The finite element method is in general a linear analysis technique, so that special solution procedures must be used for nonlinear applications. In LD3DX, it is assumed that member strains are small so that the material behaves in a linearly elastic manner, but rigid body motions may be large so geometric nonlinearities must be considered in solving the equilibrium equations. Details of this analysis are beyond the scope of this present paper (see Smith, 1969), so only a brief description is included herein.

The solution procedure is a form of the Newton-Raphson iteration technique, illustrated schematically in Figure 28-2. For a given loading, R, an initial deformed configuration, r_0, is assumed or computed using the initial linear solution. Internal resisting forces, R_0, are computed for this configuration and compared to the applied external loading, R. The resulting set of out-of-balance forces

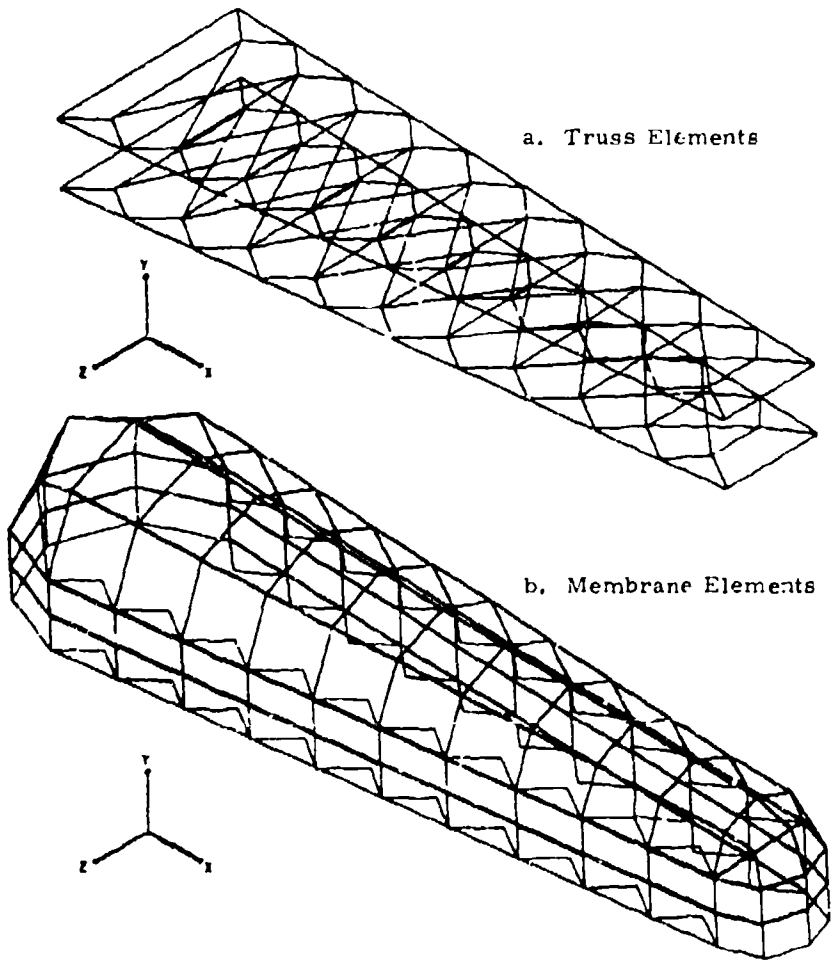

Figure 28-1. Sample Plot of Finite Element Model

are then applied to the deformed structure at point 0 resulting in a new set of deflections at point 1. The procedure is repeated until the unbalanced forces become less than a specified tolerance.

For some problems, numerical difficulties are experienced if the total external load is applied in one step. Often convergence to the correct solution is aided by applying the load in two or more increments, as illustrated in Figure 28-3. A load value, R', smaller than the total R is applied, and the iterative solution yields the corresponding equilibrium position, r'. This configuration is then used as the starting point for applying the remainder of the load R. In addition to aiding in convergence of the iteration procedure, this incremental load technique

allows deflections and stresses to be obtained for various loading conditions and intensities.

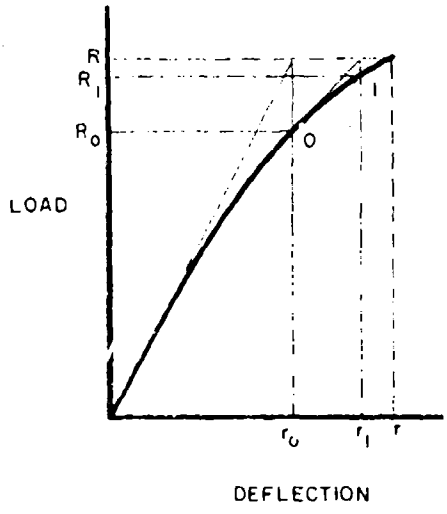

Figure 28-2. Illustration of Load-Deflection Iteration Technique

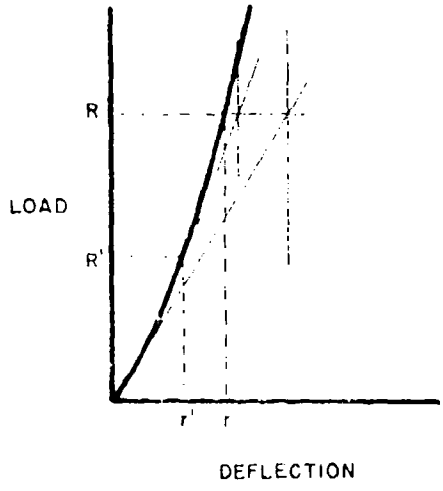

Figure 28-3. Illustration of Load-Deflection Iteration With Incremented Loading

28-3. MATERIAL PROPERTIES

The behavior of the membrane material in the program is assumed to be that of a general anisotropic linearly elastic material in a state of plane stress. The stresses and strains in two orthogonal directions, 1 and 2, are related by the generalized form of Hooke's law:

$$\sigma_{11} = C_{11}\epsilon_{11} + C_{12}\epsilon_{22} + C_{13}\gamma_{12}$$

$$\sigma_{22} = C_{21}\epsilon_{11} + C_{22}\epsilon_{22} + C_{23}\gamma_{12}$$

$$\tau_{12} = C_{31}\epsilon_{11} + C_{32}\epsilon_{22} + C_{33}\gamma_{12}$$

where σ_{11} and σ_{22} are direct stresses, τ_{12} is the shear stress, ϵ_{11} and ϵ_{22} are direct strains, and γ_{12} is the shear strain. The coefficients C_{ij} are called elastic constants.

The analysis theory used requires a Hookian material for which the elastic constants are symmetrical. Thus, only six coefficients are required: C_{11}, C_{12}, C_{13}, C_{22}, C_{23}, and C_{33}. However, for fabric materials often utilized in inflatable structures, it is known that material strains are not conservative, so that all nine elastic constants are independent (Alley and Faison, 1970). In this case, it is necessary to use an averaging technique to approximate the material behavior with six constants.

For an isotropic material, the elastic constants can be computed directly from Young's modulus and Poisson's ratio. Elastic constants for anisotropic fabrics can be obtained by means of a biaxial stress test machine developed expressly for this purpose. In this test setup, shown in Figure 28-4, a cylinder is fabricated from the material and is subjected to various combinations of pressure, longitudinal, and torque loadings. The elastic constants can then be calculated from known applied stresses and corresponding measured strains.

Figure 28-4. Biaxial Stress Cylinder Test

Most fabric-type materials exhibit a certain amount of nonlinear behavior, especially at higher stress levels. Since the program assumes linear material behavior, it is sometimes necessary to approximate the actual stress-strain relationship with a linearized approximation in the range of interest. Also, the program has a restart feature, whereby the loading can be incremented and the elastic constants revised at the start of each new increment to reflect changing stress levels.

Material properties for rod elements are simply Young's modulus and cross-sectional area.

28-4. APPLIED LOADING

Loads applied to the structure are of two general types:

(1) Concentrated nodal forces and

(2) Element loads, either gravity or normal pressure type.

The element type loads are converted by the program into equivalent nodal forces. However, directions of these nodal forces depend on the geometry and thus change with each iteration. The concentrated nodal forces input remain constant in magnitude and direction referenced to a global coordinate system.

Loads can be applied in increments as previously discussed. Each load set can be independently sequenced so that the same load factor need not be applied to all load sets. This feature is convenient for some inflatable structure problems when, for example, it is desirable to apply internal pressurization loads first and then apply subsequent service loads with pressure held constant.

28-5. APPLICATIONS

Applications of the program include stress and deformation analysis of inflatable structures and similar type problems which exhibit geometrically nonlinear behavior. Previous problems analyzed with the program include balloons, inflatable buildings, pressurized diaphragms, and cable suspension systems. As examples, two analysis problems will be discussed briefly in this section.

The first example is the stress and deformation analysis of the hull and suspension line system of a 250,000 cubic foot tethered balloon. The finite element model for this analysis is sketched in Figure 28-5. Since both the structure and all loading cases considered are symmetrical about the center vertical plane, only one-half the structure is analyzed. Boundary conditions are specified such that symmetry is forced in the plane of symmetry. All deflections are restrained at

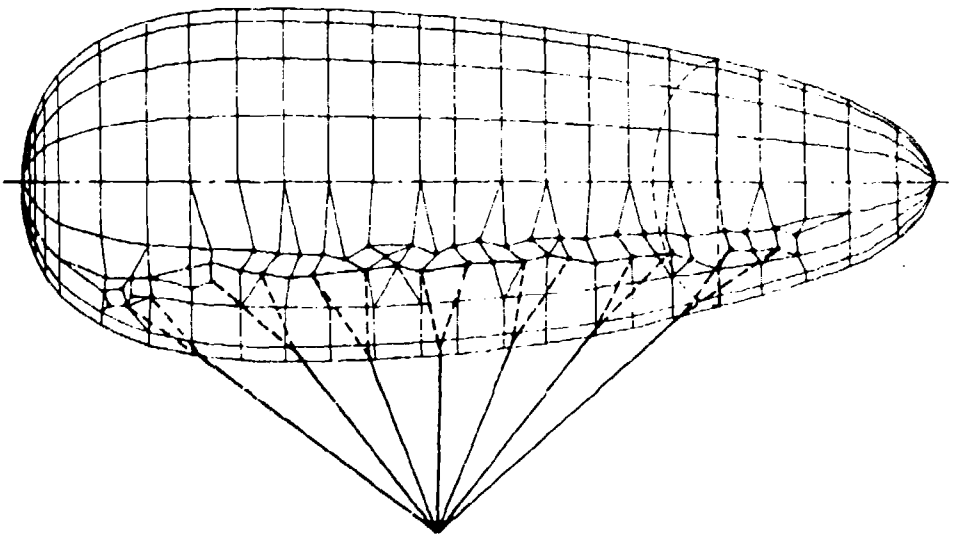

Figure 28-5. Model for Tethered Balloon Hull-Suspension Line Analysis

the tether confluence point. In this model, there are 287 nodal points, 23 truss elements, and 276 membrane elements.

Six load sets were considered:

(1) Internal pressurization
(2) Net buoyant lift
(3) Payload concentrated forces
(4) Aerodynamic pressure
(5) Empennage net aerodynamic lift and drag
(6) Hull skin friction drag.

The aerodynamic loads were determined from rigid model wind tunnel tests. These loads were applied in four load increments: first pressurization, then buoyant lift and payload, then two increments for adding aerodynamic loads. Stresses and deflections were obtained for each load increment.

The results of this analysis allow the engineer to predict the magnitude and location of the maximum direct and shear stresses in the material, suspension line loads, possible areas of wrinkling or hull buckling, hull growth due to pressurization, and hull deformation due to external loads.

This problem was run on the CDC 6600 computer. The amount of central processor (CP) time, which is the primary factor in the machine cost, varied with each load increment depending on the number of iterations required for convergence. The average for each increment was about four iterations with a CP time of about 3 minutes.

The second example problem is the analysis of one side of the horizontal stabilizer of the same tethered balloon. Figure 28-6 is a plot of the membrane elements used in the analysis model. Not shown in the plot are the internal laced

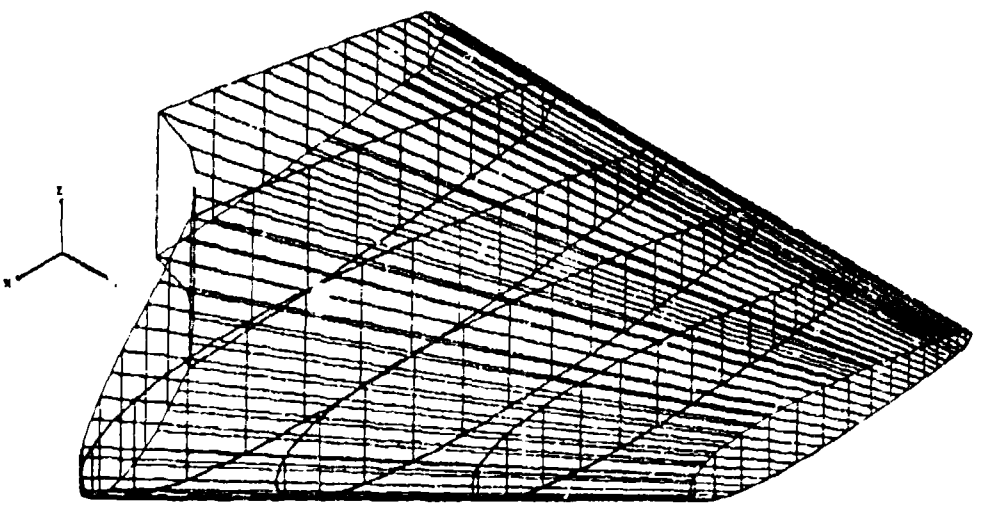

Figure 28-6. Model for Tethered Balloon Horizontal Stabilizer Analysis

rib members and external support guy lines. Also not shown are flexible support members at the root which were used to simulate the flexible hull. This model has 386 points, 70 truss elements, and 437 membrane elements.

For this problem, the loading conditions imposed on the structure were internal pressurization, aerodynamic pressure distribution, and skin friction drag. These loads were all applied in a single load increment, although different load values were analyzed in separate computer runs. Three iterations were required for convergence for the load increment with a machine time of about 4 CP minutes.

Output for this problem included membrane stresses in all the elements, rib lacing and guy line loads and deformations of the fin. Also, loads in the fin root supports were obtained which could be used in further analysis of the hull-fin intersection region.

28-6. VERIFICATION

Numerous test problems have been analyzed to determine the validity of the program. Comparisons with theoretical results have been made for various

pressurized structure problems and simple truss instability problems. Also analysis results have been compared to experimental measurements for pressurized shells, pressurized diaphragms, and a cable suspension system. It is concluded that good results can be obtained from these types of analyses, assuming reasonable care is exercised in modeling the structure and that material properties are adequately represented.

References

Alley, V. L., Jr., and Faison, R. W. (1970) Decelerator Fabric Constants Required by the Generalized Form of Hooke's Law, AIAA Aerodynamic Deceleration Systems Conference, Dayton, Ohio, Sept. 14-16.

Przemieniecki, J. S. (1968) Theory of Matrix Structural Analysis, McGraw-Hill, New York.

Smith, P. G. (1969) Membrane Shapes for Shell Structures, thesis presented to the Univ. of California, Berkeley, in partial fulfillment of the requirement for the degree of Doctor of Philosophy.

Smith, P. G., and Wilson, E. L. (1971) Automatic design of shell structures, J. Structural Division 97(No. ST1) ASCE, Proc. Paper 7825:191-201.

Contents

29. A New Brittleness Criterion for Low Density Polyethylene Balloon Films

Dr. D. Weissmann
Stevens Institute of Technology
Hoboken, New Jersey

Abstract

The brittle rupture of polyethylene films may be one of the main causes of failure of high altitude balloons in the stratosphere. If the material can deform in a plastic manner, there is the possibility that the stress can be relieved by deformation or a ductile rupture. A ductile rupture is a local tear in the material. A brittle rupture is a shattering in a glass-like manner of large areas of the material resulting in an immediate loss of the balloon.

Since existing methods of characterizing the film performance regarding brittleness were found to be unsatisfactory, the present study was undertaken to investigate the brittle-ductile transition and the factors that may influence it. By defining a brittle failure under uniaxial constant strain rate test conditions, a transition temperature from ductile to brittle failure was established at each strain rate. It was found that at low strain rates the transition temperature is almost independent of the strain rate. This temperature is suggested as the "cold brittleness temperature."

This cold brittleness temperature is related to the energy dissipation ability of the material as found from dynamic mechanical tests. The correlation between the uniaxial constant strain rate test and the dynamic mechanical data was checked mathematically by using a viscoelastic model.

29-1. INTRODUCTION

As the use of plastics expanded and their behavior was investigated, it became obvious that for certain applications, it is not sufficient to consider only the commonly used mechanical properties such as ultimate stress and strain or the elastic modulus. Additional aspects of the mechanical behavior must be considered to achieve satisfactory performance.

Balloon failures due to the brittleness of the film have accompanied balloon flights almost since polyethylene films were introduced as a balloon material. In the early fifties, M. M. Renfew and A. J. Freeman (1953) reported on the development of the inclined plane ball tester. This tester was developed to evaluate balloon films for brittleness. However, the inclined plane ball test, as well as the falling ball test in which the ball is dropped directly on a suspended sample rather than rolled down an inclined plane, were found to be unsatisfactory. The results obtained did not correlate well with balloon flight experience, and properties related to the surface of the ball were found to influence the test results (Winker, 1970; Nelson, 1970; Hauser and Stefan, 1970; and Mielke, 1968). A Round Robin testing program indicated little or no agreement among the results obtained at several different laboratories as was reported by Hauser (1967).

It was suggested by Roth and Manmood, (1965) that a study of tensile properties at progressively lower temperatures should yield information regarding the transition from ductile to brittle behavior. However, the difference between ductile and brittle rupture as is found in the ruptures induced by biaxial loading (Figures 29-1 and 29-2) is not observable in uniaxial testing. This necessitates the establishment of an independent criterion for ductile and brittle behavior. The criterion suggested by this paper is based on the observations of Amborski and Mecca (1960). They showed that at a constant temperature a curve of the ultimate strain versus log (strain rate) yields a sudden transition from a large ultimate strain to a much smaller strain in a narrow range of strain rates, as can be seen in Figure 29-3. The strain rate at which this transition occurs is defined as the critical strain rate (CSR) at the given temperature. Ductile behavior is therefore associated with large ultimate deformations, while the brittle behavior is associated with much smaller ultimate deformations.

It can be expected that repeating these tests at various temperatures would yield a similar transition at each temperature with the CSR moving to higher strain rates as the temperature is increased. Plotting the same data as ultimate strain versus temperature at a constant strain rate should yield a similar transition on the temperature axis as Amborski and Mecca observed on the strain rate axis. It is then possible to define a critical temperature (CT) equivalent to the CSR.

Figure 29-1. Ductile Rupture

Figure 29-2. Brittle Rupture

Extrapolating these results to very low strain rates yields a new criterion for cold brittleness in the establishment of a cold brittleness temperature (CBT).

29-2. EXPERIMENTAL RESULTS

The experimental program leading to the establishment of the CBT consisted only of constant strain rate uniaxial tests conducted on an Instron tensile tester. Tests were run at a number of strain rates between 50 and 5000 percent per minute

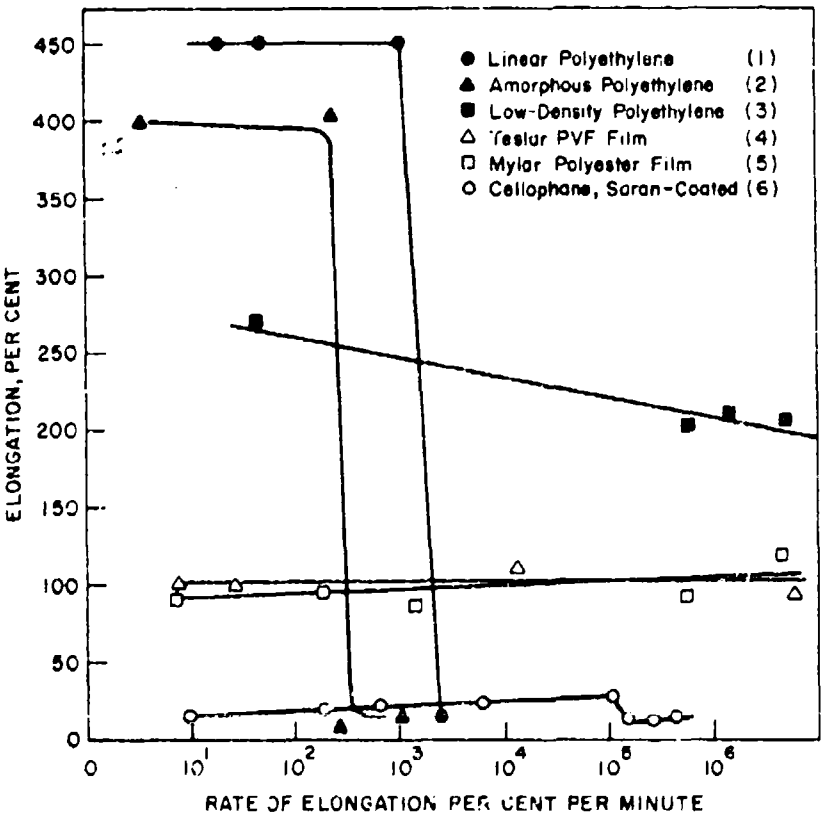

Figure 29-3. Critical Strain Rate
(Temp. 23.5°C; from Amborski and Mecca, 1960)

at temperatures from room temperature to -75°C at intervals of 8 to 10 degrees on 1-inch gage length samples, 1/2-inch wide. Samples were cut in the machine and transverse directions from a single roll of film. Most of the tests were performed on 2.0-mil StratoFilm® with some limited testing done on 1.5-mil X-124. The Instron used is a table model machine, equipped with a constant temperature chamber. More details about the materials and test methods will be available in a report for Stevens Institute now in preparation.

Typical Instron output is shown in Figure 29-4. It can be seen that at some temperature the ultimate strain starts to decrease. The curves do not show the "classical" brittle behavior (rupture without yield). In order to obtain this kind of behavior, much lower temperatures must be used. At those temperatures, the samples become highly sensitive to defects due to preparation or material imperfections.

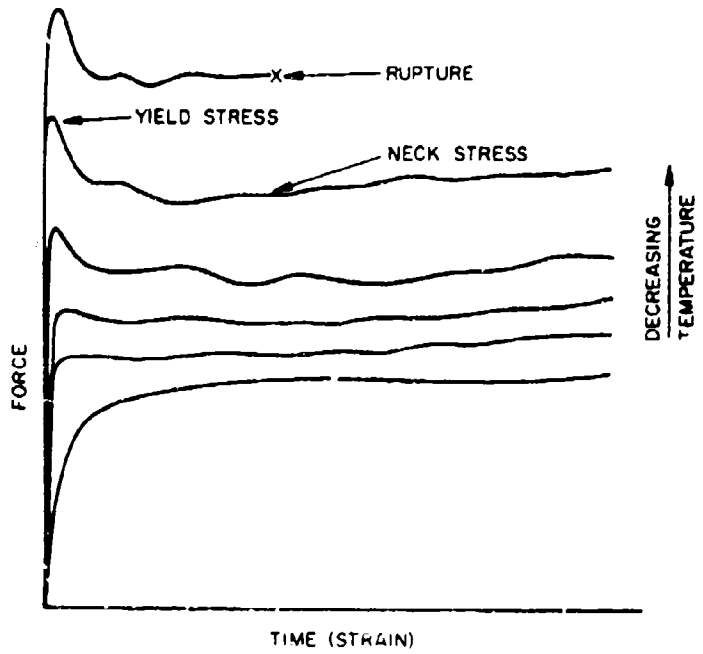

Figure 29-4. Typical Instron Data at Different Temperatures (at Constant Strain Rate)

It was first attempted to reproduce the characteristics of Amborski and Mecca's curve shown in Figure 29-3. Figure 29-5 shows that at -40°C, the CSR cannot be observed in the range of available strain rates, but at -52°C, it is clearly visible.

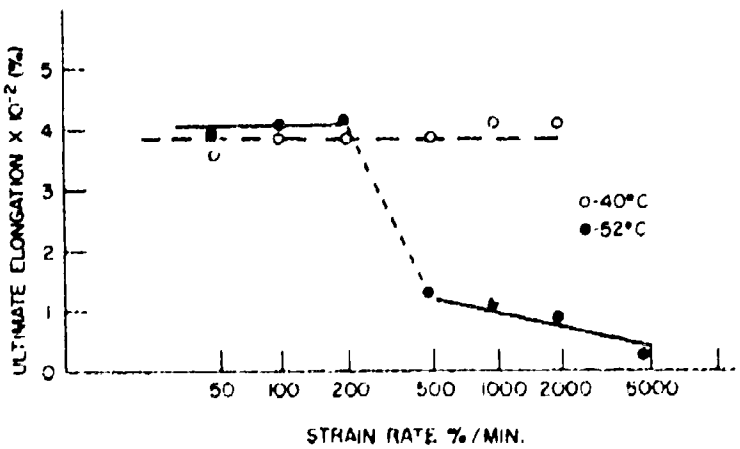

Figure 29-5. Attempt to Reproduce CSR Curve of Amborski and Mecca (1969)

All of the data were then plotted as ultimate strain versus temperature at a constant strain rate. Figure 29-6a contains the results for the machine direction, and Figure 29-6b shows results for the transverse direction. At each strain rate the critical temperature is defined. The maximum travel of the crosshead was restricted to 500 percent elongation to avoid excessive slippage from within the jaws. Combining the critical temperatures and their respective strain rates yields Figure 29-7. The points of this plot fall on a straight line divided into two sections, one for the lower strain rates (<732 percent min.) and the other for the higher strain rates (>732 percent min.). The approximation by straight lines on a plot of logarithm of rate versus reciprocal absolute temperature is typical for viscoelastic materials in which the relaxation process can be described by an Arrhenius type rate equation. This is, therefore, frequently referred to as an Arrhenius plot, and a straight line region indicates conformity to a single mechanism. Based on the Arrhenius equation, the activation energy for the high strain rates region was found to be 10 Kcal/mole which is a typical value for a flow process.

The straight vertical line in the low strain rate region indicates that the response of the viscous part of the material becomes of secondary importance, since this is the only part which is time or rate dependent. This suggests that the brittle failure is associated with a lack of viscous response, or a lack of ability to dissipate strain energy. If the strain energy buildup rate is larger than the rate of energy dissipation, the result is rupture, the fastest energy release mechanism through the formation of new surfaces.

The temperature at which the viscous response became independent of rate (time) is suggested as the cold brittleness (CBT). For Stratoflex®, this temperature was found to be -52°C. Because of the way the CBT was defined, it was expected that the CBT would be somewhat higher than the usually obtained values, but a review of the literature showed the temperature of -52°C to fall within the published data for polyethylene (Webber, 1958; Hoff and Turner, 1957). In addition to yielding the CBT, Figure 29-7 gives the relationship between strain rate and the temperature needed to yield brittle rupture at temperatures higher than the CBT.

29-3. DISCUSSION

As was shown in the previous section, the ductile behavior is due to the plastic deformation by which the material can relieve stored strain energy, while the brittle rupture occurs when the strain energy level is greater than the material can sustain. It is relieved by forming new surfaces at the rupture process and releasing the remaining elastic energy.

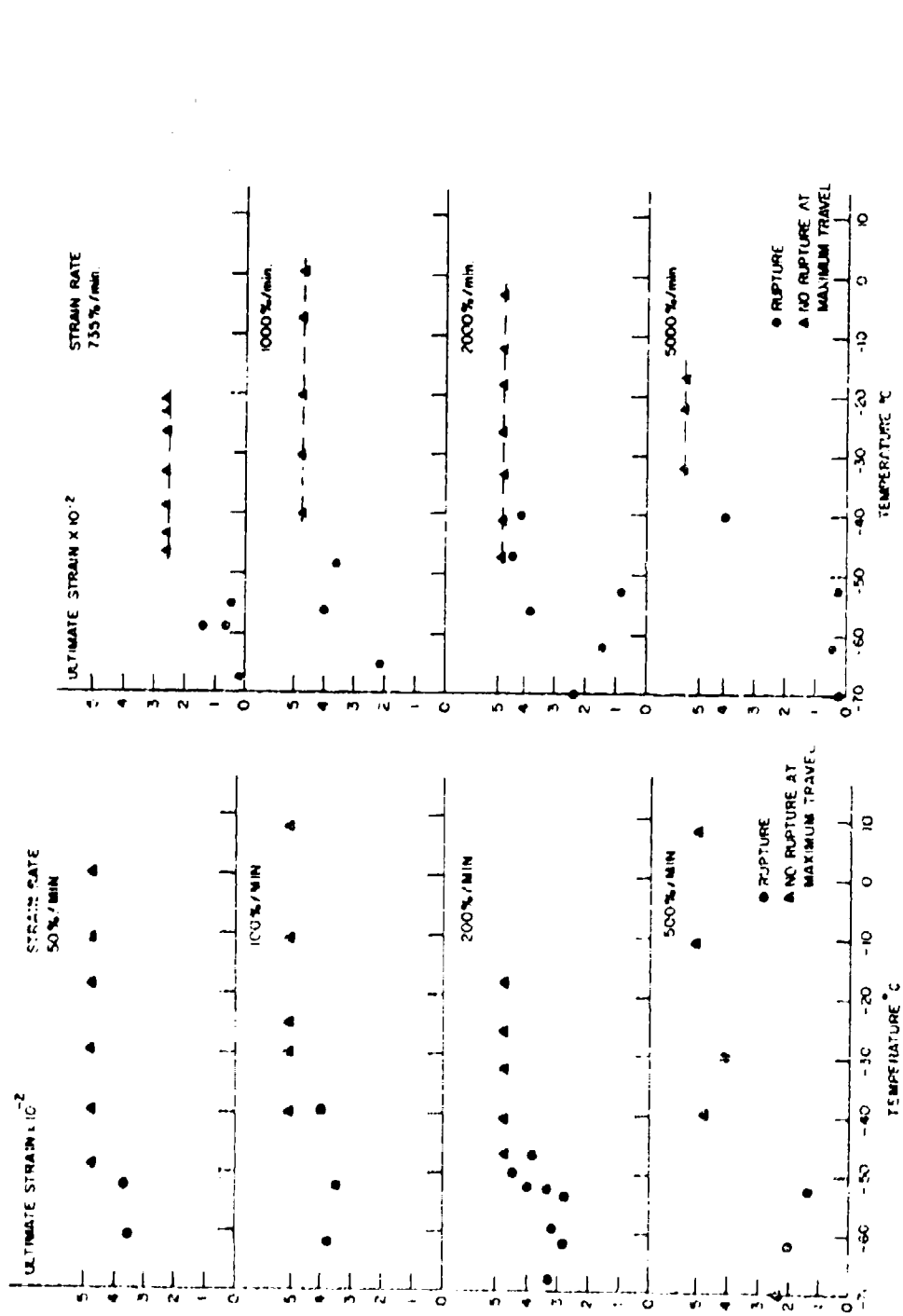

2. StratoFilm®, Machine Direction
Figure 29-6. Evaluation of the Critical Temperature (CT)

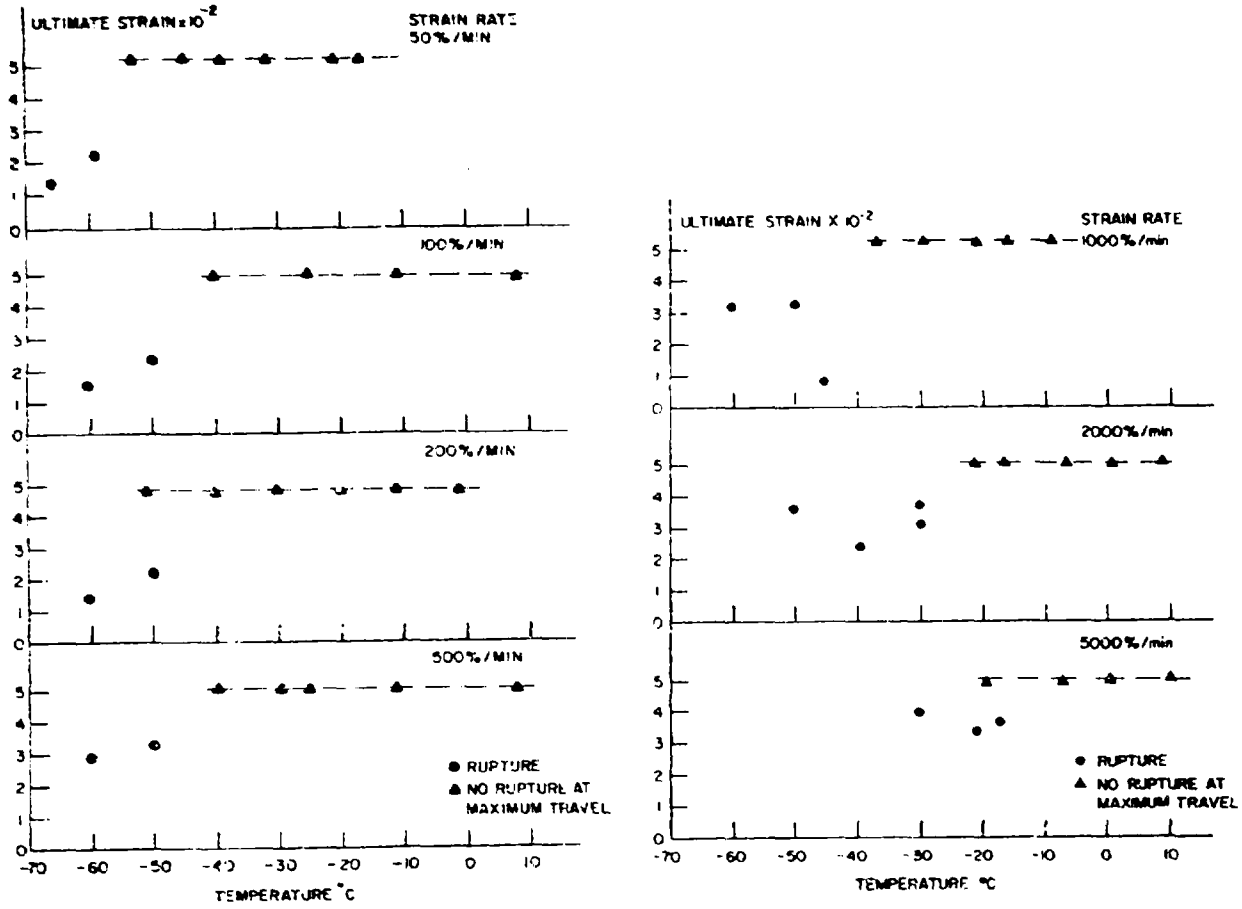

b. StratoFilm®, Transverse Direction

Figure 29-6. Evaluation of the Critical Temperature (CT)

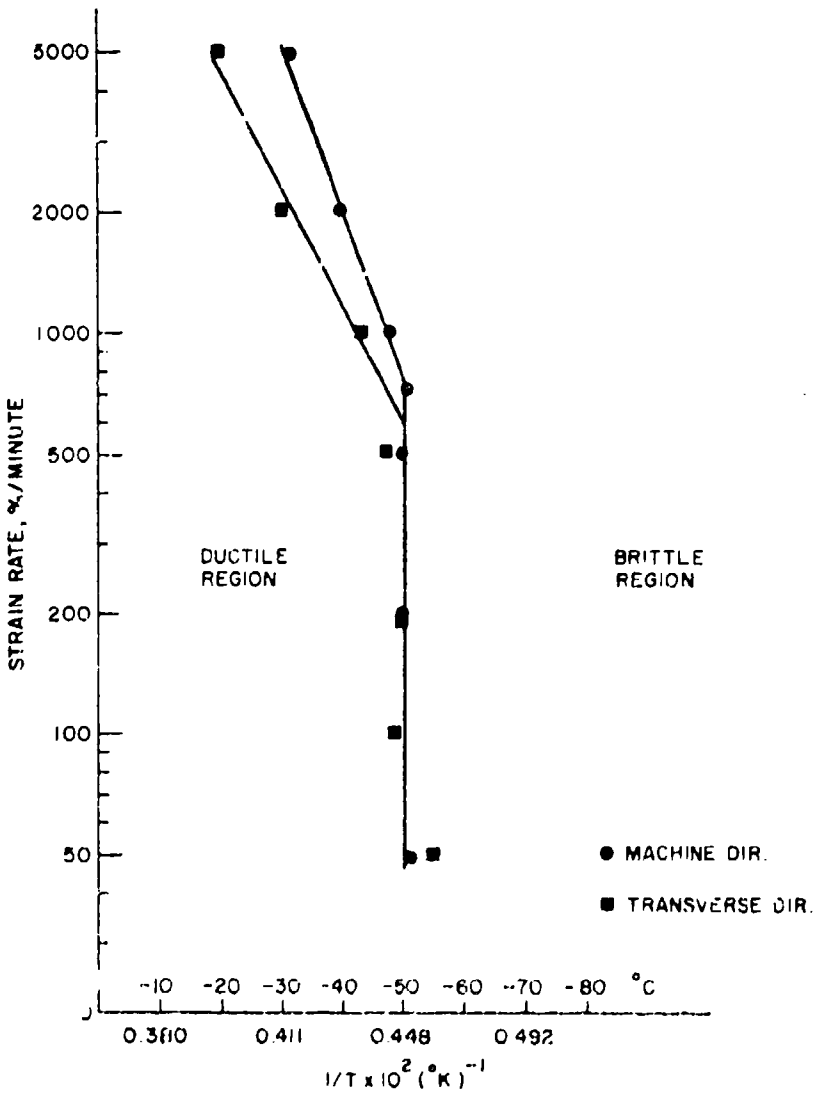

Figure 20-7. Plot of Critical Temperature (CT) Versus Strain Rate

The ability of a given material to dissipate energy is directly related to the damping properties as presented by the loss modulus E'' and the tan δ, the phase shift in a dynamic mechanical test. A series of dynamic mechanical tests were performed on a Rheovibron to evaluate E'' and tan δ curves for StratoFilm . The resulting characteristics are given in Figures 29-8 and 29-9.

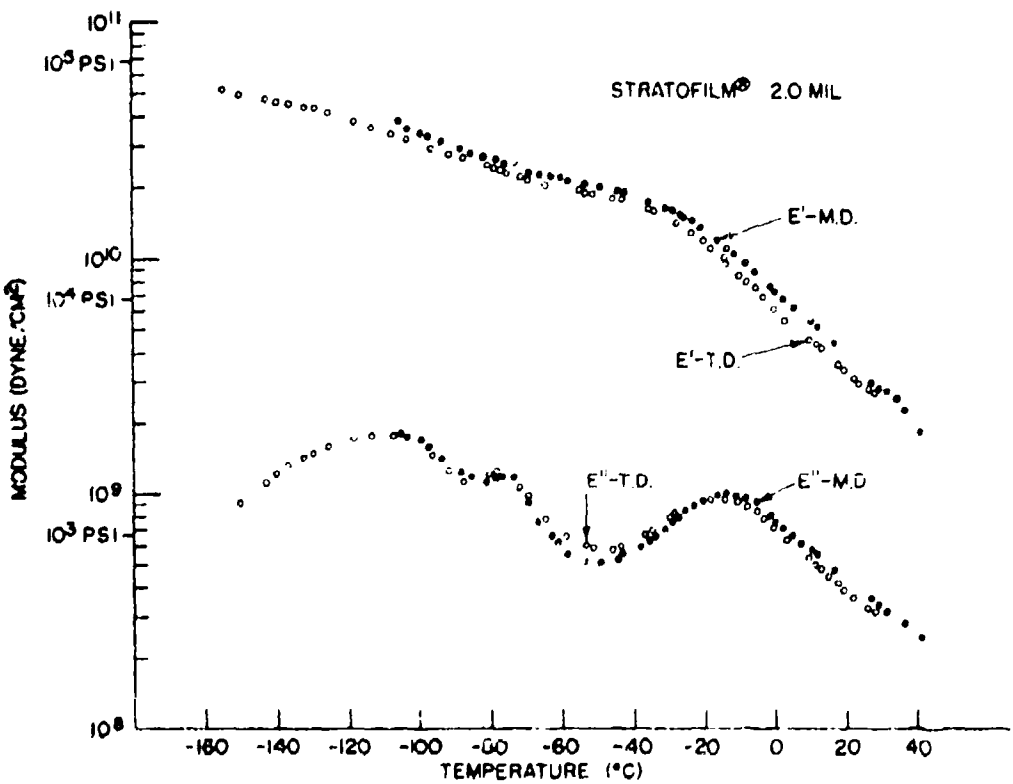

Figure 29-8. Storage and Loss Moduli Versus Temperature for StratoFilm®

It is clear that the CBT of -52°C falls in the area of a relative minimum of the E'' or the tan δ versus temperature curves. The different peaks are indicative of the various relaxation mechanisms that appear at various temperatures at this test frequency (110 cps). The low temperature, γ, transition peak is due to restricted local motion with the exact mechanism yet to be determined. At the β transition in the temperature range of 0°C, large chain segments gain mobility needed for plastic flow. The dissipation of energy is due to flow of those chain

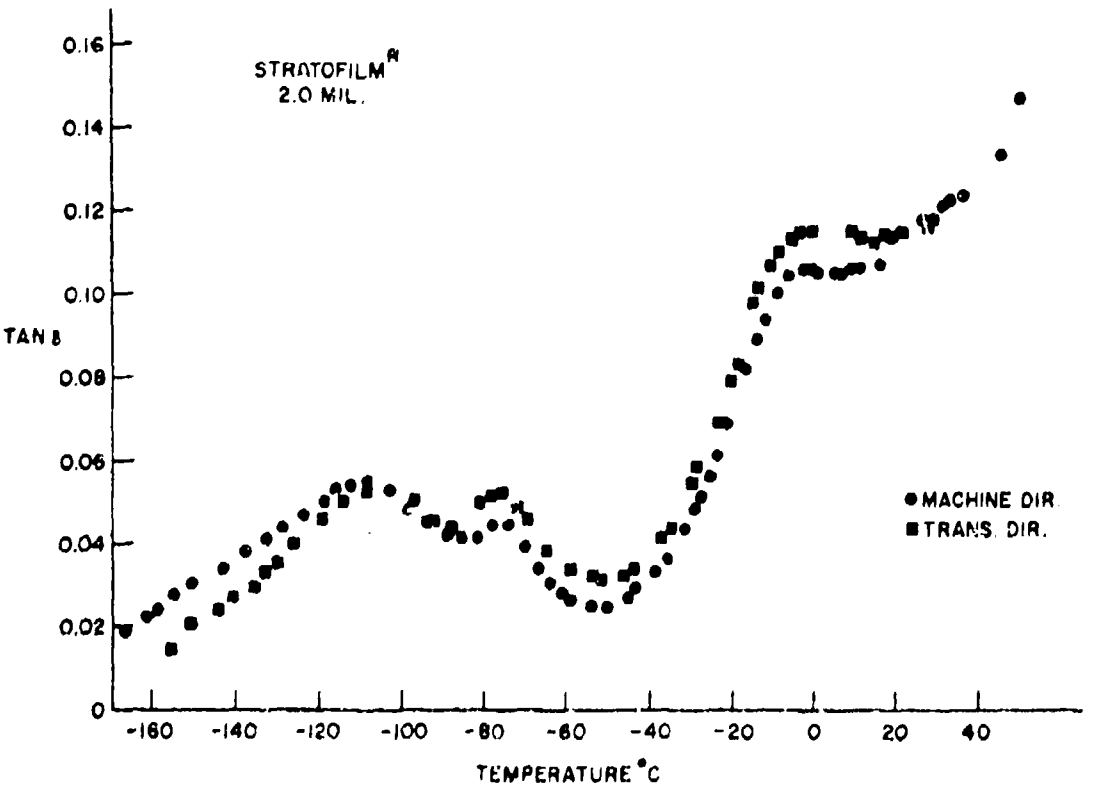

Figure 29-9. Tan δ Curve for StratoFilm®

segments (Matsuoka et al, 1967; Matsuoka and Ishioa, 1966). The domination of the β relaxation mechanism starts at the minimum between the γ and the β transitions in the region of the CHT.

To determine whether the relationship between the dissipation spectra, as given by tan δ or E", and the behavior found in the Instron tests is peculiar to this low density polyethylene or is characteristic of a viscoelastic material of similar nature, a theoretical analysis was performed. The assumption underlying this analysis was that fracture occurs if the stored strain energy exceeds a critical level. A three-element model, Figure 29-10, was utilized. The parameters of the models were evaluated as functions of temperature from the tan δ and E" data available from the dynamic mechanical tests, as will be described in detail in the Stevens Institute Report. After calculating the parameters E_1, E_2, and η, the model's response to constant rate stretching was determined analytically, looking for the ultimate strain at which the critical energy was reached.

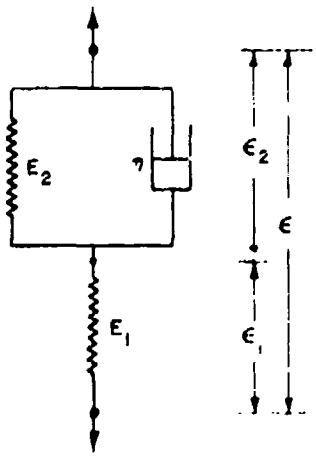

Figure 29-10. Three Element Model

A typical result of this analysis is given in Figure 29-11 (the governing equations and the computer program are included in the appendix). The ultimate elongation is small and almost constant until a temperature is reached at which the elongation starts to increase due to the response of the viscous part and energy dissipating. At the lower strain rates which correspond to the low rates of the Instron, the deflection point where the elongation starts to increase is at the same temperature. However, at the faster rates this point shifts to higher and higher temperatures similar to what was found experimentally.

It is recognized that the three-element model used does not characterize the material behavior under creep conditions. A four-element model, including an additional dashpot in series with the present model, would yield better results. For this analysis, however, the three-element model is sufficient, as the additional dashpot would not yield any additional elongation in the low temperature range, but would only increase the ultimate elongation after the deflection point of the curve. Since no attempt was made to achieve quantitative agreement between the model and the actual tests, it was not necessary to use a more complicated model in this work.

29-4. CONCLUSIONS

A systematic testing program was introduced to determine the cold brittleness temperature of low density polyethylene films. This procedure yields, in addition to the cold brittleness temperature, the relationship between the transition from

ductile to brittle behavior and the strain rate and temperature. It was shown that for low density polyethylene, the ductile-brittle transition is related to the transition from the β relaxation mechanism to the γ relaxation mechanism and to the dissipation spectra of the material.

Theoretical model analysis showed that the relationship between the E'' and tan δ versus temperature curves and the ultimate elongation versus temperature curves obtained by constant strain rate uniaxial testing is a result of the viscoelastic nature of the material and could be expected to be the same for similar materials.

References

Amborski, L. E., and Mecca, T. D. (1960) J. Polymer Sci. 4:332.

Bland, D. R. (1960) The Theory of Linear Viscoelasticity, Pergamon Press, New York, p. 12.

Hauser, R. L. (1967) Proc., Fourth AFCRL Scientific Balloon Sym., J. F. Dwyer, Ed., p. 125.

Hauser, R. L., and Stefan, K. (1970) Proc., Sixth AFCRL Scientific Balloon Sym., L. A. Grass, Ed., p. 335.

Hoff, E. A. W., and Turner, S. (1957) ASTM Bull. 225:58.

Matsuoka, S., Aloisio, C. J., and Daane, J. H. (1967) Appl. Polymer Sci. 5:103.

Matsuoka, S., and Ishida, Y. (1966) Transitions and relaxations in polymers, J. Polymer Sci. (Symposium) R. F. Boyer, Ed., Interscience, New York, C14:247.

Mielke, L. (1968) Proc., Fifth AFCRL Scientific Balloon Sym., L. A. Grass, Ed., p. 131.

Nelson, J. R. (1970) Proc., Sixth AFCRL Scientific Balloon Sym., L. A. Grass, Ed., p. 329.

Renfew, M. M., and Freeman, A. J. (1953) Modern Packaging 26:121.

Roth, D. I., and Mahmoodi, P. (1965) Testing of Polymers, J. V. Schmitz, Ed., Interscience, New York, 3:81.

Webber, A. C. (1952) ASTM Bull. 227:40.

Weissmann, D. ( ) Stevens Institute report in preparation.

Winker, J. A. (1970) Proc., Sixth AFCRL Scientific Balloon Sym., L. A. Grass, Ed., p. 325.

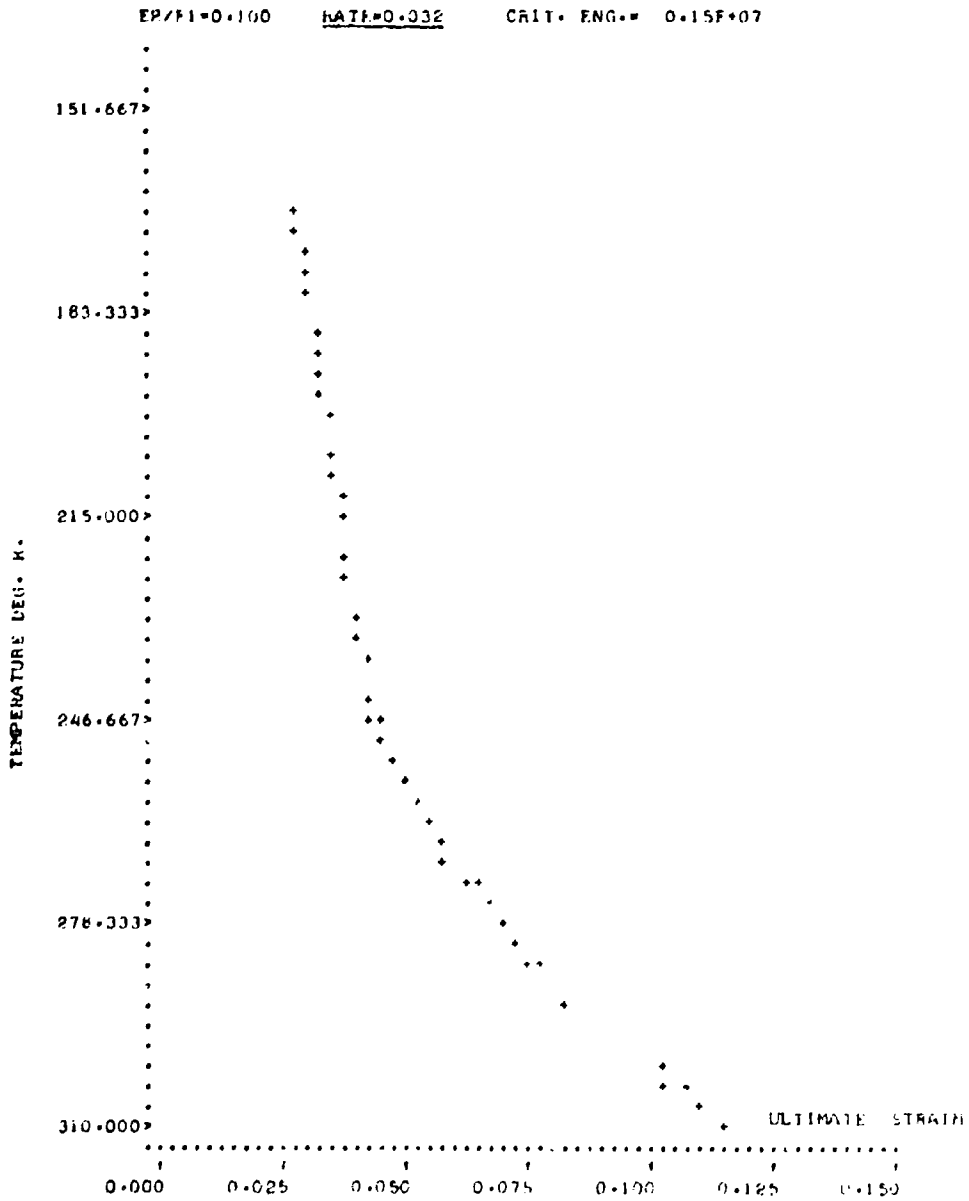

Figure 29-11a. Ultimate Strain for Three-Element Model; 2 Mil StratoFilm®, Machine Direction (cont)

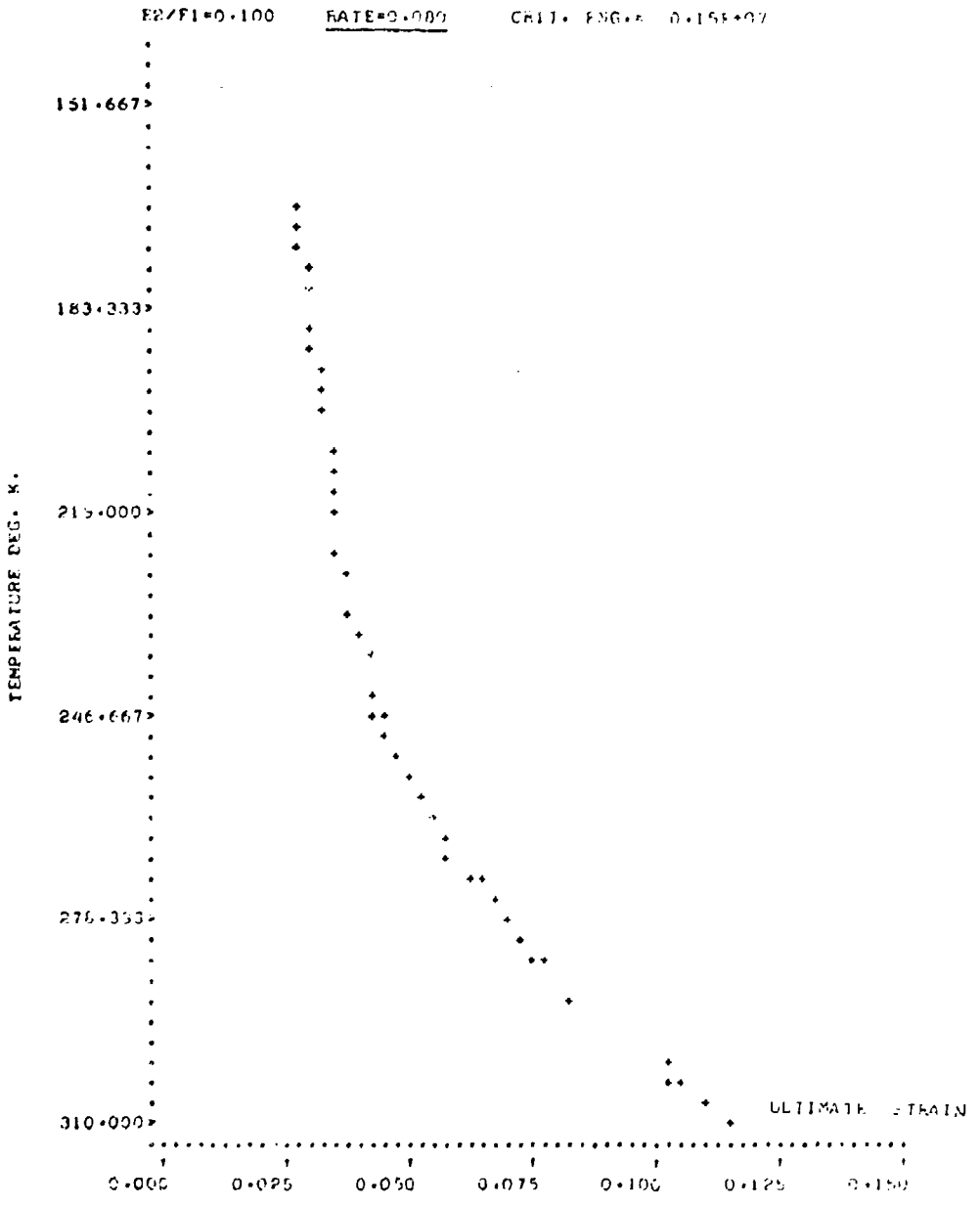

Figure 29-11b, Ultimate Strain for Three-Element Model; 2 Mil StratoFilm®, Machine Direction (cont)

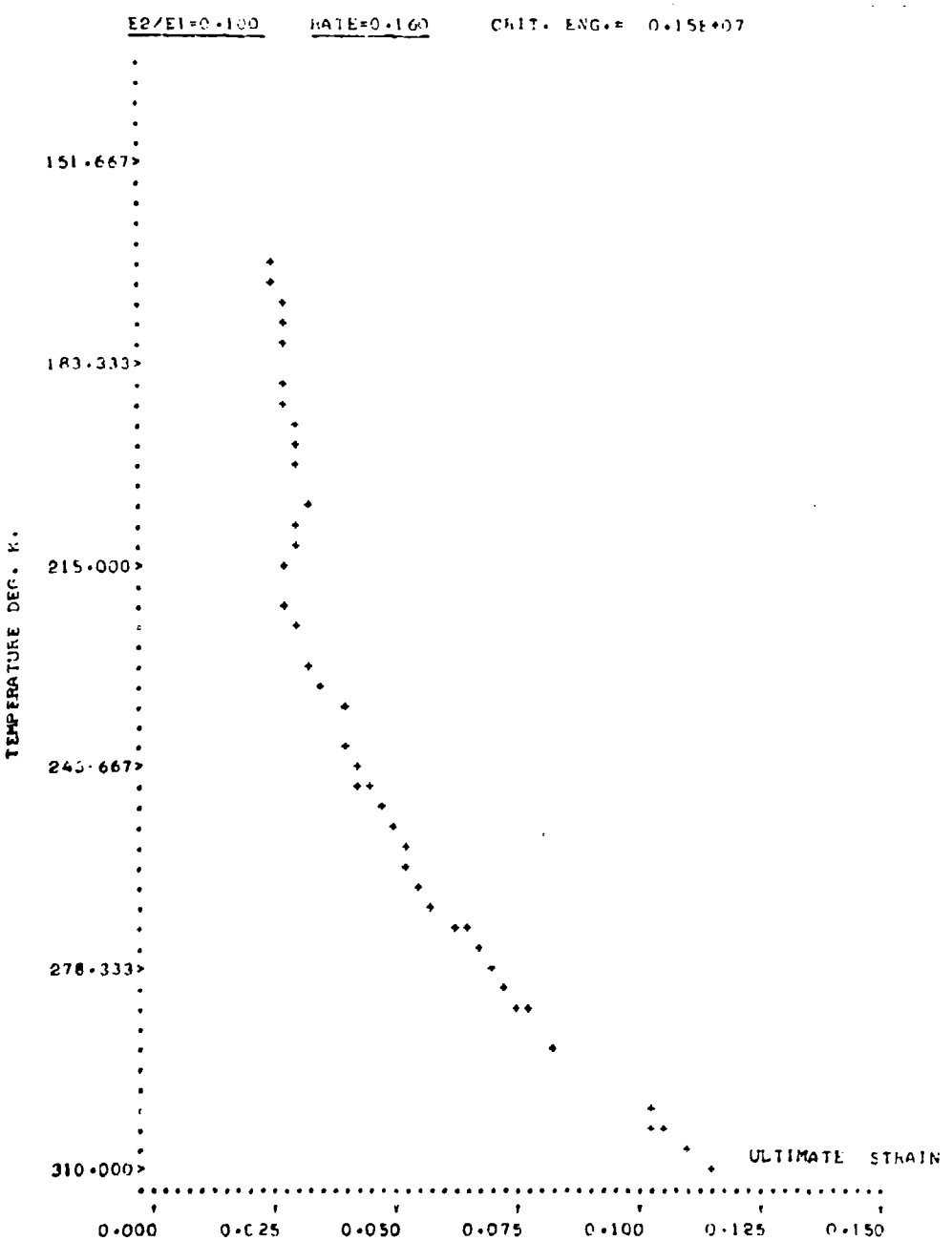

Figure 29-11c. Ultimate Strain for Three-Element Model; 2 Mil StratoFilm®, Machine Direction (cont)

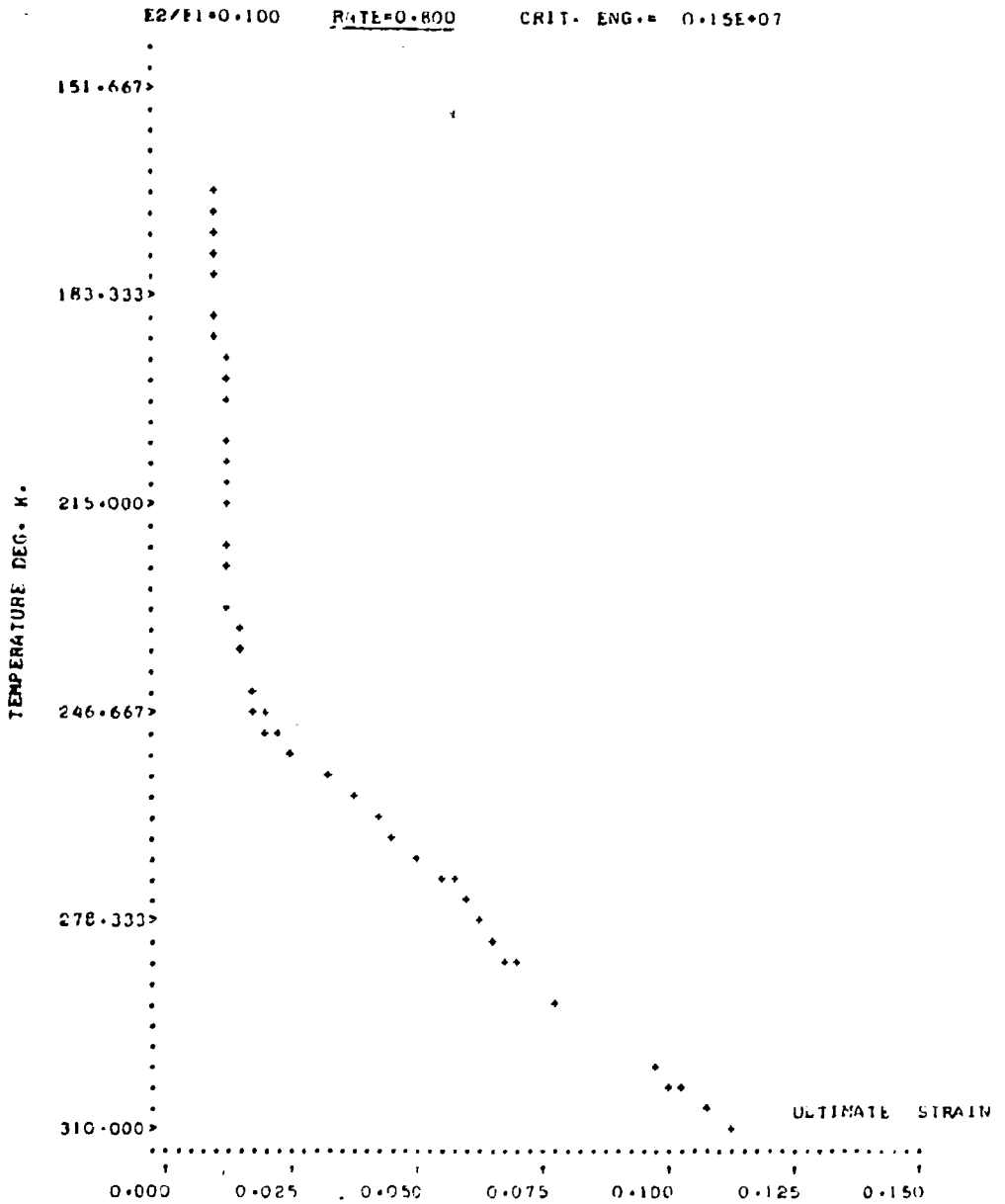

Figure 29-11e. Ultimate Strain for Three-Element Model; 2 Mil StratoFilm®, Machine Direction

Appendix A

Model Analysis Governing Equations

The complex modulus obtained from dynamic test data on the three-element model of Figure 29-10 is given by

$$E^* = E' + i\,E'' = \left(\frac{1}{E_2 + i\,\omega\eta} + \frac{1}{E_1}\right)^{-1}$$

where ω is the frequency of the test (Bland, 1960). After some algebraic manipulation, this yields

$$E' = \frac{E_1\left[E_2^2 + E_1E_2 + (\omega\eta)^2\right]}{\left(E_1 + E_2\right)^2 + (\omega\eta)^2}; \quad E'' = \frac{E_1^2\omega\eta}{\left(E_1 + E_2\right)^2 + (\omega\eta)^2};$$

introducing $\tan\delta = \frac{E''}{E'}$ and $A = \frac{E_2}{E_1}$, $E_1 = E_1(E'', \tan\delta, A)$

and $\eta = \eta\ (E'', \tan\delta, A)$ can be determined.

The differential equation for the model is

$$\sigma + \frac{E_1}{\eta}(1 + A)\sigma = \frac{AE_1^2\epsilon}{\eta} + E_1\dot{\epsilon}$$

where σ is the applied stress, ϵ is the total strain and the $(\cdot)$ represents differentiation with respect to time.

The solution of this equation with initial conditions corresponding to a constant strain rate tensile test yields

$$\sigma = C[1-\exp(-\Omega t)] + Bt$$

where B, C and Ω are combined constants including E_1, A and η, and t is time. By substituting $t = \frac{\epsilon}{R}$ where R is the rate of elongation, and separating ϵ into ϵ_1 and ϵ_2 where ϵ_1 is the deformation of the single spring and ϵ_2 is the deformation of the Voigt model, we can calculate the stored energy in the two springs. Equating this energy with the critical energy V_{cr} will yield the ultimate elongation (ϵ_u).

The computer program that was written to calculate the behavior of the model as a function of temperature under the above assumptions can be found in Appendix 29-B.

Appendix B

Computer Program for Ultimate Strain of a Three Element Model

```
      DIMENSION T(60), TD(60), EF(60), ETA(60), EONE(60),
     X  US(60)
      CALL IFILE(1,'ULTS')
      READ(1,100) J,E,L,V,G,FILM1,FILM2,FILM3,FILM4
      WRITE(6,104)FILM1,FILM2,FILM3,FILM4
      WRITE (6,102) A,E,V
      WRITE(6,105)
      READ(1,101) (T(I),I=1,J),(TD(I),I=1,J),(EF(I),I=1,J)
      W=2*3.14*F
      DO 70 I=1,J
      T(I)=-(273.-T(I))
      PARA=1.+(1.-4.*TT(I)*TD(I)*A*(1.+A))**0.5
      PARA=PARA/(2.*W*TD(I))
      EONE(I)=(1.+F)*EF(I)*((1.+A)**2+(W*PARA)**2)/(4.*PARA)
      ETA(I)=EONE(I)*PARA
      OMEGA=EONE(I)*(1.+A)/ETA(I)
      R=A*EONE(I)*EONE(I)*L/(ETA(I)*OMEGA)
      C=(EONE(I)*A/OMEGA)*(1.-A*EONE(I)/(ETA(I)*OMEGA))
      US(I)=0.1
      DO 50 N=1,100
      CD=C*(1.-EXP(-OMEGA*US(I)/R))+F*US(I)/R
      CDD=(C*OMEGA/R)*EXP(-OMEGA*US(I)/R)+F/R
      FUN=CD**2/EONE(I)+((EONE(I)*US(I)-CD)**2)*A/EONE(I)-2.*U
      FUNP=2.*CD*CDD/EONE(I)+2.*A*(EONE(I)*US(I)-CD)*(EONE(I)-
     X  CDD)/EONE(I)
      IF(ABS(FUN/(FUNP*US(I))) .LE. .00001) GO TO 60
      US(I)=US(I)-FUN/FUNP
   50 CONTINUE
      WRITE(6,106)
      GO TO 70
   60 WRITE(6,103)T(I),US(I),EONE(I),ETA(I)
   70 CONTINUE
  100 FORMAT(I,4F,4A5)
  101 FORMAT(10F)
  102 FORMAT(T10,'F2/F1=',F5.3,T25,'RATE=',F5.3,T40,'CRIT. ENG.=',
     X  E10.2,//)
  103 FORMAT(2E15.4,2E15.4)
  104 FORMAT(///,' ULTIMATE STRAIN FOR 3 ELEMENT MODEL OF',4A5,///)
  105 FORMAT(T10,'TEMP.',T20,'ULT. FLOW.',T30,'E1',T50,'ETA')
  106 FORMAT('SOLUTION FAILED TO CONVERGED')
      CALL GRAPHM(0,US,T,J,1,1,0.,.15,-310.,,-120.)
      STOP
      END
```

Program Nomenclature

T = Temperature
EDP = E'', loss modulus
TD = tan δ
EONE = E_1, spring modulus
ETA = η, dashpot viscosity
US = ϵ_u, ultimate strain
J = number of observations
F = Frequency
F = strain rate
V = V_{cr}, critical strain energy
A = Ratio between E_1 and E_2 in the model
FILM = Identification.

Appendix A

Publications of Proceedings of Past AFCRL Balloon Symposia and Workshops

Due to interest expressed in the proceedings of past AFCRL balloon symposia and workshops, and because the report series for these reports has been changed, a listing of the proceedings of all past AFCRL balloon symposia and workshops follows.

TITLE	AFCRL REPORT NO. AND DATE
Proceedings of the AFCRL Ballon Symposium	AFCRL-63-919, Dec. 1963 (AD614065)
Proceedings, 1964 AFCRL Scientific Balloon Symposium	AFCRL-65-486, Jul. 1965 (AD619695)
Proceedings, AFCRL Scientific Balloon Workshop, 1965	AFCRL-66-309, May 1966 (AD634765)
Proceedings, Fourth AFCRL Scientific Balloon Symposium	AFCRL-67-0075, Jan. 1967 (AD656692)
Proceedings, AFCRL Tethered Balloon Workshop, 1967	AFCRL-68-0097, Mar. 1968 (AD676037)
Proceedings, Fifth AFCRL Scientific Balloon Symposium	AFCRL-68-0661, Dec. 1968 (AD685726)
Proceedings, Sixth AFCRL Scientific Balloon Symposium	AFCRL-70-0543, Oct. 1970 (AD717149)